Universidad de Concepción
Dirección de Postgrado
Facultad de Ciencias Químicas - Programa de Doctorado en Ciencias Geológicas

El rift de Domeyko en la evolución de Gondwana suroccidental e
implicancias en la construcción del orógeno Andino

(The Domeyko rift in the
evolution of southwestern Gondwana and insights on the Andean building)

Tesis para optar al grado de Doctor en Ciencias Geológicas

MAURICIO ESTEBAN ESPINOZA VARGAS
CONCEPCIÓN-CHILE
2019

Profesor Guía: Verónica Oliveros Clavijo
Dpto. de Ciencias de la Tierra, Facultad de Ciencias Químicas
Universidad de Concepción

"El mundo no es, el mundo está siendo"

P. Freire

A Laura, por su insondable juventud

Agradecimientos

Gracias Nonoka, mi amor, por alentarme en los momentos difíciles y sacar siempre lo mejor de mí. Por esforzarnos infatigablemente en construir un hermoso futuro juntos. Gracias Camilo, mi chasconcito, porque desde tu infinita ternura me reconfortas y me enseñas el verdadero valor de las cosas.

Gracias a mis papás y herman@s por amarme incondicionalmente. A mi familia putativa, los Álvarez-Amado, por quererme como a uno de ellos.

Gracias a Verónica, mi tutora, por confiar siempre en mí y enseñarme con su ejemplo la pasión y perseverancia en lo que se hace. Gracias a Paulina, mi co-tutora, por el apoyo y sabiduría entregado en cada etapa.

A mis hermanos y camaradas de Deriva, por los sueños compartidos, el amor fraterno y la admiración que me despiertan.

Agradezco a tod@s quienes de una u otra forma me ayudaron a llevar a cabo esta tesis: a los colegas de Geología Regional y a l@s funcionarios del Laboratorio de Sernageomin, a las funcionarias del laboratorio de separación de arcillas del GEA, al inigualable Flaco Lemp, a los colegas de la UCN, al equipo del Laboratorio de Tectónica del IANIGLA, al equipo del Laboratorio de Estudios Isotópicos de la UNAM, al equipo del Laboratorio de Ar-Ar de la USGS, a mis compañeros de La Cabina, a l@s increíbles estudiantes de pregrado, los funcionarios (en especial a María Esperanza) y acádemicos del DCT de la UdeC (en especial a Andrés Tassara, Alfonso Encinas y Jorge Quezada, mi comisión de avances).

¡Muchas gracias!.

Resumen

Las cuencas de *rift* son lugares altamente dinámicos, donde se conjugan el fallamiento activo, el magmatismo, y la sedimentación, representando un contexto ideal para la preservación del registro geológico. Por otro lado, la reactivación de sus estructuras ejerce un control sustancial en la construcción orogéni*ca.* Durante el Triásico, la Cuenca de Domeyko correspondió a una de las cuencas de *rift* desarrolladas en Gondwana Suroccidental. La ausencia de un modelo tectonoestratigráfico integrado, las discrepancias respecto al contexto geotectónico durante la etapa de *rifting* y el posible control de la fábrica gondwánica en la posterior evolución orogénica motivan el desarrollo de esta tesis.

En base a análisis estratigráficos, sedimentológicos y geocronológicos, se determinó que la fase *synrift* del *rift* de Domeyko se habría desarrollado en dos períodos: *Synrift I* (Ladiniano – Carniano), con la apertura de la subcuenca Sierra Exploradora (SESB) y *Synrift II* (Nórico – Rético), en el que se inició la Subcuenca Sierra de Varas (SVSB) y se reactivó la SESB. El paso entre ambas etapas se correlacionaría con una reconfiguración de primer orden de la cinemática de placas durante el Triásico.

Durante el *Synrift II*, se habría registrado una fase de climax del *rift* asociada a la unión de las fallas maestras de la SVSB, generando un *rift* de rumbo ~NS por aproximadamente 400 km. Fallas maestras de rumbo ~NS a ~NNE coexistieron con fallas secundarias de rumbo NNO a NO, sugiriendo un régimen transtensional (sinistral) asociado a un sistema de *rift* oblicuo. La orientación del eje del *rift* habría estado controlada principalmente por el *slab-pull* de una losa subductante (*rift*-asociado a subducción), y de manera secundaria a esfuerzos de campo lejano provenientes de la fragmentación de Pangea.

Por otro lado, termocronología detrítica ^{40}Ar-^{39}Ar sugiere que los basamentos de ambas subcuencas (SVSB y SESB) habrían tenido una historia de enfriamiento/alzamiento contrastante, sugiriendo una segmentación tectónica a través de una estructura cortical de rumbo NO durante el Pérmico Superior. Esta estructura habría controlado la posición de un alto estructural que separó ambas subcuencas durante el *rifting*.

Posteriormente, durante la orogénesis Incaica (Eoceno), la inversión de las fallas maestras del *rift* dio lugar a la principal construcción de la Cordillera de Domeyko, en un estilo de deformación principal de piel gruesa y vergencia al oeste del flanco occidental de la sierra, donde cambios locales del estilo estructural estuvieron controlados por la arquitectura primaria del *rift* triásico. La inversión de las fallas de alto ángulo del *rift* de Domeyko habría sido facilitada mediante una tectónica transpresional, permitiendo la nucleación de las estructuras occidentales del Sistema de Fallas de Domeyko.

De esta manera, la generación y posterior inversión de cuencas mesozoicas habría constituido un mecanismo eficiente para la adquisición de la vergencia occidental del flanco occidental de los Andes Centrales, configurando así un orógeno bi-vergente.

Abstract

Rift basins are highly dynamic places, where active faulting, magmatism, and sedimentation are intimately conjugated, representing an ideal context for the preservation of the geological record. On the other hand, the reactivation of rift structures exerts substantial control in the orogenic building. During the Triassic, the Domeyko Basin corresponded to one of the rift basins developed in southwestern Gondwana. The lack of a unified tectonostratigraphic model, the discrepancies regarding the geotectonic context during the rifting, and the possible control of the gondwanic fabric on the later orogenic building, motivate this thesis.

The synrift phase of the Domeyko rift developed in two periods: Synrift I (Ladinian - Carnian), with the opening of the Sierra Exploradora sub-basin (SESB) and Synrift II (Norian - Rhaetian), which initiated the Sierra de Varas sub-basin (SVSB) and reactivated the SESB. The change between both stages roughly correlates with a first-order plate kinematic reconfiguration during the Triassic.

During the Synrift II, a rift climax phase associated with the fault-linkage stage of SVSB master faults would have occurred, configuring a ~NS striking rift by approximately ~400 km. Master NS to NNE striking faults developed with secondary NW to NNW striking faults, suggesting a transtensional kinematic system (sinistral) related to an oblique rift. The rift axis orientation would have been controlled mainly by the slab-pull force from a convergent slab (subduction-related rift), and secondarily by far-field stresses arising from the Pangea breakup.

On the other hand, ^{40}Ar-^{39}Ar detrital thermochronology indicates a strong contrast between both sub-basins basement cooling/uplift history, suggesting a tectonic segmentation through a crustal NW-striking structure during the Upper Permian. This structure would have controlled the position of a structural high separating both sub-basins during the synrift phase.

Later on, during the Incaic orogeny (Eocene), the inversion of the master rift faults led to the main building of the Domeyko Range, mainly by a thick-skinned and westward-vergent structural style along the western flank of the range. Local variations in this structural style were controlled by the ancient Triassic rift architecture. The inversion of high-angle rift faults would have been facilitated by transpressional tectonics, allowing the inception of the western structures of the Domeyko Fault System.

Finally, the inversion of Mesozoic extensional basins would have provided an efficient mechanism for the acquisition of the western vergence along the western flank of the Central Andes, configuring a bi-vergent orogen.

Índice de contenidos

Índice de figuras

Índice de tablas

Capítulo 1: Introducción

1.1 Formulación del problema

Los procesos tectónicos controlan en último término la ubicación, inicio y evolución de las cuencas sedimentarias. De esta manera, el registro sedimentario y volcánico que se alberga en ellas, junto con el estilo y dinámica de las estructuras sincrónicas asociadas, son el resultado de una configuración geotectónica particular (Ingersoll, 2012). Por otro lado, la reactivación de sistemas inicialmente extensionales ha sido reconocido como un mecanismo esencial durante la construcción de numerosos orógenos alrededor del mundo (Butler, 1989; Lacombe y Mouthereau, 2002; Butler *et al*., 2006). De esta manera, el estudio de una cuenca desde su incepción hasta el momento en que es invertida es fundamental para comprender la evolución tectónica de largo plazo de una región en particular.

En el norte de Chile, la Cuenca de Domeyko comprende depósitos sedimentarios y volcánicos que van desde el Triásico al Cretácico Temprano (Ardill, 1996; Ardill *et al*., 1998), expuestos en la Cordillera de Domeyko, entre los 21°-27°S (Fig. 1.1B). Durante el Triásico, esta cuenca se formó mediante adelgazamiento mecánico (Suárez y Bell, 1992; Ardill et al. 1998), formando parte de un sistema de cuencas de rumbo principal NNO en el margen suroccidental de Gondwana (Fig. 1.1A; Charrier, 1979; Suárez y Bell, 1992; Charrier *et al*., 2007). Durante ese periodo, Gondwana se encontraba en una etapa cuasi-estacionaria (Vilas y Valencio, 1978; Matthews *et al*., 2016). Lo anterior, junto con el desarrollo de un ingente volcanismo silícico (Grupo Choiyoi; Kleiman y Japas, 2009; Sato *et al*., 2015) ha sido relacionado clásicamente al cese de la subducción en el margen suroccidental del supercontinente (Mpodozis y Kay, 1992; Franzese y Spalletti, 2001). En consecuencia, la Cuenca de Domeyko ha sido considerada como una cuenca de *rift* intracontinental durante este período (Charrier, 1979; Ramos y Kay, 1991; Mpodozis y Kay, 1992; Suárez y Bell, 1992; Ardill *et al*., 1998).
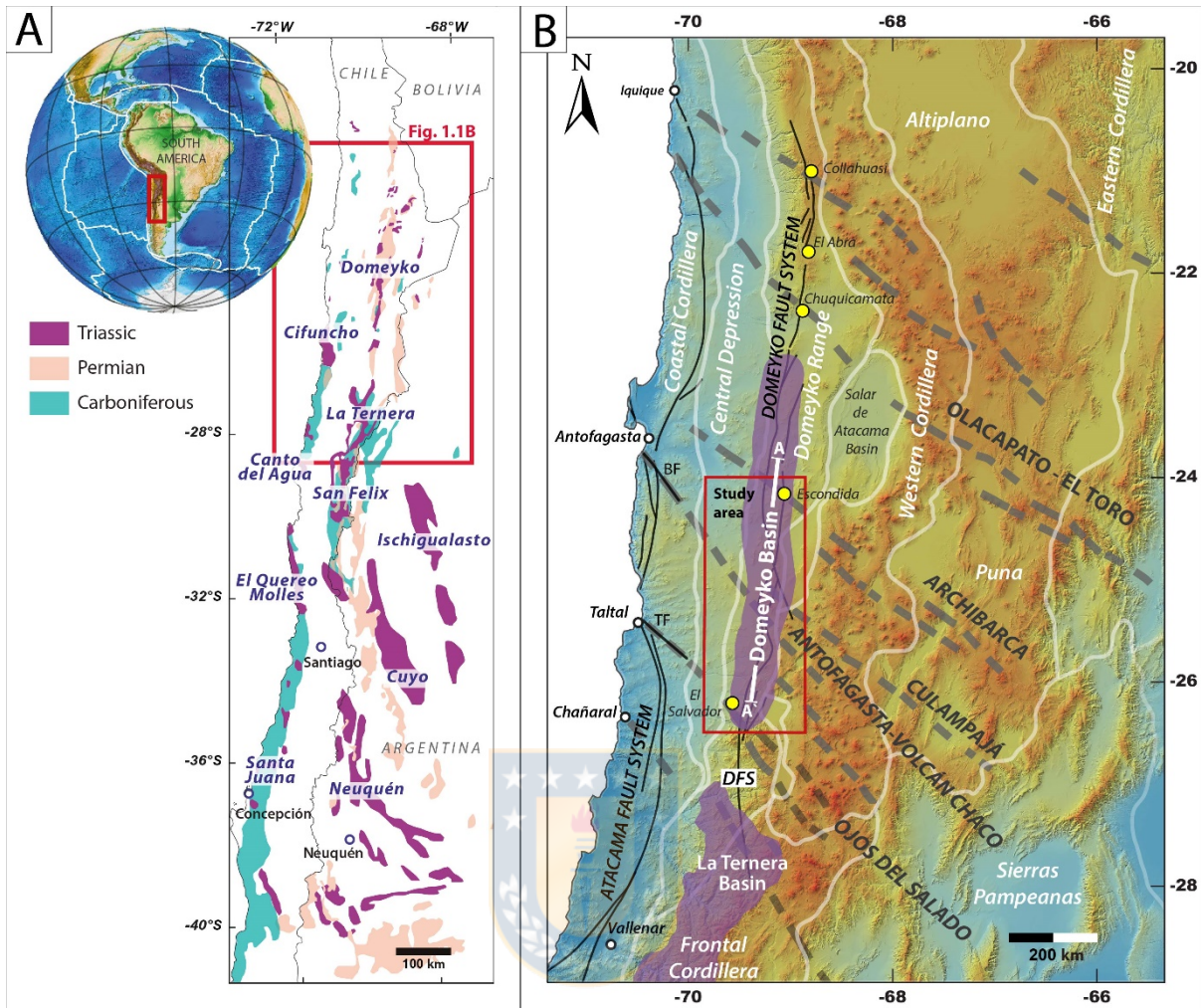
Figura 1.1: A) Afloramientos presentes en los Andes Chileno-Argentinos asociados a las cuencas extensionales desarrolladas en el margen suroccidental de Gondwana durante el Triásico (color morado). En la imagen se aprecia además la distribución del basamento Carbonífero y Pérmico, y su ubicación en Sudamérica señalada por un rectángulo de color rojo. B) Mapa topográfico con la ubicación de las principales morfoestructuras de los Andes en Chile y Argentina. En morado, la distribución de las cuencas de Domeyko y La Ternera. El área de estudio comprende el rectángulo rojo. En línea roja la ubicación de la sección estructural de Amilibia *et al*. (2008) ilustrada en la Figura 1.3. Los lineamientos en continentales en gris están basados en el trabajo de (Petrinovic y Colombo Piñol, 2006; Petrinovic *et al*., 2006)

Sin embargo, modelos recientes basados en las características geoquímicas de los productos magmáticos pre-andinos (*e.g.* magmas calcoalcalinos, anomalías negativas de Nb/Ta, alta razón LILE/HFSE, etc.) han propuesto el desarrollo de la subducción de manera ininterrumpida desde el Carbonífero al Reciente (Coloma *et al*., 2017; del Rey *et al*., 2016; González *et al*., 2017; Oliveros *et al*., 2017). De esta manera, existen discrepancias significativas respecto a la configuración geodinámica durante la etapa de *rift* triásica. En este sentido, diversas causas se han propuesto

2

para explicar el proceso de 'rifting' a escala continental, tales como: esfuerzos de campo lejano asociados a la fragmentación de Pangea (Uliana *et al*., 1989; Bechis, 2009), colapso orogénico post-sanrafaélico (Uliana y Legarreta, 1993; Kleiman y Japas, 2009), subducción tipo 'rollback' (Alvarez y Ramos, 1999; Oliveros *et al*., 2017), o una combinación de éstas (Giambiagi *et al*., 2008b). Además, algunos autores han planteado una gran relevancia en el rol de las estructuras previas heredadas del basamento paleozoico (Charrier, 1979; Bechis *et al*., 2014), asociadas a la historia acrecionaria del amalgamiento de Pangea (Ramos, 1994). Sin embargo, en el caso de la Cuenca de Domeyko, el control de estructuras previas en su génesis ha sido propuesto sólo de manera especulativa, sin pruebas directas de la existencia de estas estructuras ni del rol que habrían jugado en la extensión.

Por otro lado, si bien el proceso de *rifting* se encuentra definido por un adelgazamiento mecánico de la litosfera (Sengör, 1995), existen diversas configuraciones geodinámicas que pueden gatillar este proceso (plumas mantélicas, sistemas de subducción, colapso orogénico o sistemas transformantes; Fig. 1.2), las cuales serían determinantes para la clasificación del tipo de rift (Merle, 2011). De esta manera, aun cuando existe consenso respecto a que la tectónica extensional controló el desarrollo del sistema de rift triásico a escala continental, en el caso de la Cuenca de Domeyko, aun es una incógnita cuáles habrían sido los mecanismos geotectónicos que controlaron el proceso de *rifting* y por ende a qué tipo de rift pertenece. Más aún, se desconoce qué impacto tuvo tal configuración en la dinámica interna de la cuenca (*e.g.* magmatismo, fallamiento, sedimentación) y cómo se refleja esto en el registro tectonoestratigráfico.

Además, en contraste con el mayor entendimiento de la estratigrafía y tectónica de las cuencas triásicas desarrollado en la vertiente argentina (Ramos y Kay, 1991; Spalletti, 1999; Llambías *et al*., 2007; Bechis *et al*., 2014), aún existen interrogantes específicas acerca de la evolución de la etapa de *rift* de la Cuenca de Domeyko. Así, aun cuando el relleno sedimentario continental domina en la sucesión *synrift*, trabajos previos se han enfocado en las sucesiones marinas de la etapa post-*rift*, describiendo de manera menos precisa la etapa inicial volcanosedimentaria (Chong y Hilldebrandt, 1985; Bell y Suárez, 1991; Prinz *et al*., 1994; Marinovic *et al*., 1995; Ardill *et al*., 1998).

Esto se debió en parte al menor control cronoestratigráfico en las secuencias continentales, pobres en material fosilífero de alta resolución temporal. Lo anterior, sumado a la intensa deformación andina que afecta a las sucesiones mesozoicas, ha dificultado una comprensión de la arquitectura inicial de la cuen*ca.* De esta manera, surgen preguntas específicas tales como ¿cuál fue la temporalidad del proceso de *rifting*?, ¿Cuál fue la geometría y arquitectura primaria de estas cuencas?, ¿Bajo qué campo de deformación se desarrolló el proceso de extensión?, etc. Trabajos de cartografía regional recientes han generado una relevante información geocronológica y estratigráfica de las sucesiones triásicas (Cornejo *et al*., 2009; Venegas *et al*., 2013; González *et al*., 2015; Astudillo *et al*., 2017), sin embargo aún no existe un modelo evolutivo del *rift* triásico a la escala de la cuenca completa.
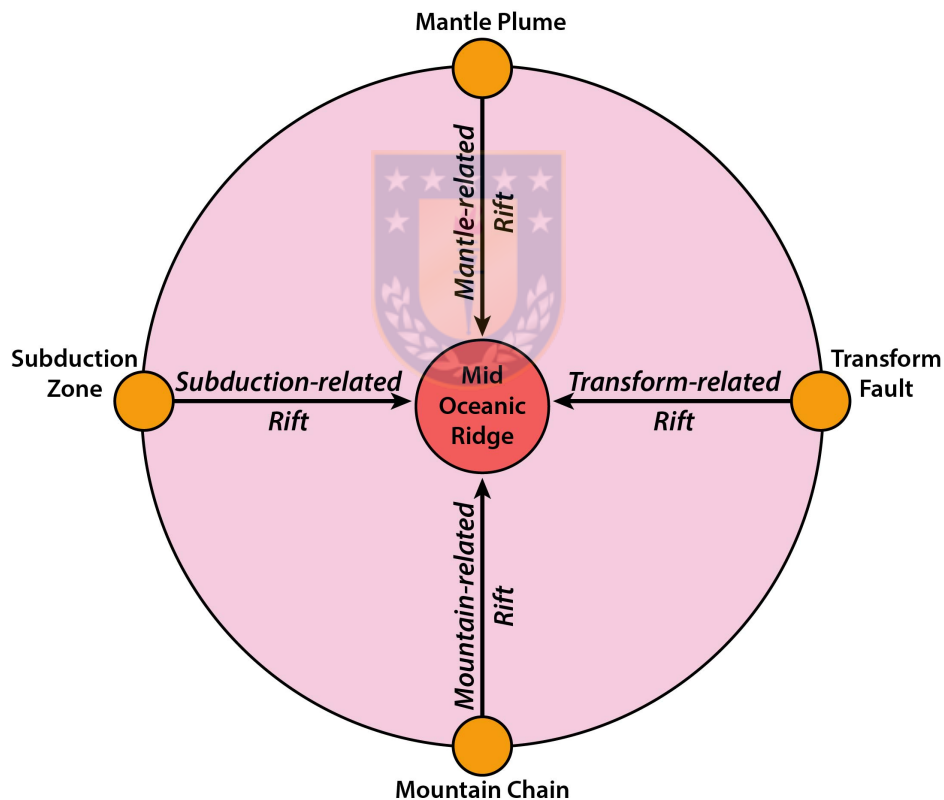
Figura 1.2: Clasificación de cuencas de *rift* propuesta por Merle (2011) basada en la definición de Sengör (1995).

Por otro lado, luego de la etapa de *synrift* triásica, durante el jurásico en la Cuenca de Domeyko se desarrolló una etapa de subsidencia termal (*postrift*) marcada por el desarrollo de sedimentación marina con pulsos episódicos de actividad

extensional, dando paso hacia el Jurásico Tardío/Cretácico Temprano a la continentalización y cierre de la cuenca (Ardill, 1996; Vicente, 2005; Charrier *et al*., 2007; Oliveros *et al*., 2012). Posteriormente, durante el Cretácico Tardío, el cambio en las condiciones de estrés desde un campo extensional/neutro a uno compresional asociado a la apertura del Atlántico, habría producido un evento de deformación regional en el norte de Chile conocido como 'Fase Peruana' (Steinman, 1929; Arriagada *et al*., 2008). Este evento ha sido asociado a la incepción de la proto-Cordillera de Domeyko a partir de evidencias de sedimentación sinorogénica presentes en las sucesiones cretácicas de la Cuenca del Salar de Atacama (Mpodozis *et al*., 2005; Arriagada *et al*., 2006; Amilibia *et al*., 2008). Acorde con Bascuñán *et al*. (2015), esta fase tectónica habría tenido un primer episodio en la Cordillera de la Costa (Peruana I, *ca*. 107 Ma) para posteriormente migrar hacia el este alcanzando la Cordillera de Domeyko (Peruana II, *ca*. 79 Ma).

La Cordillera de Domeyko corresponde a un cinturón de piel gruesa y piel delgada formado por un núcleo de basamento de edad Carbonífero-Pérmico el que se encuentra alzado sobre la cobertura mesozoica a través de fallas de alto ángulo con vergencia variable (Elderry *et al*., 1996; Mpodozis *et al*., 2005; Amilibia *et al*., 2008). Las hipótesis iniciales acerca del origen de la Cordillera de Domeyko, la consideraban el producto de una deformación principalmente transcurrente a transpresiva desarrollada durante el Eoceno-Oligoceno 'temprano' durante la orogénesis Incaica y asociada al emplazamiento de los sistemas de pórfidos cupríferos (Tomlinson *et al*., 1993; Reutter *et al*., 1996; Tomlinson y Blanco, 1997; Maksaev y Zentilli, 1999; Niemeyer y Urrutia, 2009). Sin embargo, trabajos recientes han presentado evidencias que favorecen un rol preponderante de la tectónica compresional asociada a la inversión de la Cuenca de Domeyko a partir del Cretácico Superior (Mpodozis *et al*., 2005; Muñoz *et al*., 2005; Arriagada *et al*., 2006; Amilibia *et al*., 2008; Martínez *et al*., 2018a). De esta manera, a través del proceso de inversión tectónica, el estilo estructural de la Cordillera de Domeyko se encontraría íntimamente ligado al desarrollo de la etapa extensional mesozoica.

La inversión tectónica de cuencas ha sido planteada como un mecanismo fundamental en la construcción del orógeno de los Andes Centrales (Charrier *et al*.,

2002; Carrera *et al*., 2006; Pinto *et al*., 2010; Carrera y Munoz, 2013; Martínez *et al*., 2016, 2018c; Perez *et al*., 2016a; Martínez y Cristallini, 2017). En particular, evidencias de la inversión de cuencas de *rift* triásicas se han presentado para la Cuenca Mitu en Perú (Eude *et al*., 2015; Perez *et al*., 2016a, 2016b), la Cuenca Neuquina (Giambiagi *et al*., 2003, 2008a, 2015; Mescua y Giambiagi, 2012; Mescua *et al*., 2014), y la Cuenca de Domeyko en la Depresión Pre-Andina (Martínez *et al*., 2018b, 2018a).

Por otro lado, trabajos sistemáticos realizados en la Cordillera de Domeyko bajo el enfoque de la inversión tectónica son escasos, siendo el de principal importancia el realizado por Amilibia *et al*. (2008). Este trabajo permite una comprensión del estilo principal de la Cordillera de Domeyko a través de la inversión de las cuencas mesozoicas, poniendo énfasis en la reactivación de las cuencas jurásico-cretácicas y asignando un rol menor a la geometría inicial del *rift* triásico. Sin embargo, Amilibia *et al*. (2008) no presentan un control preciso de la estratigrafía y la geometría de la cuenca triásica por lo que no es posible evaluar en detalle el rol de la arquitectura del *rift* triásico en la posterior inversión. Por otro lado, como algunos autores notaron (Zentilli *et al*., 2018), la gran coincidencia espacial entre el magmatismo eoceno-oligoceno en el núcleo de la Cordillera de Domeyko y las unidades triásicas sugiere un control subestimado de la etapa *synrift* de la Cuenca de Domeyko en el control de la estructura principal de la cordillera. De esta manera, aún es un problema abierto de qué manera particular se expresa la herencia tectónica del *rift* triásico en la posterior evolución meso-cenozoica de la región y en la construcción del flanco occidental de los Andes Centrales.

Esta tesis se enfoca en estudiar la evolución tectonoestratigráfica de la etapa de *rift* de la Cuenca de Domeyko e inferir sobre esta base las condiciones geodinámicas en las que se habría formado. Adicionalmente, se pretende comprender cómo las características iniciales de la cuenca habrían influido en la posterior evolución tectónica meso-cenozoica de la Cordillera de Domeyko. Las metodologías utilizadas comprenden estudios estratigráficos (análisis de facies), geocronológicos (dataciones U-Pb en circón y ^{40}Ar-^{39}Ar en muscovita) y estructurales (análisis cinemático y balance estructural).

En el Capítulo II, se presenta una breve síntesis de las unidades triásicas presentes entre los 22°-26° S. En el Capítulo III, se aborda la evolución tectonoestratigráfica de la Cuenca de Domeyko con énfasis en la interacción de los procesos sedimentarios, volcánicos y tectónicos, presentándose un modelo integrado de la cuen*ca.* En el Capítulo IV se aborda el rol de la herencia tectónica en la construcción de la Cordillera de Domeyko y en la incepción del Sistema de Fallas de Domeyko. En el Capítulo V, se discute el modelo de la etapa *synrift* de la Cuenca de Domeyko en el contexto de la evolución de Gondwana suroccidental y la influencia de la arquitectura del *rift* triásico en la vergencia del flanco occidental del orógeno andino. En el Capítulo VI se presentan las conclusiones obtenidas en esta tesis. Finalmente, en los anexos de esta tesis se presentan las publicaciones científicas resultantes de esta tesis (artículos publicados, manuscritos en revisión y presentaciones en congresos, Anexos 1 y 9) junto a una descripción más detallada de los métodos utilizados y los resultados obtenidos (Anexos 2 a 8)

1.2 Hipótesis

Durante el Triásico la Cuenca de Domeyko correspondió a un *rift* asociado a subducción y su evolución estuvo determinada por la interacción de procesos tectónicos, sedimentarios y volcánicos. La arquitectura de esta cuenca determinó posteriormente el estilo estructural de la Cordillera de Domeyko.

1.3 Objetivos

1.3.1 Objetivo general

Establecer la evolución tectonoestratigráfica de la Cuenca de Domeyko durante la etapa de *rift* (Triásico) y relacionarla con la posterior evolución Meso-Cenozoica de la Cordillera de Domeyko.

1.3.2 Objetivos específicos

1.- Determinar la temporalidad de la etapa de *rift* de la Cuenca de Domeyko

2.- Identificar los ambientes sedimentarios y establecer la paleogeografía de la etapa de *rift* de la Cuenca de Domeyko

3.- Especificar la proveniencia sedimentaria de la cuenca y la historia de enfriamiento/exhumación de las fuentes sedimentarias.

4.- Caracterizar la arquitectura, el estilo estructural y la cinemática de la etapa *synrift*

5.- Determinar el estilo y la evolución estructural de la Cordillera de Domeyko

1.4 Métodos

A continuación se presenta la metodología empleada con el objeto de alcanzar cada uno de los objetivos específicos.

1.4.1 Metodología asociada al Objetivo Específico 1: Geocronología U-Pb en circones

Análisis geocronológicos U-Pb en circones ígneos (IZ, 6 muestras) y detríticos (DZ, 16 muestras) fueron llevados a cabo usando Espectrometría de Masas con Plasma Acoplado Inductivamente (LA-ICP-MS y LA-MC-ICP-MS) en 22 muestras. Las unidades muestreadas corresponden a las formaciones Cerro Guanaco (1 IZ), Sierra de Varas (8 DZ y 3 IZ), Quebrada del Salitre (5 DZ y 1 IZ), La Ternera (2 DZ y 1 IZ) y el batolito Sierra Castillo (1 IZ).

Los minerales pesados fueron concentrados mediante chancado estándar, separación gravimétrica por mesa Gemini, líquidos densos no tóxicos de heteropolitungstato de litio (LST; 2.9 gr/cm^3 a 27°C) y separación magnética en el Servicio Nacional de Geología y Minería (SERNAGEOMIN) y en el Instituto de Geología Económica Aplicada (GEA). Finalmente, los granos de circón fueron elegidos de manera manual mediante lupa binocular, montados mediante resina *epoxy*, y pulidos para exponer su centro para obtener imágenes de catodoluminiscencia.

Las muestras fueron analizadas en el Arizona LaserChron Center de la Universidad de Arizona (5 muestras) durante los meses de abril y mayo de 2015, y en el Laboratorio de Estudios Isotópicos del Centro de Geociencias de la Universidad Autónoma de México (17 muestras) durante los meses de enero y febrero de 2017. Las edades de Concordia y de promedio ponderado fueron calculadas utilizando el software Isoplot v. 4. 15 (Ludwig, 2008). Se aplicó un filtro de discordancia menor al 15% para los análisis en circones ígneos, uno menor a un 25% para los análisis en circones detríticos y un filtro de discordancia reversa menor a -5%. Edades $^{206}Pb/^{238}U$ fueron consideradas para circones menores a <1.0 Ga, mientras que edades $^{207}Pb/^{206}Pb$ fueron consideradas para circones mayores a esa edad (Gehrels, 2011). Una descripción detallada de los métodos específicos utilizados se encuentra en el

9

Anexo 4. La ubicación y litología de cada muestra se encuentran en las tablas 3.3 y 4.1, mientras que los datos resultados específicos para cada circón se encuentran en el Anexo 7.

1.4.2 Metodología asociada al Objetivo Específico 2: Análisis de facies

Se realizó un análisis de facies para las sucesiones sedimentarias y volcánicas triásicas comprendidas entre los 24°-26° S basado en 12 secciones estratigráficas generalizadas (ver ubicación en Figura 3.2 en el Capítulo 3). Las secciones S6, S7, S8, S10A, S10B y S11 fueron medidas por el autor mientras que las secciones S2, S3 fueron obtenidas del trabajo de Montecino (2015). Además, se extrapoló el análisis de facies a secciones obtenidas a partir de información bibliográfica: S1 (Valenzuela, 2011); S4 y S5 (Contreras, 2014), S9 (Cornejo *et al*. 2009) y S12 (Tomlinson *et al*. 1999). El análisis de facies fue complementado con los estudios litoestratigráficos llevados a cabo por Suarez y Bell (1992) y Mpodozis y Cornejo (1997) en la parte sur del área de estudio.

La nomenclatura de facies utilizada es acorde a Miall (2006) para las rocas sedimentarias siliciclásticas, Branney y Kokelaar (2002) para las rocas piroclásticas y D´Elia *et al*. (2012) para rocas volcánicas y volcanosedimentarias. Una descripción detallada de las facies y sus interpretaciones genéticas se encuentra en el Anexo 2. Un resumen con los códigos utilizados y las asociaciones de facies se encuentra en las tablas 3.1 y 3.2 en el Capítulo 3. Por otro lado, un resumen con las localidades donde se reconoció cada *facies* se encuentra en el Anexo 3.

1.4.3 Metodología asociada al Objetivo Específico 3: Termocronología Ar-Ar en muscovita detrítica

Dataciones de ^{40}Ar-^{39}Ar de muscovitas detríticas mediante fusión total se realizaron en cuatro muestras, analizando 87 granos individuales por muestra, sumando un total de 348 granos detríticos. Las unidades muestreadas corresponden a las formaciones Sierra de Varas (1 muestra), Quebrada del Salitre (2 muestras) y La Ternera (1 muestra).

Las muscovitas fueron extraídas de la roca mediante molienda por chancador primario de mandíbula y triturador de rodillo. Posteriormente, se tamizaron para las fracciones menores a 1,0-0,5 mm y 0,5-0,25 mm. Finalmente, micas entre 0,5 y 2 mm con las menores evidencias de alteración fueron seleccionadas manualmente mediante lupa binocular. Los análisis radiométricos se realizaron en el ^{40}Ar-^{39}Ar Laboratory of the U.S. Geological Survey (USGS), USA, durante el mes de enero de 2017. Los detalles de los factores de corrección, constantes y métodos específicos empleados pueden ser consultados en el Anexo 5. La ubicación de las muestras y su litología se encuentra en la Tabla 4.1. Una tabla con los resultados específicos para cada muscovita se presenta en el Anexo 8.

1.4.4 Metodología asociada al Objetivo Específico 4: Análisis cinemático

Análisis cinemáticos se desarrollaron en fallas normales sin-sedimentarias de pequeña escala (centímetros a metros de desplazamiento). Se identificaron 67 fallas desarrolladas durante la etapa *synrift* (Noriano – Rético) y de *postrift* temprano (Rético-Hetangiano) las cuales mostraban clara evidencia de depositación sin-sedimentaria (*e.g.* estratos de crecimiento o estar selladas por estratos más jóvenes). La cinemática del fallamiento y la dirección de desplazamiento del bloque colgante se determinó mediante marcadores cinemáticos (*e.g.* estriaciones y fracturas secundarias) de acuerdo a los criterios propuestos por Petit (1987). Considerando la posterior deformación compresiva que sufrieron las sucesiones mesozoicas, las fallas normales fueron llevadas a su posición pre-deformacional mediante una rotación basada en la actitud de los estratos del bloque yaciente. Los ejes principales del elipsoide de *strain* se obtuvieron a través de una distribución estadística de Bingham (Marrett y Allmendinger, 1990) mediante el software FaultKinWin (Allmendinger *et al*., 2001). Una tabla con los datos estructurales utilizados para realizar los cálculos se encuentra en el Anexo 6.

1.4.5 Metodología asociada al Objetivo Específico 5: Balance estructural

Se realizaron tres secciones estructurales entre los 25° y 26°S basadas en la geología superficial. Las secciones fueron balanceadas mediante modelamiento *forward* utilizando el software MOVE (Midland Valley Exploration Ltd.), comenzando desde una geometría pre-deformacional del *rift* Triásico constreñida por datos estratigráficos, con el objetivo de igualar la actual configuración estructural. Se utilizó el algoritmo de *Simple Shear* para el fallamiento normal desde la etapa pre-*rift* (Withjack y Peterson, 1993) mientras que el algoritmo de *Trishear* fue usado para modelar la inversión de la cuenca y el fallamiento inverso (Erslev, 1991). El algoritmo de *Trishear* se implementó usando un ángulo apical para la zona de *trishear* de 50° para todas las estructuras y, dependiendo de la geometría del plegamiento, se utilizó una razón de propagación versus desplazamiento (P/S) entre 1.5 y 15, con el objetivo de generar pliegues por propagación de falla o de flexura de falla (Allmendinger *et al*., 2004). La deformación en el limbo trasero fue modelada usando el algoritmo de *Inclined Shear* para fallas normales reactivadas de manera inversa, con un ángulo de cizalle entre 60° y 80°, y el algoritmo *fault-parallel flow* para fallas nuevas.

Basado en observaciones de terreno se modeló la geometría de las fallas maestras del *rift* con una geometría lístrica. Las zonas de despegue profundas se asumieron entre 12-15 km de profundidad basado en la transición frágil-dúctil más somera, de acuerdo a modelos termomecánicos recientes (Giambiagi *et al*., 2015; Julve, Tassara, Echeverria, y Stotz, 2018).

Capítulo 2: Unidades triásicas en el norte de Chile entre los 22° y los 26° S[1].

En el segmento que comprende el área de estudio (22° - 26° S), las rocas de edad triásica afloran típicamente en tres unidades morfoestructurales: Cuenca del Salar de Atacama, Cordillera de Domeyko y Cordillera de la Costa (Fig. 2.1). En esta sección se exponen los antecedentes respecto a las unidades litoestratigráficas triásicas conocidos previos a la realización de esta tesis doctoral.

2.1 Cuenca del Salar de Atacama

En las inmediaciones de Peine, se presentan secuencias volcánicas con intercalaciones sedimentarias, correspondientes a coladas y brechas andesíticas, tobas dacíticas y aglomerados de la Formación Cas (Moraga et al. 1974; Niemeyer, 2013) formadas durante el Pérmico Tardío-Triásico Medio (260-240 Ma; Breitkreuz and Van Schmus, 1996; Maksaev et al., 2014). Coetánemente, se habría desarrollado un volcanismo pricipalmente andesítico y sedimentación continental en sistemas fluviales representados por la unidad Estratos de Cerros Negros (~247 Ma; Niemeyer, 2013).

2.2 Cordillera de Domeyko

Durante el Triásico Temprano a Medio se desarrolló un volcanismo y sedimentación continental cuyos afloramientos yacen típicamente en discordancia sobre rocas del Carbonífero Superior-Pérmico (Figs. 2.2 y 2.3). En las inmediaciones de Calama, conglomerados y areniscas de los Estratos de Quetena (Triásico Medio; Tomlinson et al., 2010) son sobreyacidos por lavas andesíticas y subordinadamente dacíticas y riolíticas de los Estratos de Chuquicamata (~235-231 Ma; Tomlinson and Blanco, 2008). Esta unidad se encuentra intruída por granodioritas con edades U-Pb

---

[1] Este capítulo esta basado en una parte escrita por el autor para el capítulo "The Early Stages of the Magmatic Arc in the Southern Central Andes" (Oliveros et al. 2018). Oliveros, V., González, J., Espinoza, M., Vásquez, P., Rossel, P., Creixell, C., ... and Bastías, F. (2018). The Early Stages of the Magmatic Arc in the Southern Central Andes. In *The Evolution of the Chilean-Argentinean Andes* (pp. 165-190). Springer, Cham.

de *ca.* 227-233 Ma (Proffett y Dilles, 2007; Tomlinson et al., 2010). En el margen oriental de la Cordillera de Domeyko, en las proximidades de los cerros de Tuina, se exponen andesitas y en menor medida dacitas y riolitas de la Formación Tuina (Marinovic and Lahsen, 1984), formadas durante el Pérmico Superior-Triásico Medio (~253-236 Ma; Henriquez et al., 2014). Hacia el sur, en el margen occidental del Salar de Atacama, los Estratos el Bordo (Fortt, 1981) corresponden a lavas andesíticas a daciandesíticas, intercaladas con rocas sedimentarias lacustres (~240 Ma; Basso and Mpodozis, 2012). Rocas equivalentes a esta unidad se presentan al norte de la Sierra Mariposas (Cortés, 2012) y en los Cerrillos de Imilac (Solari et al., 2015). Por otro lado, a lo largo de las sierras Eploradora y Castillo, se exponen rocas de origen fluvio-aluvial con potentes intercalaciones de basaltos, dacitas y rocas piroclásticas del Miembro Inferior de la Formación Quebrada del Salitre (Naranjo and Puig, 1984; Mpodozis and Cornejo, 1997; Venegas et al., 2013), el cual es intruído por domos riolíticos de *ca.* 232 Ma (Cornejo et al., 2009).

Por otro lado, durante el Nórico y el Rético en la Cordillera de Domeyko se desarrolla un segundo periodo de intensa actividad volcánica y sedimentación continental. En los Cerros de Caracoles, los Estratos Las Lomas, corresponden a lavas dacíticas y andesíticas junto con tobas (~206 Ma; Marinovic y Gacía, 1999; Basso y Mpodozis, 2012). Hacia el sur, rocas piroclásticas y volcánicas andesíticas con menores proporciones de basaltos, dacitas y riolitas, se habrían depositado en cuencas de origen lacustre. Estas unidades corresponden a la Formación Cerro La Ballena (Muñoz, 1989), la que presenta edades U-Pb entre los 218-195 Ma (Marinovic et al., 2007; Astudillo et al., 2017) y las formaciones Cerro Guanaco (~213-200 Ma) y Sierra de Varas (~211-206 Ma; González et al., 2015), presentes en la sierra homónima. El volcanismo y sedimentación representado por estas unidades, se habría desarrollado coetáneamente al desarrollo de sistemas fluvio-aluviales de la Formación Quebrada del Salitre en las sierras Exploradora, Castillo e Inés Chica (Miembro Superior; Cornejo et al. 2009). Asimismo, el miembro superior de la Formación Quebrada del Salitre ha sido asignada en la Sierra Vaquillas Altas (Naranjo y Puig, 1984; Venegas et al. 2013), donde se han obtenido edades U-Pb entre los ~ 214-212 Ma (Venegas et al., 2013). Posteriormente, durante el Rético, se desarrolló una

extensa transgresión marina la cual es representada en la Sierra del Jardín por los Estratos de Rencoret (Tobar, 1996; Marinovic, 2007), y en las sierras de Varas y Vaquillas Altas por la Formación Profeta (Chong, 1973), mientras que en la Sierra Exploradora correspondería a parte del Miembro Superior de la Formación Quebrada del Salitre (Cornejo et al., 2009). Sin embargo, la parte marina de este miembro fue separado en la Formación Las Bateas por Álvarez et al. 2003, en base a las facies sedimentarias presentes y su contenido fosilífero.

2.3 Cordillera de la Costa

En esta morfoestructura, las rocas más antiguas de edad triásica corresponden a secuencias sedimentarias con intercalaciones piroclásticas (~ 242 Ma), reconocidas al norte de la ciudad de Paposo y asignadas a la Formación Cifuncho (Álvarez et al., 2016), aun cuando esta unidad presenta una edad Triásico Superior en su localidad tipo en las cercanías de Taltal (Naranjo y Puig, 1984; Contreras et al., 2013). Además, escasos afloramientos de rocas plutónicas con una edad de *ca.* 246 Ma se presentan en las cercanías de las ciudades de Taltal (Granodiorita Agua Verde, Espinoza et al., 2011) y Paposo (Tonalita Cerro Carnero, Álvarez et al. 2016). Por otro lado, al este de la ciudad de Mejillones, se presentan tobas y domos de composición riolítica (Riolitas de Cerro Miranda-Cerro Camaleón) asignadas al Triásico Medio-Superior (Basso, 2004). Durante el Nórico y el Rético, de forma coetánea a la actividad volcánica y sedimentaria presente en la Cordillera de Domeyko, en esta morfoestructura se desarrolló un plutonismo representado por el Complejo Plutónico Anchuña de *ca.* 214-200 Ma (Escribano et al., 2013), el Sienogranito Capitana (*ca.* 215-207 Ma; Godoy y Lara, 1998; Espinoza et al., 2014) y tonalitas de hornblenda-biotita al oeste de Mejillones (*ca.* 208 Ma; Casquet et al., 2013).

Por otro lado, en las cercanías de Taltal, la Formación Cifuncho expone rocas sedimentarias de origen fluvio-aluvial junto a rocas piroclásticas con edades U-Pb entre los ~210-208 Ma (Contreras et al., 2013). Hacia el sur, la Formación Agua Chica (Suárez et al., 1985), presenta lavas e hipabisales andesíticos con una edad cercana a los ~200 Ma (Espinoza et al., 2015). Durante el Nórico alto- Rético se desarrolla en

15

la Cordillera de la Costa una transgresión marina representada por las formaciones Estratos de Rencoret en las cercanías de Antofagasta y por la Formación Pan de Ázucar en las inmediaciones de la ciudad de Taltal (Naranjo y Puig, 1984; González y Niemeyer, 2005; Contreras et al., 2013).
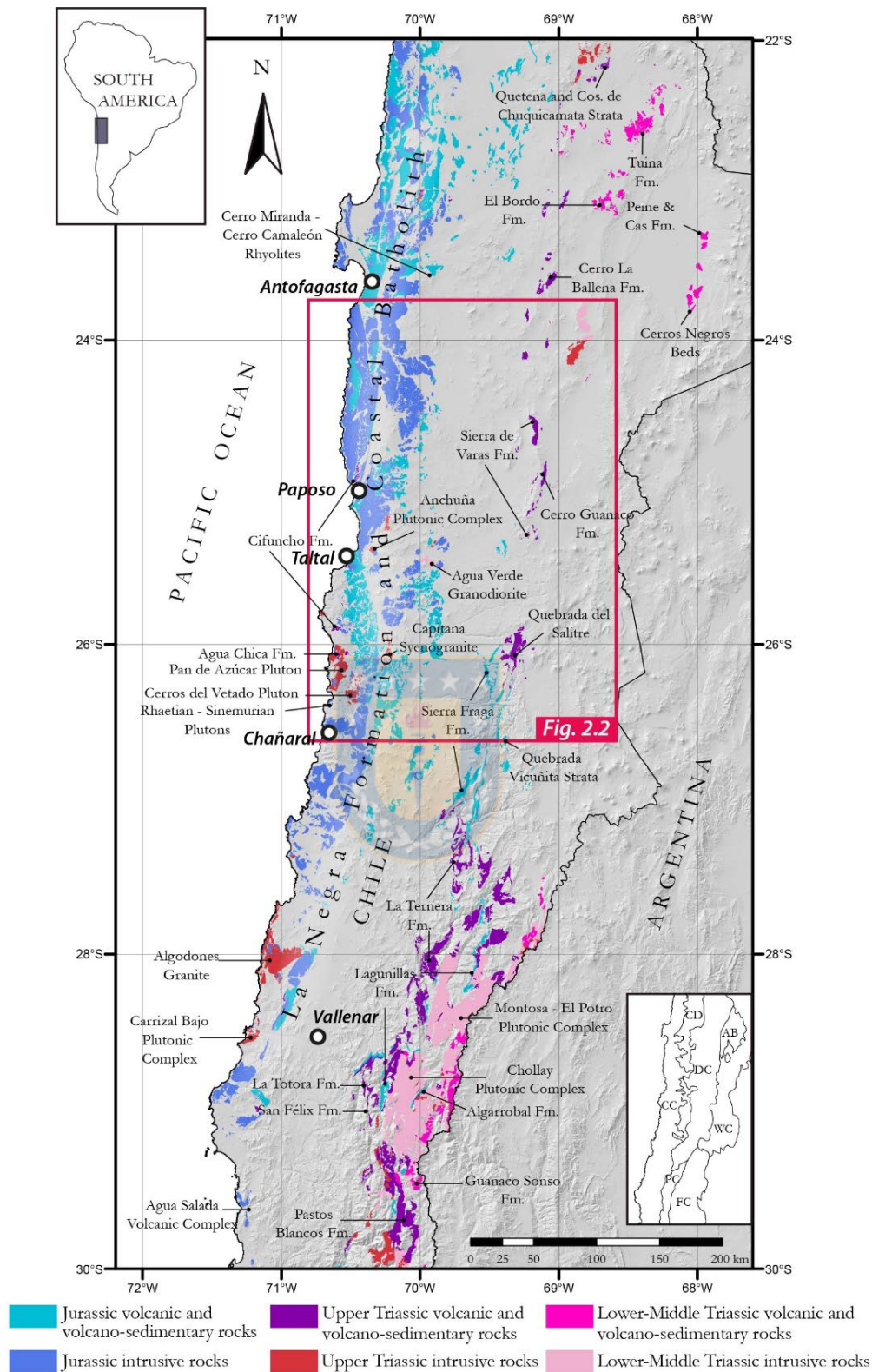
Figura 2.1: Localidades donde afloran las unidades ígneas y volcanosedimentarias triásicas y jurásicas en los Andes Centrales del Sur entre los 22° y 30° S. Mapa basado en los recientes mapas geológicos escala 1:100.000 generados por el Servicio Nacional de Geología y Minería.

17
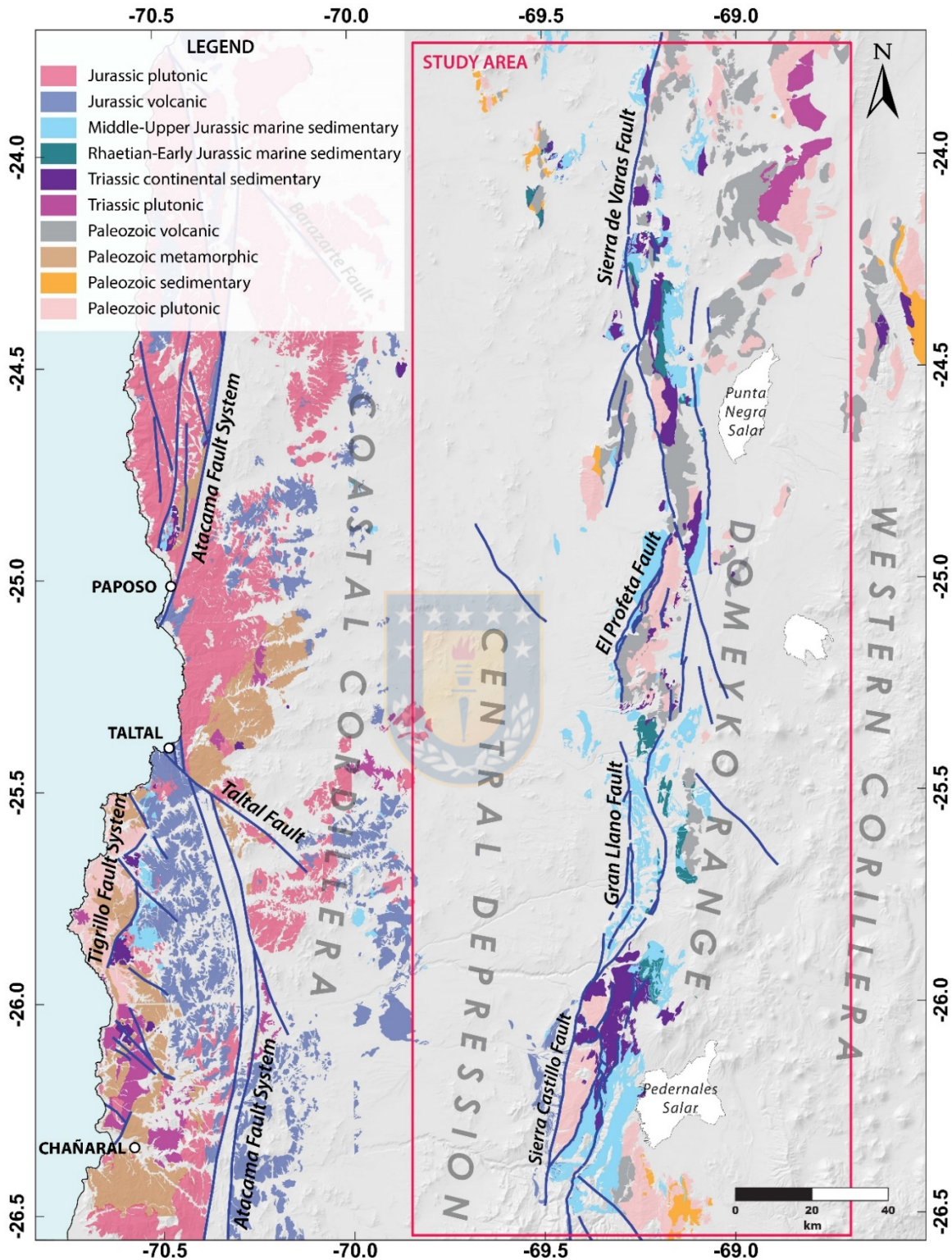
Figura 2.2: Mapa geológico del antearco chileno que muestra las unidades triásicas y jurásicas presentes entre los 23.5° – 26.5° S, indicando el área de estudio (rectángulo rojo) y las principales fallas en este dominio. Mapa basado en los recientes mapas geológicos escala 1:100.000 generados por el Servicio Nacional de Geología y Minería. Referencias específicas se encuentran en el texto.

18
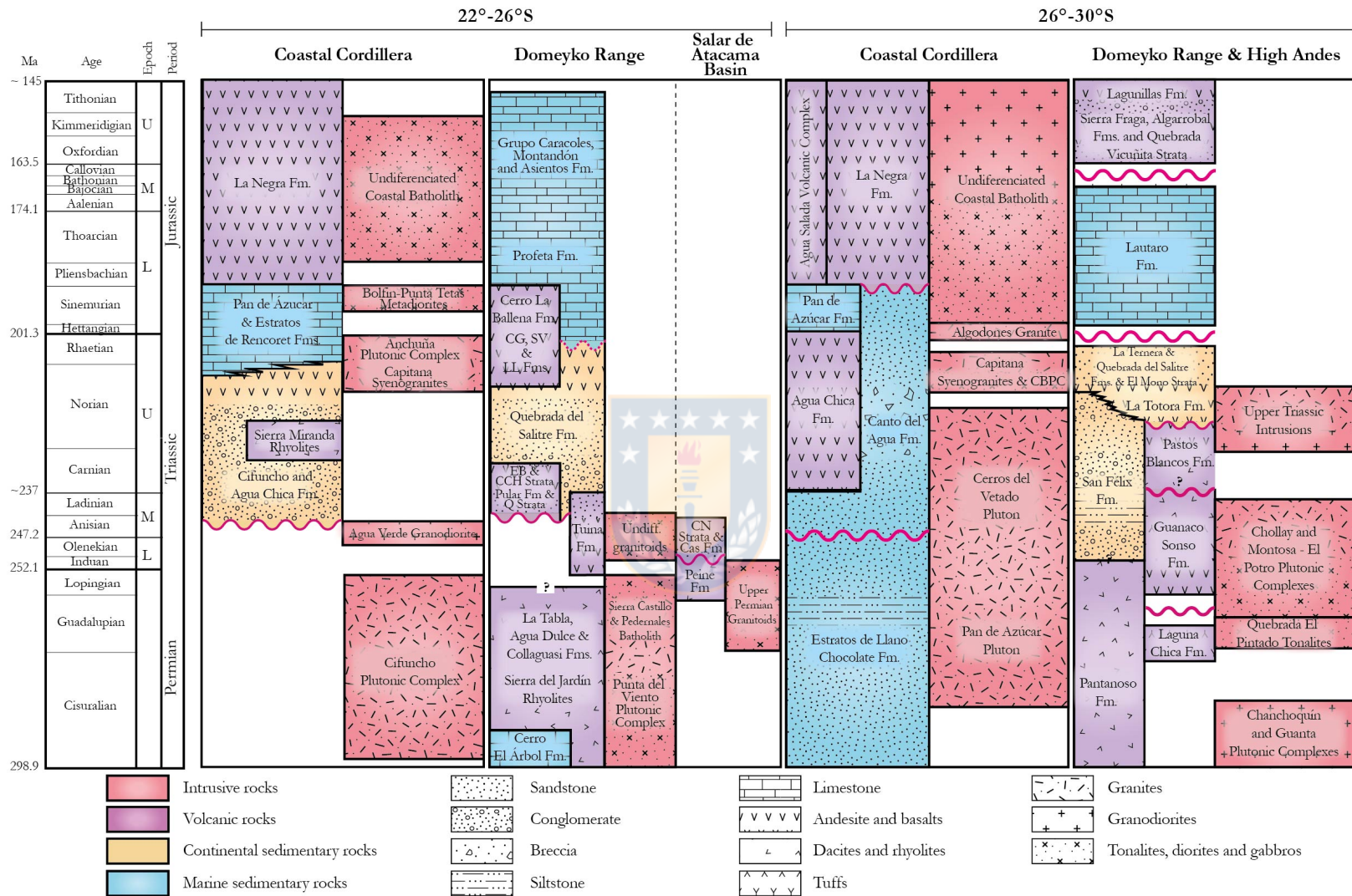
Figura 2.3: Cuadro cronoestratigráfico con las unidades triásicas y jurásicas presentes en las distintas unidades morfoestructurales del antearco chileno entre los 22°-26°S y los 26°-30° S. Esquema basado en los recientes mapas geológicos escala 1:100.000 generados por el Servicio Nacional de Geología y Minería. Referencias específicas se encuentran en el texto.

19

Capítulo 3: The synrift phase of the early Domeyko Basin (Triassic, northern Chile): Sedimentary, volcanic and tectonic interplay in the evolution of an ancient subduction-related rift basin[2].

Mauricio Espinoza [1*], Diego Montecino[2], Verónica Oliveros[1], Natalia Astudillo[2], Paulina Vásquez[2], Robinson Reyes[1], Christopher Celis[1], Rodrigo González[3], Juan Contreras[5], Christian Creixell[2], Amancay Martínez[4]

(1) Departamento Ciencias de la Tierra, Universidad de Concepción, Víctor Lamas 1290, Casilla 160-C, Concepción, Chile.

(2) Servicio Nacional de Geología y Minería (SERNAGEOMIN), Santa María 0104, Providencia, Santiago, Región Metropolitana, Chile.

(3) Departamento de Ciencias Geológicas, Universidad Católica del Norte, Avenida Angamos 0610, Antofagasta, Chile.

(4) Departamento de Geología, FCFMyN, Universidad Nacional de San Luis, Ejercito de Los Andes 950, San Luis, Argentina.

(5) Área de Minería y Metalurgia, Universidad Tecnológica de Chile (INACAP), Iquique, Chile.

Abstract

The geodynamic setting along the SW Gondwana margin during its early breakup (Triassic) remains poorly understood. Recent models calling for an uninterrupted subduction since Late Paleozoic only slightly consider the geotectonic significance of coeval basins. The Domeyko Basin initiated as a rift basin during the Triassic being filled by sedimentary and volcanic deposits. Stratigraphic, sedimentological and geochronological analyses are presented in order to determine

---

[2] El Material Suplementario referenciado en este trabajo se encuentra disponible en el siguiente enlace https://onlinelibrary.wiley.com/doi/full/10.1111/bre.12305 y en la sección de Anexos.

the tectonostratigraphic evolution of this basin and to propose a tectonic model suitable for other SW Gondwana-margin rift basins.

The Domeyko Basin recorded two synrift stages. The Synrift I (~240-225 Ma) initiated the Sierra Exploradora sub-basin while the Synrift II (~217-200 Ma) reactivated this sub-basin and originated small depocenters grouped in the Sierra de Varas sub-basin. During the rift evolution, the sedimentary systems developed were largely controlled by the interplay between tectonics and volcanism through the accommodation/sediment supply ratio (A/S). High-volcaniclastic depocenters record a net dominance of the syn-eruptive period lacking rift-climax sequences, while low-volcaniclastic depocenters of the Sierra de Varas sub-basin developed a complete rift cycle during the Synrift II stage.

The architecture of the Domeyko Basin suggests a transtensional kinematic where N-S master faults interacted with ~NW-SE basement structures producing highly asymmetric releasing bends. We suggest that the early Domeyko Basin was a continental subduction-related rift basin likely developed under an oblique convergence in a back-arc setting. Subduction would have acted as a primary driving mechanism for the extension along the Gondwanan margin, unlike inland rift basins. Slab-induced dynamic can strongly influence the tectonostratigraphic evolution of subduction-related rift basins through controls in the localization and style of magmatism and faulting, settling the interplay between tectonics, volcanism, and sedimentation during the rifting.

3.1 Introduction

Subduction-related rift basins are the result of mechanical subsidence driven by lithospheric thinning at the vicinity of a subduction zone in extensional arcs (Sengör and Natal'in, 2001; Merle, 2011) (see Supplementary Material SM1). Current examples of such arcs are less common than their compressional or neutral stress counterparts (Jarrard, 1986; Busby, 2012) and they often develop in oceanic crust (*e.g.* Western Pacific subduction zones). Few examples of extensional, subduction-related basins in continental settings are known: the Okinawa Trough (Lee *et al*., 1980), the intra-arc basins of the Taupo arc (Villamor *et al*., 2017) and the grabens of southern Japan (Kamata and Kodama, 1994), while extinct examples are the Eo-Oligocene evolution

of the Basin and Range (Ingersoll, 2012) and the Late Cretaceous Western Peruvian Trough (Polliand *et al*., 2005). Recent studies from the Taupo intra-arc rift, have shed light on the uniqueness of subduction-related rifts, such as their rapid evolution compared to intraplate continental rifts, which is due to the role of active magmatism in weakening of the crust during the early rift stages (Ellis *et al*., 2014; Villamor *et al*., 2017).
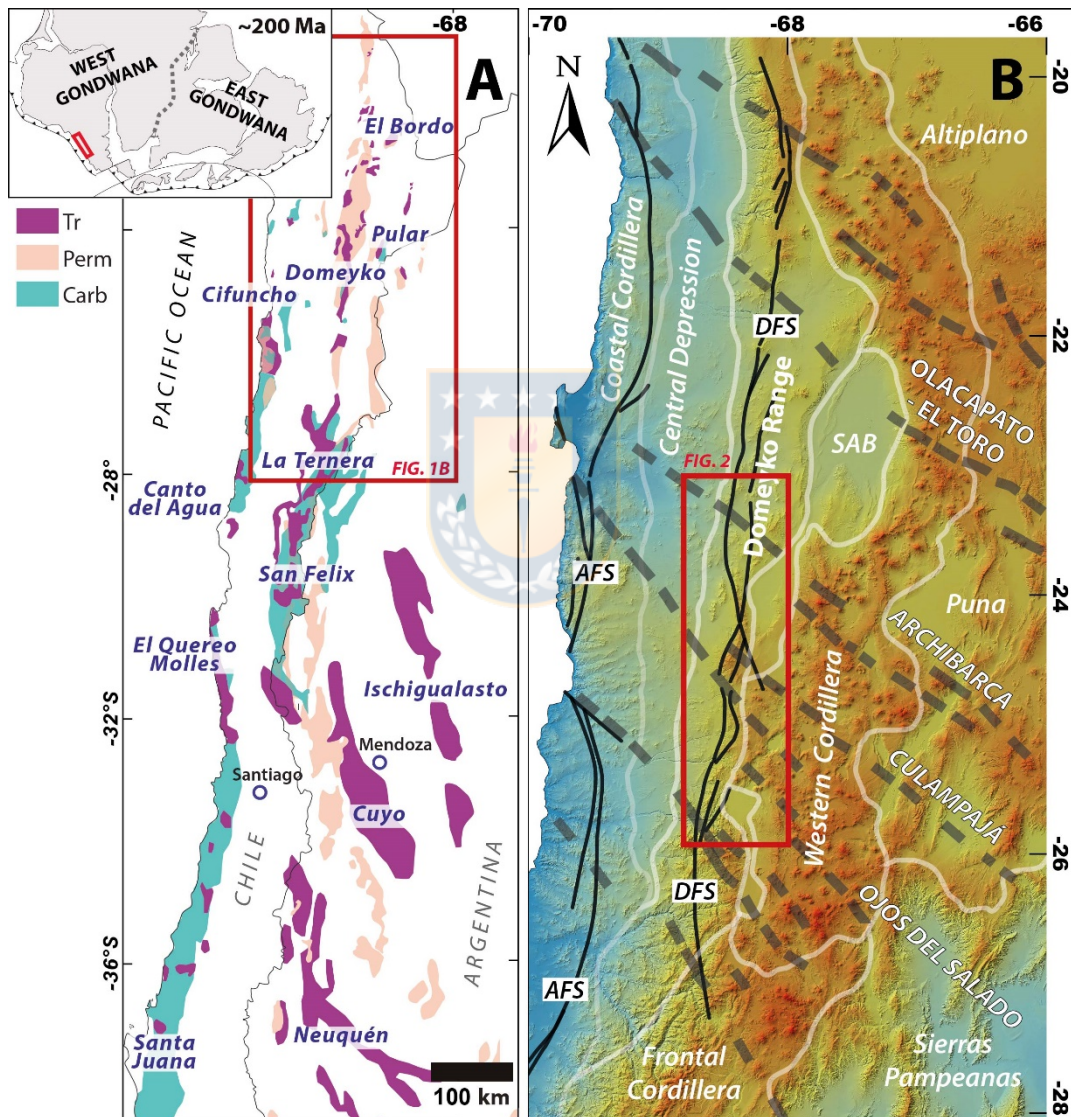
Figure 3.1: A) Distribution of Triassic basins of Chile and Argentina. The inset shows the reconstruction of Gondwana at 200 Ma according to Torsvik and Cocks (2013). B) Map of NW Chile and adjacent Argentina, showing main morphostructural units. Main tectonic features include the Atacama Fault System (AFS), the Domeyko Fault System (DFS) and main continental NW-SE lineaments (Abels and Bischoff, 1999; Petrinovic *et al*., 2005). The red rectangle indicates the study area showed in Figure 3.2.

Even though continental subduction-related rifts are scarce in modern settings, they could have been far more common along the "Pangean rim of fire" developed during the Late Triassic (Hadlari *et al*., 2017), where unique global tectonic conditions such as very low convergence rates and subduction of relatively old and cold oceanic plates (Matthews *et al*., 2016; Müller *et al*., 2016) would have favored the development of continental rift basins (Schellart, 2005; Stephenson and Schellart, 2010) associated with contemporaneous arc magmatism along the northwestern (Busby-Spera, 1988) and southwestern (Poma *et al*., 2014; Coloma *et al*., 2017; González *et al*., 2017; Oliveros *et al*., 2017) Gondwana margins. The identification and study of those basins in the Triassic Gondwanean record is crucial to understand the processes that took place at the margin of the supercontinent during the early stages of its breakup (~ 200 Ma; Lamotte *et al*., 2015).

In addition to their scarcity in the global geological record, subduction-related rift basins are difficult to identify because of their intrinsic relationship to arc volcanism, generating complex stratigraphic records where primary and secondary volcano-sedimentary deposits evolve in tandem (Martin and Németh, 2007; D'Elia *et al*., 2016), in strong contrast to the non-volcanic basins for which most tectonostratigraphic models have been proposed (*e.g.* Gulf of Suez and North Sea rifts; Schlische, 1991; Gawthorpe and Leeder, 2000; Withjack *et al*., 2002). For example, the larger volume and supply rates of sedimentation in magma-rich basins (Muravchik *et al*., 2011) results in low accommodation space-sediment supply ratios (A/S) during the syn-eruptive period, creating thick aggradational successions that often interfere with normal siliciclastic or carbonatic deposition (Martin and Németh, 2007). Hence, typical features developed in many non-volcanic intracontinental rifts such as the tripartite succession representing the alluvial-lacustrine-fluvial deposition (Schlische, 1991; Withjack *et al*., 2002), are not always observed in volcano-sedimentary basins. Furthermore, new advances in the study of subduction-related rift basins have highlighted the link between key volcanic parameters (type of edifices, style and scale of eruptions, etc.) and main features of the basin internal dynamics (synrift stratigraphic infill and subsidence pattern), distinguishing two-end members models depending on the amount of volcaniclastic input to the basin (low/high volcaniclastic depocenters; *e.g.* D'Elia *et al*., 2016). How

can these models be applied to continental subduction-related rift basins? What controls the development of low/high volcaniclastic depocenters in this particular tectonic scenario? A detailed characterization of the main volcanic parameters and their impact on the accommodation and material supply ratios is key to address these questions.

The Domeyko Basin of northern Chile (Figs. 3.1 and 3.2) provides an excellent opportunity to study the relationship between tectonism, magmatism, and sedimentation in a subduction-related rift developed on the Gondwana continent. It began as a rift basin during the Triassic (Charrier, 1979; Suárez and Bell, 1992), though its position with respect to the arc remains unknown (Suárez and Bell, 1992; Poma *et al.*, 2014; Oliveros *et al.*, 2017). During the synrift stage, continental and later marine deposition was coeval with profuse volcanism of variable composition, ranging from basalts to rhyolites (Chong and Hilldebrandt, 1985; Cornejo *et al.*, 2009; Venegas *et al.*, 2013; Astudillo *et al.*, 2017), with mainly calcalkaline affinities (González *et al.*, 2015; Espinoza *et al.*, 2016; Oliveros *et al.*, 2017). The end of the mechanical subsidence at the post-rift stage is thought to have taken place during the earliest Jurassic (Suárez and Bell, 1992; Ardill *et al.*, 1998). Even though the continental infill dominates the synrift succession, previous works focused on the marine successions of post-rift stage, paying little attention to the initial volcano-sedimentary successions (Chong and Hilldebrandt, 1985; Bell and Suárez, 1991; Prinz *et al.*, 1994; Marinovic *et al.*, 1995; Ardill *et al.*, 1998). This was partly due to the lack of adequate chronostratigraphic constraints in the fossil-poor continental syn-rift successions and to the strong deformation resulting from the tectonic inversion of the basin since the Late Cretaceous (Amilibia *et al.*, 2008; Bascuñán *et al.*, 2015), that hampered the understanding of the synrift architecture of the Domeyko Basin. Recent geological field surveys have generated significant geochronological and stratigraphic information of the Triassic successions (Cornejo *et al.*, 2009; Venegas *et al.*, 2013; González *et al.*, 2015; Astudillo *et al.*, 2017) without interpreting that information in the context of the architecture, kinematics and driving mechanisms of the synrift stage. Thus, tectonostratigraphic models which integrate this data at the entire basin scale are still lacking.

The aims of this paper are twofold. In order to get insights about the evolution of subduction-related basins, we attempt to unravel the tectonostratigraphic evolution of the synrift Domeyko Basin by addressing the interplay between volcanic, sedimentary and tectonic processes. Secondly, on a broader scale, we aim to assess the geologic processes acting at the southwestern margin of Gondwana during the early stages of its breakup and propose a coherent tectonic model for extensional basins developed on a continental margin. To achieve these goals we carried a sedimentological and U-Pb geochronological study focused on the continental Triassic deposits cropping out in the Domeyko Range (Fig. 3.2).

3.2 Geological setting

3.2.1 Overview of the Domeyko Basin

The Domeyko Basin comprises deposits from the Triassic to Lower Cretaceous (Ardill, 1996; Ardill *et al*., 1998), cropping out in the western margin of the Domeyko Range of northern Chile, between 21°-27°S (Figs. 3.1 and 3.2). The Domeyko Basin developed in its earliest stages under active lithospheric stretching, producing a continental rift basin (Charrier, 1979; Suárez and Bell, 1992). The synrift deposits occur mainly in volcanic and continental sedimentary rocks, which unconformably overlie 'upper' Carboniferous to Permian acidic igneous rocks (Fig. 3.3). Master extensional faults have been inferred to have been inverted post-rifting (Amilibia *et al*., 2008), while secondary normal faults show displacements from meters to tens of meters (Fig. 3.4). The pre-rift basement in part comprises rocks of the Choiyoi magmatic province, which is typically exposed across the Principal Cordillera of Chile and Argentina (Llambías *et al*., 2003; Kleiman and Japas, 2009).

WESTERN DOMEYKO RANGE
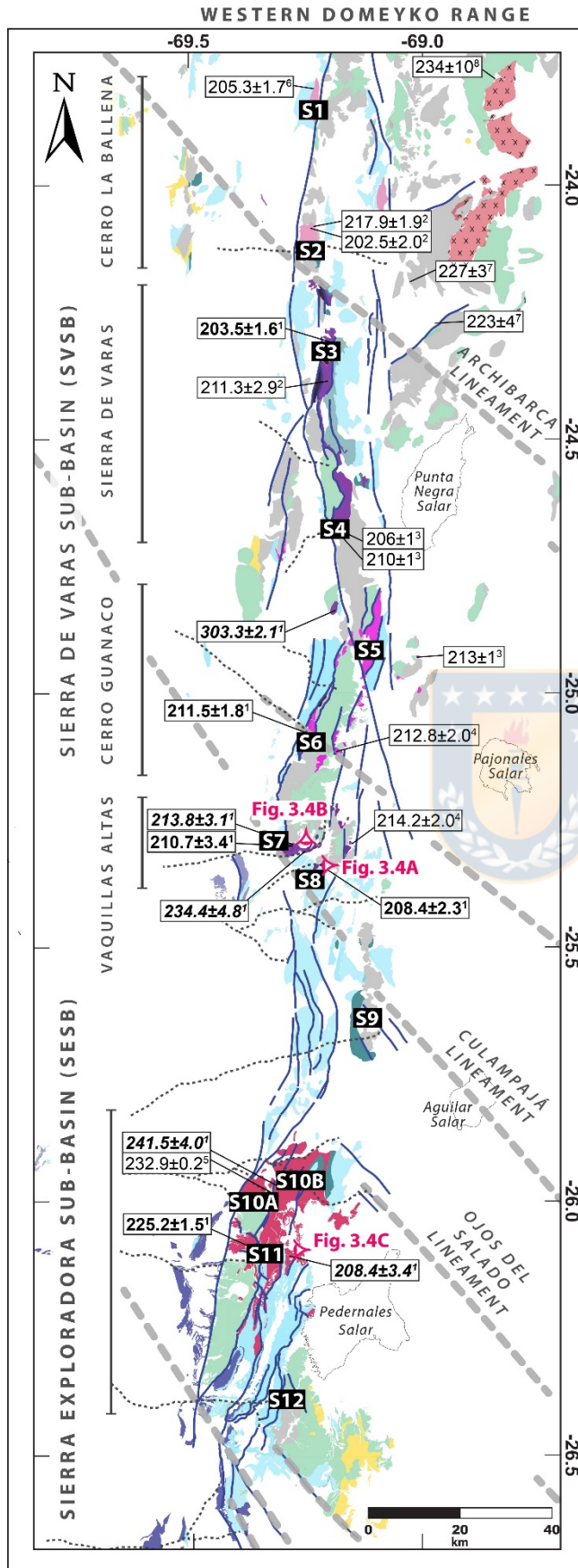
LEGEND

225.2±1.5[1] *IZ Crystallization age (* **this work bolded** *)*
208.4±3.4[1] *DZ Max. depositional age (* **this work bolded** *)*
— — — *Continental-scale lineament*
——— *Regional faults*
S1 *Stratigraphic sections location (Fig. 3.9)*

Jurassic volcanic/volcanosedimentary
Jurassic marine — **Postrift**
U. Triassic/L. Jurassic shallow marine

Triassic volcanic and continental rocks

Quebrada del Salitre Fm. (QSF)
Sierra de Varas Fm. (SVF)
Cerro Guanaco Fm. (CGF) — **Synrift**
Cerro La Ballena Fm. (CLBF)
Cerro Rincones Beds (CRB)
Triassic plutons

Carboniferous/Permian volcanics
Carboniferous/Permian plutons — **Prerift**
Upper Paleozoic sedimentary

Stratigraphic sections location keys
S1 Cerro La Ballena
S2 Cerro Pascua
S3 north portion of Sierra de Varas
S4 Quebrada Mármol
S5 Cerro Guanaco
S6 Quebrada Punta del Viento
S7 Quebrada Los Pozos
S8 Quebrada La Carreta
S9 Cerro Danko
S10A Quebrada La Perra
S10B Quebrada del Salitre
S11 Quebrada Doña Inés Chica
S12 Cerro Pedernales

26
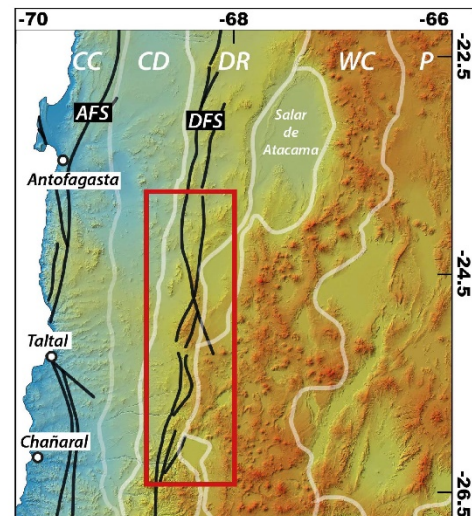
Figure 3.2: Geologic map of the study area showing the distribution of pre-rift, synrift and post-rift units and main tectonic features. U-Pb ages are from: [1] this work (bolded), [2] Astudillo *et al*. (2017), [3] González *et al*. (2015), [4] Venegas *et al*. (2013), [5] Cornejo *et al*. (2009), [6] Matthews *et al*. (2007) in Valenzuela (2014), [7] Marinovic (2009), [8] Urzúa (2009). IZ are igneous zircons and DZ are detrital zircons. Please note the location of stratigraphic sections (S1 to S12) presented in Figure 3.9.

Overlying the synrift deposits are sedimentary rocks that represent a marine transgression that took place in several depocenters during the Late Triassic (Chong, 1973; Chong and Hilldebrandt, 1985). This transgression was followed by an abrupt global rise of the sea level during the Hettangian (Ardill *et al*., 1998). The positive tectonic inversion of the basin took place during the Andean orogeny, which shaped the Domeyko Range through the Domeyko Fault System since the Late Cretaceous (Muñoz *et al*., 2005; Amilibia *et al*., 2008). The subsequent deformation imposed on the synrift successions hindered the recognition of the primary basin geometry and most of its large-scale architectural elements.

3.2.2 Sub-basins and synrift lithostratigraphic units

In the study area (Fig 3.2; 24°-26°30'S), the Domeyko Basin comprises two major synrift sub-basins: the Sierra de Varas sub-basin (SVSB) and the Sierra Exploradora sub-basin (SESB). In this section, we briefly describe the synrift units following the lithostratigraphic schemes outlined by recent studies (Álvarez, 2003; Cornejo *et al*., 2009; Venegas *et al*., 2013; González *et al*., 2015; Montecino, 2015; Astudillo *et al*., 2017; Fig. 3.3).

Sierra de Varas sub-basin

The units representing the SVSB crop out as several small synrift depocenters disrupting the continuity of the current Domeyko Range (Fig. 3.2). The synrift units unconformably overlie acidic volcanic and granitic rocks of Upper Carboniferous-Early Permian age (La Tabla Formation and Punta del Viento Plutonic Complex) and are conformably overlain by the lower member of the Profeta Formation.
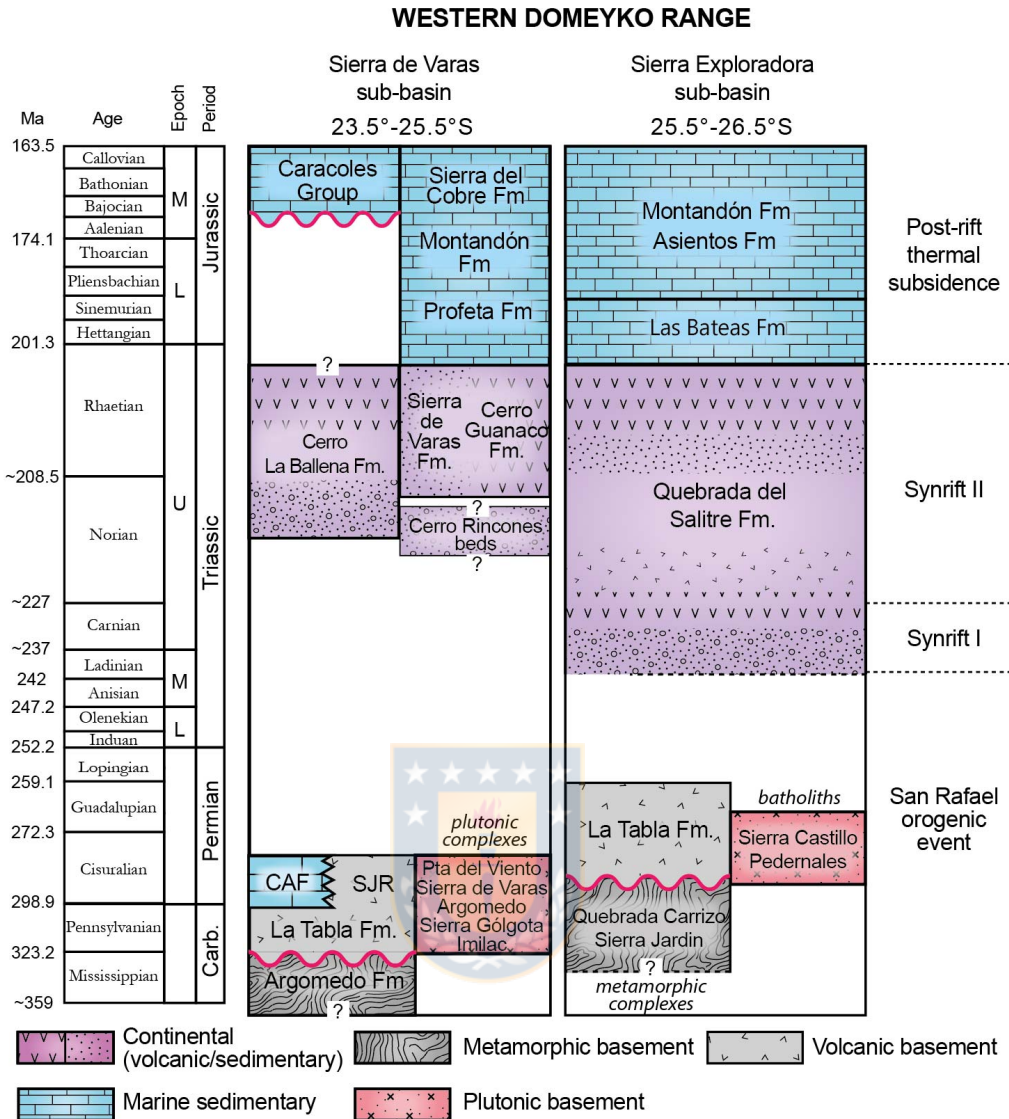
Figure 3.3: Lithostratigraphic scheme of the western margin of the Domeyko Range based on the work of Tomlinson *et al.*, (1999); Álvarez, (2003); Cornejo *et al.*, (2009); Naranjo and Puig (1984); González *et al.*, (2015) and Astudillo *et al.*, (2017). CAF: Cerro del Árbol formation; SJR: Sierra del Jardín Metamorphic Complex.

At the Cerro La Ballena depocenter (24°45'S - 24°09'S), the Cerro La Ballena Formation comprises ~650 m of welded tuffs, calcarenites, stromatolitic limestones and basalts to basaltic andesites (Muñoz, 1989; Marinovic, 2007; Valenzuela, 2014; Astudillo *et al.*, 2017). Zircon U-Pb ages indicate an age interval of *ca.* 218-203 Ma for this unit (Cornejo *et al.*, 2007; Astudillo *et al.*, 2017). A mildly younger age for this unit (194.4 +7.9 -9.2 Ma; Marinovic, 2007) is based on just two zircons with a different

weighted mean age as the reported, so we discard it due to its poor statistical signification.
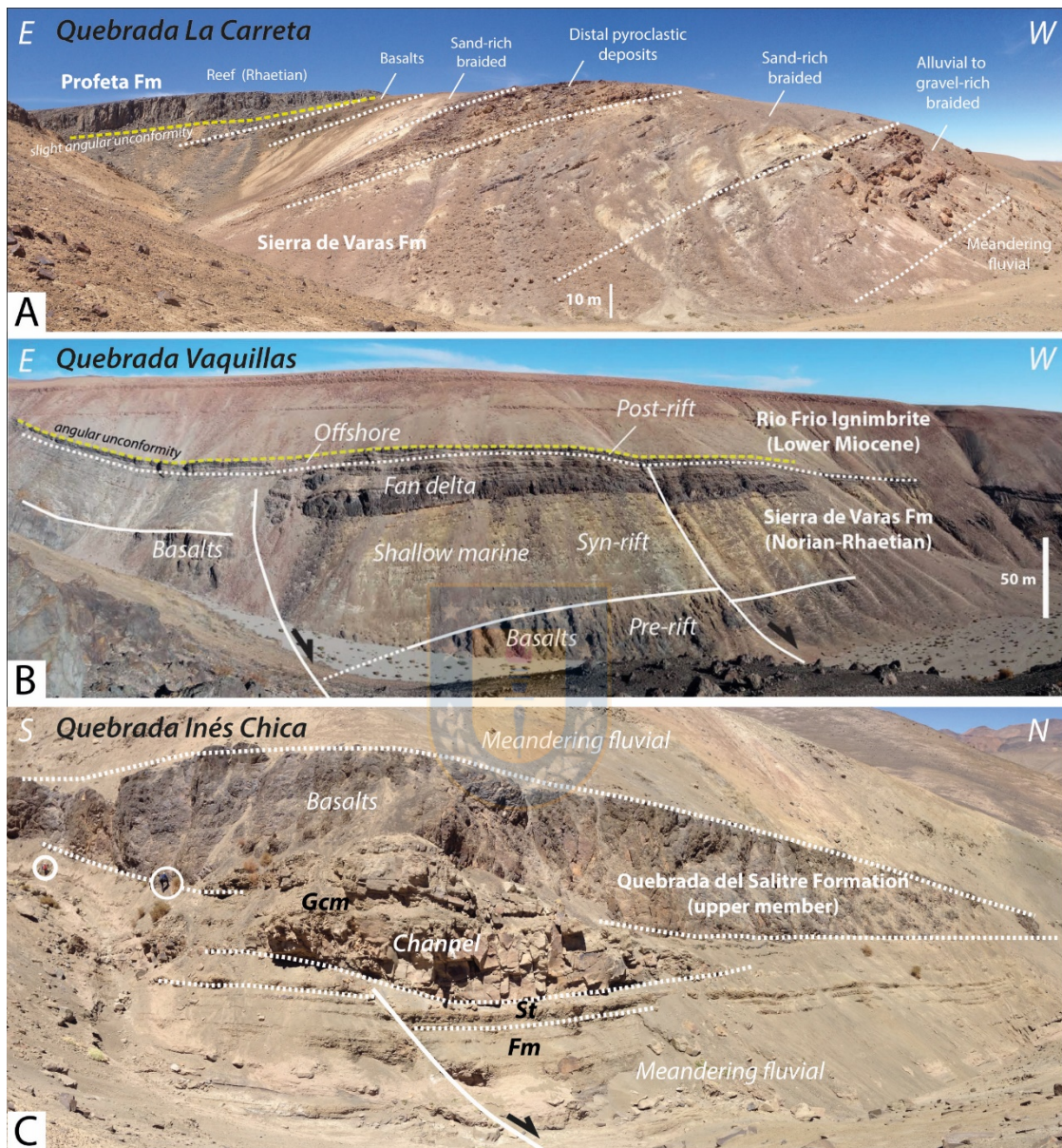
Figure 3.4: A) Slight angular unconformity between the reef facies of the Profeta Formation and the fluvial and volcanic successions of the Sierra de Varas Formation (SVF) at column S8. B) Synrift listric faults affecting deltaic facies from the Sierra de Varas Formation at column S7. C) Synsedimentary extensional fault controlling the location of a fluvial paleochannel, growth strata and basaltic lava flow thickness from the Quebrada del Salitre Formation at S11. Image locations is shown in figure 3.2.

At the Sierra de Varas depocenter (24°11'S and 24°42'S), ~600 m of bouldery-grained conglomerates and breccias from the Cerro Rincones Beds crop out at the

western flank of the Sierra de Varas range (Astudillo *et al*., 2017; Montecino, 2015). A maximum depositional zircon U-Pb age of *ca*. 276.2 ± 6.6 Ma and stratigraphic relationships constrain its age to the Permian-Late Triassic (Astudillo *et al*., 2017). In the same depocenter, the Sierra de Varas Formation comprises >650 m of siliciclastic and carbonate sedimentary rocks intercalated with pyroclastic rocks (Astudillo *et al*., 2017; Marinovic *et al*., 1995; Contreras, 2014; González *et al*., 2015; Montecino, 2015). U-Pb ages indicate a range of ~211-206 Ma for this unit (Astudillo *et al*., 2017; González *et al*., 2015).

In the Cerro Guanaco depocenter (24°47'S and 25°10'S), the Cerro Guanaco Formation crops out along the flanks of the Sierra de Varas range and is composed of ~1300 m of andesitic to dacitic lavas and pyroclastic rocks (Alfaro, 2014; González *et al*., 2015). U-Pb zircon geochronology constrains the age of this unit to *ca*. 213-200 Ma (González *et al*., 2015). Isolated gravel-rich outcrops which are similar to those from the Cerro Rincones Beds have been assigned by González *et al*. (2015) to the basal member of the Sierra de Varas Formation. These breccias unconformably overlie Permian plutonic rocks (288 ± 7 Ma; Marinovic *et al*., 1995) and are discordantly overlain by Hettangian marine rocks from the Profeta Formation (Chong, 1973; Marinovic *et al*., 1995), though a fault contact between these units has been proposed recently (González *et al*., 2015).

The Late Triassic marine transgression is represented by the lower member of the Profeta Formation (Chong and Hilldebrandt, 1985; Venegas *et al*., 2013; González *et al*., 2015; Astudillo *et al*., 2017), which comprises gravel-rich siliciclastic beds, calcareous sandstones and coral-rich boundstones of a Rhaetian age (Astudillo *et al*., 2017; Chong and Hilldebrandt, 1985; Prinz-Grimm, 1995; González *et al*., 2015). This unit conformably overlies the previous synrift units, though local angular unconformities are observed in Quebrada La Carreta (Fig. 3.4A) and Quebrada Punta del Viento (Chong and Hilldebrandt, 1985; Fig. 3.5).
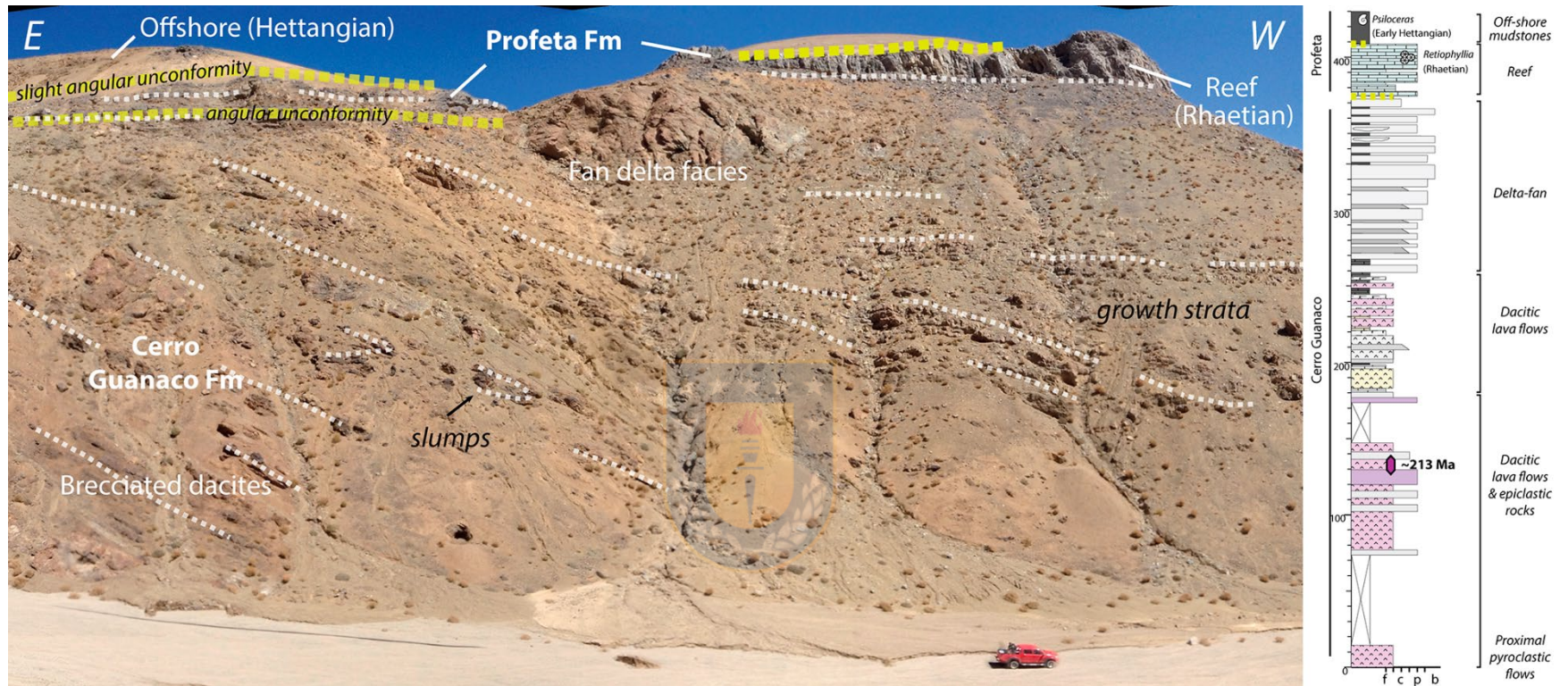
Figure 3.5: A) Slight angular unconformity between the reef facies of the Profeta Formation and the fluvial and volcanic successions of the Sierra de Varas Formation (SVF) at S8. B) Synrift listric faults affecting deltaic facies from the SVF at S7. C) Synsedimentary extensional fault controlling the location of a fluvial paleochannel, growth strata and basaltic lava flow thickness from the Quebrada del Salitre Formation at S11.

Sierra Exploradora sub-basin

To the south of the study area (Fig. 3.2), the SESB is represented by a voluminous succession of volcanic and sedimentary rocks known as the Quebrada del Salitre Formation (Naranjo and Puig, 1984; Tomlinson *et al*., 1999; Cornejo *et al*., 2009). The lower member of this unit unconformably overlies Permian plutonic rocks (Tomlinson *et al*., 1999; Cornejo *et al*., 2009), including a thick succession of coarse sedimentary rocks and a suite of dacitic, rhyolitic and basaltic volcanic rocks (Cornejo and Mpodozis, 1996; Cornejo *et al*., 2009). According to Cornejo *et al*., (2009), the upper member corresponds to transitional to marine facies, which underlies Pliensbachian beds from the Montandón Formation. However, based on the difference between the continental and marine lithofacies, we agree with the proposal of Álvarez (2003) who separates the initial shallow marine successions in the Las Bateas Formation (Rhaetian – Sinemurian). Hence, we consider the upper member of the Quebrada del Salitre Formation corresponds mainly to the continental and transitional successions developed prior to the well-developed marine deposits (Las Bateas Formation). This division has lithostratigraphic and chronostratigraphic significance, helping to make regional correlations between the sub-basins. The lower levels of the Las Bateas Formation comprise quartz-rich sandstones, conglomerates and coral-rich boundstones (Rhaetian?; Alvarez *et al*., 2003) correlating with the basal member of the Profeta Formation (González *et al*., 2015; Astudillo *et al*., 2017).

3.3 Lithofacies association and depositional environments

We performed a comprehensive facies analysis focused on the continental volcanic and sedimentary Triassic successions of the Domeyko Basin (24° - 26°S). A summary of the volcanic and sedimentary facies, their codes and interpreted genetic processes is presented in Table 3.1, while a detailed description of individual facies and interpretations can be found in the Supplementary Material SM2 (Annexe 2). Facies nomenclature follows Miall (2006) for sedimentary siliciclastic rocks, Branney and Kokelaar (1997) for pyroclastic rocks and D´Elia *et al*. (2012) for volcanic and

volcano-sedimentary rocks. Facies analysis is based on measured stratigraphic sections, field survey of key localities and complemented with lithostratigraphic studies carried out by Suarez and Bell (1992), Cornejo *et al*. (2006) and Mpodozis and Cornejo (1997) in the southern part of the studied area.

3.3.1 Facies associations

The sedimentary versus volcanic infill of the synrift stage of the Domeyko Basin present large variations across the depocenters with sedimentary deposits comprising ~60% of the observed rocks. The sedimentary assemblages developed during this stage include alluvial fan, sand-rich braided and meandering fluvial systems, lacustrine, deltaic and shallow carbonate platform assemblages. Here we present a synthesis of main facies associations and the interpreted depositional environments where they were originated (Table 3.2). Main localities of facies associations are listed in Supplementary Material SM7 (Annexe 3).

3.3.1.1 Sedimentary facies

Alluvial fan facies

Facies Association A1: Debris flows (Gmm, Sm).

This facies assemblage is mainly represented by Gmm gravel facies, corresponding to massive, matrix-supported and poorly sorted breccias (Fig. 3.6A), developing crude horizontal stratification (<5 m thick). Decimeter- to meter-scale intercalations of massive sandstone facies (Sm) are common. Gmm facies represent debris flows deposits, developed in sub-aerial to sub-aqueous conditions (Miall, 2006). Due to the lack of marine or lacustrine features (*e.g.* wave reworking, subaqueous fossils, calcareous or muddy matrix) we interpret this association as corresponding to the proximal portion of alluvial fans (Nemec and Steel, 1984; Blair and McPherson, 1994). Given that the generation of this type of *en-masse* flows is favored by steep

slopes, and its preservation in the geological record requires a high subsidence, these assemblages are inferred here to be deposited in proximity to uplifted structural blocks (Blair and McPherson, 1994, 2009). Given the inferred extensional setting, these structural blocks were likely formed via fault slip along high-angle, predominantly dip-slip normal faults.

Facies Association A2: Channelized flows (Gcm, St, Sm).

Channelized gravel bodies show lenticular to tabular geometries and are formed by clast-supported, poorly to moderately sorted, massive conglomerates of decimetric to metric scale thick (Gcm facies, Fig. 3.7G). This facies occasionally grade upward into medium- to pebbly- sized massive (Sm) and trough cross-bedded sandstones (St). This association represents the deposition of channels and/or longitudinal bars (Gcm) and sediment gravity flows (Sm) in the active lobes of alluvial fans (Selley, 2000; Miall, 2006; Nichols, 2009).

Facies Association A3: Sheetfloods (Gcm, Sh).

This facies association is mainly represented by well-stratified, tabular bodies of oligomictic and clast-supported conglomerates (Gcm), occasionally intercalated with sheets of horizontal laminated and normal graded tuffaceous sandstones (Sh). Gcm facies were originated by pseudo-plastic debris flows, while parallel-laminated sandstones (Sh) were deposited under upper flow regime conditions (Miall, 1978, 2006). This association records sheetfloods originated by turbulent flows (Koster and Steel, 1984; Nichols, 2009).

Code	Lithology	Description	Interpretation
Sedimentary			
Gmm	Breccia	Poorly sorted, massive, matrix-supported conglomerate showing crude horizontal stratification. Gravel clasts are angular to subangular ranging from pebbles to boulders	Plastic, high-strength debris flow.
Gcm	Conglomerate	Moderately sorted, massive, clast-supported conglomerate. Clasts range from pebble to large boulder and are moderately to well rounded	Pseudoplastic debris flows; hyper- concentrated flows
Gmg	Conglomerate	Matrix-supported conglomerate, normal or inverse grading	Pseudoplastic, low-strength debris flow
Sh	Sandstone	Medium- to fine-grained sandstones with horizontal lamination	Plane bed flow (critical flow)
Sm	Sandstone	Massive, very fine- to coarse-grained sandstone containing roots	Sediment gravity flow.
Sp/St	Sandstone	Cross stratified, medium to coarse grained sandstone	2-D and 3-D dune migration under lower regime conditions
Ss	Sandstone	Thin-bedded stratified sandstones; occurs as thin lenses within or alternates with facies Gmm	Scour fills
Fl	Siltstone	Interlaminated, mudstone, siltstone, and fine-grained sandstone; locally containing plant fossils	Overbank, abandoned channel, or warning flood deposits
Fm	Siltstone	Massive siltstone and mudstone; locally containing plant fossils	Deposition from suspension; back swamp, abandoned channel deposits
W, M	Limestone	Laminated and massive calcareous mudstones and wackestones	Calcareous deposition from suspension in restricted shallow marine environment
Fo	Limestone	Oncolytic floatstone	Algae originated under shallow subaqueous conditions
R	Limestone	Coarse, clast-supported bioclastic mudstones	Deposition in carbonate platform in high-energy conditions
B	Limestone	Coral-rich boundstones	Framework reefal carbonate
Bs	Limestone	Stromatolitic boundstone	Algal mats originated under shallow subaqueous conditions and low siliciclastic input
P	Limestone	Packstone limestones	Deposition in carbonate platform in high to medium energy conditions
Extrusive			
cB	Basalt	Coherent aphanitic and microporphiritic lava flows. Highly vesiculated and amygdaloidal, very altered	Subaerial mafic lava flows related to fissural volcanism
brB	Basalt	Brecciated and highly vesiculated lava flows with moderate development of peperitic textures and pseudo pillows	Hydroclastic reaction of mafic flows in contact with water or wet sediments. Subaqueous lava flows.
cA	Andesite	Coherent porphyritic lavas. Locally highly amygdaloidal	Subaerial intermediate lava flows
cD	Dacite	Coherent and massive lava flows, show aphanitic and porphyritic texture	Subaerial acidic lava flows
brA/brD	Andesite/Dacite	Autobrecciated lava flows with angular clasts in a matrix-supported fabrics and crystalline groundmass	
bcR/cjD	Rhyolite/Dacite	Coherent vitrophiric and porphyritic lavas showing flow banded textures with vertical disjunctions. Fault related	Acidic domes and necks.
Pyroclastic			
mBr	Pyroclastic breccia	Massive monomictic breccia, non-graded, seriated, poorly sorted and ash supported. Juvenile pyroclasts are dacitic porphyritic rocks	Block and ash pyroclastic flows related to dome collapse
mLT	Lapilli tuff	Massive lapilli tuff	Fluid escape-dominated flow boundary zone. Partial elutriation of fine ash and absence of tractional segregation
p-xsLT	Lapilli tuff	Pumice rich, cross stratified lapilli tuff, low angle troughs, basal scoured and moderately to well sorted	Deposition from traction-dominated flow boundary conditions. Probable surge deposits.
emLT	Tuff	Massive vitrophiric lapilli-tuff and vitric tuff, present moderately developed eutaxitic texture	Welding deformation in pyroclastic flow due to burden during hot emplacement
mT	Tuff	Massive vitric and vitric-crystal tuff	Fallout deposits
p-//sT	Tuff	Pumice rich, parallel-laminated tuff	Pumice rich fallout deposits

Table 3.1. Lithofacies codes and corresponding depositional processes interpreted in this study.

Type	Depositional environment	Facies association	Code	Facies
Sedimentary	Alluvial fan	Debris flow	A1	*Gmm, Sm*
		Channelized flows	A2	*Gcm, St, Sm*
		Sheetflood flows	A3	*Gcm, Sh*
	Fluvial	Sand-rich braided river	F1	*Gcm, St, Sp, Sh, Sm, Fm*
		Meandering river	F2	*Fl, Fm, Sm, Sh*
	Lacustrine	Marginal lacustrine	L1	*Fo, Bs, Gmm, Gcm*
		Basinal lacustrine	L2	*Fl, Sm*
	Shallow marine	Delta-fan	SM1	*Gmg, Gmm, Gcm, St, Ss, M*
		Rimmed carbonate shelf	SM2	*B, R, P, W, M, Sm*
Volcanic	Basaltic volcanism	Basaltic subaerial & partly subaqueous volcanism	VB1	*cB, brB*
	Intermediate volcanism	Intermediate subaerial lava flows	VI1	*cA, cD, brA, brD*
	Silicic explosive volcanism	Silicic domes & proximal pyroclastic deposits	VS1	*bcR, cjD, mBr, emLT*
		Medium to distal pyroclastic deposits	VS2	*mT,//sT, p-//sT*

Table 3.2. Facies association codes defined in this study. Locations where each facies is found can be found in the Supplementary Material

Fluvial facies

Facies Association F1: Sand-rich braided rivers (Gcm, St, Sp, Sh, Sm, Fm).

The architecture of this facies assemblage corresponds to channel bedforms embedded in thick overbank deposits (Fig. 3.6). Channelized bedforms are represented by trough-cross bedded sandstones (St) formed by 3-D dune migration, and massive sandstones (Sm). Fine facies (Fm) represents deposition from standing water in the floodplain during low-stage abandonment of channels. Occasional Sh facies would represents sporadic spill out floods into the overbank area (Miall, 2006).

Facies Association F2: Meandering rivers (Fl, Fm, Sm, Sh).

This facies association corresponds to massive and laminated fine facies (Fm and Fl), formed by quartz-rich siltstones to very fine sandstones, intercalated with thin sheets of massive (Sm) and horizontally stratified sandstones (Sh) (Fig. 3.6C). Fine facies occasionally incorporates Late Triassic fossil flora (Fig. 3.6B; see Supplementary Material SM6 for detailed descriptions) indicating deposition in a floodplain with

36

abundant vegetation (Miall, 2006). The presence of siderite nodules points to a deposition under reducing conditions with a mixing of seawater and freshwater (Nichols, 2009), suggesting a coastal meandering fluvial origin for these facies. On the other hand, sandy facies represents sediment gravity flows (Sm) and deposition under upper plane conditions (Sh), probably related to sporadic bank collapse and/or crevasse splays over the floodplain environment (Walker and James, 1992; Miall, 2006).

Lacustrine facies

Facies Association L1: Basinal lacustrine (Fl, Sm).

Finely laminated mudstones (Fl facies) corresponds to greyish to greenish mudstones, displaying millimetric lamination ('laminites', Fig. 3.6E), with common intercalations of pyroclastic fall deposits (//sT facies). Occasionally, they present centimetric-scale 'cast and flame' load structures and ripple bedding. Fine facies represents deposition by suspension and weak traction currents (Miall, 2006). The well-preserved 'laminites' indicates the absence of bioturbating bottom fauna and seasonal variation in phytoplankton production, pointing to a deposition under open water lake conditions in a deep basinal setting (Platt and Wright, 1991), while Sm facies and the load-cast features suggest the development of sporadic sandy turbidites (Nichols, 2009), probably in a high-gradient, bench type margin lake (Platt and Wright, 1991).

Facies Association L2: Marginal lacustrine facies (Fo, Bs, Gmm, Gcm).

Stromatolitic boundstone facies (Bs), is formed by dark-greyish microbial limestones (algal mats and stromatolites) showing parallel and convolute bedding, originated in shallow lake shorelines under good illumination conditions (Nichols, 2009). Oncolytic floatstone facies (Fo, Fig. 3.6F) exhibits intercalations of coarse siliciclastic beds (Gmm, Gcm), indicating progradation of alluvial fans over swamps in a palustrine environment (Wright and Platt, 1995; Alonso-Zarza and Tanner, 2009). These marginal

lacustrine facies were formed in shallow and ephemeral lakes associated with a low-gradient ramp margin, where the sediment supply and accommodation space were similar (Platt and Wright, 1991).

Shallow marine facies

Facies Association SM1: Delta fans (Gmg, Gmm, Gcm, St, Ss, M).

Gravel-facies consist of pale grey Gmm, Gcm and Gmg facies, corresponding to debris flows (Miall, 2006) deposited first in alluvial fans, and then into a shallow marine carbonate platform as indicated by the intercalations of limestones (M facies) and the increasing input of bioclastic fragments (McPherson *et al.*, 1987; Benvenuti, 2003; Blair and McPherson, 2009). Conglomerates display poor sorting and coarsening-upward cycles with clast sizes ranging from pebbles to large boulders (Fig. 3.5) with outsized clasts that are up to 1.12 m in diameter (Fig. 3.6D), immersed in a fine-grained calcareous matrix. Intercalated in these facies are green calcareous mudstones and medium- to pebble-sized calcareous sandstones, with trough cross stratification (St facies) and scoured bases (Ss facies).

Facies Association SM2: Rimmed carbonate shelf (B, R, P, W, M, Sm).

This facies association is characterized by calcareous coral-rich facies formed by greyish, irregular beds of coral-rich boundstones (B facies, Figs. 5 and 6G), bearing Late Triassic Retiophyllia sp. and Thecosmilia sp. fossil flora corresponding to the core of reefal frameworks (Chong, 1977; Ardill *et al.*, 1998; Montecino, 2015; González *et al.*, 2015). Intercalations of rudstone (R facies) and packstone limestones (P facies) are composed of fragments of bivalves, brachiopods, shell debris and corals. According to Nichols (2009), the local, intercalations of massive litharenites (Sm) and laminated calcareous mudstones (M facies) would indicate a deposition by suspension fallout in protected areas, probably in a back-reef to lagoon environment. This assemblage represents a shallow marine carbonate platform limited by a mounded-reef ('rimmed

carbonate shelf') with an intermittent siliciclastic input (Nichols, 2009). This reefal facies marks the beginning of a marine transgression of regional significance along the Domeyko Range (Chong, 1973; Chong and Hilldebrandt, 1985; Gröschke *et al.*, 1988). The presence of Retiophyllia sp. and Choristoceras sp. in equivalent facies across the Domeyko Basin indicates a Rhaetian age for the onset of the marine transgression (Chong and Hilldebrandt, 1985; Ardill, 1996; Navea *et al.*, 2015).

3.3.1.2 Volcanic facies

Volcanic lithofacies present important variations across the sub-basins, with a mainly intermediate composition (andesites to dacites) at the Sierra de Varas sub-basin and a predominant mafic composition (basalts to basaltic andesites) with acidic and minor intermediate volcanic deposits at the Sierra Exploradora sub-basin.

Volcanic facies of basaltic composition

Facies Association VB1: Basaltic subaerial and partly subaqueous volcanism (cB, brB).

Mafic volcanic rocks crop out extensively in the southern portion of the study area (see Table T2), with thicknesses varying from tens of meters (~ 60 m) in Quebrada Los Pozos (S7, Fig. 3.2) to hundreds of meters (>600 m, Fig. 3.7C) in Quebrada del Salitre (S10, Fig. 3.2). This facies assemblage mainly corresponds to dark-green, coherent basalts and basaltic andesites (cB facies, Fig. 3.7C) which form decimetric to metric scale irregular beds displaying a high proportion of vesicles and calcite-filled amygdales. Coherent basaltic facies (cB) represents subaerial mafic effusive volcanism (McPhie *et al.*, 1993). Locally, basalts exhibit a brecciated texture (brB facies), corresponding to mixed lava fragments and silicified red-colored sediments (peperitic texture, Fig. 3.7E), indicating interaction of lava and wet sediments (Busby-Spera and White, 1987; Doyle, 2000), or pillow-breccias (Fig. 3.7B), evidencing partial deposition under subaqueous conditions (Cas and Wright, 1988; White and Houghton, 2006).

Figure 3.6: A) Gmm facies developed in proximal alluvial fan facies (debris flows) from the basal member of Sierra de Varas Formation (SVF) at Sierra de Varas depocenter. B) Late Triassic fossil flora developed in floodplain assemblage from SVF at S7. C) A synsedimentary extensional fault affecting meandering fluvial assemblages from basal successions of the SVF at S7. D) Matrix-supported gravel facies developed in a fan delta assemblage from the Cerro Guanaco Formation at S6. E) Basinal lacustrine facies (Fl facies) from SVF at S7. F) Oncolite-bearing floatstone facies deposited in marginal lacustrine conditions from the SVF at S3. G) Boundstone facies from the Las Bateas Formation bearing Late Triassic corals (Retiophyllia sp.) at S11.

Volcanic facies of intermediate composition

Facies Association VI1: Intermediate subaerial lava flows (cA, cD, brA, brD).

Intermediate composition volcanic rocks crop out discontinuously across the entire Domeyko Range. Andesitic volcanism is common in the northern portion of the study area (Cerro La Ballena depocenter), while dacitic and subordinate andesitic volcanism predominates to the south (Vaquillas Altas depocenter and SESB). Andesitic to dacitic coherent facies (cA and cD facies), form massive and vesiculated beds (0.4 – 2 m thick), showing a porphyritic texture (Fig. 3.5) composed by medium-grained phenocrysts (pg + amph ± qtz) embedded in a glassy or microcrystalline groundmass. These facies correspond to lava flows originated under low shear rates in subaerial conditions (Stewart and McPhie, 2003). Locally, matrix-supported, brecciated dacites and andesites (brD, Fig. 3.7F, and brA facies) were originated by an autoclastic, brittle fragmentation mechanism, due to the lateral transport of lava flows under subaerial conditions (McPhie *et al*., 1993; Stewart and McPhie, 2006).

Subvolcanic and pyroclastic silicic facies

Facies Association VA1: Silicic domes and proximal pyroclastic deposits (bcR, cjD, mBr, mLT).

Coherent vitrophyric rhyolites (bcR) and dacites (cjD) present flow banding and vertical columnar jointing (Fig. 3.7D), indicating the flow advance and cooling margins of small domes and vents (Fink and Anderson, 2000). At SESB, these domes form elongated bodies (1.6 to 2.2 km long) which are spatially associated with ~NS trending extensional faults (Cornejo *et al*., 2009). Large vents are recorded by sub-circular silicic domes bounded by arcuate ring normal faults (~5 km of diameter, Tomlinson *et al*., 1999) associated with dome-margin breccias (mBr), suggesting an extensional origin for these vents, with a plate (piston) mechanism for the subsidence (Lipman, 2000).

At Cerro Guanaco depocenter (S5 and S6 in Fig. 3.9), matrix-supported, and monomictic massive pyroclastic breccias (mBr) are spatially associated with dacitic

domes and are interpreted as block-and-ash pyroclastic flow deposits related to the gravitational collapse of lava domes (Cas and Wright, 1988; Freundt *et al*., 2000; Branney and Kokelaar, 2002). Ignimbrite deposits are recorded by very poorly sorted massive lapilli-tuffs (mLT facies), which are formed by lapilli-sized pumice, crystal fragments and lithics in a vitric matrix. The common thickness of mLT facies at Vaquillas Altas depocenter are up to ~30 m thick, though similar facies can be thicker at Cerro Guanaco (Alfaro, 2014; González *et al*., 2015) and Cerro La Ballena (Valenzuela, 2014) depocenters. There is a general lack of evidence of high-temperature welding (*e.g.* sintering of glass shards, rheomorphism, etc.), with some ignimbrites showing a pseudo-eutaxitic texture due to diagenetic alteration.

Facies Association VA2: Medium to distal pyroclastic deposits (mT, sT, p-//sT).

Reddish- to greenish- massive tuffs (mT) are composed of well-sorted pumice, crystals and minor lithics in a vitreous ash-sized matrix, making up centimetric beds (< 1 m). This facies can corresponds to the deposition of fine-grained distal ignimbrites or fallout deposits (Fisher and Schmincke, 1984; Cas and Wright, 1988; Branney and Kokelaar, 2002). On the other hand, well-stratified (occasionally laminated) and very well-sorted //sT facies present a similar composition that mT facies. The //sT facies could represent distal fallout of eruption plumes, ash-rich pyroclastic density currents or surges deposits (Cas and Wright, 1988; Branney and Kokelaar, 2002), however its common association with lacustrine mudstones, its generally low thickness (0.3-0.6 m) and the absence of lateral transport evidences (scours, cross-stratification, low-angle truncations), points to a fallout origin (Cas and Wright, 1988; McPhie *et al*., 1993; Branney and Kokelaar, 2002; D'Elia *et al*., 2012). Occasionally, similar pumiceous-rich tuffs (p-//sT facies) show subangular pumice clasts indicating a similar fallout origin (Branney and Kokelaar, 2002).
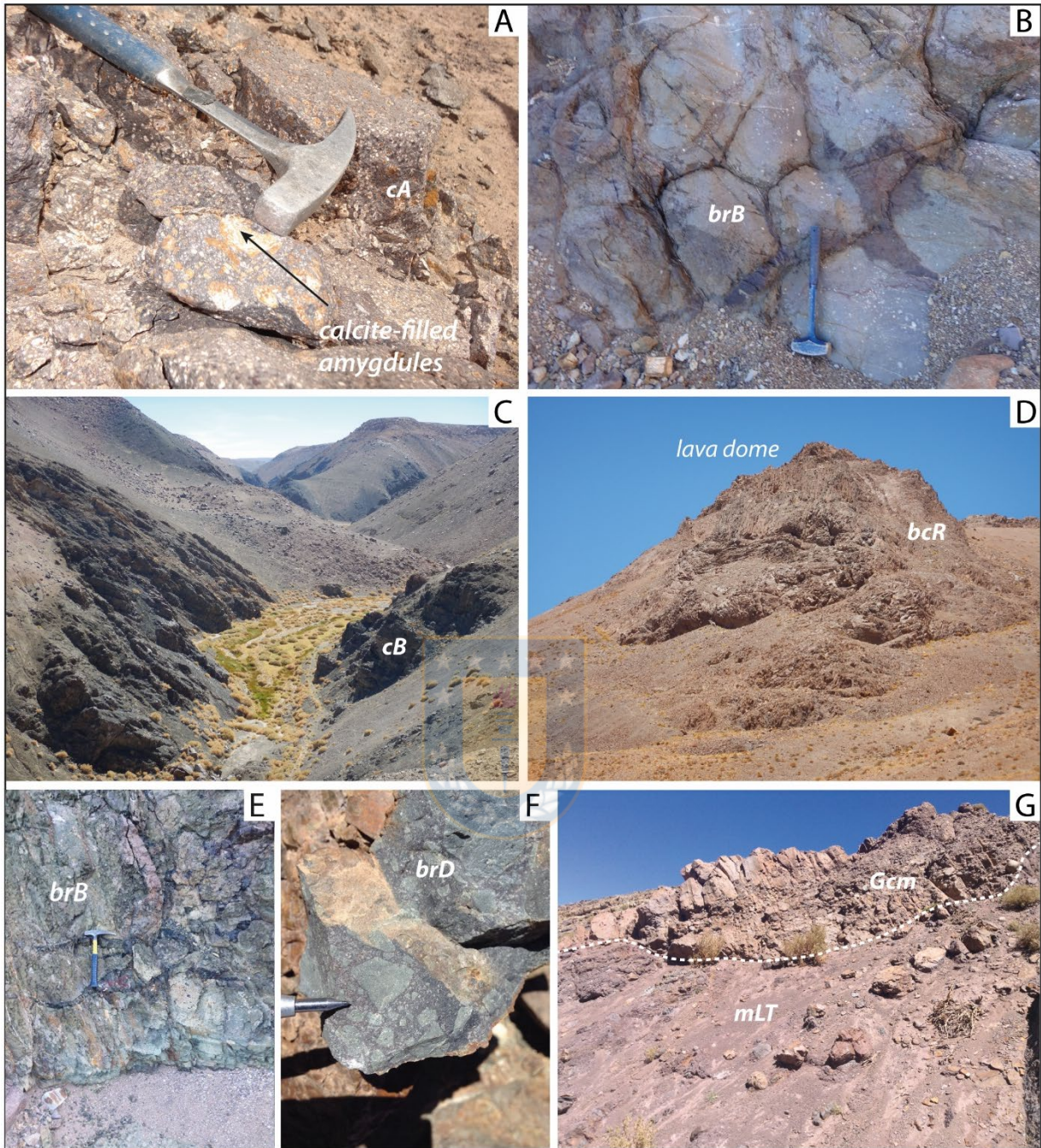
Figure 3.7: Volcanic facies at the studied sub-basins. A) Coherent andesites (cA) from Cerro La Ballena Formation at S1. B) Brecciated basalts (brB) from Quebrada del Salitre Formation showing pseudo-pillow structures at S7. C) Coherent basalts (cB) successions at S10. D) Silicic lava dome formed by coherent rhyolites (bcR) from the Quebrada del Salitre Formation showing vertical columnar jointing at Cerro Colorado. E) Peperites. F) Brecciated dacites facies (brD) at S6. G) Channelized flows (alluvial fan) incised over massive lapilli-tuffs (mLT) from the SVF at S7.

3.4 Geochronological analysis

3.4.1 Analytical methods

U-Pb igneous and detrital zircon analyses were performed using laser-ablation inductively-coupled-plasma mass-spectrometry (LA-ICP-MS and LA-MC-ICP-MS) method in ten samples. Lithostratigraphic units sampled correspond to the continental, sedimentary and volcanic, Sierra de Varas, Cerro Guanaco and, Quebrada del Salitre formations.

Heavy minerals were concentrated by standard crushing, Gemini table, LST heavy liquid (2.9 gr/cm3) and magnetic separation techniques at Servicio Nacional de Geología and Minería and University of Concepción. Finally, zircon grains were handpicked under a binocular microscope, mounted in epoxy, and polished to expose grain centers for cathodoluminescence (CL) imaging. U-Pb analysis of samples CPV-14-157, CPV-14-254, CPV-14-261, and CPV-14-268 were performed at the Arizona LaserChron Center (ALC), University of Arizona, while samples CPV-15-310, CPV-15-316, CPV-15-324, CPV-15-342, CPV-15-350 and CPV-16-400 were analyzed at the Laboratorio de Estudios Isotópicos (LEI), Centro de Geociencias, UNAM. Concordia and average ages were calculated using Isoplot v. 4.15 (Ludwig, 2008). We apply a discordance filter of < 15 % for igneous analyses, while for detrital analyses, a discordance filter < 25 %, and a reverse discordance filter of > -5 % were used. 206Pb/238U ages are preferred for zircons younger than <1.0 Ga, while 207Pb/206Pb ages are reported for zircons older than that age (Gehrels, 2011). A detailed description of the analytical techniques is in Supplementary Material SM5 (Annexe 4).

3.4.2 U-Pb geochronology

Geochronological results and sample locations are summarized in Table 3.3 and Figure 3.8. Errors are reported as 2σ and maximum depositional ages (MDA) were calculated averaging the 3 or more zircons overlapping at 2σ error, except for sample CPV-14-254, where 2 zircons overlapping at 1σ error was used (Dickinson and

Gehrels, 2009). Detailed isotopic and rejected data of U-Pb analysis are found in Supplementary Material SM3 and SM4 (Annexe 8).

U-Pb geochronology			Sample Location			Igneous Zircon (IZ)		Detrital Zircon (DZ)	
Sample	Lithology	Lithostratigraphic unit	UTM N	UTM E	n	Concordia Age (Ma)	Weighted Mean Age (Ma)	Maximum Depositional Age (Ma)*	Major Peak (Ma)
CPV-14-157	Volcanic breccia	Cerro Guanaco	7225857	475701	33	211.5±1.8 (n=28)	-	-	-
CPV-15-400	Vitric tuff	Sierra de Varas	7197540	477638	15	208.4±2.3 (n=8)	-	-	-
CPV-14-268	Vitric tuff	Sierra de Varas	7311340	480355	35	-	203.5±1.6 (n=20)	-	-
CPV-15-310	Rhyolite	Quebrada del Salitre	7114194	462332	38	-	225.2±1.5 (n=26)	-	-
CPV-15-350	Lapilli tuff	Sierra de Varas	7201630	471834	31	-	210.7±3.4 (n=3)	-	-
CPV-14-254	Quartz-rich sandstone	Sierra de Varas	7200644	475282	105	-	-	234.4±4.8 (n=2)**	~297
CPV-15-342	Quartz-rich sandstone	Sierra de Varas.	7201928	471961	107	-	-	213.8±3.1 (n=4)	~292
CPV-14-261	Breccia	Sierra de Varas	7252939	479730	35	-	-	303.3±2.1 (n=33)	~303
CPV-15-316	Sandstone	Quebrada del Salitre	7125508	468083	120	-	-	241.5±4.0 (n=3)	~294
CPV-15-324	Sandstone	Quebrada del Salitre	7115254	470733	35	-	-	208.4±3.4 (n=3)	~260

*Maximum depositional age calculated from the 3 or more zircons overlapping at 2σ which define a separate peak

**Maximum depositional age calculated from the 2 youngest zircons overlapping at 1σ

Tabla 3.3. U-Pb geochronological data from this study

3.4.2.1 Sierra de Varas Formation

Detrital zircons (DZ) from a coarse-grained sandstone intercalated in monomictic massive breccias (CPV-14-261) corresponding to the Lower Member of the Sierra de Varas Formation (González *et al.*, 2015), yielded a unimodal age distribution with a weighted mean age of 303.3 ± 2.1 Ma which is interpreted as the MDA. The breccias overly in unconformity Permian plutonic rocks with a K-Ar (biotite) age of 288 ± 7 Ma (Marinovic *et al.*, 1995), suggesting a significant gap between the MDA and the depositional age for this unit.

DZ age distribution from a coarse sandstone intercalated in conglomeratic facies at the base of the Sierra de Varas Formation (CPV-15-342) shows the main peak at *ca.* 292 Ma (~80%) and a minor peak at *ca.* 246 Ma (~12%) with an MDA of 213.8 ± 3.1 Ma. Another DZ sample from this unit (CPV-14-254), a quartz-rich sandstone directly overlying Carboniferous-Permian plutonic rocks (Punta del Viento Plutonic

Complex), shows a main age peak at ~297 Ma (77%) and two smaller groups at ~479 Ma (9%) and ~246 Ma (3%), with scarce zircons older than 500 Ma and a MDA of 234.4 ± 4.8 Ma. Thus, both samples from the basal successions indicate the main source from the Permian basement (292-297 Ma), with more restricted secondary sources from Middle Triassic (~246 Ma) and Ordovician (~478 Ma) rocks.

Igneous zircon (IZ) from a lapilli-tuff sampled 40 m above the base of the unit (CPV-15-350) yielded a major peak at *ca.* 227 Ma and a secondary peak at *ca.* 211 Ma. We interpret the youngest peak as the age of the eruptive event, yielding a weighted mean age (WMA) of 210.7±3.4, while the secondary peak at *ca.* 227 Ma would correspond mostly to accessory sources. A vitric tuff (CPV-14-268) intercalated in the upper levels of a lacustrine succession (Fig. 3.8) yielded a WMA of 203.5 ± 1.6 Ma interpreted as the age of the volcanic event. An older small peak at *ca.* 283 Ma is probably associated to accidental fragments. On the other hand, an IZ sample from a vitric-tuff intercalated in fluvial deposits (CPV-15-400) yielded a Concordia age of 208.6 ± 2.3 Ma, interpreted as the crystallization age of the pyroclastic event.

3.4.2.2 Cerro Guanaco Formation

IZ from a brecciated dacite (CPV-14-157) yielded a Concordia age of 211.5 ±1.8 interpreted as the crystallization age. This lithostratigraphic unit was formerly assigned to the Carboniferous-Permian La Tabla Formation (Venegas *et al*., 2013). However, taking into account the Norian crystallization age and the interpretation of the dated level as part of proximal acidic dome deposits, we assign these outcrops to the Cerro Guanaco Formation (Alfaro, 2014; González *et al*., 2015).

3.4.2.3 Quebrada del Salitre Formation

IZ from a banded rhyolite belonging to a silicic dome (CPV-15-310) yielded a WMA of 226.7 ± 1.4 Ma interpreted as the timing of the volcanic event, while a secondary group at *ca.* 241 Ma is inferred to represent accessory material from the volcanic conduit. A litharenite corresponding to sand-rich fluvial deposits from the basal

member of this unit (CPV-15-316) yielded an MDA of 241.5±4.0 Ma with a major peak at ca 294 Ma (41%) and a secondary peak at ~267 Ma (12%). Another DZ sample from a tuffaceous sandstone corresponding to meandering fluvial facies from the upper continental member of this unit, shows an MDA of 208.4±3.4 Ma and major peaks at *ca.* 258 Ma (47%) and *ca.* 272 Ma (24%).
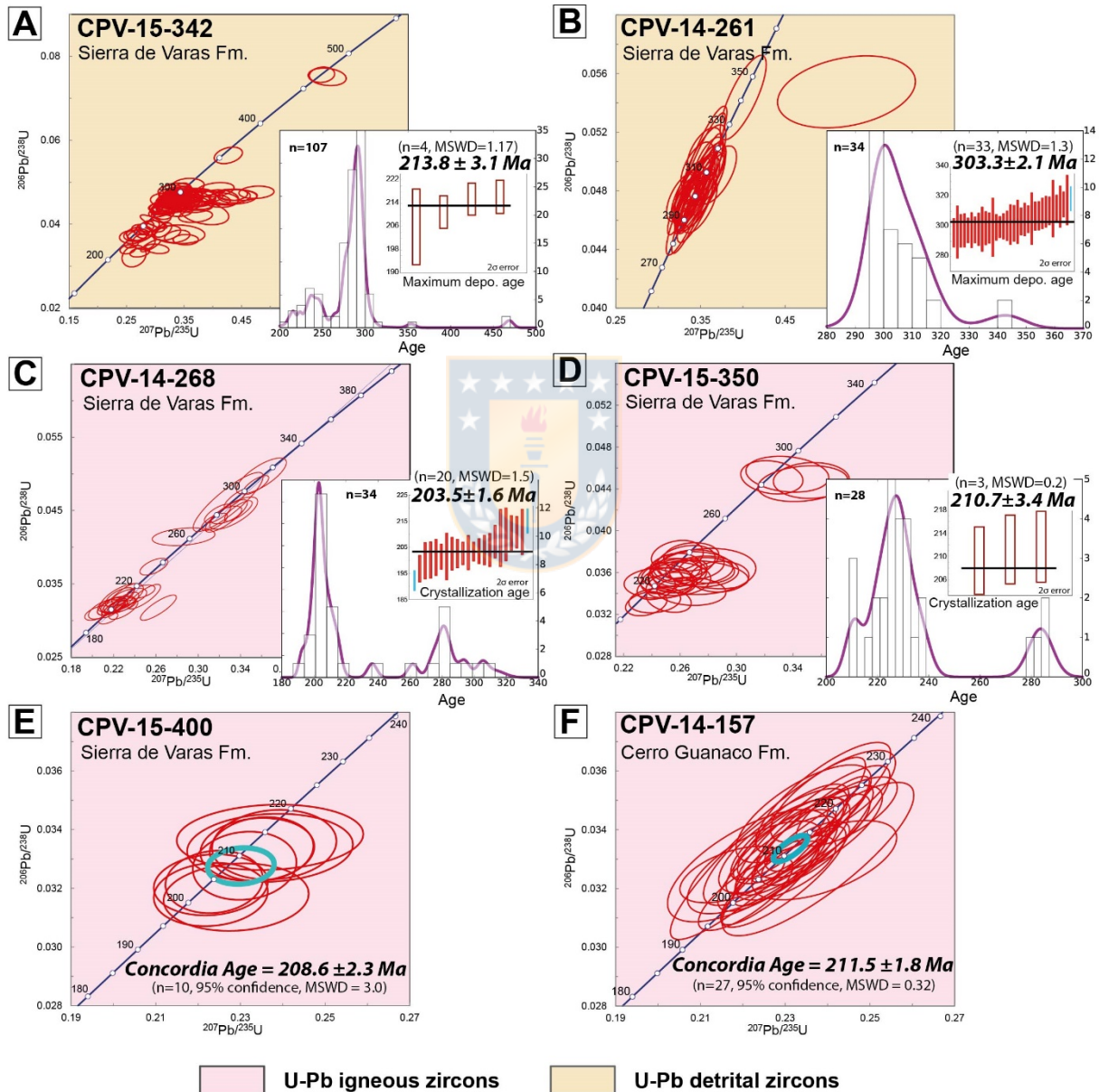
Figure 3.8: U-Pb in zircon geochronological data from this study. Orange/pink filled graphs are detrital/igneous analyses.
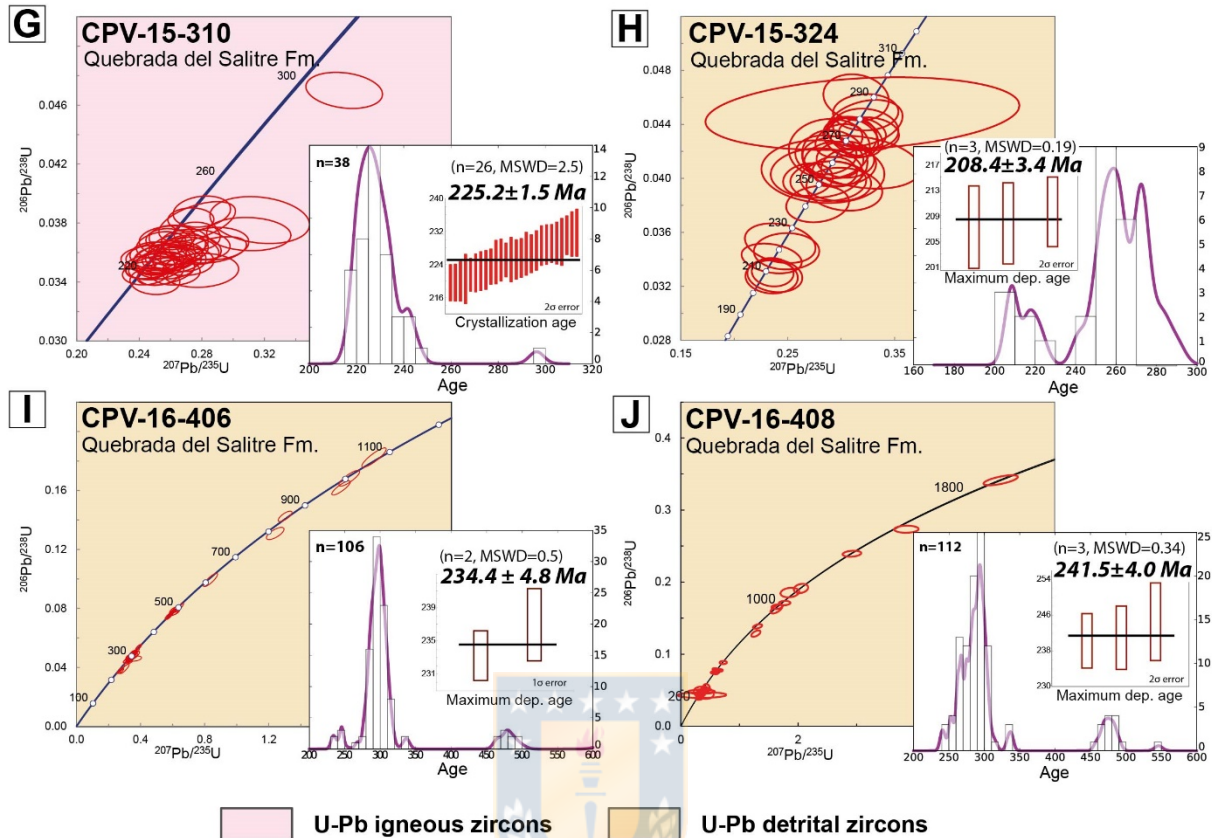
Figure 3.8: (continuation)

3.5 Discussion

3.5.1 Stratigraphic correlations across the Domeyko Basin

Given the abrupt facies changes across depocenters and the common incomplete exposure of many sections due to Cenozoic Andean faulting, there are scarce correlations for the logged synrift deposits. The most easily correlated unit is the 'upper' Rhaetian marine transgression marked by the presence of coral-rich reef boundstones (Fig. 3.6G) developed in a rimmed carbonate shelf at the base of the Profeta and Las Bateas formations (Chong and Hilldebrandt, 1985; Ardill *et al.*, 1998; Álvarez, 2003; Cornejo *et al.*, 2009; Venegas *et al.*, 2013; González *et al.*, 2015; Astudillo *et al.*, 2017), which is observed in most of the depocenters (Fig. 3.9). The beginning of the synrift can be correlated at the base of the sections S7 and S8 in the

48

Vaquillas Altas depocenter for the Sierra de Varas Formation and between the base of S4 and S5 sections in the Sierra de Varas and the Cerro Guanaco depocenters for the Sierra de Varas and the Cerro Guanaco formations, respectively. Secondary correlations based on sedimentary facies can be suggested between the meandering fluvial systems that follow the thick basaltic successions of the Quebrada del Salitre Formation (S10 and S11) and the Sierra de Varas Formation (S7 and S8) at the Vaquillas Altas depocenter (Fig. 3.9).

3.5.2 Timeframe of the synrift activity

In the Domeyko Basin, we propose that two stages of major mechanical subsidence and associated sedimentation were developed during the Triassic (Fig. 3.10). The Synrift I would have taken place in the SESB, during the Ladinian – Carnian (~240 - 225 Ma). The lower limit is constrained by the DZ MDA of 241.5 ± 4.0 Ma from sand-rich braided fluvial facies (CPV-15-316; Figs 3.8J and S10 in Fig. 3.9) and the upper limit by the IZ age of rhyolitic domes which have been dated at 225.2±1.5 Ma (CPV-15-310, Fig. 3.8G and S10 in Fig. 3.9). The Synrift II ('upper' Norian – Rhaetian; 217-200 Ma) is well constrained by the initiation of the SVSB at *ca.* ~213-210 Ma (Figs. 3.9 and 3.10). The upper limit of the Synrift II is constrained by the Rhaetian marine transgression and a U-Pb IZ age of 200±2 Ma (González *et al*., 2015) from the uppermost synrift beds in the Cerro Guanaco depocenter (section S5, Fig. 3.9). The activity of the SESB during the Synrift II can be established by the DZ MDA of meandering fluvial facies (208.4±3.4 Ma) which are overlain by Rhaetian shallow marine facies from the Las Bateas Formation (Álvarez, 2003). The initiation age of Synrift II at SESB is very problematic to resolve due to the low zircon fertility of basaltic lavas inferred to represent the basal part of the Synrift II (S10, Fig. 3.9). The later raise the possibility that a relatively continuous deposition took place at the SESB, without the inferred hiatus between the two synrift stages. However, considering a more regional context, the scattered sedimentary record from the 'Synrift I stage' occurred mainly in isolated small basins peripheral to the Domeyko Range which do not record deposition during the Synrift II stage, such as the El Bordo (Basso and Marinovic,

2003), Tuina (Henríquez *et al*. 2014) and Pular (Solari *et al*. 2015) formations (Fig. 3.1), suggesting that the volcanism and sedimentation during the Synrift I stage was discontinuous to the Synrift II stage. On the other hand, the well-marked initiation of depocenters at ~212 Ma such as the SVSB and the Cifuncho basin at the Coastal Cordillera (Contreras *et al*., 2013; Espinoza *et al*., 2015) seems to indicate that the Synrift II stage was a well distinguishable event across the paleo-margin. We propose both stages were clearly differentiated and infer that the activity of the SESB during the Synrift II stage took place in a similar timeframe as the SVSB, though further geochronological constraints are needed to confirm this hypothesis.

D O M E Y K O   B A S I N   S Y N - R I F T   A R C H I T E C T U R E

51
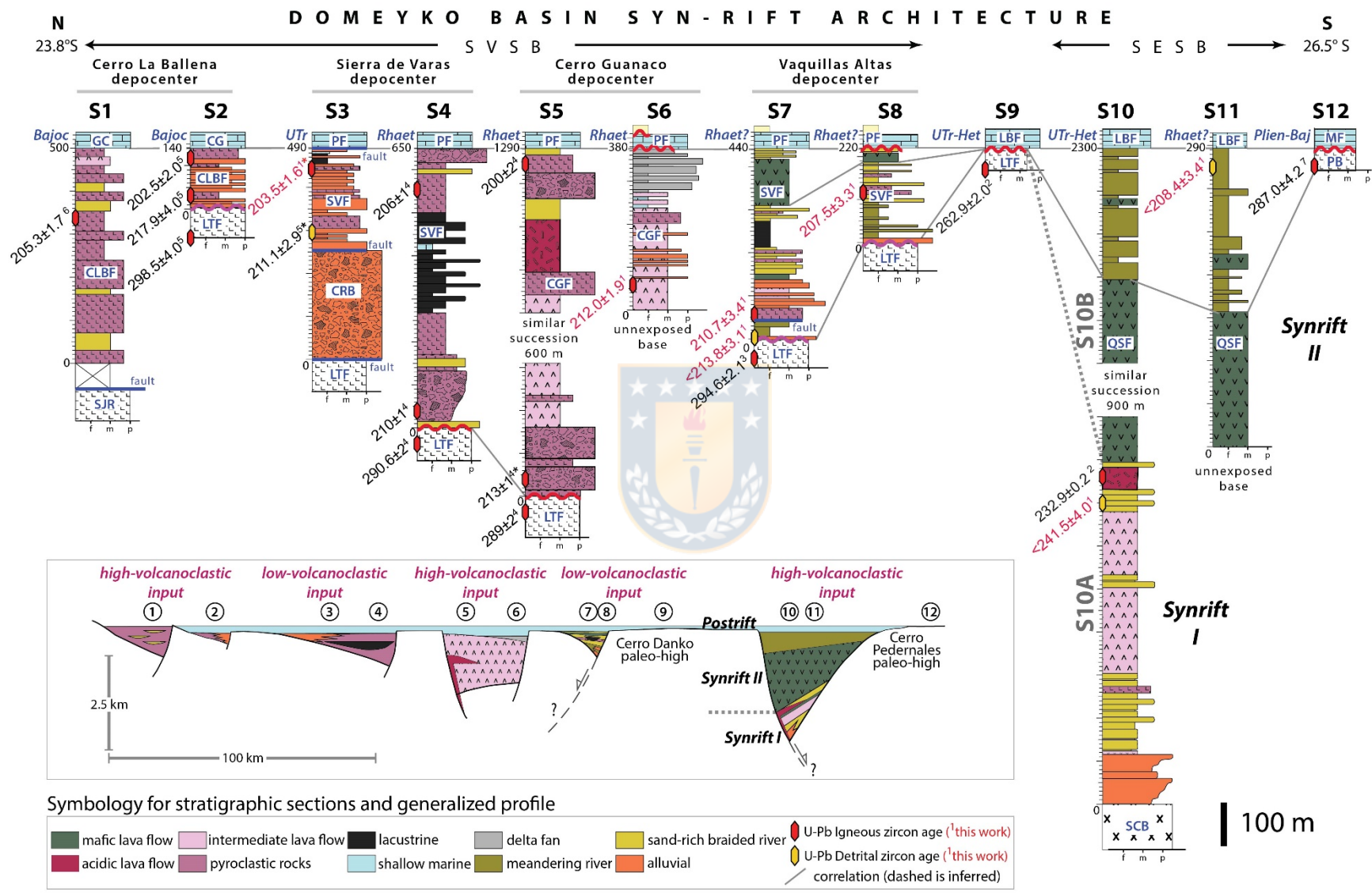
Figure 3.9: Domeyko Basin synrift architecture based in generalized sections across the Domeyko Range. References for sections are: this work (S2, S3, S6, S7 and S8); this work and Cornejo *et al*. 2009 (S10); this work and Suárez and Bell 1992 (S11); Valenzuela, 2014 (S1); Contreras, 2014 (S4): González *et al*. 2015 (S5); Cornejo *et al*., 2009 (S9) and Tomlinson *et al*. 1999 (S12) (for section locations see Figure 3.2). Lithostratigraphic unit abbreviations are as follow: SJR (Sierra Jardín Rhyolites), CLBF (Cerro La Ballena Formation), CG (Caracoles Group), LTF (La Tabla Formation), PF (Profeta Formation), SVF (Sierra de Varas Formation), CRB (Cerro Rincones Beds), CGF (Cerro Guanaco Formation), LBF (Las Bateas Formation), QSF (Quebrada del Salitre Formation), SCB (Sierra Castillo batholith), MF (Montandón Formation) and PB (Pedernales batholith). References for U-Pb ages are: [1] (this work, red colored), [2] (Cornejo *et al*., 2009), [3] (Venegas *et al*., 2013), [4] (González *et al*., 2015), [5] (Astudillo *et al*., 2017), [6] (Matthews *et al*., 2007), [7] (Maksaev *et al*., 2014). In the generañized profile (N-S direction), extensional structures correspond to oblique NW-SE inferred basin margin faults. Different depocenters have been classified as "lower/high-volcaniclastic" based on the impact of volcanism in the evolution of sedimentary systems (D'Elia *et al*., 2016).

3.5.3 Tectonostratigraphic evolution of the synrift Domeyko Basin: an interaction between sedimentary, volcanic and tectonic processes

Sedimentary systems are the result of the balance between the accommodation space (A) and sediment supply (S) to the basin. The accommodation space is related to the space available below the base level in order for sediments to accumulate (Jervey, 1988). In non-marine environments, base level is better defined by the 'stratigraphic base level' (Martinsen *et al*., 1999), which is the equilibrium surface that "describes the direction in which a stratigraphic system is likely to move, toward sedimentation and stratigraphic preservation or sediment bypass and erosion" (Shanley and McCabe, 1994). Thus, we use the 'subaerial accommodation space' defined as 'the space developed between successive depositional surfaces of different ages' (Muto and Steel, 2000), which is most commonly driven by changing subsidence, uplift or eustatic sea level and is represented by the thickness of preserved sediment in the stratigraphic record (Muto and Steel, 2000). In non-marine basins, eustatic level changes are negligible (Martinsen *et al*., 1999). On the other hand, tectonic subsidence commonly affects strongly the accommodation space than climatic effects (Schlische, 1991; Prosser, 1993; Derer *et al*., 2005; Martins-Neto and Catuneanu, 2010). However, the later can account for higher frequency changes in sedimentary environments (Carroll and Bohacs, 1999), as observed in some rift lakes from East Africa (Lake Tanganyika, Lake Malawi and Lake Turkana; Scholz *et al*., 1990; Scholz *et al*., 2007;

Johnson *et al*., 1987) and United States (Lake Lahonton; Benson and Thomson, 1987). During the Triassic, major climatic fluctuations at the Domeyko Basin are poorly recorded, maintaining a main subtropical climate, though sporadic drought episodes have been proposed at the Coastal Cordillera (Suárez and Bell, 1994, 2010). However, the development of very different sedimentary environments in both sub-basins during a similar period (Synrift II stage), such as lacustrine and alluvial facies associations in the SVSB and meandering rivers in the SESB, let us to infer that the base level variations were mainly controlled by local variations in the subsidence regime rather than climatic fluctuations which should have allowed the development of similar sedimentary environments in a broader area.

In the following section, the evolution of the synrift stages in the SVSB and SESB is analyzed interpreting changes in the stratigraphic record (A/S) as due to the interplay between sedimentary, volcanic and tectonic processes.

3.5.3.1 Synrift I (~240 - 225 Ma)

3.5.3.1.1 Sierra Exploradora sub-basin

The Synrift I stage (Fig. 3.12A) recorded the deposition of coarse alluvial fan facies (A/S < 1; Martinsen *et al*., 1999) with a thickening-upward trend (base of S10, Fig. 3.9), that according to (Gawthorpe and Leeder, 2000), would result from very low A/S due to low subsidence rates during basin initiation. The alluvial fans are followed by sand-rich braided rivers indicating a slight increase in the A/S ratio (S10 in Fig. 3.9). This was accompanied by subaerial intermediate volcanism which added a significant supply to the basin (S10, Fig. 3.9). During the Carnian, deposition to the basin was marked by a profuse silicic magmatism evidenced by the extrusion of rhyolitic domes spatially related to high-angle extensional structures with a current ~NS trend (Fig. 3.12A). Explosive volcanic activity is recorded by the proximal deposition of ignimbrites near to silicic vents. The scarcity of major epiclastic sedimentation indicates the predominance of a high volcaniclastic material supply during this period, with restricted deposition of sand-rich braided fluvial facies (A/S < 1 ratio).
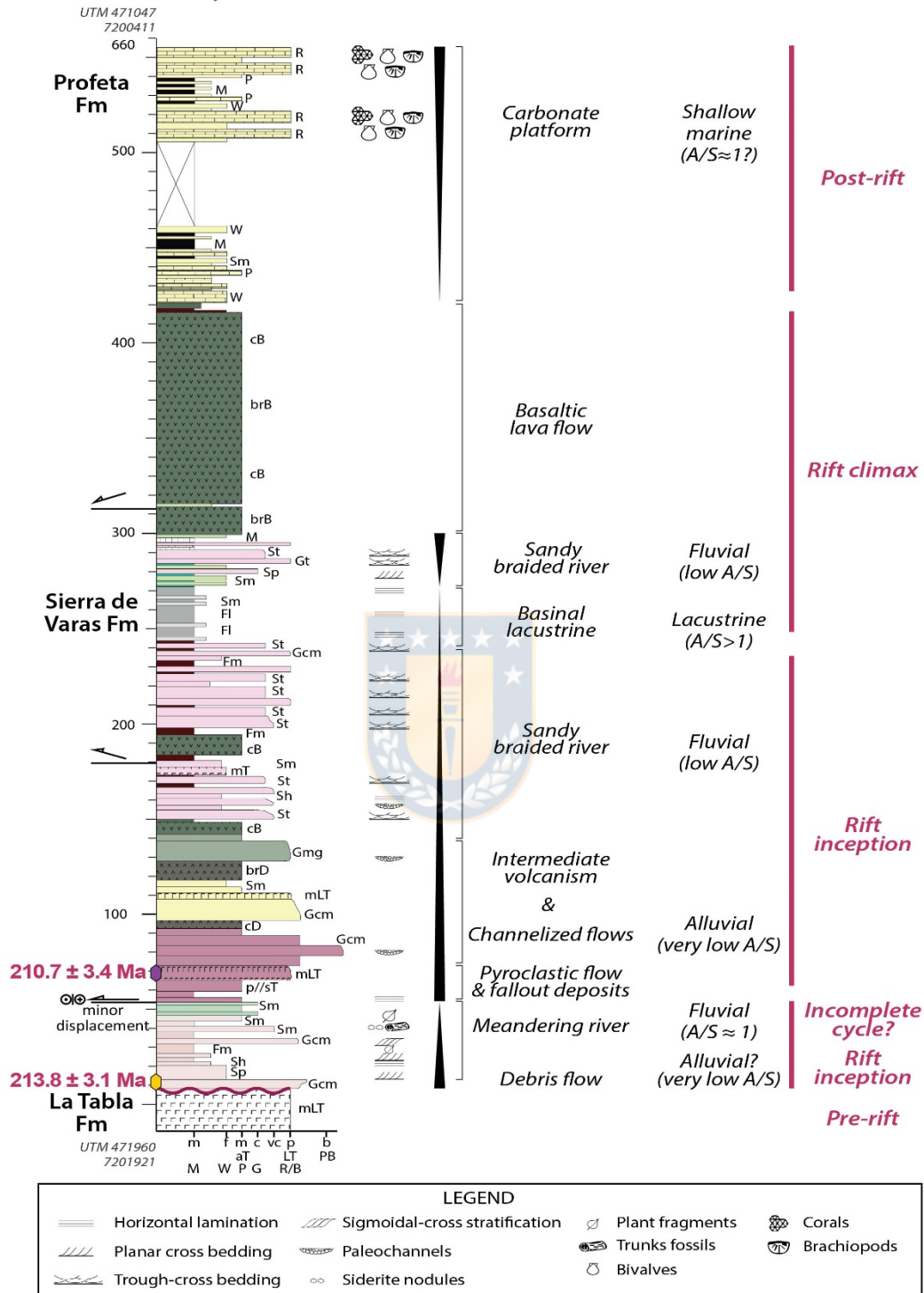
Figure 3.10: Generalized stratigraphic section S7 (Figs. 3.2, 3.9) showing a complete rift cycle during the Synrift II stage. Rift inception record alluvial and fluvial with an A/S < 1, rift climax record basinal lacustrine facies with an A/S>1 indicating an abrupt increase of subsidence and the post-rift phase is marked by shallow marine facies indicating a decrease of the subsidence and supply to the basin. Approximate lithology outcrop-color is indicated.
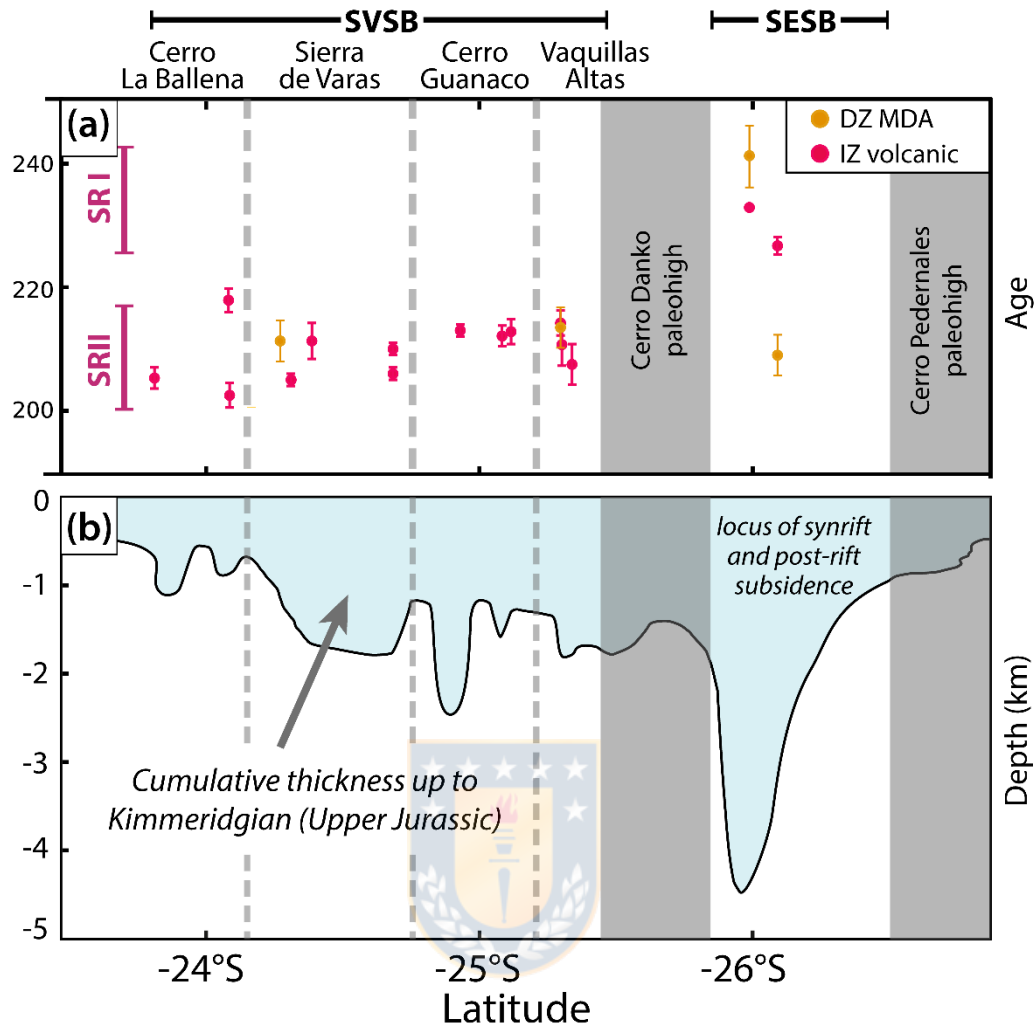
Figure 3.11: A) Compilation of volcanic and detrital (MDA) U-Pb ages from Triassic units exposed at the western margin of the Domeyko Range (69º - 69.5º W). The two synrift stages are indicated. References for geochronological data are the same that in Fig. 3.9. B) Minimum cumulative thickness of outcropping successions up to Kimmeridgian (based on the work of Prinz *et al.* (1994) and graphically updated by the thickness of Triassic successions presented in this work).

3.5.3.2 Synrift II (~217 - 200 Ma)

3.5.3.2.1 Sierra de Varas sub-basin

The initiation of rifting in the Sierra de Varas sub-basin (Norian) was accompanied by the deposition of proximal alluvial fan facies (A/S<1) from the Cerro Rincones Beds (S3 in Fig. 3.9) and the basal member of the Sierra de Varas Formation (S4 in Fig. 3.9). At the Vaquillas Altas depocenter (S7 in Fig. 3.9), the alluvial deposition

(A/S<1) was followed by meandering rivers (A/S ≈ 1, Martinsen *et al*., 1999) carrying a Late Triassic fossil flora (Fig. 3.6B), evidencing an increase in the accommodation space during the inception of the rift. This phase experienced negligible volcanism, evidenced by the mature composition of sediments and scarce DZ juvenile sources (Fig. 3.8E).

During the Norian-Rhaetian, the variable supply of volcanic products across the SVSB resulted in "high- or low-volcaniclastic" depocenters based on the sedimentary systems developed (Fig. 3.9; D'Elia *et al*., 2016). At the Cerro La Ballena and Cerro Guanaco volcanic depocenters, intermediate to silicic volcanism formed composite vents and proximal pyroclastic deposits (block-and-ash and ignimbrites). Restricted coarse-grained sedimentary systems were developed (A/S<1), such as alluvial fans and braided rivers at Cerro La Ballena depocenter and progradational delta-fans at the Cerro Guanaco depocenter (S2 and S6, Fig. 3.9).

In Sierra de Varas and Vaquillas Altas depocenters, a low-volcaniclastic input allowed the deposition of sedimentary systems with only medial to distal pyroclastic assemblages (distal ignimbrites and/or fallout deposits). A complete synrift cycle is recorded at the Vaquillas Altas depocenter (S7 in Fig. 3.9 and Fig. 3.10), from alluvial fans (A/S<1), basinal lacustrine (A/S>1) and braided fluvial systems, with restricted pyroclastic (mainly fallout deposits) and dacitic to basaltic volcanism (Fig. 3.10). This succession would represents the transition from rift inception (very low A/S), climax (high A/S) and post-rift sequences (moderate A/S), reflecting the rapid increase and posterior cease of mechanical subsidence (Prosser, 1993; Schlische and Anders, 1996; Withjack *et al*., 2002; Barredo *et al*., 2012). The rift climax is referred to the 'time of maximum rate of displacement on a fault' (Prosser, 1993). This period is characterized by the linkage of previous small and isolated faults into a fully linked fault array (Cowie *et al*., 2000; Gawthorpe and Leeder, 2000) producing a maximum subsidence where the sedimentation is likely to be outpaced by the accommodation space, generating characteristic relatively fine-grained basinal depositional systems (lacustrine, marine gulf) due to the starvation of the basin (McCann and Saintot, 2003; Prosser, 1993). Thus, the development of basinal lacustrine rift-climax facies (Prosser, 1993) across the Sierra de Varas and the Vaquillas Altas sub-basins (*e.g.* at S4, S7

sections), suggests an abrupt increase of the accommodation space which would be related to the fault linkage and consequent increase in mechanical subsidence across the SVSB (Fig. 3.12B; Schlische, 1991; Gawthorpe and Leeder, 2000; Withjack *et al*., 2002).

It should be noted that the succession recording the complete rift cycle (S7), was previously assigned to the Quebrada del Salitre Formation (Naranjo and Puig, 1984; Venegas *et al*., 2013). We suggest that these deposits would be better assigned to the Sierra de Varas Formation based on its completeness: (1) the presence of lacustrine facies which are absent in the type locality of the Quebrada del Salitre Formation, (2) its Norian-Rhaetian age which is younger than a significant portion of the Quebrada del Salitre Formation, and (3) its location in a structurally separated depocenter.

3.5.3.2.2 Sierra Exploradora sub-basin

The Synrift II stage in the SESB (Fig. 3.12B), recorded the deposition of meandering rivers and mafic lava flows (S10 and S11) with no development of rift-climax sequences (Prosser, 1993). The development of meandering rivers (A/S ≈ 1, Martinsen *et al*., 1999) suggest that the thick basaltic infill (>1300 m; S10, Fig. 3.9) match the high accommodation space and inhibited the development of water-deep facies during the high-subsidence of the basin. An outcrop scale example of this is preserved in the Quebrada del Salitre Formation (Fig. 3.4C), where syntectonic troughs were filled by basaltic lavas during meandering fluvial deposition (S11 in Fig. 3.9). This indicates an important role of the volcanism in the depositional systems developed in the SESB (high-volcaniclastic input).

3.5.3.3 Post-rift transition ('latest' Rhaetian)

During the uppermost Rhaetian (Fig. 3.12C), a broad and thin (< 50 m) shallow marine surface formed in carbonate shelves mantled the hanging- and foot-walls of both sub-basins (see section 5.1), indicating a generalized and abrupt reduction of the mechanical subsidence and the onset of the post-rift stage. At the Vaquillas Altas

depocenter, exceptional exposures of synsedimentary faults evidence the post-rift character of the carbonate platform assemblage (Fig. 3.4B). Previous works roughly delineated the onset of the post-rift at the Hettangian (*e.g.* Ardill *et al*., 1998), when deep marine facies were developed during a global sea rise (Ardill *et al*., 1998). However, these facies are better assigned to a late post-rift phase (Fig. 3.12D; Prosser, 1993).

3.5.4 Synrift architecture of the Domeyko Basin

Regarding to the main rift structures of the Domeyko Basin, we suggest that major N-S basin bounding faults were located at the western margin of the basin based on the predominance of thick, monomictic and coarse debris flow deposits, covering small areas near to the westernmost N-S faults of the Cenozoic Domeyko Fault System (DFS; Fig. 3.2). This proximal alluvial fan facies requires high-slopes to be formed and fast subsidence to be preserved, suggesting the proximity to high-angle faults (Blair and McPherson, 1994, 2009), in contrast to wider medial to distal assemblages (sheetfloods and channelized flows) developed at flexural margins. The proximity of this facies to the DFS suggests the reactivation of this structure, which usually occurs at the master faults of previous extensional systems (Butler, 1989; Amilibia *et al*., 2008; Bonini *et al*., 2012). At the SESB, elongated silicic domes were associated with ~N-S trending faults (Fig. 3.12A).

On the other hand, abrupt lithofacies changes and strong thickness asymmetry of the Domeyko Basin through the N-S direction, suggest basin segmentation was controlled by oblique, NW-SE striking faults (inset in Fig. 3.9). Moreover, several paleo-highs can be recognized longitudinally along the Domeyko Basin (*e.g.* Cerro Danko and Cerro Pedernales paleo-highs) based on the unconformable contact between the pre-rift basement and post-rift marine facies (Fig. 3.9). Major paleo-highs coincide with the tip of SVSB and SESB and correlates with large-scale NW lineaments (Figs. 3.1 and 3.2; Salfity, 1985; Abels and Bischoff, 1999; Petrinovic *et al*., 2006), suggesting pre-existing basement fabrics exhibit a strong control on the segmentation of the basin (Fig. 3.12). Additionally, Triassic NW-SE trending cataclasites (238 ± 10 Ma, K-Ar

whole rock age) crop out at the Sierra de Varas depocenter (Padilla, 1988; Niemeyer *et al.*, 2004) while prevailing, centi- to meter-scale Triassic NNW-SSE to NW-SE synsedimentary extensional faults have been identified at the SVSB (Espinoza *et al.*, 2016).
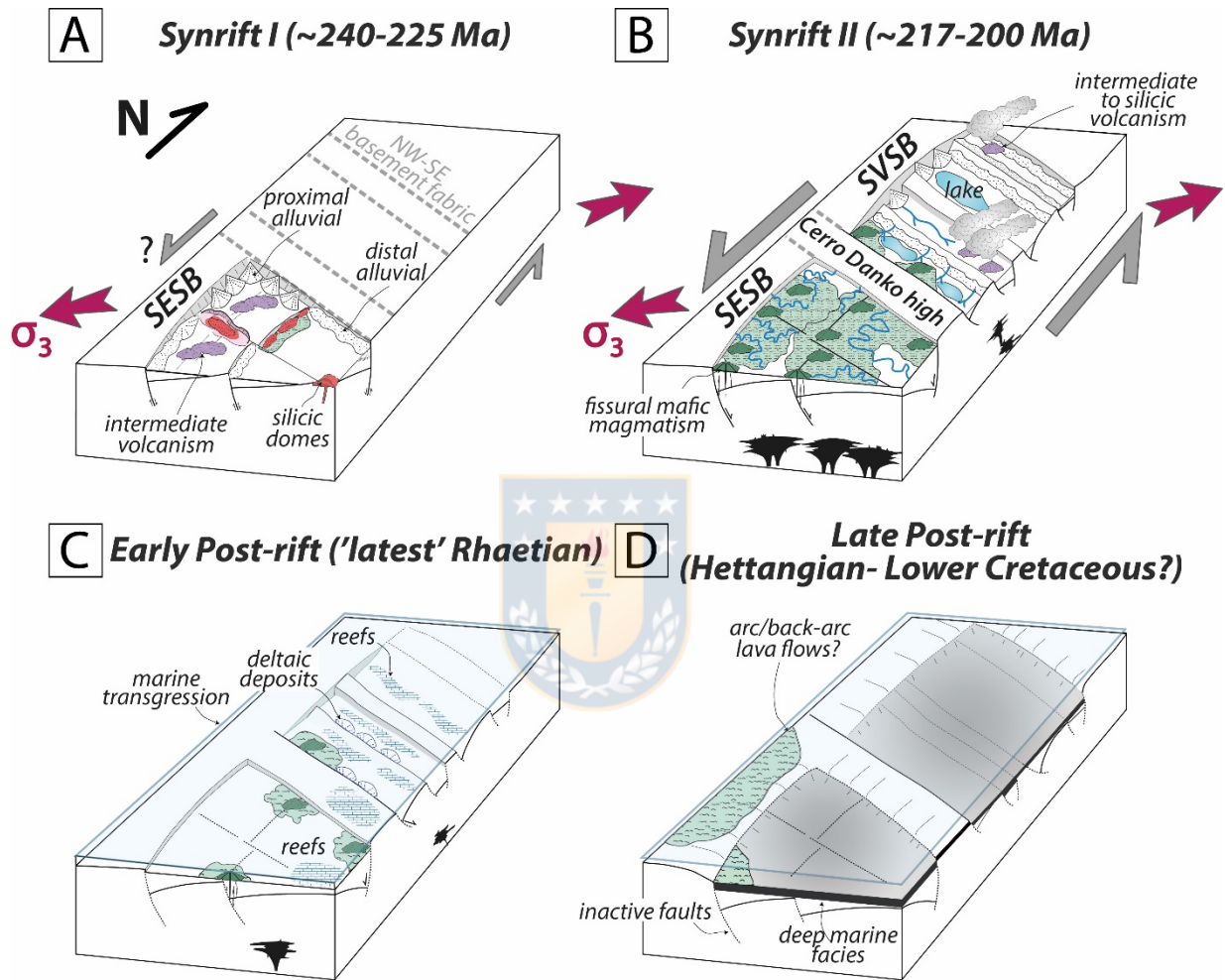
Figure 3.12: Conceptual basin-evolution model of the Synrift I, II and post-rift phase of the Domeyko Basin. A) Synrift I stage (~240-225 Ma): Initiation of the SESB in a mainly extensional setting occupying the NW-SE basement fabric. B) Synrift II stage (~217-200 Ma): Aperture of the SVSB and likely reactivation of the SESB in a mainly transtensional (sinistral) setting. During this stage, rift inception to rift climax sequences were developed at the SVSB due to an ongoing fault linkage through a ~N-S trending fault system. C) Early Postrift ('latest' Rhaetian): An abrupt reduction of the mechanical subsidence allowed the settlement of a shallow sea due to the initiation of the thermal subsidence phase. D) Late Post-rift stage (Hettangian-Lower Cretaceous?): The ongoing thermal subsidence coupled with a global rise of the sea-level controlled the deposition of deep marine facies across the mechanically inactive sub-basins.

We suggest that the interaction between major N-S structures and NW-SE oblique discontinuities can be explained by a transtensional model, partitioning the deformation into extensional and sinistral strike-slip components, where the NW-SE structures acted as releasing bends (Fig. 3.12). Several key features developed in transtensional basins are recognized in the Domeyko Basin: (1) a strong longitudinal and lateral asymmetry (Christie-Blick and Biddle, 1985), (2) narrow basins and rapid changes in lateral and vertical facies, thickness, and geometry of near depocenters (Christie-Blick and Biddle, 1985; Belt, 2012; Dorsey and Umhoefer, 2012), (3) common unconformities from one basin to another marking the migration of depocenters (Christie-Blick and Biddle, 1985; Busby and Bassett, 2007), such as those recorded at S6 and S8 in Vaquillas Altas and Cerro Guanaco depocenters (Fig. 3.9), (4) prominent topographic margins (Nilsen and Sylvester, 1998), which is in agreement with the unimodal provenance evidenced by the DZ data (Fig. 3.8), pointing to close and highly compartmentalized depocenters. Additionally, a strike-slip component has been suggested for the Jurassic back-arc phase of the Domeyko Basin, based on the "en-echelon" distribution of depocenters (Prinz et al., 1994; Vicente, 2005). Similar transtensional continental rift basins were developed during the Late Triassic-Lower Jurassic arc of the northwestern Gondwana (Busby and Bassett, 2007; Busby, 2012). In modern times, the dextral transtensional Walker Lane belt (United States) host the largest volcanic vents at releasing bends (Busby, 2013), and we infer a similar setting for the major volcanic centers developed in the Domeyko Basin.

During the post-rift stage (mainly Jurassic to Lower Cretaceous), the location of the thickest cumulative infills coincide with the deepest subsiding depocenters formed during the synrift stage (Fig. 3.11), suggesting a strong control of the synrift architecture over the differential thermal subsidence during the post-rift phase of the Domeyko basin, similar to that proposed by Cristallini et al. (2009) for the Jurassic back-arc Neuquén Basin of South America.

3.5.5 Geotectonic significance of the Domeyko Basin in the Southwestern Gondwana

During the Synrift II stage, the Cifuncho Basin (Fig. 3.1) was filled by volcanic and sedimentary rocks in the Coastal Cordillera in a similar timespan (212-200 Ma; Contreras *et al*., 2013; Espinoza *et al*., 2015). The scattered plutonic rocks of this age (Godoy and Lara, 1998; Escribano *et al*., 2013; Espinoza *et al*., 2014) and the intermediate to silicic, calcalkaline volcanism at the Coastal Cordillera would indicate a back-arc position for the synrift Domeyko Basin which hosts both calcalkaline and tholeiitic magmas (Espinoza *et al*., 2016; Oliveros *et al*., 2017). The later points to a more distal position of the Domeyko Basin with respect to the arc-axis, where the influence of released fluids from the slab in the genesis of magmas is less pronounced (Hochstaedter *et al*., 1990; Stern *et al*., 1990; Sayit *et al*., 2017).

The strong possibility that the subduction would have been active in northern Chile at least during the Late Triassic (Poma *et al*., 2014; del Rey *et al*., 2016; Coloma *et al*., 2017; González *et al*., 2017; Oliveros *et al*., 2017), suggests that the slab-pull would have played an important role as a driving mechanism of rifting at the southwestern margin of Gondwana during its early breakup. The oblique convergence required to sustain the sinistral transtension for the Domeyko Basin is in agreement with recent Triassic kinematic reconstructions (Matthews *et al*., 2016; Müller *et al*., 2016). The slab-pull in a retreating trench, would be coexisting with others driving mechanisms, such as far-field stresses (Giambiagi *et al*., 2009), which would have been more relevant for inboard basins at this time, such as the Ischigualasto and Cuyo basins (Fig. 3.1A). We suggest that the influence of the subduction system at the Gondwanan margin would have controlled the basin geometry, kinematics and ultimately the tectonostratigraphic evolution of the synrift Domeyko Basin.

3.6 Conclusions

In the Domeyko Basin, two synrift periods were developed during the Triassic: The Synrift I (~240 - 225 Ma) with the aperture of the Sierra Exploradora sub-basin (SESB) and the Synrift II (217-200 Ma), which led to the opening of the Sierra de Varas sub-basin (SVSB) and the reactivation of the SESB. These volcano-sedimentary sub-basins present striking differences in the sedimentary and volcanic infill of its

depocenters, evidencing a strong influence of the volcanic input (low or high) and the mechanical subsidence in the sedimentary depositional systems developed (A/S ratio). In low-volcaniclastic depocenters, a complete rift cycle is recorded (alluvial-lacustrine-fluvial), with rift-climax basinal lacustrine facies (A/S>1) indicating the fault-linkage of the SVSB during the Synrift II. In high-volcaniclastic depocenters of the SVSB and SESB, the development of low to very low A/S facies (A/S ≤ 1) during high mechanical subsidence suggests that volcanic supply inhibited the development of rift-climax facies (basinal deep-water facies). The post-rift transition took place at the 'latest' Rhaetian where the thermal subsidence allows a wide transgression of shallow marine facies, bypassing the footwalls of the Domeyko Basin.

We suggest that the architecture of the synrift Domeyko Basin was controlled by the interaction between major N-S faults and oblique ~NW-SE discontinuities, generating asymmetric half-graben depocenters and structural highs in a left-lateral transtensional model (pull-apart or releasing bend). The oblique discontinuities would correspond to NW-SE continental-scale lineaments, suggesting that inherited basement weakness controlled the segmentation of the Domeyko Basin.

The strong possibility that the Domeyko Basin would have been formed as subduction-related rift basin in a back-arc position during the Late Triassic, highlights the slab-pull as probable driving mechanism for extension at the Southwestern Gondwana margin during its early breakup, unlike other inland rift basins driven by far-field stresses (Cuyo, Ischigualasto and Neuquén basins, Fig. 3.1A). Therefore, slab-induced tectonics can control the first-order features of subduction-related rifts, such as the rift position (*e.g.* intra-arc or back-arc basins), the volcanism style and composition, and the rift kinematics (purely extensional versus transtensional tectonics). These features would have controlled the tectonostratigraphic evolution of the synrift stage of the Domeyko Basin through the localization of volcanic centers (high-volcaniclastic depocenters) and the deformation at releasing stepovers (transtensional kinematics). Given that only a moderate amount of subduction obliquity would be required to develop a strike-slip component during rifting (> ~30º; Philippon and Corti, 2016), the transtensional Domeyko rift may correspond to an underestimated example of the tectonostratigraphic evolution of Gondwanean continental subduction-related basins.

3.7 Acknowledgements

3.8 References

ABELS, A., and BISCHOFF, L. (1999) Clockwise block rotations in northern Chile: Indications for a large-scale domino mechanism during the middle-late Eocene. Geology, 0–3.

ALFARO, R. (2014) Estratigrafia de las rocas triásicas de la Formación Cerro Guanaco (Nueva Unidad) en la Cordillera de Domeyko, sector Sierra de Varas. Región de Antofagasta.(24º 48'–25º 00' Lat. Sur). Memoria de título, Antofagasta (unpublished), pp. 95. Chile.

ALONSO-ZARZA, A. M., and TANNER, L. H. (2009) Carbonates in continental settings: facies, environments, and processes, Vol. 61. Elsevier.

ÁLVAREZ, P. (2003) Análisis litofacial de la Formación Las Bateas. In: X Congreso Geológico Chileno. Concepción, Chile.

AMILIBIA, A., SÀBAT, F., MCCLAY, K. R., MUÑOZ, J. A., ROCA, E., and CHONG, G. (2008) The role of inherited tectono-sedimentary architecture in the development of the central Andean mountain belt: Insights from the Cordillera de Domeyko. J. Struct. Geol., 30, 1520–1539.

ARDILL, J. (1996) Sequence stratigraphy of the Mesozoic Domeyko basin, northern Chile. University of Liverpool.

ARDILL, J., FLINT, S., CHONG, G., and WILKE, H. (1998) Sequence stratigraphy of the Mesozoic Domeyko Basin, northern Chile. J. Geol. Soc. London., 155, 71–88.

ASTUDILLO, N., FERRANDO, R., MONTECINO, D., ESPINOZA, F., MATTHEWS, S., CORNEJO, P., and ARÉVALO, C. (2017) Carta Augusta Victoria, Región de Antofagasta. Servicio Nacional de Geología y Minería. Carta Geológica de Chile, Serie Geología Básica XXX. 1 mapa escala 1:100.000. Santiago, Chile.

BARREDO, S., CHEMALE, F., MARSICANO, C., ÁVILA, J. N., OTTONE, E. G., and RAMOS, V. A. (2012) Tectono-sequence stratigraphy and U-Pb zircon ages of the Rincón Blanco Depocenter, northern Cuyo Rift, Argentina. Gondwana Res., 21, 624–636.

BASCUÑÁN, S., ARRIAGADA, C., LE ROUX, J., and DECKART, K. (2015) Unraveling the Peruvian Phase of the Central Andes: stratigraphy, sedimentology and geochronology of the Salar de Atacama Basin (22°30-23°S), northern Chile. Basin Res., 28, 365–392.

BASSO, M., and MARINOVIC, N. (2003) Antecedentes geocronológicos de volcanismo triásico en la zona de los Estratos El Bordo, Antofagasta, Chile. In: X Congreso Geológico Chileno. Concepción.

BELL, C. M., and SUÁREZ, M. (1991) Late Triassic fluvial and marine shelf succession, Quebrada Doña Inés Chica, Atacama region, northern Chile. J. South Am. Earth Sci., 4, 287–293.

BELT, L. (2012) Active transtensional intracontinental basins: Walker Lane belt in the Western Great Basin. In: Tectonics of Sedimentary Basins: Recent Advances, pp. 226–248.

BENSON, L. V., and THOMPSON, R. S. (1987) Lake-level variation in the Lahontan basin for the past 50,000 years. Quat. Res., 28, 69–85.

BENVENUTI, M. (2003) Facies analysis and tectonic significance of lacustrine fan-deltaic successions in the Pliocene–Pleistocene Mugello Basin, Central Italy. Sediment. Geol., 157, 197–234.

BLAIR, T. C., and MCPHERSON, J. G. (1994) Alluvial Fans and their Natural Distinction from Rivers Based on Morphology, Hydraulic Processes, Sedimentary Processes, and Facies Assemblages. SEPM J. Sediment. Res., 64A, 450–489.

BLAIR, T. C., and MCPHERSON, J. G. (2009) Processes and Forms of Alluvial Fans. In: Geomorphology of Desert Environments, 2nd edn. (Ed. by A. J. Parsons and A. D. Abrahams), pp. 413–467. Springer Netherlands.

BONINI, M., SANI, F., and ANTONIELLI, B. (2012) Basin inversion and contractional reactivation of inherited normal faults: A review based on previous and new experimental models. Tectonophysics, 522, 55–88.

BRANNEY, M., and KOKELAAR, P. (2002) Interpreting ignimbrite lithofacies. In: Pyroclastic Density Currents and the Sedimentation of Ignimbrites, pp. 51–85. The Geological Society of London, London.

BUSBY-SPERA, C. J. (1988) Speculative tectonic model for the early Mesozoic arc of the southwest Cordilleran United States. Geology, 16, 1121–1125.

BUSBY-SPERA, C. J., and WHITE, J. D. L. (1987) Variation in peperite textures associated with differing host-sediment properties. Bull. Volcanol., 49, 765–776.

BUSBY, C. (2012) Extensional and transtensional continental arc basins: case studies from the southwestern United States. In: Tectonics of Sedimentary Basins: Recent Advances, (Ed. by C. Busby and A. Azor), pp. 382–404. Wiley-Blackwell.

BUSBY, C. (2013) Birth of a plate boundary at ca. 12 Ma in the Ancestral Cascades arc, Walker Lane belt of California and Nevada. Geosphere, 9, 1147–1160.

BUSBY, C., and BASSETT, K. N. (2007) Volcanic facies architecture of an intra-arc strike-slip basin, Santa Rita Mountains, Southern Arizona. Bull. Volcanol., 70, 85–103.

BUTLER, R. W. H. (1989) The influence of pre-existing basin structure on thrust system evolution in the Western Alps. Geol. Soc. London, Spec. Publ., 44, 105–122.

CARROLL, A. R., and BOHACS, K. M. (1999) Stratigraphic classification of ancient lakes: Balancing tectonic and climatic controls. Geology, 27, 99–102.

CAS, R., and WRIGHT, J. V (1988) Volcanic successions modern and ancient: A geological approach to processes, products and successions. Springer Science and Business Media.

CHARRIER, R. (1979) El Triásico en Chile y regiones adyacentes de Argentina: Una reconstrucción paleogeográfica y paleoclimática. Comun. Dep. Geol. Univ. Chile, 26, 1–47.

CHONG, G. (1973) Reconocimiento Geológico del Área Catalina, Sierra de Varas y estratigrafía del Jurásico del Profeta, Provincia de Antofagasta. Memoria de título, Universidad de Chile (unpublished), pp. 284.

CHONG, G. (1977) Contribution to the knowledge of the Domeyko range in the Andes of northern Chile. Geol. Rundschau, 66, 374–404.

CHONG, G., and HILLDEBRANDT, A. (1985) El Triásico PreAndino de Chile entre los 23°30´ y 26°00´ de lat. sur. In: IV Congreso Geológico Chileno. Antofagasta, Chile.

CHRISTIE-BLICK, N., and BIDDLE, K. (1985) Deformation and Basin Formation Along Strike-Slip Faults. SEPM (Society Sediment. Geol. Spec. Publ., 37, 1–33.

COLOMA, F., VALIN, X., OLIVEROS, V., VÁSQUEZ, P., CREIXELL, C., SALAZAR, E., DUCEA, M., and VALLEJOS, D. (2017) Geochemistry of Permian to Triassic igneous rocks from northern Chile (28o-29o30'S): Implications on the dynamics of the proto-Andean margin. Andean Geol., 44, 147–178.

CONTRERAS, J. F. (2014) Estratigrafía de la Formación Sierra de Varas, Cordillera de Domeyko, Región de Antofagasta entre las coordenadas 7.273. 103–7.268. 892 m N; 481.320–482.290 m E, Memoria de título, Antofagasta (unpublished), pp. 105. Universidad Católica del Norte, Antofagasta, Chile.

CONTRERAS, J. P., ESPINOZA, M., JORQUERA, R., KRAUS, S., RAMÍREZ, C., DE LA CRUZ, R., NARANJO, J. A., ESCRIBANO, J. and MARTÍNEZ, P. (2013). Carta Cifuncho, Regiones de Antofagasta y Atacama. Servicio Nacional de Geología y Minería. Carta Geológica de Chile, Serie Geología Básica 161, 1 mapa escala. 1:100.000. Santiago, Chile.

CORNEJO, P. and MPODOZIS, C. (1996) Geología de la Región de Sierra Exploradora (Cordillera de Domeyko 25°-26°S). Servicio Nacional de Geología y Minería - CODELCO, Informe Registrado, IR-96-09, 1-330, 9 mapas escala 1:50.000. Santiago.

CORNEJO, P., MPODOZIS, M., RIVERA, O. and MATTHEWS, S. (2009) Carta Exploradora, Regiones de Antofagasta y Atacama. Servicio Nacional de Geología y Minería, Carta Geológica de Chile, Serie Geología Básica, 119, 1-103. 1 mapa escala 1:100.000.Santiago, Chile.

COWIE, P. A., GUPTA, S., and DAWERS, N. H. (2000) Implications of fault array evolution for synrift depocentre development: Insights from a numerical fault growth model. Basin Res., 12, 241–261.

CRISTALLINI, E., TOMEZZOLI, R. N., PANDO, G., GAZZERA, C., MARTÍNEZ, J. M., QUIROGA, J., BUHLER, M., BECHIS, F., BARREDO, S., and ZAMBRANO, O. (2009) Controles precuyanos en la estructura de la cuenca neuquina. Rev. La Asoc. Geológica Argentina, 65, 248–264.

D'ELIA, L., MARTÍ, J., MURAVCHIK, M., BILMES, A., and FRANZESE, J. R. (2016) Impact of volcanism on the sedimentary record of the Neuquén rift basin, Argentina: Towards a cause and effect model. Basin Res.

D'ELIA, L., MURAVCHIK, M., FRANZESE, J. R., and LÓPEZ, L. (2012) Tectonostratigraphic analysis of the Late Triassic-Early Jurassic syn-rift sequence of the Neuquén Basin in the Sañicó depocentre , Neuquén Province , Argentina. Andean Geol., 39, 133–157.

DERER, C. E., SCHUMACHER, M. E., and SCHÄFER, A. (2005). The northern Upper Rhine Graben: basin geometry and early syn-rift tectono-sedimentary evolution. Int. J. Earth Sci., 94, 640–656.

DICKINSON, W. R., and GEHRELS, G. E. (2009) Use of U-Pb ages of detrital zircons to infer maximum depositional ages of strata: A test against a Colorado Plateau Mesozoic database. Earth Planet. Sci. Lett., 288, 115–125.

DORSEY, R. J., and UMHOEFER, P. J. (2012) Influence of Sediment Input and Plate-Motion Obliquity on Basin Development Along an Active Oblique-Divergent Plate Boundary: Gulf of California and Salton Trough. In: Tectonics of Sedimentary Basins: Recent Advances, pp. 209–225.

DOYLE, M. G. (2000) Clast shape and textural associations in peperite as a guide to hydromagmatic interactions: Upper Permian basaltic and basaltic andesite examples from Kiama, Australia. Aust. J. Earth Sci., 47, 167–177.

ESCRIBANO, J., MARTÍNEZ, P., DOMAGALA, J., PADEL, M., ESPINOZA, M., JORQUERA, R., CONTRERAS, J., DE LA CRUZ, R. and CALDERÓN, M. (2013) Cartas Bahía Isla Blanca y Taltal. Escala 1:100.000. Servicio Nacional de Geología y Minería, Carta Geológica de Chile, Serie Geología Básica, 164-165. 1-75. 1 mapa escala 1:100.000. Santiago.

ESPINOZA, M., CONTRERAS, J. P., KRAUS, S., DE LA CRUZ, R., JORQUERA, R., RAMIREZ, C. and NARANJO, J. A. (2014) Carta Cerro del Pingo, Regiones de Antofagasta y Atacama. Servicio Nacional de Geología y Minería, Carta Geológica de Chile, Serie Geología Básica XXX. 1 mapa escala 1:100.000. Santiago.

ESPINOZA, M., OLIVEROS, V., and CELIS, C. (2016) Geochronology, Geochemistry and Tectonics of Subduction-Related Late Triassic Rift Basins in Northern Chile (24o-26oS). In: American Geophysical Union, Fall General Assembly 2016, p. T51D–2975. San Francisco, United States.

ESPINOZA, M., OLIVEROS, V., VÁSQUEZ, P., and BECHIS, F. (2015) U-Pb geochronology and kinematic preliminary analyses of Late Triassic-Early Jurassic basins in northern Chile (24.5o-26oS). In: XIV Congreso Geológico Chileno, pp. 840–843. La Serena, Chile.

FINK, J. H., and ANDERSON, S. W. (2000) Lava domes and coulees. In: Encyclopedia of volcanoes, (Ed. by B. F. Houghton, S. McNutt, H. Rymer, and J. Stix), pp. 307–319. Academic Press San Diego.

FISHER, R. V, and SCHMINCKE, H.-U. (1984) Pyroclastic Rocks and Tectonic Environment. In: Pyroclastic rocks, pp. 383–409. Springer.

FREUNDT, A., WILSON, C. J. N., and CAREY, S. N. (2000) Ignimbrites and block-and-ash flow deposits. In: Encyclopedia of volcanoes, (Ed. by H. Sigurdsson), pp. 581–599. Academic Press, New York.

GAWTHORPE, R., FRASER, A., and COLLIER, R. (1994) Sequence stratigraphy in active extensional basins: implications for the interpretation of ancient basin-fills. Mar. Pet. Geol., 11, 642–658.

GAWTHORPE, R., and LEEDER, M. (2000) Tectono-sedimentary evolution of active extensional basins. Basin Res., 12, 195–218.

GEHRELS, G. (2011) Detrital Zircon U-Pb Geochronology: Current Methods and New Opportunities. In: Tectonics of Sedimentary Basins: Recent Advances, (Ed. by C. J. Busby and A. Azor), pp. 45–62.

GIAMBIAGI, L., TUNIK, M., BARREDO, S., BECHIS, F., GHIGLIONE, M., ALVAREZ, P., and DROSINA, M. (2009) Cinemática de apertura del sector norte de la cuenca neuquina. Rev. La Asoc. Geológica Argentina, 65, 278–292.

GODOY, E. and LARA, L. (1998) Hojas Chañaral y Diego de Almagro, Región de Atacama. Servicio Nacional de Geologia y Minería, Mapas Geológicos No. 5-6. 1 mapa escala 1:100.000, Santiago.

GONZÁLEZ, J., OLIVEROS, V., CREIXELL, C., VELÁSQUEZ, R., VÁSQUEZ, P., and LUCASSEN, F. (2017) The Triassic magmatism and its relation with the Pre-Andean tectonic evolution: Geochemical and petrographic constrains from the High Andes of north central Chile (29o 30' - 30o S). J. South Am. Earth Sci., 1–18.

GONZÁLEZ, R., WILKE, H. G., MENZIES, A. H., ESPINOZA, F., RIQUELME, R. and HERRERA, C. (2015) Carta Sierra de Varas, Región de Antofagasta. Servicio Nacional de Geología y Minería, Carta Geológica de Chile, Serie Geología Básica 178. 114 p, 1 mapa escala 1:100.000. Santiago.

GRÖSCHKE, M., V. HILLEBRANDT, A., PRINZ, P., QUINZIO, L. A., and WILKE, H.-G. (1988) Marine mesozoic paleogeography in Northern Chile between 21°–26°S. In: The Southern Central Andes SE - 7, (Ed. by H. Bahlburg, C. Breitkreuz, and P. Giese), Vol. 17, pp. 103–117. Springer Berlin Heidelberg.

HADLARI, T., MIDWINTER, D., POULTON, T. P., and MATTHEWS, W. A. (2017) A Pangean rim of fire: Reviewing the Triassic of western Laurentia. Lithosphere, L643.1.

HENRÍQUEZ, S. (2014) Geología del área San Pedro de Atacama, Región de Antofagasta. Servicio Nacional de Geología y Minería. Carta Geológica de Chile, Serie Geología Básica 171. 111 p., 1 mapa escala 1:100.000. Santiago.

HOCHSTAEDTER, A. G., GILL, J. B., and MORRIS, J. D. (1990) Volcanism in the Sumisu Rift, II. Subduction and non-subduction related components. Earth Planet. Sci. Lett., 100, 195–209.

INGERSOLL, R. V. (2012) Tectonics of Sedimentary Basins, with Revised Nomenclature. In: Tectonics of Sedimentary Basins: Recent Advances, pp. 1–43.

JARRARD, R. D. (1986) Relations among subduction parameters. Rev. Geophys., 24, 780–783.

JOHNSON, T. C., HALFMAN, J. D., ROSENDAHL, B. R., and LISTER, G. S. (1987) Climatic and tectonic effects on sedimentation in a rift-valley lake: evidence from high-resolution seismic profiles, Lake Turkana, Kenya. Geol. Soc. Am. Bull., 98, 439–447.

KAMATA, H., and KODAMA, K. (1994) Tectonics of an arc-arc junction: an example from Kyushu Island at the junction of the Southwest Japan Arc and the Ryukyu Arc. Tectonophysics, 233, 69–81.

KLEIMAN, L. E., and JAPAS, M. S. (2009) The Choiyoi volcanic province at 34°S–36°S (San Rafael, Mendoza, Argentina): Implications for the Late Palaeozoic evolution of the southwestern margin of Gondwana. Tectonophysics, 473, 283–299.

KOSTER, E. H., and STEEL, R. J. (1984) Sedimentology of gravels and conglomerates, Vol. 10. Canadian Society of Petroleum Geologists, Calgary.

LEE, C.-S., SHOR, G. G., BIBEE, L. D., LU, R. S., and HILDE, T. W. C. (1980) Okinawa Trough: Origin of a back-arc basin. Mar. Geol., 35, 219–241.

LEEDER, M., and GAWTHORPE, R. (1987) Sedimentary models for extensional tilt-block/half-graben basins. Geol. Soc. London, Spec. Publ., 28, 139–152.

LAMOTTE, D., FOURDAN, B., LELEU, S., LEPARMENTIER, F., CLARENS, P. (2015) Style of rifting and the stages of Pangea breakup. Tectonics, 34, 5, (1009-1029).

LIPMAN, P. W. (2000) Calderas. In: Encyclopedia of Volcanoes, (Ed. by H. Sigurdsson, B. Houghton, S. McNutt, H. Rymer, and J. Stix), pp. 643–662. Academic Press.

LLAMBÍAS, E. J., QUENARDELLE, S., and MONTENEGRO, T. (2003) The Choiyoi Group from central Argentina: a subalkaline transitional to alkaline association in the craton adjacent to the active margin of the Gondwana continent. J. South Am. Earth Sci., 16, 243–257.

LUDWIG, K. R. (2008) Isoplot 3.7: A geochronological toolkit for Microsoft Excel. Berkeley Geochronology Center Special Publication.

MARINOVIC, N. (2007) Carta Oficina Domeyko, Región de Antofagasta. Servicio Nacional de Geología y Minería, Carta Geológica de Chile, Serie Geológica Básica, 105, 1-41. 1 mapa escala 1:100.000, Santiago.

MARINOVIC, N., SMOJE, I., MAKSAEV, V., HERVÉ, M. and MPODOZIS, C. (1995) Hoja Aguas Blancas. Servicio Nacional de Geología y Minería, Carta Geológica de Chile, 70, 1-150. 1 mapa escala 1:250.000, Santiago.

MCCANN, T., and SAINTOT, A. (2003) Tracing tectonic deformation using the sedimentary record: an overview. Geol. Soc. London, Spec. Publ., 208, 1–28.

MUTO, T., and STEEL, R. J. (2000) The accommodation concept in sequence stratigraphy: Some dimensional problems and possible redefinition. Sediment. Geol., 130, 1–10.

NÉMETH, K., and ULRIKE, M. (2007) Practical Volcanology. Lecture notes for understanding volcanic rocks from field-based studies. In: Occasional Papers of the Geological Institute of Hungary, 27, 1-221. Budapest.

MARTINS-NETO, M. A., and CATUNEANU, O. (2010) Rift sequence stratigraphy. Mar. Pet. Geol., 27, 247–253.

MARTINSEN, O. J., RYSETH, A. L. F., HELLAND-HANSEN, W., FLESCHE, H., TORKILDSEN, G., and IDIL, S. (1999) Stratigraphic base level and fluvial architecture: Ericson Sandstone (Campanian), Rock Springs Uplift, SW Wyoming, USA. Sedimentology, 46, 235–263.

MATTHEWS, K. J., MALONEY, K. T., ZAHIROVIC, S., WILLIAMS, S. E., SETON, M., and MILLER, R. D. (2016) Global plate boundary evolution and kinematics since the late Paleozoic. Glob. Planet. Change, 146, 226–250.

MCPHERSON, J. G., SHANMUGAM, G., and MOIOLA, R. J. (1987) Fan-deltas and braid deltas : Varieties of coarse- grained deltas. Geol. Soc. Am. Bull., 99, 331–340.

MCPHIE, J., DOYLE, M. G., and ALLEN, R. (1993) Volcanic textures: a guide to the interpretation of textures in volcanic rocks. CODES-University of Tasmania, Hobart.

MERLE, O. (2011) A simple continental rift classification. Tectonophysics, 513, 88–95.

MIALL, A. D. (1978) Lithofacies types and vertical profile models in braided river deposits: a summary. Fluv. Sedimentol., 5, 597–600.

MIALL, A. D. (2006) The Geology of Fluvial Deposits. Springer, Berlin.

MONTECINO, D. (2015) Nuevo esquema estratigráfico, condiciones de sedimentación y evolución de la cuenca triásica entre los 24°00'-24°30' S y 69°00'-69°30' W, Región de Antofagasta, Chile. Memoria de título, Universidad de Concepción (unpublished), pp. 177. Concepción.

MPODOZIS, C. and CORNEJO, P. (1997) El rift triásico-sinemuriano de Sierra Exploradora, Cordillera de Domeyko (25°-26°S): Asociaciones de facies y reconstrucción tectónica. In: VIII Congreso Geólogico Chileno, pp. 550–554.

MÜLLER, R. D., SETON, M., ZAHIROVIC, S., WILLIAMS, S. E., MATTHEWS, K. J., WRIGHT, N. M., SHEPHARD, G. E., MALONEY, K. T., BARNETT-MOORE, N., BOWER, D. J., and CANNON, J. (2016) Ocean basin evolution and global-scale reorganization events since Pangea breakup. Annu. Rev. Earth Planet. Sci. Lett., 107–138.

MUÑOZ, J., AMILIBIA, A., CARRERA, N., MON, R., CHONG, G., ROCA, E. and SÀBAT, F. (2005) A geological cross-section of the Andean orogen at 25.5° LS. In VI International Symposium on Andean Geodynamics, 536–539. Barcelona, España.

MUÑOZ, N. (1989) Estudio geológico estratigráfico de las Hojas Baquedano y Pampa Unión, II Región de Antofagasta, Chile. Memoria de Título, Universidad de Chile (unpublished), Departamento de Geología, pp. 161. Santiago.

MURAVCHIK, M., D'ELIA, L., BILMES, A., and FRANZESE, J. R. (2011) Syn-eruptive/inter-eruptive relations in the syn-rift deposits of the Precuyano Cycle, Sierra de Chacaico, Neuquén Basin, Argentina. Sediment. Geol., 238, 132–144.

NARANJO, J. A. and PUIG, A. (1984) Hojas Taltal y Chañaral, Regiones de Antofagasta y Atacama. Servicio Nacional de Geología y Minería, Carta Geológica de Chile, 62-63, 1-146. 1 mapa escala 1:250.000, Santiago.

NAVEA, A., WILKE, H.-G. and GONZÁLEZ, R. (2015) Naturaleza de la transgresión marina triásica superior en Sierra Áspera de Argomedo y Sierra de Varas , Región de. In XIV Congreso Geológico Chileno, 808–811. La Serena, Universidad de Chile.

NEMEC, W., and STEEL, R. J. (1984) Alluvial and coastal conglomerates: their significant features and some comments on gravelly mass-flow deposits. Sedimentol. Gravels Conglomerates, 10, 1–31.

NICHOLS, G. (2009) Sedimentology and stratigraphy. John Wiley and Sons.

NIEMEYER, H., BERRÍOS, H., and RUIZ CRUZ, M. D. (2004) Temperaturas de formación en cataclasitas triásicas de la Cordillera Domeyko, Antofagasta, Chile. Rev. Geológica Chile, 31, 3–18.

NILSEN, T. H., and SYLVESTER, A. G. (1998) Strike-Slip Basins. In: Tectonics of sedimentary basins, (Ed. by C. Busby and R. Ingersoll), pp. 425–456. Willey.

OLIVEROS, V., GONZÁLEZ, J., ESPINOZA VARGAS, M., VÁSQUEZ, P., ROSSEL, P., CREIXELL, C., SEPÚLVEDA, F., and BASTÍAS, F. (2017) The early stages of the magmatic arc in the Southern Central Andes. In: The Evolution of the Chilean-Argentinean Andes, (Ed. by A. Folguera, E. Contreras-Reyes, N. Heredia, A. Encinas, V. Oliveros, F. Dávila, and G. Collo), pp. 185–212. Springer.

PADILLA, H. (1988) Eventos intrusivos y deformaciones en la Cordillera de Domeyko a la latitud del Salar de Punta Negra. Antecedentes geocronológicos K-Ar. In: V Congreso Geológico Chileno, pp. 229–243. Santiago, Chile.

PETRINOVIC, I. A., RILLER, U., and BROD, J. A. (2005) The Negra Muerta Volcanic Complex, southern Central Andes: Geochemical characteristics and magmatic evolution of an episodically active volcanic centre. J. Volcanol. Geotherm. Res., 140, 295–320.

PHILIPPON, M., and CORTI, G. (2016) Obliquity along plate boundaries. Tectonophysics, 693, 171–182.

PLATT, N. H., and WRIGHT, V. P. (1991) Lacustrine carbonates: facies models, facies distributions and hydrocarbon aspects. Spec. Publ. Internatinal Assoc. Sedimentol., 13, 57–74.

POLLIAND, M., SCHALTEGGER, U., FRANK, M., and FONTBOTÉ, L. (2005) Formation of intra-arc volcanosedimentary basins in the western flank of the central Peruvian Andes during Late Cretaceous oblique subduction: Field evidence and constraints from U-Pb ages and Hf isotopes. Int. J. Earth Sci., 94, 231–242.

POMA, S., ZAPPETTINI, E. O., QUENARDELLE, S., SANTOS, J. O., KOUKHARSKY, M., BELOUSOVA, E., and MCNAUGHTON, N. (2014) Geochemistry, U-Pb SHRIMP zircon dating and Hf isotopes of the Gondwanan magmatism in NW Argentina: petrogenesis and geodynamic implications. Andean Geol., 41, 267–292.

PRINZ-GRIMM, P. (1995) Triassiche Korallen der südlichen Zentral-Anden. Geol. Palaeontol., 29, 233–234.

PRINZ, P., WILKE, H.-G., and VON HILLEBRANDT, A. (1994) Sediment accumulation and subsidence history in the Mesozoic marginal basin of northern Chile. In: Tectonics of the Southern Central Andes, (Ed. by K. J. Reutter, E. Scheuber, and P. J. Wigger), pp. 219–232. Springer-Verlag, Berlin.

PROSSER, S. (1993) Rift-related linked depositional systems and their seismic expression. Geol. Soc. London, Spec. Publ., 71, 35–66.

DEL REY, A., DECKART, K., ARRIAGADA, C., and MARTÍNEZ, F. (2016) Resolving the paradigm of the late Paleozoic–Triassic Chilean magmatism: Isotopic approach. Gondwana Res., 37, 172–181.

SAYIT, K., BEDI, Y., TEKIN, U. K., GÖNCÜOGLU, M. C., and OKUYUCU, C. (2017) Middle Triassic Back-arc Basalts from the Blocks in the Mersin Mélange, southern Turkey: Implications for the Geodynamic Evolution of the Northern Neotethys. Lithos, 268–271, 102–113.

SCHELLART, W. P. (2005) Influence of the subducting plate velocity on the geometry of the slab and migration of the subduction hinge. Earth Planet. Sci. Lett., 231, 197–219.

SCHLISCHE, R. W. (1991) Half-graben basin filling models: new constraints on continental extensional basin development. Basin Res., 3, 123–141.

SCHLISCHE, R. W., and ANDERS, M. H. (1996) Stratigraphic effects and tectonic implications of the growth of normal faults and extensional basins. Geol. Soc. Am. Spec. Pap., 303, 183–203.

SCHOLZ, C. A., JOHNSON, T. C., COHEN, A. S., KING, J. W., PECK, J. A., OVERPECK, J. T., TALBOT, M. R., BROWN, E. T., KALINDEKAFE, L., AMOAKO, P. Y. O., LYONS, R. P., SHANAHAN, T. M., CASTANEDA, I. S., HEIL, C. W., FORMAN, S. L., MCHARGUE, L. R., BEUNING, K. R., GOMEZ, J., and PIERSON, J. (2007) East African megadroughts between 135 and 75 thousand years ago and bearing on early-modern human origins. Proc. Natl. Acad. Sci., 104, 16416–16421.

SCHOLZ, C. A., ROSENDAHL, B. R., and SCOTT, D. L. (1990) Development of coarse grained-facies in lacustrine rift basins: Example from East Africa. Geology, 18, 140–144.

SELLEY, R. C. (2000) Applied sedimentology. Academic Press.

SENGÖR, A. M. C., and NATAL'IN, B. A. (2001) Rifts of the world. In: Special Paper 352: Mantle plumes: their identification through time, Vol. 352, pp. 389–482.

SHANLEY, K. W., and MCCABE, P. J. (1994) Perspectives on the sequence stratigraphy of continental strata. Am. Assoc. Pet. Geol. Bull., 78, 544–568.

SOLARI, M., MONTECINOS, D., VENEGAS, C., and ESPINOZA, F. (2015) Hallazgo de unidades volcánicas del Triásico Medio en la sierra de Imilac, Segunda Región de Antofagasta. In: XIV Congreso Geológico Chileno, pp. 0–2.

STEPHENSON, R. A., and SCHELLART, W. P. (2010) The Black Sea back-arc basin: insights to its origin from geodynamic models of modern analogues. Geol. Soc. London, Spec. Publ., 340, 11–21.

STERN, R. J., LIN, P. N., MORRIS, J. D., JACKSON, M. C., FRYER, P., BLOOMER, S. H., and ITO, E. (1990) Enriched back-arc basin basalts from the northern Mariana Trough: implications for the magmatic evolution of back-arc basins. Earth Planet. Sci. Lett., 100, 210–225.

STEWART, A. L., and MCPHIE, J. (2003) Internal structure and emplacement of an Upper Pliocene dacite cryptodome, Milos Island, Greece. J. Volcanol. Geotherm. Res., 124, 129–148.

STEWART, A. L., and MCPHIE, J. (2006) Facies architecture and Late Pliocene - Pleistocene evolution of a felsic volcanic island, Milos, Greece. Bull. Volcanol., 68, 703–726.

SUÁREZ, M., and BELL, C. (2010) Sabkhas continentales y costeros en el Triásico Superior-Cretácico Inferior de Atacama, Chile. Rev. Geológica Chile, 145–153.

SUÁREZ, M., and BELL, C. M. (1994) Braided Rivers, Lakes and Sabkhas of the Upper Triassic Cifuncho Formation, Atacama Region, Chile. J. South Am. Earth Sci., 7, 25–33.

SUÁREZ, M., and BELL, C. (1992) Triassic rift-related sedimentary basins in northern Chile (24°-29°S). J. South Am. Earth Sci., 6, 109–121.

TOMLINSON, A. J., CORNEJO, P. and MPODOZIS, C. (1999) Hoja Potrerillos, Región de Atacama. Servicio Nacional de Geología y Minería (Chile), Mapas Geológicos, No. 14, 1 mapa escala 1:100.000, Santiago.

TORSVIK, T. H., and COCKS, L. R. M. (2013) Gondwana from top to base in space and time. Gondwana Res., 24, 999–1030.

VALENZUELA, J. (2014) Estratigrafía y geología estructural de la región de Cerro La Ballena-Portezuelo Azabache (Cordillera de Domeyko 23° 40'-24° 00'S). MSc. Thesis, Universidad de Chile, pp. 147. Santiago de Chile.

VENEGAS, C., CERVETTO, M., ASTUDILLO, N., ESPINOZA, F., CORNEJO, P., MPODOZIS, C., and RIVERA, O. (2013) Carta Sierra Vaquillas Altas, Regiones de Antofagasta y Atacama. Servicio Nacional de Geología y Minería, Carta Geológica de Chile, Serie Geología Básica 159, 1-87. 1 mapa escala 1:100.000. Santiago.

VICENTE, J. C. (2005) Dynamic paleogeography of the Jurassic Andean Basin: pattern of transgression and localisation of main straits through the magmatic arc. Rev. La Asoc. Geológica Argentina, 60, 221–250.

VILLAMOR, P., BERRYMAN, K. R., ELLIS, S. M., SCHREURS, G., WALLACE, L. M., LEONARD, G. S., LANGRIDGE, R. M., and RIES, W. F. (2017) Rapid Evolution of Subduction-Related Continental Intraarc Rifts: The Taupo Rift, New Zealand. Tectonics, 36, 2250–2272.

WALKER, R. G., and JAMES, N. P. (1992) Facies models: response to sea level change. Geological Association of Canada.

WHITE, J. D. L., and HOUGHTON, B. F. (2006) Primary volcaniclastic rocks. Geology, 34, 677–680.

WITHJACK, M. O., SCHLISCHE, R. W., and OLSEN, P. E. (2002) Rift-basin structure and its influence on sedimentary systems. In: Sedimentation in continental Rifts, (Ed. by R. . Renaut and G. M. Ashley), pp. 57–81. Society of Economic Paleontologists and Mineralogists (SEPM), Special Publication 73, Tulsa.

WRIGHT, V. P., and PLATT, N. H. (1995) Seasonal wetland carbonate sequences and dynamic catenas: a re-appraisal of palustrine limestones. Sediment. Geol., 99, 65–71.

Capítulo 4: Gondwanic inheritance on the building of the western Central Andes (Domeyko Range, Chile): Structural and thermochronological approach (U-Pb and ^{40}Ar-^{39}Ar)[3]

Mauricio Espinoza[1], Verónica Oliveros[1], Paulina Vásquez[2], Laura Giambiagi[3], Leah Morgan[4], Rodrigo González[5], Luigi Solari[6], Florencia Bechis[7]

(1) Departamento Ciencias de la Tierra, Universidad de Concepción, Víctor Lamas 1290, Casilla 160-C, Concepción, Chile.
(2) Servicio Nacional de Geología y Minería (SERNAGEOMIN), Santa María 0104, Providencia, Santiago, Región Metropolitana, Chile.
(3) IANIGLA, CCT Mendoza, Centro Regional de Investigaciones Científicas y Tecnológicas, Parque San Martín s/n, 5500 Mendoza, Argentina.
(4) U.S. Geological Survey, Denver Federal Center, Denver, CO, USA.
(5) Departamento de Ciencias Geológicas, Universidad Católica del Norte, Avenida Angamos 0610, Antofagasta, Chile.
(6) Centro de Geociencias, Universidad Nacional Autónoma de México, Juriquilla 76230, Querétaro, México.
(7) Instituto de Investigaciones en Diversidad Cultural y Procesos de Cambio (IIDyPCa), CONICET - Universidad Nacional de Río Negro, San Carlos de Bariloche, Argentina.
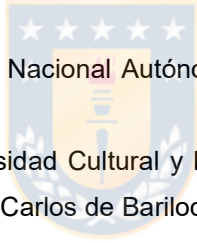
Key Points

• The synrift Domeyko Basin (Triassic) developed as an oblique rift driven by subduction dynamics and far-field Pangea-breakup stresses

• During rift inversion, the metallogenic-fertile Domeyko Fault System nucleated over the former Domeyko Basin master rift faults

• Gondwanic NNW-striking structures controlled Paleozoic exhumation, synrift basin segmentation, and the main Domeyko Range structural style

---

[3] Manuscrito sometido a revista Tectonics el 19 de Marzo de 2019. El Material Suplementariio referenciado en este trabajo se encuentra disponible en la sección de Anexos.

Abstract

Tectonics inheritance controlled the evolution of many orogens. In order to unravel the role of the Gondwanic heritage over the building of the Central Andes in northern Chile (Domeyko Range), we performed detrital U-Pb zircon and Ar muscovite geochronology together with structural analyses (kinematics and structural balancing). Ar detrital muscovite dating reveals contrasting cooling histories of the Paleozoic basement between Triassic rift sub-basins, pointing to a ~NW striking cortical structure segmenting the region since at least the Guadalupian, likely related to the accretional evolution of SW Gondwana. Later on, this structure controlled the location of a structural high separating rift sub-basins. During the Late Triassic, ~NS striking master faults and secondary NW to NNW-striking faults configured a narrow oblique rift primarily driven by subduction dynamics. Compressional tectonics began at Late Cretaceous, whereas the specific inversion of the Triassic rift likely occurred during the Eocene, resulting in the inception of the transpressional Domeyko Fault System at the western slope of the Domeyko Range. The overall structural style of this range was determined by the architecture of the Triassic rift, where the inversion of deep-seated detached faults accounted for west-vergent thick- and thin-skinned structures. In contrast, where only postrift deposition took place, east-vergent, thin-skinned structures were developed. Pre-Andean NW-striking crustal structures also accommodated tectonic rotations during the Incaic orogeny and might delimit the rupture zone of large historical earthquakes, suggesting an underestimated role of such old discontinuities in Andean neotectonics.

4.1 Introduction

The Domeyko Range (Precordillera) of northern Chile represents the western slope of the Central Andes, conforming a ~800 km long, north-south trending belt (Fig. 4.1B), hosting some of the most gigantic porphyry Cu-Mo deposits of the world, including the Eocene-Oligocene '*behemoths*' Chuquicamata and La Escondida deposits (Camus and Dilles, 2001; Cooke *et al*., 2008). This belt is formed by a core of Upper Paleozoic basement rocks thrusted over Mesozoic sedimentary units formerly deposited in a long-lived depocenter known as the Domeyko Basin (Fig. 4.1).

The formation of this late Eocene-Oligocene metallogenic belt was intimately related to the inception of the Domeyko Fault System (DFS), a trench-linked strike-slip structural system that controlled the intrusion of porphyries, especially at the intersection with continental-scale NW to WNW trending 'lineaments' (Chernicoff *et al*., 2002; Richards, 2003). These oblique-trending crustal lineaments have been associated with a pre-Andean basement fabric acquired during the Lower Paleozoic accretional evolution (Chernicoff *et al*., 2002; Ramos, 1994; Salfity, 1985). Although this fabric has been intensely modified by Meso-Cenozoic tectonomagmatic events, these lineaments can be traced based on scattered NW-striking faults exposed from Coastal Cordillera to the Domeyko Range (Fig. 4.1B), as well as volcanic alignments and strike-slip faults from the Altiplano and Puna.

Major strike-slip movements have been proposed for the DFS during the Eocene-Oligocene (Maksaev and Zentilli, 1999; Tomlinson and Blanco, 1997). Additionally, growing evidence suggests that inversion of the former Mesozoic basin and protracted Andean compressional tectonics accounted for the main range building (Amilibia *et al*., 2008; Martínez *et al*., 2018; Muñoz, 1992). Basin inversion comprises an essential mechanism during the building of many orogens (Butler, 1989; Butler *et al*., 2006; Lacombe and Mouthereau, 2002), including the Central Andes (Charrier *et al*., 2002; Giambiagi *et al*., 2015; Martínez *et al*., 2016; Perez *et al*., 2016). Although the previous extensional phase seems to have strongly influenced the Domeyko Range building (Amilibia *et al*., 2008), some key aspect of the rifting process, such as the basin architecture and kinematics, have remained poorly constrained (Espinoza *et al*., 2019). Moreover, debate exists about the driving mechanism of the Domeyko Basin synrift

phase, such as (1) gravitational collapse of the former Permian orogen (Kleiman and Japas, 2009), (2) slab collapse and delamination (Mpodozis and Kay, 1992), or (3) slab-rollback subduction (Espinoza *et al.*, 2019). Therefore, a proper understanding of the specific control of the basin architecture on the structural style of the Domeyko Range is still lacking.
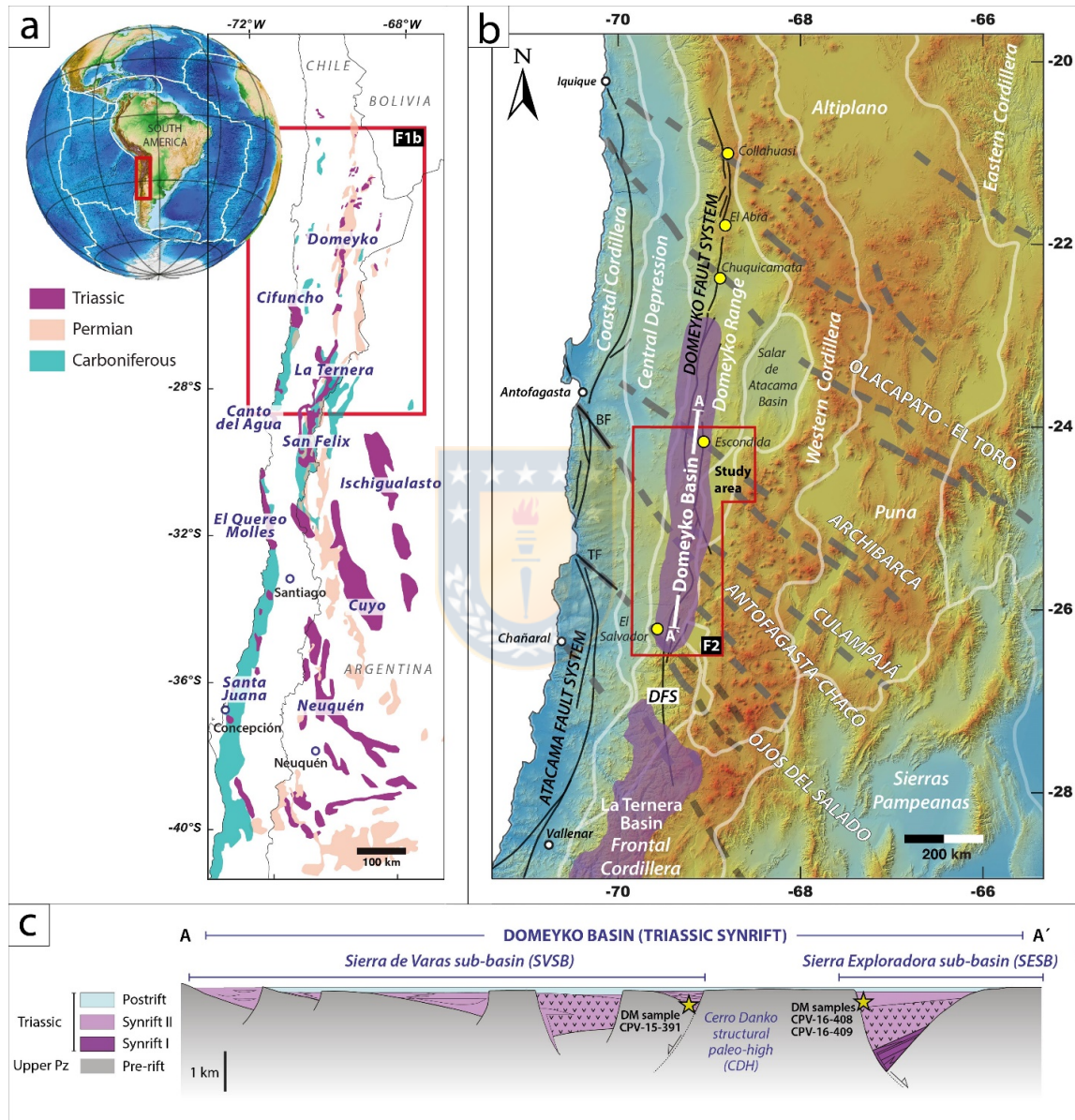
Figure 4.1: A) Gondwanic (Carboniferous-Early Permian) and Pre-Andean (Late Permian-Triassic) cycles units (Charrier *et al.*, 2007) developed at the SW Gondwana margin, including the distribution of Triassic rift basins. B) Map showing main structural systems and morphostructural units of the Chilean-Argentinean Andes (20° to 28°S). Purple areas show the Domeyko and La Ternera basins distributions. Grey segmented lines represent continental-scale NW lineaments after Petrinovic *et al.* (2006). Yellow circles mark giant Cu-Mo porphyry copper deposits. Abbreviations are Barazarte (BZ) and Taltal (TF) faults. C) Simplified geometry of the Domeyko rift basin through an N-S section along the Domeyko Range (A-A' in Fig. 4.1B), showing the schematic location of Ar detrital muscovite (DM) samples.

High-temperature thermochronometers (*e.g.*, U-Pb apatite, [40]Ar-[39]Ar muscovite) resulted in powerful tools in order to unravel the thermal history of source terranes, because their high closure temperature compared to low-temperature thermochronometers (*e.g.*, fission-track and (U-Th)/He methods) (Cochrane *et al.*, 2014; Haines *et al.*, 2004; Hodges, 2005), allowing to interpret exhumation histories related to ancient orogenic processes (Carrapa *et al.*, 2004, 2009). Moreover, the coupling with a high-temperature geochronometer such as detrital zircon U-Pb dating can potentially reveal the crystallization age and the cooling and exhumation age of a region (Carrapa *et al.*, 2009; Haines *et al.*, 2004).

In this paper, we aim to unravel the role of the mechanical anisotropy acquired during Gondwanic tectonic events over the evolution of the western slope of the Central Andes. In particular, we strive to answer how did the Paleozoic accretional history and the rift stage of the Domeyko Basin determine the structural style of the Domeyko Range, and how this heritage controlled the inception of a channel for the ascent of metal-fertile magmas such as the Domeyko Fault System. We present new structural, thermochronological (Ar detrital muscovite dating) and geochronological (U-Pb detrital zircon) data, as well as kinematic analysis of the synrift stage, and structural balancing from the Domeyko Range in northern Chile (22º - 26º S).

4.2 Geological background

The Domeyko Range is a thick- and thin-skinned belt formed by a basement core of Late Paleozoic igneous rocks, uplifted over a Mesozoic stratified cover by steep reverse faults in a double-vergent structural style (Amilibia *et al.*, 2008). Mesozoic successions were initially deposited in the Domeyko Basin, which experienced synrift and postrift deposition from Triassic to Early Cretaceous (Ardill *et al.*, 1998; Vicente, 2005), and is now exposed through ~800 km along the Domeyko Range (Fig. 4.1).

Further south, La Ternera Basin (filled by the homonymous unit), comprises another Triassic rift depocenter, exposed along the present-day Frontal Cordillera (Fig. 4.1B). Geochronological analyses were performed in La Ternera Formation in order to

contrast results from the Domeyko Basin, though a comprehensive depiction of this unit is beyond the scope of this study.

4.2.1 The Domeyko Basin (Triassic - Early Cretaceous)

4.2.1.1 Synrift phase

The synrift phase of the Domeyko Basin took place in two stages (Espinoza *et al*., 2019): (1) the Synrift I (*ca.* 241-226 Ma), with the aperture of the Sierra Exploradora sub-basin (SESB) and (2) the Synrift II (*ca.* 217-200 Ma) with the opening of the Sierra de Varas sub-basin (SVSB) and the reactivation of the SESB. Both sub-basins were separated by a structural high that was by-passed during the postrift phase (Cerro Danko high, Fig. 4.2). The synrift units unconformably overlie Carboniferous to Permian silicic igneous rocks (*e.g.*, La Tabla Formation and plutonic complexes), partly correlated to the Choiyoi igneous province (Kleiman and Japas, 2009). The synrift phase was marked by the deposition of continental sedimentary rocks showing abrupt lithofacies changes between close depocenters (*e.g.,* Quebrada del Salitre, Sierra de Varas and Cerro Guanaco formations). Coeval volcanism comprised an important volume of the infill, ranging from basaltic to rhyolitic lavas and subvolcanic rocks (González *et al*., 2015). On the other hand, low-volcaniclastic depocenters recorded a complete rift cycle during the Synrift II stage in the SVSB, from rift inception alluvial facies to rift climax basinal lacustrine deposits during fault linkage (Sierra de Varas Formation; Espinoza *et al*., 2019).

4.2.1.2 Post-rift phase

The continental synrift deposition was succeeded by a marine transgression during the Rhaetian, developing carbonate platforms with typical coral-rich reef deposits (*e.g.*, Las Bateas and the 'lowest' Profeta units; Álvarez, 2003; Chong and Hilldebrandt, 1985; González *et al*., 2015). These deposits are related to a regional episode of low-accommodation and low-sediment supply to the basin, marking the

onset of the early post-rift phase (Espinoza *et al*., 2019; Prosser, 1993). Marine deposition under thermal subsidence was mainly controlled by global eustatic changes during the Early-Middle Jurassic (*e.g.*, Montandón and Profeta formations) resulting in two transgression-regression cycles (Ardill *et al*., 1998). During the Oxfordian, the basin experienced a continental-scale regression, resulting in the deposition of typical evaporites (*e.g.*, Asientos Formation). Continental-scale sea-level changes during the Bathonian to Valanginian (Middle Jurassic-Early Cretaceous) were the result of regional extensional tectonics (Ardill *et al*., 1998) associated with back-arc volcanism (*e.g.*, Candeleros, Quebrada Vicuñita, and Sierra Fraga formations). The final closing and transitional continentalization of the Domeyko Basin occurred during the Late Jurassic-Early Cretaceous ('upper' Profeta and Quebrada del Chaco Beds; Oliveros *et al*., 2012; Venegas *et al*., 2013).

4.2.2 Basin Inversion and Domeyko Range Building

The inversion of the Domeyko Basin is presumed to have started during the onset of the Andean orogeny (Late Cretaceous) by an event known as the 'Peruana phase' (Steinman, 1929), which resulted in the proto-Domeyko Range, roughly constrained at *ca.* 90-78 Ma (Amilibia *et al*., 2008; Arriagada, *et al*., 2006; Mpodozis *et al*., 2005). At the Salar de Atacama Basin, based on synorogenic deposits provenance, Bascuñán *et al*. (2015) proposed a maximum age of *ca.* 79 Ma for the uplift of the Domeyko Range. However, due to the depositional hiatus during part of the Late Cretaceous (Fig. 4.2B), the onset of compressional tectonics is poorly constrained along the western flank of the Domeyko Range (Ferrando and Espinoza, 2015).
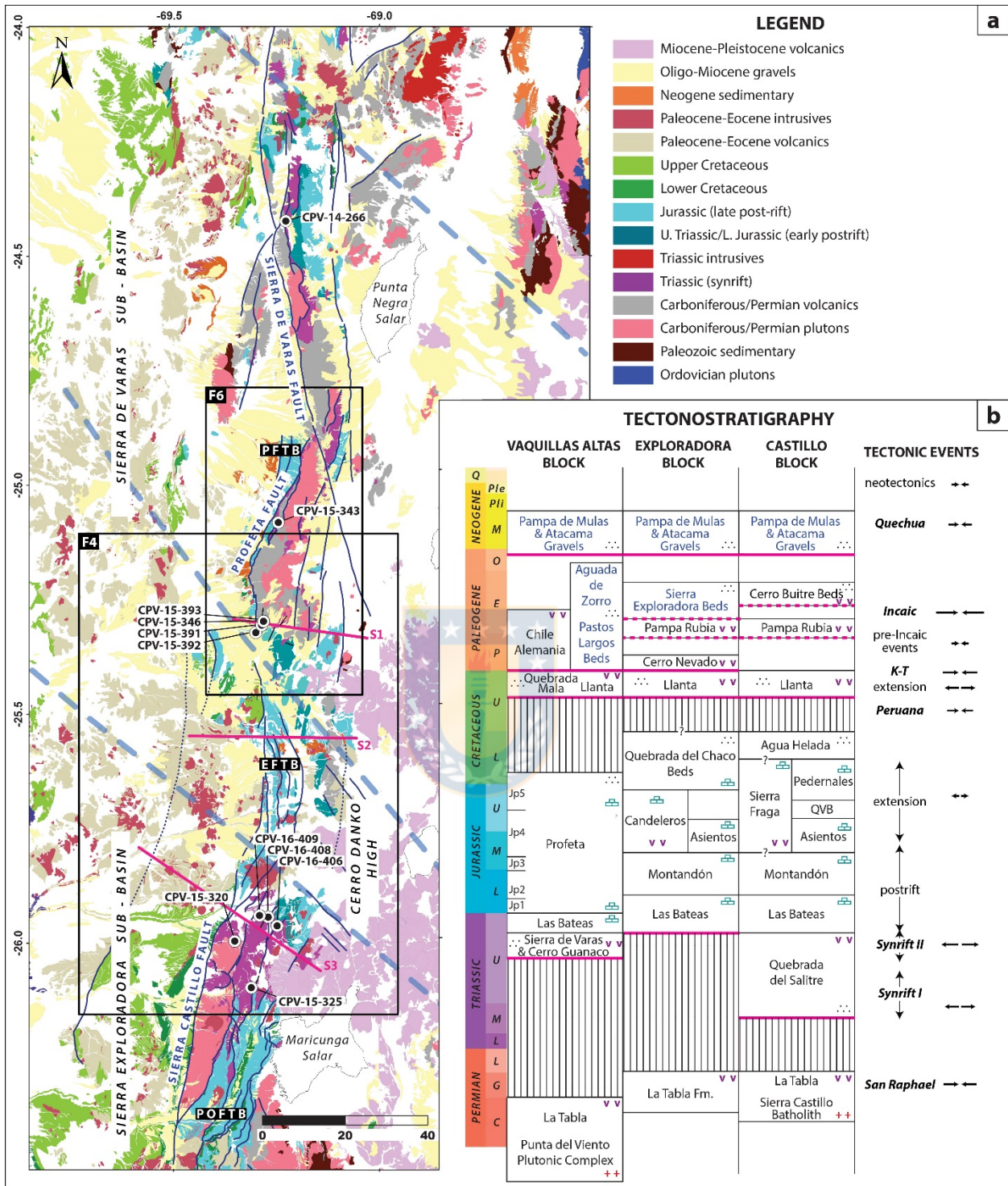
Figure 4.2: A) Geological map of the study area (map references in Text S1 in the Supporting Information section) showing the location of structural sections (S1, S2, and S3) and the Profeta (PFTB), Exploradora (EFTB) and Potrerillos (POFTB) fold-thrust belts. Black dots indicate sample locations and segmented blue lines main lineaments dividing structural blocks. B) Tectonostratigraphic scheme along the study area (block locations in Fig. 4.4). Synorogenic units are in blue. Solid (segmented) magenta lines indicate main (minor scale) unconformities. Vertical lines represent significant hiatus.

77
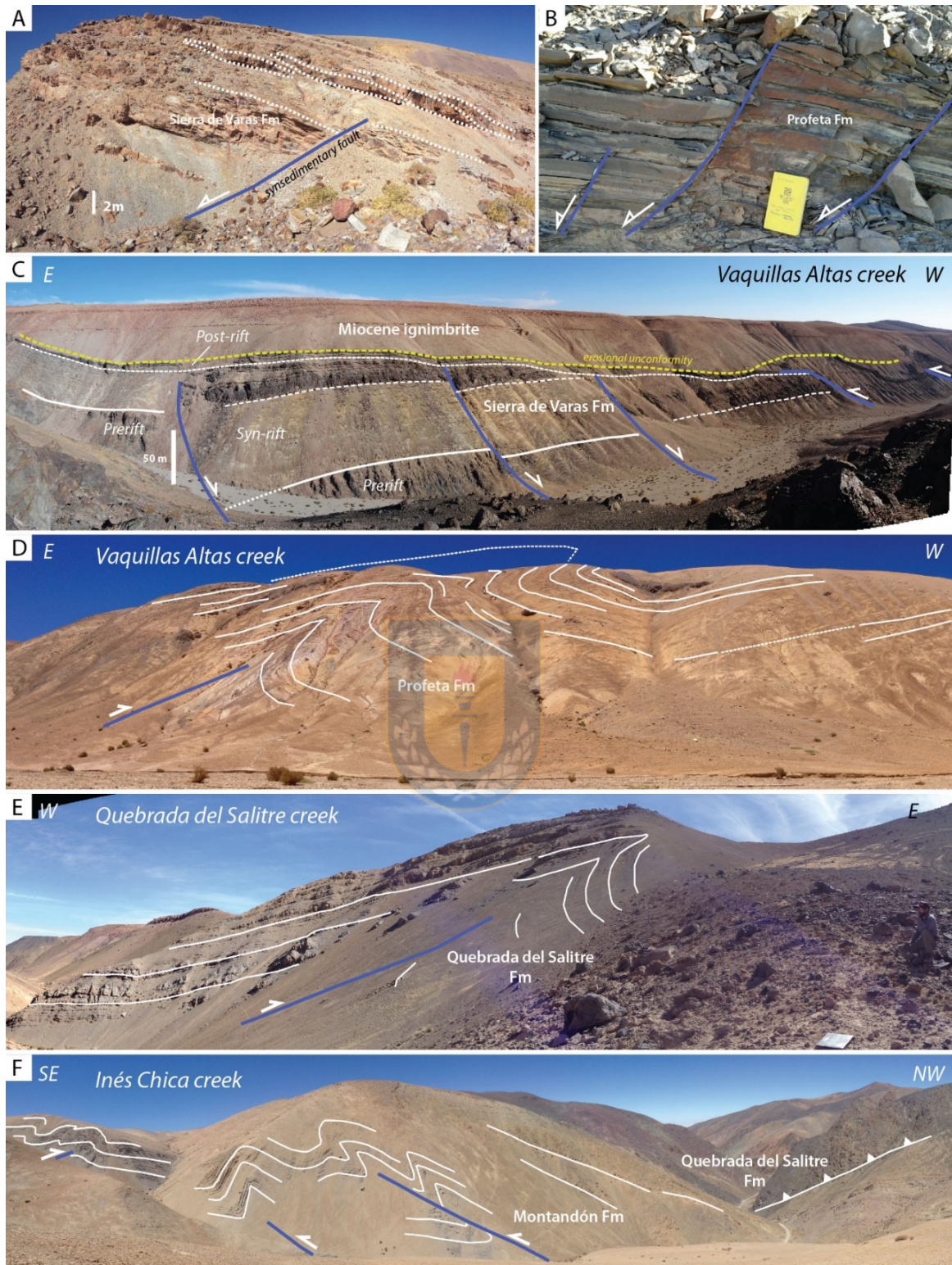
Figure 4.3: A-B) Small-scale synsedimentary normal faults affecting the Sierra de Varas and Profeta formations. C) Listric normal faulting sealed by the Profeta Formation. The flexural border of this hemigraben shows contractional faulting. D-E) Fault-propagation folds affecting the post-rift Profeta and synrift Quebrada del Salitre formations. F) East-vergent, thin-skinned thrusting in the Potrerillos fold-thrust belt.

Subsequent compressional events are recorded during the Cretaceous-Paleocene limit ('K-T' phase; Cornejo *et al*., 2003) and the Eocene-Oligocene "Incaic" phase (Hammerschmidt, 1992; Steinman, 1929). The latter corresponded to an intense period of deformation which comprised the exhumation of Paleozoic plutonic complexes (Maksaev and Zentilli, 1999) as well as the development of thin-skinned Profeta (PFT), Exploradora (EFTB) and Pedernales (POFTB) fold-thrust belts (Fig. 4.2; Cornejo *et al*., 2009; Tomlinson *et al*., 1993). Contemporaneously, a trench-parallel strike-slip structural system (*e.g.*, Domeyko Fault System) was developed, displaying mainly sinistral movements (*e.g.*, Sierra de Varas and Sierra Castillo faults) though dextral reversals have been reported (Niemeyer, 1999; Reutter *et al*., 1996; Tomlinson *et al*., 1994). Transpressional tectonics were associated with the emplacement of giant-scale porphyry copper deposits (Mpodozis *et al*., 2005; Tomlinson and Blanco, 1997), and vertical-axis rotations (Arriagada *et al*., 2006). Synorogenic deposits can be identified from their deposition adjacent to the range front and in between thrust sheets (Pastos Largos, Aguada de Zorro, and Sierra Exploradora Beds units; Cornejo *et al*., 2009; González *et al*., 2015; Venegas *et al*., 2013). Finally, during the Neogene intense denudation of the belt resulted in the aggradation of a thick mantle of partially consolidated synorogenic deposits near the Domeyko Range (*e.g.*, Pampa de Mulas and Atacama gravels; Nalpas *et al*., 2008).

4.3 Methods

4.3.1 U-Pb Geochronology

U-Pb zircon analyses were performed using laser-ablation inductively-coupled-plasma mass-spectrometry (LA-ICP-MS) in 10 detrital and 2 igneous zircon samples. Heavy minerals were separated by standard methods. Finally, zircon grains were handpicked under a binocular microscope, mounted in epoxy, and polished to expose grain centers for cathodoluminescence imaging. U-Pb analyses were performed at the Laboratorio de Estudios Isotópicos (Centro de Geociencias, UNAM), and the Arizona LaserChron Center (University of Arizona). Concordia and average ages were

calculated using Isoplot v. 4.15 (Ludwig, 2011). We applied a discordance filter for igneous (< 5 %) and detrital (< 25 %) analyses, with a reverse discordance filter (> -5 %).

4.3.2 ^{40}Ar-^{39}Ar Detrital Muscovite Thermochronology

Ar detrital muscovite (DM) total fusion dates were performed in four samples, with 87 individual grains analyzed per sample, for a total of 348 detrital grains. Detrital grains were extracted by jaw crusher and roller grinding, sieved by 1.0-0.5 mm and 0.5-0.25 mm fractions. Finally, micas ranging 0.3-2 mm were hand-picked under a binocular microscope. Analyses were conducted in the 40Ar-39Ar laboratory of the U.S. Geological Survey (USGS) in Denver, USA (see Text S2 in the Supporting Information section or Annexe 5).

4.3.3 Kinematic Analysis

Kinematic analyses were performed in small synsedimentary normal faults (centimeter to meter-scale, Fig. 4.3). We identified 67 fault-slip data from synrift (Norian-Rhaetian, five stations) and early postrift (Rhaetian-Hettangian, three stations) units, showing clear evidence of synsedimentary faulting (*e.g.*, growth strata). The direction and sense of slip were determined using kinematic indicators (*e.g.*, mechanical striations and secondary fractures), according to the criteria proposed by Petit (1987). Main axes of the strain ellipsoid were obtained by Bingham distribution statistics (Marrett and Allmendinger, 1990) using the FaultKinWin software (Allmendinger, Cardozo, and Fisher, 2012)
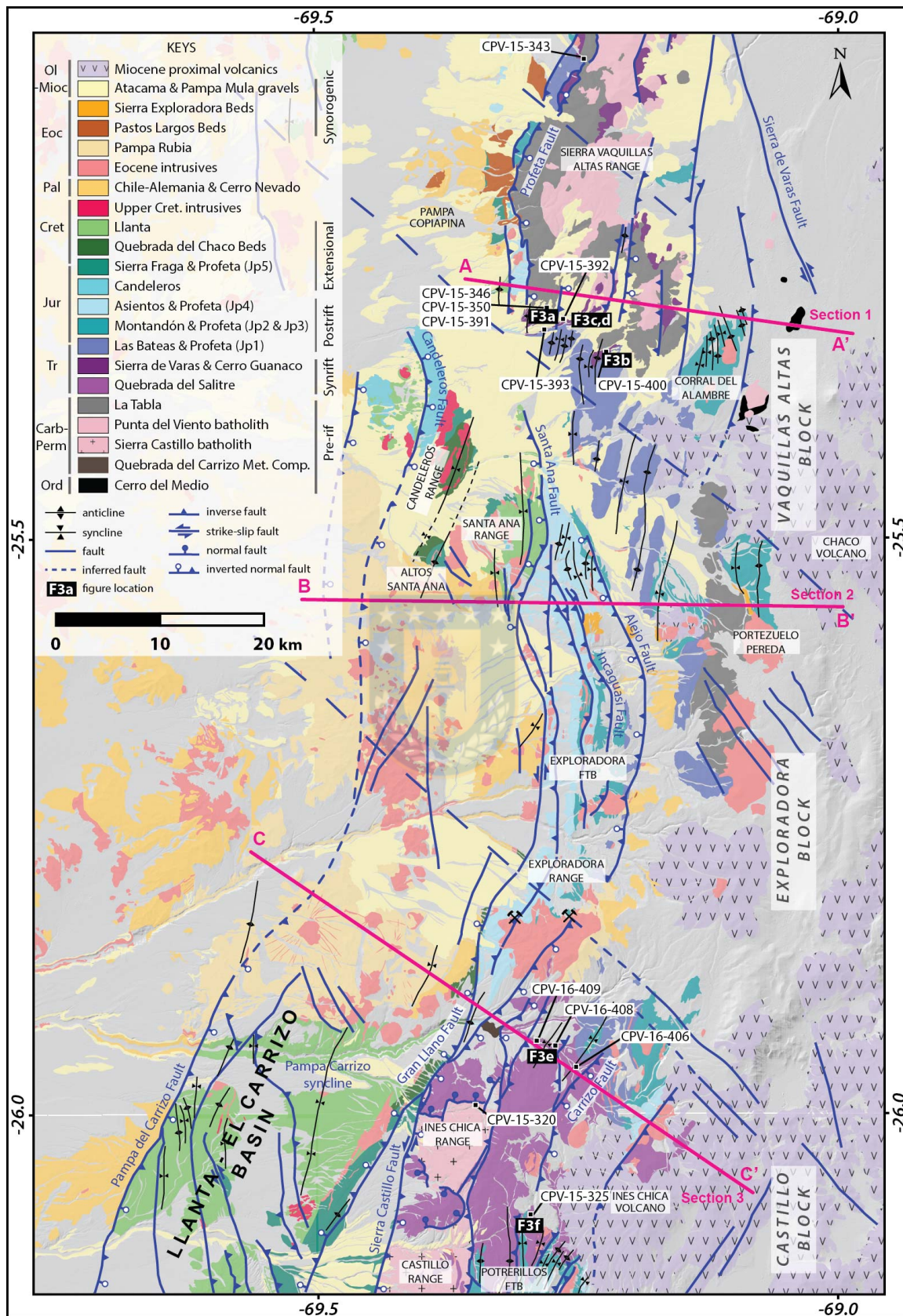
Figure 4.4: Structural map of the study area showing the location of cross sections.

4.3.4 Balanced Cross Sections

Three structural cross-sections where constructed along the Domeyko Range (Fig. 4.4). The main limitation in the reconstruction of deep structures is the lack of seismic profiles and borehole data. However, recent geological mapping considerably improved the stratigraphic, geochronological and structural constraints (Cornejo *et al*., 2009; Venegas *et al*., 2013), allowing us to interpret the sub-surface geometry. Sections were balanced by forward-modeling using MOVE software (Midland Valley Exploration Ltd.). We used Simple Shear algorithm for normal faulting since the pre-rift state (Withjack and Peterson, 1993) whereas Trishear algorithm was used for basin inversion and thrusting (Erslev, 1991). Trishear algorithm was implemented using a trishear apical angle of 50° and propagation versus displacement ratio (P/S) between 1.5 and 15 in order to generate fault-propagation folds and fault-bend folds (Allmendinger *et al*., 2004). Backlimb deformation was accommodated using the inclined shear algorithm for inverted faults, with a shear angle between 60° and 80°, and the fault-parallel flow algorithm for newly formed thrusts. Synrift master faults (Sections S1-S3) were modelled as listric structures based on field observations (Fig. 4.3C), with deep detachments (12-15 km b.s.l.) based on the shallow brittle-ductile transition from thermomechanical models (Giambiagi *et al*., 2015; Julve *et al*., 2018).

4.4 Results

4.4.1 U-Pb detrital zircon geochronology

Detrital zircons U-Pb analyses (DZ) were carried out to reconstruct the provenance of the exposed Triassic units and also to infer the tectonic setting during the depositional stages (Cawood *et al*., 2012). Figure 4.5 summarizes the DZ results for each sample. Sample location coordinates (Table 4.1) and analytical results (Tables S1-S2) can be found in the Supporting Information section (Annexe 8).

4.4.1.1 Sierra de Varas Formation

Five samples yielded DZ ages between 195 and 325 Ma with few grains >500 Ma (Fig. 4.5A). Samples CPV-15-393 (conglomeratic sandstone) and CPV-15-346 (very fine-grained sandstone) were collected from the lower section of the Sierra de Varas Formation (SVF), yielding major components at ~298-296 Ma and a secondary group at ~278-274 Ma (Fig. 4.5A). Three samples were obtained from the upper section of the SVF. Sample CPV-15-343 (tuffaceous sandstone) yielded a unimodal age distribution with the main peak at *ca.* 206 Ma whereas the sample CPV-15-392 shows a prominent peak at *ca.* 212 Ma with a minor group at *ca.* 295 Ma. Sample CPV-14-266 yielded the main peak at *ca.* 297 Ma and a secondary peak at *ca.* 208 Ma.

4.4.1.2 Quebrada del Salitre Formation

Three samples from the upper section of the Quebrada del Salitre Formation (Synrift II) were collected (Fig. 4.5B). Sample CPV-15-325 (medium-grained arkose) yielded the main age group ranging 233-287 Ma centered at *ca.* 259 Ma, and a minor group at 448-460 Ma. Sample CPV-16-406 (coarse-grained sandstone) shows the main age group between 245-295 Ma centered at *ca.* 267 Ma, and a small cluster between 451-480 Ma, whereas the sample CPV-16-408 (very fine-grained sandstone) shows the main group between 261-292 Ma with the major peak at *ca.* 277 Ma.

4.4.1.3 La Ternera Formation

Sample CPV-16-411 was collected from the upper section of the unit exposed in Quebrada Paipote. This sample shows a broad and unimodal age distribution with the main age group spanning 225-295 Ma with a major peak at ~250 Ma and a secondary peak at ~226 Ma. Sample CPV-15-272 (gravelly sandstone) was collected from the upper member in the Río Jorquera creek. This sample displays the main age group between 220-265 Ma with the major peak at ~255 Ma and significant peaks at ~244 Ma and ~226 Ma (Fig. 4.5C). A minor age cluster is defined at *ca.* 285-297.

U-Pb detrital zircon (DZ)

DZ by sample

DZ by unit

Ar detrital muscovite (DM)

Figure 4.5: (A-C) DZ plots from Triassic synrift units. (D-F) Summed DZ plots (all samples) and histograms for each unit. (G-I) DM age distributions from Triassic synrift units, including the percentage of 40Ar radiogenic for each grain (magenta dots).

84

Sample	UTM E	UTM N	Unit	U-Pb IZ	U-Pb DZ	Ar DM	Depositional age (Ma)
CPV-14-266	477331	7298697	Sierra de Varas		x		205
CPV-15-343	475524	7225799	Sierra de Varas		x		206
CPV-15-346	471952	7201896	Sierra de Varas		x		212
CPV-15-392	471504	7200954	Sierra de Varas		x		201
CPV-15-393	470076	7199157	Sierra de Varas		x		212
CPV-15-391	471998	7201940	Sierra de Varas			x	-
CPV-15-325	469000	7113292	Quebrada del Salitre		x		205
CPV-16-406	475253	7128240	Quebrada del Salitre		x		210
CPV-16-408	473084	7130367	Quebrada del Salitre		x	x	220
CPV-16-409	470999	7130750	Quebrada del Salitre			x	-
CPV-15-272	406908	6898788	La Ternera		x		220
CPV-16-411	417696	6998730	La Ternera		x	x	210
CPV-15-279	448251	6933987	La Ternera	x			-
CPV-15-320	465519	7125144	Sierra Castillo batolith	x			-

Table 4.1 Sample identification, location (UTM 19S) and estimated depositional age of analyzed samples (U-Pb zircon and Ar detrital muscovite).

4.4.2 U-Pb igneous zircon geochronology

4.4.2.1 Sierra Castillo batholith

In order to compare the DZ age distribution of the Quebrada del Salitre Formation with the age of the plutonic basement, we sampled the Sierra Castillo batholith (Tomlinson *et al.*, 1999). Sample CPV-15-320 (granodiorite) yielded a Concordia age of 278.9 ± 2.4 Ma (Figure S1a in the Supporting Information section).

4.4.2.2 La Ternera Formation

To provide an absolute constraint for the depositional age of La Ternera Formation, we sampled a lapilli-tuff from the upper section of this unit cropping out in

the Rio Turbio Creek (CPV-15-279), yielding a weighted mean age of 219.4 +3.4/-2.0 Ma (Figure S1b in the Supporting Information section).

4.4.3 ^{40}Ar-^{39}Ar thermochronology

In order to reveal the cooling history of Triassic sources, we performed Ar detrital muscovite dating (DM) in 4 samples deposited during the Synrift II stage (Espinoza *et al*., 2019). A comprehensive list of the analytical results is in the Supporting Information section (Table S3) or Annexe 9.

4.4.3.1 Sierra de Varas Formation

Sample CPV-15-391 (matrix-supported conglomerate) was sampled at the base of the Sierra de Varas Formation in the SVSB. Muscovites extracted from the sand-sized fraction yielded DM dates between 245-193 Ma with the main age peak at *ca.* 202 Ma showing a right-skewed distribution with its long tail lying towards the *ca.* 245 Ma peak (Fig. 4.5G). Fused muscovites showed high radiogenic ^{40}Ar values (80% - 95 %).

4.4.3.2 Quebrada del Salitre Formation

Two samples (CPV-16-408 and CPV-16-409) were collected from fluvial facies (medium-grained sandstones) at the SESB (Fig. 4.5H). Sample CPV-16-408 yielded DM dates between 194 - 271 Ma showing a nearly unimodal distribution with the main component at 264.6 ± 0.3 Ma (98% of the population) and a small component at 195.6 ± 3.4 Ma (2% of the population). Fused muscovites showed high radiogenic 40Ar values (>86%). Sample CPV-16-409 presents a similar DM distribution as the sample CPV-16-408, with the main component at 261.6 ± 0.2 Ma (74% of the population) and small components at 249.7 ± 0.5 (15% of the population) and 238.0 ±0.8 Ma (11% of the population). Radiogenic ^{40}Ar is relatively high (>73%) especially close to the main component (>92%).

4.4.3.3 La Ternera Formation

Sample CPV-16-411 (see Section 4.1.3) yielded a complex DM distribution with the main group of ages ranging from 72 to 118 Ma and centered at ~91 Ma (Fig. 4.5I) showing very low radiogenic 40Ar values (from 40% to 90%). Minor age clusters at ~273-255 Ma, ~239-245 Ma, and 220 Ma show high values of radiogenic ^{40}Ar (92% - 99%).

4.4.4 Triassic rift architecture

Due to the Andean orogeny, major Mesozoic normal faults in the Domeyko Basin were inverted. Hence, the identification of synrift master faults was based on (1) the recognition of significant changes in the structural style of the range, (2) the location of proximal deposits, abrupt lateral facies and thickness variations, and (3) evidence of active deformation during sedimentation (*e.g.* synsedimentary faulting, and slumping). Thereby, we identified major NS to NNE striking faults as the master synrift Triassic faults in the Sierra de Varas (Sierra de Varas and Profeta faults) and Sierra Exploradora sub-basins (Sierra Castillo Fault). The geometry of these east-dipping faults is inferred to be listric, as can be observed in second-order synsedimentary faults (Fig. 4.3C). Adjacent to these faults, proximal deposits were derived from the local Carboniferous-Permian basement, whereas minor sources (Middle Triassic, Famatinian and Grenvillian) were transported from the east through the hanging wall, as evidenced by the DZ fingerprint of synrift units (Fig. 4.5A-F).

Figure 4.6: A) Structural map of the Vaquillas Altas block showing tilting-corrected fault-slip solutions. Raw data can be found in Table S4 (Supporting Information section) or Annexe 7. B) The oblique rifting model proposed for the synrift phase of the Domeyko Basin showing the interaction between ~NS and ~NW normal faults. C) DZ discrimination plot (after Cawood *et al.*, 2012) for Triassic synrift units (N=1196 zircons), including four samples reported by Espinoza *et al.* (2019). Estimated depositional age for individual samples can be found in Table S5 in Supporting Information or Annexe 6.

4.4.5 Kinematic Analysis

Eight stations were measured in the Vaquillas Altas block of the SVSB (Fig. 4.6A). In most synrift stations, normal faults show the main extension direction (T axis) between NE and ENE orientations, indicating that secondary NNW to NW striking

88

normal faults occurred together with the NS to NNE striking master faults in the Vaquillas Altas block. Postrift normal faults are less common and smaller than synrift structures and are likely associated with differential accommodation during thermal subsidence (Cristallini *et al*., 2009). Interestingly, early postrift sites show a distinct WNW to NW extension direction. This result might suggest a change in the regional stress field during the postrift phase related to the ceasing of the tensional stresses and the predominance of the major N-S to NNE-striking structures. Conversely, the postrift station at Cerro Guanaco shows a distinct ~NE main extensional direction (Fig. 4.6A) which could be explained by (1) later tectonic rotations accommodated by the Sierra de Varas Fault, such as those reported since the Paleogene (Arriagada *et al*., 2000) or (2) a non-uniform strain field from the northern and southern depocenters of the SVSB, though more data is necessary to explain this variability.

4.4.6 Balanced cross sections

In this section, we describe the structural styles recognized along the southern Domeyko Range (25º-26.5º S) based on the structural balancing process of three sections located in key structural blocks (Vaquillas Altas, Exploradora and Castillo blocks, Fig. 4.4). Due to the lack of thermochronological data, the fault sequence was based on the analog-modeling of inverted basins (McClay and Buchanan, 1992) and cross-cutting relationships.

4.4.6.1 Section 1: Vaquillas Altas block

This section runs at the southern tip of the Sierra Vaquillas Altas range (SVAR). The front of the SVAR is marked by the high-angle Profeta Fault (PF), which uplifts the Paleozoic basement over the Jurassic-Upper Cretaceous stratified cover (Fig. 4.7). Based on the relationship between Triassic deposits and this fault, we consider that evidences for the inversion of the Triassic rift at this section are: 1) the location of Triassic sequences restricted to the hanging-wall of the PF, (2) the record of Triassic proximal facies adjacent to this fault (Fig. 4.6A), and (3) the recognition of inversion-

related fold geometries (*buttressing* folding) as first reported by Amilibia *et al*. (2008). These observations point to the Profeta Fault as the former master rift fault (Fig. 4.7A).

This fault was likely inverted during the Eocene-Oligocene 'Incaic phase' (Maksaev and Zentilli, 1999; Mpodozis *et al*., 2005). Older regional deformational events, such as the Late Cretaceous 'Peruana phase' (Steinman, 1929) and the Cretaceous-Paleocene 'K-T phase' (Cornejo *et al*., 2003), cannot be assessed due to the absence of surface data from Mesozoic successions to the west of the Profeta Fault. However, we infer they likely occurred in a similar way as recognized in Section 2-3.

Paleogene synorogenic deposits of the Pastos Largos Beds and Aguada de Zorro Formation, suggest westward thrust propagation through short-cut faulting at the SVAR front (Figs. 4.6 and 4.7B), likely related to the development of the thin-skinned Profeta fold-thrust belt to the north of this section (Fig. 4.2). Basement-involved faulting showing variable vergence to the east of the Profeta fault, was interpreted here as out-of-sequence inversion of inferred normal faults and backthrusting (Fig. 4.7B). West-vergent thrusting of the Ordovician and Carboniferous basement over Jurassic cover through a major NNE-striking located to the east, was interpreted here as a newly formed fault (Fig. 4.7C). Thin-skinned folding and thrusting at the Corral del Alambre (Fig. 4.7C) are interpreted as short-cut faults propagated upwards through a shallow detachment likely located at the basement-postrift interface. The latter, together with the likely inversion of the Profeta Fault involving crystalline basement, configure the Sierra Vaquillas Altas range (SVAR), as a west-vergent, thick- and thin-skinned belt.
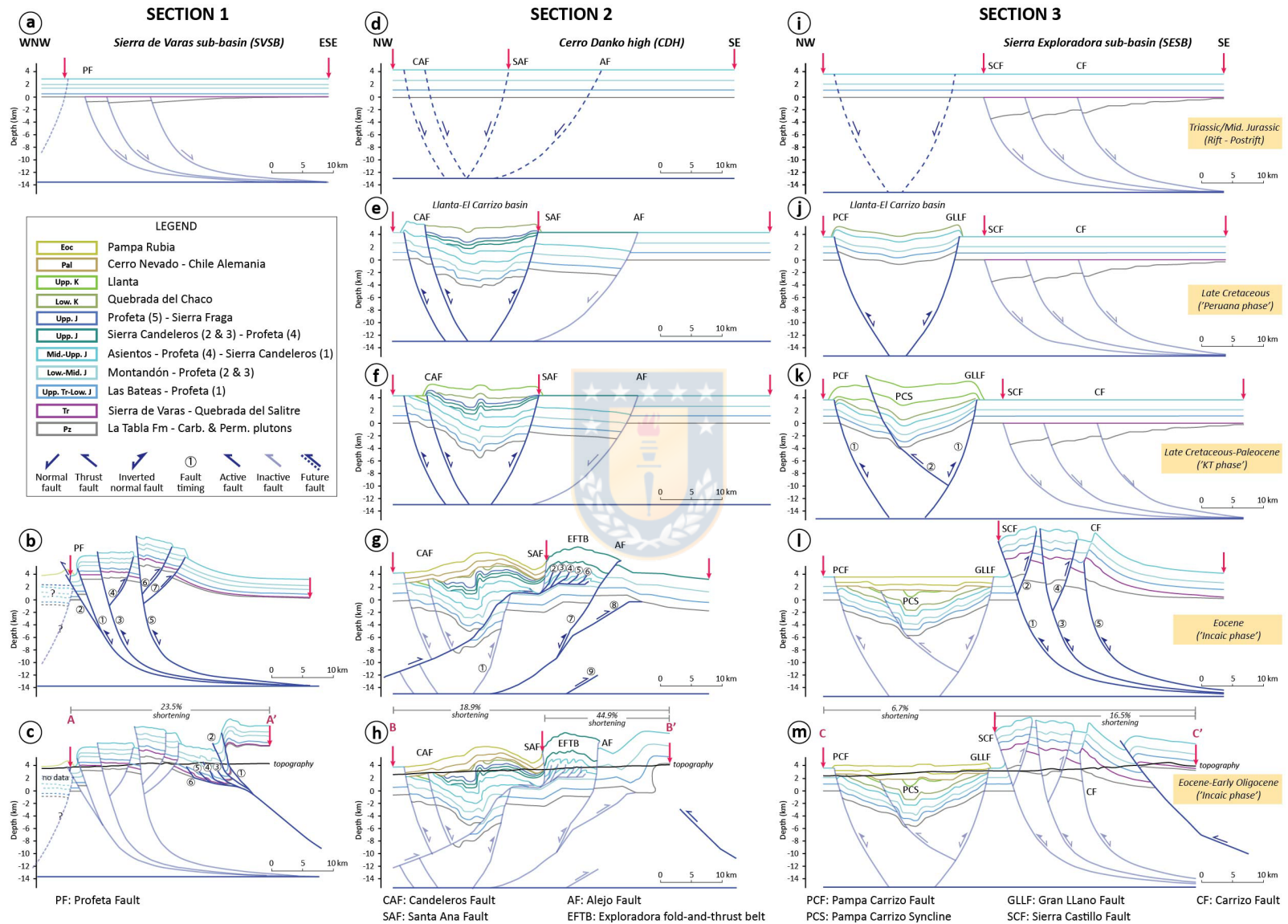
Figure 4.7: Forward modeling of Section 1 (A-C), Section 2 (D-H) and Section 3 (I-M).

91

4.4.6.2 Section 2: Exploradora block

Section 2 is located in the northern part of the Exploradora block, which represented a structural high during the Triassic synrift phase, recording only postrift deposition (Fig. 4.7D; Espinoza *et al*., 2019). This block displays two structural domains delimited by the Santa Ana Fault (SAF). To the west, Middle Jurassic to Upper Cretaceous sequences are deformed in open folds with ~NNE, and ~NNW oriented axes (Fig. 4.4). Due to the thick pile of Jurassic-Cretaceous successions delimited by the SAF, we interpret it as a west-dipping, originally Jurassic and later inverted normal fault, corresponding to the prolongation of the inverted Gran Llano Fault (Amilibia *et al*., 2008). The western part of the section was projected from the northern Sierra Candeleros Range, showing a major N-S inverted normal fault (Candeleros Fault, CAF), which initially controlled the deposition of Upper Jurassic-Lower Cretaceous units (Fig. 4.7E) and later uplifted them over Upper Cretaceous volcanic rocks (73-68 Ma; Venegas *et al*., 2013). We interpret the CAF as an antithetic structure related to the SAF, both representing the northern prolongation of the Llanta-El Carrizo basin (Fig. 4.4; Cornejo *et al*., 2009). A slight angular unconformity between Upper Jurassic and Upper Cretaceous units (Venegas *et al*., 2013) suggests that the compression and associated tectonic inversion occurred during the Late Cretaceous 'Peruana phase' (Fig. 4.7E). On the other hand, a well-developed unconformity between Lower Cretaceous and Paleocene successions in the Alto de Santa Ana anticline (Fig. 4.4) was likely formed during the Cretaceous-Paleocene 'K-T phase' (Fig. 4.7F).

To the east of the SAF, the thin-skinned, east-vergent Exploradora fold-thrust belt (EFTB) involves only Jurassic postrift sequences, likely formed by a shallow detachment at Oxfordian evaporites (Asientos Formation). In order to fit the geometry and present position of folds and faults, the EFTB was interpreted as likely formed by the decapitation of normal faults of the Llanta-El Carrizo basin related to the transfer of the deformation to the eastern domain (Fig. 4.7G). The eastern limit of the EFTB is marked by the Don Alejo Fault (AF), a Jurassic normal structure (Cornejo *et al*., 2009) interpreted as inverted through the advance of the EFTB. Slightly asymmetric folding affected postrift successions and the effusive Paleozoic basement (La Tabla

Formation), interpreted as the result of in-sequence thrust propagation using a shallow detachment at the basement-postrift interface (Fig. 4.7G). The timing of the EFTB activity is constrained by Eocene synorogenic deposition between thrust sheets (Sierra Exploradora Beds). A basement-cored anticline located to the east (Fig. 4.7H) is inferred to have been produced by later west-vergent blind faulting. Eocene subvolcanic intrusions at the hinge anticline suggest an Eocene date for this event (Fig. 4.4).

4.4.6.3 Section 3: Castillo block

This section is located in the northern part of the Castillo block (Fig. 4.4), where the Sierra Exploradora sub-basin (SESB) formerly developed. Two structural domains are limited by the Gran Llano Fault (GLLF), a high-angle inverted normal fault (Amilibia *et al*., 2008). To the west, the Upper Cretaceous Llanta Formation displays an open and symmetric syncline (Pampa del Carrizo syncline, PCS) limited to the west by the Pampa del Carrizo Fault (PCF). We interpret the large-wavelength and symmetry of the PCS as the result of the inversion of a wide graben bounded by the GLLF and PCF (Fig. 4.7I), as depicted by the analog-modeling of inverted grabens (Brun and Nalpas, 1996). This graben was likely related to volcano-tectonic subsidence, controlling the deposition of a thick pile of Upper Jurassic to Upper Cretaceous successions (Llanta-El Carrizo basin).

A slight angular unconformity between Lower and Upper Cretaceous rocks at the eastern limb of the PCS would represent a Late Cretaceous compressional event (Fig. 4.7J). Unconformably overlying the PCS, Paleogene units are gently folded, constraining an inversion episode of the Llanta-El Carrizo basin to the Cretaceous-Paleocene limit ('K-T' phase). We interpret that basin inversion included backthrust faulting related to the reactivation of the GLLF (Fig. 4.7K).

To the east of the GLLF, complex faulting and small-wavelength, close and asymmetric folding of synrift and postrift successions highly contrasts with the structural style of the likely inverted Carrizo-Llanta basin graben (Fig. 4.7L). These sequences are limited to the west by the high-angle Sierra Castillo Fault (SCF), a transpressive

fault active during the Eocene (Niemeyer, 1999; Tomlinson *et al*., 1993). However, the adjacent location of Triassic proximal deposits (*Synrift I*) points to a former activity of the SCF as the master rift fault of the SESB.

Variable vergence of reverse faults affecting the crystalline basement were interpreted here as originated by the out-of-sequence inversion of Triassic normal faults and accompanying backthrusting in a similar way as inferred in Section 1. The inversion of another inverted normal fault (Carrizo Fault, CF) formed a closed footwall syncline later cut by a backthrust, locally defining a triangular zone (Fig. 4.7L). Later on, a west-vergent thrust equivalent to those recognized in the eastern part of Section 1-2 was developed (Fig. 4.7M). Based on the similarity of this thick and thin-skinned, west-vergent belt with the structural style of Section 1, where Eocene synorogenic deposits are present at the range front, we infer that inversion of the Triassic rift at this area was probably developed during the Eocene 'Incaic phase'.

4.5 Discussion

4.5.1 Triassic synrift tectonics

Major NS to NNE striking master faults (Sierra de Varas, Profeta, and Sierra Castillo faults), controlled the development of a long and narrow rift system (Fig. 4.8B). On the other hand, NW to WNW secondary normal faults from the Vaquillas Altas block (Section 4.3) suggests a significant obliquity with respect to the strike of master faults. Evidence of regional NNW to NW striking structures along the rift axis include: (1) Triassic NNW striking cataclasites in the SVSB (Niemeyer *et al*., 2004), (2) local and regional ~NNW to ~NW lineaments (Fig. 4.8) cutting across the Domeyko Range (Abels and Bischoff, 1999; Salfity, 1985) and (3) abrupt facies changes and local structural highs delimiting depocenters along the Domeyko Basin.

We propose that the synrift Domeyko Basin evolved as an oblique rifting (Brune *et al*., 2018; Tron and Brun, 1991), where basin-bounding NS to NNE striking structures acted as oblique faults, with inferred sinistral and normal movements, whereas NW to WNW striking structures represented pure normal faults in a transtensional system (Fig.

4.6B). Furthermore, several key features of transtensional basins can be identified in the Domeyko Basin, such as (1) a strong longitudinal and lateral asymmetry (Christie-Blick and Biddle, 1985), (2) narrow basins and rapid changes in lateral facies and thickness between near depocenters (Belt, 2012; Dorsey and Umhoefer, 2012) and (3) prominent topographic margins (Nilsen and Sylvester, 1998), as evidenced by the local sediment provenance (Fig. 4.5).

The NNW to NW-striking structures related to the Triassic rifting in Southwestern Gondwana (Charrier, 1979) have been associated with a pre-existing basement fabric acquired during the accretionary evolution of the margin (Ramos, 1994). However, unlike oblique rifts where pre-existing structures control the orientation of major basin-bounding faults (Bellahsen *et al*., 2006; Morley, 2007), such as the Atuel depocenter of the Neuquén Basin (Bechis *et al*., 2010, 2014), the Domeyko Basin master faults apparently did not nucleated over the former weaknesses. Instead, the pervasive ~NNW striking fabric interacted with the ~NS master faults producing highly asymmetric releasing bends (Espinoza *et al*., 2019). We propose that the orientation of master faults was controlled by parallel-margin weaknesses associated with the slab-pull force of active subduction. Near the continental margin, the slab-pull from a retreating trench would have acted in combination with far-field tectonic stresses arising from the breakup of Pangea, which controlled the extension of inboard depocenters such as the Neuquén, Ischigualasto and Cuyo basins (Giambiagi *et al*., 2009, 2011). Additionally, plate-kinematic models suggest a slight oblique convergence compatible with sinistral movements during the *Synrift II* stage (*e.g.*, Matthews *et al*., 2016), which would have enhanced the development of transtensional tectonics. Triassic active subduction along the southwestern Gondwana has been supported by recent geochemical studies (Coloma *et al*., 2017; del Rey *et al*., 2016; González *et al*., 2017; Oliveros *et al*., 2017). This hypothesis is supported by the detrital zircon fingerprint of Triassic units of the Domeyko Basin, plotting in the subduction field of the tectonic discrimination diagram (Fig. 4.6C) proposed by Cawood *et al*. (2012).

Significant tectonic rotations mainly related to the building of the Bolivian orocline are recorded in northern Chile since the Paleogene (Arriagada *et al*., 2006). To the west of the study area, pre-Miocene units show ~30° clockwise rotations (Fig.

4.8A). Therefore, the rift axis likely presented a ~NNW to ~NS orientation before the oroclinal curvature acquisition. However, local vertical-axis correction for secondary NNW to NW normal faults cannot be performed because of a paleomagnetic data gap in the Vaquillas Altas block. Despite this, the oblique rifting model agrees with all the evidence mentioned above, though the specific obliquity of the system remains undetermined.
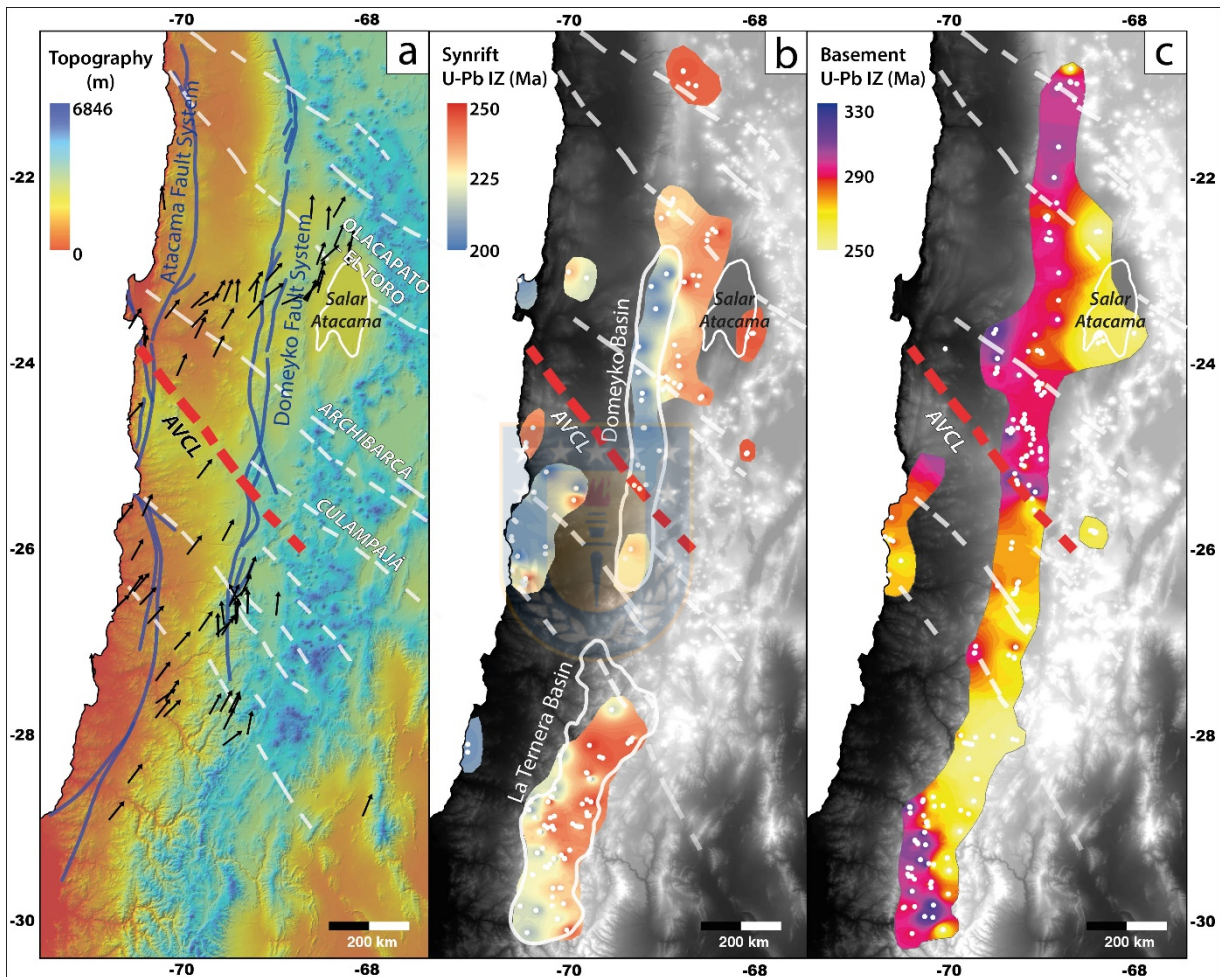
Figure 4.8: (A) Topographic map showing NW continental-scale lineaments (Petrinovic *et al*. 2006). AVCL (Antofagasta-Volcán Chaco lineament). Black arrows indicate paleomagnetic rotations (Arriagada *et al*., 2006). (B-C) Inverse Distance Weighting interpolation of Triassic and Paleozoic igneous zircon U-Pb ages (white points).

4.5.2 Cooling history of triassic synrift sources

In the SESB, U-Pb detrital zircon ages (DZ) from the Quebrada del Salitre Formation show a single source at ~277 Ma (Fig. 4.9C), similar to the 278.9 ± 2.4 Ma

age obtained for the Sierra Castillo batholith. On the other hand, the Ar detrital muscovite (DM) age distribution shows the main peak at *ca.* 262-267 Ma with minor peaks at ~250 and ~238 Ma (Fig. 4.9C). The DM well-defined significant peak and the small difference between both the crystallization (DZ) and cooling (DM) age distributions of the sources point to a discrete cooling event during the Guadalupian (262-267 Ma). We interpret this as the exhumation of the Permian (Cisularian) batholith in the SESB. This event coincides with the 'San Rafael phase' recorded near Calama (~280-260 Ma), associated with the exhumation of Early Paleozoic high-pressure metamorphic rocks (Lucassen *et al.*, 1999; Tomlinson *et al.*, 2007), indicating the younger activity of this orogenic event in the Castillo structural block (Fig. 4.10A).

On the other hand, DM results from the SVSB show striking differences with respect to the SESB. Thus, DZ ages from the base of the Sierra de Varas Formation show the main age group between *ca.* 270-310 Ma with a peak at ~292 Ma (Fig. 4.9B), and minor ages between 210-250 Ma (Espinoza *et al.*, 2019). In contrast, DM results show a complex distribution ranging between 192-243 Ma with the main peak at ~202 Ma. The broad distribution and its much younger peak compared to the age of the primary source (Cislurian) can be related to (1) multiple sources or (2) a gradual uplift of a slowly exhumed terrain, according to Haines *et al*. (2004). Based on the predominance of local Permian sources in the Sierra de Varas Formation (Fig. 4.5A), and the muscovite-poor nature of coeval Triassic sources, we discard the existence of multiple sources with different unroofing histories. Notwithstanding, we propose the DM distribution in the SVSB reflects a gradual uplift of the Paleozoic plutonic basement since ~243 Ma, without experiencing the 'San Raphael' event recorded in the SESB.

Interestingly, the main DM peak in the SVSB is younger than the depositional age of the succession (~212-210 Ma; Espinoza *et al.*, 2019), suggesting an aperture of the Ar system close to ~192 Ma (Fig. 4.9B). The coincidence of this age with the youngest altered K-Ar ages from the Paleozoic plutonic basement (weighted mean of 191.9±2.3 Ma, Fig. 4.9A), points to a regional thermal event rather than processes such as burial metamorphism or diagenetic alteration. We propose that this thermal event could be related to the oldest and poorly dated Jurassic back-arc volcanism in the study area (Sierra Fraga Formation). This hypothetical age of the initial back-arc magmatism

is in agreement with the Sinemurian-Pliensbachian oldest arc-volcanism of La Negra Formation in the Coastal Cordillera (Escribano *et al*., 2013).

Alternatively, the DM distribution in the SVSB could be interpreted as primarily similar to the DM distribution in the SESB, but suffering a strong reset during the Lower Jurassic thermal event. We discard this hypothesis based on the DM results from La Ternera Basin (Fig. 4.9D). Here, a full-reset of the DM dates occurred between *ca.* 110-72 Ma, much younger than the depositional age of the succession (~219 Ma) and coinciding with the 'Peruana phase' timespan (Bascuñán *et al*., 2015). Unlike the DM of the SVSB, the full-reset in La Ternera Basin shows low radiogenic 40Ar values (Fig. 4.5I). Furthermore, relict DM dates still reflect the Permo-Triassic cooling age of the sources indicated by DZ data. Thus, we distinguish the DM partial reset occurred in the SVSB, to the DM full-reset occurred in the La Ternera Basin.
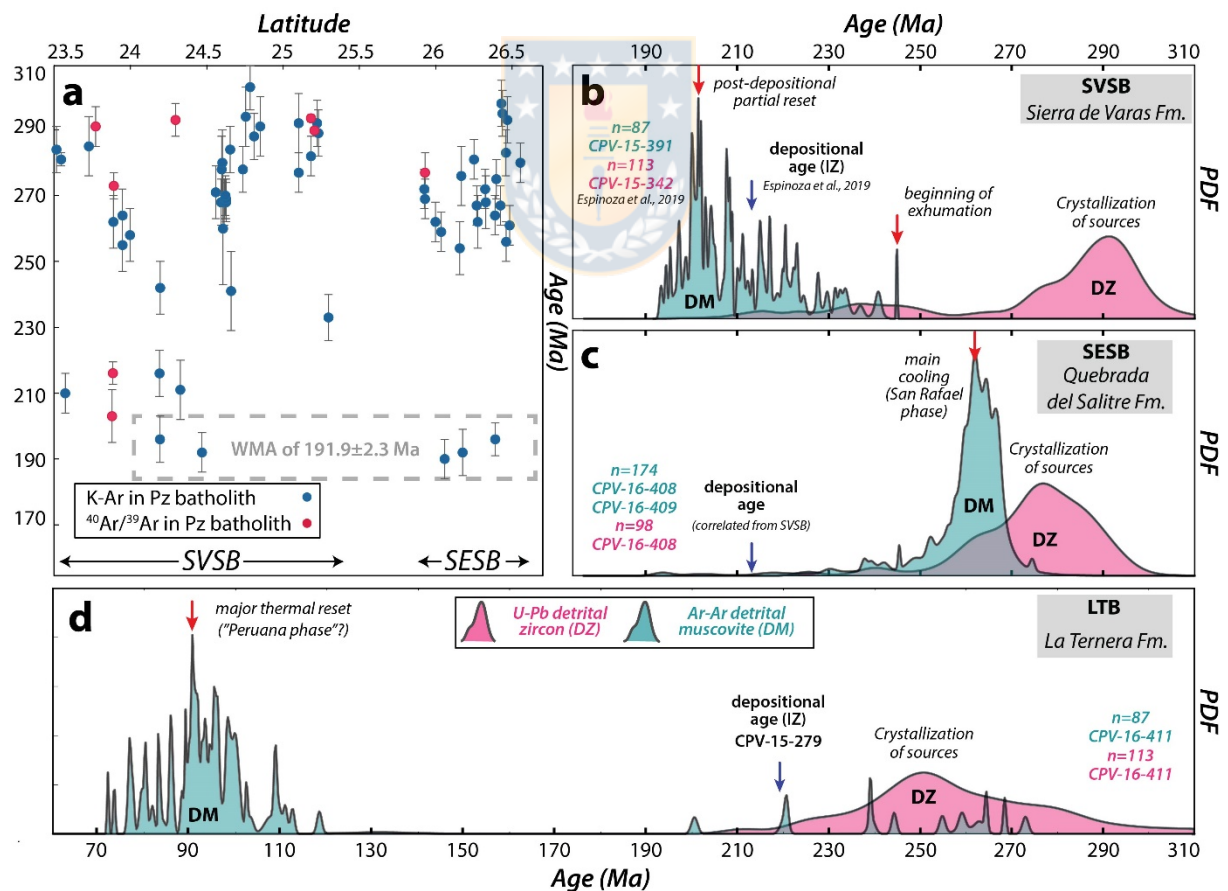
Figure 4.9: (A) K-Ar and 40Ar-39Ar dates from the Paleozoic plutonic basement in the Domeyko Range. References in Text S3 in the Supporting Information. (B-D) Combined DZ and DM probability density plots from Triassic synrift units.

4.5.3 Inheritance over the western Central Andes building

In this section, we discuss how ancient Gondwanic processes (*e.g.*, accretion and rifting) inherited an indelible mechanical anisotropy during the evolution of the Central Andean forearc.Firstly, the DM dating revealed a major cooling event during the Guadalupian (*ca.* 262-267 Ma), corresponding to the San Rafael orogenic event, extending the area of influence of this well-recognized orogeny in western Argentina (Kleiman and Japas, 2009) and Chilean Frontal Cordillera (Mpodozis and Kay, 1992), settling a protracted period of mountain-building and exhumation during *ca.* 280-260 Ma. However, as evidenced by the local exhumation of the Limon Verde metamorphic complex near Calama (Tomlinson *et al*., 2007), this orogenic event seems to have occurred by segments (Fig. 4.10A). Thus, the San Rafael phase was recorded in the Castillo block but not in the Vaquillas Altas block, which began to slowly cool since the Middle Triassic (Fig. 4.10A), coeval to the activity of extensional depocenters near the Salar de Atacama Basin (El Bordo Beds, Tuina and Pular formations; Cortés, 2012; Henríquez *et al*., 2014; Solari, 2017). We explain this by the existence of a major NW structure segmenting the Paleozoic basement since at least ~265 Ma (Antofagasta-Volcán Chaco lineament, AVCL). The AVCL correlates with a noteworthy break in the ages of the Paleozoic basement (Fig. 4.8C), pointing to a first-order segmentation of the Gondwanic magmatic belt (Fig. 4.10A).

Later on, the AVCL would have defined the position of a significant structural-high (Cerro Danko high), which separated both sub-basins of the Domeyko Basin (SVSB and SESB) during the Triassic rifting (Fig. 4.10B). Additionally, during the Synrift II stage (*ca.* 217-200 Ma; Espinoza *et al*., 2019), the development of rift climax sequences along the SVSB evidences a fault linkage process (Gawthorpe and Leeder, 2000), which resulted in a ~600 km long ~NS trending rift. We propose that the interaction between ~NS master faults and the pervasive NNW to NW basement fabric configured an oblique transtensional rift, mainly controlled by slab-rollback and secondary Pangea-breakup far-field stresses (Fig. 4.10B).
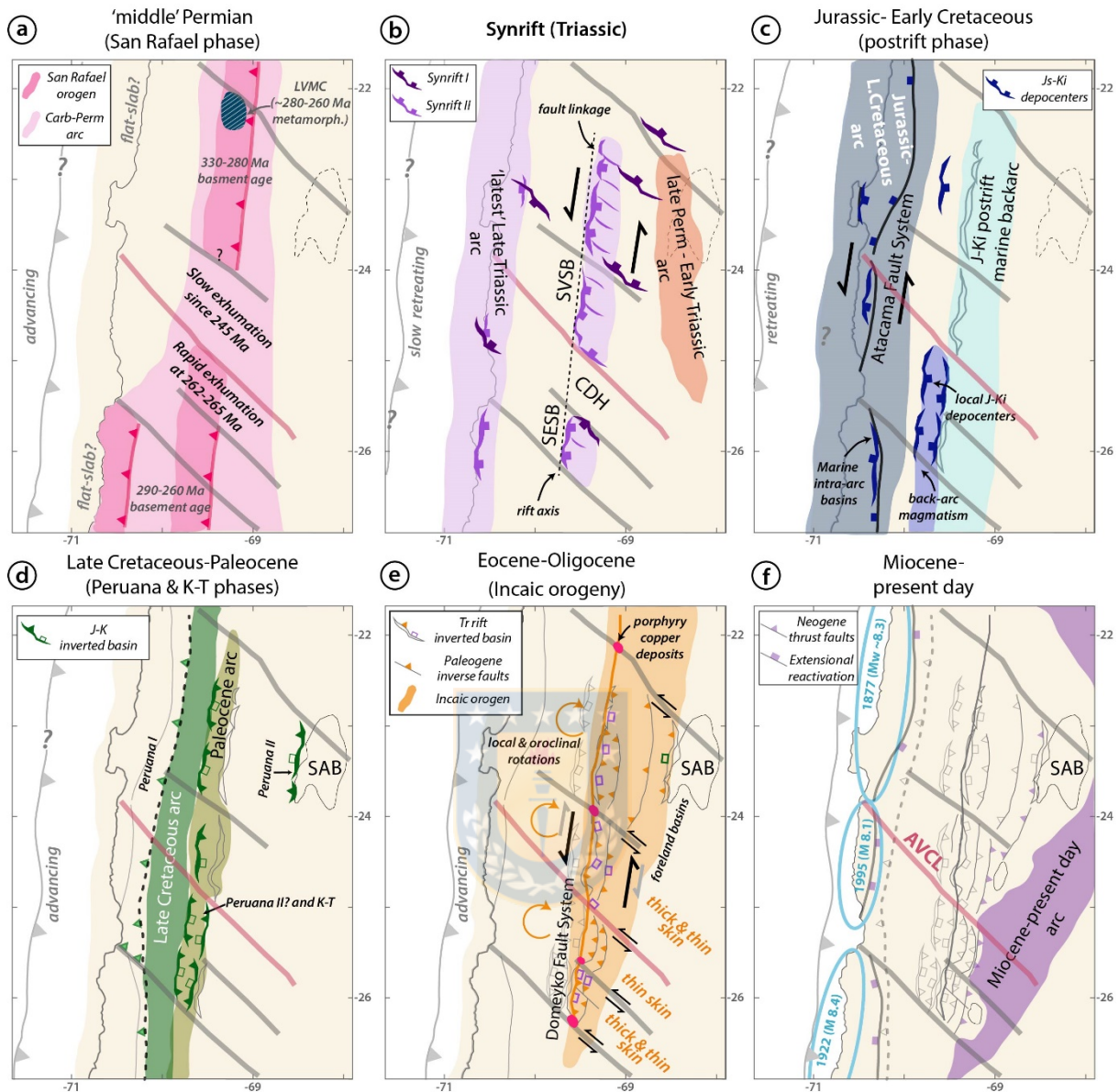
Figure 4.10: (A) San Rafael orogeny: Carboniferous-Permian batholiths were exhumed in discrete segments controlled by NW pre-Andean structures. (B) Triassic rifting: Sub-basins of the Domeyko Basins (Sierra de Varas and Sierra Exploradora sub-basins; SVSB and SESB, respectively) were limited by the Cerro Danko high (CDH), controlled by an NW-striking cortical structure. Oblique rifting during the 'Synrift II' (217-200 Ma) led to a transtensional (sinistral) system. (C) Jurassic-Early Cretaceous: Postrift back-arc basin took place in the former synrift. Also, principal curvatures and offsets of the Atacama Fault System correlate with the position of the main NW-trending lineaments. (D) Late Cretaceous-Paleocene: 'Peruana phase' led to the uplift of the Coastal Cordillera ('Peruana I' event) and the inversion of local Late Jurassic to Late Cretaceous depocenters ('Peruana II' and K-T events)(SAB: Salar Atacama basin). (E) Eocene-Oligocene 'Incaic orogeny': Rift inversion and Domeyko Fault System inception over the former 'Synrift II' rift. Thick- and thin-skinned structures were controlled by the sites where synrift took place. (F) Miocene-present day: Migration of the deformation to the eastern margin of the Domeyko Range. Major earthquake ruptures zones correlate with domains defined by NW cortical structures.

During the Late Jurassic-Early Cretaceous and after the postrift period, extensional tectonics was focused along the Coastal Cordillera by the settlement of the transtensional Atacama Fault System (AFS). There is a noteworthy match between first-order curvatures of the AFS and significant NW-striking faults in the Coastal Cordillera (Fig. 4.2, Taltal and Barazarte faults), which defined the limits of a crustal-scale sliver ('Paposo sliver'; Veloso *et al.*, 2015), suggesting that NW-striking pre-Andean structures delimited rigid blocks which segmented the AFS during the Late Jurassic-Early Cretaceous.

At the Domeyko Range, Late Jurassic-Early Cretaceous basins were formed west of the former rift axis (Fig. 4.10C). These depocenters were partially inverted during the Late Cretaceous 'Peruana II phase' (*ca.* 78 Ma; Bascuñán *et al.*, 2015), though the precise timing and significance of this event remain poorly constrained in the study area (Fig. 4.10D). This contractional phase seems to coincide with the development of intra-arc extensional basins (*e.g.,* Llanta-El Carrizo basin, LLCB) during the Late Cretaceous (Mpodozis *et al.*, 2005). However, based on the precise age of the Llanta Formation in the study area (73-68 Ma; Venegas *et al.*, 2011), we interpret that the LLCB represents the extensional reactivation of the former Late Jurassic-Early Cretaceous inverted basin. The LLCB corresponded to a wide volcano-tectonic graben later inverted during the well-recorded Cretaceous-Paleocene 'K-T phase' (Cornejo *et al.*, 2003).

Nevertheless, the most critical control of the former Gondwanic fabric over the Andean building took place during the Paleogene. We propose that the Eocene-Oligocene Domeyko Fault System (DFS) nucleated over the former ~NS trending Triassic rift. This inception was possible due to the efficient fault-linkage process during the rift climax phase in the SVSB (Espinoza *et al.*, 2019). The rift system shows a high-spatial coincidence with the Eocene-Oligocene magmatic and metallogenic belt, allowing the ascent of deeply sourced magmas (Camus and Dilles, 2001). Furthermore, highly focused conduits which promoted the emplacement of giant porphyry-Cu deposits would have been created at the intersection of the DFS with NW pre-Andean crustal structures (Fig. 4.10E; Richards, 2003). The importance of (1) a preexisting fabric, (2) extensional deep-seated master faults and (3) the later coincident with

subduction-related magmatism, has been proposed as a key combination in the development of large porphyry-Cu-Au deposits (Gow and Walshe, 2005).

Together with the inception of the DFS, rift inversion and basement exhumation (≥ 4-5 km, Maksaev and Zentilli, 1999) took place during the Eocene-Oligocene 'Incaic' orogeny. Due to the high-angle dip of master rift faults, they were unlikely inverted as pure contractional structures. Instead, basin inversion would have been facilitated by oblique faulting in a transpressional setting (inverse and sinistral strike-slip). Contemporaneously, NW striking pre-Andean structures acted as sinistral transfer zones (Fig. 4.10E; Tomlinson *et al*., 1993), accommodating local vertical-axis rotations of major structural blocks (Abels and Bischoff, 1999).

During basin inversion, the rift architecture controlled main structural style changes of the Domeyko Range. In sites where synrift deposition occurred (SVSB and SESB), shortening was accommodated by basin inversion together with hybrid thick- and thin-skinned, west-vergent structures, whereas where only postrift deposition took place, thin-skinned structures (Exploradora fold-thrust belt, EFTB) were developed (Fig. 4.10E). In thick-skinned blocks, inverted normal faults were modeled with a deep detachment in the mid-crust (~13-16 km, Fig. 4.7), following other rift-rooted orogens (*e.g.*, Lacombe and Mouthereau, 2002) and coherent with the brittle-ductile transition predicted by thermomechanical models (Giambiagi *et al*., 2015; Julve *et al*., 2018). Deep-detached faults allowed the later uplift of the Paleozoic crystalline and metamorphic basement. Due to the highly faulted and asymmetric rift hemigraben, basin inversion involved a complex sequence of faulting, together with backthrust and short-cut faulting (Fig. 4.7). On the contrary, where postrift deposition took place directly over basement rocks (Exploradora block), thin-skinned structures were developed (Fig. 4.10E, EFTB). The east-vergent EFTB likely resulted from the upward propagation of a bypass fault related to the decapitation of the Llanta Carrizo Basin (Fig. 4.7), using a shallow detachment at the gypsum horizons of the Asientos Formation.

Later on, west-vergent, newly formed thrusts likely developed at the eastern edge of the Domeyko Range during the Eocene (Figs. 4.7C, H and M). After this, the interaction between these structures and NW-striking faults seems to have controlled the westernmost emplacement of some Miocene volcanoes (*e.g.*, Doña Inés Chica and

Chaco volcanoes; Figs. 4.4 and 4.10F). Finally, some of the most conspicuous NW-striking structures (pre-Andean?) at the Coastal Cordillera correlate with the rupture zones of major historical earthquakes (>8 Mw; Melnick *et al*., 2009), suggesting their neotectonic activity defining major structural crustal blocks along the Central Andean forearc (Fig. 4.10F).

4.6 Conclusions

In northern Chile, several lines of evidence show how processes occurred before the breakup of Gondwana played a significant role during the Andean building. Ar detrital muscovite dating shows different cooling histories between the Triassic Domeyko rift sub-basins. In the Sierra Exploradora sub-basin (SESB) a rapid exhumation took place at *ca*. 262-265 Ma during the San Raphael orogeny. In contrast, in the Sierra de Varas sub-basin (SVSB) slow cooling and gradual uplift of the crystalline basement occurred since Middle Triassic (*ca*. 243 Ma). We explain this difference by the activity of a NW-striking crustal structure (Antofagasta-Volcán Chaco lineament, AVCL) segmenting the region since at least the Cisularian and likely related to the tectonic fabric acquired during the accretional history of the margin.

During the Triassic rift, the AVCL defined the position of a structural high separating the SVSB and the SESB. The fault linkage developed during the Synrift II stage (*ca*. 217-200 Ma) led to the formation of a long and narrow ~NS rift, which interacted with the former NW-trending fabric producing a transtensional system in an oblique rift setting. The rift orientation was likely controlled by parallel-margin weaknesses driven by slab-rollback subduction.

The structural balance evidence that the Triassic rift strongly determined the later structural style of the Domeyko Range. Along both sub-basins (SVSB and SESB) deep-seated master faults were likely inverted during the Eocene-Oligocene Incaic orogeny, producing west-vergent, thick- and thin-skinned tectonics at the core of the Domeyko Range. In contrast, in sites where only postrift deposition took place, east-vergent thin-skinned structures were developed. The reactivation of the rift master faults would have been facilitated by oblique faulting leading to the inception of the

transpressional Domeyko Fault System (DFS). The intersection between the DFS and pre-Andean NW-striking crustal structures seems to have promoted the emplacement of large Cu-Mo porphyry copper deposits. NW-striking structures also accommodated Paleogene tectonic rotations unexplained solely by oroclinal bending, defining blocks that match with the rupture zone of large historical earthquakes, suggesting an important role in the neotectonics of the Andean forearc.

4.7 Acknowledgments

4.8 References

Abels, A., and Bischoff, L. (1999). Clockwise block rotations in northern Chile: Indications for a large-scale domino mechanism during the middle-late Eocene. *Geology*, *27*(8), 751–754. https://doi.org/10.1130/0091-7613(1999)027<0751:CBRINC>2.3.CO;2

Allmendinger, R. W., Cardozo, N. C., and Fisher, D. (2012). *Structural Geology Algorithms: Vectors & Tensors*. Cambridge, England, Cambridge University Press.

Álvarez, P. (2003). Análisis litofacial de la Formación Las Bateas. In *X Congreso Geológico Chileno*. Concepción, Chile.

Amilibia, A., Sàbat, F., McClay, K. R., Muñoz, J. A., Roca, E., and Chong, G. (2008). The role of inherited tectono-sedimentary architecture in the development of the central Andean mountain belt: Insights from the Cordillera de Domeyko. *Journal of Structural Geology*, *30*(12), 1520–1539. https://doi.org/10.1016/j.jsg.2008.08.005

Ardill, J., Flint, S., Chong, G., and Wilke, H. (1998). Sequence stratigraphy of the Mesozoic Domeyko Basin, northern Chile. *Journal of the Geological Society*, *155*, 71–88. https://doi.org/10.1144/gsjgs.155.1.0071

Arriagada, C., Cobbold, P., and Roperch, P. (2006). Salar de Atacama basin: A record of compressional tectonics in the central Andes since the mid-Cretaceous. *Tectonics*, *25*(1), TC1008. https://doi.org/10.1029/2004TC001770

Arriagada, C., Roperch, P., and Mpodozis, C. (2000). Clockwise block rotations along the eastern border of the Cordillera de Domeyko, Northern Chile (22°45'–23°30'S). *Tectonophysics*, *326*, 153–171.

Arriagada, C., Roperch, P., Mpodozis, C., and Fernandez, R. (2006). Paleomagnetism and tectonics of the southern Atacama Desert (25-28°S), northern Chile. *Tectonics*, *25*(4), TC4001. https://doi.org/10.1029/2005TC001923

Astudillo, N., Ferrando, R., Montecino, D., Espinoza, F., Matthews, S., Cornejo, P., and Arévalo, C. (2017). *Carta Augusta Victoria, Región de Antofagasta. Servicio Nacional de Geología y Minería, Carta Geológica de Chile, Serie Geología Básica 189. 1 mapa escala 1:100.000. Santiago, Chile.*

Bascuñán, S., Arriagada, C., Le Roux, J., and Deckart, K. (2015). Unraveling the Peruvian Phase of the Central Andes: stratigraphy, sedimentology, and geochronology of the Salar de Atacama Basin (22°30-23°S), northern Chile. *Basin Research*, *28*(3), 365–392. https://doi.org/10.1111/bre.12114

Bechis, F., Cristallini, E. O., Giambiagi, L. B., Yagupsky, D. L., Guzmán, C. G., and García, V. H. (2014). Transtensional tectonics induced by oblique reactivation of previous lithospheric anisotropies during the Late Triassic to Early Jurassic rifting in the Neuquén basin: Insights from analog models. *Journal of Geodynamics*, *79*, 1–17. https://doi.org/10.1016/j.jog.2014.04.010

Bechis, F., Giambiagi, L., García, V., Lanés, S., Cristallini, E., and Tunik, M. (2010). Kinematic analysis of a transtensional fault system: The Atuel depocenter of the Neuquén basin, southern Central Andes, Argentina. *Journal of Structural Geology*, *32*(7), 886–899. https://doi.org/10.1016/j.jsg.2010.03.009

Bellahsen, N., Fournier, M., d'Acremont, E., Leroy, S., and Daniel, J. M. (2006). Fault reactivation and rift localization: Northeastern Gulf of Aden margin. *Tectonics*, *25*(1), 1–14. https://doi.org/10.1029/2004TC001626

Belt, L. (2012). Active transtensional intracontinental basins: Walker Lane belt in the Western Great Basin. In *Tectonics of Sedimentary Basins: Recent Advances* (pp. 226–248).

Brun, J. P., and Nalpas, T. (1996). Graben inversion in nature and experiments. *Tectonics*, *15*(3), 677–687. https://doi.org/10.1029/95TC03853

Brune, S., Willliams, S. E., and Müller, R. D. (2018). Oblique rifting: the rule, not the exception. *Solid Earth Discussions*, 1–26. https://doi.org/10.5194/se-2018-63

Butler, R. W. ., Tavarnelli, E., and Grasso, M. (2006). Structural inheritance in mountain belts: An Alpine-Apennine perspective. *Journal of Structural Geology*, *28*(11), 1893–1908. https://doi.org/10.1016/j.jsg.2006.09.006

Butler, R. W. H. (1989). The influence of pre-existing basin structure on thrust system evolution in the Western Alps. *Geological Society, London, Special Publications*, *44*(1), 105–122. https://doi.org/10.1144/gsl.sp.1989.044.01.07

Camus, F., and Dilles, J. H. (2001). A Special Issue Devoted to Porphyry Copper Deposits of Northern Chile. *Economic Geology*, *96*(2), 233–237. https://doi.org/10.2113/gsecongeo.96.2.233

Carrapa, B., DeCelles, P. G., Reiners, P. W., Gehrels, G. E., and Sudo, M. (2009). Apatite triple dating and white mica 40Ar/39Ar thermochronology of syntectonic detritus in the Central Andes: A multiphase tectonothermal history. *Geology*, *37*(5), 407–410. https://doi.org/10.1130/G25698A.1

Carrapa, B., Wijbrans, J. R., and Bertotti, G. (2004). Detecting provenance variations and cooling patterns within the western Alpine orogen through 40Ar/39Ar geochronology on detrital sediments: The Tertiary Piedmont Basin, northwest Italy. *Geological Society of America Special Papers*, *378*, 67–103. https://doi.org/10.1130/1052-5173(2004)014<0033:BU>2.0.CO;2

Cawood, P. a., Hawkesworth, C. J., and Dhuime, B. (2012). Detrital zircon record and tectonic setting. *Geology*, *40*(10), 875–878. https://doi.org/10.1130/G32945.1

Charrier, R. (1979). El Triásico en Chile y regiones adyacentes de Argentina: Una reconstrucción paleogeográfica y paleoclimática. *Comunicaciones, Departamento de Geología, Universidad de Chile*, *26*, 1–47.

Charrier, R., Baeza, O., Elgueta, S., Flynn, J. J., Gans, P., Kay, S. M., … Zurita, E. (2002). Evidence for Cenozoic extensional basin development and tectonic inversion south of the flat-slab segment, southern Central Andes, Chile (33–36 SL). *Journal of South American Earth Sciences*, *15*(1), 117–139. https://doi.org/10.1016/S0895-9811(02)00009-3

Charrier, R., Pinto, L., and Rodriguez, M. P. (2007). Tectonostratigraphic evolution of the Andean Orogen in Chile. In T. Moreno and W. Gibbons (Eds.), *The Geology of Chile* (pp. 21–114). London: Geological Society of London.

Chernicoff, C. J., Richards, J. P., and Zappettini, E. O. (2002). Crustal lineament control on magmatism and mineralization in northwestern Argentina: Geological, geophysical, and remote sensing evidence. *Ore Geology Reviews*, *21*(3–4), 127–155. https://doi.org/10.1016/S0169-1368(02)00087-2

Chong, G., and Hilldebrandt, A. (1985). El Triásico PreAndino de Chile entre los 23°30´ y 26°00´ de lat. sur. In *IV Congreso Geológico Chileno*. Antofagasta, Chile.

Christie-Blick, N., and Biddle, K. (1985). Deformation and Basin Formation Along Strike-Slip Faults. *SEPM (Society for Sedimentary Geology) Special Publication*, *37*, 1–33. https://doi.org/10.2110/pec.85.37.0001

Cochrane, R., Spikings, R. A., Chew, D., Wotzlaw, J. F., Chiaradia, M., Tyrrell, S., … Van der Lelij, R. (2014). High temperature (>350°C) thermochronology and mechanisms of Pb loss in apatite. *Geochimica et Cosmochimica Acta*, *127*, 39–56. https://doi.org/10.1016/j.g*ca*.2013.11.028

Coloma, F., Valin, X., Oliveros, V., Vásquez, P., Creixell, C., Salazar, E., … Vallejos, D. (2017). Geochemistry of Permian to Triassic igneous rocks from northern Chile (28º-29º30'S): Implications on the dynamics of the proto-Andean margin. *Andean Geology*, *44*(2), 147–178. https://doi.org/0.5027/andgeoV44n2-a03

Cooke, D. R., Hollings, P., and Walshe, J. L. (2008). Giant Porphyry Deposits: Characteristics, Distribution, and Tectonic Controls. *Economic Geology*, *100*(5), 801–818.

Cornejo, P., Matthews, S., Marinovic, N., and Pérez de Arce, C. P. (2006). Alteración Hidrotermal Y Mineralización Recurrente De Cu Y Cu-Mo Durante El Pérmico Y El Triásico En La Cordillera De Domeyko (Zona De Zaldívar-Salar De Los Morros): Antecedentes Geocronológicos. In *XI Congreso Geológico Chileno* (pp. 219–222).

Cornejo, P., Matthews, S., and Pérez de Arce, C. (2003). The'KT'compressive deformation event in northern Chile (24-27 S). In *Congreso Geológico Chileno* (Vol. 10, p. 11).

Cornejo, P., and Mpodozis, C. (1996). *Geología de la Región de Sierra Exploradora (Cordillera de Domeyko 25°-26°S). Servicio Nacional de Geología y Minería-CODELCO, Informe Registrado, IR-96-09, 330 p. 9 mapas escala 1:50.000.* Santiago.

Cornejo, P., Mpodozis, C., Ramírez, C. F., and Tomlinson, A. J. (1993). *Estudio geológico de la región del Potrerillos y El Salvador (26° - 27° Lat. S). Servicio Nacional de Geología y Minería – CODELCO, Informe Registrado IR – 93-01, Santiago, 280 pp*.

Cornejo, P., Mpodozis, M., Rivera, O., and Matthews, S. (2009). *Carta Exploradora, Regiones de Antofagasta y Atacama. Servicio Nacional de Geología y Minería, Carta Geológica de Chile, Serie Geología Básica 119: 103 p., 1 mapa escala 1:100.000.*

Cortés, J. (2012). *Carta Sierra Mariposa, Región de Antofagasta. Servicio Nacional de Geología y Minería, Carta Geológica de Chile, Serie Geología Básica 119: 30 p., 1 mapa escala 1:100.000*.

Cristallini, E., Tomezzoli, R. N., Pando, G., Gazzera, C., Martínez, J. M., Quiroga, J., … Zambrano, O. (2009). Controles precuyanos en la estructura de la cuenca neuquina. *Revista de La Asociación Geológica Argentina*, *65*(2), 248–264.

del Rey, A., Deckart, K., Arriagada, C., and Martínez, F. (2016). Resolving the paradigm of the late Paleozoic–Triassic Chilean magmatism: Isotopic approach. *Gondwana Research*, *37*, 172–181. https://doi.org/10.1016/j.gr.2016.06.008

Dorsey, R. J., and Umhoefer, P. J. (2012). Influence of Sediment Input and Plate-Motion Obliquity on Basin Development Along an Active Oblique-Divergent Plate Boundary: Gulf of California and Salton Trough. In *Tectonics of Sedimentary Basins: Recent Advances* (pp. 209–225). https://doi.org/10.1002/9781444347166.ch10

Erslev, E. A. (1991). Trishear fault-propagation folding. *Geology*, *19*(6), 617–620. https://doi.org/10.1130/0091-7613(1991)019<0617:TFPF>2.3.CO;2

Escribano, J., Martínez, P., Domagala, J., Padel, M., Espinoza, M., Jorquera, R., … Calderón, M. (2013). *Cartas Bahía Isla Blanca y Taltal. Escala 1:100.000. Servicio Nacional de Geología y Minería, Carta Geológica de Chile, Serie Geología Básica (nos. 164-165): 75 pp. 1 mapa escala 1:100.000. Santiago.*

Espinoza, M., Montecino, D., Oliveros, V., Astudillo, N., Vásquez, P., Reyes, R., … Martínez, A. (2019). The synrift phase of the early Domeyko Basin (Triassic, northern Chile): Sedimentary, volcanic and tectonic interplay in the evolution of an ancient subduction-related rift basin. *Basin Research*, *31*(1), 4–32. https://doi.org/10.1111/bre.12305

Ferrando, R., and Espinoza, F. (2015). Revisión y nuevos antecedentes del Cretácico Superior en la depresión Central de la región de Antofagasta. In *XIV Congreso Geológico Chileno* (pp. 37–42). La Serena, Chile.

Gawthorpe, R., and Leeder, M. (2000). Tectono-sedimentary evolution of active extensional basins. *Basin Research*, *12*(3–4), 195–218. https://doi.org/10.1046/j.1365-2117.2000.00121.x

Gehrels, G. E., Valencia, V. A., and Ruiz, J. (2008). Enhanced precision, accuracy, efficiency, and spatial resolution of U-Pb ages by laser ablation–multicollector–inductively coupled plasma–mass

spectrometry. *Geochemistry, Geophysics, Geosystems*, *9*(3), Q03017. https://doi.org/10.1029/2007GC001805.

Giambiagi, L., Mescua, J., Bechis, F., Martinez, a., and Folguera, a. (2011). Pre-Andean deformation of the Precordillera southern sector, southern Central Andes. *Geosphere*, *7*(1), 219–239. https://doi.org/10.1130/GES00572.1

Giambiagi, L., Spagnotto, S., Moreiras, S. M., Gómez, G., Stahlschmidt, E., and Mescua, J. (2015). Three-dimensional approach to understanding the relationship between the Plio-Quaternary stress field and tectonic inversion in the Triassic Cuyo Basin, Argentina. *Solid Earth*, *6*(2), 747–763. https://doi.org/10.5194/se-6-747-2015

Giambiagi, L., Tunik, M., Barredo, S., Bechis, F., Ghiglione, M., Alvarez, P., and Drosina, M. (2009). Cinemática de apertura del sector norte de la cuenca neuquina. *Revista de La Asociación Geológica Argentina*, *65*(2), 278–292.

González, J., Oliveros, V., Creixell, C., Velásquez, R., Vásquez, P., and Lucassen, F. (2017). The Triassic magmatism and its relation with the Pre-Andean tectonic evolution: Geochemical and petrographic constrains from the High Andes of north central Chile (29º 30' - 30º S). *Journal of South American Earth Sciences*, *87*(November), 95–112. https://doi.org/10.1016/j.jsames.2017.12.009

González, R., Wilke, H. G., Menzies, A. H., Espinoza, F., Riquelme, R., and Herrera, C. (2015). *Carta Sierra de Varas, Región de Antofagasta. Servicio Nacional de Geología y Minería, Carta Geológica de Chile, Serie Geología Básica XXX, 1 mapa escala 1:100.000. Santiago.*

Gow, P. A., and Walshe, J. L. (2005). The role of preexisting geologic architecture in the formation of giant porphyry-related Cu - Au deposits: Examples from New Guinea and Chile. *Economic Geology*, *100*(5), 819–833. https://doi.org/10.2113/gsecongeo.100.5.819

Haines, P. W., Turner, S. P., Kelley, S. P., Wartho, J. A., and Sherlock, S. C. (2004). 40Ar-39Ar dating of detrital muscovite in provenance investigations: A case study from the Adelaide Rift Complex, South Australia. *Earth and Planetary Science Letters*, *227*(3–4), 297–311. https://doi.org/10.1016/j.epsl.2004.08.020

Hammerschmidt, K. (1992). Implication of 40Ar / 39Ar dating of Early Tertiary volcanic rocks from the north-Chilean Precordillera. *Tectonophysics*, *202*(1), 55–81.

Heller, P., and Paola, C. (1992). The large-scale dynamics of grain-size variation in alluvial basins, 2: Application to syntectonic conglomerate. *Basin Research*, *4*(2), 91–102. https://doi.org/10.1111/j.1365-2117.1992.tb00146.x

Henríquez, S., Becerra, J., and Arriagada, C. (2014). *Geología del área San Pedro de Atacama, Región de Antofagasta. Servicio Nacional de Geología y Minería. Carta Geológica de Chile, Serie Geología Básica 171, 111 p., 1 mapa escala 1:100.000. Santiago. Carta Geológica de Chile.*

Hodges, K. V. (2005). 40Ar/39Ar Thermochronology of Detrital Minerals. *Reviews in Mineralogy and Geochemistry*, *58*, 239–257. https://doi.org/10.2138/rmg.2005.58.9

Julve, J., Tassara, A., Echeverria, I., and Stotz, I. (2018). Rol del régimen termal y mecánico de la litósfera en la deformación cortical bajo los Andes del Sur. In *XV Congreso Geológico Chileno* (p. 1190). Concepción.

Kleiman, L. E., and Japas, M. S. (2009). The Choiyoi volcanic province at 34°S–36°S (San Rafael, Mendoza, Argentina): Implications for the Late Palaeozoic evolution of the southwestern margin of Gondwana. *Tectonophysics*, *473*(3–4), 283–299. https://doi.org/10.1016/j.tecto.2009.02.046

Kuiper, K. F., Deino, A., Hilgen, F. J., Krijgsman, W., Renne, P. R., and Wijbrans, J. R. (2008). Synchronizing Rock Clocks of Earth History. *Science*, *320*(5875), 500–504. https://doi.org/10.1126/science.1154339

Lacombe, O., and Mouthereau, F. (2002). Basement-involved shortening and deep detachment tectonics in forelands of orogens: Insights from recent collision belts (Taiwan, Western Alps, Pyrenees). *Tectonics*, *21*(4). https://doi.org/10.1029/2001TC901018

Lee, J. Y., Marti, K., Severinghaus, J. P., Kawamura, K., Yoo, H. S., Lee, J. B., and Kim, J. S. (2006). A redetermination of the isotopic abundances of atmospheric Ar. *Geochimica et Cosmochimica Acta*, *70*(17), 4507–4512. https://doi.org/10.1016/j.g*ca*.2006.06.1563

Lucassen, F., Franz, G., and Laber, A. (1999). Permian high pressure rocks—The basement of the Sierra de Limón Verde in northern Chile. *Journal of South American Earth Sciences*, *12*(2), 183–199. https://doi.org/10.1016/S0895-9811(99)00013-9

Ludwig, K. R. (2011). Isoplot v. 4.15: A Geochronological Toolkit for Microsoft Excel. *Berkeley*

Geochronology Center Special Publication, *4*, 75.

Maksaev, V., and Zentilli, M. (1999). Fission track thermochronology of the Domeyko Cordillera, northern Chile; implications for Andean tectonics and porphyry copper metallogenesis. *Exploration and Mining Geology*, *8*(1–2), 65–89.

Marinovic, N. (2007). *Carta Oficina Domeyko, Región de Antofagasta. Servicio Nacional de Geología y Minería, Carta Geológica de Chile, Serie Geológica Básica, No. 105, 41 p., 1 mapa escala 1:100.000. Santiago*.

Marinovic, N., Smoje, I., Maksaev, V., Hervé, M., and Mpodozis, C. (1995). *Hoja Aguas Blancas. Servicio Nacional de Geología y Minería, Carta Geológica de Chile, No. 70, 150 p., 1 mapa escala 1:250.000. Santiago.*

Marrett, R. A., and Allmendinger, R. W. (1990). Kinematic analysis of fault-slip data. *Journal of Structural Geology*, *12*, 973–986.

Martínez, F., Arriagada, C., Peña, M., Deckart, K., and Charrier, R. (2016). Tectonic styles and crustal shortening of the Central Andes "Pampean" flat-slab segment in northern Chile (27–29°S). *Tectonophysics*, *667*, 144–162. https://doi.org/10.1016/j.tecto.2015.11.019

Martínez, F., Gonzalez, R., Bascuñan, S., and Arriagada, C. (2018). Structural styles of the Salar de Punta Negra Basin in the Preandean Depression (24°-25°S) of the Central Andes. *Journal of South American Earth Sciences*, *87*, 188–199. https://doi.org/10.1016/j.jsames.2017.08.004

Martínez, F., López, C., Bascuñan, S., and Arriagada, C. (2018). Tectonic interaction between Mesozoic to Cenozoic extensional and contractional structures in the Preandean Depression (23°–25°S): Geologic implications for the Central Andes. *Tectonophysics*, *744*, 333–349. https://doi.org/10.1016/j.tecto.2018.07.016

Matthews, K. J., Maloney, K. T., Zahirovic, S., Williams, S. E., Seton, M., and Miller, R. D. (2016). Global plate boundary evolution and kinematics since the late Paleozoic. *Global and Planetary Change*, *146*, 226–250. https://doi.org/10.1016/j.gloplacha.2016.10.002

McClay, K., and Buchanan, P. (1992). Thrust faults in inverted extensional basins. In *Thrust tectonics* (pp. 93–104). Springer.

McDougall, I., and Harrison, T. M. (1999). *Geochronology and thermochronology by the 40Ar/39Ar method*. New York: Oxford University Press.

Melnick, D., Bookhagen, B., Strecker, M. R., and Echtler, H. P. (2009). Segmentation of megathrust rupture zones from fore-arc deformation patterns over hundreds to millions of years, Arauco peninsula, Chile. *Journal of Geophysical Research: Solid Earth*, *114*(1), 1–23. https://doi.org/10.1029/2008JB005788

Min, K., Mundil, R., Renne, P. R., and Ludwig, K. R. (2000). A test for systematic errors in 40Ar/39Ar geochronology through comparison with U/Pb analysis of a 1.1-Ga rhyolite. *Geochimica et Cosmochimica Acta*, *64*(1), 73–98. https://doi.org/10.1016/S0016-7037(99)00204-5

Morley, C. K. (2007). Variations in Late Cenozoic-Recent strike-slip and oblique-extensional geometries, within Indochina: The influence of pre-existing fabrics. *Journal of Structural Geology*, *29*, 36–58. https://doi.org/10.1016/j.jsg.2006.07.003

Mpodozis, C., Arriagada, C., Basso, M., Roperch, P., Cobbold, P., and Reich, M. (2005). Late Mesozoic to Paleogene stratigraphy of the Salar de Atacama Basin, Antofagasta, Northern Chile: Implications for the tectonic evolution of the Central Andes. *Tectonophysics*, *399*(1–4 SPEC. ISS.), 125–154. https://doi.org/10.1016/j.tecto.2004.12.019

Mpodozis, C., and Kay, S. (1992). Late Paleozoic to Triassic evolution of the Gondwana margin: Evidence from Chilean Frontal Cordilleran batholiths (28° S to 31° S). *Geological Society of America Bulletin*, *104*(8), 999–1014.

Muñoz, J. A. (1992). Evolution of a continental collision belt: ECORS-Pyrenees crustal balanced cross-section. *Thrust Tectonics*, 235–246. https://doi.org/10.1007/978-94-011-3066-0_21

Nalpas, T., Dabard, M. P., Ruffet, G., Vernon, A., Mpodozis, C., Loi, A., and Hérail, G. (2008). Sedimentation and preservation of the Miocene Atacama Gravels in the Pedernales-Chañaral Area, Northern Chile: Climatic or tectonic control? *Tectonophysics*, *459*(1–4), 161–173. https://doi.org/10.1016/j.tecto.2007.10.013

Naranjo, J. A., and Puig, A. (1984). *Hojas Taltal y Chañaral, Regiones de Antofagasta y Atacama. Servicio Nacional de Geología y Minería, Carta Geológica de Chile, Nº 62-63,1-146. 1 mapa escala 1:250.000, Santiago.*

Niemeyer, H. (1999). Nuevos datos cinemáticos para la Falla Sierra Castillo en Quebrada del Carrizo,

Precordillera de la Región de Atacama, Chile. *Revista Geológica de Chile*, *26*(2), 159–174.

Niemeyer, H., Berríos, H., and Ruiz Cruz, M. D. (2004). Temperaturas de formación en cataclasitas triásicas de la Cordillera Domeyko, Antofagasta, Chile. *Revista Geológica de Chile*, *31*(1), 3–18. https://doi.org/10.4067/S0716-02082004000100001

Nilsen, T. H., and Sylvester, A. G. (1998). Strike-Slip Basins. In C. Busby and R. Ingersoll (Eds.), *Tectonics of sedimentary basins* (pp. 425–456). Willey.

Oliveros, V., González, J., Espinoza, M., Vásquez, P., Rossel, P., Creixell, C., … Bastias, F. (2017). The early stages of the volcanic arc in the Southern Central Andes. *The Evolution of the Chilean-Argentinean Andes*, 156–185. https://doi.org/10.1007/978-3-319-67774-3

Oliveros, V., Labbé, M., Rossel, P., Charrier, R., and Encinas, A. (2012). Late Jurassic paleogeographic evolution of the Andean back-arc basin: New constrains from the Lagunillas Formation, northern Chile (27°30'–28°30'S). *Journal of South American Earth Sciences*, *37*, 25–40. https://doi.org/10.1016/j.jsames.2011.12.005

Paton, C., Woodhead, J. D., Hellstrom, J. C., Hergt, J. M., Greig, A., and Maas, R. (2010). Improved laser ablation U-Pb zircon geochronology through robust downhole fractionation correction. *Geochemistry, Geophysics, Geosystems*, *11*(3), 1–36. https://doi.org/10.1029/2009GC002618

Perez, N. D., Horton, B. K., McQuarrie, N., Stübner, K., and Ehlers, T. A. (2016). Andean shortening, inversion and exhumation associated with thin- and thick-skinned deformation in southern Peru. *Geological Magazine*, *153*(5–6), 1013–1041. https://doi.org/10.1017/S0016756816000121

Petit, J. P. (1987). Criteria for the sense of movement on fault surfaces in brittle rocks. *Journal of Structural Geology*, *9*(5–6), 597–608.

Petrinovic, I. A., Riller, U., Brod, J. A., Alvarado, G., and Arnosio, M. (2006). Bimodal volcanism in a tectonic transfer zone: Evidence for tectonically controlled magmatism in the southern Central Andes, NW Argentina. *Journal of Volcanology and Geothermal Research*, *152*(3–4), 240–252. https://doi.org/10.1016/j.jvolgeores.2005.10.008

Prosser, S. (1993). Rift-related linked depositional systems and their seismic expression. *Geological Society, London, Special Publications*, *71*(1), 35–66. https://doi.org/10.1144/GSL.SP.1993.071.01.03

Ramos, V. (1994). Terranes of Southern Gondwanaland and Their Control in the Andean Structure (30°-33° S Latitude). In *Tectonics of the Southern Central Andes* (pp. 249–261).

Reutter, K., Scheuber, E., and Chong, G. (1996). The Precordilleran fault system of Chuquicamata, Northern Chile: evidence for reversals along arc-parallel strike-slip faults. *Tectonophysics*, *259*(1–3), 213–228. https://doi.org/10.1016/0040-1951(95)00109-3

Richards, J. ., Noble, S. R., and Pringle, M. S. (1999). A revised late Eocene age for porphyry Cu magmatism in the Escondida area, northern Chile. *Economic Geology*, *94*(8), 1231–1247. https://doi.org/10.2113/gsecongeo.94.8.1231

Richards, J. P. (2003). Tectono-magmatic precursors for porphyry Cu-(Mo-Au) deposit formation. *Economic Geology*, *98*(8), 1515–1533. https://doi.org/10.2113/gsecongeo.98.8.1515

Salfity, J. A. (1985). Lineamentos transversales al rumbo andino en el Noroeste Argentino. In *IV Congreso Geologico Chileno* (Vol. 2, pp. 119–137).

Schmitz, M. D., and Schoene, B. (2007). Derivation of isotope ratios, errors, and error correlations for U-Pb geochronology using 205Pb-235U-(233U)-spiked isotope dilution thermal ionization mass spectrometric data. *Geochemistry, Geophysics, Geosystems*, *8*(8), Q08006. https://doi.org/10.1029/2006GC001492

Solari, L. A., González-León, C. M., Ortega-Obregón, C., Valencia-Moreno, M., and Rascón-Heimpel, M. A. (2018). The Proterozoic of NW Mexico revisited : U – Pb geochronology and Hf isotopes of Sonoran rocks and their tectonic implications. *International Journal of Earth Sciences*, *107*(3), 845–861. https://doi.org/10.1007/s00531-017-1517-2

Solari, L. A., and Tanner, M. (2011). UPb.age, a fast data reduction script for LA-ICP-MS U-Pb geochronology. *Revista Mexicana de Ciencias Geológicas*, *28*(1), 83–91.

Solari, M., Venegas, C., Montecino, D., Astudillo, N., Cortés, J., Bahamondes, B., and Espinoza, F. (2017). *Geología del área Imilac-Quebrada Guanaqueros. Escala 1:100.000. Servicio Nacional de Geología y Minería, Carta Geológica de Chile, Serie Geología Básica (n. 191): 81 pp. 1 mapa escala 1:100.000. Santiago.*

Steinman, G. (1929). *Geologie von Peru*. Heidelberg: Karl Winters Universitats-Buchhandlung.

Suárez, M., and Bell, C. M. (1992). Triassic rift-related sedimentary basins in northern Chile (24°-29°S).

Journal of South American Earth Sciences, *6*(3), 109–121.

Tomlinson, A., and Blanco, N. (1997). Structural evolution and displacement history of the West fault System, Precordillera, Chile: Part 1, synmineral history. In *Proccedings 8th Congreso Geológico Chileno* (pp. 1873–1877). Antofagasta.

Tomlinson, A., Blanco, N., García, M., Baeza, L., Alcota, H., Ladino, M., … Martin, M. W. (2015). Permian exhumation of metamorphic complexes in the Calama area : Evidence for flat-slab subduction in northern Chile during the San Rafael tectonic phase and origin of the Central Andean Gravity High. In *XIV Congreso Geológico Chileno* (pp. 212–214). La Serena, Chile.

Tomlinson, A., Cornejo, P., and Mpodozis, C. (1999). *Hoja Potrerillos, Región de Atacama. Servicio Nacional de Geología y Minería (Chile), Mapas Geológicos, No. 14, 1 mapa escala 1:100.000, Santiago*.

Tomlinson, A., Mpodozis, C., Cornejo, P., and Ramirez, C. (1993). Structural Geology of the Sierra Castillo - Agua Amarga Fault System, Precordillera of Chile, El Salvador-Potrerillos. In *Second ISAG* (pp. 259–262). Oxford, United Kingdom.

Tomlinson, A., Mpodozis, C., Cornejo, P., Ramírez, C. F., and Dumitru, T. (1994). El Sistema de fallas Sierra Castillo-Agua Amarga: transpresión sinistral eocena en la Precordillera de Potrerillos-El Salvador. In *VII Congreso Geológico Chileno* (pp. 1459–1463). Concepción, Chile.

Tron, V., and Brun, J. P. (1991). Experiments on oblique rifting in brittle-ductile systems. *Tectonophysics*, *188*(1–2), 71–84. https://doi.org/10.1016/0040-1951(91)90315-J

Urzúa, F. (2009). *Structural Evolution of La Escondida Copper District, Northern Chile*. University of Tasmania, Hobart, Australia.

Veloso, E. E., Gomila, R., Cembrano, J., González, R., Jensen, E., and Arancibia, G. (2015). Stress fields recorded on large-scale strike-slip fault systems: Effects on the tectonic evolution of crustal slivers during oblique subduction. *Tectonophysics*, *664*, 244–255. https://doi.org/10.1016/j.tecto.2015.09.022

Venegas, C., Cervetto, M., Astudillo, N., Espinoza, F., Cornejo, P., Mpodozis, C., and Rivera, O. (2013). *Carta Sierra Vaquillas Altas, Regiones de Antofagasta y Atacama. Servicio Nacional de Geología y Minería, Carta Geológica de Chile, Serie Geología Básica 159, 1-87. 1 mapa escala 1:100.000. Santiago.*

Vicente, J. C. (2005). Dynamic paleogeography of the Jurassic Andean Basin: pattern of transgression and localisation of main straits through the magmatic arc. *Revista de La Asociación Geológica Argentina*, *60*(1), 221–250.

Withjack, M. O., and Peterson, E. T. (1993). Prediction of normal-fault geometries--a sensitivity analysis. *AAPG Bulletin*, *77*(11), 1860–1873.

Capítulo 5: Discusión

5.1 El rift de Domeyko en la evolución de Gondwana suroccidental

Los resultados e interpretaciones expuestos previamente referentes a la geocronología, sedimentología y cinemática de la etapa de *rift* de la Cuenca de Domeyko permiten proponer lo siguiente (capítulos III y IV):

- La fase de subsidencia mecánica en el *rift* de Domeyko habría tenido lugar en dos períodos: *Synrift I* (Ladiniano – Carniano; *ca*. 240 - 225 Ma), gatillándose la apertura de la subcuenca Sierra Exploradora (SESB) y *Synrift II* (Nórico – Rético; *ca*. 217- 200 Ma), en el que se inició la Subcuenca Sierra de Varas (SVSB) y se reactivó la depositación en la Subcuenca Sierra Exploradora.

- Durante el *Synrift II*, en la SVSB se desarrollaron discretos depocentros (Cerro La Ballena, Sierra de Varas, Cerro Guanaco y Vaquillas Altas), en los cuales se depositaron sucesiones continentales sedimentarias y volcánicas (Fig. 3.9). En aquellos depocentros donde se desarrolló un menor aporte volcánico *("low-volcanoclastic input depocenters";* Sierra de Varas y Vaquillas Altas), se registró una sucesión tripartita (aluvial, fluvial y lacustre) la que estaría asociada a la progresión de la subsidencia tectónica (Fig. 3.10). El desarrollo de sistemas lacustres profundos estaría asociado a un aumento brusco del espacio de acomodación, indicando una fase de climax del *rift*, probablemente relacionado a la unión de las fallas maestras ("*fault linkage stage*"), generando un sistema de *rift* elongado y angosto (*ca*. 400 km de largo) con un rumbo actual ~NS a ~NNE (Fig. 4.8).

- Junto a las fallas maestras de orientación ~NS a ~NNE (Fallas Profeta, Sierra Castillo y Sierra de Varas) y manteo hacia el este, se desarrollaron fallas secundarias de rumbo NNO-SSE a NO-SE. Ambos sistemas estructurales se habrían generado mediante un régimen transtensional (sinistral) el que habría dado origen a un sistema de *rift* oblicuo (Figs. 4.6 y 4.10B).

Con el fin de inferir el significado geodinámico del *rift* de Domeyko en el contexto de la evolución de Gondwana Suroccidental durante el Triásico (Fig. 5.1), en las siguientes secciones se integrarán los resultados enunciados previamente con

antecedentes compilados a partir de otras cuencas de *rift* coetáneas (*e.g.* dataciones U-Pb en circón y geoquímica de rocas ígneas).
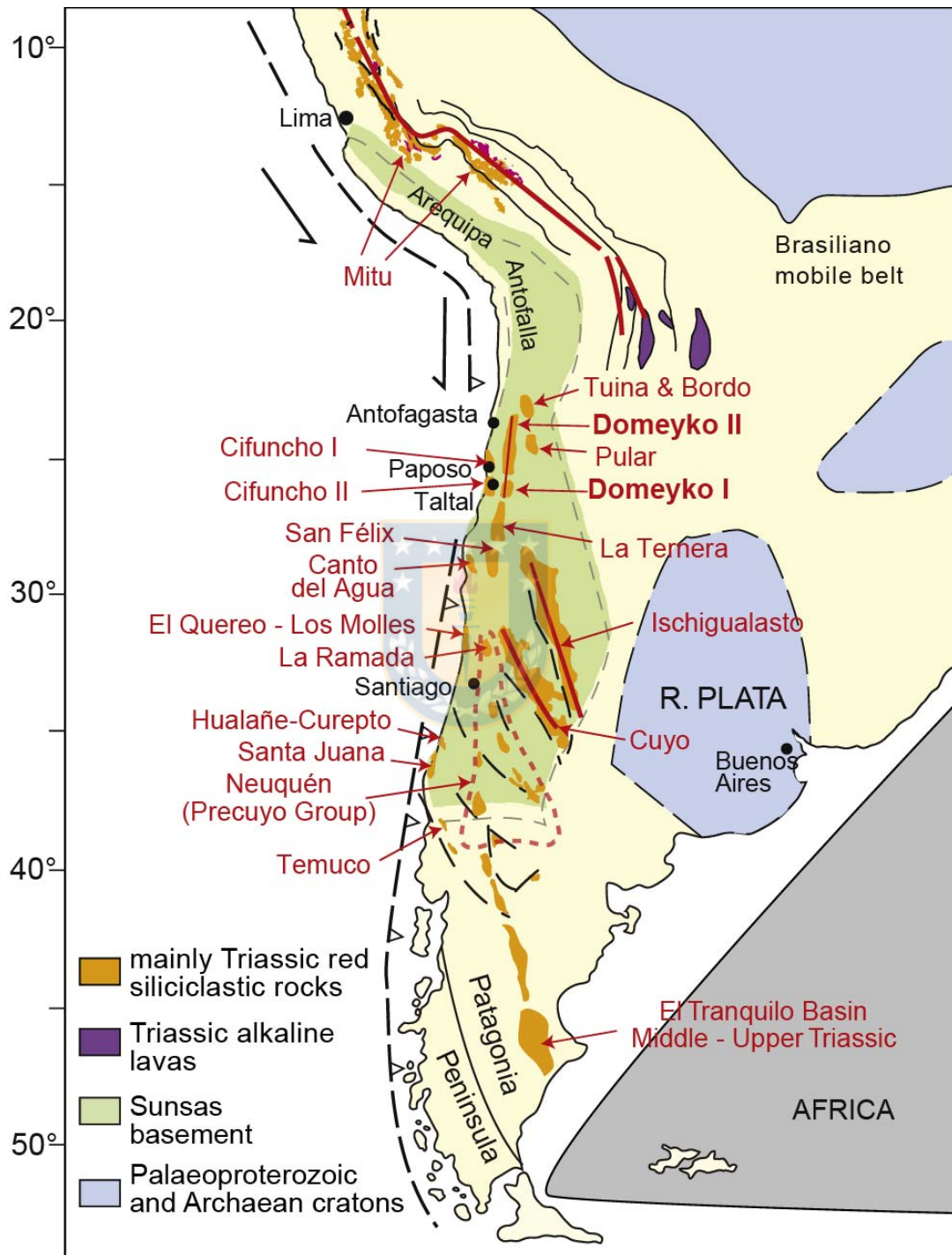
Figura 5.1: Cuencas de *rift* desarrolladas durante el Triásico-Jurásico Inferior en Gondwana Suroccidental. Modificado de Spikings *et al*. (2016).

5.1.1 Etapas synrift en el norte de Chile

Charrier *et al*. (2007) propusieron que la subsidencia mecánica de las cuencas pre-Andinas en Chile se habría desarrollado en dos períodos: Primera Etapa (Lopingiano – Ladiniano tardío) y Segunda Etapa (Nórico-Sinemuriano). Posteriormente, para el segmento entre los 31° - 37° S en Chile y Argentina, Charrier *et al*. (2014) refinaron los límites de estos períodos a una Primera Etapa (Lopingiano – Ladiniano a Cárnico) y una Segunda Etapa (post-Cárnico – Pliensbachiano). Acorde a estos autores, ambas etapas estarían separadas por un pulso silícico y volcanoclástico Ladiniano-Cárnico (La Totora-Pichidangui). Por otro lado, en la Cordillera Frontal, Salazar *et al*. (*in press*) distinguieron dos etapas de subsidencia mecánica (Primera Etapa durante el Lopingiano-Triásico Medio alto y Segunda Etapa durante el Nórico - Rético), separadas por una fase de alzamiento (discordancia Carniana) durante el Ladiniano-Cárnico. En relación a estos límites y considerando la cronoestratigrafía observada entre los 23° - 27°S, es posible discutir que:

- La expresión local de los depocentros volcanoclásticos silícicos desarrollados durante el Lopingiano – Triásico Inferior y expuestos en el actual borde del Salar de Atacama (*e.g.* formaciones Cas y Peine; Niemeyer, 2013), junto a su contemporaneidad con los registros más jóvenes del volcanismo de la provincia magmática de Choiyoi (286-247 Ma; Sato *et al*., 2015), permite interpretar que estos depocentros se habrían formado mediante subsidencia volcanotectónica (Fig. 5.2), no correspondiendo a cuencas de *rift sensu stricto* (Sengör, 1995; Sengör y Natal'in, 2001). Fuera del área de estudio, en el sector de la Cordillera Frontal de Vallenar, sucesiones parcialmente equivalentes corresponderían a la Formación Guanaco Sonso, desarrollada en un sistema tipo caldera (López, 2015; Salazar y Coloma, 2016). De esta manera, los depocentros de *rift* se habrían generado posterior al magmatismo de Choiyoi (Permo - Triásico) en el norte de Chile y Argentina.
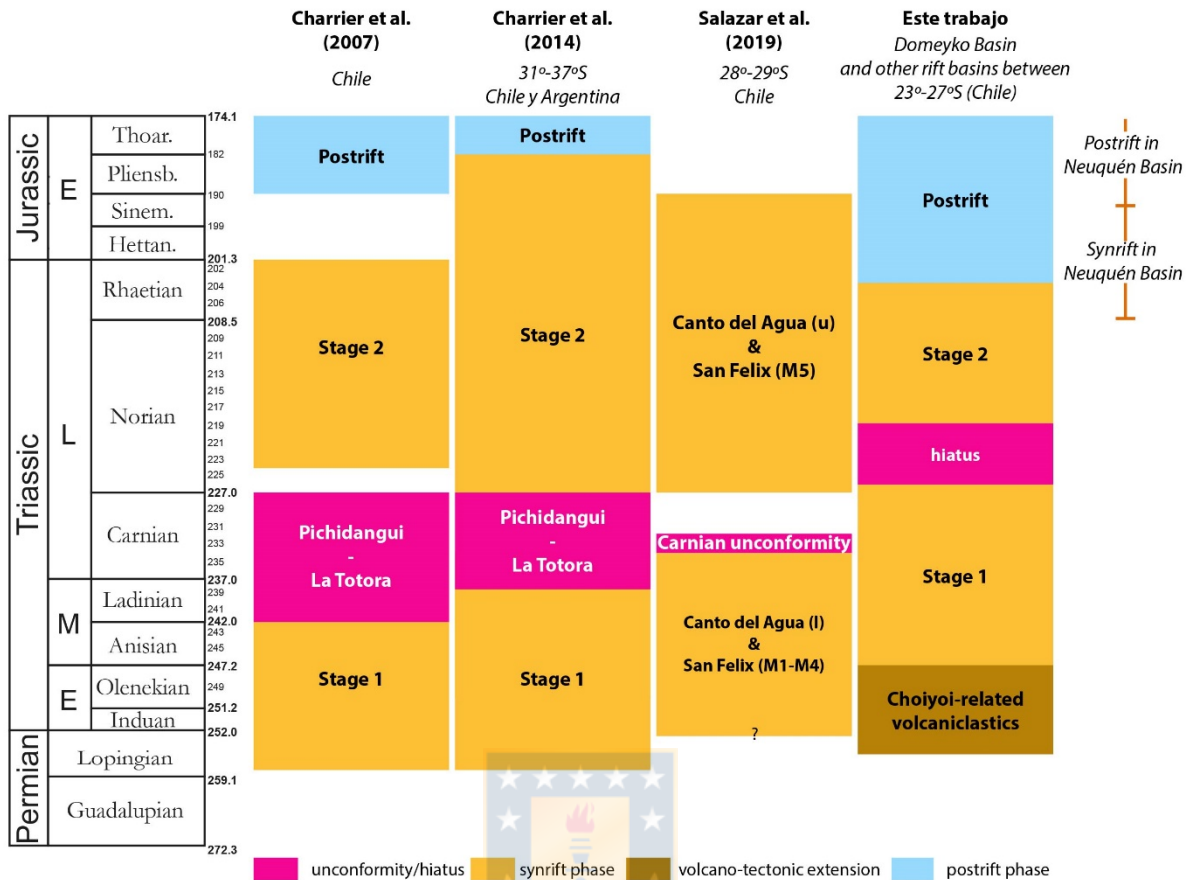
Figura 5.2: Esquemas cronoestratigráficos en Chile para el *rift* triásico y comparación con la Cuenca Neuquina. Referencia para esta última cuenca es acorde a Bechis et al. (2014).

- La discordancia Carniana (Fig. 5.2), asociada al alzamiento del batolito Chollay en la Cordillera Frontal de Chile (Salazar *et al*., *in press*) no se registraría entre los 23° - 27° S. Más aún, los datos de termocronología de muscovitas detríticas presentados en el Capítulo IV (sección 4.5.2), indican que al menos parte del basamento de esta región experimentó un enfriamiento sostenido y lento a partir de los *ca*. 243 Ma, posiblemente asociado al alzamiento isostático asociado al desarrollo de las cuencas extensionales coetáneas. Por otro lado, Kato y Godoy (2015) propusieron la existencia de un evento de deformación transpresivo post-Triásico Inferior (Triásico Medio-Superior?), el cual habría exhumado los complejos acrecionarios Gondwánicos entre los 26° - 42° S. De esta manera, se observa un contraste en la deformación intra-triásica entre los dominios al norte y sur de los 27°S. Esta diferencia se evidencia además en el disímil volumen de exposición de las raíces del arco

magmático Triásico Inferior-Medio entre ambos dominios. Lo anterior permite sugerir una segmentación del paleomargen de Gondwana aproximadamente a los 27°S, la cual se extendería hacia el Jurásico (Oliveros *et al*., 2018).

- En relación al inicio de la etapa *postrift,* entre los 23° - 26° S existen una serie de evidencias que indican que esta habría comenzado durante el Rético alto (Ardill *et al*., 1998; Amilibia, 2002), tales como: (1) la depositación de facies arrecifales del Rético (formaciones Profeta y Las Bateas), sobre una gran área de la Cordillera de Domeyko (Chong y Hilldebrandt, 1985; Ardill *et al*., 1998; Venegas *et al*., 2013; González *et al*., 2015; Astudillo *et al*., 2017), las que se habrían relacionado a bajas tasas de acomodación y aporte sedimentario, marcando una disminución abrupta de la subsidencia mecánica (sección 3.5.3.2); (2) evidencias de sellamientos postrift en unidades hetangianas (Formación Profeta) sobre fallas normales sinsedimentarias (Fig. 3.4B); (3) discordancias angulares locales asociadas a la depositación de las facies arrecifales (Fig. 3.5) y (4) la menor frecuencia y desplazamiento de las fallas normales sinsedimentarias que afectan las sucesiones depositadas durante el Rético-Hetangiano. De esta manera, la fase de *synrift* entre los 23° - 26° S estaría circunscrita únicamente al Triásico. Sucesiones *synrift* desarrolladas durante el Jurásico Inferior (Rético-Sinemuriano) han sido bien descritas en Argentina (Grupo Pre-Cuyo; Giambiagi *et al*., 2008, 2009; Cristallini *et al*., 2009; Bechis *et al*., 2010, 2014; Drosina *et al*., 2017) y correlacionadas entre los 31° - 37° S en Chile (Charrier *et al*., 2014). Lo anterior sugiere una migración del foco de la extensión, volviéndose más joven hacia el sur. La posibilidad de que sucesiones *synrift* se hayan desarrollado en el norte de Chile (23º - 27º S) durante el intervalo Hetangiano-Sinemuriano, constituyendo un nuevo pulso de subsidencia mecánica, es difícil de evaluar dada la coincidencia con un alza relativa del nivel del mar a nivel global durante el Hetangiano (Ardill *et al*., 1998), por lo que estudios detallados deberían desarrollarse a la hora de testear esta posibilidad.

De esta manera, se propone que entre los 23° - 27° S, se desarrollaron tres períodos de extensión (Fig. 5.2): una primera subsidencia volcanotectónica asociada al magmatismo de Choiyoi durante el Pérmico Superior – Triásico inferior (*ca*. 256 –

247; Lopingiano – Olenekiano), seguida de dos etapas de subsidencia mecánica (*synrift*): Primera Etapa (*ca*. 246-227 Ma; Anisiano – Carniano) y Segunda Etapa (*ca*. 219-202 Ma). El período intermedio entre ambas etapas de subsidencia mecánica coincide parcialmente con el desarrollo de intrusiones sub-volcánicas intermedias a silícicas registradas en las cercanías de Calama (Tomlinson *et al*., 2001; Tomlinson y Blanco, 2008).

5.1.2   El rift Triásico-Jurásico en Gondwana SW y el hiatus del Nórico bajo

Contemporáneamente a la etapa de *Synrift I* de la Cuenca de Domeyko (Fig. 5.3), el *rift* de la Cuenca de Mitu en Perú (*ca*. 240 – 220 Ma) fue rellenado mediante sedimentación continental y un volcanismo basáltico alcalino/subalcalino para el cual ha sido propuesta tanto una configuración de *rift* intracontinental (Spikings *et al*., 2016) como de cuenca de trasarco (Reitsma, 2012). En Chile, en las proximidades de la Depresión Pre-Andina y del borde oriental de la Cordillera de Domeyko se desarrollaron discretos depocentros entre los *ca*. 247 – 232 Ma donde se depositaron las formaciones Pular (Niemeyer *et al*., 2008; Solari *et al*., 2017), Tuina (Henríquez *et al*., 2014) y los Estratos El Bordo (Basso y Mpodozis, 2012). En la Cordillera de la Costa, afloramientos menores en el sector de Paposo (Formación Cifuncho) indican una depositación entre los *ca*. 242 - 226 Ma asociados a volcanismo explosivo (Álvarez *et al*., 2016), mientras que material fosilífero y edades máximas de circones detríticos sugieren la depositación de la Formación Canto del Agua entre el Anisiano 'superior' y el Cárnico 'bajo' a la latitud de Vallenar (Salazar *et al*., *in press*). En la Cordillera Frontal, los miembros M1 a M4 de la Formación San Félix se habrían depositado después de los 254 Ma y hasta el Anisiano 'superior' (Salazar *et al*., *in press*). Actividad extensional durante un intervalo similar tuvo lugar en Argentina en la Cuenca Cuyana entre los *ca*. 240-230 Ma (Ávila *et al*., 2006; Spalletti *et al*., 2008; Mancuso *et al*., 2010; Barredo *et al*., 2012; Ottone *et al*., 2014) y en la Cuenca de Ischigualasto entre los *ca*. 252 – 226 Ma (Rogers *et al*., 1993; Shipman, 2004; Martinez *et al*., 2011; Kent *et al*., 2014; Marsicano *et al*., 2016).

Durante la etapa de *Synrift II* de la Cuenca de Domeyko, en la Cordillera de la Costa (sector Taltal; Figura 5.1) se depositaron rocas sedimentarias continentales y volcánicas intermedias a ácidas en la Cuenca Cifuncho entre los 212 - 200 Ma (Contreras *et al*., 2013; Espinoza *et al*., 2015a; Figura 5.4), mientras que en las cercanías de Vallenar se depositó el miembro superior de la Formación Canto del Agua (< *ca*. 216 Ma; Nórico – Rético; Salazar *et al*., *in press*). A esta misma latitud en la Cordillera Frontal, el Miembro M5 de la Formación San Félix se depositó discordante sobre el basamento plutónico del Triásico Medio durante el Nórico – Rético (< *ca*. 212 Ma; Salazar *et al*., 2013). Por otro lado, una relación similar se observa en la principalmente volcánica Formación la Totora (*ca*. 218 – 210 Ma; Salazar et al. 2013). También en la Cordillera Frontal, contenido fosilífero vegetal (Reyes, 2017) y una edad U-Pb de *ca*. 219,4 +3,4/-2,0 Ma obtenida en una toba de la sección superior de la Formación La Ternera, indicaría que esta unidad se habría depositado en la cuenca homónima durante el Nórico – Rético (Fig. 4.5 y secciones 4.4.1.3 y 4.4.2.2). Por otra parte, en la Cordillera Principal de Chile y Argentina (31°- 33° S), en base a su contenido fosilífero y recientes edades U-Pb, la Cuenca Mercedario se habría desarrollado durante el Rético tardío - Sinemuriano (Alvarez y Ramos, 1999; Mackaman-lofland *et al*., 2019). Más al sur, numerosas edades ígneas U-Pb indican que las unidades *synrift* de la Cuenca Neuquina (Grupo Pre-Cuyo) se habrían desarrollado aproximadamente entre los 211 y 192 Ma (Bermudez *et al*., 2002; Schiuma y Llambías, 2008; Spalletti *et al*., 2010; Barrionuevo *et al*., 2011; Naipauer *et al*., 2016; Mackaman-lofland *et al*., 2019).
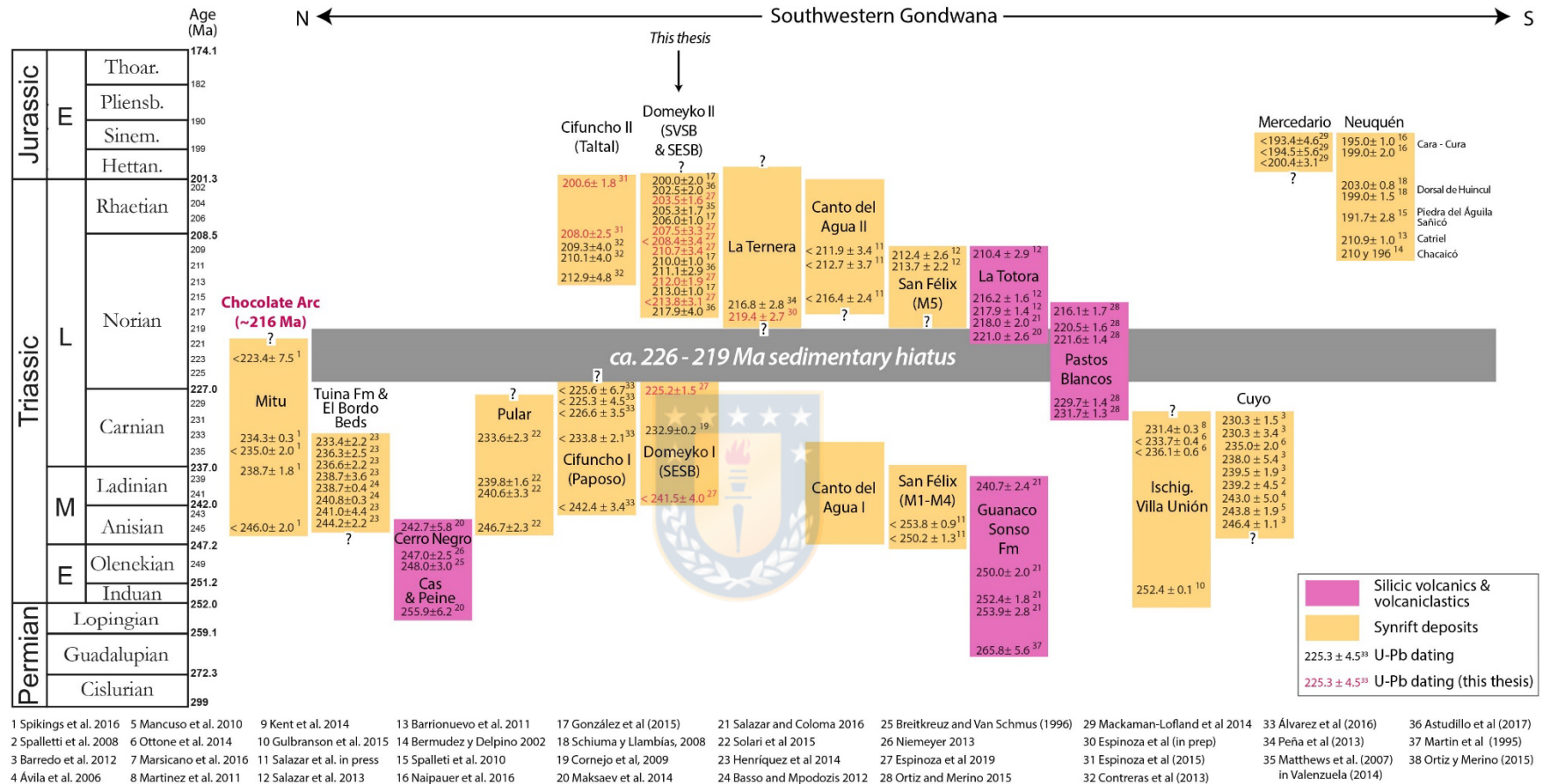
Figura 5.3: Cronoestratigrafía generalizada las cuencas triásicas desarrolladas en Gondwana Suroccidental durante el Pérmico-Jurásico Inferior.
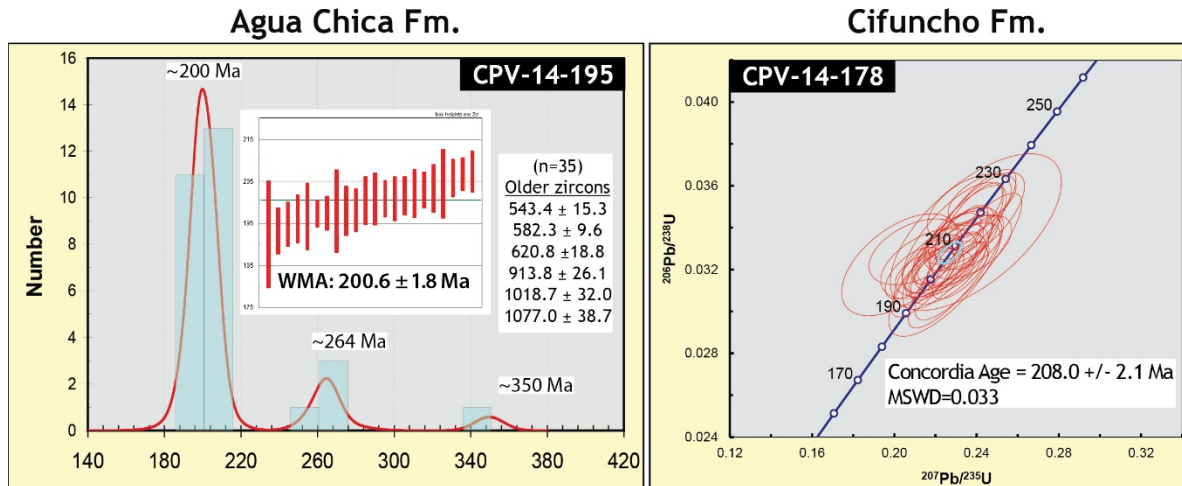
Figura 5.4: Edades U-Pb en circones de tobas pertenecientes a la Formación Cifuncho y Agua Chica, en las cercanías de Taltal (Espinoza *et al*., 2015a)

Un análisis de la cronoestratigrafía de las sucesiones triásicas expuestas en Chile, Argentina y Perú, basado en la compilación de edades U-Pb en circón (Fig. 5.3), evidencia una disminución significativa del registro sedimentario en Gondwana Suroccidental (hiatus deposicional) entre los *ca*. 226-219 Ma. De esta manera, la sedimentación triásica a gran escala parece haberse desarrollado en dos grandes períodos, aun cuando los límites temporales individuales entre las distintas cuencas son diacrónicos y algunos eventos de deformación intra-triásica parecieran presentar una mayor o menor expresión en función de una segmentación del paleomargen gondwánico. Estos períodos coinciden con las etapas de *synrift* propuestas en este trabajo para la Cuenca de Domeyko (*Synrift I* y *Synrift II*) y las observadas en el norte de Chile entre los 23 - 27ºS.

El inicio del hiatus deposicional coincide aproximadamente con una reconfiguración de la cinemática de placas ocurrida a los *ca*. 228 Ma (Fig. 5.5), como lo muestran recientes modelos de cinemática de placas (Matthews *et al*., 2016; Müller *et al*., 2016). Acorde a estos modelos, previo a los *ca*. 228 Ma el paleomargen habría presentado una subducción con una losa oceánica convergiendo con una alta oblicuidad de cinemática dextral, mientras que posteriormente la velocidad de convergencia habría disminuido y se habría desarrollado una ligera oblicuidad de cinemática sinestral. Lo anterior es coherente con la cinemática sinestral del sistema de *rift* oblicuo propuesto para la Cuenca de Domeyko durante la etapa de *Synrift* II.

119
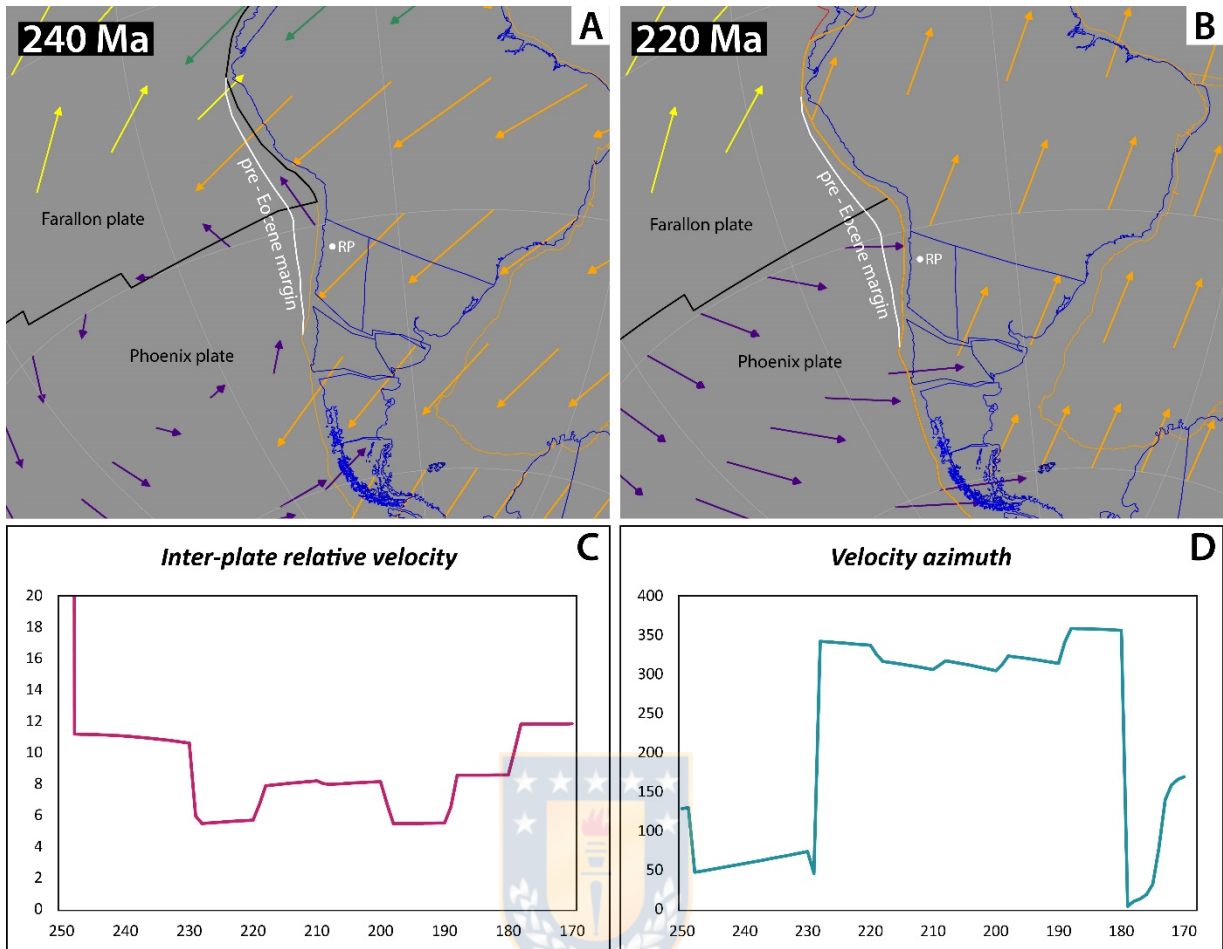
Figura 5.5: Configuración de placas en el margen suroccidental de Gondwana para los A) 240 Ma y los B) 220 Ma. C) Velocidad interplacas (placas Phoenix y punto de referencia en Chilenia; RP: Punto de referencia) entre los 250-170 Ma y D) Velocidad azimutal de RP entre el mismo periodo. El modelo cinemático utilizado corresponde a Matthews et al. (2016) y fue implementado en el software *GPlates*.

5.1.3 Ambiente geotectónico durante el rift de Domeyko

Durante el Triásico Medio – Superior bajo (*Synrift* I), la actividad plutónica en Perú tuvo lugar al este del Grupo Mitu, en la Cordillera de Carabaya (Reitsma, 2012; Spikings *et al*., 2016), mientras que en el norte de Chile, abundante plutonismo de esta edad se registra entre los 28° - 30° S en la Cordillera Frontal (e.g complejos plutónicos Chollay y Montosa – El Potro; Coloma *et al*., 2017), marcando claramente la posición del eje magmático del período. Por otra parte, cuerpos plutónicos de menor dimensión se reconocen localmente al norte de los 27°S en la Cordillera de la Costa en las proximidades de Paposo, Taltal y Chañaral (*ca*. 230-245; Godoy y Lara, 1998;

Matthews *et al*., 2010; Escribano *et al*., 2013; Álvarez *et al*., 2016), en el borde oriental de la Cordillera de Domeyko (Complejo Intrusivo Varilla Norte, *ca*. 239-225 Ma; Solari *et al*., 2017) y en la Puna (*ca*. 246-247; Poma *et al*., 2014).

Recientes investigaciones que integran la geoquímica de estos cuerpos plutónicos indican que sus características se corresponden a la de magmas generados mediante la subducción de una losa oceánica (*e.g.* presencia de minerales hidratados, alta razón LILE/HFSE, anomalía negativa Nb-Ta; Coloma *et al*., 2017; del Rey *et al*., 2016; González *et al*., 2017; Oliveros *et al*., 2018). Sin embargo, a diferencia de lo que ocurre al sur de los 27º S, en el área de estudio, la presencia de plutonismo tiene un volumen restringido pero distribuido sobre una gran extensión lateral, abarcando desde la Cordillera de la Costa hasta la Puna, dificultando la distinción del eje del arco magmático. Es posible que la distribución del magmatismo en este segmento esté relacionada al desarrollo de una subducción de bajo ángulo, aunque no suficiente para suprimir el magmatismo (>30º), en la cual el magmatismo es distribuido en un sector amplio de la corteza, tal como ha sido planteado para el suroeste norteamericano durante el Paleógeno (Keith, 1978). En el contexto de una subducción de bajo ángulo, es probable que el mecanismo de subsidencia mecánica desarrollado durante la etapa de *Synrift I* entre los 23 - 27º S haya sido relativamente débil. Este mecanismo pudo estar relacionado únicamente a esfuerzos de campo lejano asociados a la fragmentación de Pangea, dando lugar a depocentros menores, de distribución local y aislada, los que habrían nucleado preferentemente en zonas de debilidad previas (Fig. 4.10B).

Durante este periodo (*Synrift* I), en las cuencas de *rift* del oeste argentino (cuencas de Ischigualasto y Cuyo) se desarrolló un magmatismo petrográficamente bimodal y de afinidad alcalina, el que se ha usado como evidencia de la ausencia de subducción durante el Triásico (Ramos y Kay, 1991; Rocher *et al*., 2016). Por otra parte, afinidades puramente alcalinas de intraplaca como las reportadas hacia el este de la cuenca de Ischigualasto (Sommer *et al*., 2018), coexisten con aquellas que presentan tanto una afinidad alcalina en las componentes basálticas (tipo OIB) y calcoalcalina en aquellas silícicas (Orellano *et al*., 2019) al oeste de la cuenca Cuyana. De esta manera, en términos de la geoquímica de sus productos magmáticos y la

distancia al posible arco magmático, es posible considerar las cuencas desarrolladas hacia el interior de Gondwana suroccidental (Fig. 5.1) como un sistema progresivamente dominado por una dinámica intracontinental.

Por otro lado, durante el *Synrift II* (post *ca*. 217 Ma) la actividad plutónica migró claramente a la Cordillera de la Costa tanto al norte como al sur de los 27º S: Granito Algodones y Complejo Plutónico Carrizal Bajo (Vallenar; Arévalo y Welkner, 2008), Sienogranito Capitana (Chañaral; Espinoza *et al*., 2014; Godoy y Lara, 1998), Complejo Intrusivo Anchuña (Taltal; Escribano *et al*., 2013) y Tonalita Morro Mejillones (Casquet *et al*., 2013). Entre los 24.5º-26.5º S, el plutonismo estuvo acompañado de volcanismo intermedio a silícico de las formaciones Agua Chica y Cifuncho entre los *ca*. 213 – 200 Ma (Godoy y Lara, 1998; Contreras *et al*., 2013; Espinoza *et al*., 2015a). De forma contemporánea, en la Cordillera de Domeyko se desarrolló un volcanismo basáltico (Formación Quebrada del Salitre) a intermedio-silícico (formaciones Cerro Guanaco y Sierra de Varas). En ambos dominios (C. Costa y C. Domeyko), la geoquímica volcánica indica un *trend* calcoalcalino (Fig. 5.6A), con una alta razón LILE/HFSE y una anomalía negativa de Nb-Ta, P y Ti (Fig. 5.6E), signatura típica de magmas generados a partir de la presencia de fluidos procedentes de una losa subductante (Espinoza *et al*., 2016). Sin embargo, la amplia variabilidad composicional de la Formación Quebrada del Salitre (Fig. 5.6B), así como una anomalía de Nb menos pronunciada que su contraparte costera y una clasificación en los diagramas discriminadores tectónicos que va desde rocas de arco a intraplaca, sugieren una menor influencia de los fluidos liberados por el *slab* en la génesis de estos magmas (Sayit *et al*., 2017). Un comportamiento similar se observa en rocas volcánicas generadas en cuencas de *rift* ubicadas en una posición de trasarco (e.g Sumisu *rift*; Hochstaedter *et al*., 1990; Rossel *et al*., 2013) las que se asemejan geoquímicamente a los basaltos de trasarco *(back-arc basin basalts*, BABB; Stern *et al*., 1990).

Lo anterior, junto a la posición de los plutones del Triásico Superior (post- *ca*. 218 Ma), sugiere que durante la etapa *Synrift II*, la Cuenca de Domeyko se desarrolló en una posición de trasarco mientras que la Cuenca Cifuncho constituiría una cuenca de intra-arco. Como se propuso en los Capítulos 3 y 4 (secciones 3.5.5 y 4.5.1 respectivamente), el *rift* de Domeyko durante esta etapa correspondería entonces a un

rift oblicuo asociado a subducción (*subduction-related rift*; Merle, 2011) el cual se habría formado bajo dos campos de esfuerzos: uno local asociado al *slab-pull* de la losa subductante tipo *rollback* y otro de campo lejano asociado al desmembramiento de Pangea. De esta manera, la mayor velocidad de convergencia de la placa Phoenix durante el *Synrift* II con respecto al *Synrift* I, podría estar asociado a un aumento del *slab-pull,* intensificando la apertura de las cuencas más cercanas al paleomargen gondwánico, reconociéndose durante esta etapa un aumento en la actividad extensional en el margen chileno (Charrier *et al*., 2007).

Por otro lado, dada la clara migración del magmatismo de arco hacia la Cordillera de la Costa posterior a los 218 Ma, desde Perú (arco volcánico de Chocolate, *ca*. 216 - 135 Ma; Boekhout *et al*., 2012; Spikings *et al*., 2016) hasta al menos los 29° S, inferimos una posición de trasarco para las cuencas de *rift* de La Ternera, San Félix (miembro M5), Mercedario y Neuquén (Fig. 5.1).
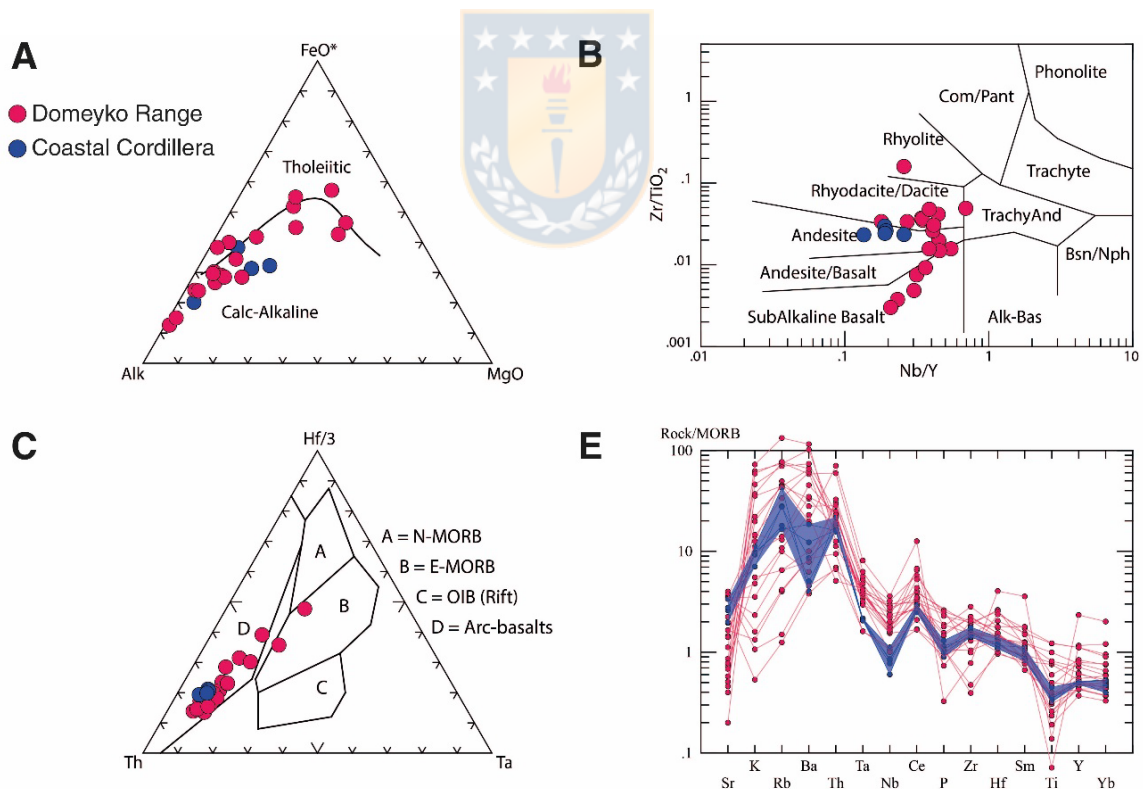
Figura 5.6: Geoquímica de las rocas volcánicas triásicas de la Cordillera de Domeyko (círculos magenta) y Cordillera de la Costa (círculos azules). Tomado de Espinoza *et al*. (2016) y Celis (2018). A) Clasificación de rocas alteradas (Winchester y Floyd, 1977). B) Diagrama AFM (Irvine y Baragar, 1971). C) Diagrama de discriminación geotectónica (Wood, 1980). Diagrama *Spider* de tierras raras (Pearce *et al*., 1984).

5.2 Inversión del rift de Domeyko: Implicancias en la construcción de los Andes Centrales

Los resultados e interpretaciones expuestas en el Capítulo 4, referentes a la geocronología detrítica (Ar-Ar en muscovitas y U-Pb en circón), junto con al balance estructural de la Cordillera de Domeyko, nos permiten proponer que:

- La historia de enfriamiento de las fuentes sedimentarias de la subcuenca Sierra Exploradora (SESB) indicaría un enfriamiento rápido del basamento de este depocentro durante el Pérmico Superior (262-265 Ma), el que se asociaría a la etapa más joven de la Fase San Rafael. Por otro lado, el basamento de la subcuenca Sierra de Varas (SVSB) habría registrado un enfriamiento lento asociado a un alzamiento gradual a partir de los *ca*. 243 Ma. Este contraste se habría generado a partir de la actividad de una estructural cortical de probable rumbo noroeste (AVCHL; lineamiento Antofagasta-Volcán Chaco), la que habría segmentado ambos dominios desde al menos el Pérmico Superior.

- Durante la etapa de *rift* de la Cuenca de Domeyko, la posición inferida para el AVCHL coincide aproximadamente con la posición de un alto estructural que separó las subcuencas de la Cuenca de Domeyko (SVSB y SESB).

- Durante la orogénesis Incaica (Eoceno tardío), ambas subcuencas (SESB y SVSB) habrían experimentado inversión tectónica, dando lugar a la exhumación del basamento plutónico Paleozoico en un estilo de deformación de piel gruesa y de vergencia principal al oeste. Por otro lado, en el bloque que constituyó un alto estructural durante la etapa *synrift*, se desarrolló una deformación de piel delgada y de vergencia al este en el núcleo de la Cordillera de Domeyko.

- La inversión de las fallas maestras del *rift* de Domeyko mediante tectónica transpresional habría permitido la incepción de las estructuras occidentales del Sistema de Fallas de Domeyko.

Con el objetivo de discutir el rol que habría jugado la inversión del *rift* triásico en la orogénesis andina, en esta sección se entregan antecedentes adicionales correspondientes a información geocronológica, estratigráfica y estructural referente a la geología regional de la Cordillera de Domeyko entre los 23°- 27° S.

5.2.1 Estilo estructural y temporalidad de la deformación de la Cordillera de Domeyko.

En el área de estudio es posible distinguir un dominio oriental, conformado por el flanco occidental de la Cordillera de Domeyko y un dominio occidental formado por el extremo oriental de la Depresión Central. El límite entre ambos dominios está marcado por estructuras de alto ángulo que generan un cambio abrupto en la topografía del área (*e.g.* fallas Profeta, Gran Llano y Sierra Castillo). La evolución geológica del área a partir del Paleozoico Superior generó una segmentación a lo largo del eje de la Cordillera de Domeyko, la cual posteriormente controló la ubicación de las subcuencas del *rift* de Domeyko (Capítulo IV). En base a tal segmentación y correlacionando la presencia de estructuras locales de rumbo NO-SE con lineamientos de escala cortical presentes en el antearco, se dividió la región en tres bloques estructurales: Vaquillas Altas, Exploradora y Castillo (Fig. 5.7A).

5.2.1.1 Estilo estructural del flanco occidental de la Cordillera de Domeyko

El estilo estructural del dominio occidental de los bloques centro (Exploradora) y sur (Castillo) es interpretado como correspondiente a la inversión de una cuenca extensional activa durante el Jurásico Superior-Cretácico (Cuenca Llanta-Carrizo). Las unidades involucradas se encuentran deformadas en pliegues abiertos y simétricos de gran longitud de onda (Fig. 5.7D). En este sentido, considerando modelos análogos de inversión (Brun y Nalpas, 1996), el desarrollo de un sinclinal central de gran longitud de onda (*e.g.* Sinclinal de Pampa del Carrizo) es interpretado como una geometría asociada a la inversión de un depocentro original tipo graben (Fig. 5.8). Por otro lado, en el bloque Exploradora, se interpreta que posterior a la inversión del graben, se habría desarrollado una falla de sobrepaso de vergencia este (*bypass* fault), la que cortaría la Cuenca Llanta-Carrizo y se anclaría hacia el este en los niveles de baja competencia de la sucesión postrift jurásica (*e.g.* yeso oxfordiano en Formación Asientos). Esta transferencia de la deformación hacia el dominio oriental habría sido facilitada por la ausencia de basamento plutónico en este sector, el que actuaría como un bloque rígido en las demás secciones.

a

KEYS

Ol-Mioc
- Miocene proximal volcanics
- Atacama & Pampa Mula gravels

Eoc
- Sierra Exploradora Beds
- Pastos Largos Beds
- Pampa Rubia

Pal
- Eocene intrusives
- Chile-Alemania & Cerro Nevado

Cret
- Upper Cret. intrusives
- Llanta
- Quebrada del Chaco Beds
- Sierra Fraga & Profeta (Jp5)

Jur
- Candeleros
- Asientos & Profeta (Jp4)
- Montandón & Profeta (Jp2 & Jp3)
- Las Bateas & Profeta (Jp1)

Tr
- Sierra de Varas & Cerro Guanaco
- Quebrada del Salitre

Carb-Perm
- La Tabla
- Punta del Viento batholith
- Sierra Castillo batholith
- Quebrada del Carrizo Met. Comp.

Ord
- Cerro del Medio

- anticline
- syncline
- fault
- inferred fault
- inverse fault
- strike-slip fault
- normal fault
- inverted normal fault

Scale 0 10 20 km

b

23.5% shortening

A — A'

no data

topography

PF: Profeta Fault

c

18.9% shortening   44.9% shortening

B — B'

CF   SAF   EFTB   AF

topography

CAF: Candeleros Fault   AF: Alejo Fault
SAF: Santa Ana Fault   EFTB: Exploradora fold-and-thrust belt

d

6.7% shortening   16.5% shortening

C — C'

PCF   GLLF   SCF

PCS   CF   topography

PCF: Pampa Carrizo Fault   GLLF: Gran LLano Fault   CAF: Carrizo Fault
PCS: Pampa Carrizo Syncline   SCF: Sierra Castillo Fault

LEGEND

Eoc — Pampa Rubia
Pal — Co Nevado- Chile Alemania
Upp. K — Llanta
Low. K — Quebrada del Chaco
Upp. J — Profeta (5) - Sierra Fraga
Upp. J — Sierra Candeleros (2 & 3) Profeta (4)
Mld.-Upp. J — Asientos - Profeta (4) Sierra Candeleros (1)
Low.-Mid. J — Montandón - Profeta (2 & 3)
Upp. Tr-Low. J — Las Bateas - Profeta (1)
Tr — Sierra de Varas Quebrada del Salitre
Pz — La Tabla Fm Carb. & Perm. plutons

- Normal fault
- Thrust fault
- Inverted normal fault
- ① Fault timing
- Active fault
- Inactive fault
- Future fault

126

Más aún, actividad neotectónica en el dominio occidental del bloque Exploradora, correspondiente a fallamiento de bloque hundido hacia el este (Fig. 5.9), ha sido interpretada como originadas por la reactivación de fallas inversas "volcadas" (Audin *et al*., 2003). Lo anterior resulta compatible con un basculamiento de las fallas invertidas del flanco oriental de la Cuenca Llanta Carrizo durante el traslado pasivo a través de la estructura de sobrepaso inferida (Fig. 5.7C). En particular, las fallas marginales de vergencia opuesta propuestas en el modelo de Audin *et al*. (2003), corresponderían a las que aquí se interpretan como las fallas de borde invertidas del graben. En el bloque Vaquillas Altas, dada la gran cobertura de unidades neógenas, no fue posible determinar la geometría en profundidad del dominio occidental. Sin embargo, se interpreta que habría experimentado una evolución similar a la del bloque Castillo.

(modified from Badley et al., 1989)

Figura 5.8: Ejemplo de graben invertido (Sole Pit Basin; Badley *et al*., 1989). Tomado de Brun y Nalpas (1996).

Por otro lado, el estilo estructural del dominio oriental de los bloques norte (Vaquillas Altas) y sur (Castillo) correspondería a uno de piel gruesa asociado a la exhumación del basamento cristalino paleozoico a través de la inversión de las fallas

maestras del *rift* triásico, generando una vergencia principal hacia el oeste del flanco occidental de la Cordillera de Domeyko. El proceso de inversión de estas fallas de alto ángulo habría sido facilitado mediante una cinemática transpresional y habría involucrado el desarrollo de fallas de atajo y retrocorrimientos mediante fallamiento fuera de secuencia, como lo mostraron McClay y Buchanan (1992) mediante modelos análogos. Esta compleja deformación generó una geometría que contrasta con la inversión del graben de la Cuenca Llanta-Carrizo, caracterizándose por pliegues cerrados y de corta longitud de onda. Además, el cambio de vergencia de las fallas asociado a la generación de retrocorrimientos, habría formado geometrías tipo *pop-up* y zonas triangulares (Fig. 5.7). Esta compleja deformación es típica de regiones que experimentan inversión tectónica (Cooper *et al*., 1989; McClay, 1989; Colletta *et al*., 1997). Posterior a la inversión del *rift*, en el borde de la Cordillera Occidental se habría desarrollado un fallamiento de vergencia oeste que alzó el basamento plutónico y sedimentario paleozoico.

Por otro lado, en el bloque Exploradora se desarrolló un estilo de piel delgada y vergencia hacia el este, correspondiente a la Faja Plegada y Corrida Exploradora (Cornejo *et al*., 2009). En esta tesis se interpreta que este sistema estaría asociado a la propagación de la deformación a niveles más someros a través de la falla de sobrepaso inferida desde el dominio occidental de este bloque (Fig. 5.7C). El alzamiento del basamento volcánico paleozoico desde el este se interpretó como ocasionado por fallamiento de vergencia occidental similar al desarrollado en los bloques Vaquillas Altas y Castillo en el borde de la Cordillera Occidental, aunque en este bloque esta estructura sería ciega. La intrusión de hipabisales con edades entre los 39-38 Ma siguiendo el eje de esta falla inferida (Cornejo *et al*. 2009), sugiere una temporalidad eocena para esta estructura.
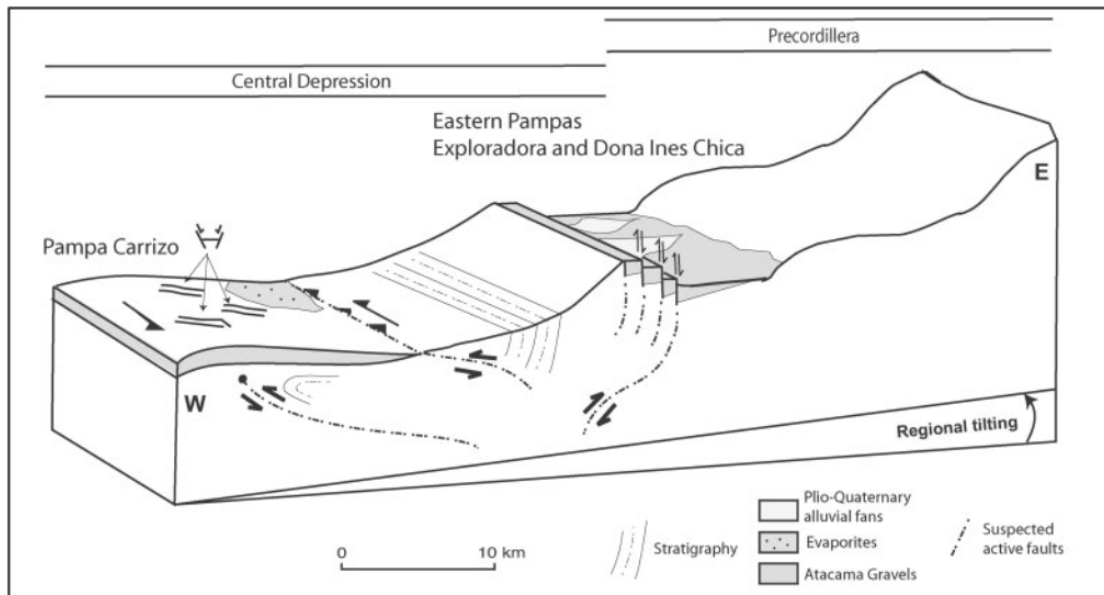
Figura 5.9: Esquema de la deformación neotectónica en el área de estudio. Tomado de Audin *et al*. (2003).

5.2.1.2 Temporalidad de la deformación en el flanco occidental de la Cordillera de Domeyko

Para constreñir la temporalidad de la deformación en el modelo forward (Capítulo IV), se utilizaron principalmente relaciones de corte observadas en campo, bibliografía disponible (*e.g.* Tomlinson *et al*., 1999; Cornejo *et al*., 2009; Venegas *et al*., 2013) e información termocronológica disponible en el área de estudio (Maksaev y Zentilli, 1999).

Posterior a la etapa *synrift* (Triásico Medio-Superior) y postrift (Jurásico Inferior-Medio), se desarrollaron depocentros extensionales menores hacia el oeste de la actual Cordillera de Domeyko, donde se depositaron unidades sedimentarias marinas (formaciones Asientos, Profeta y Pedernales), volcanosedimentarias (formaciones Candeleros, Sierra Fraga y Quebrada Vicuñitas) y sedimentarias continentales (Estratos Quebrada del Chaco y Formación Agua Helada) durante el lapso Jurásico Medio-Cretácico Inferior.

Un primer evento de deformación contraccional se registraría durante el Cretácico Superior en la suave discordancia angular que separa las unidades del Cretácico Inferior (Estratos Quebrada del Chaco y parte superior de la Formación Sierra Fraga) de la Formación Llanta (Cornejo *et al*., 2009; Venegas *et al*., 2013). Una relación discordante similar ha sido reportada al norte del área de estudio entre unidades del Cretácico Inferior (Estratos Areniscas Islote y Estratos de Paradero El Desierto) y del Cretácico Superior (Formación Quebrada Mala) (Muñoz, 1989; Ferrando y Espinoza, 2015; Mardonez *et al*., 2015). La intrusión de cuerpos hipabisales de *ca*. 86 Ma (Venegas *et al*., 2013) en el eje de pliegues desarrollados en secuencias del Cretácico Inferior en el sector de la Sierra Candeleros posiblemente datarían este evento, correspondiente a la fase Peruana.

Posterior a la fase de deformación Peruana, tuvo lugar la depositación de la Formación Llanta (73-68 Ma; Cornejo *et al*., 2009; Venegas *et al*., 2013) en una cuenca extensional (Cuenca Llanta-Carrizo; Cornejo *et al*., 2009), correspondiente a un paleocentro emisor distal con respecto al arco volcánico del Cretácico Superior (Venegas *et al*., 2013). Dado el gran aporte volcánico y su geometría interpretada como graben, en esta tesis se interpreta que el mecanismo de extensión correspondería a subsidencia volcanotectónica, similar a lo propuesto para la Formación Quebrada Mala al norte del área de estudio (Ferrando y Espinoza, 2015). Estas unidades se encuentran deformadas y en discordancia angular bajo unidades volcánicas paleocenas (Formación Cerro Nevado; Cornejo *et al*. 2009), constriñendo un nuevo evento de deformación entre los *ca*. 67-64 Ma (Fase K-T; Cornejo *et al*., 2003).

Posteriormente, durante el Eoceno, se evidencia la mayor deformación y exhumación en el núcleo de la Cordillera de Domeyko, constituyéndose el orógeno Incaico (Charrier *et al*., 2007). En el bloque Vaquillas, los Estratos de Quebrada Pastos Largos (Venegas *et al*., 2013) fueron depositados inmediatamente al oeste del frente cordillerano. Circones detríticos de esta unidad sinorogénica indican que el basamento paleozoico y las unidades depositadas durante el *Synrift II* (*ca*. 217-200 Ma) constituyeron una fuente sedimentaria con posterioridad a los *ca*. 54 Ma (Fig. 5.10A; Venegas *et al*. 2013), durante el alzamiento del bloque occidental de la Cordillera de Domeyko. Esta unidad es equivalente a la sinorogénica Formación Aguada de Zorro

(Eoceno-Oligoceno) ubicada al oeste de la Faja Plegada y Corrida Profeta, la cual también presenta una procedencia sedimentaria del basamento paleozoico ubicado hacia el este (González *et al*., 2015).

En el bloque Exploradora, depósitos sinorogénicos (Estratos de Sierra Exploradora) habrían sido depositados también durante el Eoceno medio (Cornejo *et al*., 2009). La distribución de esta unidad hacia el este del frente de deformación y entre las láminas tectónicas de la Faja Plegada y Corrida de Exploradora es coherente con una vergencia hacia el este en este dominio. Por otro lado, hacia el sur del bloque Castillo, termocronología de trazas de fisión en apatito indican una exhumación acelerada entre los 46-44 Ma (Eoceno 'medio'), la cual sería responsable de una erosión superficial de entre 4 a 5 km (Maksaev y Zentilli, 1999). También en este bloque, Tomlinson *et al*. (1994) interpretan una actividad entre los ~42-39 Ma para el Sistema de Falla Sierra Castillo-Agua Amarga basados en las edades de pórfidos y cuerpos hipabisales emplazados sintectónicamente.
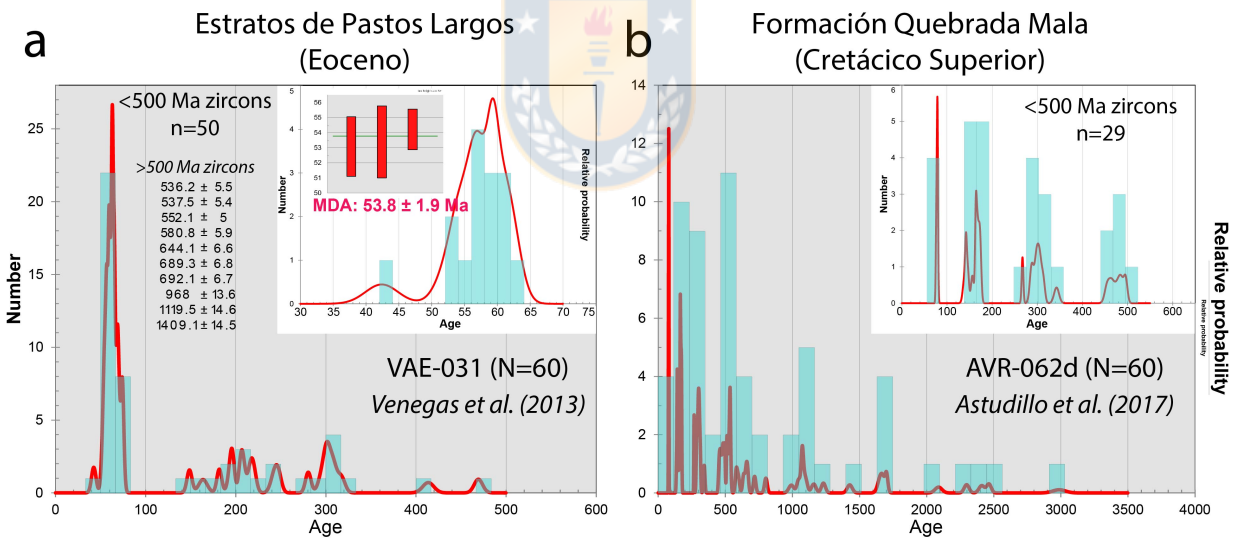
Figura 5.10: Dataciones U-Pb en circones detríticos de unidades cercanas al frente cordillerano del flanco occidental de la Cordillera de Domeyko (referencias en la figura).

Posterior al Eoceno, solo se habría producido una deformación de menor magnitud en el margen occidental de la Cordillera de Domeyko, como lo evidencia el suave plegamiento de las unidades del Paleoceno-Eoceno ubicadas al oeste de la Cordillera de Domeyko. La depositación de las Gravas de Atacama y de la Formación

Pampa de Mulas durante el Oligoceno-Mioceno indicaría un importante periodo de denudación, el cual no estaría relacionado a una reactivación importante de fallas en el flanco occidental de la Cordillera de Domeyko, sino más bien a un basculamiento general del antearco (Riquelme *et al*., 2003) y con la migración del foco de la deformación a la Puna y el Sistema de Santa Bárbara.

5.2.1.3 Contraste del alzamiento entre ambas vertientes de la Cordillera de Domeyko

Por otro lado, deformación y alzamiento en la Cordillera de Domeyko a partir del Cretácico Superior (< 86 Ma; Fase Peruana) ha sido propuesto en base al reconocimiento de sedimentación sinorogénica en sucesiones cretácicas de la Cuenca del Salar de Atacama (Mpodozis *et al*., 2005; Arriagada *et al*., 2006; Amilibia *et al*., 2008). Estudios de proveniencia sedimentaria en estas sucesiones indicaría un proceso de *unroofing* del basamento paleozoico adyacente, evidenciado por el aporte desde fuentes ordovícicas y triásicas (*ca.* 252-228 Ma) en la Formación Tonel, seguido de un gran aporte del basamento paleozoico Pérmico y una disminución del aporte triásico durante la depositación de sobreyacente Formación Purilactis (Bascuñán *et al*., 2015). Considerando las edades de las fuentes triásicas, estas provendrían de la exhumación de los depocentros cercanos al Salar de Atacama, correspondientes a las cuencas asociadas al Choiyoi (fomaciones Cas y Peine) y *Synrift I* (formaciones Tuina, El Bordo, Pular). Sin embargo, en las sucesiones cretácicas del Salar de Atacama no se registran fuentes depositadas durante la fase de *Synrift II* (217-200 Ma) desarrollada en el margen occidental de la actual Cordillera de Domeyko.

Por otro lado, aún cuando la Cordillera de Domeyko presenta una vergencia oeste en su flanco occidental, depósitos sinorogénicos de edad Cretácico Superior ubicados al oeste de esta sierra no se han reportado entre los 23° - 27°S (dominio de la Cuenca de Domeyko). En contraste, entre los 20°- 22° S, la formación Tambillos indicaría el desarrollo de una cuenca de antepaís al oeste de la Sierra de Moreno durante el Cretácico Superior-Paleoceno(?) (Tomlinson et al. 2001). Más aún, las unidades del Cretácico Superior entre los 24°-27°S en la Depresión Central y el borde

occidental de la Cordillera de Domeyko, correspondientes a las formaciones Llanta y Quebrada Mala (*ca*. 80-65; Cornejo *et al*., 2009; Venegas *et al*., 2013; González *et al*., 2015; Astudillo *et al*., 2017), se habrían depositado en cuencas extensionales formadas mediante subsidencia volcanotectónica (Espinoza *et al*., 2015), evidenciando un evento extensional post-Peruano (Espinoza *et al*., 2015; Ferrando y Espinoza, 2015; Mardonez *et al*., 2015) y previo a la deformación K-T.

Además, edades de circones detríticos procedentes de la Formación Quebrada Mala (Fig. 5.10B) evidencian un gran aporte de fuentes jurásicas y paleozoicas (Astudillo *et al*., 2017). Aun cuando las fuentes paleozoicas podrían provenir desde la Cordillera de Domeyko, el significativo aporte de fuentes jurásicas y la ausencia de fuentes triásicas asociadas a la exhumación del *Synrift II.* De esta forma, la procedencia sedimentaria de esta unidad sugiere su fuente en la Cordillera de la Costa, probablemente asociada al alzamiento de esta unidad durante la Fase Peruana I (110-100 Ma), como lo propusieron Bascuñán *et al.* (2015). Además, el significativo aporte cratónico que evidencia esta muestra sugiere que no habría existido una barrera topográfica importante hacia el interior del continente.

En contraste, como se discutió en la sección anterior, sedimentación sinorogénica durante el Eoceno se registra al oeste de las fallas de vergencia occidental de la Cordillera de Domeyko. De esta manera, proponemos que durante el Eoceno, la inversión del *rift* de Domeyko habría generado la vergencia oeste del flanco occidental de la sierra. Por otro lado, resultados termocronológicos indican que durante el Eoceno y hasta el Oligoceno, el sistema de vergencia oriental adyacente al Salar de Atacama habría estado activo (Reiners *et al*., 2015; Henriquez *et al*., 2019). De esta manera, durante la orogenia Incaica se habría desarrollado la doble vergencia observada en la actualidad en la Cordillera de Domeyko (Mpodozis y Ramos, 1989; Buddin *et al*., 1993), constituyendo la etapa principal de construcción de la Cordillera de Domeyko.

Lo anterior indicaría que la evolución de la Cordillera de Domeyko habría sido compleja y habría respondido de forma heterogénea durante la deformación andina. En este sentido, la inversión del *rift* de Domeyko durante la orogenia Incaica y la vergencia occidental que habría generado en el margen occidental de la Cordillera de

Domeyko, podría ser interpretada como un retrocorrimiento de escala cortical, el que habría sido controlado conjuntamente por la pre-existencia de un sistema estructural continuo y de gran longitud generado durante la fase de climax del *rift* y el debilitamiento mecánico asociado a la migración del arco magmático Eoceno-Oligoceno. Es posible hipotetizar que el alzamiento temprano del margen oriental de la Cordillera de Domeyko habría estado asociado a la reactivación de las estructuras extensionales cercanas a la Cuenca del Salar de Atacama, desarrolladas durante las etapas tardías del magmatismo de Choiyoi y la Primera Etapa de *rift* triásico.

5.2.2 Inversión tectónica y su rol en la vergencia del flanco occidental de los Andes Centrales del sur.

El crecimiento andino se ha interpretado clásicamente como una retro-cuña de vergencia al este (Isacks, 1988; Mpodozis y Ramos, 1989; Kley, 1999; Charrier *et al*., 2007; Giambiagi *et al*., 2014). Por otro lado, en las secciones anteriores se argumentó que durante la inversión tectónica del *rift* de Domeyko (Eoceno), el flanco occidental de la Cordillera de Domeyko habría adquirido una vergencia hacia el oeste. De manera similar, diversos trabajos han reconocido segmentos de los Andes Centrales cuyo flanco occidental presenta una vergencia hacia el oeste, aun cuando el estilo estructural y la temporalidad de la deformación varían un segmento a otro (Fig. 5.11).

Entre los 18º - 21º S (Fig. 5.11C-D), la Precordillera exhibe una serie de estructuras monoclinales (Victor *et al*., 2004; García *et al*., 2011; Charrier *et al*., 2013), las que se habrían generado a partir de fallas inversas ciegas, de alto ángulo y vergencia al oeste. Estas estructuras se habrían desarrollado como un retrocorrimiento asociado a un sistema de rampa-flat de escala cortical (Fig. 5.11C-D) durante el Oligoceno tardío-Mioceno temprano y/o Mioceno (Farías *et al*., 2005; Charrier *et al*., 2013; Herrera *et al*., 2017b). El desarrollo de un sistema de vergencia oriental en la Cordillera Occidental, reflejaría una estructura general de tipo *pop-up* (Charrier *et al*., 2013; Herrera *et al*., 2017b). A los 21º S esta geometría ha sido relacionada genéticamente con la actividad dextral transpresiva del Sistema de Fallas de la

Precordillera (Victor *et al*., 2004), el cual corresponde a la prolongación norte del Sistema de Fallas de Domeyko (Fig. 5.11E).

a

Victor et al. (2004)

b

Rodríguez et al. (2018)

c

Charrier et al. (2013)

d

Herrera et al. (2017)

e

Victor et al. (2004)

f

Rodríguez et al. (2018)

g

Farías et al. (2010)
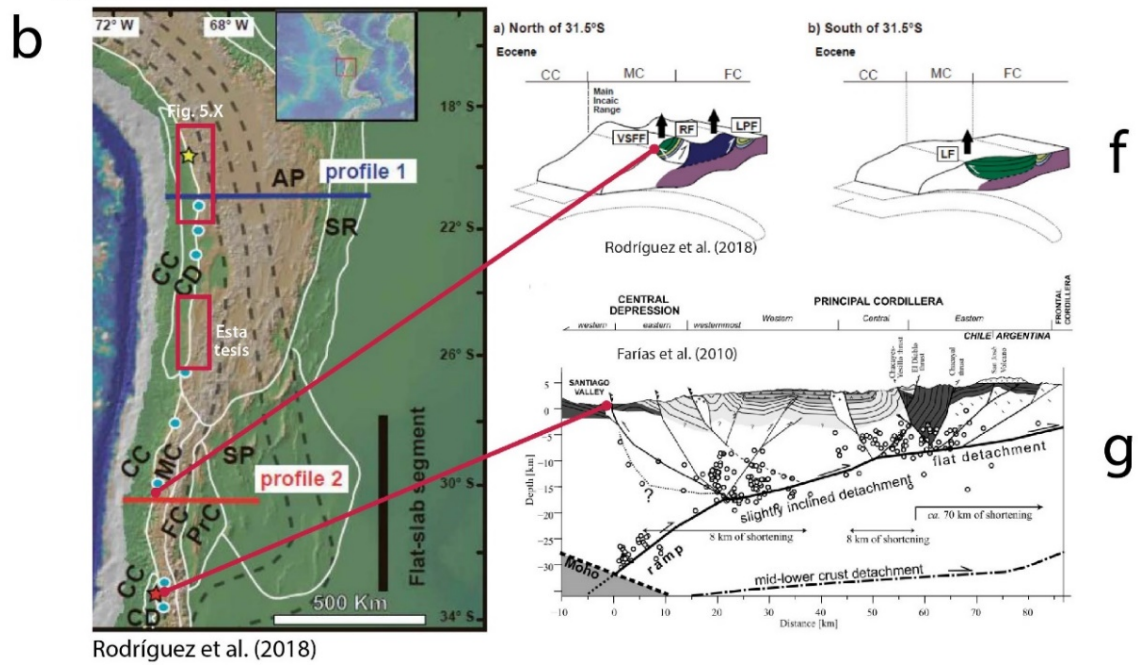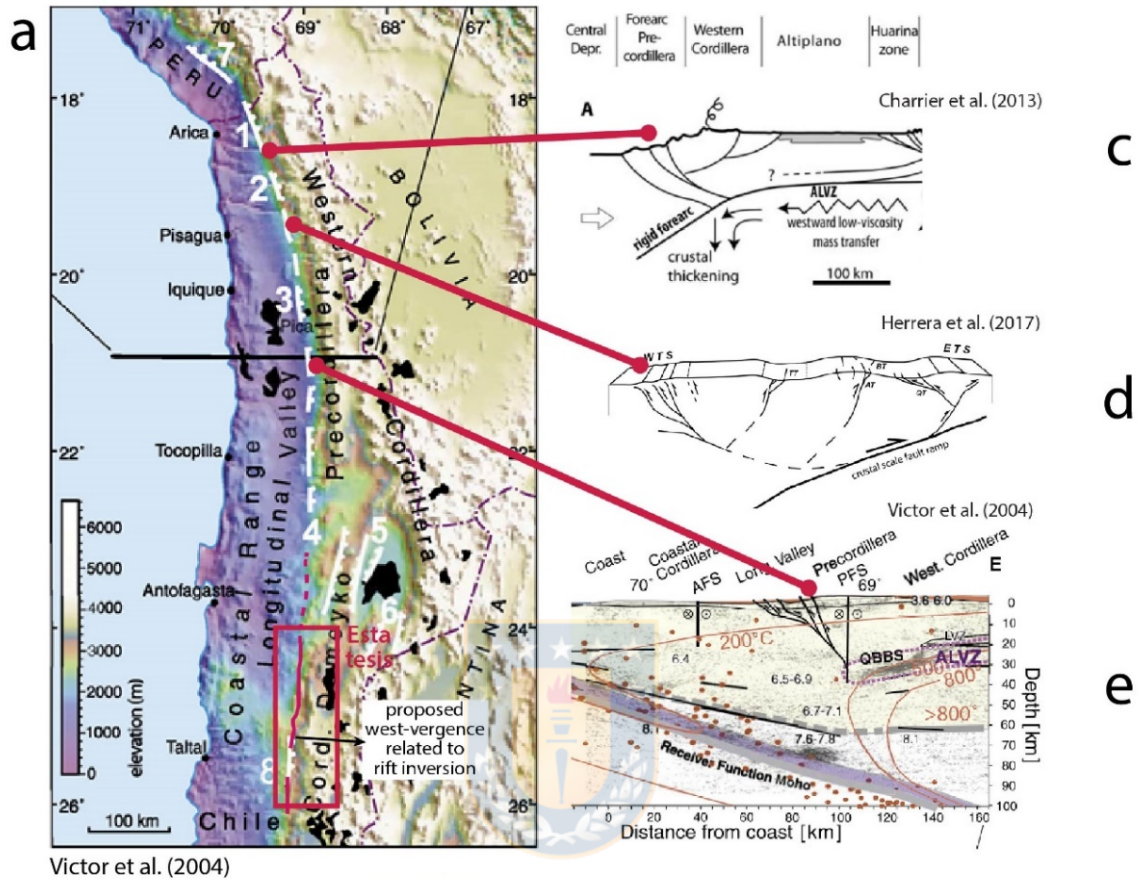
Figura 5.11: Segmentos del antearco chileno donde se ha reconocido el desarrollo de una vergencia oeste del flanco occidental de los Andes Centrales del Sur (referencias en la figura).

En la zona sur de los Andes Centrales (28º - 31º S), el flanco occidental de la Cordillera Principal presentaría una vergencia hacia el oeste (*e.g.* Falla Vicuña - San Félix), la que estaría asociada a la inversión de la cuenca mesozoica durante el Eoceno (Rodríguez *et al*., 2018). La reactivación de las fallas marginales de la cuenca durante la inversión habría generado una geometría general tipo "*pop-up*" (Fig. 5.11F). Este segmento marca el límite sur del prominente alzamiento y exhumación que experimentó el margen occidental de los Andes Centrales durante el Eoceno, conformando el orógeno Incaico (Maksaev y Zentilli, 1999; Charrier *et al*., 2013; Lossada *et al*., 2017; Rodríguez *et al*., 2018; Sánchez *et al*., 2018).

Por otro lado, en Chile Central (~33-34º S), el flanco occidental de la Cordillera Principal está dominado por un sistema de fallas y pliegues de vergencia al oeste (Fig. 5.11G; Thiele, 1980; Charrier *et al*., 2002; Fock *et al*., 2006; Armijo *et al*., 2010; Farías *et al*., 2010; Vargas *et al*., 2014). La evolución de este segmento está marcado por la inversión de la cuenca de Abanico (Eoceno medio (?) - Mioceno temprano; Charrier *et al*., 2002, 2005), durante el Oligoceno superior – Mioceno, siendo este último período de deformación el que ocasionaría la vergencia occidental del sistema (Fock *et al*., 2006), aun cuando algunas de las fallas que participarían en la extensión y posterior inversión de la cuenca (*e.g.* Falla San Ramón-Pocuro) presentarían actividad neotectónica (Charrier *et al*., 2005; Díaz *et al*., 2014; Vargas *et al*., 2014).

En este último segmento, se han planteado dos grandes hipótesis acerca del origen de la vergencia occidental de la Cordillera Principal: (i) acorde al modelo clásico, Farías *et al*. (2010) propusieron un despegue cortical de manteo hacia la fosa como estructura de primer orden del orógeno andino, en el cual la vergencia occidental del antearco correspondería a un retrocorrimiento de segundo orden asociado al cambio de pendiente del despegue principal (geometría rampa-flat), de manera análoga a lo que ocurriría en el segmento entre los 18º - 21º S. (ii) Por otro lado, Armijo *et al*. (2010) propusieron que las fallas del borde occidental de la Cordillera Principal corresponderían a un sistema de faja plegada y corrida con vergencia al oeste (*Western Andean Fold and Thrust Belt*, WAFTB; Riesner *et al*., 2017, 2018), el que habría evolucionado mediante fallamiento en secuencia a partir de los *ca.* 25 Ma

(Armijo *et al.*, 2010; Riesner *et al.*, 2018). En este modelo, el despegue cortical principal mantea hacia el este, generando la subducción del antearco en relación al cratón sudamericano (Fig. 5.12).
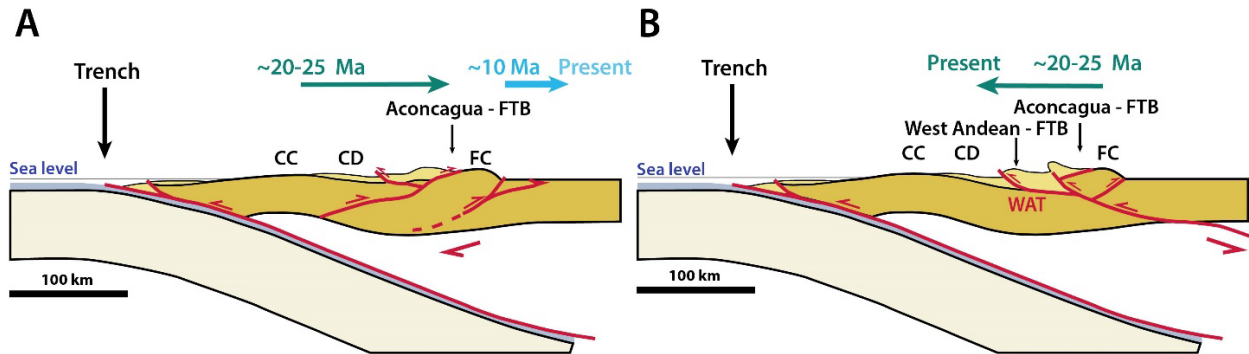
Figura 5.12: Modelos contrastantes acerca de la estructura de los Andes a los 34°S (tomado de Riesner et al. 2018). A) modelo de retrocuña de vergencia oriental (Giambiagi *et al.*, 2014). B) modelo de orógeno bi-vergente con predominancia de la vergencia occidental propuesto por Armijo *et al.* (2010).

En relación a la vergencia oeste observada en el flanco occidental de la Cordillera de Domeyko y la arquitectura estructural de los Andes Centrales en el segmento estudiado, es posible discutir que:

- El fenómeno de inversión de cuencas habría jugado un rol clave para la nucleación de las fallas de vergencia oeste del flanco occidental de los Andes Centrales en diferentes segmentos (23°-26° y 28°-31° S para la Cuenca Mesozoica temprana y ~34° S para la Cuenca de Abanico). En particular, entre los 23°-26° (esta tesis) y entre los 28°- 31° S (Rodríguez *et al.*, 2018), la inversión de la cuenca mesozoica temprana asociada a la construcción principal de las Cordilleras de Domeyko y Principal, se correlaciona con una fase acelerada de alzamiento durante la orogénesis Incaica (Eoceno medio-tardío). Por otro lado, hacia el segmento norte (18°-21°S), donde no se ha registrado la inversión de un sistema de *rift* en el antearco, el mayor alzamiento se alcanzaría durante el Mioceno (Farías *et al.*, 2005; Charrier *et al.*, 2013). Asimismo, hacia el sur de los 31° S, el principal alzamiento ocurriría durante el Mioceno-Plioceno (Maksaev *et al.*, 2009; Rodríguez *et al.*, 2018). Rodríguez *et al.* (2018) explican el contraste en la historia de exhumación al norte y sur de los 31°S

137

debido a la ausencia del basamento cristalino Paleozoico en la Cordillera Principal en el segmento sur, el que habría actuado como "butress" de la deformación en el segmento norte, concentrándola hacia los márgenes del orógeno incaico.

- Posterior a la construcción bi-vergente de la Cordillera de Domeyko durante el Eoceno, la deformación habría migrado hacia la Puna durante el Eoceno tardío y a la Cordillera Oriental en el Oligoceno temprano-Mioceno (Grier *et al*., 1991; Coutand *et al*., 2001), mientras que el alzamiento principal de la Puna se habría alcanzado entre los 5-10 Ma (Allmendinger, 1986). Como se discutió en la sección anterior, en el segmento estudiado no se registra mayor deformación orogénica asociada a fallas ubicadas al oeste de la Cordillera de Domeyko luego del Eoceno superior-Oligoceno temprano. De esta manera, considerando la secuencia de la migración de la deformación, se descarta que en este segmento opere el modelo de orógeno bivergente con transporte tectónico preferencial hacia el oeste (Armijo *et al*., 2010; Riesner *et al*., 2018). Por otro lado, es posible que la inversión de las fallas occidentales de la cuenca de Domeyko actúen como "backstop" para la transferencia preferencial de la deformación hacia el este, de manera similar a lo propuesto por Herrera *et al*. (2017a) en base al modelamiento análogo de la inversión de la cuenca de Abanico a los 34°S.

Capítulo 6: Conclusiones

La fase *synrift* de la Cuenca de Domeyko (*rift* de Domeyko) se habría desarrollado en dos períodos: *Synrift I* (Ladiniano – Carniano; *ca*. 240 - 225 Ma), con la apertura de la subcuenca Sierra Exploradora (SESB) y *Synrift II* (Nórico – Rético; *ca*. 217-200 Ma), en el que se inició la Subcuenca Sierra de Varas (SVSB) y se reactivó la extensión en la Subcuenca Sierra Exploradora.

El desarrollo de los sistemas sedimentarios del *rift* de Domeyko habría estado controlado principalmente por la subsidencia tectónica y la magnitud del aporte sedimentario mediante la razón A/S (acomodación/aporte sedimentario). Durante el *Synrift II*, en aquellos depocentros donde se desarrolló un menor aporte volcánico *(low-volcanoclastic input depocenters)* se registró un ciclo de *rift* completo, incluyendo una fase de climax asociada a la unión de las fallas maestras del *rift*. Mediante esta unión de fallas, se generó un sistema de *rift* elongado, de rumbo actual ~NS. Junto a las fallas maestras de orientación ~NS a ~NNE, se desarrollaron fallas secundarias de rumbo NNO-SSE a NO-SE. Ambos sistemas se habrían generado mediante un régimen transtensional (sinestral) el que habría dado origen a un sistema de *rift* oblicuo.

Las etapas *synrift* del *rift* de Domeyko se correlacionarían con dos etapas de desarrollo de cuencas de *rift* en Gondwana Suroccidental, separadas por una disminución significativa del registro sedimentario (¿hiatus?) entre los *ca*. 226-219 Ma. El inicio de este hiatus correspondería a una reconfiguración de primer orden de la cinemática de placas durante el Triásico. Aun cuando ambas etapas del *rift* de Domeyko habrían correspondido a un "*rift*-asociado a subducción", durante el *Synrift* I el plutonismo ocupó una extensa área, dificultando la distinción de una zona de arco. En contraste, durante el *Synrift* II el arco magmático se instaló en la Cordillera de la Costa, generando un sistema de cuenca de intra-arco y de trasarco en las Cordilleras de la Costa y Domeyko respectivamente.

Por otro lado, termocronología detrítica Ar-Ar indica que la historia de enfriamiento de las fuentes sedimentarias de ambas subcuencas es contrastante. En la SESB habría ocurrido un enfriamiento rápido del basamento durante el Pérmico Superior (262-265 Ma), el que se asociaría a la Fase San Rafael. Por otro lado, el

basamento de la SVSB se habría alzado lentamente a partir de los *ca*. 243 Ma. Este contraste sugiere la actividad de una estructura cortical de probable rumbo noroeste segmentando tectónicamente ambos dominios desde al menos el Pérmico Superior. Durante la etapa de *rift* esta estructura cortical coincidiría con la posición de un alto estructural que separó las subcuencas de la Cuenca de Domeyko (SVSB y SESB).

Posteriormente, durante la orogénesis Incaica, los bloques donde se desarrolló fallamiento *synrift* (SVSB y SESB), experimentaron inversión tectónica dando lugar a la exhumación del basamento plutónico Paleozoico en un estilo de deformación de piel gruesa y de vergencia principal al oeste. Por otro lado, en el bloque transicional se desarrolló una deformación de piel delgada y de vergencia hacia el este en el núcleo de la Cordillera de Domeyko. Además, la inversión de las fallas maestras del *rift* de Domeyko mediante tectónica transpresional habría permitido la incepción de las estructuras occidentales del Sistema de Fallas de Domeyko, configurando una vergencia principal hacia el oeste del flanco occidental de la Cordillera de Domeyko.

De esta manera, la generación y posterior inversión de las cuencas Meso-Cenozoicas habría jugado un rol clave para la adquisición de la vergencia oeste del flanco occidental de los Andes Centrales. En particular, entre los 23°-32° S, la inversión de las cuencas mesozoicas durante la orogénesis Incaica habría generado una estructura tipo *pop-up* en el margen occidental (Cordilleras de Domeyko y Principal).

Se infiere que la vergencia oriental de la Cordillera de Domeyko se habría comenzado a desarrollar durante el Cretácico Superior, mientras que la vergencia occidental asociada a la inversión del *rift* de Domeyko se desarrollaría principalmente durante el Eoceno, posiblemente correspondiendo a un retrocorrimiento de escala cortical.

Capítulo 7: Referencias

Allmendinger, R.W., 1986, Tectonic development, southeastern border of the Puna Plateau, northwestern Argentine Andes: Geological Society of America Bulletin, v. 97, p. 1070–1082.

Álvarez, J., Jorquera, R., Miralles, C., Padel, M., and Martinez, P., 2016, Cartas Punta Posallaves y Sierra Vicuña Mackenna, Región de Antofagasta. Escala 1:100.000. Servicio Nacional de Geología y Minería, Carta Geológica de Chile, Serie Geología Básica (nos. 183-184): 151 pp. 1 mapa escala 1:100.000. Santiago.

Alvarez, P.P., and Ramos, V.A., 1999, The Mercedario rift system in the Principal Cordillera of Argentina and Chile (32° SL): Journal of South American Earth Sciences, v. 12, p. 17–31.

Amilibia, A., 2002, Inversión tectónica en la Cordillera de Domeyko, Andes del Norte de Chile: Doctoral thesis. Universitat de Barcelona.

Amilibia, A., Sàbat, F., McClay, K.R., Muñoz, J.A., Roca, E., and Chong, G., 2008, The role of inherited tectono-sedimentary architecture in the development of the central Andean mountain belt: Insights from the Cordillera de Domeyko: Journal of Structural Geology, v. 30, p. 1520–1539.

Ardill, J., 1996, Sequence stratigraphy of the Mesozoic Domeyko basin, northern Chile: University of Liverpool, 1-245 p.

Ardill, J., Flint, S., Chong, G., and Wilke, H., 1998, Sequence stratigraphy of the Mesozoic Domeyko Basin, northern Chile: Journal of the Geological Society, v. 155, p. 71–88.

Arévalo, C., and Welkner, D., 2008, Geología del área Carrizal Bajo-Chacritas, Región de Atacama. Servicio Nacional de Geología y Minería. Serie Geología Básica 111, 67 p.

Armijo, R., Rauld, R., Thiele, R., Vargas, G., Campos, J., Lacassin, R., and Kausel, E., 2010, The West Andean Thrust (WAT), the San Ramón Fault and the seismic hazard for Santiago (Chile): Tectonics, v. 29, p. 1–34.

Arriagada, C., Cobbold, P., and Roperch, P., 2006, Salar de Atacama basin: A record of compressional tectonics in the central Andes since the mid-Cretaceous: Tectonics, v. 25, p. TC1008.

Arriagada, C., Roperch, P., Mpodozis, C., and Cobbold, P.R., 2008, Paleogene building of the Bolivian Orocline: Tectonic Restoration of the Central Andes in 2D Map View: Tectonics, v. 27.

Astudillo, N., Ferrando, R., Montecino, D., Espinoza, F., Matthews, S., Cornejo, P., and Arévalo, C., 2017, Carta Augusta Victoria, Región de Antofagasta. Servicio Nacional de Geología y Minería, Carta Geológica de Chile, Serie Geología Básica 189. 1 mapa escala 1:100.000. Santiago, Chile.

Audin, L., Herail, G., Riquelme, R., Darrozes, J., Martinod, J., and Font, E., 2003, Geomorphological markers of faulting and neotectonic activity along the western Andean margin, northern Chile: Journal of Quaternary Science, v. 18, p. 681–694.

Ávila, J.N., Chemale, J., Mallmann, G., Kawashita, K., and Armstrong, R. a., 2006, Combined stratigraphic and isotopic studies of Triassic strata, Cuyo Basin, Argentine Precordillera: Bulletin of the Geological Society of America, v. 118, p.

1088–1098.

Badley, M.E., Price, J.D., and Backshall, L.C., 1989, Inversion, reactivated faults and related structures: seismic examples from the southern North Sea: Geological Society, London, Special Publications, v. 44, p. 201 LP-219.

Barredo, S., Chemale, F., Marsicano, C., Ávila, J.N., Ottone, *E.G.*, and Ramos, V. a., 2012, Tectono-sequence stratigraphy and U-Pb zircon ages of the Rincón Blanco Depocenter, northern Cuyo Rift, Argentina: Gondwana Research, v. 21, p. 624–636.

Barrionuevo, M., Arnosio, M., and Llambías, J., 2011, Nuevas Edades Para Rocas Volcánicas Aflorantes Y De Subsuelo En El Oeste De La Pampa. Implicancias Estratigráficas: ¿Choiyoi O Precuyo?, *in* XVIII Congreso Geológico Argentino, Neuquén, Argentina, p. 77–78.

Bascuñán, S., Arriagada, C., Le Roux, J., and Deckart, K., 2015, Unraveling the Peruvian Phase of the Central Andes: stratigraphy, sedimentology and geochronology of the Salar de Atacama Basin (22°30-23°S), northern Chile: Basin Research, v. 28, p. 365–392.

Basso, M., and Mpodozis, M., 2012, Carta Cerro del Quimal, Región de Antofagasta. Servicio Nacional de Geología y Minería, Carta Geológica de Chile, Serie Geología Básica143. Mapa geológico a escala 1:100.000.

Bechis, F., 2009, Deformcaión transtensiva de la cuenca neuquina: Análisis a partir de ejemplos de campo y modelos análogos: Universidad de Buenos Aires, 265 p.

Bechis, F., Cristallini, E.O., Giambiagi, L.B., Yagupsky, D.L., Guzmán, C.G., and García, V.H., 2014, Transtensional tectonics induced by oblique reactivation of previous lithospheric anisotropies during the Late Triassic to Early Jurassic rifting in the Neuquén basin: Insights from analog models: Journal of Geodynamics, v. 79, p. 1–17.

Bechis, F., Giambiagi, L., García, V., Lanés, S., Cristallini, E., and Tunik, M., 2010, Kinematic analysis of a transtensional fault system: The Atuel depocenter of the Neuquén basin, southern Central Andes, Argentina: Journal of Structural Geology, v. 32, p. 886–899.

Bell, C.M., and Suárez, M., 1991, Late Triassic fluvial and marine shelf succession, Quebrada Doña Inés Chica, Atacama region, northern Chile: Journal of South American Earth Sciences, v. 4, p. 287–293.

Bermudez, A., Delpino, D., and Pángaro, F., 2002, Volcanismo de arco asociado a procesos de subducción-extensión durante el Triásico Superior-Jurásico Inferior (Precuyano). Área Cerro Bandera, Cuenca Neuquina, Argentina, *in* 5º Congreso de Exploración y Desarrollo de Hidrocarburos, Mar del Plata, Argentina, p. 11.

Boekhout, F., Spikings, R., Sempere, T., Chiaradia, M., Ulianov, A., and Schaltegger, U., 2012, Mesozoic arc magmatism along the southern Peruvian margin during Gondwana breakup and dispersal: Lithos, v. 146, p. 48–64.

Brun, J.P., and Nalpas, T., 1996, Graben inversion in nature and experiments: Tectonics, v. 15, p. 677–687.

Buddin, T.S., Stimpson, I.G., and Williams, G.D., 1993, North Chilean forearc tectonics and cenozoic plate kinematics: Tectonophysics, v. 220, p. 193–203.

Butler, R.W.H.W.H., 1989, The influence of pre-existing basin structure on thrust system evolution in the Western Alps: Geological Society, London, Special

Publications, v. 44, p. 105–122.

Butler, R.W.., Tavarnelli, E., and Grasso, M., 2006, Structural inheritance in mountain belts: An Alpine-Apennine perspective: Journal of Structural Geology, v. 28, p. 1893–1908.

Carrera, N., and Munoz, J. a., 2013, Thick-skinned tectonic style resulting from the inversion of previous structures in the southern Cordillera Oriental (NW Argentine Andes): Geological Society, London, Special Publications, v. 377, p. 77–100.

Carrera, N., Muñoz, J.A., Sàbat, F., Mon, R., and Roca, E., 2006, The role of inversion tectonics in the structure of the Cordillera Oriental (NW Argentinean Andes): Journal of Structural Geology, v. 28, p. 1921–1932.

Casquet, C., Hervé, F., Pankhurst, R.J., Baldo, E., Calderón, M., Fanning, C.M., Rapela, C.W., and Dahlquist, J., 2013, The Mejillonia suspect terrane (Northern Chile): Late Triassic fast burial and metamorphism of sediments in a magmatic arc environment extending into the Early Jurassic: Gondwana Research, v. 25, p. 1272–1286.

Celis, C., 2018, Petrografía y Geoquímica de las rocas volcánicas y volcanoclásticas del triásico del triásico superior de la Cordillera de la Costa y la Coordillera de Domeyco entre las coordenadas 23°50´- 26°10´S, Chile: Universidad de Concepción, 179 p.

Charrier, R., 1979, El Triásico en Chile y regiones adyacentes de Argentina: Una reconstrucción paleogeográfica y paleoclimática: Comunicaciones, Departamento de Geología, Universidad de Chile, v. 26, p. 1–47.

Charrier, R., Bustamante, M., Comte, D., Elgueta, S., Flynn, J.J., Iturra, N., Muñoz, N., Pardo, M., Thiele, R., Wyss, A.R., 2005, The Abanico extensional basin: Regional extension, chronology of tectonic inversion and relation to shallow seismic activity and Andean uplift: Neues Jahrbuch Fur Geologie Und Palaontologie-Abhandlungen, v. 236, p. 43–77.

Charrier, R., Baeza, O., Elgueta, S., Flynn, J.J., Gans, P., Kay, S.M., Muñoz, N., Wyss, A.R., and Zurita, E., 2002, Evidence for Cenozoic extensional basin development and tectonic inversion south of the flat-slab segment, southern Central Andes, Chile (33–36 SL): Journal of South American Earth Sciences, v. 15, p. 117–139.

Charrier, R., Hérail, G., Pinto, L., García, M., Riquelme, R., Farías, M., and Muñoz, N., 2013, Cenozoic tectonic evolution in the Central Andes in northern Chile and west central Bolivia: Implications for paleogeographic, magmatic and mountain building evolution: International Journal of Earth Sciences, v. 102, p. 235–264.

Charrier, R., Pinto, L., and Rodriguez, M.P., 2007, Tectonostratigraphic evolution of the Andean Orogen in Chile, in Moreno, T. and Gibbons, W. eds., The Geology of Chile, London, Geological Society of London, p. 21–114.

Charrier, R., Ramos, V.A., Tapia, F., and Sagripanti, L., 2014, Tectono-stratigraphic evolution of the Andean Orogen between 31 and 37°S (Chile and Western Argentina): Geological Society, London, Special Publications, v. 399, p. 13–61.

Chong, G., and Hilldebrandt, A., 1985, El Triásico PreAndino de Chile entre los 23°30´ y 26°00´ de lat. sur., in IV Congreso Geológico Chileno, Antofagasta, Chile.

Colletta, B., Roure, F., De Toni, B., Loureiro, D., Passalacqua, H., and Gou, Y., 1997, Tectonic inheritance, crustal architecture, and contrasting structural styles in the Venezuela Andes: Tectonics, v. 16, p. 777–794.

Coloma, F., Valin, X., Oliveros, V., Vásquez, P., Creixel, C., Salazar, E., Ducea, M., Vallejos, D., 2017, Geochemistry of Permian to Triassic igneous rocks from northern Chile (28º-29º30'S): Implications on the dynamics of the proto-Andean margin: Andean Geology, v. 44, 2, p. 147-178.

Contreras, J.P., Espinoza, M., Jorquera, R., Kraus, S., Ramírez, C., De la Cruz, R., Naranjo, J. a., Escribano, J., and Martínez, P., 2013, Carta Cifuncho, Regiones de Antofagasta y Atacama. Servicio Nacional de Geología y Minería, Carta Geológica de Chile, Serie Geología Básica 161, 1 mapa escala 1:100.000. Santiago.:

Cooper, M.A., Williams, G.D., de Graciansky, P.C., Murphy, R.W., Needham, T., de Paor, D., Stoneley, R., Todd, S.P., Turner, J.P., and Ziegler, P.A., 1989, Inversion tectonics -- a discussion: Geological Society, London, Special Publications, v. 44, p. 335–347.

Cornejo, P., Matthews, S., and Pérez de Arce, C., 2003, The'KT'compressive deformation event in northern Chile (24-27 S), *in* Congreso Geológico Chileno, v. 10, p. 11.

Cornejo, P., Mpodozis, M., Rivera, O., and Matthews, S., 2009, Carta Exploradora, Regiones de Antofagasta y Atacama. Servicio Nacional de Geología y Minería, Carta Geológica de Chile, Serie Geología Básica 119: 103 p., 1 mapa escala 1:100.000.:

Coutand, I., Cobbold, P.R., de Urreiztieta, M., Gautier, P., Chauvin, A., Gapais, D., Rossello, E.A., and López-Gamundí, O., 2001, Style and history of Andean deformation, Puna plateau, northwestern Argentina: Tectonics, v. 20, p. 210–234.

Cristallini, E., Tomezzoli, R.N., Pando, G., Gazzera, C., Martínez, J.M., Quiroga, J., Buhler, M., Bechis, F., Barredo, S., and Zambrano, O., 2009, Controles precuyanos en la estructura de la cuenca neuquina: Revista de la Asociación Geológica Argentina, v. 65, p. 248–264.

Díaz, D., Maksymowicz, A., Vargas, G., Vera, E., Contreras-Reyes, E., and Rebolledo, S., 2014, Exploring the shallow structure of the San Ramón thrust fault in Santiago, Chile (~33.5° S), using active seismic and electric methods: Solid Earth, v. 5, p. 837–849.

Drosina, M., Barredo, S., Martinez, A., and Giambiagi, L., 2017, Facies volcaniclásticas del ciclo precuyano en el sector norte de la sierra de la cara cura, Mendoza: Revista de la Asociacion Geologica Argentina, v. 74, p. 179–190.

Elderry, S.M., Diaz, G.C., Prior, D.J., and Flint, S.S., 1996, Structural Styles in the Domeyko Range, Northern Chile, *in* Third ISAG, St. Malo, France, p. 439–442.

Escribano, J., Martínez, P., Domagala, J., Padel, M., Espinoza, M., Jorquera, R., Contreras, J., De la Cruz, R., and Calderón, M., 2013, Cartas Bahía Isla Blanca y Taltal. Escala 1:100.000. Servicio Nacional de Geología y Minería, Carta Geológica de Chile, Serie Geología Básica (nos. 164-165): 75 pp. 1 mapa escala 1:100.000. Santiago.

Espinoza, M., Contreras, J.P., Kraus, S., De la Cruz, R., Jorquera, R., Ramirez, C., and Naranjo, J.A., 2014, Carta Cerro del Pingo, Regiones de Antofagasta y Atacama. Servicio Nacional de Geología y Minería, Carta Geológica de Chile, Serie Geología Básica 169, 1 mapa escala 1:100.000. Santiago.

Espinoza, M., Oliveros, V., and Celis, C., 2016, Geochronology, Geochemistry and Tectonics of Subduction-Related Late Triassic Rift Basins in Northern Chile (24º-

26ºS)., *in* American Geophysical Union, Fall General Assembly 2016, San Francisco, United States, p. T51D–2975.

Espinoza, M., Oliveros, V., Vásquez, P., and Bechis, F., 2015a, U-Pb geochronology and kinematic preliminary analyses of Late Triassic-Early Jurassic basins in northern Chile (24.5º-26ºS), *in* XIV Congreso Geológico Chileno, La Serena, Chile, p. 840–843.

Espinoza, F., Venegas, C., Astudillo, N., and Cervetto, M., 2015b, Nuevos antecedentes cronoestratigráficos para la Sierra de Santa Ana, precordillera de Antofagasta., *in* XIV Congreso Geológico Chileno, La Serena, Chile, p. 178–181.

Eude, A., Roddaz, M., Brichau, S., Brusset, S., Calderon, Y., Baby, P., and Soula, J., 2015, Controls on timing of exhumation and deformation in the northern Peruvian eastern Andean wedge as inferred from low-temperature thermochronology and balanced cross section: Tectonics, v. 34, p. 715–730.

Farías, M., Charrier, R., Comte, D., Martinod, J., and Hérail, G., 2005, Late Cenozoic deformation and uplift of the western flank of the Altiplano: Evidence from the depositional, tectonic, and geomorphologic evolution and shallow seismic activity (northern Chile at 19°30′S): Tectonics, v. 24, p. 1–27.

Farías, M., Comte, D., Charrier, R., Martinod, J., David, C., Tassara, A., Tapia, F., and Fock, A., 2010, Crustal-scale structural architecture in central Chile based on seismicity and surface geology: Implications for Andean mountain building: Tectonics, v. 29.

Ferrando, R., and Espinoza, F., 2015, Revisión y nuevos antecedentes del Cretácico Superior en la depresión Central de la región de Antofagasta, *in* XIV Congreso Geológico Chileno, La Serena, Chile, p. 37–42.

Fock, A., Charrier, R., Farías, M., and Muñoz, M., 2006, Fallas de vergencia oeste en la Cordillera Principal de Chile Central: Inversión de la Cuenca de Abanico (33°-34°S): Revista de la Asociación Geológica Argentina, p. 48–55.

Franzese, J.R., and Spalletti, L. a., 2001, Late Triassic–early Jurassic continental extension in southwestern Gondwana: tectonic segmentation and pre-break-up rifting: Journal of South American Earth Sciences, v. 14, p. 257–270.

Garcia, M., Riquelme, R., Farias, M., Herail, G., and Charrier, R., 2011, Late Miocene-Holocene canyon incision in the western Altiplano, northern Chile: tectonic or climatic forcing?: Journal of the Geological Society, v. 168, p. 1047–1060.

Giambiagi, L., Tassara, A., Mescua, J., Tunik, M., Alvarez, P., Godoy, E., Hoke, G., Pinto, L., Spagnotto, S., Porras, H., Tapia, F., Jara, P., Bechis, F., Garcia, V. H., Suriano, J., Moreiras, S. M., Pagano, S. D. 2014, Evolution of shallow and deep structures along the Maipo-Tunuyan transect (33 40'S): from the Pacific coast to the Andean foreland: Geological Society, London, Special Publications, v. 399, p. 63–82.

Giambiagi, L., Alvarez, P., Godoy, E., and Ramos, V., 2003, The control of pre-existing extensional structures on the evolution of the southern sector of the Aconcagua fold and thrust belt, southern Andes: Tectonophysics, v. 369, p. 1–19.

Giambiagi, L., Bechis, F., García, V., and Clark, A., 2008a, Temporal and spatial relationships of thick- and thin-skinned deformation: A case study from the Malargüe fold-and-thrust belt, southern Central Andes: Tectonophysics, v. 459, p. 123–139.

145

Giambiagi, L., Bechis, F., Lanés, S., Tunik, M., García, V., Suriano, J., Mescua, J., and José, M., 2008b, Formación y evolución triásico-jurásica del depocentro Atuel, Cuenca Neuquina, provincia de Mendoza: Revista de la Asociación Geológica Argentina, v. 63, p. 520–533.

Giambiagi, L., Spagnotto, S., Moreiras, S.M., Gómez, G., Stahlschmidt, E., and Mescua, J., 2015, Three-dimensional approach to understanding the relationship between the Plio-Quaternary stress field and tectonic inversion in the Triassic Cuyo Basin, Argentina: Solid Earth, v. 6, p. 747–763.

Giambiagi, L., Tunik, M., Barredo, S., Bechis, F., Ghiglione, M., Alvarez, P., and Drosina, M., 2009, Cinemática de apertura del sector norte de la cuenca neuquina: Revista de la Asociación Geológica Argentina, v. 65, p. 278–292.

Godoy, E., and Lara, L., 1998, Hojas Chañaral y Diego de Almagro, Región de Atacama. Servicio Nacional de Geologia y Minería, Mapas Geológicos No. 5-6, 1 mapa escala 1:100.000, Santiago

González, J., Oliveros, V., Creixell, C., Velásquez, R., Vásquez, P., and Lucassen, F., 2017, The Triassic magmatism and its relation with the Pre-Andean tectonic evolution: Geochemical and petrographic constrains from the High Andes of north central Chile (29º 30' - 30º S): Journal of South American Earth Sciences, v. 87, p. 95–112.

González, R., Wilke, H.G., Menzies, A.H., Espinoza, F., Riquelme, R., and Herrera, C., 2015, Carta Sierra de Varas, Región de Antofagasta. Servicio Nacional de Geología y Minería, Carta Geológica de Chile, Serie Geología Básica 178, 1 mapa escala 1:100.000. Santiago.

Grier, M.E., Salfity, J.A., and Allmendinger, R.W., 1991, Andean reactivation of the Cretaceous Salta Rift, northwestern Argentina: Journal of South American Earth Sciences, v. 4.

Henríquez, S., Becerra, J., and Arriagada, C., 2014, Geología del área San Pedro de Atacama, Región de Antofagasta. Servicio Nacional de Geología y Minería. Carta Geológica de Chile, Serie Geología Básica 171, 111 p., 1 mapa escala 1:100.000. Santiago.

Henriquez, S., DeCelles, P.G., and Carrapa, B., 2019, Cretaceous to Middle Cenozoic Exhumation History of the Cordillera de Domeyko and Salar de Atacama Basin, Northern Chile: Tectonics.

Herrera, S., Farias, M., Pinto, L., Yagupsky, D., Guzmán, C., and Charrier, R., 2017a, Analogue modeling of rotational orogenic wedges : implications for the Neogene structural evolution of the Southern Central Andes, in American Geophysical Union, Fall Meeting 2017, p. 2–3.

Herrera, S., Pinto, L., and Deckart, K., 2017b, Cenozoic tectonostratigraphic evolution and architecture of the Central Andes in northern Chile based on the Aquine region , Western Cordillera (19 ° -19º30 ' S): Andean Geology, v. 44, p. 87–122.

Hochstaedter, A.G., Gill, J.B., and Morris, J.D., 1990, Volcanism in the Sumisu Rift, II. Subduction and non-subduction related components: Earth and Planetary Science Letters, v. 100, p. 195–209.

Ingersoll, R. V., 2012, Tectonics of Sedimentary Basins, with Revised Nomenclature, in Tectonics of Sedimentary Basins: Recent Advances, p. 1–43.

Irvine, T.N.J., and Baragar, W.R.A., 1971, A guide to the chemical classification of the

common volcanic rocks: Canadian journal of earth sciences, v. 8, p. 523–548.

Isacks, B.L., 1988, Uplift of the Central Andean Plateau and Bending of the Bolivian Orocline: Journal of Geophysical Research, v. 93.

Kato, T.T., and Godoy, E., 2015, Middle to late Triassic mélange exhumation along a pre-Andean transpressional fault system: coastal Chile (26°–42° S): International Geology Review, v. 57, p. 606–628.

Keith, S.B., 1978, Paleosubduction geometries Inferred from Cretaceous and Tertiary magmatic patterns in southwestern North America: Geology, v. 6, p. 516–521.

Kent, D. V., Malnis, P.S., Colombi, C.E., Alcober, O.A., Martínez, R.N., Santi Malnis, P., Colombi, C.E., Alcober, O.A., and Martinez, R.N., 2014, Age constraints on the dispersal of dinosaurs in the Late Triassic from magnetochronology of the Los Colorados Formation (Argentina): Proceedings of the National Academy of Sciences, v. 111, p. 7958–7963.

Kleiman, L.E., and Japas, M.S., 2009, The Choiyoi volcanic province at 34°S–36°S (San Rafael, Mendoza, Argentina): Implications for the Late Palaeozoic evolution of the southwestern margin of Gondwana: Tectonophysics, v. 473, p. 283–299.

Kley, J., 1999, Geologic and geometric constraints on a kinematic model of the Bolivian orocline: Journal of South American Earth Sciences, v. 12, p. 221–235.

Lacombe, O., and Mouthereau, F., 2002, Basement-involved shortening and deep detachment tectonics in forelands of orogens: Insights from recent collision belts (Taiwan, Western Alps, Pyrenees): Tectonics, v. 21.

Llambías, E.J., Leanza, H. a., and Carbone, O., 2007, Evolución Tectono-magmática durante el pérmico al Jurásico temprano en la Cordillera del Viento (37°05′S - 37°15′S): Nuevas evidencias geológicas y geoquímicas Del Inicio de la Cuencas Neuquina: Revista de la Asociación Geológica Argentina, v. 62, p. 217–235.

López, N., 2015, Análisis de Facies Volcanoclásticas y Control Estructural de una Sección de los Estratos de Guanaco Sonso, a los 29°S, Cordillera Frontal, Región de Atacama, in XIV Congreso Geológico Chileno, La Serena, Chile.

Lossada, A.C., Giambiagi, L., Hoke, G.D., Fitzgerald, P.G., Creixell, C., Murillo, I., Mardonez, D., Velásquez, R., and Suriano, J., 2017, Thermochronologic Evidence for Late Eocene Andean Mountain Building at 30°S: Tectonics, v. 36, p. 2693–2713.

Mackaman-lofland, C., Horton, B.K., Fuentes, F., Constenius, K.N., and Stockli, D.F., 2019, Mesozoic to Cenozoic retroarc basin evolution during changes in tectonic regime , southern Central Andes (31 – 33 ° S): Insights from zircon U-Pb geochronology: Journal of South American Earth Sciences, v. 89, p. 299–318.

Maksaev, V., Munizaga, F., Zentilli, M., and Charrier, R., 2009, Fission track thermochronology of Neogene plutons in the Principal Andean Cordillera of central Chile (33-35°S): Implications for tectonic evolution and porphyry Cu-Mo mineralization: Andean Geology, v. 36, p. 153–171.

Maksaev, V., and Zentilli, M., 1999, Fission track thermochronology of the Domeyko Cordillera, northern Chile; implications for Andean tectonics and porphyry copper metallogenesis: Exploration and Mining Geology, v. 8, p. 65–89.

Mancuso, a. C., Chemale, F., Barredo, S., Ávila, J.N., Ottone, *E.G.*, and Marsicano, C., 2010, Age constraints for the northernmost outcrops of the Triassic Cuyana Basin, Argentina: Journal of South American Earth Sciences, v. 30, p. 97–103.

147

Mardonez, D., Espinoza, F., and Quinzio, L.A., 2015, Geología del sector Cerro Islote (25ºS), Depresión Central, Región de Antofagasta, Chile: XIV Congreso Geológico Chileno, p. 189–192.

Marinovic, N., Smoje, I., Maksaev, V., Hervé, M., and Mpodozis, C., 1995, Hoja Aguas Blancas. Servicio Nacional de Geología y Minería, Carta Geológica de Chile, No. 70, 150 p., 1 mapa escala 1:250.000. Santiago.

Marsicano, C.A., Irmis, R.B., Mancuso, A.C., Mundil, R., and Chemale, F., 2016, The precise temporal calibration of dinosaur origins: Proceedings of the National Academy of Sciences, v. 113, p. 509–513.

Martínez, F., Bonini, M., Montanari, D., and Corti, G., 2016, Tectonic inversion and magmatism in the Lautaro Basin, northern Chile, Central Andes: A comparative approach from field data and analog models: Journal of Geodynamics, v. 94–95, p. 68–83.

Martínez, F., and Cristallini, E., 2017, The doubly vergent inverted structures in the Mesozoic basins of northern Chile (28°S): A comparative analysis from field data and analogue modeling: Journal of South American Earth Sciences, v. 77, p. 327–340.

Martínez, F., González, R., Bascuñan, S., and Arriagada, C., 2018a, Structural styes of the Salar de Punta Negra Basin in the Pre-Andean Depression (24º-25ºS) of the Central Andes: Journal of South American Earth Sciences, v. 87, p. 188–199.

Martínez, F., López, C., Bascuñan, S., and Arriagada, C., 2018b, Tectonic interaction between Mesozoic to Cenozoic extensional and contractional structures in the Preandean Depression (23°–25°S): Geologic implications for the Central Andes: Tectonophysics, v. 744, p. 333–349.

Martínez, F., Montanari, D., Del Ventisette, C., Bonini, M., and Corti, G., 2018c, Basin inversion and magma migration and emplacement: Insights from basins of northern Chile: Journal of Structural Geology.

Martinez, R.N., Sereno, P.C., Alcober, O.A., Colombi, C.E., Renne, P.R., Montanez, I.P., and Currie, B.S., 2011, A Basal Dinosaur from the Dawn of the Dinosaur Era in Southwestern Pangaea: Science, v. 331, p. 206–210.

Matthews, S., Espinoza, F., Cornejo, P., and Venegas, C., 2010, Carta Altamira, Regiones de Antofagasta y Atacama. Servicio Nacional de Geología y Minería, Carta Geológica de Chile, Serie Geología Básica 121: 66 p., 1 mapa escala 1:100.000.

Matthews, K.J., Maloney, K.T., Zahirovic, S., Williams, S.E., Seton, M., and Miller, R.D., 2016, Global plate boundary evolution and kinematics since the late Paleozoic: Global and Planetary Change, v. 146, p. 226–250.

McClay, K.R., 1989, Analogue models of inversion tectonics: Geological Society, London, Special Publications, v. 44, p. 41–59.

McClay, K., and Buchanan, P., 1992, Thrust faults in inverted extensional basins, *in* Thrust tectonics, Springer, p. 93–104.

Merle, O., 2011, A simple continental rift classification: Tectonophysics, v. 513, p. 88–95.

Mescua, J., and Giambiagi, L., 2012, Fault inversion vs. new thrust generation: A case study in the Malargüe fold-and-thrust belt, Andes of Argentina: Journal of Structural Geology, v. 35, p. 51–63.

Mescua, J., Giambiagi, L., Tassara, A., Gimenez, M., and Ramos, V., 2014, Influence of pre-Andean history over Cenozoic foreland deformation: Structural styles in the Malargue fold-and-thrust belt at 35 S, Andes of Argentina: Geosphere, v. 10, p. 585–609.

Mpodozis, C., Arriagada, C., Basso, M., Roperch, P., Cobbold, P., and Reich, M., 2005, Late Mesozoic to Paleogene stratigraphy of the Salar de Atacama Basin, Antofagasta, Northern Chile: Implications for the tectonic evolution of the Central Andes: Tectonophysics, v. 399, p. 125–154.

Mpodozis, C., and Kay, S., 1992, Late Paleozoic to Triassic evolution of the Gondwana margin: Evidence from Chilean Frontal Cordilleran batholiths (28° S to 31° S): Geological Society of America Bulletin, v. 104, p. 999–1014.

Mpodozis, M., and Ramos, V., 1989, The Andes of Chile and Argentina, in Ericksen, G.E., Cañas, M.T., and Reinemund, J.A. eds., Geology of the Andes and its relation to hydrocarbon and energy resources, Houston, Circum Pacific Council for Energy and Hydrotermal Resources, p. 59–90.

Müller, R.D., Seton, M., Zahirovic, S., Williams, S., Matthews, K.J., Wright, N.M., Shephard, G.E., Maloney, K., Barnett-Moore, N., Bower, D.J., Cannon, J., Hosseinpour, M., Bower, D.J., Cannon, J., 2016, Ocean basin evolution and global-scale reorganization events since Pangea breakup: Annual Review of Earth and Planetary Science Letters, v. 44, p. 107–138.

Muñoz, N., 1989, Estudio geológico estratigráfico de las Hojas Baquedano y Pampa Unión, II Región de Antofagasta, Chile. Memoria de Título (Inédito), Universidad de Chile, Departamento de Geología: 161 p. Santiago.

Muñoz, J., Amilibia, A., Carrera, N., Mon, R., Chong, G., Roca, E., and Sàbat, F., 2005, A geological cross-section of the Andean orogen at 25.5° LS, in VI International Symposium on Andean Geodynamics, Barcelona, España, p. 536–539.

Naipauer, M., Fennell, L., Folguera, A., Pimentel, M., and Ramos, V., 2016, Edades U-Pb SHRIMP de volcanitas del Ciclo Precuyano: Controles temporales en la extensión del depocentro Cara Cura - Reyes (36°30' LS), Norte de la Cuenca Neuquina, in Primer Simposio de Tectónica Sudamericana, Santiago, v. 1, p. 74.

Niemeyer, H.R., 2013, Geología del Área Cerro Lila-Peine, Región de Antofagasta. Servicio Nacional de Geología y Minería, Serie Geológica Básica 147, 1 mapa escala 1: 100.000.

Niemeyer, H., and Urrutia, C., 2009, Transcurrencia a lo largo de la Falla Sierra de Varas (Sistema de fallas de la Cordillera de Domeyko), norte de Chile: Andean Geology, v. 36, p. 37–49.

Niemeyer, H., Zavattieri, A.M., Ballent, S., Zamuner, A., and Gallego, O., 2008, Triassic age of the continental Pular Formation, Sierra de Almeida, Antofagasta, northern Chile: Revista Geológica de Chile, v. 35, p. 147–161.

Oliveros, V., González, J., Espinoza Vargas, M., Vásquez, P., Rossel, P., Creixell, C., Sepúlveda, F., and Bastias, F., 2018, The Early Stages of the Magmatic Arc in the Southern Central Andes, in Folguera, A. et al. eds., The Evolution of the Chilean-Argentinean Andes, Cham, Springer International Publishing, p. 165–190.

Oliveros, V., Labbé, M., Rossel, P., Charrier, R., and Encinas, A., 2012, Late Jurassic paleogeographic evolution of the Andean back-arc basin: New constrains from the Lagunillas Formation, northern Chile (27°30'–28°30'S): Journal of South American

Earth Sciences, v. 37, p. 25–40.

Orellano, A., Rubinstein, N., and Carrasquero, S., 2019, Petrogenesis of the Triassic Cuyo basin magmatism: Controls on the magmatic evolution of passive rifts basins in Western Gondwana: Journal of South American Earth Sciences.

Ottone, *E.G.*, Monti, M., Marsicano, C.A., de la Fuente, M.S., Naipauer, M., Armstrong, R., and Mancuso, A.C., 2014, A new Late Triassic age for the Puesto Viejo Group (San Rafael depocenter, Argentina): SHRIMP U–Pb zircon dating and biostratigraphic correlations across southern Gondwana: Journal of South American Earth Sciences, v. 56, p. 186–199.

Pearce, J.A., Harris, N.B.W., and Tindle, A.G., 1984, Trace element discrimination diagrams for the tectonic interpretation of granitic rocks: Journal of petrology, v. 25, p. 956–983.

Perez, N.D., Horton, B.K., and Carlotto, V., 2016a, Structural inheritance and selective reactivation in the central Andes: Cenozoic deformation guided by pre-Andean structures in southern Peru: Tectonophysics, v. 671, p. 264–280.

Perez, N.D., Horton, B.K., McQuarrie, N., Stübner, K., and Ehlers, T.A., 2016b, Andean shortening, inversion and exhumation associated with thin- and thick-skinned deformation in southern Peru: Geological Magazine, v. 153, p. 1013–1041.

Petrinovic, I.A., and Colombo Piñol, F., 2006, Phreatomagmatic and phreatic eruptions in locally extensive settings of Southern Central Andes: The Tocomar Volcanic Centre (24°10′S–66°34′W), Argentina: Journal of Volcanology and Geothermal Research, v. 158, p. 37–50.

Petrinovic, I.A., Riller, U., Brod, J.A., Alvarado, G., and Arnosio, M., 2006, Bimodal volcanism in a tectonic transfer zone: Evidence for tectonically controlled magmatism in the southern Central Andes, NW Argentina: Journal of Volcanology and Geothermal Research, v. 152, p. 240–252.

Pinto, L., Muñoz, C., Nalpas, T., and Charrier, R., 2010, Role of sedimentation during basin inversion in analogue modelling: Journal of Structural Geology, v. 32, p. 554–565.

Poma, S., Zappettini, E.O., Quenardelle, S., Santos, J.O., Koukharsky, M., Belousova, E., and McNaughton, N., 2014, Geochemistry, U-Pb SHRIMP zircon dating and Hf isotopes of the Gondwanan magmatism in NW Argentina : petrogenesis and geodynamic implications: Andean Geology, v. 41, p. 267–292.

Prinz, P., Wilke, H.-G., and von Hillebrandt, A., 1994, Sediment accumulation and subsidence history in the Mesozoic marginal basin of northern Chile, *in* Reutter, K.J., Scheuber, E., and Wigger, P.J. eds., Tectonics of the Southern Central Andes, Berlin, Springer-Verlag, p. 219–232.

Ramos, V., 1994, Terranes of Southern Gondwanaland and Their Control in the Andean Structure (30°-33° S Latitude), *in* Tectonics of the Southern Central Andes, p. 249–261.

Ramos, V., and Kay, S.M., 1991, Triassic rifting and associated basalts in the Cuyo basin , central Argentina central Argentina: Geological Society of America Special Papers, v. 265, p. 79–92.

Reiners, P., Thomson, S., Vernon, A., Willett, S., Zattin, M., Einhorn, J., Gehrels, G., Quade, J., Pearson, D., Murray, K., Cavazza, W., 2015, Low-temperature thermochronologic trends across the central Andes , 21 ° S – 28 ° S: Memoir of

the Geological Society of America, v. 212, p. 215–249.

Reitsma, M.J., 2012, Reconstructing the Late Paleozoic: early Mesozoic plutonic and sedimentary record of south-east Peru: Orphaned back-arcs along the western margin of Gondwana: University of Geneva, 246 p.

Reutter, K., Scheuber, E., and Chong, G., 1996, The Precordilleran fault system of Chuquicamata, Northern Chile: evidence for reversals along arc-parallel strike-slip faults: Tectonophysics, v. 259, p. 213–228.

del Rey, A., Deckart, K., Arriagada, C., and Martínez, F., 2016, Resolving the paradigm of the late Paleozoic–Triassic Chilean magmatism: Isotopic approach: Gondwana Research, v. 37, p. 172–181.

Reyes, R., 2017, Nuevas localidades fosilíferas del triásico de la Cordillera de Domeyko, Región de Antofagasta: Estratigrafía, ambientes de sedimentación y paleobotánica: Universidad de Concepcion, 144 p.

Riesner, M., Lacassin, R., Simoes, M., Armijo, R., Rauld, R., and Vargas, G., 2017, Kinematics of the active West Andean fold-and-thrust belt (central Chile): Structure and long-term shortening rate: Tectonics, v. 36, p. 287–303.

Riesner, M., Lacassin, R., Simoes, M., Carrizo, D., and Armijo, R., 2018, Revisiting the Crustal Structure and Kinematics of the Central Andes at 33.5°S: Implications for the Mechanics of Andean Mountain Building: Tectonics, v. 37, p. 1347–1375.

Riquelme, R., Martinod, J., Hérail, G., Darrozes, J., and Charrier, R., 2003, A geomorphological approach to determining the Neogene to Recent tectonic deformation in the Coastal Cordillera of northern Chile (Atacama): Tectonophysics, v. 361, p. 255–275.

Rocher, S., Abarzúa, F., Tapia Baldis, C., López, M.G., 2016, Volcanism of the Triassic Cuyo Basin in the Calingasta-Barreal Valley, Western Argentina. In: Acta geológica lilloana 28: III Jornadas de Geología de Precordillera.

Rodríguez, M.P., Charrier, R., Brichau, S., Carretier, S., Farías, M., de Parseval, P., and Ketcham, R.A., 2018, Latitudinal and Longitudinal Patterns of Exhumation in the Andes of North-Central Chile: Tectonics, v. 37, p. 2863–2886.

Rogers, R.R., Swisher III, C.C., Sereno, P.C., Forster, C.A., and Monetta, A.M., 1993, The Ischigualasto tetrapod assemblage (Late Triassic) and 40Ar/39Ar calibration of dinosaur origins. Science, v. 260, p. 794–797.

Rossel, P., Oliveros, V., Ducea, M.N., Charrier, R., Scaillet, S., Retamal, L., and Figueroa, O., 2013, The Early Andean subduction system as an analog to island arcs: Evidence from across-arc geochemical variations in northern Chile: Lithos, v. 179, p. 211–230.

Salazar, E., and Coloma, F., 2016, Geología del área Cantaritos-Laguna Chica, Región de Atacama. Servicio Nacional de Geología y Minería, Carta Geológica de Chile, Serie Geología Básica. 1 mapa escala 1:100.000. Santiago.

Salazar, E., Coloma, F., and Creixell, C., 2013, Geología del Área El Tránsito-Lagunillas, Servicio Nacional de Geología y Minería-Gobierno Regional de Atacama. 1 Mapa escala 1:100.000. Santiago.

Salazar, E., Vásquez, P., Vallejos, D., Creixell, C., Oliveros, V., and Mihai, D., *in press*, Stratigraphic and provenance analysis of Triassic rock units between 28-29°S, northern Chile: implications on the tectonic and paleogeographic evolution of the southwestern margin of Gondwana: Andean Geology.

Sanchez, C., Brichau, S., Riquelme, R., Carretier, S., Bissig, T., Lopez, C., Mpodozis, C., Campos, E., Regard, V., Hérail, G., Marquardt, C., 2018, Exhumation history and timing of supergene copper mineralisation in an arid climate: New thermochronological data from the Centinela District, Atacama, Chile: Terra Nova, v. 30, p. 78–85.

Sato, A.M., Llambías, E.J., Basei, M.A.S.S., and Castro, C.E., 2015, Three stages in the Late Paleozoic to Triassic magmatism of southwestern Gondwana, and the relationships with the volcanogenic events in coeval basins: Journal of South American Earth Sciences, v. 63, p. 48–69.

Sayit, K., Bedi, Y., Tekin, U.K., Göncüoglu, M.C., and Okuyucu, C., 2017, Middle Triassic Back-arc Basalts from the Blocks in the Mersin Mélange, southern Turkey: Implications for the Geodynamic Evolution of the Northern Neotethys: Lithos, v. 268–271, p. 102–113.

Schiuma, M., and Llambías, E.J., 2008, New ages and chemical analysis on lower jurassic volcanism close to the dorsal de Huincul, Neuquén: Revista de la Asociacion Geologica Argentina, v. 63, p. 644–652.

Sengör, A.M.C., 1995, Sedimentation and Tectonics of Fossil Rifts: in Busby, C.J., and Ingersoll, R.V., eds., Tectonics ofsedimentary basins. Oxford, Blackwell Science, p. 53–117.

Sengör, A.M.C., and Natal'in, B.A., 2001, Rifts of the world, *in* Special Paper 352: Mantle plumes: their identification through time, v. 352, p. 389–482.

Shipman, T.C., 2004, Links between sediment accumulation rates and the development of alluvial architecture: Triassic Ischigualasto Formation, northwestern Argentina: University of Arizona, 188 p.

Solari, M., Venegas, C., Montecino, D., Astudillo, N., Cortés, J., Bahamondes, B., and Espinoza, F., 2017, Geología del área Imilac-Quebrada Guanaqueros. Escala 1:100.000. Servicio Nacional de Geología y Minería, Carta Geológica de Chile, Serie Geología Básica (n. 191): 81 pp. 1 mapa escala 1:100.000. Santiago.

Sommer, C.A., Barreto, C.J.S., Lafon, J.M., Lima, E.F. de, Alexandre, F.M., Chemale Jr., F., and Koester, E., 2018, Pb isotope geochemistry and reappraisal of Sr-Nd isotopes of the Cerro Morado basic magmatism (Ischigualasto-Villa Union Triassic basin, NW Argentina): Implications for the mantle sources: Brazilian Journal of Geology, v. 48, p. 115–126.

Spalletti, L.A., 1999, Cuencas triásicas del Oeste argentino : origen y evolución: Acta geológica hispanica, v. 32, p. 29–50.

Spalletti, L. a., Fanning, C.M., Rapela, C.W.C., Fanning, M., and Rapela, C.W.C., 2008, Dating the Triassic continental rift in the southern Andes: The Potrerillos Formation, Cuyo Basin, Argentina: Geologica Acta, v. 3, p. 267–283.

Spalletti, L., Franzese, J., Morel, E., D'Elia, L., Zúñiga, A., and Fanning, C.M., 2010, Consideraciones acerca de la sedimentología, paleobotánica y geocronología de la Formación Piedra del Águila (Jurásico Inferior, Neuquén): Revista de la Asociacion Geologica Argentina, v. 66, p. 305–313.

Spikings, R., Reitsma, M.J., Boekhout, F., Mišković, A., Ulianov, A., Chiaradia, M., Gerdes, A., and Schaltegger, U., 2016, Characterization of Triassic Rifting in Peru and implications for the early disassembly of western Pangaea: Gondwana Research.

Steinman, G., 1929, Geologie von Peru: Heidelberg, Karl Winters Universitats-Buchhandlung, 448 p.

Stern, R.J., Lin, P.N., Morris, J.D., Jackson, M.C., Fryer, P., Bloomer, S.H., and Ito, E., 1990, Enriched back-arc basin basalts from the northern Mariana Trough: implications for the magmatic evolution of back-arc basins: Earth and Planetary Science Letters, v. 100, p. 210–225.

Suárez, M., and Bell, C.M., 1992, Triassic rift-related sedimentary basins in northern Chile (24°-29°S): Journal of South American Earth Sciences, v. 6, p. 109–121.

Thiele, R., 1980, Hoja Santiago, Región Metropolitana, Carta Geol. Chile 39, 51 pp., Inst. de Invest. Geol., Santiago, Chile.

Tomlinson, A., and Blanco, N., 2008, Geología de la franja El Abra-Chuquicamata, II Región (21°45'-22°30'S). Servicio Nacional de Geología y Minería, Informe Registrado IR-08-35: 196 p. Santiago.

Tomlinson, A., and Blanco, N., 1997, Structural evolution and displacement history of the West fault System, Precordillera, Chile: Part 1, synmineral history, *in* Proccedings 8th Congreso Geológico Chileno, Antofagasta, p. 1873–1877.

Tomlinson, A., Blanco, N., Maksaev, V., Dilles, J.H., Grunder, A.L., and Ladino, M., 2001, Geología de la Precordillera Andina de Quebrada Blanca-Chuquicamata, Regiones I y II (20°30'-22°30'S). Servicio Nacional de Geología y Minería, Informe Registrado IR-01-20: 444 p. Santiago.

Tomlinson, A., Cornejo, P., and Mpodozis, C., 1999, Hoja Potrerillos, Región de Atacama. Servicio Nacional de Geología y Minería (Chile), Mapas Geológicos, No. 14, 1 mapa escala 1:100.000, Santiago.

Tomlinson, A., Mpodozis, C., Cornejo, P., and Ramirez, C., 1993, Structural Geology of the Sierra Castillo - Agua Amarga Fault System, Precordillera of Chile, El Salvador-Potrerillos, *in* Second ISAG, Oxford, United Kingdom, p. 259–262.

Tomlinson, A., Mpodozis, C., Cornejo, P., Ramírez, C.F., and Dumitru, T., 1994, El Sistema de fallas Sierra Castillo-Agua Amarga: transpresión sinistral eocena en la Precordillera de Potrerillos-El Salvador, *in* VII Congreso Geológico Chileno, Concepción, Chile, p. 1459–1463.

Uliana, M.A., Biddle, K.T., Cerdan, J., Tankard, A.J., and Balkwill, H.R., 1989, Mesozoic extension and the formation of Argentine sedimentary basins, *in* Extensional tectonics and stratigraphy of the North Atlantic margins, American Association of Petroleum Geologists Tulsa Oklahoma, v. 46, p. 599–614.

Uliana, M.A., and Legarreta, L., 1993, Hydrocarbons Habitat in a Triassic-To-Cretaceous Sub-Andean Setting: Neuquén Basin, Argentina: Journal of Petroleum Geology, v. 16, p. 397–420.

De Urreiztieta, M., Gapais, D., Corre, C. Le, Cobbold, P.R., and Rossello, E., 1996, Cenozoic dextral transpression and basin development at the southern edge of the Puna Plateau, northwestern Argentina: Tectonophysics, v. 254, p. 17–39.

Vargas, G., Klinger, Y., Rockwell, T. K., Forman, S. L., Rebolledo, S., Baize, S., Lacassin, R., Armijo, R., 2014, Probing large intraplate earthquakes at the west flank of the Andes: Geology, p. 1–4.

Venegas, C., Cervetto, M., Astudillo, N., Espinoza, F., Cornejo, P., Mpodozis, C., and Rivera, O., 2013, Carta Sierra Vaquillas Altas, Regiones de Antofagasta y Atacama. Servicio Nacional de Geología y Minería, Carta Geológica de Chile,

Serie Geología Básica 159, 1-87. 1 mapa escala 1:100.000. Santiago.

Vicente, J.C., 2005, Dynamic paleogeography of the Jurassic Andean Basin: pattern of transgression and localisation of main straits through the magmatic arc: Revista de la Asociación Geológica Argentina, v. 60, p. 221–250.

Victor, P., Oncken, O., and Glodny, J., 2004, Uplift of the western Altiplano plateau: Evidence from the Precordillera between 20° and 21°S (northern Chile): Tectonics, v. 23.

Vilas, J.F., and Valencio, D., 1978, Paleomagnetism of South American and African rocks and the age of the South Atlantic: Revista Brasileira de Geociencias, v. 8, p. 3–10.

Winchester, J., and Floyd, P., 1977, Geochemical discrimination of different magma series and their differentiation products using immobile elements: Chemical geology, v. 20, p. 325–343.

Wood, D.A., 1980, The application of a Th sbnd Hf sbnd Ta diagram to problems of tectonomagmatic classification and to establishing the nature of crustal contamination of basaltic lavas of the British Tertiary Volcanic Province: Earth and Planetary Science Letters, v. 50, p. 11–30.

Zentilli, M., Maksaev, V., Boric, R., and Wilson, J., 2018, Spatial coincidence and similar geochemistry of Late Triassic and Eocene–Oligocene magmatism in the Andes of northern Chile: evidence from the MMH porphyry type Cu–Mo deposit, Chuquicamata District: International Journal of Earth Sciences, v. 107, p. 1097–1126.

Capítulo 8: Anexos

Anexo 1: Publicaciones y resúmenes resultantes de esta investigación

Publicaciones

Oliveros, V., González, J., Espinoza, M., Vásquez, P., Rossel, P., Creixell, C., ... and Bastias, F. (2018). The Early Stages of the Magmatic Arc in the Southern Central Andes. In The Evolution of the Chilean-Argentinean Andes (pp. 165-190). Springer, Cham.

Espinoza, M., Montecino D., Oliveros V, et al. The synrift phase of the early Domeyko Basin (Triassic, northern Chile): Sedimentary, volcanic, and tectonic interplay in the evolution of an ancient subduction-related rift basin. Basin Res. 2019; 31:4–32. https://doi.org/10.1111/bre.12305

Espinoza, M., Oliveros, V., Vásquez, P., Giambiagi, L., Morgan, L., González, R., Solari, L. and Bechis, F. Gondwanic inheritance on the building of the western Central Andes (Domeyko Range, Chile): Structural and Thermochronological Approach (U-Pb and 40Ar-39Ar). Manuscrito sometido a revista Tectonics el 19 de Marzo de 2019.

Oliveros, V., Vásquez, P., Creixell, C., Lucassen, F., Ducea, M., Ciocca, I., González, J., Espinoza, M., Salazar, E., Coloma, F. Lithospheric evolution of the Early Andean convergent margin, Chile. Manuscrito sometido a revista Gondwana Research el 29 de Marzo de 2019.

González, R., Espinoza D., Rogers, H., Espinoza, M., Torres, P., Robledo Carbajal, F. Jaldín, D. Polyphasic deformation related to the origin and evolution of a rift-basin and its inversion in a long-live subduction convergent margin: the case of the Late Cretaceous tectonic inversion of the Late Triassic Domeyko Basin in the Sierra de Varas, Andean Precordillera of northern Chile. Manuscrito sometido a revista Journal of Structural Geology el 5 de Abril de 2019.

Resúmenes presentados en conferencias

Mauricio Espinoza, Verónica Oliveros, Paulina Vásquez, Laura Giambiagi, Florencia Bechis, Leah Morgan (2018). Revealing the Early Mesozoic tectonic inheritance of the western Central Andes (Domeyko Range, northern Chile): A structural, geochronological and 40Ar-39Ar thermochronological approach. XV Congreso Geológico Chileno, Concepción, Chile.

Mauricio Espinoza, Verónica Oliveros, Diego Montecino, Rodrigo González, Paulina Vásquez (2018). The interplay between volcanic, tectonic and sedimentary processes in an ancient subduction-related rift basin: The early Domeyko Basin (Triassic, northern Chile). XV Congreso Geológico Chileno, Concepción, Chile.

Mauricio Espinoza, Verónica Oliveros, Leah Morgan, Michael Cosca, Luigi Solari (2017). The synrift evolution of the early Domeyko Basin (Domeyko Range, northern Chile): Coupling detrital 40Ar-39Ar white mica and U-Pb zircon analysis into a tectonostratigraphic framework. AGU Fall Meeting, New Orleans, EE.UU.

Mauricio Espinoza, Verónica Oliveros, Paulina Vásquez, Christopher Celis, Robinson Reyes. (2017) Evolución geológica y tectónica de las cuencas triásicas en el norte de chile (C. Costa y C. Domeyko, 24°- 26°S): Evidencias de un rift asociado a subducción (2017). I Simposio de Tectónica Sudamericana, Santiago, Chile.

Mauricio Espinoza, Verónica Oliveros, Diego Montecino, Paulina Vásquez. Synrift stage of the Domeyko Basin (Triassic): Architecture, provenance and tectonics of a subduction-related basin (Domeyko Range, 23°30'-26°30'S) (2017). XX Congreso Geológico Argentino, Tucumán, Argentina.

Verónica Oliveros, Paulina Vásquez, Christian Creixell, Javiera González, Mauricio Espinoza, Friedrich Lucassen, Mihai Ducea, Evolución litosférica en el margen suroccidental de Gondwana entre el Pérmico y el Jurásico: Evidencias geológicas y geoquímicas a partir de unidades ígneas en el norte de Chile (25° - 30°S) (2017). I Simposio de Tectónica Sudamericana, Santiago, Chile.

Christopher Celis, Verónica Oliveros, Mauricio Espinoza, Paulina Vásquez, Cristian Creixell, Antecedentes petrográficos y geoquímicos de las rocas volcánicas del Triásico Superior de la Cordillera de la Costa y la Precordillera entre las coordenadas 24°30´S-26°S, Chile (2017). I Simposio de Tectónica Sudamericana, Santiago, Chile.

Verónica Oliveros, Paulina Vásquez, Christian Creixell, Javiera González, Mauricio Espinoza, Friedrich Lucassen, Mihai Ducea, Lithospheric loss in the Andean convergent margin during the Triassic: Evidence from Nd-Sr-Pb isotopes of igneous rocks of northern chile (24°30'– 30°00'S) (2017). X South American Symposium on Isotope Geology, Puerto Vallarta, México.

Robinson Reyes, Philippe Moisan, Mauricio Espinoza, Verónica Oliveros (2017). La sucesión basal con flora Triásica de la Formación Quebrada del Salitre, Cordillera de Domeyko, Región de Antofagasta, Chile, V Simposio de Paleontología en Chile, Concepción, Chile.

Mauricio Espinoza, Verónica Oliveros, Christopher Celis, Paulina Vásquez, Florencia Bechis, Geochronology, Geochemistry and Tectonics of Subduction Related Late Triassic Rift Basins in Northern Chile (24º26 ºS) (2016). 2016 AGU Fall Meeting, San Francisco, EE.UU.

Mauricio Espinoza, Verónica Oliveros, Paulina Vásquez, Florencia Bechis (2015). A tectonostratigraphic study of late Triassic-Early Jurassic basins in northern Chile (24.5º-26ºs): Kinematic preliminary results. Reunión de Tectónica, General Roca, Argentina.

Mauricio Espinoza, Verónica Oliveros, Paulina Vásquez, Florencia Bechis (2015). U-Pb geochronology and kinematic preliminary analyses of Late Triassic-Early Jurassic basins in northern Chile (24.5º-26ºS). XIV Congreso Geológico Chileno, La Serena, Chile.

Verónica Oliveros, Christopher Celis, Paulina Vásquez, Mauricio Espinoza, Christian Creixell, Diego Montecinos, Amancay Martinez, Friedrich Lucassen, Rodrigo González (2015). Caracterización Petrográfica y Geoquímica de las unidades del Triásico superior entre los 24°30' y los 26°00', norte de Chile. XIV Congreso Geológico Chileno, La Serena, Chile.

Verónica Oliveros, Christian Creixell, Mihai Ducea, Mauricio Espinoza, Javiera González, Friedrich Lucassen, Paulina Vásquez, Lithospheric loss in the Andean convergent margin during the Triassic: geochemical evidence from igneous rocks of northern Chile (24°30' - 30°00'S). XIV Congreso Geológico Chileno, La Serena, Chile.

Anexo 2: Facies descriptions

1. Sedimentary facies

1.1 _Gmm_ and _Gmg_ facies (_matrix-supported, massive conglomerate_):

Description: _Gmm_ facies is formed by pale grey to reddish, massive, matrix-supported breccias wich show crude horizontal stratification of decimeter- to meter-scale thick (<5m). The sorting is very poor, with clast size ranging from pebbles to boulders showing a mean size of 30-40 cm and outsize clasts up to 3 m. Clasts of _Gmm_ are subrounded to angular with very homogeneous compositions, corresponding mainly to phaneritic and porphyritic acidic subvolcanic rocks from La Tabla Formation (Carboniferous-Permian) in Sierra de Varas, Aguada de Varas and Quebrada Ceballos.

On the other hand, at Quebrada Punta del Viento, _Gmm_ facies show a tabular stratification (0.1-2.0 m thick) and describe local cycles of coarsening upward grain size and inverse grading (_Gmg_ facies), with outsized clasts up to 1.12 m which are immersed in a fine-grained calcareous matrix. At this location the clasts correspond mainly to acidic volcanic rocks, with a minor proportion of lapilli-tuff rocks and mudstone intraclasts, while the upper levels also incorporate bioclastic fragments from marine fossils (mainly brachiopods and bivalves).

Equivalent facies to _Gmm_ have been described in Sierra Exploradora by Cornejo and Mpodozis (1996) and Cornejo _et al_. (2009). The later facies crops out at Quebrada La Perra and north of Quebrada La Encantada between the Sierra de Varas and the Barrancas faults, incorporating gravel to boulder clasts (> 1 m sized) of Permian foliated tonalities (Cornejo _et al_., 2009). On the other hand, similar facies ("rhyolitic breccias") were identified by Tomlinson _et al_. (1999) associated to acidic domes at Quebrada Doña Inés Chi_ca._

Interpretation: The _Gmm_ and _Gmg_ facies were originated by plastic, high-strength debris flows (Miall, 1977, 2006) developed in sub-aerial to sub-aqueous conditions (Miall, 2006). This facies commonly occurs either in the proximal portion of alluvial fans (Nemec and Steel, 1984; Nichols, 2009) or in fan-delta environments (Horton and Schmitt, 1996; Nemec and Steel, 1988).

1.2 _Gcm_ facies (_clast-supported massive conglomerate_):

Description: _Gcm_ facies correspond to massive, well-stratified, tabular and lenticular bodies of oligomictic and clast-supported conglomerates showing sharp basal contacts. Gravel sheets are decimeter to meter scale thickness, generally showing moderate to poor sorting with rounded clasts of a mean size of 0.5-15 cm and outsize clasts of 40 cm large. At Sierra de Varas range, this facies occasionally fining upward into decimeter- to meter- scale thick, medium to pebbly grain sized, massive (_Sm_) and trough cross-bedded sandstones (_St)._ Clasts are composed by acid porphyritic subvolcanic rocks and a minor proportion of greyish quartzites. At Quebrada La Carreta, a drastic lateral change of clast composition is recorded by the predominance of andesites and banded rhyolites in _Gcm_ facies. To the south of the study area (Quebrada La Perra), this facies present imbricated clasts, normal grading with a size ranging from 0.2-13 cm long, corresponding mainly to reddish porphyritic volcanic rocks and greyish quartzites with minor proportion of milky grains of metamorphic quartz and plutonic rocks.

Interpretation: _Gcm_ facies were originated by low-strength, pseudoplastic debris flows (Miall, 2006), related to a high sediment and water discharge floods with rapid transport and deposition (Horton and Schmitt, 1996).

1.3 _Sh_ facies (_horizontal-laminated sandstone_):

Description: _Sh_ facies corresponds to decimeter-scale thick, tabular sheets of grain-supported, fine- to coarse-grained and horizontal laminated tuffaceous sandstones, showing moderately sorting and exhibiting and locally, normal grading. Lithology corresponds mainly to immature litharenites, with angular to subrounded fragments of volcanic and pyroclastic lithics, quartz and feldspar.

Interpretation: _Sh_ facies were deposited under upper flow regime conditions at the transition from subcritical to supercritical flows (Miall, 1978, 2006), developed in sporadic flashfloods (Horton and Schmitt, 1996).

1.4 _Sm_ facies (_massive sandstone_):

Description: This facies includes ungraded, massive, moderately to good sorted, medium- to very coarse-grained litharenites with granular outsized clasts. _Sm_ facies are matrix- to grain- supported and

forms thin (< 1 m thick) and wide (<15 m) tabular beds with sharp contacts, locally forming deci- metric scale lenticular and convex-upward channel bodies. At Quebrada Punta del Viento this facies locally record slump structures.

Interpretation: *Sm* facies can be formed by the deposition of sediment gravity flows (Miall, 1978, 2006) or by subaerial hyperconcentrated flows from turbulent suspension with insufficient time for bedform development (Smith, 1986). On the other hand, massive sandstones can also be formed by the obliteration of primary structures related to an intense bioturbation (Miall, 2006).

1.5 *St and Sp* facies (*through and planar cross-bedded sandstone*):

Description: *St* facies corresponds to deci- to meter-scale thickness, moderately to well- sorted, medium- to pebbly-sized litharenites, which display trough cross stratification (*St* facies). Beds are tabular to gently lens-shaped thin sandy sheets, showing gradational to sharp basal contacts. Clast composition corresponds mainly to volcanic and pyroclastic rocks with quartz and feldspar crystaloclasts. On the other hand, *Sp* facies has a minor occurrence across the study area, corresponding to pink-colored, medium- to coarse-grained and decimeter-scale thick sandstones, which develop planar cross stratification. Clast composition records a significant proportion of dark-green and pink aphanite fragments of volcanic origin.

Interpretation: *St* (*Sp)* facies represents the migration of sinuously crested (transverse) and linguoid 3-D (2-D) dunes under lower-flow-regime conditions (Miall, 1978, 2006).

1.6 *Ss* facies (*scoured sandstone*):

Description: *Ss* facies presents minor occurrence being recognized only at Quebrada Punta del Viento where it is interbedded with *Gmm* and *Gmg* facies. Herein, decimeter-scale thickness of medium- to pebbly-sized calcareous sandstones show gently to abrupt scoured bases. This facies displays a poor sorting with a calcareous cement with a composition dominated by acidic volcanic clasts though mudstones intraclasts are common.

Interpretation: This facies is originated by the rapid deposition of coarse bed load, which could be related to basal fills of channels or scour fills (Miall, 1996, 2006).

1.7 *Fl* facies (*laminated fine*):

Description: This facies correspond to grey and greyish-green, milli- to centi-meter scale laminated siltstones and mudstones ('laminites'), which form tabular beds of centi- to meter-scale thickness (up to 25 m). Occasionally, they present centimeter-scale '*cast and flame*' load structures and ripple bedding. Intercalation of air-fall pyroclastic facies (*mT*) are common in this facies. *Fl* facies crop out in the northern portion of Sierra de Varas and Sierra de Vaquillas Altas ranges (Quebrada Los Pozos, Quebrada La Mina and Quebrada Vaquillas Altas).

Interpretation: The fine *Fl* facies represents deposition by suspension and weak traction currents typically occurring in overbank, stagnant water bodies or warning flood deposits (Miall, 1978, 1996).

1.8 *Fm* facies (*massive fine*):

This facies corresponds to thick fine deposits formed by grey to dark, massive, very fine sandstones to mudstones forming 0.1-3 m thick beds. *Fm* facies form tabular beds of milli- to meter-scale thickness, occasionally displaying fossil flora and siderite nodules. At Quebrada Los Pozos (Sierra Vaquillas Altas range), fossil flora was assigned by Reyes (2017) to the following genus/species: *Neocalamites* sp.*, Pterophyllum* sp., *Pterophyllum valdivianum*, *Pterophyllum* cf. *azcaratei*, *Dicroidium odontopteroides*, *Dicroidium* cf. *crassum, Heidiphyllum elongatum, Cladophlebis* cf. *Mendozaensis* and *Dicroidium* cf. *crissum*. These fossil flora indicate a Late Triassic age for the rocks that incorporate them. Furthermore, because of the abundance of genus, which are common during the Jurassic (*e.g. Pterophyllum sp.)*, they probably correspond to the latest Late Triassic (for detailed descriptions, see Supplementary Material SM4).

Interpretation: Fine massive facies (*Fm*) represents the deposition from ponds of water during low-stage abandonment of channels and correspond to floodplain facies (Miall, 2006). The occasional fossil flora (*Fl* and *Fm*) points to an overbank deposition (Miall, 2006), indicating that most of the sedimentation was by suspension fallout occurring in a floodplain with abundant vegetation. Siderite nodules point to a

deposition in waterlogged and freshwater to brackish reducing conditions, where there is mixing of seawater and freshwater (Nichols, 2009).

1.10 *M* (*mudstone facies*):
M facies is formed by dark- to brown-colored calcareous *mudstones* which form deci- meter scale beds. *M* facies present a moderately developed lamination and present scarce *Otapiria* sp. bivalve fossils (Montecino, 2015).
Interpretation: M facies was deposited by suspension fallout in protected areas under the fair-weather wave base (Lehrmann *et al*., 1998).

1.11 *Fo* facies (*oncolytic floatstone*):
Description: *Fo* facies corresponds to dark to yellow, matrix-supported limestones bearing oncolites (floatstones), which form decimeter-scale tabular bodies. Centimeter-scale oncolites display spheroidal to oval rims bounded by a muddy to sandy calcareous matrix. This facies present a minor occurrence being identified at the northern portion of the Sierra de Varas and Cerro Rincones.
Interpretation: This facies is interpreted to have been formed in shallow swamps with significant lighting (Nichols, 2009; Platt and Wright, 1991). Actual oncolites are present at lacustrine environments with low sedimentation rates near to the coast in gently wave- agitated zones (Matter and Tucker, 1978).

1.12 *R* facies (*rudstone*):
Description: This facies is formed by greyish, clast-supported, pebbly-grained calcareous rocks (*rudstones*) formed by fragments of bivalves, brachiopods, gastropods, shell debris and corals. Lenticular beds are deci- to meter-scale thickness and display irregular basal contacts.
Interpretation: Rudstones breccias are originated typically at moderate to high-energy conditions developed at the front of fringing reefs (Nichols, 2009).

1.13 *B* facies (*coral-rich boundstone*):
Description: *B* facies corresponds to greyish, irregular and lenticular massive beds, meter-scale thickness composed by coral-rich *boundstones* limestones bearing *Retiophyllia* sp., *Astraeomorpha?* sp. (Astudillo *et al*., in press; González *et al*., 2015; Montecino, 2015) and *Thecosmilia* sp. fossils, with associated solitary corals, bivalves (*e.g. Septocardia?* sp.) and brachiopods (J. Ardill *et al*., 1998; John Ardill, 1996; Chong, 1973).
Interpretation: *B* facies usually preserves coral fossils in life position and is interpreted as have been originated in the core of a reefal framework originated in shallow waters on carbonate platforms with high-energy conditions (Braga *et al*., 1990; Nichols, 2009).

1.14 *Bs* facies (*stromatolitic boundstone*):
Description: This facies corresponds to dark-greyish, stromatolitic and microbial *boundstone* limestones (*algal mats*), which form decimeter-scale tabular bodies and locally, exhibits parallel and convolute lamination. *Bs* facies present minor occurrence being identified in the northern portion of the Sierra de Varas.
Interpretation: Stromatolitic boundstone facies (*B*) were originated in shallow water (<10m) under good illumination conditions allowing the development of cyanobacteria colonies (Nichols, 2009). Stromatolites are developed in hypersaline subaquatic conditions, typically corresponding to a palustrine environment in lake shorelines (Alonso-Zarza and Tanner, 2009; Alonso-Zarza and Wright, 2010).

1.15 *P and W* facies (*packstone and wackestone*):
Description: *P* facies corresponds to centi- to deci-meter scale thickness beds of pale gray, clast-supported, mud-poor limestones (*packstones*) with scarce micritic matrix. Clast composition corresponds to rounded calcareous intraclasts, bioclasts (bivalves, gastropods and corals) and terrigenous fragments corresponding to volcanic lithics and quartz crystaloclasts. Locally this facies presents asymmetric ripples. *W* facies corresponds to greyish *wackstones* which form beds of deci-meter scale thickness. This facies is formed by bioclastic fragments (*e.g.* bivalves, gastropods and ostreids) and minor terrigenous clasts of volcanic lithics and crystaloclasts (coarse to pebbly-sized) immersed in a fine calcareous matrix.

Interpretation: Disarticulated marine bioclastic fragments forming *P* and *W* facies indicate a deposition in a medium- to high-energy shallow marine, shallow subtidal and wave winnowed environment (Lehrmann *et al*., 1998), probably recording sporadic storm reworking. The lack of micritic matrix would indicate the action of energetic currents able to remove the fine mud.

2. Volcanic facies:

2.1 *cB* facies (*coherent basalts and basaltic andesites*):
Description: This facies corresponds to meter to decameter- scale thick irregular beds corresponding to dark-green, coherent basalts and basaltic andesites, which commonly display a high proportion of vesicles and amygdales. Its texture is porphyritic, formed by fine to medium-grained phenocrysts (ranging from 18% to 26%) of plagioclase + clinopyroxene ± olivine, forming intersertal and intergranular groundmass textures. Calcite-filled amygdales and vesicles are usually elongated subparallel to the bedding plane. This facies is common in the southern portion of the study area (Quebrada Vaquillas Altas, Quebrada Doña Inés Chica and Quebrada del Salitre creeks).
Interpretation: Coherent basaltic facies (*cB*) represent the cooling and solidification of molten lava related to a subaerial mafic effusive volcanism (McPhie *et al*., 1993). Coherent facies record gentle shear rates and moderately to fast cooling rates (A. L. Stewart and McPhie, 2003).

2.2 *brB* facies (*brecciated basalts and basaltic andesites*):
Description: This facies present a minor occurrence and is formed by dark to greenish, brecciated basalts and basaltic andesites. Basalts and basaltic andesites present a similar composition than the *cB* facies, though commonly present a higher proportion of vesicles and amygdales. Fragmentation can be depicted by a mixing between lava fragments and silicified red-colored sediments (peperites) or by the development of ellipsoidal decimetric-scale fragments bounded by a vitreous matrix (pillow-breccias).
Interpretation: Peperitic texture indicates interaction (fragmentation and mingling) of lava with unconsolidated, soft and wet sediments with in situ deposition (Busby-Spera and White, 1987; Doyle, 2000). On the other hand, pillow-breccia texture (*hyaloclastite*) records chilling and fragmentation of flowing lava or magma in contact with water (Cas and Wright, 1988; White and Houghton, 2006). Thus, both facies indicate a primary volcanoclastic deposition under a subaqueous environment.

2.3 *cA* and *cD* facies (*coherent andesites and dacites*):
Description: Andesitic to dacitic coherent facies (*cA* and *cD*), form massive and poorly vesiculated beds ranging 0.4-2 m thick, usually displaying flow aligned crystals. These facies present porphyritic or glomeroporphiritic textures, formed by medium-grained phenocrysts of plagioclase + amphibole (andesites) ± quartz (dacites), embedded in a glassy or microcrystalline groundmass.
Interpretation: Coherent *cA* and *cD* facies record gentle shear rates and moderately to fast cooling rates (A. L. Stewart and McPhie, 2003), and correspond to intermediate-composition lava flows originated under subaerial conditions. Coherent facies record gentle shear rates and moderately to fast cooling rates (A. L. Stewart and McPhie, 2003).

2.4 *brA* and *brD* facies (*brecciated andesites and dacites*):
Description: These facies correspond to fragmented, matrix-supported, intermediate volcanic rocks (andesites and dacites), which are formed by greenish porphyritic clasts (<10 cm) embedded in a groundmass composed by monomictic clasts and fine- to medium- size phenocrysts (< 1mm) of plagioclase, amphibole and minor quartz. These facies form well-defined tabular beds of 2-3 m thick showing irregular basal contacts.
Interpretation: Features of brecciated facies, such as: (1) rotated clasts, (2) well-defined bedding, (3) monomictic composition, (4) porphyritic texture and (5) the absence of hyaloclastic textures, indicate an autoclastic, brittle fragmentation mechanism, due to the lateral transport of lava flows (McPhie *et al*., 1993; A. L. Stewart and McPhie, 2006). These facies record subaerial fragmentation of intermediate composition lava flows.

2.5 *bcR* and *cjD* facies (*banded coherent rhyolites and columnar-jointed dacites*):

Description: These facies correspond to vitrophyric rhyolites, which present milli- to centi-meter scale flow banding (*bcR*), and coherent vitrophyric dacites (*cjD*), which display vertical columnar jointing. At Sierra de Doña Inés Chica range, *bcR* facies forms prominent sub-circular acidic bodies (~5 km of diameter). At the same locality, *cjD* facies forms elongated dacitic bodies (1.6 to 2.2 km long), cropping out along the Sierra Doña Inés Chica Fault.

Interpretation: We interpret these coherent facies (*cR* and *cD*) as the record of acidic small domes and vents resulting from an endogenic growth, where columnar jointing indicates up flow direction within dome necks (Fink and Anderson, 2000). The close spatial relationship of the domes with extensional faults suggest that shallow level intrusions occupied these faults to supply magma into the basin (Busby and Bassett, 2007).

3. Pyroclastic facies

3.1 *mBr* facies (*massive lithic breccias*):

Description: Facies *mBr* corresponds to greyish to purple massive breccias, which define meter-scale, poorly stratified beds (0.3-1.7 m). Its fabric is matrix-supported and poorly sorted, displaying a seriate grain size ranging from ash (<2mm) to blocks (up to 30 cm). Fragments are composed by subangular to angular, locally prismatic jointed, monomictic dacitic fragments with porphyritic texture and irregular and fractured, medium-sized crystaloclasts of plagioclase.

Interpretation: Massive lithic breccias (*mBr*) are interpreted as block- and ash-flow tuffs deposits based on: (1) dacitic monomictic composition, (2) poorly sorted and matrix-supported fabric, (3) seriate grain size from ash to block, (4) evidence of prismatic jointed blocks (M. L. Stewart *et al*., 2003). This facies corresponds to proximal, small volume deposits (< 1 km^3) of pyroclastic flows generated by the subaerial gravitational collapse of a lava dome (Branney and Kokelaar, 2002; Cas and Wright, 1988; Freundt *et al*., 2000).

3.2 *mLT* and *emLT* facies (*massive lapilli-tuffs and eutaxitic massive lapilli-tuffs*):

Description: This facies corresponds to purple to greenish, massive lapilli-tuffs (*mLT* facies), which form centi- to metric- scale (up to 5.2 m) tabular beds commonly displaying sharp basal contacts. Its fabric is matrix-supported, poorly sorted and locally displays inverse grading. Fragments are composed mainly by acidic lithics and minor basalts and banded rhyolites, pumice and crystaloclasts (*qz*, *pg* and/or *bt*), ranging from ash to blocks sizes (up to ~30 cm) immersed in a fine-grained felsofidic groundmass. Locally, pumice juvenile fragments display a moderately developed *eutaxitic* texture (*emLT* facies).

Interpretation: Lithofacies *mLT* indicate a fluid escape-dominated flow boundary zone, with partial elutriation of fine ash and absence of tractional segregation (Branney and Kokelaar, 2002). We interpret this facies as corresponding to the result of: (1) pyroclastic flows developed under subaerial conditions and originated by the collapse of a lava-dome or eruption column, or (2) an air-fall origin (Cas and Wright, 1988; McPhie *et al*., 1993). Eutaxitic massive lapilli-tuffs (*emLT*), which have a minor occurrence, would correspond to proximal, low-grade welded pyroclastic flows associated with the rhyolitic domes.

3.3 *p-xsLT* facies (*pumiceous-rich, cross-stratified lapilli-tuffs*):

Description: This facies corresponds to ~40 m of grey to pink, pumiceous-rich lapilli-tuffs which present centi- to deci-meter scale cross stratification. Individual beds are 0.2 to 1.2 m thick, show moderate sorting and are grain-supported with fragments ranging from 0.3-1.2 cm. Fragments correspond mainly to acidic aphanitic rocks, elongated pumice and plagioclase crystaloclasts. Basal scouring is common and low angle cross sets (<30°) show normal and locally inverse grading. This facies presents a minor occurrence being identified at the southern edge of the Sierra Vaquillas Altas range (Quebrada Los Pozos).

Interpretation: Low angle cross-bedding (<30°) of *p-xsLT* facies indicates deposition from traction-dominated flow boundary conditions (Branney and Kokelaar, 2002). This facies would corresponds to pyroclastic surge deposits, which are originated by low particle concentration pyroclastic flows (Cas and Wright, 1988).

3.4 *mT* facies (*massive tuffs*):

Description: This facies corresponds to well sorted, greyish- to greenish- colored, massive tuffs (vitric, crystal and lithic), with a dominance of vitric tuffs. Fine tuffs are well stratified forming decimetric-scale

tabular beds (0.1-0.6 m). Fragments correspond mainly to intermediate juvenile and minor andesitic to rhyolitic volcanic rocks, together with crystaloclasts (*pg* and *qz*) immersed in a well devitrified groundmass altered to illite and smectite.

Interpretation: The good sorting of *mT* facies and the absence of flow textures suggest an air-fall origin for this lithofacies (Cas and Wright, 1988).

References

ALONSO-ZARZA, A. M., AND TANNER, L. H. (2009) *Carbonates in continental settings: facies, environments, and processes*, Vol. 61. Elsevier.

ALONSO-ZARZA, A. M., AND WRIGHT, V. P. (2010) Palustrine Carbonates. In: *Carbonates in continental settings: facies, environments, and processes*, (Ed. by A. M. Alonso-Zarza and L. H. Tanner), Vol. 61, pp. 103–131.

ARDILL, J. (1996) *Sequence stratigraphy of the Mesozoic Domeyko basin, northern Chile*. University of Liverpool.

ARDILL, J., FLINT, S., CHONG, G., AND WILKE, H. (1998) Sequence stratigraphy of the Mesozoic Domeyko Basin, northern Chile. *J. Geol. Soc. London.*, 155, 71–88.

ASTUDILLO, N., FERRANDO, R., MONTECINO, D., ESPINOZA, F., MATTHEWS, S., CORNEJO, P., AND ARÉVALO, C. (in press) *Carta Augusta Victoria, Región de Antofagasta. Servicio Nacional de Geología y Minería, Carta Geológica de Chile, Serie Geología Básica XXX. 1 mapa escala 1:100.000. Santiago, Chile.*

BRAGA, J. C., MARTIN, J. M., AND ALCALA, B. (1990) Coral reefs in coarse-terrigenous sedimentary environments (Upper Tortonian, Granada Basin, southern Spain). *Sediment. Geol.*, 66, 135–150.

BRANNEY, M., AND KOKELAAR, P. (2002) Interpreting ignimbrite lithofacies. In: *Pyroclastic Density Currents and the Sedimentation of Ignimbrites*, pp. 51–85. The Geological Society of London, London.

BUSBY-SPERA, C. J., AND WHITE, J. D. L. (1987) Variation in peperite textures associated with differing host-sediment properties. *Bull. Volcanol.*, 49, 765–776.

BUSBY, C., AND BASSETT, K. N. (2007) Volcanic facies architecture of an intra-arc strike-slip basin, Santa Rita Mountains, Southern Arizona. *Bull. Volcanol.*, 70, 85–103.

CAS, R. A. F., AND WRIGHT, J. V (1988) *Volcanic successions modern and ancient: A geological approach to processes, products and successions*. Springer Science and Business Media.

CHONG, G. (1973) *Reconocimiento Geológico del Área Catalina, Sierra de Varas y estratigrafía del Jurásico del Profeta, Provincia de Antofagasta*. Universidad de Chile, Santiago de Chile.

CORNEJO, P., AND MPODOZIS, C. (1996) *Geología de la Región de Sierra Exploradora (Cordillera de Domeyko 25°-26°S). Servicio Nacional de Geología y Minería-CODELCO, Informe Registrado, IR-96-09, 330 p. 9 mapas escala 1:50.000.* Santiago.

CORNEJO, P., MPODOZIS, M., RIVERA, O., AND MATTHEWS, S. (2009) *Carta Exploradora, Regiones de Antofagasta y Atacama. Servicio Nacional de Geología y Minería, Carta Geológica de Chile, Serie Geología Básica 119: 103 p., 1 mapa escala 1:100.000.*

DOYLE, M. G. (2000) Clast shape and textural associations in peperite as a guide to hydromagmatic interactions: Upper Permian basaltic and basaltic andesite examples from Kiama, Australia. *Aust. J. Earth Sci.*, 47, 167–177.

FREUNDT, A., WILSON, C. J. N., AND CAREY, S. N. (2000) Ignimbrites and block-and-ash flow deposits. In: *Encyclopedia of volcanoes*, (Ed. by H. Sigurdsson), pp. 581–599. Academic Press, New York.

GONZÁLEZ, R., WILKE, H. G., MENZIES, A. H., ESPINOZA, F., RIQUELME, R., AND HERRERA, C. (2015) *Carta Sierra de Varas, Región de Antofagasta. Servicio Nacional de Geología y Minería, Carta Geológica de Chile, Serie Geología Básica XXX, 1 mapa escala 1:100.000. Santiago.*

HORTON, B. K., AND SCHMITT, J. G. (1996) Sedimentology of a lacustrine fan-delta system, Miocene Horse Camp Formation, Nevada, USA. *Sedimentology*, 43, 133–155.

LEHRMANN, D. J., WEI, J., AND ENOS, P. (1998) CONTROLS ON FACIES ARCHITECTURE OF A LARGE TRIASSIC CARBONATE PLATFORM : THE GREAT BANK OF GUIZHOU , NANPANJIANG BASIN , SOUTH CHINA.

MATTER, A., AND TUCKER, M. E. (EDS.) (1978) *Modern and ancient lake sediments*. Blackwell Publishing Ltd.

MCPHIE, J., DOYLE, M. G., AND ALLEN, R. (1993) *Volcanic textures: a guide to the interpretation of textures in volcanic rocks*. CODES-University of Tasmania, Hobart.

MIALL, A. D. (1977) A review of the braided-river depositional environment. *Earth Sci. Rev.*, 13, 1–62.

MIALL, A. D. (1978) Lithofacies types and vertical profile models in braided river deposits: a summary. *Fluv. Sedimentol.*, 5, 597–600.

MIALL, A. D. (1996) *The Geology of Fluvial Deposits: Sedimentary Facies, basin analysis, and petroleum geology*. Springer-Verlag, Berlin.

MIALL, A. D. (2006) *The Geology of Fluvial Deposits*. Springer, Berlin.

MONTECINO, D. (2015) *Nuevo esquema estratigráfico, condiciones de sedimentación y evolución de la cuenca triásica entre los 24°00'-24°30' S y 69°00'-69°30' W, Región de Antofagasta, Chile*. Universidad de Concepción, Concepción.

NEMEC, W., AND STEEL, R. J. (1984) Alluvial and coastal conglomerates: their significant features and some comments on gravelly mass-flow deposits. *Sedimentol. Gravels Conglomerates*, 10, 1–31.

NEMEC, W., AND STEEL, R. J. (1988) What is a fan delta and how do we recognize it? In: *Fan Deltas: Sedimentology and Tectonic Settings*.

NICHOLS, G. (2009) *Sedimentology and stratigraphy*. John Wiley and Sons.

PLATT, N. H., AND WRIGHT, V. P. (1991) Lacustrine carbonates: facies models, facies distributions and hydrocarbon aspects. *Spec. Publ. Internatinal Assoc. Sedimentol.*, 13, 57–74.

REYES, R. (2017) *Nuevas localidades fosilíferas del triásico de la Cordillera de Domeyko, Región de Antofagasta: estratigrafía, ambientes de sedimentación y paleobotánica*. Universidad de Concepcion, Concepción.

SMITH, G. A. (1986) Coarse-grained nonmarine volcaniclastic sediment: Terminology and depositional process. *Geol. Soc. Am. Bull.*, 97, 1–10.

STEWART, A. L., AND MCPHIE, J. (2003) Internal structure and emplacement of an Upper Pliocene dacite cryptodome, Milos Island, Greece. *J. Volcanol. Geotherm. Res.*, 124, 129–148.

STEWART, A. L., AND MCPHIE, J. (2006) Facies architecture and Late Pliocene - Pleistocene evolution of a felsic volcanic island, Milos, Greece. *Bull. Volcanol.*, 68, 703–726.

STEWART, M. L., RUSSELL, J. K., AND HICKSON, C. J. (2003) Discrimination of hot versus cold avalanche deposits: Implications for hazard assessment at Mount Meager, B.C. *Nat. Hazards Earth Syst. Sci.*, 3, 713–724.

TOMLINSON, A. J., CORNEJO, P., AND MPODOZIS, C. (1999) *Hoja Potrerillos, Región de Atacama. Servicio Nacional de Geología y Minería (Chile), Mapas Geológicos, No. 14, 1 mapa escala 1:100.000, Santiago*.

WHITE, J. D. L., AND HOUGHTON, B. F. (2006) Primary volcaniclastic rocks. *Geology*, 34, 677–680.

Anexo 3: Facies association codes and main outcrop localities

Location keys: Aguada de Varas (AV), Cerro Rincones (CR), northern portion of Sierra de Varas (NSV), Quebrada Ceballos (QC), Quebrada Caletones (QCA), west flank of Sierra Inés Chica (WSI), Quebrada Agua Escondida (QAE), Quebrada La Perra (QLP), Cerro Pascua (CP), tributary Quebrada Los Pozos (TQP), Quebrada La Carreta (QLC), Quebrada La Mina (QLM), Alto de Vaquillas (AV), Quebrada Agua Dulce (QAD), Quebrada Inés Chica (QIC), Quebrada del Salitre (QS), Cerro Guanaco (CG), Quebrada Mármol (QM), Cerro La Ballena (CB), Quebrada del Carrizo (QCR), Quebrada Vaquillas (QV), Quebrada Punta del Viento (QPV), Cerro Amarillo (CA), Quebrada de Las Cenizas (QLC), Sierra Áspera (SA), Portezuelo de la Sal (PS), Quebrada Los Guindos (QG), Quebrada del Salitre (QS), Cerro Don Alejo (CDA), Quebrada Las Bateas (QLB), Quebrada del Diablo (QDD), Quebrada Doña Inés Chica (QICH), east flank of Cerro Morales (ECM), west margin of the Salar de Pedernales (WSP), Cerro Colorado (CC), Cerro Manchón (CMA), east flank Cerro Punta del Viento (ECPV), Sierra Gólgota (SG).

Type	Depositional environment	Facies Association	Code	Facies	Localities at SVSB	Localities at SESB
Sedimentary	Alluvial	Debris flow	A1	*Gmm, Sm*	AV, CR, NSV, QC	QCA, WSI, QAE
		Channelized flows	A2	*Gcm, St, Sm*	CP, NSV, TQP, QLC, QLM, AV	QLP, QAD, WSI, QCA
		Sheetflood flows	A3	*Gcm, Sh*	CP, NSV	
	Fluvial	Sand-rich braided river	F1	*Gcm, St, Sp, Sh, Sm, Fm*	TQP, QLC, QLM, CG?, QM?	QLP
		Meandering river	F2	*Fl, Fm, Sm, Sh*	TQP, QLC	QIC, QS, QCR
	Lacustrine	Marginal lacustrine	L1	*Fo, Bs, Gmm, Gcm*	NSV	
		Basinal lacustrine	L2	*Fl, Sm*	QM, NSV, TQP, QLM, QV	
	Shallow marine	Delta-fan	SM1	*Gmg, Gmm, Gcm, St, Ss, M*	QPV, QV, NSV	
		Rimmed carbonate shelf	SM2	*B, R, P, W, M, Sm*	QLC, QPV, QV, NSV, SA, CG, PS, QG, CR	CA, QLC, QS, CDA?, QLB, QDD
Volcanic	Basaltic volcanism	Basaltic subaerial & partly subaqueous volcanism	VB1	*cB, brB*	QV, QLC	QCR, QICH, QAD, ECM
	Intermediate volcanism	Intermediate subaerial lava flows	VI1	*cA, cD, brA, brD*	CB, CMA, QV, QPV, TQP, ECPV, PS, CG, SG	QAD
	Acidic & Explosive volcanism	Acid domes & proximal pyroclastic deposits	VA1	*bcR, cjD, mBr, emLT*	CG, QPV, CMA	CC, QICH, WSP
		Medium to distal pyroclastic deposits	VA2	*mLT, mT, p-xsLT, sT, p-//sT*	QM, NSV	TQP, QVA, QICH, QAD, QLC

Anexo 4: U-Pb geochronology methods

1. Laboratorio de Estudios Isotópicos (UNAM).

The analytical work at LEI was undertaken using a Resonetics Resolution M50 193 nm laser Excimer (LPX 220) connected to a "Thermo ICap Qc" single quadrupole (SQ) mass spectrometer, following analytical procedures and technical details after Solari *et al.* (2010). The employed laser diameter for ablation was 23 μm. Standards used were 91500 zircon (1062 ± 1 Ma; Wiedenbeck *et al.*, 1995) and Plešovice zircon (337.13 ± 0.37 Ma, Sláma *et al.*, 2008), while linear calibration curves were obtained using NIST SRM 612 glasses as standards. Data reduction was performed using Iolite software (Paton *et al.*, 2011).

2. Arizona LaserChron Center.

At the Arizona LaserChron Center (Gehrels *et al.*, 2008), U-Pb geochronology of zircons was conducted by LA-MC-ICP-MS. The analyses involve ablation of zircon with a New Wave/Lambda Physik DUV193 Excimer laser (operating at a wavelength of 193 nm) using a spot diameter of 25 or 35 mm. The ablated material is carried with helium gas into the plasma source of a GV Instruments Isoprobe, which is equipped with a flight tube of sufficient width that U, Th, and Pb isotopes are measured simultaneously. All measurements are made in static mode, using Faraday detectors for ^{238}U and ^{232}Th, an ion-counting channel for ^{204}Pb, and either Faraday collectors or ion counting channels for $^{208-206}$Pb. Ion yields are ~1 mV ppm−1. Each analysis consists of one 20 s-integration on peaks with the laser off (for backgrounds), twenty 1 s-integrations with the laser firing, and a 30 s delay to purge the previous sample and to prepare for the next analysis. The ablation pit is ~15 mm in depth.

For each analysis, the errors in determining ^{206}Pb/^{238}U and ^{206}Pb/^{204}Pb result in a measurement error of ~1% (at 2σ level) in the ^{206}Pb/^{238}U age. The errors in measurement of ^{206}Pb/^{207}Pb and ^{206}Pb/^{204}Pb also result in ~1% (2σ) uncertainty in age for grains that are >1.0 Ga, but are substantially larger for younger grains due to low intensity of the ^{207}Pb signal. For most analyses, the crossover in precision of ^{206}Pb/^{238}U and ^{206}Pb/^{207}Pb ages occurs at ~1.0 Ga. Common Pb correction is accomplished by using the measured ^{204}Pb and assuming an initial Pb composition from Stacey and Kramers (1975) (with uncertainties of 1.0 for ^{206}Pb/^{204}Pb and 0.3 for ^{207}Pb/^{204}Pb). The measurement of ^{204}Pb is unaffected by the presence of ^{204}Hg because backgrounds are measured on peaks (thereby subtracting any background ^{204}Hg and ^{204}Pb), and because very little Hg is present in the argon gas. Inter-element fractionation of Pb/U is generally ~20%, whereas fractionation of Pb isotopes is generally <2%. In-run analysis of fragments of a large Sri Lanka zircon crystal (generally every fifth measurement) with known age of 564 ± 4 Ma (2σ error) is used to correct for this fractionation (see Gehrels *et al.*, 2008). The uncertainty resulting from the calibration correction is generally ~1% (2σ) for both ^{206}Pb/^{207}Pb and ^{206}Pb/^{238}U ages. The reported ages are determined from the weighted mean of the ^{206}Pb/^{238}U ages of the concordant and overlapping analyses (Ludwig, 2003). The reported uncertainty (labeled "mean") is based on the scatter and precision of the set of ^{206}Pb/^{238}U or ^{206}Pb/^{207}Pb ages, weighted according to their measurement errors (shown at 1s). The systematic error, which includes contributions from the standard calibration, age of the calibration standard, composition of common Pb and U decay constants, is generally ~1–2% (2σ).

GEHRELS, G. E., VALENCIA, V. A., AND RUIZ, J. (2008) Enhanced precision, accuracy, efficiency, and spatial resolution of U-Pb ages by laser ablation–multicollector–inductively coupled plasma–mass spectrometry. *Geochemistry, Geophys. Geosystems*, 9.

PATON, C., HELLSTROM, J., PAUL, B., WOODHEAD, J., AND HERGT, J. (2011) Iolite: Freeware for the visualisation and processing of mass spectrometric data. *J. Anal. At. Spectrom.*, 26, 2508–2518.

SOLARI, L. A., GÓMEZ-TUENA, A., BERNAL, J. P., PÉREZ-ARVIZU, O., AND TANNER, M. (2010) U-Pb zircon geochronology with an integrated la-icp-ms microanalytical workstation: Achievements in precision and accuracy. *Geostand. Geoanalytical Res.*, 34, 5–18.

STACEY, J. S. T, AND KRAMERS, 1JD (1975) Approximation of terrestrial lead isotope evolution by a two-stage model. *Earth Planet. Sci. Lett.*, 26, 207–221.

WIEDENBECK, M., ALLE, P., CORFU, F., GRIFFIN, W. L., MEIER, M., OBERLI, F. V, QUADT, A. VON, RODDICK, J. C., AND SPIEGEL, W. (1995) Three natural zircon standards for U-Th-Pb, Lu-Hf, trace element and REE analyses. *Geostand. Geoanalytical Res.*, 19, 1–23.

Anexo 5: $^{40}Ar/^{39}Ar$ geochronology methods

White micas have been chosen because of their resistance to resetting by mild thermal disturbances owing to their sufficiently high closure temperature (350–420°C; McDougall and Harrison, 1999), and their resistance to mechanical and chemical breakdown (Heller and Paola, 1992).

Detrital muscovite grains were separated from the samples by jaw crusher and roller grinding, sieved by 1.0-0.5 mm and 0.5-0.25 mm fractions and finally, white micas of sizes ranging from 0.5-2 mm were hand-picked under a binocular microscope.

Total fusion Ar ages were obtained from 87 individual muscovite grains per sample (4 samples) adding total 348 detrital grains analyzed. Analyses were conducted in the $^{40}Ar/^{39}Ar$ laboratory at the U.S. Geological Survey (USGS) in Denver, USA. Seven samples and standards of Fish Canyon sanidine with an age of 28.201 ± 0.023 Ma (1σ) (Kuiper *et al.*, 2008) were packaged and irradiated for 20 h, in the central thimble position of the USGS TRIGA reactor in Denver, USA. Cadmium shielding was used to minimize any nucleogenic ^{40}Ar production from ^{40}K.

Analyses were conducted with a CO2 laser operating at conditions of 12 W, with a spot diameter of 3 mm and a total duration of ablation of 90 s (60 seconds at requested power) to extract gas from the samples. Blanks were run at the start and the end of every experiment and after every five unknowns and present little variations throughout the $^{40}Ar/^{39}Ar$ experiments. Backgrounds subtracted from ion beam measurements were arithmetic averages and standard deviations. Data were collected by ion counting on a Thermo Scientific ARGUS VI and were corrected for blanks, mass discrimination and nucleogenic isotopic interferences from irradiated CaF2. Typical values of isotopic interferences production ratios were measured as follows: $(^{36}Ar/^{37}Ar)_{Ca}$ = 2.673 e-4 ± 8.14 e-7, $(^{39}Ar/^{37}Ar)_{Ca}$ = 7.54 e-4 ± 3.75 e-5, $(^{38}Ar/^{39}Ar)_K$ = 1.29 e-2± 2.60 e-4 and $(^{40}Ar/^{39}Ar)_K$ = 1.51 e-3±6.12 e-4. Non-radiogenic argon was corrected to an atmospheric value of $(^{40}Ar/^{36}Ar)_{atm}$=298.56 ± 0.31 (Lee *et al.*, 2006), and ages were calculated using the decay constants in (Min, Mundil, Renne, and Ludwig, 2000). Calculated J-value for the batch of samples was 0,0044988 ± 0,0000063409.

Heller, P., and Paola, C. (1992). The large-scale dynamics of grain-size variation in alluvial basins, 2: Application to syntectonic conglomerate. *Basin Research*, *4*, 91–103. Retrieved from http://www.earthdoc.org/publication/publicationdetails/?publication=62573

Kuiper, K. F., Deino, A., Hilgen, F. J., Krijgsman, W., Renne, P. R., and Wijbrans, J. R. (2008). Synchronizing Rock Clocks of Earth History. *Science*, *320*(5875), 500–504. https://doi.org/10.1126/science.1154339

Lee, J. Y., Marti, K., Severinghaus, J. P., Kawamura, K., Yoo, H. S., Lee, J. B., and Kim, J. S. (2006). A redetermination of the isotopic abundances of atmospheric Ar. *Geochimica et Cosmochimica Acta*, *70*(17), 4507–4512. https://doi.org/10.1016/j.g*ca*.2006.06.1563

McDougall, I., and Harrison, T. M. (1999). *Geochronology and thermochronology by the 40Ar/39Ar method*. New York: Oxford University Press.

Min, K., Mundil, R., Renne, P. R., and Ludwig, K. R. (2000). A test for systematic errors in 40Ar/39Ar geochronology through comparison with U/Pb analysis of a 1.1-Ga rhyolite. *Geochimica et Cosmochimica Acta*, *64*(1), 73–98. https://doi.org/10.1016/S0016-7037(99)00204-5

Anexo 6: Fault-slip data from synrift/postrift structures.

Locality	Fault strike	Fault dip	Striae trend	Striae plunge	Sense Slip	Lat	Long	Bedd. strike	Bedd. dip	Unit
Quebrada Encuentro	133	82	311	15	N	-24,9297	-69,1067	43	85	Profeta
Quebrada Encuentro	126	75	302	13	N	-24,9297	-69,1067	43	85	Profeta
Quebrada Encuentro	128	66	302	13	N	-24,9297	-69,1067	43	85	Profeta
Quebrada Encuentro	136	82	315	14	N	-24,9297	-69,1067	43	85	Profeta
Quebrada Encuentro	137	82	315	14	N	-24,9297	-69,1067	43	85	Profeta
Quebrada Encuentro	130	82	308	15	NR	-24,9297	-69,1067	45	72	Profeta
Quebrada Encuentro	128	76	303	20	NR	-24,9297	-69,1067	45	72	Profeta
Quebrada Encuentro	129	49	290	21	NR	-24,9297	-69,1067	45	72	Profeta
Quebrada Encuentro	123	83	302	7	NR	-24,9297	-69,1067	45	72	Profeta
Quebrada Encuentro	323	85	324	12	NL	-24,9297	-69,1067	45	72	Profeta
Quebrada Encuentro	126	72	301	14	NR	-24,9297	-69,1067	45	72	Profeta
Quebrada Encuentro	341	85	161	3	NR	-24,9297	-69,1067	55	78	Profeta
Quebrada Encuentro	112	86	291	8	NR	-24,9297	-69,1067	55	78	Profeta
Quebrada Encuentro	106	57	285	2	NR	-24,9297	-69,1067	55	78	Profeta
Quebrada Encuentro	110	62	288	4	NR	-24,9297	-69,1067	55	78	Profeta
Quebrada Encuentro	106	79	284	10	NR	-24,9297	-69,1067	55	78	Profeta
Quebrada Encuentro	107	78	286	6	NR	-24,9297	-69,1067	55	78	Profeta
Quebrada Encuentro	118	84	119	9	NL	-24,9297	-69,1067	33	79	Profeta
Quebrada Encuentro	141	83	143	13	NL	-24,9297	-69,1067	33	79	Profeta
Punta del Viento	36	58	157	34	N	-25,0844	-69,2441	151	23	Profeta
Punta del Viento	23	84	33	59	NL	-25,0844	-69,2441	146	60	Profeta
Punta del Viento	211	80	295	80	NL	-25,0844	-69,2441	162	54	Profeta
Punta del Viento	45	53	89	43	NL	-25,0844	-69,2441	162	54	Profeta
Punta del Viento	34	58	169	48	NR	-25,0844	-69,2441	141	22	Profeta
Punta del Viento	33	58	155	54	NR	-25,0844	-69,2441	141	22	Profeta

Punta del Viento	176	75	218	68	NL	-25,0844	-69,2441	102	28	Profeta
Quebrada Vaquillas	105	61	278	31	N	-25,3229	-69,2882	23	34	Sierra de Varas
Quebrada Vaquillas	307	55	333	28	N	-25,3229	-69,2882	19	27	Sierra de Varas
Quebrada Vaquillas	344	58	348	35	N	-25,3229	-69,2882	46	35	Sierra de Varas
Quebrada Vaquillas	342	82	345	23	N	-25,3229	-69,2882	48	46	Sierra de Varas
Quebrada Vaquillas	325	80	351	68	N	-25,3229	-69,2882	59	41	Sierra de Varas
Quebrada Vaquillas	298	58	349	51	N	-25,3229	-69,2882	59	41	Sierra de Varas
Quebrada Vaquillas	160	80	323	59	N	-25,3229	-69,2882	59	41	Sierra de Varas
Quebrada Vaquillas	133	80	293	63	N	-25,3229	-69,2882	58	38	Sierra de Varas
Quebrada Vaquillas	0	63	26	41	N	-25,3229	-69,2882	58	38	Sierra de Varas
Quebrada Vaquillas	343	70	354	28	N	-25,3229	-69,2882	58	38	Sierra de Varas
Quebrada Vaquillas	330	82	338	44	N	-25,3229	-69,2882	58	38	Sierra de Varas
Quebrada Vaquillas	177	44	204	25	N	-25,3139	-69,2628	153	87	Sierra de Varas
Quebrada Vaquillas	153	87	155	41	N	-25,3139	-69,2628	151	47	Sierra de Varas
Quebrada Vaquillas	318	79	138	0	N	-25,3139	-69,2628	193	38	Sierra de Varas
Quebrada Vaquillas	358	45	68	49	N	-25,3139	-69,2628	181	34	Sierra de Varas
Quebrada Vaquillas	331	86	146	64	N	-25,3139	-69,2628	213	33	Sierra de Varas
Quebrada Vaquillas	166	72	197	26	N	-25,3139	-69,2628	190	41	Sierra de Varas
Quebrada Vaquillas	144	87	149	57	N	-25,3139	-69,2628	191	34	Sierra de Varas
Quebrada Vaquillas	18	69	112	66	N	-25,3139	-69,2628	183	39	Sierra de Varas
Quebrada Vaquillas	10	23	101	22	N	-25,3139	-69,2628	189	37	Sierra de Varas
Quebrada Vaquillas	335	87	153	16	N	-25,3139	-69,2628	179	29	Sierra de Varas
Quebrada Vaquillas	350	75	352	67	N	-25,3139	-69,2628	184	25	Sierra de Varas
Quebrada Los Pozos	346	73	165	0	N	-25,2990	-69,2783	102	39	Sierra de Varas
Quebrada Los Pozos	12	81	192	2	N	-25,2990	-69,2783	102	33	Sierra de Varas
Quebrada Los Pozos	340	86	160	9	N	-25,2990	-69,2783	74	39	Sierra de Varas
Quebrada Los Pozos	41	58	82	3	N	-25,2990	-69,2783	74	39	Sierra de Varas
Quebrada Los Pozos	152	86	325	55	N	-25,2990	-69,2783	82	39	Sierra de Varas
Quebrada Los Pozos	153	82	158	25	N	-25,2990	-69,2783	70	39	Sierra de Varas
Quebrada Los Pozos	91	49	98	13	N	-25,2990	-69,2783	91	36	Sierra de Varas
Quebrada Los Pozos	22	60	29	22	N	-25,2990	-69,2783	114	40	Sierra de Varas

Quebrada Los Pozos	173	81	313	71	N	-25,3057	-69,2827	128	29	Sierra de Varas
Quebrada Los Pozos	157	62	274	55	N	-25,3057	-69,2827	128	29	Sierra de Varas
Quebrada Los Pozos	162	66	216	63	N	-25,3057	-69,2827	128	29	Sierra de Varas
La Carreta 1	161	73	174	36	NL	-25,3409	-69,2204	55	37	Sierra de Varas
La Carreta 1	337	84	338	13	ND	-25,3409	-69,2204	55	37	Sierra de Varas
La Carreta 1	347	68	17	52	N	-25,3409	-69,2204	30	28	Sierra de Varas
La Carreta 1	153	62	181	42	N	-25,3409	-69,2204	108	32	Sierra de Varas
La Carreta 2	32	54	92	40	N	-25,3384	-69,2239	145	21	Profeta
La Carreta 2	26	51	85	37	N	-25,3384	-69,2239	145	21	Profeta
La Carreta 2	165	27	279	43	N	-25,3384	-69,2239	145	21	Profeta
La Carreta 2	35	50	90	45	N	-25,3384	-69,2239	145	21	Profeta

Anexo 8: Resultados U-Pb

Análisis medidos en el Arizona LaserCron Center

Analysis	U (ppm)	$^{206}Pb/^{204}Pb$	U/Th	$^{206}Pb/^{207}Pb$	± (%)	$^{207}Pb/^{235}U$	± (%)	$^{206}Pb/^{238}U$	error corr.	$^{206}Pb/^{238}U$	±2s	$^{207}Pb/^{235}U$	±2s	$^{206}Pb/^{207}Pb$	±2s	Best age (Ma)	±2s	Disc (%)	
								CORRECTED RATIOS					CORRECTED AGES (Ma)						
CPV-14-254 (DZ)	Maximum depositinal age (2+DZ, 1σ): 234.4±4.8 Ma (MSWD = 0.5)																		
CPV-14-254-Spot 72	1298,3	157496	1,17	19,42	1,43	0,26	2,97	0,04	2,61	0,88	233,2	6,0	235,9	6,3	263,0	32,8	233,2	6,0	1,1	*
CPV-14-254-Spot 79	2448,4	222671	3,39	18,56	2,65	0,28	4,57	0,04	3,73	0,82	237,0	8,7	249,1	10,1	365,5	59,7	237,0	8,7	4,9	*
CPV-14-254-Spot 40	371,9	62858	1,11	19,06	2,63	0,28	3,32	0,04	2,02	0,61	245,7	4,9	251,4	7,4	305,2	60,0	245,7	4,9	2,3	
CPV-14-254-Spot 2	528,1	36770	1,58	19,27	2,33	0,28	3,40	0,04	2,47	0,73	246,0	6,0	249,4	7,5	280,9	53,4	246,0	6,0	1,3	
CPV-14-254-Spot 74	419,9	44849	1,62	17,92	3,80	0,30	7,93	0,04	6,96	0,88	246,9	16,9	266,8	18,6	445,0	84,5	246,9	16,9	7,4	
CPV-14-254-Spot 34	283,6	51281	0,82	18,84	2,89	0,31	3,95	0,04	2,69	0,68	268,4	7,1	275,0	9,5	331,7	65,5	268,4	7,1	2,4	
CPV-14-254-Spot 77	588,8	127008	0,71	17,91	2,28	0,34	2,92	0,04	1,83	0,62	276,5	4,9	295,2	7,5	445,8	50,8	276,5	4,9	6,3	
CPV-14-254-Spot 44	514,2	25937	1,42	19,91	3,15	0,31	3,73	0,04	1,99	0,54	278,1	5,4	270,5	8,9	205,7	73,1	278,1	5,4	-2,8	
CPV-14-254-Spot 96	1476,4	97511	1,24	19,11	2,05	0,32	3,00	0,04	2,20	0,73	280,3	6,0	282,4	7,4	300,2	46,7	280,3	6,0	0,8	
CPV-14-254-Spot 36	1454,8	201225	1,24	19,19	1,45	0,32	2,70	0,04	2,28	0,84	281,3	6,3	282,3	6,7	290,3	33,1	281,3	6,3	0,3	
CPV-14-254-Spot 35	1007,2	72472	1,48	19,30	2,38	0,32	2,94	0,04	1,73	0,59	281,9	4,8	281,5	7,2	277,7	54,4	281,9	4,8	-0,2	
CPV-14-254-Spot 14	1985,6	121275	1,09	19,06	1,80	0,33	2,53	0,05	1,77	0,70	284,1	4,9	286,5	6,3	305,8	41,0	284,1	4,9	0,8	
CPV-14-254-Spot 91	522,3	68262	1,27	19,16	1,81	0,33	2,93	0,05	2,31	0,79	285,3	6,4	286,3	7,3	294,0	41,4	285,3	6,4	0,3	
CPV-14-254-Spot 33	161,4	58668	1,69	19,16	5,70	0,33	7,36	0,05	4,65	0,63	285,6	13,0	286,4	18,4	293,2	130,3	285,6	13,0	0,3	
CPV-14-254-Spot 46	446,3	63746	0,87	19,03	4,45	0,33	4,86	0,05	1,97	0,40	285,9	5,5	288,5	12,2	309,3	101,3	285,9	5,5	0,9	
CPV-14-254-Spot 54	597,5	71990	1,39	18,20	2,18	0,34	3,73	0,05	3,02	0,81	286,2	8,5	300,1	9,7	409,6	48,9	286,2	8,5	4,6	
CPV-14-254-Spot 19	690,9	55661	1,08	19,39	1,67	0,32	2,68	0,05	2,09	0,78	286,7	5,9	284,5	6,6	266,3	38,2	286,7	5,9	-0,8	
CPV-14-254-Spot 67	975,0	45820	0,98	19,12	2,13	0,33	3,14	0,05	2,31	0,74	286,8	6,5	288,1	7,9	298,5	48,6	286,8	6,5	0,4	

Sample																		
CPV-14-254-Spot 31	306,1	87637	1,41	18,46	3,34	0,34	4,94	0,05	3,63	0,74	287,0	10,2	297,1	12,7	377,6	75,1	287,0	10,2	3,4
CPV-14-254-Spot 26	125,7	94718	1,61	19,05	4,55	0,33	5,11	0,05	2,34	0,46	288,0	6,6	290,0	12,9	306,6	103,6	288,0	6,6	0,7
CPV-14-254-Spot 37	1453,3	66035	1,01	19,32	2,07	0,33	3,42	0,05	2,72	0,79	288,2	7,7	286,8	8,5	275,3	47,5	288,2	7,7	-0,5
CPV-14-254-Spot 85	595,3	53628	1,38	19,06	2,20	0,33	3,40	0,05	2,59	0,76	288,8	7,3	290,6	8,6	305,3	50,2	288,8	7,3	0,6
CPV-14-254-Spot 108	175,1	13568	1,30	17,23	8,11	0,37	8,68	0,05	3,09	0,36	289,5	8,7	317,8	23,7	531,2	177,9	289,5	8,7	8,9
CPV-14-254-Spot 98	814,9	288394	1,58	19,32	2,14	0,33	3,48	0,05	2,75	0,79	289,6	7,8	288,0	8,7	275,0	48,9	289,6	7,8	-0,6
CPV-14-254-Spot 66	1230,0	275504	1,30	19,28	2,12	0,33	3,66	0,05	2,98	0,81	290,1	8,5	288,9	9,2	279,2	48,6	290,1	8,5	-0,4
CPV-14-254-Spot 28	872,8	72576	1,11	18,73	2,65	0,34	3,87	0,05	2,82	0,73	290,6	8,0	296,7	10,0	345,2	60,0	290,6	8,0	2,1
CPV-14-254-Spot 60	1216,1	55002	1,01	19,01	2,17	0,33	3,59	0,05	2,86	0,80	290,9	8,1	293,2	9,1	311,9	49,4	290,9	8,1	0,8
CPV-14-254-Spot 20	1524,0	186790	0,97	19,03	1,33	0,33	3,02	0,05	2,72	0,90	291,0	7,7	293,0	7,7	308,9	30,2	291,0	7,7	0,7
CPV-14-254-Spot 63	399,6	49949	1,65	19,55	2,82	0,33	3,58	0,05	2,20	0,62	291,7	6,3	286,8	9,0	247,6	65,0	291,7	6,3	-1,7
CPV-14-254-Spot 56	639,5	82591	1,63	18,61	2,15	0,34	4,03	0,05	3,40	0,85	291,9	9,7	299,6	10,4	359,9	48,5	291,9	9,7	2,6
CPV-14-254-Spot 92	414,4	96490	1,16	19,14	3,35	0,33	5,13	0,05	3,89	0,76	292,4	11,1	292,9	13,1	296,7	76,4	292,4	11,1	0,2
CPV-14-254-Spot 43	261,0	90069	1,34	19,31	3,10	0,33	4,41	0,05	3,15	0,71	292,8	9,0	290,9	11,2	275,4	70,9	292,8	9,0	-0,7
CPV-14-254-Spot 97	533,2	86523	1,03	19,58	2,89	0,33	4,58	0,05	3,56	0,78	292,8	10,2	287,5	11,5	244,6	66,5	292,8	10,2	-1,8
CPV-14-254-Spot 8	584,8	100873	1,30	18,55	2,22	0,35	4,67	0,05	4,12	0,88	292,8	11,8	301,3	12,2	367,3	49,9	292,8	11,8	2,8
CPV-14-254-Spot 107	421,7	55051	1,04	19,08	3,30	0,34	4,83	0,05	3,52	0,73	293,4	10,1	294,5	12,3	303,0	75,3	293,4	10,1	0,4
CPV-14-254-Spot 87	460,3	215828	0,83	19,01	2,89	0,34	3,65	0,05	2,24	0,61	293,6	6,4	295,6	9,4	311,4	65,7	293,6	6,4	0,7
CPV-14-254-Spot 99	956,4	94362	1,46	19,35	1,99	0,33	3,99	0,05	3,45	0,87	294,1	9,9	291,6	10,1	271,5	45,6	294,1	9,9	-0,9
CPV-14-254-Spot 11	509,0	85581	1,13	19,41	2,58	0,33	3,38	0,05	2,19	0,65	294,5	6,3	291,2	8,6	264,6	59,2	294,5	6,3	-1,1
CPV-14-254-Spot 102	307,9	16952	1,23	18,89	2,98	0,34	4,70	0,05	3,63	0,77	294,7	10,5	298,2	12,1	325,9	67,6	294,7	10,5	1,2
CPV-14-254-Spot 90	503,6	50147	1,28	18,99	2,31	0,34	3,47	0,05	2,60	0,75	295,2	7,5	297,4	9,0	314,1	52,5	295,2	7,5	0,7
CPV-14-254-Spot 73	874,7	162251	1,11	19,32	2,57	0,33	3,96	0,05	3,00	0,76	295,3	8,7	293,0	10,1	274,9	59,0	295,3	8,7	-0,8
CPV-14-254-Spot 42	1001,2	161737	0,86	19,29	1,83	0,34	4,12	0,05	3,69	0,90	295,7	10,7	293,7	10,5	277,9	41,8	295,7	10,7	-0,7
CPV-14-254-Spot 21	375,2	36593	1,05	19,69	2,26	0,33	3,21	0,05	2,29	0,71	296,2	6,6	289,0	8,1	231,1	52,2	296,2	6,6	-2,5
CPV-14-254-Spot 5	542,3	184316	1,13	18,86	2,33	0,34	3,18	0,05	2,17	0,68	296,3	6,3	300,0	8,3	329,1	52,9	296,3	6,3	1,2
CPV-14-254-Spot 71	763,8	67069	0,57	19,12	2,64	0,34	5,92	0,05	5,30	0,90	296,4	15,3	296,7	15,2	298,6	60,2	296,4	15,3	0,1
CPV-14-254-Spot 89	482,1	146589	1,55	19,08	3,00	0,34	4,45	0,05	3,28	0,74	296,6	9,5	297,4	11,5	303,6	68,4	296,6	9,5	0,3

Muestra																			
CPV-14-254-Spot 62	246,8	45066	1,39	20,00	3,21	0,33	4,22	0,05	2,74	0,65	297,1	8,0	285,8	10,5	194,6	74,6	297,1	8,0	-3,9
CPV-14-254-Spot 78	1033,1	61706	1,35	19,39	2,03	0,34	4,51	0,05	4,03	0,89	297,1	11,7	293,7	11,5	266,1	46,7	297,1	11,7	-1,2
CPV-14-254-Spot 100	504,3	314400	0,89	19,02	2,36	0,34	3,61	0,05	2,73	0,76	297,3	7,9	298,8	9,3	310,4	53,6	297,3	7,9	0,5
CPV-14-254-Spot 39	334,8	79215	1,25	19,62	3,09	0,33	4,43	0,05	3,18	0,72	297,4	9,3	291,0	11,2	239,2	71,2	297,4	9,3	-2,2
CPV-14-254-Spot 51	794,7	81033	0,96	18,91	2,27	0,35	4,96	0,05	4,41	0,89	298,2	12,9	301,1	12,9	323,7	51,5	298,2	12,9	1,0
CPV-14-254-Spot 9	1239,2	169146	1,47	19,11	1,78	0,34	2,52	0,05	1,78	0,71	298,6	5,2	298,8	6,5	300,4	40,6	298,6	5,2	0,1
CPV-14-254-Spot 105	377,1	79026	1,03	19,04	2,95	0,34	3,92	0,05	2,58	0,66	298,8	7,5	299,9	10,2	308,1	67,2	298,8	7,5	0,4
CPV-14-254-Spot 1	265,1	17224	1,97	20,44	3,67	0,32	4,64	0,05	2,83	0,61	299,0	8,3	282,5	11,4	147,5	86,1	299,0	8,3	-5,9
CPV-14-254-Spot 45	755,5	74282	1,35	18,98	2,78	0,35	3,54	0,05	2,18	0,62	299,3	6,4	301,2	9,2	315,6	63,2	299,3	6,4	0,6
CPV-14-254-Spot 10	273,3	56034	1,42	19,38	3,83	0,34	4,48	0,05	2,32	0,52	299,6	6,8	296,0	11,5	268,1	87,8	299,6	6,8	-1,2
CPV-14-254-Spot 86	565,8	170670	0,93	18,88	2,43	0,35	5,74	0,05	5,20	0,91	299,6	15,2	302,8	15,0	327,4	55,1	299,6	15,2	1,1
CPV-14-254-Spot 52	743,7	54079	1,17	19,17	2,18	0,34	3,82	0,05	3,14	0,82	299,7	9,2	298,8	9,9	292,2	49,7	299,7	9,2	-0,3
CPV-14-254-Spot 29	522,2	54163	1,28	19,76	2,87	0,33	3,44	0,05	1,90	0,55	300,1	5,6	291,5	8,7	222,9	66,3	300,1	5,6	-3,0
CPV-14-254-Spot 59	498,5	88440	1,01	18,70	2,39	0,35	3,20	0,05	2,14	0,67	300,2	6,3	305,7	8,5	348,6	53,9	300,2	6,3	1,8
CPV-14-254-Spot 82	301,7	78912	1,27	19,16	3,59	0,34	4,08	0,05	1,94	0,47	300,2	5,7	299,5	10,6	294,3	81,9	300,2	5,7	-0,2
CPV-14-254-Spot 32	491,8	90401	1,25	19,49	2,23	0,34	5,15	0,05	4,65	0,90	300,2	13,6	295,1	13,2	255,0	51,2	300,2	13,6	-1,7
CPV-14-254-Spot 61	831,8	88994	0,92	19,30	1,96	0,34	3,27	0,05	2,62	0,80	300,8	7,7	298,2	8,5	277,5	44,9	300,8	7,7	-0,9
CPV-14-254-Spot 57	263,7	1050247	1,88	18,43	4,20	0,36	5,22	0,05	3,09	0,59	301,8	9,1	311,2	14,0	382,1	94,5	301,8	9,1	3,0
CPV-14-254-Spot 3	426,0	152918	1,16	18,97	2,57	0,35	3,50	0,05	2,37	0,68	302,1	7,0	303,7	9,2	316,0	58,4	302,1	7,0	0,5
CPV-14-254-Spot 15	535,6	103623	1,35	19,08	3,19	0,35	3,91	0,05	2,27	0,58	302,1	6,7	302,3	10,2	303,4	72,7	302,1	6,7	0,0
CPV-14-254-Spot 88	451,1	86531	1,23	18,89	2,88	0,35	3,42	0,05	1,85	0,54	302,2	5,5	304,9	9,0	325,8	65,4	302,2	5,5	0,9
CPV-14-254-Spot 109	718,2	407555	1,51	19,64	2,76	0,34	3,97	0,05	2,85	0,72	303,0	8,4	295,6	10,2	237,5	63,8	303,0	8,4	-2,5
CPV-14-254-Spot 27	225,4	47536	1,24	18,28	4,56	0,36	6,72	0,05	4,94	0,73	303,6	14,6	314,9	18,2	399,9	102,1	303,6	14,6	3,6
CPV-14-254-Spot 64	629,3	111039	0,97	19,15	2,50	0,35	4,07	0,05	3,22	0,79	303,8	9,5	302,9	10,7	295,6	57,1	303,8	9,5	-0,3
CPV-14-254-Spot 17	689,2	39532	1,15	19,35	2,27	0,34	3,48	0,05	2,64	0,76	304,0	7,8	300,2	9,0	270,8	52,0	304,0	7,8	-1,3
CPV-14-254-Spot 94	567,4	285325	1,37	19,17	2,18	0,35	2,80	0,05	1,75	0,63	305,3	5,2	303,9	7,4	293,2	49,9	305,3	5,2	-0,5
CPV-14-254-Spot 6	644,6	231784	1,35	18,50	2,19	0,36	2,88	0,05	1,87	0,65	305,4	5,6	313,4	7,8	373,6	49,2	305,4	5,6	2,6
CPV-14-254-Spot 69	348,8	57649	1,17	19,28	4,15	0,35	4,92	0,05	2,64	0,54	305,8	7,9	302,7	12,9	279,3	95,0	305,8	7,9	-1,0

Muestra																			
CPV-14-254-Spot 13	1110,9	174766	0,87	18,84	2,30	0,36	2,97	0,05	1,87	0,63	306,1	5,6	309,1	7,9	332,0	52,2	306,1	5,6	1,0
CPV-14-254-Spot 25	748,1	130028	1,04	18,51	1,94	0,36	4,12	0,05	3,64	0,88	306,1	10,9	313,9	11,1	371,5	43,7	306,1	10,9	2,5
CPV-14-254-Spot 83	258,3	140328	2,09	19,23	3,06	0,35	3,76	0,05	2,19	0,58	306,3	6,6	303,9	9,9	285,2	70,0	306,3	6,6	-0,8
CPV-14-254-Spot 38	221,9	15479	1,27	20,22	3,83	0,33	4,37	0,05	2,11	0,48	307,1	6,3	291,6	11,1	169,9	89,5	307,1	6,3	-5,3
CPV-14-254-Spot 76	707,8	346913	1,03	19,00	2,26	0,36	5,00	0,05	4,46	0,89	308,6	13,4	309,1	13,3	312,5	51,4	308,6	13,4	0,1
CPV-14-254-Spot 65	422,7	115525	1,89	18,77	2,49	0,36	3,12	0,05	1,89	0,60	308,7	5,7	312,5	8,4	340,7	56,4	308,7	5,7	1,2
CPV-14-254-Spot 49	846,7	64024	1,11	19,58	2,01	0,35	4,43	0,05	3,95	0,89	309,5	11,9	301,9	11,6	244,2	46,2	309,5	11,9	-2,5
CPV-14-254-Spot 101	585,6	217700	1,38	19,73	2,16	0,34	2,94	0,05	1,99	0,68	310,5	6,0	300,8	7,6	226,4	49,8	310,5	6,0	-3,2
CPV-14-254-Spot 47	310,6	50316	1,39	19,41	3,26	0,35	3,87	0,05	2,09	0,54	310,7	6,3	305,2	10,2	263,6	74,9	310,7	6,3	-1,8
CPV-14-254-Spot 53	824,7	65824	2,34	19,73	2,53	0,35	3,86	0,05	2,92	0,76	311,5	8,9	301,8	10,1	226,9	58,5	311,5	8,9	-3,2
CPV-14-254-Spot 75	481,0	466899	1,21	18,99	2,22	0,36	3,53	0,05	2,75	0,78	312,2	8,4	312,5	9,5	314,4	50,4	312,2	8,4	0,1
CPV-14-254-Spot 22	503,6	70076	1,24	19,39	2,15	0,35	3,53	0,05	2,80	0,79	312,6	8,5	307,2	9,4	266,5	49,3	312,6	8,5	-1,8
CPV-14-254-Spot 12	947,7	381717	1,05	19,43	2,02	0,35	3,62	0,05	3,01	0,83	313,6	9,2	307,6	9,6	262,1	46,4	313,6	9,2	-2,0
CPV-14-254-Spot 110	519,3	55544	1,34	18,74	2,46	0,37	5,10	0,05	4,47	0,88	315,7	13,8	319,1	14,0	344,1	55,7	315,7	13,8	1,1
CPV-14-254-Spot 41	860,6	151572	1,20	19,36	1,97	0,36	3,07	0,05	2,36	0,77	315,8	7,3	310,4	8,2	270,0	45,2	315,8	7,3	-1,7
CPV-14-254-Spot 4	728,8	187506	2,19	19,18	2,04	0,38	3,52	0,05	2,87	0,81	335,9	9,4	330,4	9,9	291,5	46,7	335,9	9,4	-1,7
CPV-14-254-Spot 23	687,1	67470	1,70	19,02	2,12	0,39	3,55	0,05	2,84	0,80	337,6	9,3	334,2	10,1	310,6	48,3	337,6	9,3	-1,0
CPV-14-254-Spot 48	1225,0	137029	1,46	17,96	1,73	0,57	2,85	0,07	2,27	0,80	463,4	10,1	459,5	10,5	440,1	38,5	463,4	10,1	-0,8
CPV-14-254-Spot 50	1937,8	150925	2,37	17,74	1,43	0,58	3,28	0,08	2,95	0,90	467,5	13,3	467,4	12,3	467,0	31,7	467,5	13,3	0,0
CPV-14-254-Spot 104	446,7	183705	3,44	17,87	1,61	0,59	3,01	0,08	2,54	0,84	471,5	11,6	468,0	11,3	450,7	35,9	471,5	11,6	-0,8
CPV-14-254-Spot 18	1717,3	171394	1,05	17,85	1,28	0,59	2,31	0,08	1,92	0,83	477,8	8,8	473,6	8,7	453,1	28,5	477,8	8,8	-0,9
CPV-14-254-Spot 58	209,4	101731	1,85	17,55	3,11	0,61	3,84	0,08	2,26	0,59	480,0	10,4	481,8	14,7	490,4	68,6	480,0	10,4	0,4
CPV-14-254-Spot 84	278,1	76294	2,03	17,48	3,40	0,61	4,19	0,08	2,45	0,59	482,6	11,4	485,6	16,2	499,4	74,8	482,6	11,4	0,6
CPV-14-254-Spot 95	364,2	149476	1,48	17,88	2,59	0,61	3,57	0,08	2,46	0,69	488,0	11,5	481,3	13,7	449,3	57,6	488,0	11,5	-1,4
CPV-14-254-Spot 16	1774,8	344187	27,32	17,80	1,46	0,61	3,51	0,08	3,19	0,91	490,0	15,1	484,6	13,5	459,1	32,5	490,0	15,1	-1,1
CPV-14-254-Spot 55	971,8	173867	4,14	17,30	1,60	0,64	3,52	0,08	3,13	0,89	498,7	15,0	502,8	14,0	521,7	35,2	498,7	15,0	0,8
CPV-14-254-Spot 68	681,0	980608	1,59	16,37	2,26	0,84	4,36	0,10	3,73	0,85	610,2	21,7	617,0	20,2	641,8	48,6	610,2	21,7	1,1
CPV-14-254-Spot 70	183,0	391749	1,32	14,55	2,58	1,24	3,65	0,13	2,58	0,71	792,5	19,3	818,9	20,5	891,2	53,2	792,5	19,3	3,2

Sample																				
CPV-14-254-Spot 80	895,8	75835	1,06	15,09	1,79	1,30	2,71	0,14	2,04	0,75	858,6	16,4	846,5	15,6	814,9	37,5	858,6	16,4	-1,4	
CPV-14-254-Spot 24	1691,3	428707	1,95	13,63	1,70	1,70	3,12	0,17	2,62	0,84	1002,7	24,3	1009,4	20,0	1024,0	34,4	1024,0	34,4	0,7	
CPV-14-254-Spot 81	856,7	125089	1,64	13,54	1,61	1,86	3,37	0,18	2,96	0,88	1079,4	29,4	1065,8	22,3	1038,1	32,6	1038,1	32,6	-1,3	
CPV-14-254-Spot 7	806,2	541103	1,22	13,50	1,49	1,65	2,85	0,16	2,43	0,85	966,1	21,8	989,9	18,0	1043,0	30,2	1043,0	30,2	2,4	
CPV-14-254-Spot 30	459,9	796110	1,02	8,33	1,85	6,06	2,51	0,37	1,70	0,68	2010,6	29,4	1984,3	21,9	1956,9	33,0	1956,9	33,0	-1,3	
CPV-14-261 (DZ)	Maximum depositinal age (3+DZ, 2σ): 303.3±2.1 Ma (MSWD = 1.3)																			
CPV-14-261-Spot 1	126,0	19401	1,16	18,55	3,52	0,35	4,76	0,05	3,21	0,67	295,9	9,3	304,1	12,5	367,2	79,3	295,9	9,3	2,7	*
CPV-14-261-Spot 38	93,3	46085	1,82	19,24	3,12	0,34	6,72	0,05	5,95	0,89	296,4	17,2	295,0	17,2	284,4	71,4	296,4	17,2	-0,5	*
CPV-14-261-Spot 4	188,6	17380	1,31	19,30	2,14	0,34	4,28	0,05	3,70	0,87	297,3	10,8	295,0	11,0	277,0	49,1	297,3	10,8	-0,8	*
CPV-14-261-Spot 30	195,6	217441	1,11	19,12	3,16	0,34	4,89	0,05	3,74	0,76	297,5	10,9	297,7	12,6	298,6	72,0	297,5	10,9	0,0	*
CPV-14-261-Spot 19	154,9	18294	6,88	19,48	2,56	0,33	3,77	0,05	2,77	0,73	297,6	8,1	292,8	9,6	255,3	58,8	297,6	8,1	-1,6	*
CPV-14-261-Spot 18	127,3	53461	1,38	19,79	2,27	0,33	4,54	0,05	3,93	0,87	297,7	11,4	289,0	11,4	219,2	52,6	297,7	11,4	-3,0	*
CPV-14-261-Spot 13	83,5	24803	1,40	19,41	3,51	0,34	4,55	0,05	2,89	0,64	297,9	8,4	294,1	11,6	264,6	80,7	297,9	8,4	-1,3	*
CPV-14-261-Spot 29	71,9	75862	1,75	19,03	3,94	0,34	5,35	0,05	3,63	0,68	298,3	10,6	299,5	13,9	309,3	89,6	298,3	10,6	0,4	*
CPV-14-261-Spot 14	120,0	32203	1,74	18,80	3,19	0,35	5,92	0,05	4,98	0,84	298,3	14,5	302,8	15,5	337,2	72,3	298,3	14,5	1,5	*
CPV-14-261-Spot 15	89,7	48875	1,52	19,35	2,69	0,34	4,58	0,05	3,71	0,81	299,0	10,8	295,9	11,8	271,7	61,6	299,0	10,8	-1,0	*
CPV-14-261-Spot 39	120,7	18851	1,58	18,69	2,70	0,35	4,32	0,05	3,38	0,78	299,1	9,9	305,0	11,4	350,4	61,1	299,1	9,9	1,9	*
CPV-14-261-Spot 12	128,1	31831	1,20	18,96	2,74	0,35	7,12	0,05	6,57	0,92	299,6	19,2	301,7	18,6	318,3	62,2	299,6	19,2	0,7	*
CPV-14-261-Spot 35	113,3	45192	1,95	19,94	3,77	0,33	4,74	0,05	2,86	0,60	299,6	8,4	288,8	11,9	201,9	87,6	299,6	8,4	-3,8	*
CPV-14-261-Spot 25	111,4	27320	1,46	19,56	3,27	0,34	4,02	0,05	2,34	0,58	299,8	6,8	293,8	10,2	246,5	75,3	299,8	6,8	-2,0	*
CPV-14-261-Spot 5	257,0	31522	1,12	19,47	2,59	0,34	3,82	0,05	2,80	0,73	300,2	8,2	295,3	9,8	257,1	59,6	300,2	8,2	-1,6	*
CPV-14-261-Spot 24	100,9	12596	1,13	19,62	3,60	0,34	4,88	0,05	3,29	0,67	300,6	9,7	293,7	12,4	238,9	83,1	300,6	9,7	-2,4	*
CPV-14-261-Spot 9	121,3	42878	1,07	19,15	3,01	0,34	5,35	0,05	4,42	0,83	301,4	13,0	300,7	13,9	295,1	68,7	301,4	13,0	-0,2	*
CPV-14-261-Spot 37	134,7	23143	2,11	19,18	1,77	0,35	4,34	0,05	3,97	0,91	302,3	11,7	301,1	11,3	291,9	40,3	302,3	11,7	-0,4	*
CPV-14-261-Spot 17	152,0	23895	0,80	19,31	2,47	0,34	5,40	0,05	4,80	0,89	303,3	14,2	300,1	14,0	275,7	56,7	303,3	14,2	-1,0	*
CPV-14-261-Spot 26	124,9	48796	1,29	19,75	2,80	0,34	4,10	0,05	2,99	0,73	303,5	8,9	294,5	10,5	223,7	64,8	303,5	8,9	-3,1	*
CPV-14-261-Spot 23	123,5	100386	1,33	18,52	2,28	0,36	4,25	0,05	3,58	0,84	304,9	10,7	312,7	11,4	371,4	51,4	304,9	10,7	2,5	*

Sample																				
CPV-14-261-Spot 40	152,6	37601	1,61	19,32	2,22	0,35	3,68	0,05	2,94	0,80	305,1	8,8	301,6	9,6	275,1	50,8	305,1	8,8	-1,1	*
CPV-14-261-Spot 6	87,0	71445	1,41	19,22	2,09	0,35	6,08	0,05	5,70	0,94	305,4	17,0	303,2	15,9	286,2	47,9	305,4	17,0	-0,7	*
CPV-14-261-Spot 28	151,2	30842	1,18	19,11	2,77	0,35	4,14	0,05	3,08	0,74	307,1	9,2	306,3	11,0	299,8	63,2	307,1	9,2	-0,3	*
CPV-14-261-Spot 20	64,2	28510	1,51	18,92	4,06	0,36	5,10	0,05	3,09	0,61	307,3	9,3	309,1	13,6	322,9	92,2	307,3	9,3	0,6	*
CPV-14-261-Spot 16	62,0	16230	1,16	18,35	4,06	0,37	5,23	0,05	3,30	0,63	308,9	10,0	318,8	14,3	391,8	91,1	308,9	10,0	3,1	*
CPV-14-261-Spot 2	185,5	83606	1,96	18,98	3,30	0,36	4,71	0,05	3,35	0,71	310,0	10,1	310,6	12,6	315,7	75,1	310,0	10,1	0,2	*
CPV-14-261-Spot 36	175,2	686937	1,09	18,82	2,90	0,36	4,16	0,05	2,99	0,72	310,6	9,1	313,5	11,2	335,0	65,7	310,6	9,1	0,9	*
CPV-14-261-Spot 10	55,7	9683	1,91	19,51	2,73	0,35	6,70	0,05	6,12	0,91	312,1	18,6	305,1	17,7	251,8	62,7	312,1	18,6	-2,3	*
CPV-14-261-Spot 22	79,3	37830	1,69	19,79	3,64	0,35	4,54	0,05	2,72	0,60	312,5	8,3	301,8	11,9	219,8	84,3	312,5	8,3	-3,5	*
CPV-14-261-Spot 8	67,6	6417	0,93	19,40	4,00	0,35	5,97	0,05	4,43	0,74	313,3	13,6	307,8	15,9	265,9	91,9	313,3	13,6	-1,8	*
CPV-14-261-Spot 21	92,0	24388	0,99	19,18	2,98	0,36	3,98	0,05	2,64	0,66	314,8	8,1	312,0	10,7	291,1	68,0	314,8	8,1	-0,9	*
CPV-14-261-Spot 11	82,4	22279	1,32	19,62	2,91	0,36	6,01	0,05	5,25	0,87	317,8	16,3	308,5	16,0	239,4	67,2	317,8	16,3	-3,0	*
CPV-14-261-Spot 3	82,9	31376	1,07	19,72	3,84	0,35	4,66	0,05	2,63	0,56	318,7	8,2	308,1	12,4	228,2	88,8	318,7	8,2	-3,5	*
CPV-14-261-Spot 7	100,8	16086	1,13	18,72	3,48	0,40	5,55	0,05	4,32	0,78	341,3	14,4	341,9	16,1	346,3	78,8	341,3	14,4	0,2	*
~~CPV-14-261-Spot 27~~	~~117,8~~	~~30513~~	~~1,30~~	~~14,45~~	~~12,20~~	~~0,52~~	~~12,74~~	~~0,05~~	~~3,66~~	~~0,29~~	~~343,7~~	~~12,3~~	~~426,8~~	~~44,4~~	~~904,6~~	~~252,3~~	~~343,7~~	~~12,3~~	~~19,5~~	~~*~~
CPV-14-268 (IZ)	Weighted mean age: 203.5 ±1.6 Ma (MSWD = 1.5)																			
~~CPV-14-268-Spot 30~~	~~82,4~~	~~16238~~	~~0,8~~	~~10,1290~~	~~4,1~~	~~0,3709~~	~~4,8~~	~~0,0272~~	~~2,5~~	~~0,52~~	~~173,3~~	~~4,3~~	~~320,3~~	~~13,3~~	~~1600,0~~	~~77,0~~	~~173,3~~	~~4,3~~	~~45,9~~	~~**~~
~~CPV-14-268-Spot 10~~	~~127,7~~	~~7131~~	~~0,7~~	~~21,1425~~	~~4,4~~	~~0,2129~~	~~5,3~~	~~0,0326~~	~~3,0~~	~~0,57~~	~~207,1~~	~~6,1~~	~~196,0~~	~~9,5~~	~~64,3~~	~~104,2~~	~~207,1~~	~~6,1~~	~~-5,7~~	~~**~~
CPV-14-268-Spot 19	238,3	39493	1,2	19,4080	2,7	0,2151	3,4	0,0303	2,1	0,60	192,3	3,9	197,9	6,1	264,4	62,5	192,3	3,9	2,8	**
CPV-14-268-Spot 12	145,2	11964	0,7	20,8929	4,0	0,2047	4,8	0,0310	2,6	0,54	196,9	5,0	189,1	8,3	92,5	95,6	196,9	5,0	-4,1	**
CPV-14-268-Spot 6	125,1	31059	1,9	18,9452	3,4	0,2292	4,9	0,0315	3,4	0,71	199,9	6,8	209,5	9,2	319,5	78,2	199,9	6,8	4,6	**
CPV-14-268-Spot 23	110,4	10602	1,5	20,6714	4,3	0,2104	5,5	0,0315	3,5	0,63	200,2	6,8	193,9	9,7	117,7	100,7	200,2	6,8	-3,3	**
CPV-14-268-Spot 1	147,1	26659	1,8	19,8477	2,6	0,2202	4,3	0,0317	3,4	0,79	201,2	6,7	202,1	7,9	212,7	60,6	201,2	6,7	0,5	**
CPV-14-268-Spot 38	260,5	113488	1,1	19,7874	2,8	0,2212	3,6	0,0317	2,4	0,65	201,4	4,7	202,9	6,7	219,8	64,2	201,4	4,7	0,7	**
CPV-14-268-Spot 39	138,5	25955	0,7	16,6873	2,9	0,2624	5,3	0,0318	4,4	0,84	201,5	8,8	236,6	11,2	600,9	63,0	201,5	8,8	14,8	**
CPV-14-268-Spot 11	117,3	25229	1,5	20,2486	3,8	0,2174	4,8	0,0319	3,1	0,63	202,6	6,1	199,7	8,8	166,2	87,7	202,6	6,1	-1,4	**
CPV-14-268-Spot 14	377,8	31548	0,8	19,7055	2,5	0,2235	3,7	0,0319	2,6	0,72	202,7	5,3	204,8	6,8	229,3	58,4	202,7	5,3	1,0	**

CPV-14-268-Spot 13	267,7	1,9	19,6508	2,6	0,2241	3,3	0,0319	2,1	0,63	202,7	4,2	205,3	6,2	235,8	59,3	202,7	4,2	1,3	**
CPV-14-268-Spot 2	178,8	1,7	20,2092	3,9	0,2183	5,0	0,0320	3,2	0,64	203,0	6,4	200,5	9,1	170,7	90,2	203,0	6,4	-1,3	**
CPV-14-268-Spot 4	261,8	0,8	19,5013	1,8	0,2267	2,5	0,0321	1,7	0,70	203,4	3,5	207,4	4,7	253,4	41,2	203,4	3,5	1,9	**
CPV-14-268-Spot 28	211,3	1,2	19,9388	3,4	0,2218	4,1	0,0321	2,3	0,56	203,5	4,6	203,4	7,6	202,1	79,9	203,5	4,6	-0,1	**
CPV-14-268-Spot 40	72,3	2,2	19,8616	6,0	0,2232	6,6	0,0321	2,8	0,42	204,0	5,6	204,6	12,3	211,1	139,6	204,0	5,6	0,3	**
CPV-14-268-Spot 16	38,7	1,1	19,7650	5,1	0,2243	5,9	0,0322	3,1	0,52	204,0	6,2	205,5	11,1	222,4	117,6	204,0	6,2	0,7	**
CPV-14-268-Spot 20	204,2	0,9	19,4502	3,2	0,2315	4,4	0,0327	3,0	0,69	207,2	6,1	211,5	8,3	259,4	72,4	207,2	6,1	2,0	**
CPV-14-268-Spot 18	87,8	1,0	20,1611	2,8	0,2249	5,9	0,0329	5,2	0,88	208,6	10,8	206,0	11,1	176,3	65,2	208,6	10,8	-1,3	**
CPV-14-268-Spot 22	76,5	2,1	20,0570	5,6	0,2276	7,4	0,0331	4,8	0,65	209,9	10,0	208,2	13,9	188,4	130,1	209,9	10,0	-0,8	**
CPV-14-268-Spot 17	80,9	1,1	20,2701	3,7	0,2258	4,9	0,0332	3,2	0,65	210,5	6,5	206,7	9,1	163,7	86,8	210,5	6,5	-1,8	**
CPV-14-268-Spot 24	81,9	1,2	19,5053	5,0	0,2349	5,7	0,0332	2,9	0,50	210,7	6,0	214,2	11,1	252,9	114,2	210,7	6,0	1,6	**
CPV-14-268-Spot 8	99,2	1,6	18,4196	3,0	0,2489	5,1	0,0333	4,1	0,81	210,9	8,5	225,7	10,3	383,1	67,4	210,9	8,5	6,6	**
CPV-14-268-Spot 15	133,0	2,4	19,0225	3,8	0,2459	4,4	0,0339	2,2	0,50	215,1	4,7	223,2	8,9	310,3	87,0	215,1	4,7	3,7	**
CPV-14-268-Spot 9	124,8	1,5	19,9489	3,3	0,2581	4,2	0,0373	2,5	0,60	236,3	5,8	233,1	8,7	200,9	77,8	236,3	5,8	-1,4	
CPV-14-268-Spot 5	20,6	1,3	19,9594	8,1	0,2862	8,5	0,0414	2,4	0,28	261,7	6,1	255,6	19,1	199,7	189,1	261,7	6,1	-2,4	
CPV-14-268-Spot 37	340,4	0,9	19,0029	2,3	0,3154	3,2	0,0435	2,2	0,69	274,3	6,0	278,3	7,8	312,6	52,8	274,3	6,0	1,5	
CPV-14-268-Spot 21	133,6	0,9	18,6902	2,8	0,3266	5,0	0,0443	4,1	0,82	279,3	11,2	287,0	12,4	350,2	64,4	279,3	11,2	2,7	
CPV-14-268-Spot 25	199,6	1,5	18,7442	2,9	0,3266	3,7	0,0444	2,2	0,61	280,1	6,1	287,0	9,1	343,7	65,9	280,1	6,1	2,4	
CPV-14-268-Spot 35	391,3	0,7	19,3155	2,2	0,3184	3,2	0,0446	2,3	0,73	281,3	6,4	280,7	7,9	275,3	50,6	281,3	6,4	-0,2	
CPV-14-268-Spot 3	113,3	1,9	18,4549	3,8	0,3335	5,6	0,0446	4,0	0,73	281,5	11,1	292,3	14,1	378,8	85,9	281,5	11,1	3,7	
CPV-14-268-Spot 27	134,8	1,0	18,3371	1,9	0,3380	3,2	0,0449	2,5	0,79	283,4	7,0	295,6	8,1	393,2	43,5	283,4	7,0	4,1	
CPV-14-268-Spot 7	94,6	1,1	19,3865	4,1	0,3283	8,2	0,0462	7,1	0,87	290,9	20,3	288,3	20,7	267,0	94,8	290,9	20,3	-0,9	
CPV-14-268-Spot 26	394,9	0,8	19,1838	1,4	0,3353	2,6	0,0466	2,2	0,84	293,9	6,3	293,6	6,6	291,0	32,1	293,9	6,3	-0,1	
CPV-14-268-Spot 29	463,1	1,7	18,8635	1,8	0,3544	2,8	0,0485	2,2	0,77	305,2	6,5	308,0	7,5	329,3	41,2	305,2	6,5	0,9	
CPV-14-268-Spot 36	79,0	1,5	19,0617	3,6	0,3597	5,4	0,0497	4,0	0,75	312,9	12,3	312,0	14,4	305,5	81,0	312,9	12,3	-0,3	
CPV-14-157 (IZ)	Concordance age: 211.5 ±1.8 Ma (MSWD = 0.31)																		
CPV-14-157-Spot 37	417,1	1,9	19,8729	2,6	0,2207	4,1	0,0318	3,2	0,77	201,9	6,3	202,5	7,6	209,8	61,2	201,9	6,3	0,3	

176

Spot																			
CPV-14-157-Spot 35	673,3	32387	1,4	19,5932	2,1	0,2265	4,2	0,0322	3,6	0,87	204,2	7,3	207,3	7,8	242,5	48,2	204,2	7,3	1,5
CPV-14-157-Spot 18	460,7	53964	1,9	19,4638	3,0	0,2296	5,3	0,0324	4,3	0,83	205,6	8,8	209,8	10,0	257,8	67,9	205,6	8,8	2,0
CPV-14-157-Spot 29	148,9	6885	3,5	20,5813	4,0	0,2176	4,7	0,0325	2,4	0,52	206,0	4,9	199,9	8,4	128,0	93,6	206,0	4,9	-3,1
CPV-14-157-Spot 6	367,2	22204	1,8	19,6003	3,2	0,2301	4,2	0,0327	2,7	0,65	207,5	5,6	210,3	8,0	241,7	74,2	207,5	5,6	1,3
CPV-14-157-Spot 30	221,0	15545	1,6	20,2472	4,3	0,2228	5,8	0,0327	3,9	0,68	207,6	8,1	204,3	10,8	166,3	100,1	207,6	8,1	-1,6
CPV-14-157-Spot 40	112,6	9033	2,7	20,4106	5,2	0,2214	7,1	0,0328	4,8	0,67	207,9	9,7	203,1	13,0	147,5	122,7	207,9	9,7	-2,4
CPV-14-157-Spot 38	209,4	29216	2,4	19,8441	3,1	0,2282	5,1	0,0328	4,0	0,80	208,4	8,2	208,7	9,5	213,1	71,0	208,4	8,2	0,2
CPV-14-157-Spot 17	211,0	47135	2,2	18,9999	4,8	0,2392	5,8	0,0330	3,3	0,57	209,1	6,9	217,8	11,4	313,0	109,0	209,1	6,9	4,0
CPV-14-157-Spot 20	264,0	18792	2,6	19,1378	4,3	0,2378	7,8	0,0330	6,5	0,83	209,3	13,3	216,6	15,1	296,5	98,2	209,3	13,3	3,4
CPV-14-157-Spot 15	548,1	68076	1,3	19,4989	2,5	0,2348	3,6	0,0332	2,7	0,74	210,5	5,5	214,1	7,0	253,7	56,6	210,5	5,5	1,7
CPV-14-157-Spot 16	437,2	32214	2,0	20,6939	3,6	0,2222	5,5	0,0334	4,2	0,76	211,5	8,7	203,8	10,2	115,2	85,4	211,5	8,7	-3,8
CPV-14-157-Spot 39	860,3	33959	2,2	20,0816	2,6	0,2291	4,6	0,0334	3,8	0,82	211,6	7,9	209,4	8,8	185,5	61,3	211,6	7,9	-1,0
CPV-14-157-Spot 24	253,6	12737	2,5	20,3600	3,4	0,2259	8,3	0,0334	7,6	0,91	211,6	15,8	206,8	15,6	153,4	80,1	211,6	15,8	-2,3
CPV-14-157-Spot 2	279,0	21517	2,2	20,2316	3,7	0,2277	6,1	0,0334	4,9	0,80	211,9	10,1	208,3	11,5	168,1	85,9	211,9	10,1	-1,7
CPV-14-157-Spot 5	327,1	27376	1,7	20,0463	3,0	0,2299	4,3	0,0334	3,1	0,71	212,0	6,4	210,1	8,2	189,6	70,1	212,0	6,4	-0,9
CPV-14-157-Spot 22	747,6	51554	1,8	19,6997	2,8	0,2342	5,8	0,0335	5,0	0,87	212,2	10,5	213,7	11,1	230,0	65,5	212,2	10,5	0,7
CPV-14-157-Spot 3	393,9	24870	2,0	20,0809	3,8	0,2298	5,5	0,0335	4,0	0,72	212,2	8,3	210,1	10,4	185,6	88,9	212,2	8,3	-1,0
CPV-14-157-Spot 23	166,6	38957	2,6	20,8225	4,7	0,2219	7,0	0,0335	5,2	0,74	212,5	10,9	203,5	13,0	100,5	112,2	212,5	10,9	-4,4
CPV-14-157-Spot 26	283,7	89322	2,1	20,2888	2,5	0,2287	4,1	0,0336	3,3	0,80	213,3	6,9	209,1	7,8	161,6	57,9	213,3	6,9	-2,0
CPV-14-157-Spot 28	295,1	16405	2,5	20,0989	2,9	0,2313	4,4	0,0337	3,4	0,76	213,8	7,1	211,3	8,5	183,5	66,5	213,8	7,1	-1,2
CPV-14-157-Spot 4	438,6	6337	1,5	20,8249	3,7	0,2233	4,9	0,0337	3,3	0,66	213,9	6,8	204,7	9,1	100,2	87,6	213,9	6,8	-4,5
CPV-14-157-Spot 13	256,6	15576	2,0	20,5955	3,2	0,2264	4,2	0,0338	2,8	0,66	214,4	5,8	207,2	7,9	126,4	74,4	214,4	5,8	-3,5
CPV-14-157-Spot 36	269,4	26811	2,1	19,6746	2,9	0,2376	4,3	0,0339	3,2	0,74	214,9	6,7	216,4	8,3	233,0	66,3	214,9	6,7	0,7
CPV-14-157-Spot 27	149,9	30149	1,7	19,6501	3,4	0,2381	5,1	0,0339	3,8	0,74	215,1	8,0	216,9	9,9	235,9	78,6	215,1	8,0	0,8
CPV-14-157-Spot 11	286,1	37174	2,2	19,8052	3,3	0,2366	6,3	0,0340	5,3	0,85	215,4	11,2	215,6	12,2	217,7	77,4	215,4	11,2	0,1
CPV-14-157-Spot 9	384,2	32269	2,3	19,8686	2,1	0,2360	4,8	0,0340	4,3	0,90	215,6	9,2	215,2	9,3	210,3	47,9	215,6	9,2	-0,2
CPV-14-157-Spot 25	268,6	37683	2,3	14,7851	5,3	0,3174	6,1	0,0340	3,0	0,49	215,8	6,3	279,9	14,8	857,4	109,8	215,8	6,3	22,9
CPV-14-157-Spot 14	346,8	33364	1,8	20,2506	2,6	0,2341	3,8	0,0344	2,8	0,73	217,9	6,0	213,6	7,3	166,0	61,0	217,9	6,0	-2,0

Sample																			
CPV-14-157-Spot 1	268,8	107742	1,9	20,3242	3,9	0,2343	5,6	0,0345	3,9	0,71	218,9	8,5	213,8	10,7	157,5	92,1	218,9	8,5	-2,4	
CPV-14-157-Spot 12	347,3	69700	2,0	19,5195	2,9	0,2446	4,0	0,0346	2,8	0,70	219,4	6,0	222,1	7,9	251,2	65,8	219,4	6,0	1,2	
CPV-14-157-Spot 8	159,7	12913	2,3	20,2485	3,2	0,2389	5,5	0,0351	4,4	0,80	222,3	9,6	217,6	10,7	166,2	75,7	222,3	9,6	-2,2	
CPV-14-157-Spot 21	297,6	28466	2,5	20,0795	3,4	0,2413	5,0	0,0351	3,6	0,73	222,6	8,0	219,5	9,8	185,7	79,4	222,6	8,0	-1,4	
~~CPV-14-157-Spot 7~~	~~350,8~~	~~29158~~	~~1,9~~	~~20,0576~~	~~3,4~~	~~0,2342~~	~~5,1~~	~~0,0356~~	~~3,8~~	~~0,75~~	~~225,5~~	~~8,4~~	~~213,7~~	~~9,8~~	~~85,2~~	~~80,6~~	~~225,5~~	~~8,4~~	~~-5,5~~	
CPV-14-266 (DZ) Maximum depositinal age (3+DZ, 1σ): 207.3±3.1 Ma (MSWD = 0.67)																				
CPV-14-266-Spot 22	45,2	11652	1,03	19,58	6,61	0,23	8,63	0,03	5,55	0,64	204,3	11,2	207,5	16,2	243,9	152,3	204,3	11,2	1,5	*
CPV-14-266-Spot 37	143,9	13066	1,00	19,73	3,75	0,23	4,28	0,03	2,06	0,48	206,2	4,2	207,8	8,0	225,9	86,8	206,2	4,2	0,8	*
CPV-14-266-Spot 9	175,5	38216	1,39	19,69	2,73	0,23	3,75	0,03	2,58	0,69	209,6	5,3	211,5	7,2	231,6	63,0	209,6	5,3	0,9	*
~~CPV-14-266-Spot 2~~	~~51,2~~	~~13105~~	~~1,39~~	~~21,64~~	~~5,71~~	~~0,21~~	~~6,59~~	~~0,03~~	~~3,29~~	~~0,50~~	~~211,7~~	~~6,8~~	~~195,8~~	~~11,7~~	~~8,4~~	~~137,6~~	~~211,7~~	~~6,8~~	~~8,1~~	
CPV-14-266-Spot 39	147,0	64803	2,27	19,98	3,37	0,23	4,66	0,03	3,23	0,69	214,1	6,8	212,7	9,0	197,8	78,2	214,1	6,8	-0,6	
CPV-14-266-Spot 29	75,1	19689	1,66	19,23	4,51	0,27	5,55	0,04	3,25	0,58	236,0	7,5	240,5	11,9	285,0	103,1	236,0	7,5	1,9	
CPV-14-266-Spot 26	70,9	6979	2,30	19,49	4,54	0,32	8,47	0,05	7,15	0,84	287,3	20,1	283,7	21,0	254,4	104,3	287,3	20,1	-1,3	
CPV-14-266-Spot 25	95,5	40722	1,76	18,94	3,69	0,33	4,35	0,05	2,29	0,53	287,6	6,4	291,2	11,0	320,3	84,0	287,6	6,4	1,2	
CPV-14-266-Spot 40	48,7	20433	1,98	19,20	5,31	0,33	5,67	0,05	1,99	0,35	288,9	5,6	288,9	14,3	288,7	121,4	288,9	5,6	0,0	
CPV-14-266-Spot 27	120,9	29953	2,26	19,80	2,27	0,32	2,80	0,05	1,64	0,59	290,1	4,7	282,2	6,9	217,8	52,6	290,1	4,7	-2,8	
CPV-14-266-Spot 20	100,3	13394	1,93	19,94	3,24	0,32	4,44	0,05	3,04	0,68	290,4	8,6	280,9	10,9	202,2	75,2	290,4	8,6	-3,4	
~~CPV-14-266-Spot 38~~	~~30,5~~	~~5004~~	~~1,48~~	~~21,09~~	~~4,29~~	~~0,30~~	~~6,30~~	~~0,05~~	~~4,61~~	~~0,73~~	~~291,2~~	~~13,1~~	~~268,0~~	~~14,8~~	~~70,3~~	~~102,1~~	~~291,2~~	~~13,1~~	~~-8,6~~	
~~CPV-14-266-Spot 36~~	~~91,2~~	~~9284~~	~~1,05~~	~~21,02~~	~~4,76~~	~~0,30~~	~~5,81~~	~~0,05~~	~~3,34~~	~~0,57~~	~~291,5~~	~~9,5~~	~~269,0~~	~~13,7~~	~~77,8~~	~~113,0~~	~~291,5~~	~~9,5~~	~~-8,3~~	
CPV-14-266-Spot 13	161,1	98581	1,95	18,80	2,77	0,34	3,51	0,05	2,16	0,62	291,6	6,2	296,7	9,0	336,8	62,7	291,6	6,2	1,7	
CPV-14-266-Spot 6	267,8	25650	1,24	19,56	3,74	0,33	4,71	0,05	2,86	0,61	292,5	8,2	287,4	11,8	246,2	86,2	292,5	8,2	-1,8	
CPV-14-266-Spot 28	138,1	38192	1,33	19,35	3,17	0,33	4,22	0,05	2,78	0,66	293,5	8,0	291,1	10,7	271,5	72,7	293,5	8,0	-0,8	
CPV-14-266-Spot 24	58,6	74264	0,84	19,51	5,25	0,33	7,02	0,05	4,67	0,66	293,8	13,4	289,3	17,7	252,7	120,8	293,8	13,4	-1,6	
CPV-14-266-Spot 19	102,8	45223	1,53	18,89	2,87	0,34	3,84	0,05	2,54	0,66	294,3	7,3	297,9	9,9	326,3	65,2	294,3	7,3	1,2	
CPV-14-266-Spot 15	117,5	33901	1,46	19,94	2,64	0,32	3,71	0,05	2,61	0,70	295,5	7,5	285,2	9,2	201,8	61,4	295,5	7,5	-3,6	
CPV-14-266-Spot 3	153,9	27986	1,42	19,45	2,70	0,33	3,98	0,05	2,93	0,74	297,1	8,5	292,9	10,1	259,4	62,0	297,1	8,5	-1,4	
CPV-14-266-Spot 17	169,4	37073	1,65	19,14	2,79	0,34	3,73	0,05	2,47	0,66	297,3	7,2	297,2	9,6	296,6	63,7	297,3	7,2	0,0	

CPV-14-266-Spot 12	277,5	42728	1,58	18,93	2,82	0,34	4,02	0,05	2,86	0,71	297,6	8,3	300,2	10,4	321,0	64,0	297,6	8,3	0,9
CPV-14-266-Spot 4	310,4	39920	1,49	18,79	2,00	0,35	2,83	0,05	2,01	0,71	297,6	5,9	302,2	7,4	338,2	45,2	297,6	5,9	1,5
CPV-14-266-Spot 11	161,2	116016	1,40	18,98	2,57	0,34	5,01	0,05	4,30	0,86	298,7	12,6	300,6	13,0	315,7	58,3	298,7	12,6	0,6
CPV-14-266-Spot 1	568,4	51551	1,39	19,21	2,36	0,34	3,98	0,05	3,20	0,80	299,6	9,4	298,3	10,3	288,0	54,0	299,6	9,4	-0,4
CPV-14-266-Spot 8	25,8	104599	1,19	19,79	7,15	0,33	8,84	0,05	5,21	0,59	299,8	15,3	290,9	22,4	219,7	165,5	299,8	15,3	-3,1
CPV-14-266-Spot 5	193,9	33954	1,64	19,41	2,76	0,34	4,64	0,05	3,74	0,80	300,2	11,0	296,1	11,9	263,7	63,3	300,2	11,0	-1,4
CPV-14-266-Spot 7	146,4	56710	1,48	19,41	3,40	0,34	4,37	0,05	2,74	0,63	300,2	8,0	296,2	11,2	264,3	78,0	300,2	8,0	-1,4
CPV-14-266-Spot 16	284,8	28283	1,30	19,29	2,15	0,34	3,51	0,05	2,78	0,79	301,0	8,2	298,4	9,1	278,2	49,2	301,0	8,2	-0,9
CPV-14-266-Spot 10	66,3	9532	1,96	19,84	5,20	0,33	7,34	0,05	5,18	0,71	301,3	15,3	291,5	18,6	213,2	120,5	301,3	15,3	-3,4
CPV-14-266-Spot 14	162,8	59327	1,48	18,55	4,28	0,36	5,70	0,05	3,75	0,66	302,7	11,1	310,3	15,2	367,5	96,6	302,7	11,1	2,4
CPV-14-266-Spot 35	154,2	31510	0,97	18,74	3,18	0,35	6,37	0,05	5,52	0,87	303,0	16,3	307,7	16,9	344,1	71,9	303,0	16,3	1,6
CPV-14-266-Spot 18	134,7	25940	1,33	18,88	2,64	0,35	3,58	0,05	2,42	0,68	303,5	7,2	306,2	9,5	327,3	59,9	303,5	7,2	0,9
CPV-14-266-Spot 30	101,0	28916	1,44	19,44	4,03	0,34	5,62	0,05	3,92	0,70	303,5	11,6	298,6	14,5	260,1	92,6	303,5	11,6	-1,7
CPV-14-266-Spot 21	71,0	7264	1,66	19,94	3,73	0,34	6,29	0,05	5,06	0,80	310,0	15,3	297,7	16,2	202,0	86,7	310,0	15,3	-4,1
CPV-14-266-Spot 23	60,6	9578	1,31	19,79	3,94	0,35	7,07	0,05	5,87	0,83	311,6	17,9	301,0	18,4	219,3	91,3	311,6	17,9	-3,5

Análisis medidos en el Laboratorio de Estudios Isotópicos de la Universidad Autónoma de México

Analysis	U (ppm)	Th (ppm)	Th/U	CORRECTED RATIOS									CORRECTED AGES (Ma)									
				207Pb/206Pb	±2s abs	207Pb/235U	±2s abs	206Pb/238U	±2s abs	208Pb/232Th	±2s abs	Rho	206Pb/238U	±2s	207Pb/235U	±2s	207Pb/206Pb	±2s	Best age (Ma)	±2s	Disc %
CPV-16-406 (DZ)																					
Zircon_043	293,0	167,0	0,570	0,087	0,003	0,447	0,020	0,035	0,001	0,046	0,004	0,300	222,5	4,8	374,0	14,0	1356,0	68,0	222,5	4,8	40,5
Zircon_020	266,0	221,0	0,831	0,051	0,003	0,252	0,014	0,036	0,001	0,011	0,000	0,163	226,9	4,9	229,0	11,0	250,0	110,0	226,9	4,9	0,9
Zircon_022	889,0	431,0	0,485	0,055	0,002	0,279	0,011	0,038	0,001	0,010	0,000	-0,101	240,7	4,4	249,3	8,3	381,0	62,0	240,7	4,4	3,4 *
Zircon_004	406,0	323,0	0,796	0,055	0,002	0,272	0,014	0,038	0,001	0,012	0,001	0,275	241,9	4,6	243,0	11,0	373,0	86,0	241,9	4,6	0,5 *
Zircon_095	128,0	123,0	0,961	0,056	0,004	0,289	0,024	0,039	0,001	0,013	0,001	0,049	247,6	6,6	256,0	19,0	390,0	160,0	247,6	6,6	3,3 *
Zircon_099	122,0	127,0	1,041	0,052	0,004	0,283	0,024	0,039	0,001	0,013	0,001	-0,061	248,3	7,4	254,0	20,0	280,0	190,0	248,3	7,4	2,2
Zircon_038	68,0	36,0	0,529	0,056	0,007	0,308	0,034	0,039	0,001	0,014	0,001	-0,032	248,9	8,7	269,0	27,0	410,0	250,0	248,9	8,7	7,5
Zircon_067	344,0	211,0	0,613	0,064	0,029	0,320	0,170	0,040	0,003	0,015	0,001	-0,352	251,4	8,6	282,0	85,0	730,0	380,0	251,4	8,6	10,9
Zircon_042	127,0	102,0	0,803	0,051	0,004	0,273	0,025	0,040	0,001	0,013	0,001	0,271	252,5	7,0	246,0	19,0	170,0	170,0	252,5	7,0	-2,6
Zircon_051	108,0	86,0	0,796	0,061	0,007	0,331	0,034	0,040	0,001	0,013	0,001	-0,088	254,5	8,0	297,0	25,0	590,0	220,0	254,5	8,0	14,3
Zircon_068	135,0	121,0	0,896	0,058	0,005	0,310	0,030	0,040	0,001	0,014	0,001	-0,096	254,6	7,6	280,0	23,0	500,0	190,0	254,6	7,6	9,1
Zircon_014	66,0	45,0	0,682	0,055	0,006	0,308	0,030	0,041	0,002	0,012	0,001	-0,062	255,9	9,9	273,0	24,0	340,0	230,0	255,9	9,9	6,3
Zircon_061	53,0	40,0	0,755	0,056	0,008	0,298	0,044	0,041	0,002	0,014	0,001	0,071	256,0	11,0	258,0	33,0	360,0	290,0	256,0	11,0	0,8
Zircon_086	150,0	134,0	0,893	0,073	0,055	0,380	0,360	0,041	0,002	0,015	0,005	-0,235	256,0	15,0	330,0	180,0	1070,0	520,0	256,0	15,0	22,4
Zircon_071	275,0	280,0	1,018	0,056	0,013	0,290	0,130	0,041	0,002	0,013	0,003	0,192	256,2	9,2	261,0	71,0	500,0	260,0	256,2	9,2	1,8
Zircon_030	75,0	76,0	1,013	0,055	0,006	0,307	0,030	0,041	0,001	0,013	0,001	0,006	256,5	7,9	272,0	23,0	420,0	220,0	256,5	7,9	5,7
Zircon_029	82,0	107,0	1,305	0,049	0,005	0,273	0,029	0,041	0,001	0,013	0,001	-0,040	257,0	7,5	242,0	23,0	110,0	210,0	257,0	7,5	-6,2
Zircon_100	54,0	42,0	0,778	0,076	0,019	0,400	0,140	0,041	0,002	0,016	0,003	-0,069	257,0	13,0	334,0	80,0	950,0	290,0	257,0	13,0	23,1

Maximum depositional age (3+DZ, 2σ): 242.5±7.7 Ma (MSWD = 1.6)

180

Sample	C1	C2	C3	C4	C5	C6	C7	C8	C9	C10	C11	C12	C13	C14	C15	C16	C17	C18	C19	C20	C21
Zircon_003	39,0	23,0	0,590	0,058	0,009	0,309	0,042	0,041	0,002	0,013	0,002	-0,192	259,0	12,0	267,0	32,0	290,0	290,0	259,0	12,0	3,0
Zircon_062	675,0	479,0	0,710	0,060	0,002	0,339	0,014	0,041	0,001	0,014	0,000	0,334	259,9	4,5	299,0	10,0	580,0	83,0	259,9	4,5	13,1
Zircon_037	36,0	24,0	0,667	0,049	0,006	0,295	0,032	0,041	0,002	0,015	0,001	-0,038	260,0	9,4	263,0	26,0	80,0	240,0	260,0	9,4	1,1
~~Zircon_083~~	~~87,0~~	~~109,0~~	~~1,253~~	~~0,051~~	~~0,005~~	~~0,265~~	~~0,028~~	~~0,044~~	~~0,001~~	~~0,013~~	~~0,001~~	~~0,126~~	~~261,5~~	~~7,8~~	~~240,0~~	~~22,0~~	~~150,0~~	~~210,0~~	~~261,5~~	~~7,8~~	~~9,0~~
Zircon_017	70,0	52,0	0,743	0,059	0,005	0,316	0,029	0,042	0,002	0,013	0,001	0,266	262,5	9,0	281,0	21,0	550,0	170,0	262,5	9,0	6,6
Zircon_085	296,0	357,0	1,206	0,053	0,002	0,298	0,012	0,042	0,001	0,013	0,000	-0,084	262,7	5,7	264,1	9,6	305,0	84,0	262,7	5,7	0,5
Zircon_005	100,0	60,0	0,600	0,055	0,005	0,312	0,029	0,042	0,001	0,014	0,001	-0,093	262,9	5,7	273,0	21,0	400,0	180,0	262,9	5,7	3,7
Zircon_033	60,0	41,0	0,683	0,059	0,007	0,324	0,039	0,042	0,001	0,015	0,001	0,067	263,0	8,4	281,0	29,0	570,0	240,0	263,0	8,4	6,4
Zircon_098	224,0	103,0	0,460	0,055	0,003	0,298	0,016	0,042	0,001	0,013	0,001	0,104	263,4	6,5	264,0	13,0	360,0	120,0	263,4	6,5	0,2
~~Zircon_101~~	~~75,0~~	~~59,0~~	~~0,787~~	~~0,051~~	~~0,005~~	~~0,284~~	~~0,029~~	~~0,042~~	~~0,001~~	~~0,014~~	~~0,001~~	~~-0,045~~	~~263,9~~	~~8,0~~	~~251,0~~	~~22,0~~	~~210,0~~	~~200,0~~	~~263,9~~	~~8,0~~	~~-5,1~~
Zircon_018	88,0	60,0	0,682	0,055	0,005	0,306	0,026	0,042	0,002	0,012	0,001	0,026	264,1	9,4	272,0	20,0	360,0	190,0	264,1	9,4	2,9
Zircon_054	185,0	148,0	0,800	0,049	0,003	0,291	0,018	0,042	0,001	0,014	0,001	-0,023	264,3	6,4	260,0	14,0	160,0	130,0	264,3	6,4	-1,7
Zircon_072	219,0	244,0	1,114	0,060	0,003	0,309	0,021	0,042	0,001	0,014	0,000	0,002	264,9	6,3	278,0	15,0	540,0	100,0	264,9	6,3	4,7
Zircon_089	262,0	236,0	0,901	0,055	0,003	0,310	0,016	0,042	0,001	0,014	0,000	0,157	265,1	5,4	273,0	12,0	390,0	110,0	265,1	5,4	2,9
Zircon_082	56,0	48,0	0,857	0,053	0,006	0,302	0,030	0,042	0,001	0,013	0,001	-0,125	265,4	8,1	269,0	23,0	270,0	210,0	265,4	8,1	1,3
Zircon_069	55,0	49,0	0,891	0,052	0,007	0,293	0,039	0,042	0,001	0,014	0,001	-0,001	265,9	8,7	261,0	30,0	240,0	280,0	265,9	8,7	-1,9
Zircon_021	137,0	110,0	0,803	0,053	0,004	0,308	0,023	0,042	0,001	0,013	0,001	-0,071	266,1	6,6	271,0	17,0	320,0	150,0	266,1	6,6	1,8
Zircon_012	239,0	168,0	0,703	0,058	0,003	0,328	0,020	0,042	0,001	0,014	0,001	-0,037	266,8	5,6	287,0	15,0	480,0	120,0	266,8	5,6	7,0
Zircon_025	705,0	678,0	0,962	0,054	0,003	0,306	0,022	0,042	0,002	0,013	0,002	-0,009	267,3	8,4	273,0	17,0	320,0	110,0	267,3	8,4	2,1
Zircon_039	485,0	213,0	0,439	0,052	0,002	0,307	0,013	0,042	0,001	0,014	0,000	0,038	267,4	5,1	271,0	10,0	276,0	88,0	267,4	5,1	1,3
Zircon_008	364,0	278,0	0,764	0,056	0,002	0,312	0,016	0,042	0,001	0,013	0,000	0,256	268,0	5,8	275,0	12,0	423,0	91,0	268,0	5,8	2,5
Zircon_052	123,0	61,0	0,496	0,053	0,004	0,314	0,026	0,043	0,001	0,013	0,001	0,123	268,0	6,4	275,0	20,0	300,0	160,0	268,0	6,4	2,5
Zircon_096	190,0	104,0	0,547	0,052	0,004	0,295	0,021	0,043	0,001	0,013	0,001	-0,007	268,7	6,0	261,0	17,0	270,0	160,0	268,7	6,0	-3,0
~~Zircon_016~~	~~51,0~~	~~37,0~~	~~0,725~~	~~0,048~~	~~0,007~~	~~0,290~~	~~0,037~~	~~0,042~~	~~0,002~~	~~0,012~~	~~0,001~~	~~0,101~~	~~269,0~~	~~10,0~~	~~253,0~~	~~27,0~~	~~90,0~~	~~240,0~~	~~269,0~~	~~10,0~~	~~-6,3~~
Zircon_026	213,0	203,0	0,953	0,057	0,003	0,319	0,019	0,043	0,001	0,014	0,000	-0,060	269,2	5,9	283,0	15,0	460,0	120,0	269,2	5,9	4,9
Zircon_073	112,0	63,0	0,563	0,057	0,005	0,333	0,027	0,043	0,001	0,014	0,001	-0,183	269,9	7,4	289,0	20,0	500,0	170,0	269,9	7,4	6,6
Zircon_058	489,0	201,0	0,411	0,053	0,002	0,313	0,014	0,043	0,001	0,014	0,000	0,165	270,1	5,1	278,0	11,0	315,0	86,0	270,1	5,1	2,8
Zircon_040	103,0	76,0	0,738	0,054	0,006	0,308	0,029	0,043	0,001	0,014	0,001	-0,139	270,6	8,0	275,0	23,0	340,0	190,0	270,6	8,0	1,6

Sample																					
Zircon_097	779,0	1157,0	1,485	0,055	0,002	0,314	0,012	0,043	0,001	0,014	0,000	-0,173	271,0	4,2	278,7	9,0	399,0	64,0	271,0	4,2	2,8
Zircon_044	134,0	71,0	0,530	0,054	0,004	0,320	0,021	0,043	0,001	0,014	0,001	-0,042	271,1	8,0	286,0	18,0	380,0	160,0	271,1	8,0	5,2
Zircon_035	258,0	252,0	0,977	0,051	0,003	0,304	0,016	0,043	0,001	0,013	0,000	0,097	271,8	6,0	270,0	13,0	240,0	100,0	271,8	6,0	-0,7
Zircon_009	213,0	113,0	0,531	0,053	0,003	0,316	0,018	0,043	0,001	0,012	0,000	0,013	272,0	5,2	280,0	14,0	290,0	120,0	272,0	5,2	2,9
Zircon_065	554,0	387,0	0,699	0,052	0,002	0,311	0,012	0,043	0,001	0,014	0,000	-0,004	272,9	4,9	274,2	9,5	281,0	82,0	272,9	4,9	0,5
Zircon_048	605,0	605,0	1,000	0,057	0,003	0,305	0,018	0,043	0,001	0,014	0,000	0,709	273,0	6,8	269,0	14,0	469,0	97,0	273,0	6,8	-1,5
~~Zircon_050~~	~~37,0~~	~~22,0~~	~~0,595~~	~~0,079~~	~~0,010~~	~~0,477~~	~~0,062~~	~~0,043~~	~~0,002~~	~~0,017~~	~~0,002~~	~~0,122~~	~~273,0~~	~~13,0~~	~~406,0~~	~~40,0~~	~~1110,0~~	~~270,0~~	~~273,0~~	~~13,0~~	~~32,8~~
Zircon_006	79,0	59,0	0,747	0,054	0,006	0,327	0,037	0,044	0,001	0,014	0,001	0,159	274,5	8,8	283,0	30,0	380,0	220,0	274,5	8,8	3,0
Zircon_011	748,0	791,0	1,057	0,054	0,011	0,310	0,097	0,044	0,001	0,013	0,002	-0,084	274,7	5,1	274,0	57,0	340,0	270,0	274,7	5,1	-0,3
Zircon_019	218,0	213,0	0,977	0,053	0,003	0,317	0,017	0,044	0,001	0,014	0,000	-0,063	274,7	5,1	281,0	13,0	290,0	120,0	274,7	5,1	2,2
Zircon_078	248,0	164,0	0,661	0,053	0,004	0,312	0,022	0,044	0,001	0,014	0,001	-0,126	275,2	6,9	275,0	17,0	350,0	150,0	275,2	6,9	-0,1
Zircon_059	264,0	179,0	0,678	0,051	0,003	0,309	0,017	0,044	0,001	0,014	0,001	-0,145	275,9	5,3	274,0	14,0	230,0	120,0	275,9	5,3	-0,7
Zircon_077	416,0	498,0	1,197	0,052	0,002	0,308	0,013	0,044	0,001	0,014	0,000	0,357	276,5	6,1	272,3	9,8	287,0	77,0	276,5	6,1	-1,5
Zircon_032	73,0	50,0	0,685	0,054	0,005	0,339	0,025	0,044	0,001	0,013	0,001	-0,152	277,2	8,0	295,0	18,0	350,0	170,0	277,2	8,0	6,0
Zircon_090	145,0	109,0	0,752	0,053	0,003	0,319	0,022	0,044	0,001	0,014	0,001	0,160	277,8	7,9	279,0	17,0	300,0	140,0	277,8	7,9	0,4
Zircon_047	144,0	88,0	0,611	0,053	0,004	0,324	0,023	0,044	0,001	0,015	0,001	-0,032	277,8	7,0	283,0	17,0	290,0	130,0	277,8	7,0	1,8
Zircon_023	145,0	117,0	0,807	0,052	0,004	0,305	0,018	0,044	0,001	0,014	0,001	0,067	278,3	6,0	272,0	15,0	230,0	140,0	278,3	6,0	-2,3
Zircon_049	133,0	62,0	0,466	0,052	0,004	0,317	0,023	0,044	0,001	0,015	0,001	0,020	278,3	6,2	278,0	18,0	250,0	150,0	278,3	6,2	-0,1
Zircon_064	224,0	183,0	0,817	0,052	0,003	0,315	0,018	0,044	0,001	0,014	0,001	-0,184	278,4	5,1	277,0	14,0	270,0	120,0	278,4	5,1	-0,5
Zircon_075	141,0	115,0	0,816	0,052	0,003	0,322	0,023	0,044	0,001	0,014	0,001	0,148	278,4	6,1	281,0	18,0	260,0	140,0	278,4	6,1	0,9
Zircon_055	103,0	77,0	0,748	0,055	0,007	0,313	0,050	0,044	0,002	0,014	0,001	-0,130	280,0	9,5	275,0	34,0	400,0	190,0	280,0	9,5	-1,8
Zircon_063	559,0	127,0	0,227	0,054	0,002	0,315	0,012	0,044	0,002	0,015	0,001	-0,175	280,0	11,0	277,6	9,1	385,0	84,0	280,0	11,0	-0,9
Zircon_094	167,0	127,0	0,760	0,054	0,003	0,323	0,020	0,044	0,001	0,014	0,001	0,363	280,3	6,4	285,0	15,0	380,0	110,0	280,3	6,4	1,6
Zircon_057	172,0	132,0	0,767	0,053	0,003	0,328	0,021	0,045	0,001	0,014	0,001	-0,015	280,4	8,2	290,0	15,0	300,0	130,0	280,4	8,2	3,3
Zircon_056	363,0	77,0	0,212	0,054	0,003	0,324	0,016	0,045	0,001	0,015	0,001	-0,220	281,2	5,8	284,0	12,0	360,0	110,0	281,2	5,8	1,0
Zircon_076	480,0	436,0	0,908	0,054	0,003	0,324	0,020	0,045	0,001	0,015	0,000	-0,180	281,6	5,0	285,0	15,0	355,0	95,0	281,6	5,0	1,2
Zircon_013	326,0	193,0	0,592	0,052	0,003	0,323	0,018	0,045	0,001	0,014	0,000	0,005	282,7	5,3	283,0	14,0	290,0	120,0	282,7	5,3	0,1
Zircon_001	495,0	638,0	1,289	0,051	0,002	0,312	0,015	0,045	0,001	0,014	0,000	0,218	283,4	4,6	275,0	11,0	221,0	86,0	283,4	4,6	-3,1

Sample																					
Zircon_007	153,0	139,0	0,908	0,056	0,004	0,346	0,026	0,045	0,001	0,014	0,000	-0,019	285,4	7,4	299,0	19,0	410,0	150,0	285,4	7,4	4,5
Zircon_101	185,0	217,0	1,173	0,052	0,003	0,317	0,018	0,046	0,001	0,014	0,001	0,265	287,7	6,7	279,0	14,0	280,0	110,0	287,7	6,7	-3,1
Zircon_053	170,0	99,0	0,582	0,050	0,003	0,324	0,022	0,046	0,001	0,015	0,001	0,152	288,4	7,1	283,0	17,0	250,0	140,0	288,4	7,1	-1,9
Zircon_010	265,0	289,0	1,091	0,057	0,003	0,336	0,021	0,046	0,001	0,015	0,000	-0,059	288,4	5,9	293,0	16,0	460,0	130,0	288,4	5,9	1,6
Zircon_074	195,0	92,0	0,472	0,053	0,003	0,325	0,020	0,046	0,001	0,016	0,001	0,047	288,9	6,3	293,0	15,0	330,0	120,0	288,9	6,3	1,4
Zircon_002	394,0	486,0	1,234	0,053	0,002	0,328	0,014	0,046	0,001	0,014	0,000	0,357	290,4	4,8	287,0	11,0	355,0	79,0	290,4	4,8	-1,2
Zircon_015	94,0	77,0	0,819	0,054	0,004	0,326	0,028	0,046	0,002	0,013	0,001	0,350	291,7	8,9	284,0	22,0	320,0	160,0	291,7	8,9	-2,7
Zircon_088	379,0	257,0	0,678	0,066	0,005	0,418	0,035	0,047	0,001	0,016	0,001	0,246	295,8	5,1	354,0	24,0	770,0	140,0	295,8	5,1	16,4
Zircon_091	106,0	61,0	0,575	0,051	0,003	0,324	0,021	0,047	0,001	0,017	0,001	0,123	296,4	7,8	284,0	16,0	200,0	140,0	296,4	7,8	-4,4
Zircon_092	204,0	112,0	0,549	0,053	0,003	0,334	0,020	0,047	0,001	0,015	0,001	-0,026	296,8	6,1	291,0	15,0	300,0	110,0	296,8	6,1	-2,0
Zircon_024	355,0	337,0	0,949	0,059	0,004	0,385	0,024	0,048	0,001	0,016	0,001	0,193	303,4	5,0	333,0	17,0	560,0	120,0	303,4	5,0	8,9
Zircon_084	340,0	364,0	1,071	0,101	0,006	0,841	0,047	0,064	0,002	0,030	0,002	0,250	399,4	9,0	619,0	29,0	1620,0	120,0	399,4	9,0	35,5
Zircon_027	698,0	468,0	0,670	0,056	0,001	0,553	0,017	0,072	0,001	0,022	0,000	0,151	446,3	6,7	447,0	11,0	453,0	56,0	446,3	6,7	0,2
Zircon_036	204,0	263,0	1,289	0,056	0,002	0,572	0,028	0,072	0,002	0,021	0,001	0,423	450,0	10,0	458,0	19,0	453,0	89,0	450,0	10,0	1,7
Zircon_087	425,0	241,0	0,567	0,059	0,002	0,570	0,023	0,072	0,001	0,022	0,000	0,152	450,1	7,3	457,0	15,0	540,0	70,0	450,1	7,3	1,5
Zircon_041	755,0	486,0	0,644	0,059	0,002	0,570	0,020	0,074	0,001	0,024	0,000	0,078	457,5	6,9	460,0	12,0	536,0	61,0	457,5	6,9	0,5
Zircon_028	257,0	129,0	0,502	0,057	0,002	0,577	0,026	0,074	0,001	0,025	0,001	0,254	458,4	7,9	464,0	16,0	478,0	77,0	458,4	7,9	1,2
Zircon_046	488,0	307,0	0,629	0,058	0,002	0,585	0,021	0,074	0,001	0,023	0,000	0,009	460,4	7,8	467,0	14,0	523,0	67,0	460,4	7,8	1,4
Zircon_079	267,0	147,0	0,551	0,058	0,002	0,578	0,026	0,074	0,002	0,022	0,001	0,135	461,2	8,7	462,0	17,0	499,0	78,0	461,2	8,7	0,2
Zircon_060	98,0	95,0	0,969	0,059	0,003	0,581	0,076	0,076	0,005	0,024	0,001	0,491	471,0	28,0	462,0	41,0	560,0	110,0	471,0	28,0	-1,9
Zircon_031	172,0	158,0	0,919	0,056	0,002	0,592	0,032	0,077	0,002	0,024	0,001	0,136	476,0	10,0	473,0	21,0	470,0	98,0	476,0	10,0	-0,6
Zircon_080	463,0	274,0	0,592	0,056	0,002	0,597	0,027	0,078	0,001	0,027	0,001	0,385	482,5	8,5	476,0	17,0	422,0	78,0	482,5	8,5	-1,4
Zircon_093	376,0	64,0	0,170	0,063	0,002	0,697	0,062	0,086	0,005	0,036	0,001	0,471	534,0	26,0	535,0	32,0	710,0	68,0	534,0	26,0	0,2
Zircon_066	285,0	185,0	0,649	0,062	0,002	0,878	0,033	0,104	0,002	0,035	0,001	-0,053	637,0	11,0	639,0	17,0	659,0	69,0	637,0	11,0	0,3
Zircon_045	27,0	9,0	0,333	0,078	0,005	1,960	0,140	0,182	0,005	0,059	0,005	0,177	1077,0	26,0	1113,0	42,0	1180,0	110,0	1077,0	26,0	3,2
Zircon_070	100,0	45,0	0,450	0,079	0,004	1,940	0,088	0,182	0,004	0,054	0,002	-0,126	1079,0	19,0	1091,0	30,0	1145,0	91,0	1079,0	19,0	1,1
Zircon_081	221,0	301,0	1,362	0,244	0,080	1,500	1,800	0,048	0,015	0,022	0,015	-0,451	302,0	90,0	870,0	320,0	2840,0	400,0	302,0	90,0	65,3
Zircon_034	919,0	1423,0	1,548	0,224	0,023	1,420	0,230	0,045	0,002	0,024	0,004	0,800	286,0	44,0	892,0	71,0	2980,0	120,0	286,0	44,0	67,9

183

CPV-16-408 (DZ)

Maximum depositional age (3+DZ, 1σ): 240.1±4.4 Ma (MSWD = 0.041)

	104,0	105,0	1,010	0,048	0,004	0,268	0,026	0,042	0,001	0,001	0,013	0,001	0,183	264,3	8,1	242,0	20,0	60,0	180,0	264,3	8,1	9,2	
~~Zircon_01~~	104,0	105,0	1,010	0,048	0,004	0,268	0,026	0,042	0,001	0,001	0,013	0,001	0,183	264,3	8,1	242,0	20,0	60,0	180,0	264,3	8,1	9,2	
Zircon_100	573,0	589,0	1,028	0,051	0,002	0,249	0,012	0,036	0,001	0,001	0,011	0,000	0,045	225,6	5,4	225,5	9,9	206,0	97,0	225,6	5,4	0,0	
Zircon_81	117,0	83,0	0,709	0,063	0,005	0,320	0,023	0,038	0,001	0,001	0,012	0,001	-0,042	239,7	7,8	283,0	18,0	660,0	150,0	239,7	7,8	15,3	*
Zircon_21	391,0	158,0	0,404	0,052	0,003	0,274	0,015	0,038	0,001	0,001	0,013	0,001	0,002	239,9	6,7	245,0	12,0	300,0	120,0	239,9	6,7	2,1	*
Zircon_44	78,0	53,0	0,679	0,067	0,007	0,359	0,039	0,038	0,002	0,001	0,015	0,001	0,043	241,4	9,9	308,0	29,0	760,0	240,0	241,4	9,9	21,6	*
~~Zircon_65~~	266,0	277,0	1,041	0,074	0,007	0,385	0,037	0,039	0,001	0,001	0,013	0,001	0,262	244,9	8,1	335,0	28,0	1040,0	190,0	244,9	8,1	26,9	
Zircon_73	62,0	46,0	0,742	0,055	0,006	0,292	0,031	0,040	0,002	0,001	0,014	0,001	0,027	251,3	9,5	268,0	25,0	350,0	220,0	251,3	9,5	6,2	
Zircon_79	60,0	42,0	0,700	0,057	0,007	0,308	0,037	0,040	0,002	0,001	0,012	0,001	0,286	255,0	11,0	272,0	28,0	440,0	240,0	255,0	11,0	6,3	
Zircon_54	133,0	155,0	1,165	0,057	0,006	0,319	0,036	0,041	0,001	0,001	0,014	0,000	0,098	258,0	8,3	280,0	28,0	510,0	230,0	258,0	8,3	7,9	
Zircon_70	220,0	186,0	0,845	0,050	0,004	0,280	0,021	0,041	0,001	0,001	0,013	0,001	-0,037	258,9	7,2	250,0	16,0	170,0	160,0	258,9	7,2	-3,6	
Zircon_32	66,0	45,0	0,682	0,057	0,006	0,320	0,031	0,041	0,002	0,001	0,013	0,001	0,112	259,6	9,1	279,0	23,0	370,0	200,0	259,6	9,1	7,0	
Zircon_61	156,0	128,0	0,821	0,052	0,004	0,296	0,022	0,041	0,001	0,001	0,013	0,001	-0,083	259,8	7,1	262,0	17,0	250,0	150,0	259,8	7,1	0,8	
Zircon_52	71,0	51,0	0,718	0,061	0,005	0,329	0,025	0,041	0,002	0,001	0,014	0,001	-0,022	261,0	10,0	287,0	19,0	540,0	190,0	261,0	10,0	9,1	
Zircon_17	47,0	26,0	0,553	0,052	0,007	0,302	0,038	0,042	0,002	0,001	0,015	0,001	0,106	262,0	12,0	263,0	30,0	220,0	240,0	262,0	12,0	0,4	
Zircon_46	122,0	101,0	0,828	0,053	0,004	0,298	0,022	0,042	0,001	0,001	0,014	0,001	-0,121	262,0	7,7	266,0	16,0	320,0	180,0	262,0	7,7	1,5	
Zircon_08	80,0	54,0	0,675	0,054	0,005	0,311	0,030	0,042	0,001	0,001	0,013	0,000	0,140	262,3	8,1	280,0	24,0	400,0	210,0	262,3	8,1	6,3	
Zircon_59	240,0	185,0	0,771	0,050	0,003	0,291	0,016	0,042	0,001	0,001	0,013	0,001	-0,096	262,6	6,7	259,0	12,0	200,0	110,0	262,6	6,7	-1,4	
Zircon_18	190,0	108,0	0,568	0,051	0,003	0,288	0,019	0,042	0,001	0,001	0,014	0,001	-0,110	262,7	7,6	256,0	15,0	230,0	140,0	262,7	7,6	-2,6	
Zircon_15	353,0	218,0	0,618	0,051	0,003	0,302	0,018	0,042	0,001	0,001	0,013	0,000	0,156	263,6	6,5	267,0	14,0	230,0	110,0	263,6	6,5	1,3	
Zircon_28	489,0	249,0	0,509	0,051	0,002	0,298	0,015	0,042	0,001	0,001	0,013	0,000	0,274	264,6	6,1	265,0	12,0	235,0	95,0	264,6	6,1	0,2	
Zircon_07	91,0	70,0	0,769	0,053	0,004	0,304	0,023	0,042	0,002	0,001	0,014	0,001	0,129	265,6	9,4	268,0	18,0	330,0	170,0	265,6	9,4	0,9	
Zircon_42	147,0	161,0	1,095	0,061	0,004	0,356	0,025	0,042	0,001	0,001	0,014	0,001	0,138	266,2	8,1	307,0	19,0	570,0	160,0	266,2	8,1	13,3	
Zircon_31	95,0	64,0	0,674	0,050	0,004	0,297	0,025	0,043	0,001	0,001	0,013	0,001	0,058	268,9	7,8	262,0	20,0	160,0	170,0	268,9	7,8	-2,6	
Zircon_16	252,0	187,0	0,742	0,052	0,003	0,312	0,017	0,043	0,001	0,001	0,013	0,000	-0,104	269,2	6,7	275,0	13,0	290,0	120,0	269,2	6,7	2,1	
Zircon_68	177,0	141,0	0,797	0,054	0,003	0,315	0,018	0,043	0,001	0,001	0,013	0,001	0,127	269,4	7,1	277,0	14,0	340,0	120,0	269,4	7,1	2,7	
Zircon_86	63,0	49,0	0,778	0,058	0,006	0,331	0,035	0,043	0,002	0,001	0,013	0,001	-0,022	269,4	9,6	291,0	25,0	460,0	220,0	269,4	9,6	7,4	

Zircon_51	81,0	48,0	0,593	0,055	0,007	0,335	0,040	0,043	0,002	0,013	0,001	-0,292	270,0	12,0	289,0	30,0	350,0	250,0	270,0	12,0	6,6
Zircon_05	128,0	97,0	0,758	0,057	0,005	0,338	0,028	0,043	0,001	0,014	0,001	0,100	270,7	7,2	294,0	21,0	430,0	180,0	270,7	7,2	7,9
Zircon_98	265,0	154,0	0,581	0,052	0,003	0,309	0,019	0,043	0,001	0,014	0,000	0,088	270,9	7,4	277,0	15,0	320,0	120,0	270,9	7,4	2,2
Zircon_36	187,0	172,0	0,920	0,056	0,004	0,328	0,026	0,043	0,001	0,013	0,001	-0,028	270,9	7,5	295,0	19,0	440,0	170,0	270,9	7,5	8,2
Zircon_20	52,0	44,0	0,846	0,056	0,006	0,325	0,035	0,043	0,002	0,015	0,001	-0,036	271,0	11,0	291,0	25,0	380,0	230,0	271,0	11,0	6,9
Zircon_74	44,0	31,0	0,705	0,059	0,008	0,346	0,044	0,043	0,002	0,014	0,001	-0,002	271,0	11,0	296,0	33,0	460,0	270,0	271,0	11,0	8,4
Zircon_76	150,0	82,0	0,547	0,057	0,004	0,334	0,022	0,043	0,001	0,014	0,001	-0,057	272,0	7,7	294,0	17,0	460,0	150,0	272,0	7,7	7,5
Zircon_55	98,0	51,0	0,520	0,060	0,005	0,357	0,031	0,043	0,001	0,015	0,001	-0,009	272,3	8,3	308,0	23,0	560,0	200,0	272,3	8,3	11,6
Zircon_13	105,0	48,0	0,457	0,051	0,004	0,310	0,027	0,043	0,001	0,013	0,001	0,193	272,8	8,8	278,0	21,0	250,0	180,0	272,8	8,8	1,9
Zircon_57	73,0	51,0	0,699	0,054	0,005	0,319	0,032	0,043	0,002	0,013	0,001	0,181	273,0	10,0	278,0	24,0	340,0	200,0	273,0	10,0	1,8
Zircon_49	76,0	57,0	0,750	0,064	0,009	0,383	0,050	0,043	0,002	0,016	0,001	-0,281	273,0	11,0	333,0	39,0	660,0	310,0	273,0	11,0	18,0
Zircon_71	248,0	184,0	0,742	0,052	0,003	0,313	0,018	0,043	0,001	0,014	0,000	-0,015	273,5	7,5	275,0	14,0	280,0	120,0	273,5	7,5	0,5
Zircon_82	107,0	51,0	0,477	0,054	0,004	0,329	0,028	0,043	0,001	0,013	0,001	0,095	273,7	8,4	290,0	21,0	360,0	170,0	273,7	8,4	5,6
Zircon_47	245,0	289,0	1,180	0,074	0,009	0,481	0,081	0,044	0,002	0,016	0,001	0,400	274,0	12,0	396,0	56,0	1000,0	310,0	274,0	12,0	30,8
Zircon_29	183,0	161,0	0,880	0,055	0,004	0,316	0,021	0,043	0,001	0,014	0,001	0,292	274,2	7,5	278,0	16,0	350,0	140,0	274,2	7,5	1,4
Zircon_64	333,0	222,0	0,667	0,052	0,003	0,315	0,016	0,044	0,001	0,014	0,000	0,037	274,5	6,9	278,0	12,0	270,0	100,0	274,5	6,9	1,3
Zircon_22	97,0	71,0	0,732	0,053	0,004	0,319	0,022	0,044	0,001	0,014	0,001	0,112	274,5	8,9	279,0	17,0	290,0	150,0	274,5	8,9	1,6
Zircon_60	196,0	141,0	0,719	0,051	0,004	0,304	0,020	0,044	0,001	0,013	0,000	-0,113	274,9	7,0	268,0	16,0	210,0	140,0	274,9	7,0	-2,6
Zircon_48	348,0	345,0	0,991	0,051	0,002	0,306	0,015	0,044	0,001	0,013	0,000	0,442	274,9	7,2	271,0	12,0	213,0	91,0	274,9	7,2	-1,4
Zircon_56	191,0	117,0	0,613	0,052	0,003	0,312	0,021	0,044	0,001	0,014	0,001	0,180	275,6	6,7	279,0	15,0	300,0	130,0	275,6	6,7	1,2
Zircon_34	198,0	130,0	0,657	0,053	0,003	0,320	0,020	0,044	0,001	0,014	0,000	-0,028	275,6	6,8	281,0	16,0	280,0	140,0	275,6	6,8	1,9
Zircon_66	335,0	326,0	0,973	0,054	0,003	0,322	0,017	0,044	0,001	0,014	0,000	0,074	276,1	6,7	285,0	13,0	320,0	110,0	276,1	6,7	3,1
Zircon_02	250,0	173,0	0,692	0,054	0,003	0,326	0,017	0,044	0,001	0,014	0,001	0,102	276,2	6,9	286,0	13,0	330,0	110,0	276,2	6,9	3,4
Zircon_78	523,0	395,0	0,755	0,054	0,002	0,327	0,017	0,044	0,001	0,014	0,000	0,344	276,3	6,2	287,0	13,0	359,0	99,0	276,3	6,2	3,7
Zircon_11	267,0	275,0	1,030	0,053	0,003	0,314	0,017	0,044	0,001	0,014	0,000	0,107	276,4	7,1	279,0	14,0	280,0	110,0	276,4	7,1	0,9
Zircon_80	250,0	163,0	0,652	0,053	0,003	0,318	0,019	0,044	0,001	0,014	0,001	0,034	276,6	8,2	280,0	15,0	310,0	130,0	276,6	8,2	1,2
Zircon_06	204,0	187,0	0,917	0,055	0,003	0,329	0,021	0,044	0,001	0,014	0,000	-0,036	276,8	6,6	287,0	16,0	350,0	140,0	276,8	6,6	3,6
Zircon_69	63,0	50,0	0,794	0,058	0,006	0,358	0,034	0,044	0,001	0,016	0,001	0,234	276,9	8,7	308,0	26,0	530,0	190,0	276,9	8,7	10,1

Zircon_27	37,0	29,0	0,784	0,050	0,009	0,322	0,051	0,044	0,002	0,012	0,001	-0,018	277,0	13,0	277,0	40,0	220,0	330,0	277,0	13,0	0,0
Zircon_43	232,0	153,0	0,659	0,053	0,003	0,321	0,019	0,044	0,001	0,014	0,001	-0,121	277,0	7,7	284,0	14,0	290,0	130,0	277,0	7,7	2,5
Zircon_45	274,0	252,0	0,920	0,054	0,003	0,333	0,016	0,044	0,001	0,014	0,000	-0,123	277,0	7,2	291,0	12,0	370,0	110,0	277,0	7,2	4,8
Zircon_38	1486,0	2584,0	1,739	0,057	0,002	0,341	0,015	0,044	0,001	0,014	0,000	-0,240	277,6	6,6	298,0	11,0	481,0	91,0	277,6	6,6	6,8 ***
Zircon_96	125,0	78,0	0,624	0,055	0,004	0,328	0,027	0,044	0,001	0,014	0,001	0,178	278,2	8,0	288,0	21,0	350,0	160,0	278,2	8,0	3,4
Zircon_63	155,0	118,0	0,761	0,053	0,004	0,325	0,021	0,044	0,001	0,014	0,001	0,036	279,0	8,6	284,0	16,0	310,0	140,0	279,0	8,6	1,8
Zircon_85	172,0	129,0	0,750	0,054	0,004	0,324	0,023	0,044	0,001	0,013	0,000	-0,056	279,2	7,0	284,0	18,0	320,0	150,0	279,2	7,0	1,7
Zircon_89	1002,0	1139,0	1,137	0,054	0,002	0,335	0,017	0,044	0,001	0,014	0,000	0,316	279,7	6,4	293,0	13,0	390,0	100,0	279,7	6,4	4,5
Zircon_37	375,0	333,0	0,888	0,057	0,003	0,349	0,019	0,044	0,001	0,015	0,000	0,420	279,7	6,6	305,0	15,0	480,0	100,0	279,7	6,6	8,3
Zircon_87	84,0	61,0	0,726	0,055	0,005	0,332	0,030	0,044	0,002	0,014	0,001	0,171	280,0	10,0	288,0	23,0	410,0	170,0	280,0	10,0	2,8
Zircon_88	178,0	158,0	0,888	0,050	0,003	0,303	0,019	0,044	0,001	0,014	0,000	-0,110	280,3	7,5	268,0	15,0	210,0	130,0	280,3	7,5	-4,6
Zircon_24	123,0	76,0	0,618	0,055	0,004	0,337	0,023	0,045	0,001	0,015	0,001	0,027	280,5	8,5	294,0	17,0	370,0	140,0	280,5	8,5	4,6
Zircon_41	149,0	107,0	0,718	0,053	0,004	0,329	0,022	0,045	0,001	0,014	0,001	-0,086	281,0	7,6	287,0	17,0	290,0	140,0	281,0	7,6	2,1
Zircon_09	285,0	214,0	0,751	0,052	0,003	0,321	0,017	0,045	0,001	0,014	0,000	-0,036	281,1	7,1	283,0	14,0	270,0	110,0	281,1	7,1	0,7
Zircon_04	104,0	105,0	1,010	0,054	0,004	0,332	0,026	0,045	0,001	0,016	0,001	-0,148	281,3	8,5	292,0	20,0	360,0	160,0	281,3	8,5	3,7
Zircon_94	427,0	364,0	0,852	0,052	0,002	0,321	0,016	0,045	0,001	0,014	0,000	-0,131	282,0	6,2	282,0	12,0	270,0	100,0	282,0	6,2	0,0
Zircon_33	323,0	287,0	0,889	0,050	0,003	0,307	0,017	0,045	0,001	0,014	0,001	0,134	282,2	7,1	271,0	13,0	160,0	110,0	282,2	7,1	-4,1
Zircon_58	145,0	108,0	0,745	0,052	0,004	0,318	0,026	0,045	0,001	0,014	0,001	-0,103	282,6	7,8	281,0	20,0	260,0	170,0	282,6	7,8	-0,6
Zircon_72	185,0	165,0	0,892	0,053	0,004	0,326	0,021	0,045	0,001	0,014	0,001	-0,187	283,0	7,4	286,0	16,0	280,0	140,0	283,0	7,4	1,0
Zircon_99	994,0	146,0	0,147	0,056	0,004	0,347	0,025	0,045	0,001	0,016	0,001	-0,189	283,3	7,2	303,0	18,0	440,0	140,0	283,3	7,2	6,5
Zircon_40	518,0	540,0	1,042	0,055	0,002	0,345	0,015	0,045	0,001	0,014	0,000	0,121	283,6	6,4	301,0	12,0	413,0	86,0	283,6	6,4	5,8
Zircon_83	77,0	59,0	0,766	0,063	0,006	0,400	0,040	0,045	0,002	0,017	0,001	-0,006	284,4	9,6	338,0	28,0	710,0	210,0	284,4	9,6	15,9
Zircon_26	143,0	122,0	0,853	0,057	0,004	0,354	0,023	0,045	0,001	0,015	0,001	0,163	284,5	8,3	309,0	16,0	470,0	130,0	284,5	8,3	7,9
Zircon_92	333,0	213,0	0,640	0,053	0,003	0,331	0,018	0,045	0,001	0,014	0,000	-0,024	284,9	6,7	290,0	13,0	310,0	110,0	284,9	6,7	1,8
Zircon_101	237,0	214,0	0,903	0,052	0,003	0,331	0,020	0,045	0,001	0,014	0,000	0,357	285,2	7,6	291,0	15,0	270,0	110,0	285,2	7,6	2,0
Zircon_91	166,0	105,0	0,633	0,050	0,003	0,313	0,018	0,045	0,001	0,014	0,001	0,181	285,6	8,0	276,0	14,0	210,0	110,0	285,6	8,0	-3,5
Zircon_35	136,0	115,0	0,846	0,059	0,004	0,367	0,026	0,045	0,001	0,015	0,001	-0,041	286,2	8,9	315,0	19,0	510,0	150,0	286,2	8,9	9,1
Zircon_30	246,0	189,0	0,768	0,050	0,002	0,312	0,016	0,045	0,001	0,014	0,000	0,177	286,4	7,9	275,0	12,0	150,0	100,0	286,4	7,9	-4,1

Label																					
Zircon_97	1100,0	118,0	0,107	0,052	0,003	0,324	0,017	0,045	0,001	0,014	0,001	-0,274	286,4	6,6	285,0	13,0	270,0	120,0	286,4	6,6	-0,5 ***
Zircon_67	219,0	195,0	0,890	0,055	0,004	0,347	0,023	0,046	0,001	0,014	0,001	-0,183	286,7	8,3	301,0	17,0	420,0	130,0	286,7	8,3	4,8
Zircon_62	342,0	315,0	0,921	0,071	0,005	0,449	0,034	0,046	0,001	0,016	0,001	-0,049	286,7	7,6	375,0	24,0	950,0	150,0	286,7	7,6	23,5
Zircon_10	212,0	90,0	0,425	0,053	0,003	0,331	0,020	0,046	0,001	0,014	0,001	0,016	287,1	7,2	289,0	15,0	290,0	130,0	287,1	7,2	0,7
Zircon_19	294,0	191,0	0,650	0,054	0,002	0,342	0,017	0,046	0,001	0,015	0,001	0,286	287,3	7,0	298,0	13,0	360,0	93,0	287,3	7,0	3,6
Zircon_84	375,0	356,0	0,949	0,052	0,002	0,329	0,016	0,046	0,001	0,014	0,001	0,285	288,6	7,1	288,0	12,0	279,0	94,0	288,6	7,1	-0,2
Zircon_14	97,0	54,0	0,557	0,051	0,005	0,320	0,032	0,046	0,002	0,014	0,002	-0,137	288,8	9,3	279,0	24,0	170,0	200,0	288,8	9,3	-3,5
Zircon_03	170,0	127,0	0,747	0,056	0,004	0,351	0,022	0,046	0,001	0,015	0,001	-0,077	288,9	7,5	307,0	17,0	410,0	130,0	288,9	7,5	5,9
~~Zircon_25~~	66,0	50,0	0,758	0,098	0,009	0,617	0,063	0,046	0,002	0,022	0,002	0,078	289,6	9,6	492,0	39,0	1520,0	190,0	289,6	9,6	41,1
Zircon_77	210,0	141,0	0,671	0,051	0,003	0,329	0,024	0,046	0,001	0,014	0,001	0,257	290,2	7,6	288,0	18,0	240,0	140,0	290,2	7,6	-0,8
Zircon_12	121,0	93,0	0,769	0,050	0,004	0,318	0,023	0,046	0,001	0,015	0,001	-0,068	290,6	7,9	282,0	17,0	210,0	150,0	290,6	7,9	-3,0
Zircon_39	163,0	119,0	0,730	0,059	0,004	0,372	0,026	0,046	0,001	0,015	0,001	-0,045	290,8	7,2	325,0	18,0	540,0	150,0	290,8	7,2	10,5
Zircon_95	305,0	190,0	0,623	0,061	0,006	0,371	0,032	0,046	0,002	0,015	0,002	-0,420	292,0	11,0	334,0	24,0	610,0	200,0	292,0	11,0	12,6
Zircon_23	464,0	722,0	1,556	0,053	0,003	0,340	0,018	0,046	0,001	0,014	0,000	0,184	292,1	8,0	298,0	13,0	350,0	100,0	292,1	8,0	2,0
Zircon_75	349,0	168,0	0,481	0,053	0,003	0,335	0,019	0,047	0,001	0,014	0,001	0,083	293,0	7,2	293,0	14,0	290,0	120,0	293,0	7,2	0,0
Zircon_50	184,0	157,0	0,853	0,056	0,003	0,361	0,020	0,047	0,001	0,014	0,000	0,356	294,4	7,2	312,0	15,0	410,0	110,0	294,4	7,2	5,6
Zircon_102	199,0	130,0	0,653	0,055	0,004	0,347	0,022	0,047	0,002	0,014	0,001	0,242	296,0	10,0	302,0	16,0	370,0	140,0	296,0	10,0	2,0
~~Zircon_93~~	185,0	128,0	0,692	0,089	0,007	0,607	0,054	0,048	0,002	0,021	0,004	0,248	301,1	9,0	478,0	34,0	1410,0	160,0	301,1	9,0	37,0
Zircon_90	72,0	80,0	1,111	0,060	0,004	0,720	0,047	0,087	0,002	0,026	0,001	-0,145	538,0	14,0	547,0	28,0	540,0	150,0	538,0	14,0	1,6
Zircon_53	256,0	216,0	0,844	0,125	0,004	6,070	0,230	0,352	0,008	0,101	0,002	0,116	2022,0	57,0	1986,0	34,0	2022,0	57,0	2022,0	57,0	2,2

CPV-16-411 (DZ) — Maximum depositional age (3+DZ, 1σ): 224.9±5.3 Ma (MSWD = 0.28)

Label																					
~~Zircon_15~~	1695	1222	0,72	0,0826	0,0055	0,3520	0,0210	0,0306	0,0013	0,0111	0,0005	-0,22	194,5	7,9	306,0	15,0	1260,0	120,0	194,5	7,9	36,44 ***
~~Zircon_77~~	1135	656	0,58	0,0605	0,0029	0,2780	0,0140	0,0332	0,0013	0,0094	0,0004	0,11	210,4	8,0	249,0	11,0	618,0	99,0	210,4	8,0	15,50
Zircon_98	222	858	3,86	0,0656	0,0049	0,3120	0,0260	0,0335	0,0015	0,0054	0,0003	0,52	212,6	9,5	277,0	19,0	770,0	160,0	212,6	9,5	23,25
~~Zircon_32~~	3722	2652	0,71	0,0564	0,0036	0,2690	0,0150	0,0352	0,0014	0,0124	0,0004	0,09	222,8	8,6	242,0	12,0	450,0	110,0	222,8	8,6	7,93 ***
~~Zircon_78~~	122	118	0,97	0,0987	0,0083	0,4670	0,0380	0,0352	0,0019	0,0143	0,0010	0,18	223,0	12,0	386,0	26,0	1590,0	160,0	223,0	12,0	42,23
Zircon_51	165	81	0,49	0,0526	0,0047	0,2580	0,0240	0,0355	0,0015	0,0121	0,0008	0,25	225,0	9,2	232,0	19,0	310,0	170,0	225,0	9,2	3,02 *

Sample																					
Zircon_90	298	341	1,14	0,0649	0,0047	0,3220	0,0240	0,0355	0,0015	0,0123	0,0006	-0,04	225,2	9,5	282,0	18,0	750,0	150,0	225,2	9,5	20,14	*
Zircon_99	139	127	0,91	0,0648	0,0046	0,3160	0,0220	0,0356	0,0016	0,0098	0,0006	0,18	226,0	10,0	280,0	18,0	710,0	150,0	226,0	10,0	19,29	*
Zircon_102	94	146	1,55	0,0517	0,0051	0,2720	0,0260	0,0360	0,0018	0,0120	0,0007	0,14	228,0	11,0	242,0	21,0	360,0	220,0	228,0	11,0	5,79	
Zircon_06	198	243	1,23	0,0545	0,0045	0,2740	0,0220	0,0363	0,0016	0,0109	0,0005	0,36	229,8	9,8	244,0	18,0	350,0	170,0	229,8	9,8	5,82	
Zircon_14	171	118	0,69	0,0562	0,0046	0,2780	0,0220	0,0364	0,0017	0,0108	0,0006	-0,20	230,0	10,0	248,0	18,0	450,0	180,0	230,0	10,0	7,26	
Zircon_13	603	467	0,77	0,0564	0,0028	0,2870	0,0150	0,0369	0,0016	0,0111	0,0006	0,29	233,7	9,9	257,0	12,0	450,0	120,0	233,7	9,9	9,07	
Zircon_40	223	214	0,96	0,0542	0,0039	0,2810	0,0210	0,0370	0,0016	0,0117	0,0006	-0,14	234,0	9,7	257,0	17,0	380,0	160,0	234,0	9,7	8,95	
Zircon_20	227	204	0,90	0,0665	0,0046	0,3390	0,0230	0,0371	0,0016	0,0120	0,0006	0,35	235,0	10,0	296,0	17,0	810,0	130,0	235,0	10,0	20,61	
Zircon_52	182	179	0,98	0,0622	0,0044	0,3040	0,0230	0,0373	0,0017	0,0098	0,0005	0,25	236,0	10,0	269,0	18,0	620,0	150,0	236,0	10,0	12,27	
Zircon_82	96	76	0,79	0,0502	0,0047	0,2640	0,0240	0,0380	0,0018	0,0127	0,0009	0,19	240,0	11,0	236,0	19,0	170,0	180,0	240,0	11,0	-1,69	
Zircon_69	120	111	0,93	0,0517	0,0052	0,2660	0,0250	0,0379	0,0018	0,0115	0,0007	-0,14	240,0	11,0	238,0	20,0	220,0	210,0	240,0	11,0	-0,84	
Zircon_37	623	546	0,88	0,0509	0,0026	0,2690	0,0140	0,0379	0,0015	0,0121	0,0005	0,08	240,0	9,4	243,0	12,0	230,0	120,0	240,0	9,4	1,23	
Zircon_45	95	78	0,82	0,0482	0,0046	0,2530	0,0240	0,0383	0,0017	0,0129	0,0008	0,06	242,0	11,0	228,0	20,0	100,0	190,0	242,0	11,0	-6,14	
Zircon_01	68	35	0,51	0,0544	0,0073	0,2890	0,0370	0,0382	0,0019	0,0130	0,0010	-0,09	242,0	12,0	254,0	29,0	390,0	260,0	242,0	12,0	4,72	
Zircon_43	186	92	0,49	0,0546	0,0037	0,2940	0,0200	0,0382	0,0016	0,0135	0,0008	-0,09	242,0	10,0	261,0	16,0	380,0	150,0	242,0	10,0	7,28	
Zircon_74	227	211	0,93	0,0515	0,0040	0,2740	0,0210	0,0383	0,0016	0,0133	0,0007	0,21	242,1	9,8	249,0	18,0	250,0	160,0	242,1	9,8	2,77	
Zircon_47	65	33	0,51	0,0475	0,0064	0,2520	0,0340	0,0384	0,0019	0,0131	0,0013	-0,04	243,0	12,0	229,0	27,0	90,0	260,0	243,0	12,0	-6,11	
Zircon_68	251	155	0,62	0,0537	0,0031	0,2800	0,0170	0,0386	0,0016	0,0125	0,0006	0,11	244,0	10,0	250,0	13,0	340,0	120,0	244,0	10,0	2,40	
Zircon_84	448	388	0,87	0,0527	0,0032	0,2860	0,0160	0,0385	0,0016	0,0120	0,0005	-0,07	244,0	10,0	255,0	13,0	320,0	140,0	244,0	10,0	4,31	
Zircon_96	694	418	0,60	0,0559	0,0030	0,2980	0,0160	0,0386	0,0016	0,0137	0,0006	0,16	244,0	9,7	264,0	13,0	460,0	120,0	244,0	9,7	7,58	
Zircon_70	103	64	0,62	0,0589	0,0053	0,3130	0,0280	0,0388	0,0018	0,0127	0,0009	-0,01	245,0	11,0	277,0	21,0	560,0	200,0	245,0	11,0	11,55	
Zircon_49	393	230	0,59	0,0518	0,0031	0,2780	0,0170	0,0388	0,0016	0,0124	0,0006	-0,23	245,7	9,6	248,0	13,0	250,0	130,0	245,7	9,6	0,93	
Zircon_23	156	108	0,69	0,0549	0,0040	0,2900	0,0210	0,0390	0,0016	0,0122	0,0007	-0,11	247,0	10,0	258,0	17,0	360,0	160,0	247,0	10,0	4,26	
Zircon_03	119	137	1,15	0,0509	0,0048	0,2720	0,0260	0,0393	0,0019	0,0131	0,0006	0,15	248,0	12,0	242,0	21,0	180,0	200,0	248,0	12,0	-2,48	
Zircon_21	71	71	1,00	0,0524	0,0065	0,2900	0,0360	0,0393	0,0018	0,0116	0,0008	0,14	248,0	11,0	254,0	28,0	250,0	240,0	248,0	11,0	2,36	
Zircon_10	281	165	0,59	0,0531	0,0036	0,2880	0,0190	0,0393	0,0017	0,0125	0,0007	-0,20	248,0	10,0	258,0	15,0	310,0	150,0	248,0	10,0	3,88	
Zircon_05	461	319	0,69	0,0558	0,0033	0,3040	0,0180	0,0392	0,0017	0,0131	0,0007	-0,07	248,0	10,0	269,0	14,0	410,0	130,0	248,0	10,0	7,81	
Zircon_56	184	214	1,16	0,0500	0,0036	0,2720	0,0200	0,0394	0,0016	0,0126	0,0006	0,01	249,0	9,9	243,0	16,0	190,0	150,0	249,0	9,9	-2,47	

Zircon_48	466	621	1,33	0,0512	0,0029	0,2780	0,0160	0,0394	0,0016	0,0124	0,0005	0,04	249,2	9,8	249,0	13,0	260,0	120,0	249,2	9,8	-0,08
Zircon_97	727	510	0,70	0,0539	0,0025	0,2950	0,0140	0,0395	0,0016	0,0127	0,0005	0,19	249,5	9,9	262,0	11,0	360,0	110,0	249,5	9,9	4,77
Zircon_88	693	313	0,45	0,0524	0,0028	0,2890	0,0160	0,0395	0,0016	0,0115	0,0005	0,22	249,7	9,8	257,0	13,0	310,0	120,0	249,7	9,8	2,84
Zircon_94	189	137	0,72	0,0498	0,0039	0,2710	0,0210	0,0396	0,0017	0,0125	0,0007	-0,28	250,0	10,0	244,0	16,0	150,0	160,0	250,0	10,0	-2,46
Zircon_28	249	243	0,98	0,0517	0,0038	0,2810	0,0210	0,0396	0,0016	0,0123	0,0006	0,04	250,0	10,0	250,0	17,0	250,0	160,0	250,0	10,0	0,00
Zircon_71	114	88	0,77	0,0570	0,0045	0,3090	0,0250	0,0393	0,0018	0,0136	0,0009	0,07	250,0	11,0	272,0	19,0	480,0	180,0	250,0	11,0	8,09
Zircon_12	700	567	0,81	0,0509	0,0026	0,2780	0,0150	0,0397	0,0016	0,0124	0,0005	0,05	251,0	9,7	249,0	12,0	230,0	110,0	251,0	9,7	-0,80
Zircon_53	391	194	0,50	0,0521	0,0031	0,2830	0,0170	0,0397	0,0016	0,0129	0,0007	0,03	251,0	10,0	252,0	13,0	260,0	130,0	251,0	10,0	0,40
Zircon_30	754	513	0,68	0,0525	0,0027	0,2860	0,0150	0,0397	0,0016	0,0124	0,0005	0,01	251,1	9,7	255,0	12,0	290,0	120,0	251,1	9,7	1,53
Zircon_17	236	213	0,90	0,0479	0,0027	0,2720	0,0150	0,0399	0,0017	0,0128	0,0006	0,20	252,0	10,0	244,0	12,0	90,0	120,0	252,0	10,0	-3,28
Zircon_31	223	231	1,04	0,0521	0,0039	0,2800	0,0200	0,0398	0,0017	0,0122	0,0006	0,12	252,0	11,0	253,0	17,0	310,0	140,0	252,0	11,0	0,40
Zircon_27	73	35	0,48	0,0562	0,0074	0,2980	0,0380	0,0398	0,0019	0,0131	0,0011	0,03	252,0	12,0	265,0	32,0	430,0	280,0	252,0	12,0	4,91
Zircon_46	124	54	0,44	0,0526	0,0040	0,2960	0,0230	0,0400	0,0017	0,0130	0,0010	-0,09	253,0	11,0	262,0	18,0	260,0	170,0	253,0	11,0	3,44
Zircon_100	205	197	0,96	0,0499	0,0037	0,2780	0,0210	0,0402	0,0018	0,0126	0,0007	0,34	254,0	11,0	248,0	16,0	180,0	160,0	254,0	11,0	-2,42
Zircon_36	199	144	0,72	0,0522	0,0036	0,2930	0,0210	0,0402	0,0019	0,0129	0,0008	-0,08	254,0	11,0	260,0	16,0	280,0	150,0	254,0	11,0	2,31
Zircon_67	350	185	0,53	0,0533	0,0035	0,2910	0,0180	0,0401	0,0017	0,0124	0,0006	-0,04	254,0	10,0	260,0	15,0	320,0	140,0	254,0	10,0	2,31
Zircon_26	372	197	0,53	0,0513	0,0027	0,2850	0,0160	0,0403	0,0017	0,0113	0,0006	0,12	255,0	10,0	254,0	12,0	260,0	130,0	255,0	10,0	-0,39
Zircon_35	194	175	0,90	0,0514	0,0035	0,2850	0,0190	0,0404	0,0017	0,0127	0,0006	-0,08	255,0	10,0	254,0	15,0	230,0	150,0	255,0	10,0	-0,39
Zircon_95	130	75	0,58	0,0519	0,0046	0,2900	0,0270	0,0403	0,0018	0,0136	0,0009	0,09	255,0	11,0	257,0	21,0	220,0	190,0	255,0	11,0	0,78
Zircon_62	246	146	0,59	0,0533	0,0037	0,2940	0,0200	0,0403	0,0017	0,0122	0,0007	-0,02	255,0	10,0	261,0	16,0	320,0	160,0	255,0	10,0	2,30
Zircon_81	195	119	0,61	0,0528	0,0034	0,2960	0,0180	0,0405	0,0016	0,0131	0,0007	0,05	256,0	10,0	263,0	14,0	290,0	140,0	256,0	10,0	2,66
Zircon_39	238	256	1,08	0,0545	0,0035	0,3000	0,0200	0,0406	0,0017	0,0125	0,0006	0,22	256,0	11,0	268,0	16,0	370,0	140,0	256,0	11,0	4,48
Zircon_101	170	95	0,56	0,0544	0,0040	0,3100	0,0220	0,0404	0,0018	0,0128	0,0009	0,03	256,0	11,0	273,0	17,0	360,0	150,0	256,0	11,0	6,23
Zircon_59	160	169	1,06	0,0521	0,0040	0,2890	0,0220	0,0406	0,0017	0,0130	0,0007	0,10	257,0	11,0	257,0	17,0	290,0	160,0	257,0	11,0	0,00
Zircon_75	147	116	0,79	0,0531	0,0041	0,3040	0,0250	0,0410	0,0018	0,0129	0,0008	0,17	259,0	11,0	268,0	20,0	310,0	170,0	259,0	11,0	3,36
Zircon_66	224	108	0,48	0,0554	0,0033	0,3070	0,0190	0,0412	0,0017	0,0138	0,0007	0,09	260,0	11,0	272,0	15,0	420,0	140,0	260,0	11,0	4,41
Zircon_33	120	126	1,05	0,0517	0,0043	0,3000	0,0250	0,0413	0,0019	0,0134	0,0008	0,12	261,0	11,0	267,0	19,0	270,0	180,0	261,0	11,0	2,25
Zircon_38	161	64	0,40	0,0517	0,0041	0,2950	0,0230	0,0414	0,0018	0,0135	0,0010	0,00	262,0	11,0	261,0	18,0	230,0	160,0	262,0	11,0	-0,38

Zircon_19	764	335	0,44	0,0508	0,0026	0,2920	0,0160	0,0417	0,0017	0,0132	0,0006	0,16	263,0	10,0	260,0	12,0	240,0	120,0	263,0	10,0	-1,15
Zircon_72	246	227	0,92	0,0538	0,0037	0,3010	0,0210	0,0416	0,0017	0,0133	0,0006	0,23	263,0	11,0	266,0	16,0	320,0	150,0	263,0	11,0	1,13
Zircon_65	182	131	0,72	0,0516	0,0037	0,2910	0,0220	0,0419	0,0018	0,0135	0,0007	0,07	264,0	11,0	258,0	17,0	270,0	160,0	264,0	11,0	-2,33
Zircon_58	151	96	0,64	0,0601	0,0045	0,3380	0,0260	0,0418	0,0019	0,0145	0,0009	0,38	264,0	11,0	294,0	19,0	590,0	150,0	264,0	11,0	10,20
Zircon_24	211	105	0,50	0,0509	0,0035	0,2910	0,0210	0,0420	0,0018	0,0142	0,0007	0,12	265,0	11,0	258,0	16,0	200,0	150,0	265,0	11,0	-2,71
Zircon_22	129	73	0,57	0,0524	0,0046	0,3030	0,0280	0,0420	0,0019	0,0128	0,0007	0,18	265,0	12,0	267,0	22,0	290,0	190,0	265,0	12,0	0,75
Zircon_11	753	414	0,55	0,0506	0,0027	0,2940	0,0160	0,0421	0,0017	0,0122	0,0006	0,13	266,0	11,0	262,0	12,0	210,0	120,0	266,0	11,0	-1,53
Zircon_80	172	135	0,78	0,0541	0,0044	0,3170	0,0260	0,0422	0,0018	0,0138	0,0007	0,13	266,0	11,0	278,0	20,0	360,0	180,0	266,0	11,0	4,32
Zircon_42	469	195	0,42	0,0547	0,0028	0,3210	0,0170	0,0424	0,0017	0,0134	0,0007	0,08	267,0	11,0	282,0	13,0	390,0	120,0	267,0	11,0	5,32
Zircon_87	37	30	0,81	0,0535	0,0067	0,3250	0,0370	0,0424	0,0024	0,0153	0,0014	0,02	267,0	15,0	297,0	27,0	450,0	230,0	267,0	15,0	10,10
Zircon_89	26	14	0,54	0,0467	0,0077	0,2830	0,0470	0,0425	0,0024	0,0132	0,0014	0,10	268,0	15,0	257,0	37,0	110,0	310,0	268,0	15,0	-4,28
Zircon_09	863	448	0,52	0,0509	0,0027	0,2970	0,0160	0,0424	0,0017	0,0136	0,0005	-0,02	268,0	10,0	264,0	12,0	220,0	120,0	268,0	10,0	-1,52
Zircon_57	188	91	0,48	0,0546	0,0038	0,3190	0,0250	0,0424	0,0019	0,0141	0,0009	0,16	268,0	12,0	280,0	19,0	450,0	150,0	268,0	12,0	4,29
Zircon_54	109	62	0,57	0,0558	0,0041	0,3330	0,0300	0,0428	0,0024	0,0137	0,0009	0,29	270,0	15,0	295,0	21,0	420,0	130,0	270,0	15,0	8,47
Zircon_25	374	269	0,72	0,0521	0,0030	0,3070	0,0180	0,0432	0,0017	0,0140	0,0007	0,15	273,0	11,0	271,0	14,0	280,0	130,0	273,0	11,0	-0,74
Zircon_55	328	167	0,51	0,0541	0,0035	0,3220	0,0210	0,0432	0,0017	0,0141	0,0007	0,04	273,0	11,0	283,0	16,0	360,0	140,0	273,0	11,0	3,53
Zircon_73	230	119	0,52	0,0545	0,0037	0,3230	0,0230	0,0433	0,0018	0,0139	0,0008	0,15	273,0	11,0	283,0	18,0	350,0	150,0	273,0	11,0	3,53
Zircon_93	339	208	0,61	0,0519	0,0031	0,3120	0,0200	0,0435	0,0017	0,0133	0,0006	0,09	274,0	11,0	279,0	14,0	290,0	130,0	274,0	11,0	1,79
Zircon_04	780	407	0,52	0,0538	0,0026	0,3200	0,0170	0,0436	0,0018	0,0139	0,0006	0,30	275,0	11,0	282,0	13,0	350,0	110,0	275,0	11,0	2,48
Zircon_41	606	185	0,31	0,0530	0,0026	0,3230	0,0160	0,0439	0,0018	0,0149	0,0008	0,09	277,0	11,0	284,0	13,0	320,0	110,0	277,0	11,0	2,46
Zircon_18	135	96	0,71	0,0505	0,0042	0,3060	0,0250	0,0440	0,0020	0,0142	0,0008	-0,01	278,0	12,0	269,0	19,0	210,0	170,0	278,0	12,0	-3,35
Zircon_50	162	65	0,40	0,0542	0,0043	0,3330	0,0260	0,0443	0,0020	0,0149	0,0009	-0,01	279,0	12,0	290,0	20,0	340,0	180,0	279,0	12,0	3,79
Zircon_08	170	135	0,79	0,0508	0,0035	0,3110	0,0210	0,0444	0,0020	0,0142	0,0007	-0,04	280,0	12,0	274,0	16,0	230,0	140,0	280,0	12,0	-2,19
Zircon_63	396	414	1,05	0,0527	0,0029	0,3170	0,0180	0,0444	0,0018	0,0143	0,0006	0,22	280,0	11,0	279,0	14,0	290,0	130,0	280,0	11,0	-0,36
Zircon_34	113	44	0,39	0,0559	0,0054	0,3360	0,0310	0,0444	0,0019	0,0147	0,0013	0,13	280,0	12,0	291,0	24,0	390,0	210,0	280,0	12,0	3,78
Zircon_29	193	155	0,80	0,0511	0,0035	0,3130	0,0230	0,0446	0,0019	0,0136	0,0006	0,07	281,0	11,0	275,0	18,0	250,0	160,0	281,0	11,0	-2,18
Zircon_07	141	101	0,72	0,0518	0,0042	0,3180	0,0250	0,0446	0,0019	0,0143	0,0008	0,17	281,0	12,0	281,0	18,0	290,0	170,0	281,0	12,0	0,00
Zircon_83	141	87	0,62	0,0513	0,0034	0,3190	0,0210	0,0447	0,0019	0,0143	0,0008	0,09	282,0	11,0	280,0	16,0	240,0	150,0	282,0	11,0	-0,71

Sample																				
Zircon_64	192	124	0,65	0,0527	0,0032	0,3250	0,0200	0,0452	0,0019	0,0135	0,0008	0,10	285,0	0,0527→						

CPV-15-343 (DZ)

Maximum depositional age (3+DZ, 1σ): 224.9±5.3 Ma (MSWD = 0.28)

Sample																				
Zircon_64	192	124	0,65	0,0527	0,0032	0,3250	0,0200	0,0452	0,0019	0,0135	0,0008	0,10	285,0	285,0	287,0	16,0	330,0	140,0	285,0	12,0	0,70
Zircon_60	102	64	0,63	0,0538	0,0051	0,3330	0,0310	0,0453	0,0021	0,0146	0,0009	-0,08	286,0	290,0	23,0	350,0	180,0	286,0	13,0	1,38
Zircon_92	178	103	0,58	0,0534	0,0044	0,3370	0,0270	0,0457	0,0020	0,0141	0,0007	0,00	288,0	299,0	19,0	290,0	180,0	288,0	12,0	3,68
Zircon_76	146	99	0,68	0,0519	0,0043	0,3320	0,0290	0,0464	0,0020	0,0153	0,0009	0,12	292,0	289,0	22,0	300,0	170,0	292,0	13,0	-1,04
Zircon_16	281	242	0,86	0,0516	0,0031	0,3320	0,0200	0,0466	0,0018	0,0141	0,0006	0,06	293,0	290,0	15,0	260,0	130,0	293,0	11,0	-1,03
~~Zircon_85~~	~~139~~	~~101~~	~~0,73~~	~~0,0824~~	~~0,0057~~	~~0,5350~~	~~0,0380~~	~~0,0471~~	~~0,0019~~	~~0,0201~~	~~0,0013~~	~~0,20~~	~~297,0~~	~~433,0~~	~~25,0~~	~~1250,0~~	~~140,0~~	~~297,0~~	~~12,0~~	~~31,11~~
Zircon_91	150	96	0,64	0,0525	0,0036	0,3480	0,0250	0,0475	0,0020	0,0147	0,0008	0,22	299,0	302,0	19,0	320,0	160,0	299,0	12,0	0,99
~~Zircon_86~~	~~44~~	~~126~~	~~0,89~~	~~0,1390~~	~~0,0160~~	~~0,9400~~	~~0,1400~~	~~0,0475~~	~~0,0024~~	~~0,0275~~	~~0,0035~~	~~0,84~~	~~299,0~~	~~672,0~~	~~74,0~~	~~2180,0~~	~~220,0~~	~~299,0~~	~~15,0~~	~~55,54~~
Zircon_61	157	99	0,63	0,0527	0,0040	0,3410	0,0220	0,0476	0,0021	0,0151	0,0009	-0,13	300,0	299,0	17,0	350,0	150,0	300,0	13,0	-0,33
Zircon_79	397	333	0,84	0,0582	0,0032	0,3940	0,0220	0,0490	0,0020	0,0143	0,0006	0,08	308,0	336,0	16,0	520,0	120,0	308,0	12,0	8,33
~~Zircon_44~~ ***	~~1770~~	~~1662~~	~~0,94~~	~~0,0543~~	~~0,0026~~	~~0,3710~~	~~0,0190~~	~~0,0492~~	~~0,0019~~	~~0,0157~~	~~0,0006~~	~~0,03~~	~~310,0~~	~~321,0~~	~~13,0~~	~~370,0~~	~~110,0~~	~~310,0~~	~~12,0~~	~~3,43~~
Zircon_02	193	145	0,75	0,0516	0,0034	0,3590	0,0240	0,0505	0,0021	0,0157	0,0008	-0,01	318,0	311,0	18,0	250,0	140,0	318,0	13,0	-2,25
~~Zircon_01~~	~~668,0~~	~~357,0~~	~~0,534~~	~~0,048~~	~~0,004~~	~~0,218~~	~~0,020~~	~~0,034~~	~~0,001~~	~~0,011~~	~~0,001~~	~~0,168~~	~~218,2~~	~~199,0~~	~~17,0~~	~~80,0~~	~~170,0~~	~~218,2~~	~~6,3~~	~~-9,6~~
~~Zircon_93~~	~~64,0~~	~~30,0~~	~~0,469~~	~~0,103~~	~~0,033~~	~~0,400~~	~~0,200~~	~~0,028~~	~~0,001~~	~~0,016~~	~~0,008~~	~~-0,238~~	~~180,1~~	~~340,0~~	~~98,0~~	~~1590,0~~	~~320,0~~	~~180,1~~	~~8,8~~	~~47,0~~
Zircon_69	217	150	0,6912	0,0583	0,0032	0,244	0,016	0,0302	0,00062	0,01053	0,00043	0,1277	191,8	221	12	520	120	191,8	3,9	13,2127
Zircon_40	194	103	0,5309	0,0526	0,0044	0,225	0,021	0,03113	0,00066	0,01012	0,00071	0,0593	197,6	206	17	280	160	197,6	4,1	4,07767
Zircon_77 *	52	32	0,6154	0,0693	0,0065	0,293	0,035	0,03132	0,00085	0,01346	0,00096	0,2055	198,8	260	26	900	170	198,8	5,3	23,5385
Zircon_54 *	214	106	0,4953	0,0535	0,0049	0,231	0,02	0,0313	0,0011	0,01	0,001	0,1101	199	213	17	300	180	199	6,6	6,57277
Zircon_34 *	364	143	0,3929	0,0523	0,0026	0,224	0,013	0,03137	0,00067	0,00995	0,00039	0,0899	199,1	205	11	270	110	199,1	4,2	2,87805
Zircon_75 *	201	124	0,6169	0,0669	0,0042	0,29	0,02	0,0314	0,00072	0,01153	0,00057	0,0567	199,3	257	16	820	130	199,3	4,5	22,4514
Zircon_33 *	104	58	0,5577	0,0513	0,0028	0,224	0,014	0,03142	0,00076	0,01034	0,00033	0,3626	199,4	205	12	230	130	199,4	4,8	2,73171
Zircon_47 *	223	109	0,4888	0,0522	0,0048	0,233	0,021	0,03164	0,00093	0,0104	0,00075	0,116	200,8	211	18	260	190	200,8	5,8	4,83412
Zircon_72 *	271	193	0,7122	0,0619	0,0041	0,264	0,019	0,03171	0,0009	0,01117	0,00053	0,1108	201,2	239	15	630	140	201,2	5,6	15,8159
Zircon_52 *	127	85	0,6693	0,0525	0,003	0,235	0,016	0,03175	0,00082	0,01093	0,00062	0,2547	201,5	214	13	290	130	201,5	5,1	5,84112
Zircon_60 *	82	39	0,4756	0,0578	0,0063	0,247	0,026	0,0318	0,0012	0,0112	0,001	-0,127	201,7	222	22	470	230	201,7	7,2	9,14414
Zircon_64 *	102	51	0,5	0,0566	0,0031	0,25	0,018	0,03183	0,00075	0,011	0,00043	-0,043	202	228	14	460	120	202	4,8	11,4035

Sample																					
Zircon_23	128	54	0,4219	0,0508	0,0029	0,221	0,014	0,03186	0,00074	0,0101	0,00037	0,1145	202,1	4,6	204	11	240	120	202,1	4,6	0,93137	*
Zircon_03	198	148	0,7475	0,0497	0,0045	0,214	0,02	0,03188	0,00095	0,01003	0,00062	-0,286	202,3	5,9	196	17	170	200	202,3	5,9	-3,2143	*
Zircon_84	158	110	0,6962	0,0827	0,0079	0,368	0,042	0,03188	0,00091	0,01452	0,00095	0,28	202,3	5,7	217	31	1240	150	202,3	5,7	36,183	*
Zircon_70	192	94	0,4896	0,0569	0,0043	0,26	0,021	0,03194	0,00097	0,0111	0,00074	-0,139	202,7	6	234	17	440	170	202,7	6	13,3761	*
Zircon_09	61	34	0,5574	0,0494	0,0035	0,218	0,016	0,03195	0,00076	0,01014	0,00043	0,0627	202,8	4,7	199	13	130	140	202,8	4,7	-1,9095	*
Zircon_96	121	62	0,5124	0,1164	0,0096	0,51	0,042	0,03196	0,00081	0,0219	0,0012	-0,059	202,8	5,1	410	29	1890	140	202,8	5,1	51,599	*
Zircon_36	492	281	0,5711	0,0528	0,0032	0,229	0,017	0,03197	0,00096	0,01088	0,00051	-0,176	202,9	6	209	14	290	130	202,9	6	2,91866	*
Zircon_46	172	111	0,6453	0,0532	0,0035	0,235	0,018	0,03203	0,00085	0,01016	0,00063	0,0177	203,2	5,3	213	14	330	140	203,2	5,3	4,60094	*
Zircon_58	130	59	0,4538	0,0563	0,0047	0,246	0,021	0,03209	0,00092	0,00987	0,00054	0,0587	203,6	5,7	222	17	470	170	203,6	5,7	8,28829	*
Zircon_28	128	71	0,5547	0,0518	0,0039	0,228	0,017	0,03214	0,00088	0,01051	0,00045	-0,261	203,9	5,5	208	14	230	160	203,9	5,5	1,97115	*
Zircon_20	175	85	0,4857	0,0491	0,0036	0,224	0,018	0,0322	0,001	0,01107	0,0008	0,1807	204,2	6,4	204	15	210	150	204,2	6,4	-0,098	*
Zircon_45	136	67	0,4926	0,0541	0,0039	0,236	0,018	0,03218	0,00072	0,0107	0,00048	-0,071	204,2	4,5	214	14	340	150	204,2	4,5	4,57944	*
Zircon_05	45	20	0,4444	0,0491	0,0031	0,218	0,016	0,03224	0,00081	0,00961	0,00049	0,2441	204,6	5	199	13	150	130	204,6	5	-2,8141	*
Zircon_08	335	243	0,7254	0,0494	0,004	0,219	0,019	0,03212	0,00085	0,0103	0,00085	0,2464	204,6	5,6	200	16	160	170	204,6	5,6	-2,3	*
Zircon_29	212	163	0,7689	0,0509	0,0027	0,229	0,013	0,03225	0,00075	0,01003	0,00056	-0,099	204,6	4,7	209	11	210	110	204,6	4,7	2,10526	*
Zircon_14	111	47	0,4234	0,0498	0,0029	0,221	0,013	0,03228	0,00069	0,01025	0,00032	-0,102	204,8	4,3	203	11	190	120	204,8	4,3	-0,8867	*
Zircon_48	206	175	0,8495	0,0518	0,0029	0,238	0,015	0,03231	0,0007	0,01104	0,00043	-0,301	205	4,4	216	12	270	120	205	4,4	5,09259	*
Zircon_49	142	93	0,6549	0,0531	0,0034	0,237	0,016	0,03233	0,00096	0,01022	0,00046	-0,004	205,1	6	217	13	320	130	205,1	6	5,48387	*
Zircon_59	184	96	0,5217	0,0559	0,0044	0,248	0,02	0,03238	0,00073	0,01074	0,00065	-0,174	205,4	4,5	226	16	400	170	205,4	4,5	9,11504	*
Zircon_88	203	160	0,7882	0,0889	0,0059	0,392	0,032	0,03238	0,00085	0,01621	0,00071	-0,095	205,4	5,3	335	23	1360	130	205,4	5,3	38,6866	*
Zircon_22	78	46	0,5897	0,0508	0,0027	0,227	0,015	0,0324	0,00063	0,01017	0,00043	0,1997	205,5	3,9	207	12	210	120	205,5	3,9	0,72464	*
Zircon_76	197	127	0,6447	0,0677	0,0055	0,303	0,025	0,03241	0,00074	0,01164	0,00076	0,0251	205,6	4,6	268	19	820	160	205,6	4,6	23,2836	*
Zircon_02	86	51	0,593	0,0476	0,0036	0,215	0,019	0,03248	0,00091	0,01066	0,00053	0,2359	206	5,7	199	16	100	150	206	5,7	-3,5176	*
Zircon_50	278	154	0,554	0,054	0,0052	0,238	0,023	0,03247	0,00082	0,01128	0,00092	0,0543	206	5,1	218	18	340	190	206	5,1	5,50459	*
Zircon_56	108	59	0,5463	0,0579	0,0062	0,248	0,026	0,0325	0,0011	0,01155	0,00074	0,057	206	6,6	223	21	420	220	206	6,6	7,62332	*
Zircon_25	224	172	0,7679	0,051	0,0032	0,229	0,014	0,03251	0,00079	0,01147	0,00056	-0,171	206,2	4,9	209	12	220	130	206,2	4,9	1,33971	*
Zircon_38	212	137	0,6462	0,0537	0,0034	0,236	0,017	0,03252	0,00077	0,01033	0,00041	0,0177	206,3	4,8	214	14	380	140	206,3	4,8	3,59813	*
Zircon_30	361	198	0,5485	0,0521	0,0025	0,232	0,014	0,03254	0,00083	0,01013	0,00055	0,0958	206,4	5,2	211	11	320	120	206,4	5,2	2,18009	*

Sample																						
Zircon_37	204	126	0,6176	0,0528	0,0028	0,233	0,014	0,03253	0,00074	0,01024	0,00054	-0,029	206,4	4,6	214	11	300	120	206,4	3,5514	4,6	*
Zircon_51	249	132	0,5301	0,0523	0,0046	0,239	0,021	0,0325	0,0011	0,01066	0,00088	0,1452	206,4	6,6	219	17	300	180	206,4	5,75342	6,6	*
Zircon_55	248	144	0,5806	0,0548	0,0044	0,245	0,021	0,0325	0,001	0,01019	0,00067	0,0669	206,4	6,3	223	17	380	170	206,4	7,44395	6,3	*
Zircon_97	102	62	0,6078	0,124	0,011	0,538	0,05	0,03255	0,0014	0,0209	0,0014	-0,029	206,4	5,9	438	31	1950	150	206,4	52,8767	5,9	*
Zircon_06	196	134	0,6837	0,0496	0,0032	0,221	0,015	0,0326	0,00092	0,01032	0,00055	0,2241	206,8	5,7	202	13	220	130	206,8	-2,3762	5,7	*
Zircon_61	166	95	0,5723	0,054	0,0034	0,255	0,018	0,0326	0,00093	0,01028	0,00058	-0,021	206,8	5,8	230	15	380	140	206,8	10,087	5,8	*
Zircon_26	67	35	0,5224	0,0512	0,003	0,231	0,018	0,0326	0,001	0,00981	0,00061	0,2838	206,9	6,3	210	15	280	130	206,9	1,47619	6,3	*
Zircon_71	134	96	0,7164	0,0604	0,0039	0,269	0,02	0,03266	0,00093	0,01289	0,00069	0,1139	207,1	5,8	241	16	600	130	207,1	14,0664	5,8	*
Zircon_79	348	227	0,6523	0,071	0,0049	0,321	0,026	0,03266	0,00097	0,01328	0,00063	0,207	207,1	6	281	20	940	130	207,1	26,2989	6	*
Zircon_15	136	60	0,4412	0,0495	0,0022	0,224	0,012	0,03266	0,00065	0,01063	0,00047	0,2827	207,2	4	206	10	159	96	207,2	-0,5825	4	*
Zircon_39	225	121	0,5378	0,052	0,004	0,236	0,017	0,03266	0,00094	0,01086	0,0007	0,0183	207,2	5,9	215	15	290	160	207,2	3,62791	5,9	*
Zircon_65	418	305	0,7297	0,056	0,0046	0,258	0,02	0,03269	0,00093	0,01106	0,00073	-0,167	207,3	5,8	234	17	510	190	207,3	11,4103	5,8	*
Zircon_85	383	347	0,8277	0,0834	0,0054	0,384	0,027	0,03268	0,00088	0,01424	0,00081	0,014	207,3	5,5	329	20	1250	130	207,3	36,9999	5,5	*
Zircon_63	263	188	0,7148	0,0564	0,004	0,255	0,02	0,0327	0,0009	0,01108	0,00051	0,0344	207,4	5,6	232	15	460	150	207,4	10,6034	5,6	*
Zircon_31	158	76	0,481	0,0513	0,0039	0,234	0,019	0,03281	0,00085	0,01062	0,0005	0,2247	208,1	5,3	213	16	250	160	208,1	2,30047	5,3	*
Zircon_41	109	50	0,4587	0,0503	0,0033	0,236	0,017	0,03281	0,00079	0,01026	0,00049	-0,065	208,1	4,9	217	14	230	150	208,1	4,10138	4,9	*
Zircon_44	263	237	0,9011	0,0521	0,004	0,235	0,018	0,03282	0,00088	0,01077	0,00045	-0,234	208,1	5,5	218	15	260	170	208,1	4,54128	5,5	*
Zircon_21	345	420	1,2174	0,0488	0,0035	0,23	0,02	0,03287	0,00098	0,01121	0,00079	0,2224	208,4	6,1	209	17	120	150	208,4	0,28708	6,1	*
Zircon_53	180	97	0,5389	0,0546	0,005	0,246	0,021	0,0329	0,0011	0,01015	0,00069	-0,144	208,6	7	222	17	310	190	208,6	6,03604	7	*
Zircon_35	158	84	0,5316	0,0512	0,0036	0,235	0,018	0,03292	0,00095	0,01088	0,00059	0,0414	208,8	5,9	215	14	260	140	208,8	2,88372	5,9	*
Zircon_92	223	163	0,7390	0,1041	0,0089	0,469	0,043	0,03293	0,0008	0,01703	0,00099	0,2355	208,9	5	386	30	1630	160	208,9	45,8808	5	*
Zircon_19	158	80	0,5063	0,0514	0,005	0,224	0,024	0,033	0,0011	0,01093	0,0007	0,229	209,5	6,8	209	20	210	200	209,5	-0,2392	6,8	*
Zircon_13	211	155	0,7346	0,0494	0,0044	0,228	0,022	0,03307	0,00095	0,0112	0,00063	0,2193	209,7	6	207	18	190	180	209,7	-1,3043	6	*
Zircon_07	81	45	0,5556	0,0498	0,006	0,223	0,027	0,0329	0,0011	0,01092	0,00085	-0,014	209,8	6,9	205	22	130	240	209,8	-2,3415	6,9	*
Zircon_66	314	287	0,914	0,0548	0,0036	0,255	0,02	0,03314	0,00094	0,01242	0,00066	0,2309	210,2	5,9	239	16	450	140	210,2	12,0502	5,9	*
Zircon_73	215	111	0,5163	0,0625	0,0058	0,281	0,027	0,0331	0,001	0,0121	0,0012	0,0614	210,2	6,4	254	20	650	190	210,2	17,2441	6,4	*
Zircon_27	181	101	0,558	0,0525	0,002	0,235	0,012	0,03317	0,00066	0,01024	0,00037	-0,036	210,3	4,1	214	9,6	304	83	210,3	1,72897	4,1	*
Zircon_83	92	40	0,4348	0,0816	0,0061	0,379	0,028	0,03317	0,00093	0,01558	0,00092	-0,072	210,4	5,8	325	21	1200	160	210,4	35,2615	5,8	*

Zircon_43	163	75	0,4601	0,0554	0,0035	0,239	0,016	0,03319	0,00082	0,01034	0,00052	0,2962	210,5	220	5,1	13	400	140	210,5	5,1	4,31818	*
Zircon_42	339	256	0,7552	0,0539	0,0028	0,243	0,015	0,03322	0,00097	0,01055	0,00046	0,2306	210,6	220	6,1	12	350	120	210,6	6,1	4,27273	*
Zircon_24	119	56	0,4706	0,0513	0,0031	0,234	0,017	0,0332	0,0012	0,01087	0,0006	0,3498	210,8	213	7,4	14	230	130	210,8	7,4	1,03286	*
Zircon_16	243	248	1,0206	0,0504	0,0046	0,229	0,021	0,03327	0,00095	0,01064	0,00084	0,0068	210,9	210	5,9	16	180	190	210,9	5,9	-0,4286	*
Zircon_12	299	190	0,6355	0,053	0,018	0,23	0,13	0,0333	0,0021	0,0099	0,0041	-0,138	211	208	13	75	180	440	211	13	-1,4423	*
Zircon_91	174	80	0,4598	0,1035	0,0084	0,471	0,035	0,0333	0,0013	0,0177	0,0012	-0,09	211,1	390	8,1	25	1660	170	211,1	8,1	45,8718	*
Zircon_68	166	88	0,5301	0,058	0,005	0,273	0,023	0,0335	0,0013	0,01134	0,00067	0,0057	212,2	244	7,9	19	520	190	212,2	7,9	13,0328	*
Zircon_81	286	205	0,7468	0,0777	0,0068	0,343	0,028	0,0335	0,0012	0,01357	0,00087	-0,406	212,2	297	7,6	21	1100	170	212,2	7,6	28,5522	*
Zircon_89	43	17	0,3953	0,092	0,011	0,434	0,062	0,0335	0,0011	0,015	0,0013	0,2817	212,3	362	6,7	41	1480	190	212,3	6,7	41,3536	*
Zircon_32	118	70	0,5932	0,0513	0,0036	0,24	0,018	0,03352	0,00086	0,01063	0,00066	-0,055	212,5	218	5,3	14	230	150	212,5	5,3	2,52294	*
Zircon_62	185	102	0,5514	0,0568	0,0058	0,268	0,032	0,0337	0,001	0,0117	0,0013	0,2983	213,9	238	6,5	25	450	220	213,9	6,5	10,1261	*
Zircon_10	96	39	0,4063	0,049	0,004	0,231	0,018	0,0338	0,001	0,01048	0,00074	0,2544	214	210	6,5	14	210	170	214	6,5	-1,9048	*
Zircon_04	300	300	1	0,0479	0,0039	0,23	0,023	0,034	0,0014	0,01196	0,00088	0,3149	215,4	209	9	19	140	170	215,4	9	-3,0622	*
Zircon_18	153	129	0,8431	0,0506	0,0038	0,238	0,019	0,03403	0,00086	0,01109	0,00071	0,143	215,7	215	5,4	15	200	160	215,7	5,4	-0,3256	*
Zircon_17	145	73	0,5034	0,0522	0,007	0,241	0,034	0,0341	0,0015	0,0112	0,00093	0,0751	215,9	215	9,1	28	310	260	215,9	9,1	-0,4186	*
Zircon_99	109	76	0,6972	0,139	0,01	0,638	0,052	0,0341	0,001	0,0226	0,001	0,2702	216,1	507	6,4	34	2190	120	216,1	6,4	57,3767	
Zircon_80	180	67	0,3722	0,0712	0,0082	0,346	0,038	0,0342	0,0012	0,015	0,0012	-0,106	216,8	301	7,5	29	970	240	216,8	7,5	27,9734	
Zircon_57	122	76	0,623	0,0554	0,0046	0,265	0,024	0,03445	0,00099	0,01315	0,00083	0,0155	218,3	237	6,2	19	380	180	218,3	6,2	7,8903	*
Zircon_87	242	133	0,5496	0,088	0,014	0,419	0,084	0,0344	0,0011	0,0154	0,0011	0,3256	218,3	356	6,6	53	1290	290	218,3	6,6	38,6798	
Zircon_90	197	146	0,7411	0,101	0,0066	0,477	0,035	0,03465	0,00097	0,01639	0,00097	0,1996	219,6	394	6	24	1670	130	219,6	6	44,264	
Zircon_78	147	83	0,5646	0,073	0,016	0,342	0,088	0,0348	0,0018	0,013	0,005	-0,13	220	293	11	56	810	390	220	11	24,9147	
Zircon_67	150	84	0,56	0,0603	0,0044	0,279	0,02	0,03498	0,00096	0,01221	0,00068	-0,069	221,6	252	6	17	540	160	221,6	6	12,0635	
Zircon_74	210	142	0,6762	0,0649	0,0055	0,306	0,032	0,035	0,0011	0,01215	0,00087	0,3039	221,7	269	6,8	24	740	160	221,7	6,8	17,5836	
Zircon_95	63	35	0,5556	0,1091	0,0062	0,523	0,033	0,03509	0,00094	0,02338	0,00097	0,1122	222,3	429	5,9	21	1780	110	222,3	5,9	48,1818	
Zircon_94	480	389	0,8104	0,1076	0,0094	0,525	0,048	0,0354	0,0011	0,0211	0,0011	0,1876	224,3	426	6,9	31	1740	140	224,3	6,9	47,3474	
Zircon_11	377	211	0,5597	0,0476	0,004	0,243	0,021	0,0357	0,0012	0,0123	0,0011	-0,039	226	222	7,7	18	90	160	226	7,7	-1,8018	
Zircon_86	462	345	0,7468	0,0903	0,0066	0,444	0,036	0,03604	0,00095	0,0188	0,0013	0,0411	228,2	372	5,9	25	1380	140	228,2	5,9	38,6559	
Zircon_98	226	158	0,6991	0,134	0,013	0,654	0,065	0,0367	0,0017	0,0278	0,0019	0,11	232	518	11	39	2120	180	232	11	55,2124	

194

	34,806	7,1	302,5	110	1390	23	464	7,1	302,5	0,004	0,00078	0,02046	0,0012	0,048	0,035	0,582	0,0051	0,0894	0,5372	159	296	~~Zircon_82~~
	66,6365	130	2820	130	2820	44	773	7,9	257,9	0,1346	0,0034	0,0469	0,0013	0,0408	0,097	1,148	0,015	0,204	0,6081	135	222	~~Zircon_100~~
	71,1921	97	3179	97	3179	64	906	12	261	0,564	0,0044	0,0323	0,0019	0,0444	0,16	1,45	0,017	0,251	0,7256	110	164	~~Zircon_101~~
																						CPV-15-392 (DZ)
	Maximum depositional age (3+DZ, 1σ): 200.9±1.8 Ma (MSWD = 1.16)																					
	26,65	6,1	192,9	130,0	860,0	17,0	263,0	6,1	192,9	0,10	0,0006	0,0114	0,0010	0,0304	0,0220	0,2970	0,0050	0,0696	0,93	195	209	~~Zircon_93~~
*	15,88	5,2	196,0	110,0	680,0	13,0	233,0	5,2	196,0	-0,14	0,0004	0,0100	0,0008	0,0309	0,0160	0,2580	0,0033	0,0610	0,60	245	408	Zircon_32
*	23,02	5,2	198,6	100,0	810,0	13,0	258,0	5,2	198,6	-0,09	0,0003	0,0115	0,0008	0,0313	0,0170	0,2900	0,0034	0,0662	1,00	463	464	Zircon_44
*	15,95	5,7	199,2	140,0	640,0	16,0	237,0	5,7	199,2	0,15	0,0006	0,0127	0,0009	0,0314	0,0210	0,2640	0,0047	0,0622	0,55	94	170	Zircon_31
*	16,05	5,9	199,8	180,0	550,0	19,0	238,0	5,9	199,8	-0,29	0,0009	0,0122	0,0009	0,0315	0,0240	0,2670	0,0054	0,0601	0,50	57	115	Zircon_29
*	4,16	5,8	200,3	130,0	240,0	12,0	209,0	5,8	200,3	0,06	0,0007	0,0108	0,0009	0,0316	0,0150	0,2300	0,0030	0,0517	0,51	79	156	Zircon_91
*	10,09	5,5	202,3	110,0	470,0	11,0	225,0	5,5	202,3	-0,32	0,0004	0,0106	0,0009	0,0319	0,0140	0,2480	0,0031	0,0570	0,61	155	254	Zircon_19
*	19,52	6,8	202,8	190,0	720,0	29,0	252,0	6,8	202,8	0,43	0,0010	0,0119	0,0011	0,0320	0,0400	0,2840	0,0078	0,0619	0,91	348	381	Zircon_49
*	27,57	6,4	202,8	160,0	1010,0	24,0	280,0	6,4	202,8	0,35	0,0008	0,0106	0,0010	0,0320	0,0300	0,3200	0,0069	0,0709	0,82	135	165	~~Zircon_100~~
*	7,87	6,8	203,6	190,0	500,0	21,0	221,0	6,8	203,6	0,05	0,0006	0,0121	0,0011	0,0321	0,0270	0,2450	0,0057	0,0554	0,92	110	120	Zircon_18
	25,55	7,0	204,0	190,0	910,0	28,0	274,0	7,0	204,0	0,34	0,0009	0,0124	0,0011	0,0322	0,0380	0,3130	0,0078	0,0700	0,70	125	179	~~Zircon_94~~
*	11,76	5,8	205,6	150,0	470,0	17,0	233,0	5,8	205,6	0,40	0,0004	0,0114	0,0009	0,0324	0,0210	0,2590	0,0042	0,0571	0,58	155	268	Zircon_90
*	15,66	7,5	205,8	200,0	550,0	23,0	244,0	7,5	205,8	-0,10	0,0010	0,0132	0,0012	0,0324	0,0300	0,2740	0,0062	0,0600	0,53	70	131	Zircon_50
	42,00	7,0	205,9	170,0	1120,0	40,0	355,0	7,0	205,9	-0,12	0,0012	0,0139	0,0011	0,0325	0,0650	0,4200	0,0110	0,0910	0,88	176	201	~~Zircon_73~~
	19,49	5,2	206,1	140,0	710,0	16,0	256,0	5,2	206,1	0,03	0,0005	0,0116	0,0008	0,0325	0,0210	0,2890	0,0044	0,0642	0,70	203	291	Zircon_99
	13,60	5,1	206,5	130,0	580,0	14,0	239,0	5,1	206,5	-0,02	0,0003	0,0115	0,0008	0,0326	0,0180	0,2660	0,0037	0,0598	0,85	387	453	Zircon_35
	40,26	9,0	206,7	200,0	1430,0	83,0	346,0	9,0	206,7	0,08	0,0033	0,0125	0,0046	0,0326	0,1700	0,4100	0,0240	0,0820	0,99	250	252	~~Zircon_38~~
	26,63	7,9	206,9	190,0	830,0	25,0	282,0	7,9	206,9	-0,03	0,0008	0,0142	0,0013	0,0326	0,0330	0,3230	0,0070	0,0683	0,50	58	117	~~Zircon_92~~
	29,52	6,7	207,2	100,0	1120,0	18,0	294,0	6,7	207,2	0,23	0,0009	0,0149	0,0011	0,0327	0,0240	0,3310	0,0045	0,0762	0,44	58	142	~~Zircon_55~~
	7,46	6,6	207,3	130,0	500,0	16,0	224,0	6,6	207,3	0,10	0,0006	0,0109	0,0011	0,0327	0,0210	0,2480	0,0040	0,0567	0,78	150	193	Zircon_11
	36,00	5,9	208,0	150,0	1290,0	22,0	325,0	5,9	208,0	0,09	0,0009	0,0133	0,0009	0,0328	0,0310	0,3800	0,0063	0,0846	0,73	149	203	~~Zircon_33~~
	21,17	5,9	208,9	160,0	700,0	20,0	265,0	5,9	208,9	0,04	0,0006	0,0128	0,0009	0,0329	0,0260	0,3000	0,0053	0,0653	0,76	105	139	Zircon_36
	42,29	9,3	208,9	210,0	1390,0	39,0	362,0	9,3	208,9	0,22	0,0020	0,0190	0,0015	0,0330	0,0580	0,4370	0,0120	0,0910	0,44	24	55	~~Zircon_30~~

Sample																					
Zircon_40	252	165	0,65	0,0608	0,0048	0,2830	0,0250	0,0330	0,0010	0,0124	0,0005	-0,22	209,4	6,1	252,0	19,0	630,0	150,0	209,4	6,1	16,90
Zircon_16	189	155	0,82	0,0532	0,0043	0,2410	0,0190	0,0330	0,0010	0,0101	0,0006	0,36	209,5	6,4	218,0	16,0	330,0	170,0	209,5	6,4	3,90
Zircon_06	369	409	1,11	0,0610	0,0036	0,2810	0,0170	0,0331	0,0009	0,0109	0,0005	0,13	209,8	5,8	251,0	13,0	650,0	130,0	209,8	5,8	16,41
Zircon_58	161	91	0,57	0,0626	0,0045	0,2790	0,0200	0,0331	0,0010	0,0108	0,0006	-0,29	209,9	6,4	249,0	16,0	620,0	150,0	209,9	6,4	15,70
~~Zircon_84~~	~~1137~~	~~900~~	~~0,79~~	~~0,1270~~	~~0,0280~~	~~0,5700~~	~~0,3400~~	~~0,0332~~	~~0,0045~~	~~0,0200~~	~~0,0100~~	~~0,53~~	~~210,0~~	~~27,0~~	~~460,0~~	~~130,0~~	~~2050,0~~	~~200,0~~	~~210,0~~	~~27,0~~	~~54,35~~
Zircon_24	128	93	0,73	0,0542	0,0051	0,2480	0,0250	0,0332	0,0011	0,0117	0,0006	-0,09	210,3	7,2	227,0	20,0	330,0	190,0	210,3	7,2	7,36
Zircon_43	167	100	0,60	0,0524	0,0054	0,2380	0,0260	0,0332	0,0011	0,0121	0,0006	0,37	210,5	7,1	215,0	20,0	290,0	180,0	210,5	7,1	2,09
~~Zircon_53~~	~~221~~	~~202~~	~~0,91~~	~~0,0724~~	~~0,0040~~	~~0,3290~~	~~0,0200~~	~~0,0332~~	~~0,0009~~	~~0,0122~~	~~0,0004~~	~~-0,02~~	~~210,6~~	~~5,6~~	~~288,0~~	~~15,0~~	~~970,0~~	~~120,0~~	~~210,6~~	~~5,6~~	~~26,88~~
~~Zircon_83~~	~~465~~	~~498~~	~~1,07~~	~~0,1020~~	~~0,0150~~	~~0,4700~~	~~0,1400~~	~~0,0332~~	~~0,0015~~	~~0,0157~~	~~0,0042~~	~~-0,07~~	~~210,7~~	~~9,5~~	~~390,0~~	~~59,0~~	~~1650,0~~	~~180,0~~	~~210,7~~	~~9,5~~	~~45,97~~
~~Zircon_68~~	~~293~~	~~116~~	~~0,40~~	~~0,0770~~	~~0,0130~~	~~0,3360~~	~~0,0690~~	~~0,0333~~	~~0,0010~~	~~0,0158~~	~~0,0030~~	~~0,22~~	~~211,1~~	~~6,5~~	~~292,0~~	~~47,0~~	~~1050,0~~	~~250,0~~	~~211,1~~	~~6,5~~	~~27,74~~
Zircon_17	118	56	0,47	0,0483	0,0045	0,2220	0,0200	0,0334	0,0010	0,0102	0,0007	0,02	211,6	6,4	206,0	18,0	130,0	180,0	211,6	6,4	-2,72
Zircon_21	217	135	0,62	0,0591	0,0044	0,2760	0,0210	0,0335	0,0010	0,0126	0,0006	0,06	212,3	6,3	246,0	17,0	550,0	150,0	212,3	6,3	13,70
~~Zircon_63~~	~~382~~	~~275~~	~~0,72~~	~~0,0995~~	~~0,0064~~	~~0,4660~~	~~0,0320~~	~~0,0335~~	~~0,0009~~	~~0,0153~~	~~0,0007~~	~~0,10~~	~~212,3~~	~~5,9~~	~~386,0~~	~~22,0~~	~~1600,0~~	~~130,0~~	~~212,3~~	~~5,9~~	~~45,00~~
Zircon_28	125	85	0,68	0,0697	0,0063	0,3220	0,0300	0,0335	0,0011	0,0130	0,0011	0,12	212,5	6,7	282,0	23,0	910,0	170,0	212,5	6,7	24,65
Zircon_70	406	173	0,43	0,0583	0,0026	0,2690	0,0140	0,0336	0,0008	0,0113	0,0005	0,03	212,7	5,0	242,0	11,0	515,0	97,0	212,7	5,0	12,11
Zircon_23	156	80	0,51	0,0590	0,0045	0,2800	0,0230	0,0336	0,0011	0,0118	0,0008	-0,05	212,8	7,1	255,0	18,0	540,0	170,0	212,8	7,1	16,55
Zircon_69	297	208	0,70	0,0528	0,0039	0,2410	0,0190	0,0336	0,0009	0,0107	0,0004	-0,09	213,0	5,6	224,0	15,0	320,0	150,0	213,0	5,6	4,91
Zircon_47	161	57	0,35	0,0524	0,0038	0,2360	0,0160	0,0336	0,0011	0,0110	0,0007	0,24	213,1	7,1	219,0	13,0	330,0	150,0	213,1	7,1	2,69
Zircon_48	147	78	0,53	0,0635	0,0041	0,2960	0,0200	0,0336	0,0012	0,0134	0,0007	0,24	213,1	7,2	262,0	16,0	690,0	140,0	213,1	7,2	18,66
Zircon_13	176	104	0,59	0,0564	0,0047	0,2620	0,0210	0,0336	0,0012	0,0118	0,0006	-0,13	213,2	7,3	238,0	17,0	460,0	170,0	213,2	7,3	10,42
Zircon_88	360	276	0,77	0,0603	0,0033	0,2770	0,0160	0,0337	0,0010	0,0118	0,0004	0,29	213,3	6,0	248,0	12,0	600,0	120,0	213,3	6,0	13,99
~~Zircon_80~~	~~518~~	~~132~~	~~0,25~~	~~0,0894~~	~~0,0096~~	~~0,4180~~	~~0,0480~~	~~0,0336~~	~~0,0009~~	~~0,0252~~	~~0,0013~~	~~0,11~~	~~213,3~~	~~5,5~~	~~353,0~~	~~31,0~~	~~1380,0~~	~~150,0~~	~~213,3~~	~~5,5~~	~~39,58~~
~~Zircon_34~~	~~67~~	~~22~~	~~0,33~~	~~0,0906~~	~~0,0094~~	~~0,4260~~	~~0,0460~~	~~0,0337~~	~~0,0014~~	~~0,0228~~	~~0,0021~~	~~-0,07~~	~~213,4~~	~~8,5~~	~~357,0~~	~~32,0~~	~~1310,0~~	~~190,0~~	~~213,4~~	~~8,5~~	~~40,22~~
Zircon_95	178	112	0,63	0,0684	0,0077	0,3210	0,0310	0,0337	0,0011	0,0135	0,0007	-0,29	213,7	7,1	281,0	26,0	920,0	190,0	213,7	7,1	23,95
Zircon_66	143	57	0,40	0,0547	0,0048	0,2550	0,0220	0,0339	0,0011	0,0132	0,0008	0,09	215,0	7,0	229,0	19,0	320,0	190,0	215,0	7,0	6,11
Zircon_09	129	84	0,65	0,0695	0,0049	0,3130	0,0240	0,0340	0,0010	0,0124	0,0007	-0,18	215,5	6,3	275,0	19,0	860,0	170,0	215,5	6,3	21,64
Zircon_71	162	71	0,44	0,0529	0,0042	0,2500	0,0200	0,0340	0,0011	0,0119	0,0007	-0,13	215,6	7,1	226,0	16,0	270,0	170,0	215,6	7,1	4,60
Zircon_65	316	184	0,58	0,0635	0,0053	0,2970	0,0240	0,0340	0,0009	0,0128	0,0010	-0,32	215,7	5,4	263,0	18,0	650,0	160,0	215,7	5,4	17,98

Zircon_67	283	161	0,57	0,0536	0,0038	0,2480	0,0190	0,0342	0,0009	0,0107	0,0007	0,05	216,6	5,9	227,0	15,0	310,0	150,0	216,6	5,9	4,58
Zircon_57	401	202	0,50	0,0535	0,0039	0,2520	0,0170	0,0342	0,0009	0,0117	0,0005	0,14	216,6	5,8	231,0	13,0	320,0	140,0	216,6	5,8	6,23
Zircon_07	183	98	0,54	0,0922	0,0082	0,4500	0,0420	0,0342	0,0011	0,0184	0,0009	0,10	216,7	6,8	380,0	29,0	1400,0	150,0	216,7	6,8	42,97
Zircon_41	130	75	0,58	0,0654	0,0055	0,3010	0,0250	0,0343	0,0011	0,0147	0,0009	-0,09	217,7	6,9	266,0	18,0	780,0	170,0	217,7	6,9	18,16
Zircon_37	79	38	0,48	0,0998	0,0089	0,4750	0,0440	0,0344	0,0014	0,0203	0,0012	-0,21	217,7	8,7	391,0	30,0	1580,0	160,0	217,7	8,7	44,32
Zircon_45	94	48	0,51	0,0746	0,0058	0,3390	0,0280	0,0344	0,0013	0,0170	0,0010	0,10	218,1	7,9	295,0	20,0	1020,0	150,0	218,1	7,9	26,07
Zircon_08	179	87	0,49	0,0701	0,0052	0,3730	0,0250	0,0344	0,0010	0,0150	0,0008	0,21	218,2	6,2	328,0	19,0	1140,0	130,0	218,2	6,2	33,48
Zircon_27	98	52	0,53	0,0746	0,0065	0,3630	0,0290	0,0345	0,0011	0,0153	0,0010	-0,13	218,4	6,6	313,0	22,0	1020,0	160,0	218,4	6,6	30,22
Zircon_20	116	85	0,73	0,0561	0,0067	0,2600	0,0330	0,0345	0,0011	0,0128	0,0010	0,27	218,7	7,1	233,0	25,0	340,0	200,0	218,7	7,1	6,14
Zircon_72	191	117	0,61	0,0802	0,0070	0,3940	0,0380	0,0345	0,0012	0,0157	0,0011	0,07	218,8	7,2	335,0	27,0	1200,0	150,0	218,8	7,2	34,69
Zircon_12	244	231	0,95	0,0628	0,0042	0,2890	0,0180	0,0347	0,0011	0,0111	0,0005	-0,04	219,7	7,0	257,0	14,0	660,0	150,0	219,7	7,0	14,51
Zircon_01	258	114	0,44	0,0705	0,0037	0,3380	0,0200	0,0347	0,0009	0,0168	0,0007	0,26	220,0	5,8	298,0	15,0	920,0	100,0	220,0	5,8	26,17
Zircon_74	445	109	0,92	0,0954	0,0058	0,4570	0,0350	0,0349	0,0011	0,0143	0,0011	-0,07	221,3	7,0	381,0	23,0	1530,0	100,0	221,3	7,0	44,92
Zircon_03	332	117	0,35	0,1077	0,0087	0,5210	0,0480	0,0350	0,0009	0,0257	0,0019	0,42	221,8	5,8	423,0	31,0	1750,0	140,0	221,8	5,8	47,57
Zircon_14	70	51	0,73	0,0603	0,0060	0,2860	0,0290	0,0351	0,0013	0,0130	0,0010	0,06	222,1	8,4	258,0	22,0	580,0	210,0	222,1	8,4	13,91
Zircon_56	108	76	0,70	0,0745	0,0072	0,3640	0,0350	0,0351	0,0013	0,0133	0,0008	-0,16	222,1	8,2	348,0	26,0	1000,0	220,0	222,1	8,2	30,16
Zircon_97	184	110	0,76	0,0880	0,0130	0,4250	0,0760	0,0352	0,0012	0,0150	0,0026	0,22	223,3	7,7	357,0	46,0	1410,0	200,0	223,3	7,7	37,45
Zircon_85	211	151	0,71	0,0894	0,0075	0,4420	0,0390	0,0353	0,0011	0,0167	0,0009	0,26	223,4	6,6	370,0	28,0	1390,0	140,0	223,4	6,6	39,62
Zircon_26	358	148	0,41	0,0549	0,0026	0,2740	0,0140	0,0353	0,0010	0,0133	0,0008	0,19	223,6	6,0	246,0	11,0	430,0	110,0	223,6	6,0	9,11
Zircon_87	163	84	0,50	0,1140	0,0120	0,5640	0,0840	0,0354	0,0011	0,0224	0,0022	-0,11	224,1	8,7	452,0	47,0	1840,0	160,0	224,1	8,7	50,42
Zircon_96	130	95	0,73	0,0783	0,0075	0,3900	0,0440	0,0354	0,0012	0,0147	0,0009	0,10	224,3	7,0	337,0	28,0	1440,0	170,0	224,3	7,0	33,44
Zircon_46	143	84	0,59	0,0633	0,0077	0,3080	0,0410	0,0354	0,0012	0,0134	0,0011	-0,10	224,5	7,5	272,0	29,0	650,0	210,0	224,5	7,5	17,46
Zircon_75	288	169	0,59	0,0889	0,0084	0,4390	0,0450	0,0357	0,0011	0,0171	0,0017	0,08	226,1	6,5	369,0	29,0	1390,0	150,0	226,1	6,5	38,73
Zircon_89	297	228	0,77	0,1183	0,0068	0,5930	0,0420	0,0357	0,0011	0,0199	0,0011	0,49	226,1	6,7	471,0	26,0	1943,0	94,0	226,1	6,7	52,00
Zircon_86	138	109	0,79	0,1240	0,0140	0,6190	0,0970	0,0359	0,0021	0,0212	0,0021	0,33	227,4	8,2	486,0	51,0	1990,0	160,0	227,4	8,2	53,21
Zircon_15	130	80	0,62	0,0615	0,0075	0,3070	0,0380	0,0360	0,0012	0,0140	0,0009	-0,25	227,7	7,8	269,0	28,0	660,0	220,0	227,7	7,8	15,35
Zircon_54	153	81	0,53	0,0800	0,0130	0,3930	0,0790	0,0362	0,0014	0,0195	0,0028	0,29	228,9	8,4	334,0	49,0	1160,0	230,0	228,9	8,4	31,47
Zircon_64	190	125	0,66	0,0956	0,0076	0,4830	0,0430	0,0364	0,0011	0,0173	0,0010	0,14	230,6	6,8	399,0	28,0	1540,0	130,0	230,6	6,8	42,21

Amostra																					
Zircon_59	72	49	0,68	0,0922	0,0067	0,4760	0,0330	0,0368	0,0012	0,0175	0,0012	-0,18	232,7	393,0	7,6	23,0	1530,0	140,0	232,7	7,6	40,79
Zircon_10	246	234	0,95	0,1220	0,0130	0,6370	0,0830	0,0369	0,0012	0,0207	0,0018	0,34	233,3	497,0	7,3	45,0	1990,0	140,0	233,3	7,3	53,06
Zircon_79	193	175	0,91	0,1154	0,0065	0,5860	0,0340	0,0369	0,0011	0,0179	0,0009	0,04	233,7	470,0	6,6	22,0	1892,0	95,0	233,7	6,6	50,28
Zircon_42	131	96	0,73	0,1040	0,0110	0,5530	0,0660	0,0374	0,0014	0,0181	0,0015	0,05	237,0	436,0	8,4	40,0	1670,0	180,0	237,0	8,4	45,64
Zircon_82	180	110	0,61	0,1540	0,0110	0,8260	0,0630	0,0385	0,0013	0,0291	0,0014	0,08	243,7	608,0	7,8	33,0	2360,0	100,0	243,7	7,8	59,92
Zircon_76	209	104	0,72	0,1702	0,0090	0,8980	0,0520	0,0387	0,0010	0,0285	0,0010	-0,05	244,7	654,0	6,0	28,0	2543,0	82,0	244,7	6,0	62,58
Zircon_62	171	113	0,66	0,1200	0,0150	0,6230	0,0930	0,0390	0,0011	0,0224	0,0019	0,48	246,4	494,0	7,4	52,0	1890,0	170,0	246,4	7,4	50,12
Zircon_25	327	305	0,93	0,0575	0,0037	0,3400	0,0240	0,0427	0,0011	0,0143	0,0004	-0,02	269,4	296,0	7,1	18,0	470,0	140,0	269,4	7,1	8,99
Zircon_51	450	718	1,60	0,0538	0,0055	0,3210	0,0420	0,0433	0,0012	0,0133	0,0007	0,15	273,3	282,0	7,5	29,0	340,0	160,0	273,3	7,5	3,09
Zircon_52	331	291	0,88	0,0548	0,0025	0,3500	0,0190	0,0466	0,0012	0,0150	0,0005	0,36	293,6	304,0	7,1	14,0	377,0	99,0	293,6	7,1	3,42
Zircon_04	310	313	1,01	0,0687	0,0044	0,4440	0,0300	0,0468	0,0012	0,0161	0,0006	-0,28	294,7	373,0	7,3	20,0	880,0	120,0	294,7	7,3	20,99
Zircon_05	130	96	0,74	0,0643	0,0042	0,4260	0,0300	0,0473	0,0015	0,0176	0,0010	0,15	297,8	358,0	9,1	22,0	750,0	130,0	297,8	9,1	16,82
Zircon_22	177	186	1,05	0,0607	0,0043	0,4100	0,0310	0,0485	0,0013	0,0160	0,0008	0,17	305,5	347,0	8,1	22,0	630,0	130,0	305,5	8,1	11,96
Zircon_77	239	158	0,66	0,1010	0,0350	0,6900	0,4700	0,0494	0,0047	0,0250	0,0150	-0,33	311,0	530,0	28,0	150,0	1600,0	280,0	311,0	28,0	41,32
Zircon_60	264	302	1,14	0,0596	0,0031	0,4180	0,0220	0,0512	0,0013	0,0164	0,0006	-0,18	322,0	354,0	8,2	16,0	560,0	100,0	322,0	8,2	9,04
Zircon_81	191	122	0,64	0,1890	0,0170	1,0400	0,1400	0,0392	0,0017	0,0350	0,0026	0,38	248,0	724,0	11,0	59,0	2720,0	120,0	2720,0	120,0	65,75
Zircon_61	254	142	0,56	0,1950	0,0180	1,0800	0,1300	0,0402	0,0015	0,0442	0,0060	0,43	253,8	737,0	9,3	55,0	2780,0	120,0	2780,0	120,0	65,56
Zircon_02	54	27	0,50	0,2140	0,0260	1,2100	0,2000	0,0447	0,0024	0,0553	0,0070	0,45	263,0	795,0	15,0	81,0	2880,0	140,0	2880,0	140,0	66,92
Zircon_98	175	121	0,69	0,2180	0,0250	1,3300	0,2700	0,0422	0,0027	0,0374	0,0057	0,47	266,0	855,0	17,0	87,0	2980,0	130,0	2980,0	130,0	68,89
Zircon_78	124	106	0,85	0,3070	0,0230	2,7200	0,3300	0,0620	0,0033	0,0694	0,0062	0,70	388,0	1344,0	20,0	68,0	3481,0	94,0	3481,0	94,0	74,13
Zircon_39	94	42	0,45	0,4810	0,0170	4,7500	0,2500	0,0708	0,0024	0,2030	0,0052	0,37	441,0	1781,0	14,0	41,0	4190,0	50,0	4190,0	50,0	75,24
CPV-15-346 (DZ)																					
Zircon_044	164	152	0,27	0,0743	0,0039	0,2740	0,0140	0,0274	0,0006	0,0178	0,0010	0,14	174,1	247,0	3,9	11,0	1040,0	100,0	174,1	3,9	29,54
Zircon_031	278	97	0,35	0,1303	0,0096	0,5710	0,0520	0,0314	0,0009	0,0318	0,0030	0,20	199,4	456,0	5,7	32,0	2120,0	110,0	199,4	5,7	56,27
Zircon_024	268	162	0,60	0,1175	0,0076	0,5890	0,0480	0,0355	0,0011	0,0234	0,0020	0,78	225,0	471,0	6,9	32,0	1910,0	120,0	225,0	6,9	52,23
Zircon_069	221	189	0,86	0,0734	0,0038	0,3640	0,0200	0,0370	0,0013	0,0153	0,0008	0,31	234,2	315,0	7,8	14,0	980,0	110,0	234,2	7,8	25,65
Zircon_030	318	248	0,78	0,0756	0,0030	0,4400	0,0190	0,0385	0,0009	0,0164	0,0009	0,39	243,3	343,0	5,7	15,0	1072,0	81,0	243,3	5,7	29,07

Zircon_118	212	181	0,85	0,0610	0,0044	0,3300	0,0210	0,0393	0,0026	0,0135	0,0008	-0,17	248,0	16,0	288,0	16,0	600,0	140,0	248,0	16,0	13,89
Zircon_034	442	367	0,89	0,0750	0,0044	0,4180	0,0230	0,0408	0,0011	0,0161	0,0008	0,07	257,5	6,8	354,0	16,0	1090,0	100,0	257,5	6,8	27,26
Zircon_028	273	232	0,85	0,0752	0,0060	0,4350	0,0270	0,0411	0,0016	0,0163	0,0010	-0,43	259,6	9,9	366,0	19,0	1080,0	140,0	259,6	9,9	29,07
Zircon_078	323	211	0,65	0,0641	0,0027	0,3880	0,0190	0,0434	0,0010	0,0154	0,0009	0,19	273,7	6,3	334,0	14,0	727,0	89,0	273,7	6,3	18,05
Zircon_015	241	163	0,68	0,0578	0,0028	0,3490	0,0180	0,0435	0,0010	0,0155	0,0009	0,07	274,5	5,8	303,0	14,0	520,0	110,0	274,5	5,8	9,41
Zircon_117	720	573	0,80	0,0541	0,0021	0,3280	0,0140	0,0438	0,0009	0,0141	0,0007	0,17	276,5	5,5	288,0	11,0	371,0	89,0	276,5	5,5	3,99
Zircon_063	203	309	1,52	0,0553	0,0038	0,3390	0,0240	0,0439	0,0011	0,0144	0,0008	0,03	277,2	6,5	295,0	18,0	390,0	140,0	277,2	6,5	6,03
Zircon_053	399	505	1,27	0,0659	0,0049	0,3990	0,0440	0,0439	0,0011	0,0146	0,0010	-0,05	277,2	7,1	341,0	28,0	780,0	140,0	277,2	7,1	18,71
Zircon_018	285	153	0,54	0,0654	0,0038	0,3920	0,0230	0,0440	0,0009	0,0162	0,0009	0,13	277,3	5,8	337,0	16,0	760,0	120,0	277,3	5,8	17,72
Zircon_062	268	163	0,61	0,0610	0,0032	0,3670	0,0200	0,0441	0,0011	0,0146	0,0009	0,33	278,3	6,5	317,0	15,0	610,0	120,0	278,3	6,5	12,21
Zircon_055	525	301	0,57	0,0530	0,0021	0,3240	0,0150	0,0444	0,0010	0,0140	0,0008	0,10	280,3	5,9	285,0	12,0	312,0	87,0	280,3	5,9	1,65
Zircon_085	751	623	0,83	0,0650	0,0340	0,4100	0,4000	0,0446	0,0037	0,0164	0,0075	-0,08	282,0	23,0	350,0	140,0	790,0	400,0	282,0	23,0	19,43
Zircon_093	223	192	0,86	0,0630	0,0035	0,3900	0,0240	0,0448	0,00112	0,0161	0,0009	0,30	282,4	6,7	333,0	18,0	710,0	120,0	282,4	6,7	15,20
Zircon_025	219	185	0,84	0,0580	0,0150	0,3590	0,0950	0,0450	0,0014	0,0153	0,0029	0,31	283,6	8,3	310,0	53,0	480,0	260,0	283,6	8,3	8,52
Zircon_022	269	218	0,81	0,0518	0,0028	0,3230	0,0180	0,0450	0,0011	0,0142	0,0009	-0,02	283,9	6,6	285,0	14,0	270,0	120,0	283,9	6,6	0,39
Zircon_021	258	212	0,82	0,0553	0,0024	0,3420	0,0170	0,0451	0,0010	0,0152	0,0009	0,14	284,6	6,3	299,0	13,0	418,0	95,0	284,6	6,3	4,82
Zircon_032	396	319	0,81	0,0588	0,0030	0,3600	0,0180	0,0451	0,0010	0,0149	0,0008	0,20	284,6	6,2	312,0	13,0	560,0	110,0	284,6	6,2	8,78
Zircon_075	149	136	0,91	0,0548	0,0040	0,3430	0,0240	0,0453	0,0012	0,0133	0,0008	0,05	285,7	7,4	298,0	19,0	360,0	160,0	285,7	7,4	4,13
Zircon_019	316	200	0,63	0,0587	0,0028	0,3660	0,0200	0,0453	0,0010	0,0153	0,0009	0,09	285,8	6,1	318,0	14,0	540,0	110,0	285,8	6,1	10,13
Zircon_005	332	228	0,69	0,0528	0,0023	0,3290	0,0160	0,0455	0,0011	0,0147	0,0008	0,04	286,5	6,6	288,0	12,0	340,0	95,0	286,5	6,6	0,52
Zircon_027	354	309	0,87	0,0531	0,0024	0,3320	0,0150	0,0455	0,0010	0,0143	0,0008	0,20	287,1	6,1	291,0	12,0	310,0	100,0	287,1	6,1	1,34
Zircon_090	316	202	0,64	0,0564	0,0058	0,3590	0,0390	0,0456	0,0011	0,0151	0,0012	0,22	287,7	6,9	311,0	27,0	430,0	160,0	287,7	6,9	7,49
Zircon_094	326	189	0,58	0,0772	0,0047	0,4960	0,0280	0,0457	0,0013	0,0206	0,0011	-0,05	287,8	8,0	407,0	19,0	1140,0	110,0	287,8	8,0	29,29
Zircon_109	179	148	0,83	0,0564	0,0033	0,3590	0,0200	0,0457	0,0012	0,0146	0,0009	0,14	287,9	7,6	311,0	15,0	480,0	130,0	287,9	7,6	7,43
Zircon_087	296	201	0,68	0,0590	0,0110	0,3800	0,1100	0,0458	0,0014	0,0159	0,0029	0,10	288,5	8,4	329,0	47,0	570,0	230,0	288,5	8,4	12,31
Zircon_008	180	174	0,97	0,0561	0,0028	0,3550	0,0180	0,0458	0,0011	0,0145	0,0008	0,00	288,7	6,6	310,0	14,0	420,0	110,0	288,7	6,6	6,87
Zircon_040	293	263	0,90	0,0540	0,0025	0,3370	0,0160	0,0459	0,0009	0,0140	0,0008	0,13	289,4	5,5	296,0	12,0	370,0	100,0	289,4	5,5	2,23
Zircon_047	132	105	0,80	0,0544	0,0041	0,3380	0,0240	0,0459	0,0013	0,0149	0,0010	0,33	289,4	8,0	297,0	18,0	360,0	160,0	289,4	8,0	2,56

Zircon_072	202	210	1,04	0,0605	0,0042	0,3860	0,0260	0,0459	0,0011	0,0151	0,0009	-0,21	289,5	6,6	330,0	19,0	570,0	150,0	289,5	6,6	12,27
Zircon_023	59	29	0,49	0,0580	0,0053	0,3600	0,0310	0,0460	0,0018	0,0135	0,0012	-0,13	290,0	11,0	309,0	23,0	460,0	200,0	290,0	11,0	6,15
Zircon_037	251	161	0,64	0,0520	0,0027	0,3310	0,0170	0,0461	0,0011	0,0152	0,0009	-0,02	290,3	6,7	290,0	13,0	290,0	110,0	290,3	6,7	-0,10
Zircon_080	226	175	0,77	0,0554	0,0041	0,3540	0,0280	0,0461	0,0010	0,0143	0,0011	-0,04	290,3	6,3	307,0	20,0	390,0	130,0	290,3	6,3	5,44
Zircon_110	151	119	0,79	0,0554	0,0036	0,3510	0,0240	0,0461	0,0011	0,0151	0,0009	0,20	290,8	6,7	304,0	18,0	400,0	140,0	290,8	6,7	4,34
Zircon_115	385	594	1,54	0,0601	0,0040	0,3800	0,0270	0,0462	0,0010	0,0145	0,0008	0,30	290,9	6,0	325,0	19,0	550,0	130,0	290,9	6,0	10,49
Zircon_011	89	50	0,56	0,0526	0,0039	0,3290	0,0240	0,0462	0,0013	0,0148	0,0012	0,04	291,1	7,8	287,0	18,0	290,0	160,0	291,1	7,8	-1,43
Zircon_048	235	351	1,49	0,0525	0,0032	0,3310	0,0200	0,0462	0,0011	0,0142	0,0007	-0,20	291,1	6,9	289,0	15,0	280,0	130,0	291,1	6,9	-0,73
Zircon_096	174	147	0,84	0,0548	0,0039	0,3470	0,0250	0,0462	0,0012	0,0147	0,0009	0,12	291,2	7,4	301,0	19,0	350,0	160,0	291,2	7,4	3,26
Zircon_036	397	305	0,77	0,0533	0,0027	0,3340	0,0170	0,0462	0,0009	0,0146	0,0008	-0,16	291,3	5,8	295,0	13,0	330,0	110,0	291,3	5,8	1,25
Zircon_058	252	259	1,03	0,0549	0,0026	0,3460	0,0190	0,0462	0,0011	0,0145	0,0008	0,29	291,4	6,9	305,0	14,0	410,0	100,0	291,4	6,9	4,46
Zircon_106	194	150	0,77	0,0509	0,0027	0,3200	0,0170	0,0463	0,0012	0,0148	0,0009	0,08	291,7	7,1	281,0	13,0	230,0	110,0	291,7	7,1	-3,81
Zircon_091	194	92	0,47	0,0550	0,0360	0,3500	0,2900	0,0463	0,0020	0,0170	0,0130	0,24	292,0	12,0	310,0	120,0	360,0	340,0	292,0	12,0	5,81
Zircon_016	198	143	0,72	0,0560	0,0270	0,3600	0,2400	0,0464	0,0027	0,0160	0,0066	0,01	292,0	17,0	310,0	110,0	440,0	400,0	292,0	17,0	5,81
Zircon_049	220	184	0,84	0,0574	0,0029	0,3660	0,0180	0,0463	0,0014	0,0151	0,0009	0,02	292,0	8,7	316,0	13,0	470,0	110,0	292,0	8,7	7,59
Zircon_082	412	495	1,20	0,0530	0,0180	0,3400	0,1500	0,0464	0,0015	0,0141	0,0022	0,20	292,1	9,3	297,0	83,0	300,0	340,0	292,1	9,3	1,65
Zircon_013	285	191	0,67	0,0544	0,0026	0,3420	0,0170	0,0464	0,0010	0,0149	0,0009	-0,04	292,2	5,9	302,0	13,0	390,0	110,0	292,2	5,9	3,25
Zircon_100	688	492	0,72	0,0546	0,0019	0,3480	0,0150	0,0464	0,0010	0,0143	0,0007	-0,03	292,2	6,1	303,0	11,0	407,0	83,0	292,2	6,1	3,56
Zircon_104	229	246	1,07	0,0546	0,0028	0,3470	0,0200	0,0464	0,0010	0,0143	0,0008	0,35	292,3	6,3	301,0	15,0	360,0	110,0	292,3	6,3	2,89
Zircon_088	170	164	0,96	0,0544	0,0033	0,3570	0,0230	0,0464	0,0010	0,0141	0,0008	0,06	292,6	6,4	309,0	17,0	380,0	140,0	292,6	6,4	5,31
Zircon_043	274	305	1,11	0,0521	0,0024	0,3310	0,0160	0,0465	0,0009	0,0144	0,0008	0,06	292,7	5,7	290,0	12,0	270,0	100,0	292,7	5,7	-0,93
Zircon_039	274	234	0,85	0,0525	0,0023	0,3340	0,0170	0,0465	0,0011	0,0151	0,0008	0,22	292,7	6,7	292,0	13,0	300,0	100,0	292,7	6,7	-0,24
Zircon_061	190	136	0,72	0,0532	0,0034	0,3390	0,0210	0,0465	0,0012	0,0146	0,0009	0,06	292,9	7,4	298,0	17,0	340,0	140,0	292,9	7,4	1,71
Zircon_057	257	191	0,74	0,0530	0,0027	0,3350	0,0190	0,0465	0,0012	0,0140	0,0008	0,10	293,0	7,2	293,0	14,0	320,0	110,0	293,0	7,2	0,00
Zircon_052	197	129	0,65	0,0561	0,0028	0,3520	0,0190	0,0465	0,0011	0,0143	0,0009	0,25	293,0	6,9	305,0	14,0	420,0	110,0	293,0	6,9	3,93
Zircon_119	162	92	0,57	0,0590	0,0110	0,3800	0,1300	0,0465	0,0019	0,0152	0,0054	-0,12	293,0	12,0	323,0	51,0	540,0	210,0	293,0	12,0	9,29
Zircon_098	149	117	0,79	0,0530	0,0037	0,3330	0,0210	0,0465	0,0012	0,0148	0,0010	-0,16	293,1	7,6	291,0	16,0	320,0	140,0	293,1	7,6	-0,72
Zircon_060	283	223	0,79	0,0543	0,0031	0,3460	0,0200	0,0465	0,0010	0,0147	0,0008	0,04	293,1	6,3	307,0	15,0	380,0	130,0	293,1	6,3	4,53

Zircon_086	191	184	0,96	0,0570	0,0043	0,3640	0,0270	0,0466	0,0011	0,0154	0,0009	-0,06	293,3	7,0	314,0	20,0	420,0	150,0	293,3	7,0	6,59
Zircon_113	155	94	0,61	0,0531	0,0036	0,3410	0,0230	0,0466	0,0012	0,0152	0,0009	0,10	293,7	7,3	297,0	18,0	310,0	150,0	293,7	7,3	1,11
Zircon_017	258	147	0,57	0,0639	0,0036	0,4080	0,0260	0,0466	0,0011	0,0174	0,0010	0,16	293,7	6,7	349,0	18,0	730,0	130,0	293,7	6,7	15,85
Zircon_068	270	198	0,73	0,0788	0,0069	0,4990	0,0460	0,0467	0,0011	0,0185	0,0014	0,00	294,1	6,7	418,0	30,0	1160,0	150,0	294,1	6,7	29,64
Zircon_050	214	137	0,64	0,0541	0,0033	0,3430	0,0230	0,0469	0,0011	0,0153	0,0009	0,29	295,2	6,7	298,0	17,0	360,0	140,0	295,2	6,7	0,94
Zircon_111	315	322	1,02	0,0531	0,0027	0,3400	0,0170	0,0469	0,0011	0,0153	0,0009	0,12	295,6	7,0	296,0	13,0	320,0	110,0	295,6	7,0	0,14
Zircon_089	235	248	1,06	0,0606	0,0034	0,3990	0,0250	0,0470	0,0013	0,0154	0,0009	0,29	295,8	7,9	340,0	18,0	600,0	120,0	295,8	7,9	13,00
Zircon_101	322	258	0,80	0,0533	0,0027	0,3400	0,0180	0,0471	0,0011	0,0153	0,0009	0,20	296,5	6,6	296,0	13,0	320,0	120,0	296,5	6,6	-0,17
Zircon_114	120	74	0,62	0,0542	0,0044	0,3460	0,0280	0,0471	0,0010	0,0150	0,0010	0,03	296,6	6,1	302,0	22,0	330,0	170,0	296,6	6,1	1,79
Zircon_120	159	94	0,59	0,0529	0,0032	0,3510	0,0250	0,0471	0,0012	0,0158	0,0010	0,19	296,9	7,3	304,0	18,0	330,0	140,0	296,9	7,3	2,34
Zircon_092	217	185	0,85	0,0563	0,0030	0,3630	0,0200	0,0472	0,0012	0,0156	0,0010	0,03	297,0	7,7	317,0	15,0	430,0	120,0	297,0	7,7	6,31
Zircon_107	176	152	0,86	0,0680	0,0290	0,4200	0,3200	0,0472	0,0029	0,0179	0,0079	0,21	297,0	18,0	360,0	110,0	910,0	330,0	297,0	18,0	17,50
Zircon_014	306	299	0,98	0,0519	0,0026	0,3410	0,0180	0,0472	0,0010	0,0150	0,0009	-0,07	297,1	6,2	297,0	13,0	260,0	110,0	297,1	6,2	-0,03
Zircon_012	136	77	0,57	0,0576	0,0041	0,3680	0,0250	0,0472	0,0013	0,0172	0,0011	-0,19	297,2	7,9	319,0	19,0	470,0	150,0	297,2	7,9	6,83
Zircon_059	195	172	0,88	0,0582	0,0030	0,3740	0,0210	0,0472	0,0012	0,0148	0,0009	0,21	297,2	7,1	324,0	15,0	560,0	100,0	297,2	7,1	8,27
Zircon_002	186	155	0,83	0,0592	0,0033	0,3830	0,0240	0,0472	0,0013	0,0150	0,0010	0,28	297,4	8,1	328,0	18,0	560,0	130,0	297,4	8,1	9,33
Zircon_026	176	103	0,59	0,0532	0,0031	0,3490	0,0200	0,0472	0,0011	0,0149	0,0009	0,04	297,5	7,0	305,0	16,0	320,0	130,0	297,5	7,0	2,46
Zircon_103	210	130	0,62	0,0623	0,0037	0,3990	0,0250	0,0472	0,0012	0,0167	0,0011	0,24	297,5	7,2	340,0	18,0	670,0	130,0	297,5	7,2	12,50
Zircon_108	213	167	0,78	0,0532	0,0031	0,3380	0,0190	0,0472	0,0011	0,0150	0,0008	-0,12	297,6	6,8	297,0	15,0	360,0	130,0	297,6	6,8	-0,20
Zircon_102	681	336	0,49	0,0546	0,0035	0,3520	0,0180	0,0473	0,0014	0,0154	0,0011	0,10	297,9	8,8	306,0	13,0	390,0	120,0	297,9	8,8	2,65
Zircon_081	226	149	0,66	0,0523	0,0028	0,3420	0,0200	0,0473	0,0013	0,0148	0,0009	0,31	298,0	8,2	300,0	15,0	320,0	120,0	298,0	8,2	0,67
Zircon_079	148	91	0,61	0,0586	0,0044	0,3830	0,0280	0,0474	0,0012	0,0169	0,0010	-0,27	298,3	7,3	327,0	20,0	480,0	160,0	298,3	7,3	8,78
Zircon_006	343	251	0,73	0,0525	0,0025	0,3420	0,0190	0,0474	0,0011	0,0148	0,0008	0,26	298,8	6,5	301,0	15,0	359,0	99,0	298,8	6,5	0,73
Zircon_065	226	155	0,69	0,0547	0,0029	0,3550	0,0210	0,0474	0,0012	0,0144	0,0009	0,22	298,8	7,2	307,0	16,0	410,0	120,0	298,8	7,2	2,67
Zircon_073	189	126	0,67	0,0567	0,0029	0,3720	0,0200	0,0474	0,0011	0,0145	0,0009	0,10	299,1	6,6	322,0	15,0	460,0	110,0	299,1	6,6	7,11
Zircon_116	307	267	0,87	0,0518	0,0029	0,3420	0,0200	0,0476	0,0011	0,0154	0,0008	0,07	299,5	6,7	298,0	15,0	260,0	120,0	299,5	6,7	-0,50
Zircon_076	168	109	0,65	0,0546	0,0034	0,3550	0,0240	0,0476	0,0011	0,0153	0,0010	0,13	299,6	7,0	307,0	18,0	370,0	140,0	299,6	7,0	2,41
Zircon_046	200	156	0,78	0,0763	0,0047	0,4960	0,0330	0,0476	0,0012	0,0190	0,0012	0,33	299,7	7,1	407,0	22,0	1150,0	110,0	299,7	7,1	26,36

Sample																					
Zircon_004	127	107	0,84	0,0529	0,0033	0,3500	0,0260	0,0476	0,0014	0,0141	0,0010	0,36	299,8	8,6	304,0	19,0	280,0	150,0	299,8	8,6	1,38
Zircon_041	183	133	0,73	0,0533	0,0035	0,3480	0,0230	0,0476	0,0011	0,0153	0,0010	0,02	299,8	7,0	304,0	17,0	300,0	140,0	299,8	7,0	1,38
Zircon_097	168	126	0,75	0,0514	0,0031	0,3370	0,0200	0,0476	0,0013	0,0157	0,0009	0,31	299,9	8,1	296,0	16,0	250,0	120,0	299,9	8,1	-1,32
Zircon_084	155	89	0,57	0,0533	0,0027	0,3570	0,0200	0,0476	0,0012	0,0151	0,0010	0,10	299,9	7,6	309,0	15,0	320,0	110,0	299,9	7,6	2,94
Zircon_007	180	125	0,69	0,0522	0,0032	0,3350	0,0210	0,0476	0,0011	0,0152	0,0008	-0,13	300,0	6,9	293,0	16,0	260,0	130,0	300,0	6,9	-2,39
Zircon_035	210	218	1,04	0,0600	0,0800	0,4000	3,3000	0,0480	0,0300	0,0160	0,0560	0,07	300,0	170,0	330,0	380,0	550,0	530,0	300,0	170,0	9,09
Zircon_074	176	48	0,27	0,0525	0,0028	0,3410	0,0180	0,0477	0,0015	0,0163	0,0012	0,16	301,2	8,7	297,0	14,0	290,0	120,0	301,2	8,7	-1,41
Zircon_010	297	311	1,05	0,0526	0,0026	0,3450	0,0190	0,0477	0,0011	0,0156	0,0008	0,27	301,3	6,6	300,0	15,0	320,0	110,0	301,3	6,6	-0,43
Zircon_054	193	155	0,80	0,0540	0,0032	0,3530	0,0210	0,0479	0,0011	0,0148	0,0009	-0,05	301,9	6,9	306,0	16,0	370,0	130,0	301,9	6,9	1,34
Zircon_038	224	290	1,29	0,0541	0,0039	0,3530	0,0240	0,0480	0,0011	0,0150	0,0008	-0,17	302,0	7,0	305,0	18,0	350,0	160,0	302,0	7,0	0,98
Zircon_020	190	115	0,61	0,0600	0,0040	0,3950	0,0270	0,0480	0,0011	0,0176	0,0011	-0,03	302,0	7,0	339,0	19,0	540,0	150,0	302,0	7,0	10,91
Zircon_045	135	85	0,63	0,0548	0,0050	0,3550	0,0320	0,0480	0,0012	0,0171	0,0012	-0,06	302,4	7,3	311,0	23,0	410,0	170,0	302,4	7,3	2,77
Zircon_003	206	116	0,56	0,0630	0,0035	0,4120	0,0240	0,0480	0,0011	0,0183	0,0010	-0,19	302,5	6,9	352,0	17,0	680,0	130,0	302,5	6,9	14,06
Zircon_067	161	100	0,62	0,0656	0,0099	0,4360	0,0670	0,0481	0,0012	0,0199	0,0018	0,01	302,8	7,7	365,0	44,0	730,0	220,0	302,8	7,7	17,04
Zircon_056	335	286	0,85	0,0539	0,0030	0,3550	0,0200	0,0481	0,0012	0,0160	0,0009	-0,09	303,0	7,2	308,0	15,0	350,0	120,0	303,0	7,2	1,62
Zircon_029	216	186	0,86	0,0539	0,0032	0,3580	0,0200	0,0481	0,0012	0,0154	0,0008	-0,15	303,0	7,4	310,0	15,0	350,0	130,0	303,0	7,4	2,26
Zircon_064	188	130	0,69	0,0679	0,0058	0,4540	0,0410	0,0484	0,0012	0,0185	0,0014	0,36	304,6	7,4	376,0	29,0	840,0	180,0	304,6	7,4	18,99
Zircon_077	258	158	0,61	0,0611	0,0030	0,4070	0,0210	0,0484	0,0011	0,0169	0,0010	0,13	304,8	6,9	346,0	15,0	610,0	100,0	304,8	6,9	11,91
Zircon_051	270	273	1,01	0,0730	0,0660	0,5000	1,9000	0,0480	0,0160	0,0150	0,0490	0,37	305,0	91,0	400,0	270,0	1000,0	350,0	305,0	91,0	23,75
~~Zircon_033~~	~~142~~	~~126~~	~~0,89~~	~~0,0890~~	~~0,0240~~	~~0,6000~~	~~0,2300~~	~~0,0485~~	~~0,0026~~	~~0,0208~~	~~0,0037~~	~~0,61~~	~~305,0~~	~~16,0~~	~~480,0~~	~~97,0~~	~~1300,0~~	~~300,0~~	~~305,0~~	~~16,0~~	~~36,46~~
Zircon_095	134	85	0,63	0,0556	0,0035	0,3730	0,0230	0,0486	0,0013	0,0165	0,0011	-0,10	305,9	7,9	321,0	16,0	420,0	140,0	305,9	7,9	4,70
Zircon_066	473	252	0,53	0,0605	0,0028	0,4050	0,0190	0,0487	0,0011	0,0172	0,0010	-0,18	306,5	6,9	345,0	14,0	610,0	110,0	306,5	6,9	11,16
Zircon_105	150	122	0,81	0,0636	0,0066	0,4340	0,0470	0,0490	0,0013	0,0190	0,0014	0,17	308,3	8,0	370,0	33,0	720,0	210,0	308,3	8,0	16,68
Zircon_070	286	216	0,76	0,0721	0,0085	0,4870	0,0610	0,0490	0,0013	0,0175	0,0020	0,15	308,6	7,8	400,0	39,0	900,0	200,0	308,6	7,8	22,85
Zircon_042	219	231	1,05	0,0638	0,0054	0,4180	0,0410	0,0492	0,0015	0,0166	0,0014	0,23	309,3	9,1	359,0	27,0	700,0	180,0	309,3	9,1	13,84
Zircon_099	125	74	0,59	0,0502	0,0037	0,3430	0,0260	0,0492	0,0013	0,0160	0,0011	0,12	309,5	7,8	298,0	19,0	180,0	160,0	309,5	7,8	-3,86
Zircon_071	96	63	0,66	0,0671	0,0047	0,4600	0,0300	0,0498	0,0014	0,0181	0,0012	-0,06	313,0	8,6	387,0	21,0	840,0	150,0	313,0	8,6	19,12
Zircon_009	133	54	0,41	0,0524	0,0030	0,3530	0,0220	0,0498	0,0012	0,0157	0,0012	-0,01	313,2	7,3	308,0	16,0	270,0	120,0	313,2	7,3	-1,69

Sample																			
Zircon_001	344	534	1,55	0,0624	0,0052	0,4250	0,0330	0,0499	0,0175	0,0011	313,8	6,9	362,0	22,0	700,0	150,0	313,8	6,9	13,31
Zircon_112	179	250	1,40	0,0575	0,0040	0,3870	0,0270	0,0503	0,0165	0,0012	316,5	7,6	334,0	19,0	480,0	150,0	316,5	7,6	5,24
Zircon_083	154	115	0,75	0,0991	0,0064	0,7140	0,0500	0,0522	0,0233	0,0013	327,9	8,0	551,0	31,0	1610,0	120,0	327,9	8,0	40,49

CPV-15-393 (DZ) — Maximum depositional age (3+DZ, 1σ): 249.6±5.1 Ma (MSWD = 0.28)

Sample																			
Zircon_010	888	970	1,09	0,0705	0,0036	0,3660	0,0200	0,0367	0,01	0,0011	232,2	7,0	347,0	14,0	952,0	94,0	232,2	7,0	26,75
Zircon_003	86	95	1,10	0,0918	0,0092	0,4770	0,0390	0,0389	0,01	0,0014	246,2	8,9	392,0	27,0	1360,0	210,0	246,2	8,9	37,19
Zircon_052	224	157	0,70	0,0519	0,0052	0,2810	0,0140	0,0390	0,01	0,0018	247,0	11,0	251,0	11,0	280,0	170,0	247,0	11,0	1,59
Zircon_046	200	230	1,15	0,0550	0,0150	0,3000	0,0490	0,0391	0,01	0,0023	247,0	14,0	264,0	48,0	360,0	320,0	247,0	14,0	6,44
Zircon_061	438	422	0,96	0,0589	0,0034	0,3260	0,0150	0,0397	0,01	0,0011	251,1	6,6	286,0	11,0	610,0	120,0	251,1	6,6	12,20
Zircon_037	183	167	0,91	0,0810	0,0210	0,4400	0,1100	0,0398	0,01	0,0015	251,5	9,3	365,0	70,0	1180,0	260,0	251,5	9,3	31,10
Zircon_063	125	267	2,14	0,0834	0,0067	0,4570	0,0330	0,0399	0,01	0,0014	252,2	6,5	380,0	23,0	1240,0	150,0	252,2	6,5	33,63
Zircon_069	1091	648	0,59	0,0575	0,0025	0,3279	0,0098	0,0411	0,01	0,0009	259,7	5,8	287,6	7,6	494,0	89,0	259,7	5,8	9,70
Zircon_084	223	187	0,84	0,0523	0,0036	0,3040	0,0200	0,0416	0,01	0,0010	262,5	6,2	271,0	15,0	330,0	150,0	262,5	6,2	3,14
Zircon_049	225	166	0,74	0,0562	0,0040	0,3290	0,0170	0,0425	0,01	0,0012	268,6	7,7	288,0	13,0	410,0	150,0	268,6	7,7	6,74
Zircon_038	218	168	0,77	0,0540	0,0041	0,3100	0,0210	0,0426	0,01	0,0012	268,8	7,3	276,0	17,0	310,0	150,0	268,8	7,3	2,61
Zircon_056	304	200	0,66	0,0641	0,0035	0,3840	0,0190	0,0429	0,01	0,0010	270,5	6,2	329,0	14,0	740,0	120,0	270,5	6,2	17,78
Zircon_085	116	128	1,10	0,0574	0,0047	0,3300	0,0250	0,0430	0,01	0,0017	271,0	10,0	287,0	20,0	470,0	180,0	271,0	10,0	5,57
Zircon_040	659	379	0,58	0,0549	0,0024	0,3250	0,0110	0,0430	0,01	0,0008	271,1	5,2	285,8	8,6	400,0	100,0	271,1	5,2	5,14
Zircon_032	501	356	0,71	0,0527	0,0028	0,3080	0,0140	0,0431	0,01	0,0009	271,7	5,4	272,0	11,0	300,0	120,0	271,7	5,4	0,11
Zircon_034	138	114	0,83	0,0537	0,0040	0,3180	0,0240	0,0432	0,01	0,0013	272,5	8,1	280,0	19,0	340,0	150,0	272,5	8,1	2,68
Zircon_026	621	341	0,55	0,0525	0,0024	0,3160	0,0130	0,0433	0,01	0,0009	273,2	5,3	278,2	9,8	300,0	100,0	273,2	5,3	1,80
Zircon_017	87	79	0,91	0,0569	0,0085	0,3420	0,0550	0,0436	0,01	0,0019	275,0	11,0	296,0	40,0	450,0	290,0	275,0	11,0	7,09
Zircon_041	80	61	0,76	0,0543	0,0052	0,3270	0,0290	0,0438	0,01	0,0015	276,6	9,4	289,0	22,0	360,0	190,0	276,6	9,4	4,29
Zircon_089	159	128	0,81	0,0727	0,0079	0,4610	0,0420	0,0440	0,02	0,0019	277,0	12,0	380,0	30,0	960,0	220,0	277,0	12,0	27,11
Zircon_045	270	180	0,67	0,0537	0,0031	0,3250	0,0170	0,0440	0,01	0,0010	277,3	6,4	287,0	13,0	330,0	130,0	277,3	6,4	3,38
Zircon_065	104	75	0,72	0,0558	0,0052	0,3270	0,0260	0,0440	0,01	0,0014	277,7	8,6	296,0	19,0	380,0	180,0	277,7	8,6	6,18
Zircon_016	115	80	0,70	0,0501	0,0040	0,3050	0,0240	0,0441	0,01	0,0013	277,9	7,8	274,0	18,0	180,0	170,0	277,9	7,8	-1,42

Zircon_066	202	218	1,08	0,0514	0,0035	0,3130	0,0190	0,0441	0,0011	0,01	0,0007	-0,1457	277,9	6,8	275,0	14,0	220,0	150,0	277,9	6,8	-1,05
Zircon_050	219	118	0,54	0,0541	0,0038	0,3270	0,0220	0,0441	0,0011	0,02	0,0008	-0,0873	277,9	7,1	286,0	17,0	410,0	150,0	277,9	7,1	2,83
Zircon_039	240	143	0,60	0,0540	0,0058	0,3250	0,0330	0,0442	0,0036	0,01	0,0012	0,1886	279,0	22,0	292,0	24,0	310,0	200,0	279,0	22,0	4,45
Zircon_033	164	139	0,85	0,1110	0,0460	0,6800	0,6200	0,0444	0,0060	0,02	0,0035	0,2259	280,0	36,0	530,0	120,0	1790,0	330,0	280,0	36,0	47,17
Zircon_028	780	1169	1,50	0,0528	0,0025	0,3250	0,0120	0,0444	0,0009	0,01	0,0005	-0,1727	280,1	5,2	285,8	9,5	310,0	100,0	280,1	5,2	1,99
Zircon_004	212	185	0,87	0,0605	0,0046	0,3660	0,0220	0,0445	0,0012	0,02	0,0009	0,0934	280,6	7,7	315,0	16,0	580,0	150,0	280,6	7,7	10,92
Zircon_095	537	299	0,56	0,0890	0,0220	0,5800	0,1300	0,0445	0,0010	0,02	0,0010	-0,1659	280,6	6,3	452,0	68,0	1320,0	290,0	280,6	6,3	37,92
Zircon_002	236	174	0,74	0,0544	0,0035	0,3380	0,0190	0,0446	0,0010	0,02	0,0007	-0,3789	280,9	6,0	295,0	14,0	370,0	140,0	280,9	6,0	4,78
Zircon_006	224	195	0,87	0,0560	0,0037	0,3440	0,0190	0,0446	0,0011	0,02	0,0007	-0,0301	281,3	6,8	299,0	15,0	420,0	140,0	281,3	6,8	5,92
Zircon_007	180	128	0,71	0,0775	0,0049	0,4850	0,0250	0,0447	0,0012	0,02	0,0012	-0,0807	281,8	7,3	401,0	17,0	1120,0	130,0	281,8	7,3	29,73
Zircon_030	187	140	0,75	0,0551	0,0033	0,3350	0,0180	0,0448	0,0012	0,02	0,0008	-0,0071	282,4	7,5	296,0	13,0	390,0	130,0	282,4	7,5	4,59
Zircon_057	291	227	0,78	0,0535	0,0030	0,3300	0,0160	0,0449	0,0010	0,01	0,0006	0,0198	282,9	6,2	289,0	12,0	330,0	120,0	282,9	6,2	2,11
Zircon_075	134	108	0,81	0,0544	0,0055	0,3320	0,0290	0,0450	0,0012	0,01	0,0007	-0,3655	283,5	7,4	289,0	22,0	330,0	200,0	283,5	7,4	1,90
Zircon_029	252	160	0,63	0,0547	0,0032	0,3420	0,0160	0,0450	0,0010	0,01	0,0007	0,0775	283,9	6,4	296,0	12,0	410,0	120,0	283,9	6,4	4,09
Zircon_011	257	170	0,66	0,0594	0,0035	0,3740	0,0210	0,0451	0,0010	0,01	0,0008	0,4142	284,5	6,3	322,0	16,0	610,0	120,0	284,5	6,3	11,65
Zircon_086	148	186	1,26	0,1700	0,0210	1,0300	0,1200	0,0452	0,0019	0,02	0,0016	0,6133	285,0	12,0	730,0	62,0	2450,0	190,0	285,0	12,0	60,96
Zircon_088	193	157	0,81	0,0517	0,0032	0,3220	0,0170	0,0454	0,0011	0,01	0,0007	0,1886	286,1	6,7	282,0	13,0	250,0	130,0	286,1	6,7	-1,45
Zircon_008	453	267	0,59	0,0525	0,0026	0,3350	0,0150	0,0457	0,0009	0,02	0,0008	0,1265	288,3	5,3	293,0	11,0	310,0	120,0	288,3	5,3	1,60
Zircon_015	1133	1085	0,96	0,0527	0,0023	0,3360	0,0120	0,0459	0,0009	0,01	0,0005	0,0047	289,2	5,6	293,6	8,8	302,0	98,0	289,2	5,6	1,50
Zircon_044	169	135	0,80	0,0532	0,0038	0,3370	0,0220	0,0460	0,0014	0,02	0,0010	0,1532	289,6	8,5	294,0	17,0	310,0	150,0	289,6	8,5	1,50
Zircon_018	169	147	0,87	0,0529	0,0040	0,3380	0,0240	0,0460	0,0012	0,01	0,0007	0,1197	289,7	7,6	294,0	18,0	310,0	170,0	289,7	7,6	1,46
Zircon_100	375	174	0,46	0,0523	0,0040	0,3340	0,0250	0,0460	0,0011	0,02	0,0008	0,0372	290,1	6,8	292,0	18,0	280,0	150,0	290,1	6,8	0,65
Zircon_012	342	325	0,95	0,0527	0,0034	0,3310	0,0200	0,0461	0,0010	0,01	0,0006	-0,0283	290,8	6,3	290,0	15,0	270,0	140,0	290,8	6,3	-0,28
Zircon_025	420	396	0,94	0,0544	0,0031	0,3490	0,0180	0,0462	0,0010	0,01	0,0007	0,1141	291,3	6,1	303,0	13,0	370,0	120,0	291,3	6,1	3,86
Zircon_024	150	74	0,49	0,0566	0,0045	0,3610	0,0260	0,0462	0,0011	0,01	0,0009	0,0487	291,4	6,9	311,0	20,0	410,0	170,0	291,4	6,9	6,30
Zircon_079	282	256	0,91	0,0532	0,0035	0,3340	0,0170	0,0463	0,0012	0,01	0,0008	-0,2037	291,7	7,5	292,0	13,0	300,0	140,0	291,7	7,5	0,10
Zircon_080	217	150	0,69	0,1080	0,0130	0,6900	0,1200	0,0463	0,0016	0,02	0,0032	0,0849	292,0	9,9	535,0	55,0	1750,0	150,0	292,0	9,9	45,42
Zircon_083	200	116	0,58	0,0543	0,0030	0,3510	0,0170	0,0464	0,0013	0,01	0,0009	-0,2056	292,2	7,9	305,0	13,0	390,0	110,0	292,2	7,9	4,20

Zircon_023	357	239	0,67	0,0530	0,0032	0,3370	0,0170	0,0465	0,0010	0,01	0,0007	-0,0215	293,2	6,1	294,0	13,0	300,0	130,0	293,2	6,1	0,27
Zircon_099	179	153	0,85	0,0577	0,0036	0,3690	0,0200	0,0466	0,0009	0,02	0,0008	-0,4269	293,4	5,5	318,0	15,0	470,0	140,0	293,4	5,5	7,74
Zircon_093	268	282	1,05	0,0513	0,0030	0,3270	0,0190	0,0466	0,0012	0,01	0,0006	0,1159	293,5	7,1	289,0	14,0	230,0	130,0	293,5	7,1	-1,56
Zircon_096	157	115	0,73	0,0526	0,0036	0,3320	0,0190	0,0467	0,0011	0,02	0,0008	-0,1611	294,3	6,9	293,0	14,0	290,0	150,0	294,3	6,9	-0,44
Zircon_055	408	195	0,48	0,0542	0,0023	0,3510	0,0120	0,0467	0,0010	0,01	0,0006	-0,0424	294,4	6,0	305,6	8,9	368,0	93,0	294,4	6,0	3,66
Zircon_053	348	233	0,67	0,0581	0,0069	0,3720	0,0560	0,0468	0,0011	0,01	0,0008	-0,1202	294,6	7,0	320,0	35,0	490,0	160,0	294,6	7,0	7,94
Zircon_035	334	304	0,91	0,0559	0,0035	0,3620	0,0190	0,0469	0,0011	0,02	0,0007	0,0625	295,3	7,1	313,0	13,0	470,0	130,0	295,3	7,1	5,65
Zircon_020	388	455	1,17	0,0508	0,0030	0,3310	0,0170	0,0469	0,0010	0,01	0,0006	0,0896	295,4	6,2	290,0	13,0	220,0	120,0	295,4	6,2	-1,86
Zircon_022	332	114	0,34	0,0545	0,0036	0,3550	0,0190	0,0470	0,0010	0,01	0,0008	-0,2662	296,0	6,2	309,0	14,0	380,0	140,0	296,0	6,2	4,21
Zircon_091	70	35	0,50	0,0508	0,0055	0,3300	0,0340	0,0471	0,0014	0,02	0,0012	0,0484	296,4	8,8	286,0	26,0	180,0	220,0	296,4	8,8	-3,64
Zircon_067	635	388	0,61	0,0537	0,0023	0,3490	0,0120	0,0471	0,0009	0,02	0,0007	0,3096	296,5	5,7	304,0	9,0	360,0	98,0	296,5	5,7	2,47
Zircon_078	313	131	0,42	0,0521	0,0029	0,3400	0,0160	0,0472	0,0010	0,01	0,0007	-0,0840	297,0	6,4	297,0	12,0	260,0	120,0	297,0	6,4	0,00
Zircon_042	631	362	0,57	0,0598	0,0027	0,3920	0,0150	0,0472	0,0010	0,02	0,0008	0,1638	297,0	5,8	335,0	11,0	610,0	100,0	297,0	5,8	11,34
Zircon_073	199	127	0,64	0,0521	0,0032	0,3390	0,0170	0,0472	0,0012	0,01	0,0007	-0,2096	297,2	7,1	296,0	13,0	280,0	140,0	297,2	7,1	-0,41
Zircon_013	375	283	0,75	0,0530	0,0026	0,3470	0,0140	0,0473	0,0010	0,01	0,0006	-0,1236	297,9	6,2	302,0	10,0	320,0	110,0	297,9	6,2	1,36
Zircon_051	241	238	0,99	0,0676	0,0046	0,4380	0,0270	0,0473	0,0011	0,02	0,0008	0,1724	297,9	6,9	368,0	18,0	860,0	130,0	297,9	6,9	19,05
Zircon_087	310	149	0,48	0,0538	0,0033	0,3510	0,0170	0,0474	0,0011	0,01	0,0007	-0,1517	298,8	6,6	305,0	13,0	350,0	130,0	298,8	6,6	2,03
Zircon_092	211	118	0,56	0,0517	0,0071	0,3370	0,0540	0,0475	0,0023	0,02	0,0033	-0,2696	299,0	14,0	293,0	37,0	220,0	230,0	299,0	14,0	-2,05
Zircon_101	442	351	0,79	0,0517	0,0026	0,3410	0,0160	0,0475	0,0012	0,02	0,0007	0,0458	299,1	7,1	300,0	12,0	270,0	110,0	299,1	7,1	0,30
Zircon_060	89	88	0,99	0,0525	0,0047	0,3470	0,0300	0,0477	0,0014	0,01	0,0008	0,1878	300,0	8,3	300,0	23,0	280,0	190,0	300,0	8,3	0,00
Zircon_097	1330	603	0,45	0,0512	0,0030	0,3440	0,0160	0,0477	0,0009	0,02	0,0007	-0,3352	300,6	5,6	300,0	12,0	260,0	110,0	300,6	5,6	-0,20
Zircon_072	171	109	0,64	0,0551	0,0033	0,3580	0,0190	0,0477	0,0012	0,01	0,0008	0,0652	300,6	7,3	310,0	14,0	380,0	130,0	300,6	7,3	3,03
Zircon_047	201	122	0,61	0,0531	0,0033	0,3470	0,0200	0,0478	0,0013	0,02	0,0010	0,0037	301,2	7,8	305,0	14,0	320,0	140,0	301,2	7,8	1,25
Zircon_014	95	64	0,67	0,0527	0,0050	0,3490	0,0320	0,0479	0,0015	0,01	0,0010	0,0762	301,3	9,5	304,0	23,0	310,0	200,0	301,3	9,5	0,89
Zircon_094	250	100	0,40	0,0544	0,0029	0,3590	0,0170	0,0479	0,0012	0,02	0,0009	-0,0219	301,5	7,2	311,0	13,0	370,0	120,0	301,5	7,2	3,05
Zircon_090	269	206	0,77	0,0527	0,0031	0,3530	0,0180	0,0480	0,0012	0,02	0,0007	-0,0864	302,3	7,2	307,0	13,0	320,0	130,0	302,3	7,2	1,53
Zircon_019	412	199	0,48	0,0519	0,0027	0,3440	0,0150	0,0480	0,0010	0,01	0,0007	-0,1778	302,4	5,9	299,0	11,0	260,0	110,0	302,4	5,9	-1,14
Zircon_031	135	134	0,99	0,0524	0,0043	0,3520	0,0270	0,0481	0,0014	0,02	0,0008	0,0382	302,7	8,7	310,0	19,0	320,0	180,0	302,7	8,7	2,35

Zircon_036	241	92	0,38	0,0510	0,0032	0,3440	0,0200	0,0481	0,0011	0,02	0,0010	-0,0175	303,1	6,7	299,0	15,0	260,0	140,0	303,1	6,7	-1,37
Zircon_027	398	331	0,83	0,0523	0,0032	0,3490	0,0210	0,0485	0,0011	0,02	0,0007	-0,0837	305,1	6,8	303,0	15,0	310,0	130,0	305,1	6,8	-0,69
Zircon_064	250	203	0,81	0,0536	0,0031	0,3550	0,0180	0,0485	0,0012	0,02	0,0008	0,3096	305,6	7,4	310,0	14,0	320,0	130,0	305,6	7,4	1,42
Zircon_043	174	101	0,58	0,0519	0,0033	0,3470	0,0210	0,0486	0,0013	0,02	0,0010	0,2938	305,7	8,1	302,0	16,0	280,0	130,0	305,7	8,1	-1,23
Zircon_021	220	268	1,22	0,0515	0,0032	0,3480	0,0170	0,0486	0,0012	0,02	0,0006	-0,2717	305,9	7,3	303,0	13,0	250,0	140,0	305,9	7,3	-0,96
Zircon_005	283	167	0,59	0,0528	0,0029	0,3580	0,0160	0,0488	0,0011	0,02	0,0009	-0,0147	306,8	6,5	312,0	12,0	290,0	120,0	306,8	6,5	1,67
Zircon_009	76	34	0,45	0,0560	0,0053	0,3700	0,0310	0,0488	0,0014	0,02	0,0014	-0,1757	306,9	8,8	324,0	21,0	420,0	190,0	306,9	8,8	5,28
Zircon_001	474	226	0,48	0,0517	0,0026	0,3540	0,0160	0,0493	0,0010	0,02	0,0008	0,0015	310,1	6,3	307,0	12,0	260,0	110,0	310,1	6,3	-1,01
~~Zircon_054~~	107	84	0,79	0,1150	0,0075	0,7940	0,0440	0,0496	0,0014	0,02	0,0013	-0,0853	311,9	8,4	592,0	23,0	1870,0	110,0	311,9	8,4	47,31
Zircon_081	363	196	0,54	0,0536	0,0027	0,3660	0,0160	0,0497	0,0010	0,02	0,0008	0,1950	312,7	6,0	317,0	12,0	340,0	110,0	312,7	6,0	1,36
Zircon_062	128	150	1,17	0,0556	0,0061	0,3740	0,0310	0,0497	0,0017	0,02	0,0011	-0,0780	313,0	11,0	325,0	23,0	370,0	180,0	313,0	11,0	3,69
~~Zircon_074~~	89	62	0,70	0,0936	0,0080	0,6440	0,0520	0,0506	0,0013	0,02	0,0011	-0,1797	318,4	8,0	510,0	30,0	1470,0	170,0	318,4	8,0	37,57
Zircon_058	276	181	0,66	0,0684	0,0081	0,4850	0,0390	0,0512	0,0017	0,01	0,0007	0,1117	322,0	10,0	399,0	25,0	860,0	190,0	322,0	10,0	19,30
~~Zircon_077~~	178	75	0,42	0,0896	0,0041	1,0140	0,0630	0,0808	0,0044	0,02	0,0018	0,7984	501,0	26,0	708,0	30,0	1425,0	86,0	501,0	26,0	29,24
~~Zircon_070~~	102	67	0,66	0,1690	0,0160	1,4000	0,1300	0,0613	0,0019	0,04	0,0023	-0,0081	3844,0	12,0	880,0	50,0	2500,0	150,0	3844,0	12,0	56,36
~~Zircon_071~~	503	241	0,48	0,1810	0,0700	1,3000	2,2000	0,0540	0,0520	0,05	0,1500	-0,0332	340,0	250,0	860,0	310,0	2650,0	300,0	340,0	250,0	60,47
~~Zircon_068~~	101	127	1,26	0,2460	0,0310	1,8200	0,4800	0,0526	0,0029	0,03	0,0036	0,4214	330,0	18,0	1048,0	84,0	3160,0	150,0	330,0	18,0	68,51
~~Zircon_098~~	74	39	0,53	0,2840	0,0590	2,5000	2,3000	0,0640	0,0220	0,11	0,0760	0,3670	400,0	120,0	1280,0	250,0	3350,0	220,0	400,0	120,0	68,75
~~Zircon_076~~	15	38	2,53	0,3000	0,1200	1,7300	0,8400	0,0420	0,0130	0,02	0,0054	0,3079	265,0	83,0	970,0	240,0	3430,0	700,0	265,0	83,0	72,68
~~Zircon_059~~	372	178	0,48	0,3450	0,0140	3,0930	0,0980	0,0648	0,0013	0,11	0,0047	0,2213	405,0	8,2	1430,0	24,0	3688,0	57,0	405,0	8,2	71,68
~~Zircon_082~~	†	†	1,00	0,8650	0,0530	62,0000	12,0000	0,5200	0,1000	0,82	0,3200	0,9693	2690,0	410,0	4240,0	240,0	5110,0	120,0	2690,0	410,0	36,56

Maximum depositional age (2+DZ, 1σ): 222.0±4.2 Ma (MSWD = 0.18)

CPV-15-325 (DZ)

~~Zircon_074~~	101	122	1,21	0,0700	0,0300	0,3100	0,2100	0,0323	0,0019	0,0999	0,0026	-0,16	205,0	12,0	270,0	98,0	920,0	360,0	205,0	12,0	24,07	
~~Zircon_073~~	271	253	0,93	0,0719	0,0049	0,3360	0,0240	0,0338	0,0010	0,0107	0,0006	0,41	214,0	6,3	293,0	18,0	1020,0	120,0	214,0	6,3	26,96	
Zircon_087	43	28	0,65	0,0478	0,0088	0,2270	0,0430	0,0348	0,0015	0,0108	0,0013	-0,04	220,2	9,6	210,0	36,0	110,0	330,0	220,2	9,6	-4,86	*
Zircon_084	547	468	0,86	0,0510	0,0028	0,2510	0,0160	0,0351	0,0008	0,0108	0,0006	0,18	222,5	4,8	227,0	12,0	240,0	120,0	222,5	4,8	1,98	*

																					***
~~Zircon_078~~	~~2018~~	~~608~~	~~0,30~~	~~0,0550~~	~~0,0024~~	~~0,2780~~	~~0,0150~~	~~0,0366~~	~~0,0007~~	~~0,0112~~	~~0,0006~~	~~0,25~~	~~231,9~~	~~4,6~~	~~250,0~~	~~12,0~~	~~420,0~~	~~100,0~~	~~231,9~~	~~4,6~~	~~7,24~~
~~Zircon_127~~	~~122~~	~~189~~	~~1,55~~	~~0,1079~~	~~0,0098~~	~~0,5450~~	~~0,0480~~	~~0,0370~~	~~0,0012~~	~~0,0140~~	~~0,0009~~	~~0,28~~	~~233,9~~	~~7,6~~	~~445,0~~	~~30,0~~	~~1780,0~~	~~140,0~~	~~233,9~~	~~7,6~~	~~47,44~~
Zircon_121	160	191	1,19	0,0507	0,0043	0,2670	0,0240	0,0371	0,0011	0,0116	0,0007	0,14	234,5	6,7	244,0	20,0	270,0	180,0	234,5	6,7	3,89
Zircon_057	397	190	0,48	0,0514	0,0032	0,2670	0,0180	0,0373	0,0008	0,0116	0,0008	0,04	236,2	5,2	242,0	15,0	280,0	130,0	236,2	5,2	2,40
Zircon_076	229	185	0,81	0,0554	0,0038	0,2870	0,0200	0,0375	0,0010	0,0094	0,0008	-0,12	237,1	6,3	261,0	16,0	430,0	130,0	237,1	6,3	9,16
Zircon_137	330	562	1,70	0,0527	0,0036	0,2720	0,0190	0,0376	0,0009	0,0111	0,0006	0,06	238,2	5,4	244,0	15,0	310,0	140,0	238,2	5,4	2,38
Zircon_053	190	274	1,44	0,0514	0,0044	0,2760	0,0230	0,0384	0,0011	0,0126	0,0008	-0,14	243,1	6,6	246,0	18,0	250,0	180,0	243,1	6,6	1,18
Zircon_109	302	217	0,72	0,0497	0,0030	0,2670	0,0180	0,0388	0,0010	0,0119	0,0008	0,21	245,5	6,2	240,0	14,0	180,0	130,0	245,5	6,2	-2,29
~~Zircon_126~~	~~42~~	~~29~~	~~0,69~~	~~0,0970~~	~~0,0110~~	~~0,4900~~	~~0,0590~~	~~0,0388~~	~~0,0017~~	~~0,0464~~	~~0,0016~~	~~-0,02~~	~~246,0~~	~~10,0~~	~~407,0~~	~~40,0~~	~~1440,0~~	~~250,0~~	~~246,0~~	~~10,0~~	~~39,56~~
Zircon_142	1198	439	0,37	0,0597	0,0030	0,3230	0,0190	0,0389	0,0008	0,0147	0,0008	-0,11	246,2	5,1	284,0	15,0	590,0	100,0	246,2	5,1	13,31
Zircon_118	86	97	1,13	0,0490	0,0063	0,2720	0,0310	0,0391	0,0017	0,0117	0,0009	-0,03	247,0	11,0	246,0	25,0	240,0	230,0	247,0	11,0	-0,41
Zircon_114	158	144	0,91	0,0523	0,0043	0,2810	0,0240	0,0396	0,0011	0,0115	0,0007	0,16	250,0	6,7	250,0	19,0	290,0	170,0	250,0	6,7	0,00
~~Zircon_124~~	~~21~~	~~13~~	~~0,62~~	~~0,1300~~	~~0,0180~~	~~0,7010~~	~~0,0990~~	~~0,0396~~	~~0,0026~~	~~0,0292~~	~~0,0026~~	~~-0,07~~	~~250,0~~	~~16,0~~	~~525,0~~	~~58,0~~	~~2120,0~~	~~250,0~~	~~250,0~~	~~16,0~~	~~52,38~~
Zircon_065	173	387	2,24	0,0523	0,0040	0,2920	0,0230	0,0396	0,0011	0,0121	0,0007	0,16	250,3	6,6	259,0	18,0	360,0	150,0	250,3	6,6	3,36
Zircon_119	45	28	0,62	0,0588	0,0083	0,3050	0,0420	0,0397	0,0018	0,0140	0,0017	-0,04	251,0	11,0	286,0	32,0	530,0	260,0	251,0	11,0	12,24
Zircon_148	104	71	0,68	0,0549	0,0096	0,3030	0,0560	0,0398	0,0015	0,0132	0,0014	-0,06	251,6	9,0	264,0	39,0	480,0	250,0	251,6	9,0	4,70
Zircon_068	33	24	0,73	0,0577	0,0099	0,2890	0,0470	0,0398	0,0023	0,0131	0,0014	0,03	252,0	14,0	273,0	37,0	350,0	320,0	252,0	14,0	7,69
Zircon_120	123	94	0,76	0,0528	0,0038	0,2910	0,0220	0,0399	0,0012	0,0125	0,0009	-0,07	252,2	7,5	258,0	17,0	280,0	160,0	252,2	7,5	2,25
Zircon_141	273	175	0,64	0,0483	0,0035	0,2720	0,0200	0,0399	0,0010	0,0118	0,0009	-0,03	252,3	6,4	245,0	16,0	90,0	160,0	252,3	6,4	-2,98
Zircon_098	267	213	0,80	0,0511	0,0031	0,2870	0,0200	0,0399	0,0010	0,0128	0,0008	0,16	252,5	6,4	255,0	16,0	260,0	120,0	252,5	6,4	0,98
Zircon_111	54	39	0,72	0,0531	0,0059	0,3020	0,0360	0,0402	0,0014	0,0131	0,0012	0,15	254,3	8,5	268,0	27,0	330,0	230,0	254,3	8,5	5,11
Zircon_110	247	109	0,44	0,0523	0,0036	0,2920	0,0220	0,0403	0,0017	0,0111	0,0012	0,17	255,0	10,0	259,0	17,0	290,0	170,0	255,0	10,0	1,54
Zircon_116	56	33	0,59	0,0499	0,0073	0,2820	0,0400	0,0404	0,0016	0,0118	0,0010	-0,06	255,1	9,8	261,0	29,0	140,0	280,0	255,1	9,8	2,26
Zircon_100	199	159	0,80	0,0547	0,0043	0,2970	0,0240	0,0404	0,0011	0,0128	0,0008	-0,14	255,5	6,7	263,0	18,0	340,0	170,0	255,5	6,7	2,85
Zircon_123	72	55	0,76	0,0533	0,0061	0,2940	0,0340	0,0406	0,0015	0,0132	0,0010	0,30	256,4	9,1	263,0	26,0	300,0	230,0	256,4	9,1	2,51
Zircon_055	233	173	0,74	0,0536	0,0038	0,2920	0,0220	0,0406	0,0010	0,0131	0,0008	0,12	256,5	6,5	259,0	17,0	310,0	150,0	256,5	6,5	0,97
Zircon_115	281	300	1,07	0,0538	0,0036	0,2950	0,0210	0,0406	0,0009	0,0122	0,0007	0,16	256,5	5,6	261,0	17,0	320,0	150,0	256,5	5,6	1,72
Zircon_064	235	214	0,91	0,0517	0,0039	0,2940	0,0230	0,0406	0,0010	0,0125	0,0008	-0,19	256,5	6,3	263,0	18,0	300,0	160,0	256,5	6,3	2,47

Zircon_052	103	82	0,80	0,0572	0,0056	0,3090	0,0320	0,0405	0,0013	0,0128	0,0010	0,12	257,1	8,1	270,0	25,0	430,0	200,0	257,1	8,1	4,78
Zircon_132	603	351	0,58	0,0511	0,0026	0,2860	0,0170	0,0408	0,0009	0,0129	0,0007	0,12	257,5	5,4	255,0	13,0	230,0	110,0	257,5	5,4	-0,98
Zircon_136	172	170	0,99	0,0598	0,0040	0,3340	0,0250	0,0408	0,0012	0,0121	0,0009	0,23	257,8	7,3	291,0	19,0	540,0	150,0	257,8	7,3	11,41
Zircon_051	124	114	0,92	0,0570	0,0097	0,3200	0,0650	0,0409	0,0016	0,0125	0,0022	0,65	258,0	10,0	280,0	44,0	560,0	240,0	258,0	10,0	7,86
Zircon_133	477	236	0,49	0,0527	0,0031	0,3010	0,0190	0,0409	0,0009	0,0125	0,0008	-0,17	258,6	5,8	269,0	15,0	290,0	120,0	258,6	5,8	3,87
Zircon_088	318	355	1,12	0,0550	0,0035	0,3040	0,0210	0,0410	0,0011	0,0127	0,0007	-0,27	258,8	6,7	272,0	16,0	370,0	140,0	258,8	6,7	4,85
Zircon_104	177	128	0,72	0,0531	0,0034	0,2930	0,0200	0,0410	0,0011	0,0132	0,0009	0,26	259,0	6,7	264,0	16,0	330,0	130,0	259,0	6,7	1,89
Zircon_050	164	154	0,94	0,0506	0,0042	0,2820	0,0230	0,0412	0,0012	0,0131	0,0009	0,02	260,1	7,1	251,0	18,0	180,0	170,0	260,1	7,1	-3,63
Zircon_144	138	164	1,19	0,0531	0,0043	0,2980	0,0250	0,0412	0,0013	0,0130	0,0008	0,14	260,4	7,8	263,0	20,0	280,0	170,0	260,4	7,8	0,99
Zircon_058	63	64	1,02	0,0515	0,0060	0,2840	0,0340	0,0413	0,0015	0,0129	0,0010	0,25	260,7	9,6	262,0	26,0	310,0	210,0	260,7	9,6	0,50
Zircon_145	59	49	0,83	0,0551	0,0073	0,2960	0,0410	0,0411	0,0017	0,0127	0,0012	0,05	261,0	11,0	263,0	32,0	250,0	260,0	261,0	11,0	0,76
Zircon_072	293	201	0,69	0,0588	0,0033	0,3380	0,0210	0,0414	0,0010	0,0094	0,0006	0,33	261,2	6,2	298,0	16,0	570,0	130,0	261,2	6,2	12,35
Zircon_060	382	232	0,61	0,0501	0,0028	0,2900	0,0180	0,0414	0,0012	0,0125	0,0007	0,36	261,3	6,2	258,0	13,0	200,0	120,0	261,3	6,2	-1,28
Zircon_128	148	182	1,23	0,0530	0,0049	0,2970	0,0270	0,0414	0,0013	0,0131	0,0009	-0,20	261,4	8,0	264,0	21,0	280,0	200,0	261,4	8,0	0,98
Zircon_135	250	161	0,64	0,0540	0,0042	0,3060	0,0250	0,0414	0,0010	0,0124	0,0007	-0,13	261,6	6,2	272,0	19,0	340,0	170,0	261,6	6,2	3,82
Zircon_054	232	130	0,56	0,0579	0,0039	0,3290	0,0230	0,0415	0,0012	0,0118	0,0010	-0,25	262,2	7,6	290,0	18,0	530,0	150,0	262,2	7,6	9,59
Zircon_062	435	440	1,01	0,0517	0,0029	0,2960	0,0180	0,0415	0,0009	0,0129	0,0007	-0,18	262,3	5,5	263,0	14,0	250,0	120,0	262,3	5,5	0,27
Zircon_089	334	345	1,03	0,0589	0,0035	0,3300	0,0210	0,0416	0,0009	0,0140	0,0008	-0,15	262,8	5,8	289,0	16,0	530,0	130,0	262,8	5,8	9,07
Zircon_097	232	262	1,13	0,0534	0,0056	0,3060	0,0350	0,0417	0,0011	0,0130	0,0011	-0,06	263,1	7,0	274,0	26,0	340,0	180,0	263,1	7,0	3,98
Zircon_101	127	84	0,66	0,0514	0,0041	0,3010	0,0240	0,0420	0,0012	0,0139	0,0009	-0,06	265,2	7,6	266,0	19,0	260,0	160,0	265,2	7,6	0,30
~~Zircon_108~~	~~152~~	~~147~~	~~0,97~~	~~0,0480~~	~~0,0037~~	~~0,2820~~	~~0,0210~~	~~0,0420~~	~~0,0013~~	~~0,0128~~	~~0,0008~~	~~-0,10~~	~~265,4~~	~~8,1~~	~~251,0~~	~~17,0~~	~~100,0~~	~~150,0~~	~~265,4~~	~~8,1~~	~~-5,74~~
~~Zircon_105~~ ***	~~1373~~	~~854~~	~~0,62~~	~~0,0530~~	~~0,0025~~	~~0,3090~~	~~0,0180~~	~~0,0421~~	~~0,0009~~	~~0,0131~~	~~0,0008~~	~~-0,12~~	~~265,5~~	~~5,6~~	~~273,0~~	~~14,0~~	~~330,0~~	~~110,0~~	~~265,5~~	~~5,6~~	~~2,75~~
Zircon_077	255	128	0,50	0,0514	0,0031	0,2980	0,0200	0,0422	0,0011	0,0138	0,0009	0,18	266,2	6,7	266,0	16,0	240,0	130,0	266,2	6,7	-0,08
Zircon_086	411	95	0,23	0,0531	0,0029	0,3070	0,0200	0,0423	0,0010	0,0138	0,0010	0,57	267,2	6,4	272,0	15,0	330,0	130,0	267,2	6,4	1,76
Zircon_070	97	105	1,08	0,0518	0,0056	0,3070	0,0290	0,0425	0,0014	0,0131	0,0009	-0,36	268,5	8,4	270,0	23,0	240,0	210,0	268,5	8,4	0,56
Zircon_092	115	56	0,49	0,0518	0,0053	0,3070	0,0320	0,0427	0,0014	0,0125	0,0011	0,12	269,4	8,5	270,0	25,0	240,0	200,0	269,4	8,5	0,22
Zircon_106	273	280	1,03	0,0517	0,0032	0,3070	0,0210	0,0429	0,0012	0,0133	0,0008	0,15	270,5	7,3	273,0	16,0	240,0	140,0	270,5	7,3	0,92
Zircon_102	186	263	1,41	0,0602	0,0044	0,3540	0,0280	0,0431	0,0013	0,0142	0,0008	0,12	271,7	8,0	313,0	21,0	580,0	140,0	271,7	8,0	13,19

Zircon_056	533	451	0,85	0,0513	0,0027	0,3040	0,0190	0,0434	0,0009	0,0135	0,0007	0,01	273,7	5,8	269,0	15,0	240,0	120,0	273,7	5,8	-1,75
Zircon_107	55	25	0,45	0,0710	0,0380	0,4300	0,4600	0,0436	0,0050	0,0160	0,0200	-0,26	275,0	30,0	360,0	160,0	840,0	350,0	275,0	30,0	23,61
Zircon_131	574	317	0,55	0,0509	0,0029	0,3100	0,0200	0,0437	0,0010	0,0138	0,0008	0,00	275,6	6,1	273,0	16,0	240,0	130,0	275,6	6,1	-0,95
Zircon_066	1120	691	0,62	0,0545	0,0026	0,3320	0,0190	0,0440	0,0009	0,0144	0,0008	0,06	277,7	5,8	291,0	14,0	380,0	110,0	277,7	5,8	4,57
~~Zircon_090~~	~~61~~	~~61~~	~~1,00~~	~~0,0472~~	~~0,0051~~	~~0,2860~~	~~0,0300~~	~~0,0441~~	~~0,0016~~	~~0,0145~~	~~0,0011~~	~~0,06~~	~~278,0~~	~~10,0~~	~~256,0~~	~~24,0~~	~~20,0~~	~~210,0~~	~~278,0~~	~~10,0~~	~~-8,59~~
Zircon_129	282	354	1,26	0,0512	0,0032	0,3140	0,0210	0,0441	0,0012	0,0142	0,0008	0,04	278,2	7,5	279,0	17,0	260,0	150,0	278,2	7,5	0,29
Zircon_063	205	166	0,81	0,0594	0,0042	0,3570	0,0250	0,0441	0,0014	0,0130	0,0008	0,14	278,2	8,4	309,0	18,0	550,0	150,0	278,2	8,4	9,97
Zircon_061	156	136	0,87	0,0535	0,0047	0,3210	0,0280	0,0442	0,0013	0,0129	0,0009	-0,10	278,5	7,8	284,0	21,0	310,0	180,0	278,5	7,8	1,94
~~Zircon_069~~	~~79~~	~~43~~	~~0,54~~	~~0,0870~~	~~0,0100~~	~~0,5120~~	~~0,0640~~	~~0,0442~~	~~0,0013~~	~~0,0204~~	~~0,0018~~	~~0,12~~	~~278,5~~	~~8,0~~	~~413,0~~	~~39,0~~	~~1340,0~~	~~180,0~~	~~278,5~~	~~8,0~~	~~32,57~~
Zircon_085	192	99	0,52	0,0505	0,0041	0,3040	0,0260	0,0445	0,0013	0,0151	0,0010	0,04	280,3	8,2	268,0	20,0	200,0	180,0	280,3	8,2	-4,59
Zircon_103	457	186	0,41	0,0527	0,0027	0,3240	0,0190	0,0445	0,0010	0,0136	0,0009	0,12	280,4	6,3	284,0	15,0	310,0	120,0	280,4	6,3	1,27
Zircon_082	207	98	0,47	0,0526	0,0033	0,3290	0,0240	0,0448	0,0012	0,0149	0,0011	0,27	282,7	7,2	288,0	18,0	280,0	130,0	282,7	7,2	1,84
Zircon_113	293	166	0,57	0,0523	0,0033	0,3250	0,0220	0,0450	0,0012	0,0144	0,0009	0,12	283,7	7,3	285,0	17,0	280,0	140,0	283,7	7,3	0,46
Zircon_139	180	198	1,10	0,0557	0,0038	0,3390	0,0250	0,0450	0,0013	0,0153	0,0011	-0,32	283,9	7,9	298,0	18,0	410,0	150,0	283,9	7,9	4,73
Zircon_122	884	512	0,58	0,0528	0,0026	0,3290	0,0210	0,0458	0,0011	0,0146	0,0010	0,55	288,4	7,0	289,0	16,0	300,0	110,0	288,4	7,0	0,21
Zircon_093	580	366	0,63	0,0509	0,0027	0,3230	0,0200	0,0459	0,0010	0,0139	0,0008	0,03	289,3	6,0	284,0	15,0	220,0	120,0	289,3	6,0	-1,87
Zircon_099	289	111	0,38	0,0507	0,0029	0,3280	0,0210	0,0470	0,0012	0,0147	0,0010	0,08	295,9	7,2	287,0	16,0	200,0	130,0	295,9	7,2	-3,10
Zircon_094	464	237	0,51	0,0548	0,0030	0,3700	0,0220	0,0490	0,0011	0,0162	0,0009	-0,14	308,6	6,9	319,0	16,0	410,0	120,0	308,6	6,9	3,26
Zircon_117	377	144	0,38	0,0520	0,0027	0,3450	0,0200	0,0491	0,0012	0,0141	0,0009	0,10	309,2	7,7	301,0	15,0	280,0	130,0	309,2	7,7	-2,72
Zircon_130	783	239	0,31	0,0566	0,0028	0,3820	0,0220	0,0492	0,0011	0,0184	0,0010	0,12	309,7	6,9	328,0	16,0	460,0	110,0	309,7	6,9	5,58
Zircon_095	414	180	0,43	0,0612	0,0030	0,5510	0,0310	0,0663	0,0017	0,0161	0,0010	0,19	414,0	10,0	445,0	20,0	660,0	100,0	414,0	10,0	6,97
Zircon_143	325	314	0,97	0,0564	0,0034	0,5500	0,0370	0,0713	0,0018	0,0214	0,0012	-0,09	444,0	11,0	444,0	24,0	430,0	130,0	444,0	11,0	0,00
Zircon_147	280	223	0,80	0,0546	0,0032	0,5530	0,0360	0,0721	0,0016	0,0224	0,0012	0,12	448,7	9,6	445,0	23,0	430,0	140,0	448,7	9,6	-0,83
Zircon_134	279	209	0,75	0,0574	0,0032	0,5690	0,0350	0,0725	0,0017	0,0218	0,0013	0,12	451,0	10,0	460,0	22,0	520,0	120,0	451,0	10,0	1,96
~~Zircon_080~~	~~197~~	~~138~~	~~0,70~~	~~0,0842~~	~~0,0048~~	~~0,8260~~	~~0,0510~~	~~0,0724~~	~~0,0021~~	~~0,0253~~	~~0,0014~~	~~-0,17~~	~~451,0~~	~~12,0~~	~~610,0~~	~~28,0~~	~~1310,0~~	~~110,0~~	~~451,0~~	~~12,0~~	~~26,07~~
Zircon_138	375	219	0,58	0,0560	0,0030	0,5730	0,0350	0,0737	0,0016	0,0224	0,0013	0,14	458,6	9,5	459,0	22,0	450,0	120,0	458,6	9,5	0,09
Zircon_112	618	366	0,59	0,0557	0,0025	0,5710	0,0310	0,0738	0,0016	0,0233	0,0013	0,06	459,2	9,4	460,0	20,0	440,0	99,0	459,2	9,4	0,17
Zircon_096	309	217	0,70	0,0644	0,0034	0,6570	0,0430	0,0748	0,0016	0,0250	0,0013	0,49	464,9	9,6	516,0	26,0	760,0	110,0	464,9	9,6	9,90

Sample																						
Zircon_075	177	121	0,68	0,0616	0,0038	0,7270	0,0470	0,0848	0,0022	0,0188	0,0014	0,16	524,0	13,0	558,0	27,0	690,0	120,0	524,0	13,0	6,09	
Zircon_081	149	84	0,56	0,0595	0,0034	0,7030	0,0460	0,0862	0,0020	0,0267	0,0016	0,31	533,0	12,0	539,0	28,0	560,0	130,0	533,0	12,0	1,11	
Zircon_071	53	23	0,43	0,0837	0,0086	1,9200	0,1800	0,1660	0,0130	0,0292	0,0031	0,63	988,0	76,0	1080,0	75,0	1300,0	210,0	988,0	76,0	8,52	
Zircon_091	109	40	0,37	0,0752	0,0035	1,8300	0,1000	0,1778	0,0040	0,0524	0,0032	0,28	1055,0	22,0	1054,0	37,0	1064,0	94,0	1055,0	22,0	-0,09	
Zircon_083	143	100	0,70	0,0748	0,0037	1,8500	0,1000	0,1790	0,0038	0,0538	0,0029	-0,21	1061,0	21,0	1062,0	37,0	1057,0	98,0	1061,0	21,0	0,09	
Zircon_140	194	101	0,52	0,0752	0,0036	1,8900	0,1100	0,1821	0,0044	0,0532	0,0029	0,27	1078,0	24,0	1077,0	36,0	1081,0	94,0	1078,0	24,0	-0,09	
Zircon_146	113	38	0,34	0,0783	0,0041	1,9500	0,1200	0,1821	0,0043	0,0561	0,0038	-0,03	1078,0	23,0	1096,0	40,0	1130,0	110,0	1078,0	23,0	1,64	
Zircon_067	45	23	0,51	0,0924	0,0050	3,2200	0,1900	0,2520	0,0065	0,0780	0,0049	0,18	1448,0	34,0	1464,0	47,0	1480,0	100,0	1480,0	100,0	1,09	
Zircon_079	463	44	0,10	0,1061	0,0044	4,5200	0,2300	0,3088	0,0063	0,0978	0,0054	0,61	1735,0	31,0	1735,0	42,0	1731,0	77,0	1731,0	77,0	0,00	
Zircon_059	63	67	1,06	0,1138	0,0054	5,1100	0,2700	0,3296	0,0069	0,0995	0,0050	0,30	1835,0	34,0	1841,0	46,0	1843,0	85,0	1843,0	85,0	0,33	
CPV-15-272 (DZ)						Maximum depositional age (2+DZ, 1σ): 224.1±1.6 Ma (MSWD = 1.02)																
Zircon_057	106	79	0,75	0,0564	0,0054	0,2640	0,0270	0,0345	0,0011	0,0111	0,0009	0,10	218,9	7,0	239,0	21,0	400,0	200,0	218,9	7,0	8,41	*
Zircon_024	274	322	1,18	0,0593	0,0043	0,2830	0,0240	0,0346	0,0009	0,0115	0,0007	0,06	219,5	5,8	252,0	19,0	590,0	170,0	219,5	5,8	12,90	*
Zircon_047	182	178	0,98	0,0507	0,0036	0,2440	0,0200	0,0347	0,0010	0,0109	0,0007	-0,01	219,6	6,0	221,0	16,0	200,0	150,0	219,6	6,0	0,63	*
Zircon_033	127	86	0,68	0,0553	0,0046	0,2610	0,0230	0,0347	0,0012	0,0109	0,0009	-0,04	219,8	7,6	234,0	19,0	410,0	180,0	219,8	7,6	6,07	*
Zircon_038	82	58	0,71	0,0545	0,0063	0,2620	0,0310	0,0348	0,0012	0,0106	0,0010	0,02	220,5	7,5	234,0	25,0	270,0	230,0	220,5	7,5	5,77	*
Zircon_023	28	14	0,50	0,0630	0,0130	0,2940	0,0540	0,0353	0,0018	0,0120	0,0015	-0,12	223,0	11,0	259,0	41,0	460,0	380,0	223,0	11,0	13,90	*
Zircon_058	148	157	1,06	0,0526	0,0047	0,2600	0,0240	0,0353	0,0012	0,0104	0,0007	0,19	223,3	7,6	238,0	18,0	270,0	180,0	223,3	7,6	6,18	*
Zircon_008	171	169	0,99	0,0571	0,0039	0,2660	0,0200	0,0353	0,0010	0,0117	0,0008	-0,26	223,7	6,4	239,0	16,0	440,0	150,0	223,7	6,4	6,40	*
Zircon_097	417	387	0,93	0,0594	0,0031	0,2890	0,0200	0,0354	0,0010	0,0116	0,0007	0,24	224,1	6,4	259,0	15,0	580,0	110,0	224,1	6,4	13,47	*
Zircon_043	190	129	0,68	0,0530	0,0079	0,2490	0,0450	0,0355	0,0011	0,0111	0,0014	-0,14	224,8	7,0	225,0	33,0	280,0	230,0	224,8	7,0	0,09	*
~~Zircon_073~~	~~3843~~	~~6750~~	~~1,76~~	~~0,0694~~	~~0,0022~~	~~0,3410~~	~~0,0200~~	~~0,0356~~	~~0,0008~~	~~0,0066~~	~~0,0006~~	~~0,07~~	~~225,3~~	~~5,1~~	~~298,0~~	~~15,0~~	~~915,0~~	~~64,0~~	~~225,3~~	~~5,1~~	~~24,40~~	*
Zircon_019	111	85	0,77	0,0574	0,0049	0,2770	0,0260	0,0356	0,0013	0,0114	0,0009	0,19	225,7	8,0	247,0	20,0	480,0	180,0	225,7	8,0	8,62	*
Zircon_018	105	66	0,63	0,0536	0,0047	0,2610	0,0250	0,0356	0,0012	0,0117	0,0008	-0,03	226,2	7,6	234,0	21,0	280,0	180,0	226,2	7,6	3,33	*
Zircon_020	31	15	0,48	0,0580	0,0100	0,2910	0,0560	0,0359	0,0020	0,0122	0,0020	0,17	227,0	12,0	249,0	44,0	540,0	350,0	227,0	12,0	8,84	*
Zircon_064	97	55	0,57	0,0611	0,0057	0,2980	0,0290	0,0359	0,0012	0,0115	0,0009	-0,09	227,1	7,4	263,0	22,0	560,0	200,0	227,1	7,4	13,65	*
Zircon_014	155	149	0,96	0,0500	0,0037	0,2500	0,0210	0,0360	0,0010	0,0120	0,0008	-0,27	227,9	6,4	226,0	17,0	180,0	160,0	227,9	6,4	-0,84	*

Zircon_037	164	138	0,84	0,0559	0,0037	0,2830	0,0230	0,0360	0,0011	0,0112	0,0008	0,09	228,1	7,0	252,0	18,0	420,0	140,0	228,1	7,0	9,48 *
Zircon_065	292	189	0,65	0,0505	0,0024	0,2520	0,0170	0,0361	0,0010	0,0117	0,0008	0,05	228,6	6,2	229,0	13,0	230,0	110,0	228,6	6,2	0,17 *
~~Zircon_099~~	~~149~~	~~103~~	~~0,69~~	~~0,0469~~	~~0,0039~~	~~0,2360~~	~~0,0210~~	~~0,0361~~	~~0,0011~~	~~0,0119~~	~~0,0010~~	~~0,04~~	~~228,8~~	~~6,9~~	~~214,0~~	~~17,0~~	~~50,0~~	~~160,0~~	~~228,8~~	~~6,9~~	~~-6,92~~ *
Zircon_068	130	140	1,08	0,0529	0,0048	0,2690	0,0270	0,0362	0,0012	0,0121	0,0009	-0,12	229,1	7,2	240,0	21,0	300,0	200,0	229,1	7,2	4,54 *
Zircon_096	223	195	0,87	0,0598	0,0033	0,2950	0,0210	0,0365	0,0011	0,0130	0,0008	0,29	230,9	6,6	261,0	17,0	590,0	130,0	230,9	6,6	11,53	
Zircon_028	138	117	0,85	0,0525	0,0041	0,2620	0,0230	0,0367	0,0012	0,0106	0,0007	0,12	232,3	7,3	235,0	19,0	280,0	160,0	232,3	7,3	1,15	
Zircon_089	81	59	0,73	0,0643	0,0055	0,3160	0,0290	0,0368	0,0014	0,0125	0,0012	0,16	232,9	8,6	277,0	22,0	680,0	180,0	232,9	8,6	15,92	
Zircon_088	212	267	1,26	0,0652	0,0045	0,3320	0,0270	0,0370	0,0011	0,0130	0,0008	0,28	234,4	7,0	292,0	20,0	790,0	140,0	234,4	7,0	19,73	
~~Zircon_095~~	~~101~~	~~117~~	~~1,16~~	~~0,0700~~	~~0,0063~~	~~0,3600~~	~~0,0320~~	~~0,0370~~	~~0,0013~~	~~0,0134~~	~~0,0009~~	~~-0,09~~	~~234,4~~	~~8,3~~	~~310,0~~	~~24,0~~	~~910,0~~	~~190,0~~	~~234,4~~	~~8,3~~	~~24,39~~	
Zircon_003	130	138	1,06	0,0506	0,0047	0,2570	0,0250	0,0371	0,0014	0,0122	0,0009	-0,14	234,9	8,5	231,0	20,0	180,0	190,0	234,9	8,5	-1,69	
Zircon_075	150	241	1,61	0,0548	0,0039	0,2820	0,0230	0,0372	0,0011	0,0123	0,0008	0,12	235,2	6,6	251,0	19,0	400,0	150,0	235,2	6,6	6,29	
Zircon_059	153	126	0,82	0,0575	0,0042	0,2970	0,0240	0,0374	0,0011	0,0116	0,0007	-0,14	236,5	6,7	263,0	19,0	490,0	170,0	236,5	6,7	10,08	
Zircon_056	282	395	1,40	0,0526	0,0029	0,2730	0,0190	0,0375	0,0010	0,0111	0,0007	0,02	237,2	6,3	244,0	15,0	280,0	120,0	237,2	6,3	2,79	
~~Zircon_091~~	~~297~~	~~379~~	~~1,28~~	~~0,0720~~	~~0,0049~~	~~0,3720~~	~~0,0290~~	~~0,0376~~	~~0,0012~~	~~0,0155~~	~~0,0011~~	~~0,23~~	~~237,6~~	~~7,3~~	~~320,0~~	~~22,0~~	~~1000,0~~	~~140,0~~	~~237,6~~	~~7,3~~	~~25,75~~	
Zircon_032	247	115	0,47	0,0555	0,0035	0,2890	0,0240	0,0378	0,0010	0,0120	0,0010	0,02	239,0	11,0	257,0	19,0	390,0	150,0	239,0	11,0	7,00	
Zircon_040	55	44	0,80	0,0606	0,0081	0,3070	0,0400	0,0379	0,0018	0,0137	0,0013	-0,06	239,6	9,7	273,0	29,0	530,0	260,0	239,6	9,7	12,23	
Zircon_074	221	146	0,66	0,0544	0,0036	0,2850	0,0220	0,0380	0,0012	0,0126	0,0010	0,04	240,2	7,4	256,0	17,0	360,0	150,0	240,2	7,4	6,17	
Zircon_013	189	200	1,06	0,0525	0,0038	0,2780	0,0220	0,0381	0,0012	0,0119	0,0007	0,08	240,8	7,4	248,0	18,0	330,0	160,0	240,8	7,4	2,90	
Zircon_005	240	283	1,18	0,0525	0,0033	0,2810	0,0210	0,0382	0,0010	0,0116	0,0007	0,05	241,6	6,2	250,0	17,0	290,0	140,0	241,6	6,2	3,36	
Zircon_066	288	360	1,25	0,0571	0,0030	0,3010	0,0210	0,0383	0,0010	0,0121	0,0007	0,21	242,0	5,9	267,0	16,0	480,0	120,0	242,0	5,9	9,36	
Zircon_062	340	240	0,71	0,0526	0,0030	0,2760	0,0190	0,0382	0,0010	0,0123	0,0008	-0,15	242,2	6,7	247,0	15,0	300,0	120,0	242,2	6,7	1,94	
Zircon_067	392	451	1,15	0,0537	0,0029	0,2840	0,0200	0,0383	0,0011	0,0121	0,0007	-0,14	242,3	6,6	255,0	15,0	330,0	120,0	242,3	6,6	4,98	
Zircon_082	269	475	1,77	0,0546	0,0032	0,2900	0,0220	0,0383	0,0012	0,0123	0,0008	0,22	242,3	7,6	262,0	18,0	380,0	130,0	242,3	7,6	7,52	
Zircon_029	717	1433	2,00	0,0559	0,0029	0,2980	0,0190	0,0384	0,0010	0,0120	0,0007	-0,14	243,1	5,9	265,0	15,0	450,0	110,0	243,1	5,9	8,26	
Zircon_009	248	218	0,88	0,0518	0,0037	0,2730	0,0210	0,0385	0,0011	0,0118	0,0008	-0,27	243,5	6,9	244,0	17,0	240,0	150,0	243,5	6,9	0,20	
Zircon_076	353	203	0,58	0,0511	0,0025	0,2720	0,0200	0,0385	0,0010	0,0128	0,0008	0,50	244,2	6,8	246,0	16,0	240,0	110,0	244,2	6,8	0,73	
Zircon_036	264	442	1,67	0,0520	0,0030	0,2780	0,0200	0,0386	0,0010	0,0118	0,0007	0,13	244,4	6,5	249,0	16,0	270,0	130,0	244,4	6,5	1,85	
Zircon_054	177	119	0,67	0,0555	0,0042	0,2940	0,0240	0,0387	0,0010	0,0118	0,0008	-0,28	244,8	6,3	260,0	19,0	360,0	160,0	244,8	6,3	5,85	

211

Zircon_094	121	75	0,62	0,0551	0,0043	0,2970	0,0270	0,0387	0,0012	0,0129	0,0010	244,8	0,24	262,0	21,0	350,0	170,0	244,8	7,8	6,56
Zircon_045	671	1108	1,65	0,0519	0,0020	0,2770	0,0170	0,0388	0,0009	0,0118	0,0007	245,1	0,17	248,0	13,0	265,0	88,0	245,1	5,6	1,17
Zircon_079	705	270	0,38	0,0525	0,0023	0,2820	0,0170	0,0389	0,0010	0,0130	0,0008	246,0	0,13	252,0	14,0	286,0	99,0	246,0	6,1	2,38
Zircon_100	197	149	0,76	0,0565	0,0045	0,3030	0,0270	0,0390	0,0012	0,0128	0,0009	246,3	0,01	267,0	21,0	470,0	170,0	246,3	7,6	7,75
~~Zircon_084~~	157	242	1,54	0,0479	0,0037	0,2600	0,0220	0,0392	0,0011	0,0124	0,0008	247,8	-0,14	234,0	18,0	70,0	160,0	247,8	7,0	~~-5,90~~
Zircon_077	73	98	1,34	0,0578	0,0048	0,3130	0,0290	0,0393	0,0017	0,0133	0,0009	248,0	-0,17	275,0	22,0	500,0	190,0	248,0	10,0	9,82
Zircon_081	478	366	0,77	0,0525	0,0023	0,2870	0,0170	0,0395	0,0010	0,0127	0,0008	249,7	-0,03	256,0	14,0	290,0	100,0	249,7	6,2	2,46
Zircon_071	236	140	0,59	0,0567	0,0034	0,3120	0,0230	0,0395	0,0012	0,0129	0,0009	249,7	0,13	277,0	18,0	490,0	130,0	249,7	7,4	9,86
Zircon_050	190	212	1,12	0,0536	0,0042	0,2890	0,0250	0,0395	0,0010	0,0131	0,0008	249,9	-0,15	259,0	20,0	310,0	170,0	249,9	6,3	3,51
Zircon_092	332	236	0,71	0,0524	0,0024	0,2930	0,0190	0,0396	0,0011	0,0130	0,0008	250,3	0,08	261,0	15,0	302,0	97,0	250,3	6,6	4,10
Zircon_006	347	466	1,34	0,0538	0,0030	0,3010	0,0220	0,0398	0,0010	0,0119	0,0007	251,3	-0,04	266,0	17,0	370,0	130,0	251,3	6,3	5,53
Zircon_012	110	72	0,65	0,0620	0,0530	0,3300	0,6100	0,0398	0,0055	0,0140	0,0210	252,0	-0,04	290,0	210,0	600,0	500,0	252,0	33,0	13,10
Zircon_093	676	967	1,43	0,0628	0,0039	0,3510	0,0290	0,0399	0,0010	0,0140	0,0008	252,0	0,34	307,0	22,0	730,0	140,0	252,0	6,1	17,92
Zircon_069	235	178	0,76	0,0564	0,0029	0,3090	0,0200	0,0399	0,0010	0,0128	0,0008	252,4	-0,11	273,0	16,0	450,0	120,0	252,4	6,0	7,55
Zircon_072	282	128	0,45	0,0529	0,0032	0,2900	0,0200	0,0400	0,0011	0,0134	0,0009	252,9	-0,29	258,0	16,0	330,0	130,0	252,9	6,6	1,98
Zircon_027	409	477	1,17	0,0502	0,0019	0,2780	0,0170	0,0400	0,0010	0,0119	0,0007	253,0	0,21	249,0	13,0	207,0	89,0	253,0	6,0	-1,61
Zircon_017	178	130	0,73	0,0560	0,0034	0,3090	0,0230	0,0400	0,0011	0,0129	0,0009	253,0	0,02	273,0	18,0	440,0	120,0	253,0	6,7	7,33
Zircon_031	139	101	0,73	0,0542	0,0047	0,2920	0,0280	0,0402	0,0013	0,0122	0,0010	253,9	-0,02	262,0	22,0	300,0	180,0	253,9	7,8	3,09
Zircon_049	462	559	1,21	0,0543	0,0025	0,3010	0,0190	0,0402	0,0010	0,0126	0,0007	254,0	-0,13	267,0	15,0	360,0	100,0	254,0	5,9	4,87
Zircon_052	319	345	1,08	0,0521	0,0024	0,2930	0,0190	0,0404	0,0010	0,0122	0,0007	255,0	0,02	260,0	15,0	300,0	110,0	255,0	6,1	1,92
~~Zircon_044~~	84	95	1,13	0,0456	0,0049	0,2470	0,0260	0,0404	0,0014	0,0127	0,0009	255,5	0,07	233,0	22,0	10,0	200,0	255,5	8,6	~~-9,66~~
Zircon_011	520	360	0,69	0,0499	0,0019	0,2800	0,0170	0,0404	0,0010	0,0127	0,0007	255,5	0,17	250,0	13,0	193,0	91,0	255,5	6,3	-2,20
Zircon_030	277	218	0,79	0,0517	0,0025	0,2850	0,0190	0,0405	0,0011	0,0113	0,0007	256,0	0,03	254,0	15,0	250,0	110,0	256,0	6,6	-0,79
Zircon_048	172	183	1,06	0,0557	0,0040	0,3180	0,0260	0,0405	0,0012	0,0125	0,0008	256,1	0,07	279,0	20,0	430,0	150,0	256,1	7,2	8,21
Zircon_016	199	137	0,69	0,0588	0,0031	0,3330	0,0250	0,0405	0,0012	0,0129	0,0009	256,2	0,30	291,0	19,0	520,0	120,0	256,2	7,2	11,96
Zircon_053	190	109	0,57	0,0538	0,0033	0,3060	0,0240	0,0406	0,0012	0,0127	0,0009	256,5	0,08	270,0	19,0	360,0	140,0	256,5	7,2	5,00
Zircon_007	93	70	0,75	0,0510	0,0042	0,2740	0,0240	0,0407	0,0014	0,0117	0,0011	257,1	0,04	245,0	18,0	220,0	180,0	257,1	8,8	-4,94
Zircon_061	479	61	0,13	0,0508	0,0023	0,2810	0,0210	0,0407	0,0013	0,0134	0,0011	257,3	0,51	254,0	16,0	220,0	110,0	257,3	8,2	-1,30

Sample																					
Zircon_085	289	261	0,90	0,0612	0,0032	0,3390	0,0220	0,0407	0,0011	0,0142	0,0010	0,25	257,4	6,9	296,0	17,0	650,0	100,0	257,4	6,9	13,04
Zircon_002	94	116	1,23	0,0512	0,0045	0,2920	0,0280	0,0408	0,0013	0,0115	0,0008	0,21	257,8	8,0	258,0	22,0	240,0	190,0	257,8	8,0	0,08
Zircon_063	262	238	0,91	0,0527	0,0029	0,3000	0,0200	0,0409	0,0011	0,0135	0,0008	-0,03	258,2	6,7	268,0	16,0	280,0	120,0	258,2	6,7	3,66
Zircon_041	182	103	0,57	0,0541	0,0037	0,3080	0,0240	0,0409	0,0012	0,0133	0,0010	-0,23	258,4	7,4	274,0	20,0	400,0	160,0	258,4	7,4	5,69
Zircon_055	148	88	0,59	0,0528	0,0039	0,3010	0,0260	0,0411	0,0013	0,0137	0,0011	-0,02	259,4	7,9	266,0	20,0	290,0	160,0	259,4	7,9	2,48
Zircon_022	483	405	0,84	0,0520	0,0028	0,2950	0,0190	0,0412	0,0010	0,0125	0,0007	-0,15	260,1	6,5	262,0	15,0	290,0	120,0	260,1	6,5	0,73
Zircon_046	109	86	0,79	0,0535	0,0050	0,3050	0,0300	0,0413	0,0013	0,0130	0,0011	-0,24	260,8	8,2	271,0	23,0	300,0	200,0	260,8	8,2	3,76
Zircon_010	303	311	1,03	0,0523	0,0033	0,2870	0,0300	0,0413	0,0016	0,0128	0,0012	0,43	261,0	10,0	256,0	23,0	300,0	140,0	261,0	10,0	-1,95
~~Zircon_034~~	~~50~~	~~58~~	~~1,16~~	~~0,0476~~	~~0,0062~~	~~0,2680~~	~~0,0360~~	~~0,0414~~	~~0,0018~~	~~0,0128~~	~~0,0010~~	~~0,05~~	~~262,0~~	~~11,0~~	~~242,0~~	~~30,0~~	~~90,0~~	~~260,0~~	~~262,0~~	~~11,0~~	~~-8,26~~
Zircon_025	267	164	0,61	0,0529	0,0023	0,3040	0,0190	0,0416	0,0011	0,0125	0,0008	0,04	262,6	6,6	269,0	15,0	320,0	100,0	262,6	6,6	2,38
Zircon_021	159	177	1,11	0,0513	0,0033	0,2900	0,0210	0,0416	0,0011	0,0130	0,0008	-0,12	262,9	6,8	257,0	17,0	220,0	140,0	262,9	6,8	-2,30
Zircon_087	290	186	0,64	0,0567	0,0027	0,3300	0,0210	0,0417	0,0010	0,0139	0,0009	-0,08	263,3	6,5	291,0	16,0	470,0	110,0	263,3	6,5	9,52
Zircon_042	754	377	0,50	0,0537	0,0022	0,3100	0,0190	0,0417	0,0010	0,0129	0,0008	0,01	263,6	6,4	274,0	14,0	365,0	89,0	263,6	6,4	3,80
~~Zircon_035~~	~~170~~	~~204~~	~~1,20~~	~~0,0497~~	~~0,0041~~	~~0,2810~~	~~0,0260~~	~~0,0419~~	~~0,0013~~	~~0,0134~~	~~0,0008~~	~~0,23~~	~~264,4~~	~~8,3~~	~~250,0~~	~~21,0~~	~~140,0~~	~~170,0~~	~~264,4~~	~~8,3~~	~~-5,76~~
Zircon_086	348	262	0,75	0,0517	0,0028	0,3020	0,0210	0,0419	0,0011	0,0142	0,0009	0,06	264,7	6,7	268,0	16,0	280,0	120,0	264,7	6,7	1,23
Zircon_001	62	129	2,08	0,0624	0,0064	0,3600	0,0380	0,0420	0,0016	0,0130	0,0009	0,14	265,0	10,0	309,0	29,0	590,0	220,0	265,0	10,0	14,24
Zircon_070	207	162	0,78	0,0543	0,0031	0,3120	0,0230	0,0421	0,0012	0,0135	0,0009	0,32	265,6	7,7	279,0	18,0	370,0	120,0	265,6	7,7	4,80
Zircon_039	117	94	0,80	0,0617	0,0048	0,3730	0,0340	0,0436	0,0014	0,0149	0,0012	0,08	275,3	8,7	326,0	26,0	630,0	170,0	275,3	8,7	15,55
Zircon_015	229	173	0,76	0,0513	0,0031	0,3190	0,0230	0,0447	0,0013	0,0140	0,0009	0,05	282,0	7,7	280,0	18,0	220,0	130,0	282,0	7,7	-0,71
Zircon_060	88	42	0,48	0,0638	0,0076	0,3990	0,0490	0,0453	0,0015	0,0161	0,0015	-0,10	285,7	9,2	340,0	34,0	650,0	240,0	285,7	9,2	15,97
Zircon_083	258	152	0,59	0,0505	0,0029	0,3190	0,0230	0,0454	0,0012	0,0146	0,0010	0,06	286,4	7,3	280,0	18,0	200,0	130,0	286,4	7,3	-2,29
Zircon_004	160	102	0,64	0,0506	0,0039	0,3220	0,0270	0,0464	0,0013	0,0144	0,0010	-0,13	292,4	8,0	285,0	22,0	230,0	170,0	292,4	8,0	-2,60
Zircon_090	131	79	0,60	0,0564	0,0043	0,3730	0,0330	0,0470	0,0014	0,0147	0,0011	0,01	296,1	8,8	320,0	24,0	450,0	180,0	296,1	8,8	7,47
Zircon_051	241	160	0,66	0,0535	0,0027	0,3480	0,0240	0,0472	0,0013	0,0161	0,0010	0,21	297,3	7,8	302,0	18,0	340,0	120,0	297,3	7,8	1,56
~~Zircon_101~~	~~130~~	~~104~~	~~0,80~~	~~0,0910~~	~~0,0100~~	~~0,6100~~	~~0,1100~~	~~0,0480~~	~~0,0020~~	~~0,0199~~	~~0,0018~~	~~0,24~~	~~302,0~~	~~12,0~~	~~478,0~~	~~57,0~~	~~1110,0~~	~~160,0~~	~~302,0~~	~~12,0~~	~~36,92~~
Zircon_080	482	475	0,99	0,0540	0,0023	0,3690	0,0220	0,0498	0,0012	0,0151	0,0009	0,16	313,5	7,1	318,0	17,0	363,0	93,0	313,5	7,1	1,42
Zircon_026	88	37	0,42	0,0605	0,0048	0,4240	0,0380	0,0522	0,0016	0,0178	0,0014	0,20	328,0	9,5	356,0	27,0	540,0	170,0	328,0	9,5	7,87
Zircon_098	150	73	0,49	0,0561	0,0038	0,4160	0,0350	0,0538	0,0015	0,0171	0,0013	0,10	337,8	9,1	351,0	25,0	420,0	150,0	337,8	9,1	3,76

213

~~Zircon_078~~	~~3~~	~~8~~	~~2,67~~	~~0,6740~~	~~0,0880~~	~~8,8000~~	~~1,3000~~	~~0,1030~~	~~0,0712~~	~~0,0440~~	~~0,0071~~	~~0,36~~	~~629,0~~	~~78,0~~	~~2290,0~~	~~130,0~~	~~4770,0~~	~~230,0~~	~~4770,0~~	~~230,0~~	72,53
CPV-15-320 (IZ)							Crystallization age (Concordia age): 278,9 ± 2.4 Ma														
Zircon_35	176	66	0,38	0,0871	0,0051	0,4770	0,0270	0,0388	0,0012	0,01	0,0216	0,0014	245,4	7,2	395,0	19,0	1370,0	120,0	245,4	7,2	37,87
Zircon_38	178	135	0,76	0,0701	0,0045	0,3990	0,0270	0,0407	0,0009	0,09	0,0159	0,0010	257,4	5,8	340,0	19,0	950,0	120,0	257,4	5,8	24,29
Zircon_25	315	196	0,62	0,0787	0,0040	0,4490	0,0270	0,0411	0,0010	0,38	0,0180	0,0010	259,5	6,5	376,0	19,0	1157,0	99,0	259,5	6,5	30,98
Zircon_06	396	409	1,03	0,0527	0,0034	0,3120	0,0210	0,0430	0,0010	-0,25	0,0132	0,0008	271,5	6,2	276,0	16,0	310,0	130,0	271,5	6,2	1,63
Zircon_39	1076	618	0,57	0,0577	0,0024	0,3390	0,0150	0,0431	0,0009	0,54	0,0142	0,0007	272,1	5,4	296,0	11,0	508,0	94,0	272,1	5,4	8,07
Zircon_19	996	743	0,72	0,0723	0,0035	0,4360	0,0220	0,0433	0,0008	0,59	0,0152	0,0008	273,3	5,1	366,0	16,0	990,0	100,0	273,3	5,1	25,33
Zircon_16	334	253	0,76	0,0852	0,0049	0,5040	0,0340	0,0434	0,0010	0,42	0,0193	0,0010	273,6	6,0	444,0	22,0	1340,0	95,0	273,6	6,0	33,94
Zircon_34	260	313	1,20	0,0630	0,0034	0,3740	0,0210	0,0435	0,0010	-0,10	0,0144	0,0008	274,7	6,2	322,0	15,0	730,0	110,0	274,7	6,2	14,69
Zircon_36	172	95	0,55	0,0585	0,0040	0,3700	0,0230	0,0438	0,0010	-0,08	0,0163	0,0010	276,2	6,2	349,0	17,0	880,0	150,0	276,2	6,2	13,42
Zircon_10	435	329	0,76	0,0533	0,0032	0,3250	0,0210	0,0439	0,0010	-0,20	0,0132	0,0009	276,7	6,2	285,0	16,0	360,0	120,0	276,7	6,2	2,91
Zircon_23	239	258	1,08	0,0674	0,0049	0,4430	0,0350	0,0440	0,0015	0,01	0,0149	0,0011	277,3	9,2	350,0	24,0	870,0	140,0	277,3	9,2	20,77
Zircon_24	744	856	1,16	0,0598	0,0029	0,3630	0,0200	0,0441	0,0009	-0,03	0,0146	0,0008	278,1	5,4	344,0	15,0	599,0	98,0	278,1	5,4	11,43
Zircon_28	97	60	0,62	0,0652	0,0054	0,3840	0,0340	0,0441	0,0015	0,14	0,0150	0,0010	278,1	9,0	326,0	25,0	720,0	170,0	278,1	9,0	14,69
Zircon_17	506	415	0,82	0,0887	0,0050	0,5510	0,0340	0,0442	0,0011	0,55	0,0184	0,0012	278,5	6,6	443,0	23,0	1390,0	110,0	278,5	6,6	37,13
Zircon_05	387	282	0,73	0,0532	0,0024	0,3190	0,0160	0,0443	0,0009	0,28	0,0137	0,0007	279,2	5,7	282,0	12,0	320,0	100,0	279,2	5,7	0,99
Zircon_09	479	317	0,66	0,0703	0,0061	0,4290	0,0310	0,0443	0,0011	-0,31	0,0171	0,0011	279,3	7,1	362,0	21,0	940,0	140,0	279,3	7,1	22,95
Zircon_08	1483	1391	0,94	0,0525	0,0020	0,3190	0,0140	0,0443	0,0008	0,11	0,0135	0,0007	279,4	5,0	281,0	11,0	301,0	82,0	279,4	5,0	0,57
Zircon_29	522	407	0,78	0,0687	0,0037	0,4070	0,0250	0,0443	0,0011	0,30	0,0150	0,0011	279,5	6,8	349,0	18,0	870,0	110,0	279,5	6,8	19,94
Zircon_02	100	79	0,79	0,0532	0,0045	0,3220	0,0270	0,0444	0,0014	0,07	0,0140	0,0011	280,2	8,5	281,0	21,0	290,0	170,0	280,2	8,5	0,28
Zircon_04	336	240	0,71	0,0570	0,0031	0,3470	0,0180	0,0445	0,0011	-0,09	0,0142	0,0010	280,6	6,7	302,0	14,0	470,0	110,0	280,6	6,7	7,09
Zircon_33	517	471	0,91	0,0773	0,0040	0,4730	0,0280	0,0445	0,0009	-0,07	0,0178	0,0010	280,7	5,8	393,0	19,0	1119,0	91,0	280,7	5,8	28,58
Zircon_18	593	396	0,67	0,0699	0,0028	0,4240	0,0210	0,0446	0,0010	0,58	0,0175	0,0009	281,2	5,9	362,0	15,0	912,0	79,0	281,2	5,9	22,22
Zircon_26	500	351	0,70	0,0699	0,0032	0,4280	0,0220	0,0447	0,0009	0,42	0,0157	0,0010	281,6	5,6	361,0	15,0	923,0	99,0	281,6	5,6	21,99
Zircon_03	161	176	1,09	0,0613	0,0039	0,3750	0,0240	0,0447	0,0010	0,01	0,0149	0,0008	281,7	6,1	326,0	17,0	650,0	130,0	281,7	6,1	13,59
Zircon_22	441	240	0,54	0,0598	0,0029	0,3660	0,0180	0,0447	0,0009	-0,29	0,0163	0,0009	282,0	5,4	347,0	13,0	600,0	110,0	282,0	5,4	11,04

Sample																					
Zircon_20	278	184	0,66	0,0716	0,0039	0,4250	0,0230	0,0448	0,0013	0,07	0,0166	0,0011	282,3	7,7	359,0	17,0	950,0	110,0	282,3	7,7	21,26
Zircon_13	337	293	0,87	0,0615	0,0036	0,3840	0,0220	0,0449	0,0009	-0,04	0,0161	0,0008	282,9	5,8	329,0	16,0	640,0	120,0	282,9	5,8	14,01
Zircon_07	392	238	0,64	0,0577	0,0039	0,3470	0,0260	0,0449	0,0013	-0,16	0,0145	0,0011	283,1	8,1	302,0	19,0	480,0	110,0	283,1	8,1	6,29
Zircon_01	577	211	0,37	0,1007	0,0043	0,6300	0,0290	0,0453	0,0010	0,29	0,0308	0,0008	285,7	5,9	496,0	18,0	1626,0	77,0	285,7	5,9	42,40
Zircon_15	425	343	0,81	0,0704	0,0034	0,4440	0,0240	0,0454	0,0012	0,07	0,0164	0,0010	285,9	7,2	372,0	17,0	910,0	110,0	285,9	7,2	23,15
Zircon_3	182	183	1,01	0,0780	0,0066	0,4660	0,0480	0,0454	0,0013	0,39	0,0163	0,0013	286,0	7,9	386,0	32,0	1070,0	170,0	286,0	7,9	25,91
Zircon_11	707	793	1,12	0,0724	0,0037	0,4530	0,0260	0,0454	0,0013	-0,44	0,0167	0,0011	286,3	7,9	382,0	15,0	1020,0	100,0	286,3	7,9	25,05
Zircon_27	91	49	0,54	0,0788	0,0068	0,4930	0,0420	0,0457	0,0013	-0,07	0,0206	0,0015	288,0	8,2	405,0	27,0	1210,0	150,0	288,0	8,2	28,89
Zircon_12	82	68	0,83	0,0632	0,0046	0,4030	0,0320	0,0457	0,0014	0,47	0,0154	0,0011	288,1	8,7	344,0	23,0	640,0	100,0	288,1	8,7	15,51
Zircon_30	924	422	0,46	0,0533	0,0022	0,3350	0,0160	0,0459	0,0012	0,50	0,0150	0,0009	289,6	7,1	293,0	12,0	328,0	96,0	289,6	7,1	1,16
Zircon_32	410	229	0,56	0,0708	0,0032	0,4490	0,0200	0,0469	0,0010	-0,33	0,0186	0,0010	295,4	6,4	376,0	15,0	920,0	110,0	295,4	6,4	21,44
Zircon_21	257	151	0,59	0,0903	0,0054	0,5810	0,0350	0,0470	0,0011	0,42	0,0204	0,0014	296,3	6,8	464,0	22,0	1430,0	100,0	296,3	6,8	36,14
Zircon_14	106	92	0,87	0,1070	0,0130	0,7030	0,0860	0,0470	0,0013	0,27	0,0234	0,0016	296,3	7,9	538,0	51,0	1680,0	190,0	296,3	7,9	44,93
Zircon_37	206	153	0,74	0,1270	0,0420	0,8400	0,5500	0,0484	0,0043	0,04	0,0240	0,0045	307,0	26,0	620,0	150,0	2070,0	270,0	307,0	26,0	50,48

CPV-15-279 (IZ)

Crystallization age (TuffZirc age): 219,4 +3,4/-2,0 Ma

Sample																					
Zircon_105	336	285	0,85	0,0723	0,0044	0,3130	0,0210	0,0317	0,0008	0,19	0,0124	0,0007	201,3	5,0	275,0	16,0	1010,0	120,0	201,3	5,0	26,80
Zircon_121	303	245	0,81	0,0585	0,0029	0,2510	0,0130	0,0318	0,0008	0,28	0,0093	0,0006	201,5	5,3	227,0	11,0	550,0	120,0	201,5	5,3	11,23
Zircon_110	239	173	0,72	0,0700	0,0042	0,3170	0,0190	0,0320	0,0008	0,34	0,0125	0,0008	203,0	4,9	279,0	14,0	930,0	120,0	203,0	4,9	27,24
Zircon_115	244	175	0,72	0,0537	0,0036	0,2340	0,0160	0,0322	0,0008	0,36	0,0105	0,0007	204,0	4,9	213,0	13,0	310,0	150,0	204,0	4,9	4,23
Zircon_122	277	227	0,82	0,0663	0,0045	0,2910	0,0200	0,0324	0,0008	0,10	0,0103	0,0007	205,7	4,8	258,0	15,0	820,0	130,0	205,7	4,8	20,27
Zircon_107	373	315	0,84	0,0633	0,0036	0,2790	0,0160	0,0326	0,0008	0,01	0,0112	0,0007	206,8	5,1	249,0	13,0	700,0	130,0	206,8	5,1	16,95
Zircon_103	428	422	0,99	0,0584	0,0034	0,2630	0,0180	0,0331	0,0008	0,38	0,0109	0,0006	209,9	4,8	237,0	14,0	530,0	130,0	209,9	4,8	11,43
Zircon_98	357	285	0,80	0,0599	0,0030	0,2760	0,0150	0,0335	0,0007	0,20	0,0113	0,0006	212,1	4,5	250,0	12,0	590,0	120,0	212,1	4,5	15,16
Zircon_118	237	195	0,82	0,0595	0,0058	0,2740	0,0290	0,0335	0,0008	0,65	0,0091	0,0010	212,3	5,2	245,0	22,0	540,0	170,0	212,3	5,2	13,35
Zircon_95	210	93	0,44	0,0661	0,0048	0,3090	0,0230	0,0336	0,0009	-0,16	0,0133	0,0009	213,3	5,3	272,0	18,0	870,0	140,0	213,3	5,3	21,58
Zircon_102	319	220	0,69	0,0500	0,0031	0,2340	0,0150	0,0336	0,0008	0,13	0,0115	0,0008	213,7	4,9	213,0	12,0	170,0	130,0	213,7	4,9	-0,33
Zircon_119	457	517	1,13	0,0522	0,0047	0,2400	0,0240	0,0342	0,0007	0,18	0,0102	0,0007	216,8	4,4	220,0	19,0	290,0	170,0	216,8	4,4	1,45

Zircon_108	277	214	0,77	0,0586	0,0039	0,2770	0,0180	0,0342	0,0008	0,05	0,0114	0,0007	216,8	5,1	247,0	14,0	530,0	150,0	216,8	5,1	12,23
Zircon_87	289	154	0,53	0,0515	0,0032	0,2390	0,0150	0,0343	0,0008	0,36	0,0118	0,0007	217,1	5,1	217,0	13,0	260,0	130,0	217,1	5,1	-0,05
Zircon_88	160	92	0,58	0,0516	0,0042	0,2410	0,0190	0,0343	0,0009	0,16	0,0110	0,0007	217,4	5,3	222,0	16,0	220,0	150,0	217,4	5,3	2,07
Zircon_93	256	164	0,64	0,0541	0,0035	0,2560	0,0150	0,0344	0,0007	-0,03	0,0110	0,0006	217,8	4,6	234,0	12,0	370,0	130,0	217,8	4,6	6,92
Zircon_111	241	187	0,78	0,0516	0,0030	0,2440	0,0150	0,0344	0,0008	0,14	0,0105	0,0006	218,1	5,2	223,0	12,0	270,0	120,0	218,1	5,2	2,20
Zircon_114	242	184	0,76	0,0524	0,0034	0,2490	0,0170	0,0345	0,0009	0,13	0,0110	0,0007	218,5	5,6	225,0	13,0	260,0	140,0	218,5	5,6	2,89
Zircon_113	252	161	0,64	0,0574	0,0040	0,2750	0,0200	0,0345	0,0008	0,33	0,0121	0,0008	218,6	4,8	248,0	16,0	470,0	150,0	218,6	4,8	11,85
Zircon_109	165	90	0,55	0,0545	0,0046	0,2610	0,0210	0,0345	0,0009	-0,02	0,0121	0,0007	218,7	5,8	234,0	17,0	350,0	180,0	218,7	5,8	6,54
Zircon_106	265	153	0,58	0,0519	0,0032	0,2500	0,0160	0,0346	0,0008	-0,18	0,0108	0,0007	219,2	5,1	226,0	13,0	250,0	130,0	219,2	5,1	3,01
Zircon_100	317	347	1,09	0,0517	0,0029	0,2450	0,0140	0,0346	0,0007	-0,18	0,0113	0,0006	219,4	4,6	222,0	11,0	240,0	120,0	219,4	4,6	1,17
Zircon_89	342	264	0,77	0,0541	0,0028	0,2580	0,0140	0,0347	0,0007	0,30	0,0114	0,0007	219,7	4,5	233,0	11,0	350,0	110,0	219,7	4,5	5,71
Zircon_90	209	130	0,62	0,0514	0,0040	0,2470	0,0200	0,0348	0,0010	0,14	0,0113	0,0007	220,3	6,1	223,0	16,0	230,0	160,0	220,3	6,1	1,21
Zircon_120	137	79	0,58	0,0585	0,0046	0,2850	0,0200	0,0348	0,0010	-0,02	0,0132	0,0010	220,6	6,3	256,0	16,0	570,0	150,0	220,6	6,3	13,83
Zircon_94	408	362	0,89	0,0518	0,0029	0,2470	0,0150	0,0349	0,0007	0,32	0,0112	0,0007	221,4	4,6	224,0	12,0	280,0	120,0	221,4	4,6	1,16
Zircon_112	185	138	0,75	0,0549	0,0040	0,2650	0,0180	0,0351	0,0010	-0,20	0,0117	0,0007	222,5	5,9	243,0	14,0	380,0	160,0	222,5	5,9	8,44
Zircon_101	180	135	0,75	0,0510	0,0035	0,2510	0,0160	0,0352	0,0010	-0,16	0,0111	0,0007	222,7	6,1	226,0	13,0	250,0	150,0	222,7	6,1	1,46
Zircon_104	236	199	0,84	0,0518	0,0035	0,2520	0,0170	0,0352	0,0010	-0,03	0,0110	0,0006	222,8	5,9	228,0	14,0	280,0	150,0	222,8	5,9	2,28
Zircon_99	107	85	0,79	0,0943	0,0084	0,4590	0,0370	0,0352	0,0012	-0,12	0,0146	0,0010	222,8	7,7	381,0	25,0	1580,0	130,0	222,8	7,7	41,52
Zircon_92	337	249	0,74	0,0546	0,0030	0,2660	0,0150	0,0352	0,0008	0,26	0,0112	0,0007	223,0	4,9	239,0	12,0	390,0	120,0	223,0	4,9	6,69
Zircon_86	356	352	0,99	0,0499	0,0030	0,2470	0,0150	0,0352	0,0010	0,07	0,0113	0,0008	223,3	5,9	224,0	12,0	190,0	140,0	223,3	5,9	0,31
Zircon_96	151	74	0,49	0,0552	0,0040	0,2580	0,0190	0,0353	0,0009	0,02	0,0126	0,0008	223,7	5,6	236,0	16,0	380,0	150,0	223,7	5,6	5,21
Zircon_116	647	765	1,18	0,0542	0,0026	0,2640	0,0140	0,0353	0,0007	0,14	0,0111	0,0006	223,8	4,5	237,0	11,0	380,0	110,0	223,8	4,5	5,57
Zircon_91	234	172	0,74	0,0524	0,0033	0,2610	0,0170	0,0354	0,0008	0,13	0,0107	0,0006	223,9	5,3	235,0	14,0	270,0	140,0	223,9	5,3	4,72
Zircon_117	434	427	0,98	0,0511	0,0033	0,2510	0,0140	0,0358	0,0008	0,06	0,0116	0,0006	226,5	4,8	227,0	12,0	240,0	130,0	226,5	4,8	0,22
Zircon_97	79	77	0,97	0,1970	0,0130	0,9830	0,0750	0,0366	0,0014	0,56	0,0200	0,0018	233,7	8,4	698,0	35,0	2790,0	110,0	2790,0	110,0	66,84

Weighted mean age: 225.2 ±1.5 Ma (MSWD = 2.5)

CPV-15-310 (IZ)

Zircon_47	96,0	82,0	0,854	0,101	0,011	0,425	0,044	0,031	0,001	-0,053	0,010	0,001	197,9	6,2	360,0	31,0	1620,0	170,0	197,9	6,2	45,0

Zircon_67	473,0	322,0	0,681	0,054	0,003	0,250	0,013	0,034	0,001	-0,051	0,011	0,001	215,9	4,6	226,0	11,0	360,0	120,0	215,9	4,6	4,5	
Zircon_57	738,0	783,0	1,061	0,052	0,002	0,244	0,012	0,035	0,001	0,119	0,011	0,001	219,2	4,0	221,7	9,7	280,0	100,0	219,2	4,0	1,1	
~~Zircon_85~~	~~396,0~~	~~302,0~~	~~0,763~~	~~0,062~~	~~0,007~~	~~0,296~~	~~0,036~~	~~0,035~~	~~0,001~~	~~-0,177~~	~~0,012~~	~~0,001~~	~~219,5~~	~~5,6~~	~~263,0~~	~~26,0~~	~~680,0~~	~~170,0~~	~~219,5~~	~~5,6~~	~~16,5~~	**
Zircon_58	362,0	198,0	0,547	0,054	0,003	0,257	0,015	0,035	0,001	0,433	0,011	0,001	219,6	4,3	231,0	12,0	350,0	120,0	219,6	4,3	4,9	**
Zircon_44	740,0	748,0	1,011	0,055	0,003	0,263	0,013	0,035	0,001	0,070	0,011	0,001	219,6	4,4	237,0	10,0	400,0	110,0	219,6	4,4	7,3	**
Zircon_46	850,0	801,0	0,942	0,054	0,002	0,254	0,012	0,035	0,001	0,295	0,011	0,001	219,9	4,7	229,9	9,4	336,0	97,0	219,9	4,7	4,3	**
Zircon_59	270,0	181,0	0,670	0,057	0,004	0,279	0,020	0,035	0,001	0,081	0,010	0,001	220,5	5,9	248,0	15,0	490,0	150,0	220,5	5,9	11,1	**
Zircon_62	1019,0	1295,0	1,271	0,052	0,002	0,248	0,012	0,035	0,001	0,297	0,011	0,001	221,5	3,9	227,7	9,6	284,0	98,0	221,5	3,9	2,7	**
Zircon_41	526,0	371,0	0,705	0,051	0,003	0,249	0,015	0,035	0,001	0,128	0,011	0,001	222,0	4,5	225,0	12,0	240,0	120,0	222,0	4,5	1,3	**
Zircon_61	314,0	213,0	0,678	0,052	0,003	0,256	0,016	0,035	0,001	0,006	0,012	0,001	222,4	4,6	234,0	13,0	240,0	140,0	222,4	4,6	5,0	**
~~Zircon_50~~	~~508,0~~	~~374,0~~	~~0,736~~	~~0,064~~	~~0,008~~	~~0,309~~	~~0,046~~	~~0,035~~	~~0,002~~	~~0,092~~	~~0,011~~	~~0,001~~	~~222,5~~	~~6,1~~	~~273,0~~	~~32,0~~	~~780,0~~	~~170,0~~	~~222,5~~	~~6,1~~	~~18,5~~	**
Zircon_75	441,0	383,0	0,868	0,051	0,003	0,250	0,015	0,035	0,001	0,455	0,011	0,001	222,7	4,6	226,0	12,0	240,0	120,0	222,7	4,6	1,5	**
Zircon_73	1259,0	1469,0	1,167	0,052	0,002	0,251	0,011	0,035	0,001	0,169	0,011	0,001	223,5	4,2	227,1	9,0	261,0	91,0	223,5	4,2	1,6	**
Zircon_68	289,0	145,0	0,502	0,055	0,003	0,268	0,016	0,035	0,001	-0,020	0,012	0,001	224,6	5,2	240,0	13,0	390,0	130,0	224,6	5,2	6,4	**
Zircon_72	628,0	481,0	0,766	0,052	0,004	0,254	0,021	0,036	0,001	0,002	0,012	0,001	225,1	5,0	229,0	16,0	300,0	140,0	225,1	5,0	1,7	**
Zircon_65	412,0	310,0	0,752	0,054	0,003	0,259	0,014	0,036	0,001	0,129	0,012	0,001	225,1	4,0	234,0	11,0	380,0	110,0	225,1	4,0	3,8	**
Zircon_49	381,0	196,0	0,514	0,051	0,003	0,253	0,014	0,036	0,001	0,333	0,011	0,001	225,2	5,3	228,0	11,0	260,0	120,0	225,2	5,3	1,2	**
Zircon_64	356,0	206,0	0,579	0,053	0,003	0,255	0,015	0,036	0,001	0,088	0,012	0,001	225,2	4,7	232,0	13,0	290,0	130,0	225,2	4,7	2,9	**
Zircon_70	928,0	766,0	0,825	0,055	0,002	0,268	0,012	0,036	0,001	-0,061	0,011	0,001	225,6	4,6	241,2	9,9	385,0	95,0	225,6	4,6	6,5	**
Zircon_79	176,0	80,0	0,455	0,052	0,004	0,256	0,020	0,036	0,001	0,230	0,012	0,001	226,6	5,1	231,0	16,0	290,0	150,0	226,6	5,1	1,9	**
Zircon_74	628,0	557,0	0,887	0,053	0,003	0,260	0,013	0,036	0,001	0,241	0,011	0,001	226,6	4,5	234,0	11,0	300,0	110,0	226,6	4,5	3,2	**
Zircon_76	453,0	293,0	0,647	0,051	0,003	0,250	0,013	0,036	0,001	0,007	0,012	0,001	227,4	4,7	226,0	11,0	220,0	120,0	227,4	4,7	-0,6	**
~~Zircon_69~~	~~312,0~~	~~164,0~~	~~0,526~~	~~0,063~~	~~0,003~~	~~0,315~~	~~0,017~~	~~0,036~~	~~0,001~~	~~0,277~~	~~0,013~~	~~0,001~~	~~228,5~~	~~5,1~~	~~278,0~~	~~13,0~~	~~680,0~~	~~120,0~~	~~228,5~~	~~5,1~~	~~17,8~~	**
Zircon_83	570,0	423,0	0,742	0,055	0,003	0,275	0,013	0,036	0,001	-0,147	0,012	0,001	228,6	4,7	247,0	11,0	400,0	100,0	228,6	4,7	7,4	**
Zircon_54	1212,0	1121,0	0,925	0,054	0,003	0,267	0,014	0,036	0,001	0,253	0,011	0,001	228,8	4,7	240,0	11,0	360,0	100,0	228,8	4,7	4,7	**
Zircon_53	576,0	461,0	0,800	0,059	0,003	0,289	0,016	0,036	0,001	0,388	0,012	0,001	229,1	4,5	257,0	12,0	560,0	110,0	229,1	4,5	10,9	**
Zircon_56	383,0	253,0	0,661	0,055	0,003	0,274	0,015	0,036	0,001	-0,085	0,012	0,001	229,2	5,0	245,0	12,0	390,0	130,0	229,2	5,0	6,4	**
Zircon_66	312,0	182,0	0,583	0,055	0,003	0,264	0,015	0,036	0,001	0,321	0,011	0,001	229,5	5,6	238,0	12,0	390,0	110,0	229,5	5,6	3,6	**

Sample																						
Zircon_42	494,0	223,0	0,451	0,051	0,003	0,254	0,013	0,037	0,001	0,220	0,012	0,001	231,1	4,6	231,0	11,0	260,0	100,0	231,1	4,6	0,0	**
Zircon_77	331,0	218,0	0,659	0,055	0,004	0,276	0,018	0,037	0,001	-0,108	0,012	0,001	231,4	5,3	247,0	15,0	400,0	140,0	231,4	5,3	6,3	**
Zircon_52	236,0	98,0	0,415	0,056	0,004	0,288	0,018	0,037	0,001	0,105	0,013	0,001	231,7	5,6	257,0	14,0	480,0	130,0	231,7	5,6	9,8	**
Zircon_63	545,0	461,0	0,846	0,052	0,003	0,262	0,018	0,037	0,001	0,022	0,011	0,001	232,6	5,4	236,0	14,0	310,0	110,0	232,6	5,4	1,4	
Zircon_45	865,0	869,0	1,005	0,052	0,002	0,259	0,012	0,037	0,001	-0,074	0,012	0,001	232,8	4,2	233,4	9,5	270,0	98,0	232,8	4,2	0,3	
Zircon_40	147,0	77,0	0,524	0,070	0,009	0,360	0,048	0,037	0,001	0,243	0,016	0,002	233,1	6,7	309,0	34,0	870,0	220,0	233,1	6,7	24,6	
Zircon_81	1107,0	1197,0	1,081	0,051	0,002	0,261	0,012	0,037	0,001	0,059	0,012	0,001	234,3	4,2	236,6	9,4	234,0	98,0	234,3	4,2	1,0	
Zircon_60	508,0	436,0	0,858	0,054	0,003	0,277	0,012	0,037	0,001	-0,070	0,012	0,001	235,0	4,7	247,7	9,8	374,0	98,0	235,0	4,7	5,1	
Zircon_82	179,0	81,0	0,453	0,061	0,005	0,310	0,022	0,037	0,001	-0,074	0,014	0,001	235,7	5,7	273,0	16,0	580,0	170,0	235,7	5,7	13,7	
Zircon_78	305,0	160,0	0,525	0,086	0,007	0,453	0,038	0,038	0,001	0,262	0,020	0,002	238,6	5,3	381,0	25,0	1320,0	130,0	238,6	5,3	37,4	
Zircon_55	270,0	164,0	0,607	0,062	0,004	0,323	0,021	0,038	0,001	0,019	0,013	0,001	239,4	6,4	286,0	16,0	690,0	160,0	239,4	6,4	16,3	
Zircon_43	239,0	149,0	0,623	0,053	0,003	0,277	0,020	0,038	0,001	0,526	0,013	0,001	240,8	6,9	247,0	16,0	280,0	130,0	240,8	6,9	2,5	
Zircon_71	84,0	29,0	0,345	0,058	0,005	0,317	0,026	0,038	0,001	-0,193	0,013	0,001	241,6	8,1	277,0	20,0	570,0	180,0	241,6	8,1	12,8	
Zircon_48	492,0	352,0	0,715	0,110	0,006	0,581	0,031	0,038	0,001	0,244	0,020	0,001	241,8	5,9	464,0	20,0	1770,0	100,0	241,8	5,9	47,9	
Zircon_51	1185,0	1734,0	1,463	0,052	0,002	0,273	0,012	0,038	0,001	0,026	0,012	0,001	241,9	4,0	244,9	9,5	258,0	91,0	241,9	4,0	1,2	
Zircon_80	324,0	201,0	0,620	0,052	0,003	0,280	0,015	0,039	0,001	0,165	0,014	0,001	245,2	5,3	250,0	11,0	280,0	110,0	245,2	5,3	1,9	
Zircon_84	226,0	116,0	0,513	0,057	0,003	0,371	0,020	0,047	0,001	-0,215	0,016	0,001	296,3	6,1	322,0	15,0	510,0	120,0	296,3	6,1	8,0	

CPV-15-316 (DZ)

Maximum depositional age (3+DZ, 2σ): 241,4±4.0 Ma (MSWD = 0.34)

Sample																						
Zircon_024	190,0	149,0	0,784	0,052	0,004	0,280	0,022	0,038	0,001	0,012	0,001	0,134	240,3	6,1	252,0	17,0	320,0	180,0	240,3	6,1	4,6	*
Zircon_032	890,0	780,0	0,876	0,056	0,004	0,301	0,024	0,038	0,001	0,010	0,001	-0,126	241,0	7,1	267,0	17,0	460,0	130,0	241,0	7,1	9,7	*
Zircon_061	78,0	119,0	1,526	0,060	0,007	0,335	0,038	0,039	0,001	0,012	0,001	0,352	244,6	8,7	292,0	29,0	640,0	200,0	244,6	8,7	16,2	*
Zircon_089	187,0	122,0	0,652	0,053	0,004	0,282	0,022	0,040	0,001	0,010	0,001	0,348	251,5	5,9	254,0	17,0	300,0	160,0	251,5	5,9	1,0	
Zircon_076	355,0	393,0	1,107	0,055	0,004	0,295	0,020	0,040	0,001	0,012	0,001	0,076	252,1	4,8	261,0	16,0	390,0	140,0	252,1	4,8	3,4	
Zircon_078	190,0	36,0	0,189	0,053	0,004	0,294	0,027	0,040	0,001	0,014	0,001	0,380	254,9	7,2	260,0	21,0	340,0	180,0	254,9	7,2	2,0	
Zircon_079	187,0	198,0	1,059	0,053	0,004	0,286	0,020	0,040	0,001	0,013	0,001	0,229	255,5	6,1	255,0	16,0	280,0	150,0	255,5	6,1	-0,2	
Zircon_057	121,0	97,0	0,802	0,052	0,005	0,300	0,028	0,041	0,001	0,013	0,001	-0,171	260,8	7,3	272,0	20,0	350,0	200,0	260,8	7,3	4,1	
Zircon_102	799,0	495,0	0,620	0,053	0,003	0,300	0,015	0,041	0,001	0,013	0,001	0,122	261,4	3,6	266,0	12,0	330,0	110,0	261,4	3,6	1,7	

Zircon																					
Zircon_096	121,0	88,0	0,727	0,052	0,005	0,300	0,029	0,042	0,001	0,013	0,001	0,051	261,9	7,7	264,0	22,0	220,0	200,0	261,9	7,7	0,8
Zircon_085	1217,0	458,0	0,376	0,052	0,003	0,298	0,015	0,042	0,001	0,013	0,001	0,484	263,0	4,4	266,0	12,0	300,0	100,0	263,0	4,4	1,1
Zircon_109	247,0	131,0	0,530	0,051	0,003	0,292	0,018	0,042	0,001	0,013	0,001	0,014	263,1	5,1	259,0	14,0	240,0	130,0	263,1	5,1	-1,6
Zircon_026	233,0	209,0	0,897	0,053	0,004	0,314	0,022	0,042	0,001	0,013	0,001	0,002	264,5	4,8	277,0	17,0	340,0	150,0	264,5	4,8	4,5
Zircon_094	288,0	117,0	0,406	0,049	0,003	0,289	0,017	0,042	0,001	0,013	0,001	0,048	264,6	4,5	259,0	13,0	180,0	130,0	264,6	4,5	-2,2
Zircon_080	82,0	115,0	1,402	0,056	0,006	0,338	0,032	0,042	0,001	0,013	0,001	-0,169	266,5	8,3	296,0	23,0	490,0	210,0	266,5	8,3	10,0
Zircon_088	1267,0	868,0	0,685	0,053	0,002	0,305	0,014	0,042	0,001	0,013	0,001	0,036	267,1	3,8	270,0	11,0	300,0	100,0	267,1	3,8	1,1
Zircon_090	1172,0	772,0	0,659	0,052	0,002	0,299	0,014	0,042	0,001	0,012	0,001	0,045	267,8	3,6	266,0	11,0	260,0	100,0	267,8	3,6	-0,7
Zircon_095	517,0	359,0	0,694	0,054	0,003	0,310	0,015	0,042	0,001	0,012	0,001	0,034	268,2	4,3	274,0	12,0	360,0	110,0	268,2	4,3	2,1
Zircon_064	86,0	90,0	1,047	0,058	0,007	0,338	0,038	0,043	0,001	0,014	0,001	-0,473	268,2	7,4	293,0	29,0	420,0	240,0	268,2	7,4	8,5
Zircon_073	546,0	708,0	1,297	0,054	0,003	0,308	0,018	0,043	0,001	0,013	0,001	-0,198	268,9	4,2	272,0	14,0	320,0	130,0	268,9	4,2	1,1
Zircon_093	408,0	304,0	0,745	0,055	0,003	0,323	0,018	0,043	0,001	0,014	0,001	0,021	270,7	5,6	284,0	14,0	400,0	120,0	270,7	5,6	4,7
Zircon_112	125,0	102,0	0,816	0,055	0,006	0,319	0,033	0,043	0,001	0,015	0,001	0,112	272,1	7,6	282,0	25,0	350,0	200,0	272,1	7,6	3,5
Zircon_062	985,0	394,0	0,400	0,052	0,003	0,308	0,015	0,043	0,001	0,014	0,001	0,181	273,0	4,3	273,0	12,0	300,0	100,0	273,0	4,3	0,0
Zircon_019	176,0	212,0	1,205	0,059	0,039	0,360	0,340	0,043	0,003	0,014	0,003	0,073	273,0	19,0	310,0	150,0	460,0	430,0	273,0	19,0	11,9
Zircon_029	723,0	769,0	1,064	0,052	0,003	0,313	0,015	0,043	0,001	0,013	0,001	0,140	274,2	4,1	277,0	12,0	290,0	110,0	274,2	4,1	1,0
Zircon_117	160,0	102,0	0,638	0,060	0,005	0,351	0,029	0,044	0,001	0,015	0,001	-0,022	275,2	6,3	309,0	22,0	570,0	180,0	275,2	6,3	10,9
Zircon_013	925,0	92,0	0,099	0,051	0,002	0,310	0,015	0,044	0,001	0,015	0,001	0,170	275,3	4,1	275,0	11,0	240,0	110,0	275,3	4,1	-0,1
Zircon_009	159,0	120,0	0,755	0,054	0,004	0,321	0,023	0,044	0,001	0,013	0,001	-0,165	275,7	5,6	286,0	18,0	440,0	150,0	275,7	5,6	3,6
Zircon_067	55,0	37,0	0,673	0,060	0,005	0,368	0,034	0,044	0,001	0,013	0,001	0,056	277,0	8,4	316,0	23,0	580,0	170,0	277,0	8,4	12,3
Zircon_083	208,0	166,0	0,798	0,050	0,004	0,307	0,021	0,044	0,001	0,013	0,001	-0,027	278,2	6,2	271,0	16,0	200,0	150,0	278,2	6,2	-2,7
Zircon_069	204,0	166,0	0,814	0,051	0,004	0,309	0,022	0,044	0,001	0,014	0,001	0,096	278,6	7,2	272,0	17,0	220,0	150,0	278,6	7,2	-2,4
Zircon_091	228,0	131,0	0,575	0,053	0,003	0,318	0,020	0,044	0,001	0,013	0,001	0,245	279,6	6,8	281,0	15,0	340,0	140,0	279,6	6,8	0,5
Zircon_104	441,0	278,0	0,630	0,054	0,003	0,328	0,018	0,044	0,001	0,014	0,001	0,301	280,3	5,1	288,0	14,0	360,0	120,0	280,3	5,1	2,7
Zircon_041	155,0	119,0	0,768	0,053	0,005	0,319	0,029	0,045	0,001	0,014	0,001	-0,073	280,6	7,2	279,0	22,0	280,0	180,0	280,6	7,2	-0,6
Zircon_011	261,0	145,0	0,556	0,053	0,003	0,327	0,023	0,045	0,001	0,014	0,001	0,074	281,3	7,7	287,0	17,0	330,0	140,0	281,3	7,7	2,0
Zircon_105	217,0	186,0	0,857	0,055	0,003	0,332	0,021	0,045	0,001	0,014	0,001	0,286	282,0	6,5	290,0	16,0	370,0	130,0	282,0	6,5	2,8
Zircon_075	180,0	147,0	0,817	0,053	0,004	0,321	0,022	0,045	0,001	0,013	0,001	0,074	282,8	5,5	284,0	16,0	310,0	140,0	282,8	5,5	0,4

Zircon_003	170,0	88,0	0,518	0,052	0,004	0,319	0,029	0,045	0,001	0,014	0,001	0,336	283,2	280,0	21,0	300,0	170,0	283,2	6,0	6,0	-1,1
Zircon_047	166,0	157,0	0,946	0,050	0,004	0,312	0,022	0,045	0,001	0,014	0,001	0,021	283,7	275,0	17,0	260,0	160,0	283,7	7,5	7,5	-3,2
Zircon_058	246,0	268,0	1,089	0,051	0,004	0,306	0,021	0,045	0,001	0,014	0,001	0,046	283,8	271,0	17,0	210,0	160,0	283,8	4,8	4,8	-4,7
Zircon_034	238,0	185,0	0,777	0,050	0,004	0,315	0,022	0,045	0,001	0,014	0,001	0,073	283,9	277,0	17,0	200,0	150,0	283,9	6,4	6,4	-2,5
Zircon_108	543,0	299,0	0,551	0,053	0,003	0,322	0,018	0,045	0,001	0,014	0,001	0,464	284,5	285,0	14,0	290,0	120,0	284,5	4,5	4,5	0,2
Zircon_036	146,0	135,0	0,925	0,051	0,004	0,312	0,025	0,045	0,001	0,014	0,001	0,311	285,0	281,0	21,0	240,0	170,0	285,0	7,1	7,1	-1,4
Zircon_120	206,0	123,0	0,597	0,050	0,004	0,312	0,023	0,045	0,001	0,015	0,001	-0,185	285,8	274,0	18,0	210,0	160,0	285,8	6,1	6,1	-4,3
Zircon_027	230,0	136,0	0,591	0,052	0,004	0,331	0,023	0,045	0,001	0,015	0,001	-0,092	285,8	290,0	17,0	300,0	150,0	285,8	6,3	6,3	1,4
Zircon_099	391,0	487,0	1,246	0,052	0,003	0,323	0,021	0,045	0,002	0,013	0,002	0,301	285,9	284,0	15,0	250,0	120,0	285,9	9,3	9,3	-0,7
Zircon_014	260,0	196,0	0,754	0,054	0,004	0,341	0,026	0,046	0,001	0,015	0,001	0,119	286,8	296,0	20,0	340,0	150,0	286,8	4,9	4,9	3,1
Zircon_059	371,0	160,0	0,431	0,052	0,003	0,330	0,019	0,046	0,001	0,014	0,001	0,322	287,3	289,0	15,0	260,0	120,0	287,3	5,2	5,2	0,6
Zircon_038	225,0	138,0	0,613	0,054	0,004	0,341	0,023	0,046	0,001	0,015	0,001	-0,030	288,6	297,0	17,0	350,0	140,0	288,6	6,4	6,4	2,8
Zircon_031	445,0	336,0	0,755	0,055	0,003	0,345	0,018	0,046	0,001	0,015	0,001	-0,024	288,8	300,0	14,0	390,0	110,0	288,8	5,2	5,2	3,7
Zircon_018	222,0	132,0	0,595	0,053	0,004	0,331	0,025	0,046	0,001	0,015	0,001	0,082	289,7	289,0	19,0	290,0	160,0	289,7	6,0	6,0	-0,2
Zircon_023	315,0	451,0	1,432	0,054	0,003	0,339	0,020	0,046	0,001	0,014	0,001	0,085	289,7	296,0	15,0	340,0	130,0	289,7	5,2	5,2	2,1
Zircon_040	176,0	225,0	1,278	0,051	0,003	0,326	0,020	0,046	0,001	0,015	0,001	-0,086	290,3	285,0	16,0	250,0	140,0	290,3	5,4	5,4	-1,9
Zircon_119	123,0	104,0	0,846	0,055	0,004	0,343	0,026	0,046	0,001	0,014	0,001	0,359	290,7	298,0	19,0	340,0	150,0	290,7	8,1	8,1	2,4
Zircon_084	424,0	242,0	0,571	0,052	0,003	0,328	0,019	0,046	0,001	0,014	0,001	0,169	291,2	288,0	15,0	290,0	130,0	291,2	5,5	5,5	-1,1
Zircon_020	231,0	180,0	0,779	0,059	0,004	0,383	0,028	0,046	0,001	0,015	0,001	0,147	291,8	330,0	21,0	560,0	160,0	291,8	7,6	7,6	11,6
Zircon_043	285,0	186,0	0,653	0,055	0,004	0,350	0,023	0,046	0,001	0,014	0,001	-0,097	292,0	304,0	17,0	370,0	140,0	292,0	5,1	5,1	3,9
Zircon_005	242,0	148,0	0,612	0,054	0,003	0,342	0,020	0,046	0,001	0,015	0,001	-0,471	292,3	302,0	15,0	360,0	130,0	292,3	4,7	4,7	3,2
Zircon_111	175,0	173,0	0,989	0,054	0,004	0,346	0,024	0,047	0,001	0,013	0,001	0,142	292,7	300,0	18,0	380,0	150,0	292,7	6,7	6,7	2,4
Zircon_114	276,0	209,0	0,757	0,056	0,003	0,365	0,022	0,046	0,001	0,014	0,001	0,130	292,8	315,0	16,0	500,0	120,0	292,8	5,2	5,2	7,0
Zircon_030	845,0	396,0	0,469	0,054	0,005	0,390	0,140	0,046	0,007	0,016	0,002	-0,207	293,0	332,0	55,0	373,0	96,0	293,0	41,0	41,0	11,7
Zircon_021	433,0	372,0	0,859	0,052	0,003	0,342	0,017	0,047	0,001	0,015	0,001	0,164	293,1	298,0	13,0	310,0	120,0	293,1	5,0	5,0	1,6
Zircon_025	350,0	338,0	0,966	0,052	0,003	0,335	0,022	0,047	0,001	0,015	0,001	-0,072	294,1	293,0	17,0	240,0	140,0	294,1	5,5	5,5	-0,4
Zircon_092	535,0	300,0	0,561	0,053	0,003	0,339	0,017	0,047	0,001	0,014	0,001	-0,154	294,2	296,0	13,0	300,0	110,0	294,2	4,6	4,6	0,6
Zircon_100	138,0	1115,0	0,833	0,056	0,004	0,356	0,027	0,047	0,001	0,015	0,001	-0,289	294,2	308,0	20,0	390,0	170,0	294,2	6,5	6,5	4,5

Sample																					
Zircon_087	243,0	214,0	0,881	0,051	0,004	0,324	0,026	0,047	0,001	0,015	0,001	0,013	294,3	6,9	283,0	20,0	190,0	170,0	294,3	6,9	-4,0
Zircon_017	60,0	69,0	1,150	0,056	0,006	0,362	0,041	0,047	0,001	0,015	0,001	0,035	294,3	8,6	321,0	29,0	410,0	220,0	294,3	8,6	8,3
Zircon_086	201,0	135,0	0,672	0,052	0,004	0,323	0,023	0,047	0,001	0,015	0,001	0,056	295,3	4,7	288,0	17,0	230,0	150,0	295,3	4,7	-2,5
Zircon_054	168,0	138,0	0,821	0,058	0,004	0,370	0,027	0,047	0,001	0,016	0,001	0,077	295,3	6,8	318,0	20,0	460,0	160,0	295,3	6,8	7,1
Zircon_045	153,0	144,0	0,941	0,056	0,004	0,364	0,025	0,047	0,001	0,015	0,001	0,248	295,7	6,3	314,0	18,0	410,0	150,0	295,7	6,3	5,8
Zircon_037	450,0	411,0	0,913	0,053	0,003	0,346	0,019	0,047	0,001	0,015	0,001	0,028	296,1	4,8	301,0	14,0	310,0	130,0	296,1	4,8	1,6
Zircon_015	196,0	189,0	0,964	0,054	0,003	0,353	0,022	0,047	0,001	0,015	0,001	-0,068	296,5	6,3	309,0	17,0	370,0	140,0	296,5	6,3	4,0
Zircon_077	159,0	127,0	0,799	0,051	0,004	0,330	0,024	0,047	0,001	0,014	0,001	0,204	296,8	6,5	296,0	18,0	260,0	150,0	296,8	6,5	-0,3
Zircon_002	132,0	107,0	0,811	0,053	0,005	0,332	0,026	0,047	0,001	0,015	0,001	-0,139	297,3	7,3	295,0	20,0	260,0	180,0	297,3	7,3	-0,8
Zircon_110	389,0	218,0	0,560	0,057	0,003	0,364	0,019	0,047	0,001	0,015	0,001	-0,087	298,1	5,3	315,0	14,0	470,0	110,0	298,1	5,3	5,4
Zircon_098	675,0	375,0	0,556	0,054	0,003	0,347	0,018	0,048	0,001	0,014	0,001	-0,092	299,2	4,2	302,0	14,0	330,0	120,0	299,2	4,2	0,9
Zircon_115	153,0	134,0	0,876	0,053	0,004	0,341	0,026	0,048	0,001	0,015	0,001	-0,060	299,4	6,3	297,0	20,0	300,0	160,0	299,4	6,3	-0,8
Zircon_071	188,0	147,0	0,782	0,050	0,004	0,319	0,023	0,048	0,001	0,013	0,001	-0,005	299,9	6,9	284,0	18,0	150,0	160,0	299,9	6,9	-5,6
Zircon_046	223,0	137,0	0,614	0,054	0,004	0,353	0,023	0,048	0,001	0,015	0,001	0,171	300,0	6,1	306,0	18,0	360,0	150,0	300,0	6,1	2,0
Zircon_056	199,0	144,0	0,724	0,054	0,004	0,347	0,025	0,048	0,001	0,016	0,001	-0,081	300,1	8,5	307,0	18,0	370,0	160,0	300,1	8,5	2,2
Zircon_055	414,0	348,0	0,841	0,053	0,003	0,344	0,019	0,048	0,001	0,015	0,001	0,073	300,5	5,1	300,0	14,0	330,0	130,0	300,5	5,1	-0,2
Zircon_060	226,0	207,0	0,916	0,055	0,004	0,359	0,025	0,048	0,001	0,014	0,001	0,142	300,9	5,6	310,0	19,0	370,0	150,0	300,9	5,6	2,9
Zircon_044	51,0	52,0	1,020	0,053	0,022	0,350	0,190	0,048	0,003	0,015	0,002	0,036	302,0	14,0	308,0	96,0	280,0	450,0	302,0	14,0	1,9
Zircon_007	202,0	142,0	0,703	0,055	0,004	0,368	0,027	0,048	0,001	0,016	0,001	0,593	303,2	6,4	324,0	20,0	430,0	150,0	303,2	6,4	6,4
Zircon_068	268,0	231,0	0,862	0,087	0,004	0,574	0,031	0,048	0,001	0,046	0,001	0,205	304,2	5,7	460,0	21,0	1350,0	110,0	304,2	5,7	33,9
Zircon_048	122,0	81,0	0,664	0,051	0,005	0,345	0,032	0,048	0,001	0,018	0,002	-0,033	304,3	8,2	298,0	24,0	220,0	200,0	304,3	8,2	-2,1
Zircon_113	96,0	59,0	0,615	0,058	0,005	0,374	0,032	0,048	0,001	0,015	0,001	-0,149	304,5	7,5	331,0	24,0	460,0	200,0	304,5	7,5	8,0
Zircon_118	224,0	130,0	0,580	0,054	0,004	0,347	0,024	0,048	0,001	0,015	0,001	0,226	305,0	6,0	306,0	18,0	350,0	140,0	305,0	6,0	0,3
Zircon_074	115,0	116,0	1,009	0,063	0,016	0,420	0,120	0,049	0,003	0,013	0,002	-0,358	307,0	12,0	354,0	63,0	710,0	270,0	307,0	12,0	13,3
Zircon_072	69,0	51,0	0,739	0,059	0,007	0,389	0,048	0,049	0,001	0,017	0,002	0,289	307,1	9,2	338,0	32,0	550,0	210,0	307,1	9,2	9,1
Zircon_042	130,0	79,0	0,608	0,054	0,005	0,380	0,032	0,050	0,001	0,016	0,001	-0,254	315,0	7,5	325,0	23,0	370,0	190,0	315,0	7,5	3,1
Zircon_049	511,0	38,0	0,074	0,059	0,003	0,436	0,047	0,053	0,004	0,057	0,003	-0,110	334,0	27,0	367,0	31,0	630,0	120,0	334,0	27,0	9,0
Zircon_106	232,0	115,0	0,496	0,051	0,003	0,377	0,024	0,053	0,001	0,017	0,001	0,201	334,2	6,9	327,0	18,0	240,0	130,0	334,2	6,9	-2,2

Muestra	U (ppm)	Th (ppm)	Th/U	²⁰⁷Pb/²⁰⁶Pb	±	²⁰⁷Pb/²³⁵U	±	²⁰⁶Pb/²³⁸U	±	±	rho	²⁰⁶Pb/²³⁸U edad	±	²⁰⁷Pb/²³⁵U edad	±	²⁰⁷Pb/²⁰⁶Pb edad	±	Mejor edad	±	% disc
Zircon_070	72,0	43,0	0,597	0,058	0,006	0,403	0,036	0,054	0,002	0,015	0,001	-0,247	336,1	9,3	341,0	25,0	480,0	190,0	**336,1**	**9,3**	1,4
Zircon_028	250,0	75,0	0,300	0,054	0,003	0,403	0,025	0,054	0,001	0,022	0,001	-0,063	338,8	6,1	343,0	17,0	340,0	130,0	**338,8**	**6,1**	1,2
Zircon_066	178,0	55,0	0,309	0,058	0,003	0,589	0,035	0,074	0,001	0,024	0,001	-0,119	457,9	7,7	469,0	23,0	500,0	130,0	**457,9**	**7,7**	2,4
Zircon_101	265,0	70,0	0,264	0,053	0,003	0,548	0,031	0,075	0,001	0,022	0,001	0,031	463,9	7,9	447,0	21,0	320,0	120,0	**463,9**	**7,9**	-3,8
Zircon_012	277,0	244,0	0,881	0,058	0,003	0,583	0,034	0,075	0,001	0,024	0,001	0,207	468,1	7,9	465,0	22,0	490,0	120,0	**468,1**	**7,9**	-0,7
Zircon_004	832,0	469,0	0,564	0,057	0,003	0,596	0,028	0,076	0,001	0,024	0,001	0,239	469,1	6,7	474,0	18,0	500,0	100,0	**469,1**	**6,7**	1,0
Zircon_001	186,0	6,0	0,032	0,059	0,003	0,619	0,036	0,076	0,002	0,047	0,007	0,078	470,0	10,0	491,0	23,0	580,0	130,0	**470,0**	**10,0**	4,3
Zircon_008	307,0	153,0	0,498	0,056	0,003	0,601	0,032	0,076	0,001	0,022	0,001	0,085	474,5	7,7	477,0	20,0	450,0	120,0	**474,5**	**7,7**	0,5
Zircon_053	833,0	343,0	0,412	0,057	0,002	0,600	0,027	0,077	0,001	0,025	0,001	0,343	475,3	7,5	477,0	17,0	491,0	91,0	**475,3**	**7,5**	0,4
Zircon_116	134,0	175,0	1,306	0,056	0,003	0,594	0,039	0,077	0,002	0,024	0,001	0,047	476,7	9,5	471,0	25,0	420,0	140,0	**476,7**	**9,5**	-1,2
Zircon_010	179,0	88,0	0,492	0,055	0,003	0,601	0,038	0,078	0,002	0,024	0,002	0,243	482,0	11,0	477,0	24,0	400,0	120,0	**482,0**	**11,0**	-1,0
Zircon_051	324,0	98,0	0,302	0,063	0,003	0,673	0,034	0,078	0,001	0,030	0,002	-0,126	482,1	8,2	522,0	21,0	690,0	110,0	**482,1**	**8,2**	7,6
Zircon_097	95,0	53,0	0,558	0,056	0,005	0,613	0,051	0,078	0,002	0,024	0,002	-0,117	483,0	11,0	481,0	32,0	420,0	180,0	**483,0**	**11,0**	-0,4
Zircon_063	233,0	79,0	0,339	0,058	0,003	0,613	0,034	0,078	0,001	0,025	0,001	-0,001	483,4	8,2	484,0	21,0	550,0	120,0	**483,4**	**8,2**	0,1
Zircon_103	192,0	119,0	0,620	0,053	0,003	0,583	0,036	0,079	0,001	0,024	0,001	-0,069	490,5	8,0	469,0	24,0	320,0	140,0	**490,5**	**8,0**	-4,6
Zircon_035	112,0	58,0	0,518	0,059	0,004	0,723	0,051	0,088	0,002	0,027	0,002	0,024	546,0	11,0	557,0	30,0	550,0	150,0	**546,0**	**11,0**	2,0
Zircon_107	525,0	219,0	0,417	0,072	0,003	1,280	0,064	0,129	0,004	0,046	0,003	0,566	779,0	21,0	837,0	31,0	977,0	87,0	**779,0**	**21,0**	6,9
Zircon_052	214,0	36,0	0,168	0,069	0,003	1,308	0,064	0,139	0,003	0,035	0,003	0,465	836,0	14,0	848,0	26,0	888,0	92,0	**836,0**	**14,0**	1,4
Zircon_022	313,0	129,0	0,412	0,073	0,003	1,634	0,084	0,163	0,005	0,051	0,003	0,635	972,0	29,0	982,0	34,0	1007,0	88,0	**972,0**	**29,0**	1,0
Zircon_082	582,0	1067,0	1,833	0,073	0,003	1,638	0,074	0,166	0,003	0,049	0,002	0,180	989,0	14,0	984,0	29,0	1001,0	89,0	**989,0**	**14,0**	-0,5
Zircon_016	865,0	4,0	0,005	0,074	0,003	1,771	0,080	0,171	0,002	0,056	0,009	0,074	1018,0	13,0	1035,0	29,0	1032,0	85,0	**1018,0**	**13,0**	1,6
Zircon_006	51,0	28,0	0,549	0,074	0,004	1,860	0,074	0,186	0,005	0,053	0,003	0,178	1096,0	29,0	1063,0	43,0	1010,0	110,0	**1096,0**	**29,0**	-3,1
Zircon_033	372,0	99,0	0,266	0,078	0,003	2,050	0,100	0,191	0,005	0,056	0,003	0,216	1128,0	29,0	1132,0	35,0	1152,0	82,0	**1128,0**	**29,0**	0,4
Zircon_039	265,0	194,0	0,732	0,088	0,004	2,920	0,130	0,239	0,003	0,071	0,003	0,208	1384,0	18,0	1386,0	34,0	1372,0	81,0	**1384,0**	**18,0**	0,1
Zircon_081	210,0	118,0	0,562	0,102	0,004	3,850	0,170	0,273	0,004	0,083	0,004	0,056	1558,0	20,0	1602,0	36,0	1662,0	76,0	**1662,0**	**76,0**	2,7
Zircon_065	184,0	128,0	0,696	0,116	0,005	5,460	0,240	0,341	0,006	0,100	0,005	0,669	1893,0	28,0	1893,0	39,0	1886,0	73,0	**1886,0**	**73,0**	0,0
~~Zircon_050~~	~~65,0~~	~~180,0~~	~~2,008~~	~~0,203~~	~~0,015~~	~~1,470~~	~~0,110~~	~~0,052~~	~~0,002~~	~~0,017~~	~~0,001~~	~~0,146~~	~~325,6~~	~~9,0~~	~~909,0~~	~~45,0~~	~~2830,0~~	~~130,0~~	**~~2830,0~~**	**~~130,0~~**	~~64,2~~

222

CPV-15-324 (DZ)

Maximum depositional age (3+DZ, 2σ): 208.4±3.4 Ma (MSWD = 0.19)

CPV-15-324 (DZ)																					
Zircon_032	137,0	104,0	0,759	0,050	0,004	0,235	0,020	0,033	0,001	0,011	-0,054	0,001	6,4	207,2	213,0	16,0	220,0	180,0	207,2	6,4	2,7	*
Zircon_024	183,0	81,0	0,443	0,052	0,005	0,238	0,021	0,033	0,001	0,011	-0,138	0,001	6,3	207,8	218,0	17,0	250,0	180,0	207,8	6,3	4,7	*
Zircon_022	193,0	137,0	0,710	0,052	0,003	0,236	0,016	0,033	0,001	0,010	-0,073	0,001	5,4	209,6	216,0	14,0	260,0	130,0	209,6	5,4	3,0	*
Zircon_015	146,0	94,0	0,644	0,050	0,005	0,235	0,023	0,034	0,001	0,011	-0,263	0,001	5,6	215,9	213,0	19,0	150,0	190,0	215,9	5,6	-1,4	
Zircon_038	134,0	105,0	0,784	0,052	0,005	0,249	0,025	0,035	0,001	0,012	0,012	0,001	6,6	219,3	224,0	20,0	300,0	190,0	219,3	6,6	2,1	
Zircon_042	108,0	57,0	0,528	0,050	0,006	0,243	0,027	0,035	0,001	0,011	-0,245	0,001	7,2	223,0	219,0	22,0	190,0	250,0	223,0	7,2	-1,8	
Zircon_039	197,0	146,0	0,741	0,053	0,004	0,278	0,024	0,038	0,001	0,012	0,137	0,001	6,7	241,1	251,0	19,0	320,0	160,0	241,1	6,7	3,9	
Zircon_019	154,0	128,0	0,831	0,057	0,006	0,303	0,029	0,039	0,001	0,013	-0,130	0,001	8,3	247,8	266,0	23,0	410,0	210,0	247,8	8,3	6,8	
Zircon_034	100,0	88,0	0,880	0,051	0,005	0,288	0,029	0,040	0,001	0,012	0,029	0,001	7,6	251,4	255,0	22,0	240,0	200,0	251,4	7,6	1,4	
Zircon_023	136,0	175,0	1,287	0,053	0,005	0,295	0,027	0,040	0,001	0,012	-0,119	0,001	7,7	251,6	260,0	21,0	320,0	200,0	251,6	7,7	3,2	
Zircon_017	224,0	162,0	0,723	0,049	0,003	0,269	0,019	0,040	0,001	0,012	0,131	0,001	6,1	252,3	241,0	15,0	130,0	140,0	252,3	6,1	-4,7	
Zircon_049	52,0	47,0	0,904	0,049	0,006	0,277	0,035	0,040	0,002	0,013	0,053	0,002	9,1	255,3	248,0	27,0	140,0	230,0	255,3	9,1	-2,9	
Zircon_036	802,0	1195,0	1,490	0,053	0,003	0,294	0,017	0,040	0,001	0,012	-0,031	0,001	5,6	255,9	261,0	14,0	320,0	120,0	255,9	5,6	2,0	
Zircon_027	60,0	33,0	0,550	0,061	0,006	0,333	0,037	0,041	0,001	0,013	0,182	0,002	10,0	256,0	295,0	27,0	670,0	230,0	256,0	10,0	13,2	
Zircon_035	32,0	21,0	0,656	0,053	0,008	0,283	0,047	0,041	0,002	0,014	-0,081	0,002	12,0	258,0	252,0	36,0	170,0	320,0	258,0	12,0	-2,4	
Zircon_025	220,0	119,0	0,541	0,054	0,004	0,307	0,021	0,041	0,001	0,014	0,135	0,001	6,9	258,2	271,0	16,0	320,0	140,0	258,2	6,9	4,7	
Zircon_040	216,0	71,0	0,329	0,066	0,009	0,374	0,063	0,041	0,001	0,017	-0,214	0,001	7,7	259,2	332,0	40,0	870,0	230,0	259,2	7,7	21,9	
Zircon_033	50,0	35,0	0,700	0,056	0,008	0,319	0,045	0,041	0,002	0,014	-0,264	0,002	10,0	260,0	276,0	35,0	380,0	300,0	260,0	10,0	5,8	
Zircon_048	231,0	96,0	0,639	0,053	0,004	0,304	0,022	0,041	0,001	0,013	-0,021	0,001	6,8	261,7	269,0	17,0	360,0	140,0	261,7	6,8	2,7	
Zircon_047	72,0	46,0	0,639	0,053	0,005	0,294	0,025	0,042	0,002	0,012	-0,145	0,002	10,0	262,0	260,0	20,0	280,0	190,0	262,0	10,0	-0,8	
Zircon_045	253,0	315,0	1,245	0,051	0,003	0,290	0,020	0,042	0,001	0,013	0,201	0,001	6,2	262,2	262,0	14,0	210,0	140,0	262,2	6,2	-0,1	
Zircon_037	121,0	148,0	1,223	0,051	0,005	0,289	0,026	0,042	0,001	0,013	-0,150	0,001	7,8	262,5	256,0	20,0	210,0	200,0	262,5	7,8	-2,5	
Zircon_021	62,0	40,0	0,645	0,048	0,005	0,289	0,031	0,042	0,002	0,013	0,027	0,002	11,0	266,0	258,0	24,0	170,0	220,0	266,0	11,0	-3,1	
Zircon_044	301,0	31,0	0,103	0,050	0,003	0,298	0,018	0,043	0,001	0,015	0,235	0,001	6,3	270,2	264,0	14,0	190,0	120,0	270,2	6,3	-2,3	
Zircon_020	276,0	221,0	0,801	0,052	0,003	0,309	0,020	0,043	0,001	0,014	-0,034	0,001	7,3	271,7	274,0	15,0	330,0	130,0	271,7	7,3	0,8	
Zircon_043	167,0	135,0	0,808	0,052	0,004	0,309	0,021	0,043	0,001	0,013	-0,212	0,001	7,2	271,7	277,0	15,0	300,0	130,0	271,7	7,2	1,9	
Zircon_028	142,0	88,0	0,620	0,052	0,004	0,313	0,021	0,043	0,001	0,014	-0,337	0,001	7,6	272,3	278,0	17,0	300,0	160,0	272,3	7,6	2,1	

Sample																			
Zircon_018	274,0	233,0	0,850	0,053	0,004	0,315	0,022	0,043	0,001	-0,099	0,013	0,001	279,0	17,0	320,0	150,0	273,1	6,4	2,1
Zircon_030	252,0	227,0	0,901	0,055	0,004	0,326	0,023	0,043	0,001	-0,079	0,013	0,001	285,0	17,0	370,0	140,0	273,2	6,2	4,1
Zircon_046	217,0	145,0	0,668	0,054	0,004	0,323	0,025	0,044	0,001	-0,119	0,014	0,001	283,0	19,0	300,0	160,0	275,4	7,3	2,7
Zircon_041	124,0	80,0	0,645	0,052	0,004	0,322	0,029	0,044	0,001	0,297	0,013	0,001	281,0	22,0	260,0	170,0	278,0	8,5	1,1
Zircon_031	151,0	117,0	0,775	0,054	0,013	0,320	0,120	0,045	0,002	0,225	0,013	0,003	287,0	67,0	360,0	290,0	282,0	13,0	1,7
Zircon_026	168,0	128,0	0,762	0,052	0,004	0,323	0,025	0,045	0,001	0,038	0,014	0,001	283,0	19,0	250,0	160,0	283,3	6,9	-0,1
Zircon_016	125,0	100,0	0,800	0,050	0,004	0,314	0,025	0,046	0,001	-0,133	0,014	0,001	279,0	20,0	180,0	170,0	289,7	8,5	-3,8
~~Zircon_029~~	~~150,0~~	~~73,0~~	~~0,487~~	~~0,210~~	~~0,025~~	~~1,170~~	~~0,260~~	~~0,042~~	~~0,002~~	~~0,286~~	~~0,046~~	~~0,010~~	~~782,0~~	~~88,0~~	~~2880,0~~	~~150,0~~	~~265,0~~	~~15,0~~	~~66,1~~
CPV-15-342 (DZ)									Maximum depositional age (3+DZ, 2σ): 213.8±3.1 Ma (MSWD =1.17)										
~~AZircon_19~~	~~387,0~~	~~230,0~~	~~0,594~~	~~0,083~~	~~0,005~~	~~0,335~~	~~0,022~~	~~0,030~~	~~0,001~~	~~0,043~~	~~0,001~~	~~0,556~~	~~293,0~~	~~17,0~~	~~1280,0~~	~~110,0~~	~~188,4~~	~~6,8~~	~~35,7~~	*
AZircon_51	717,0	208,8	0,291	0,057	0,002	0,263	0,017	0,032	0,002	0,016	0,000	0,209	237,0	13,0	470,0	100,0	206,0	13,0	13,1	*
AZircon_27	400,0	323,0	0,808	0,060	0,003	0,273	0,014	0,033	0,001	0,011	0,001	0,307	245,0	11,0	610,0	100,0	211,1	5,6	13,8	*
AZircon_44	260,3	163,1	0,627	0,054	0,002	0,252	0,011	0,034	0,001	0,011	0,000	0,249	229,9	8,7	344,0	94,0	215,5	5,5	6,3	*
AZircon_11	1787,0	986,0	0,552	0,062	0,003	0,303	0,017	0,034	0,001	0,013	0,001	-0,232	269,0	13,0	660,0	110,0	216,3	5,7	19,6	*
AZircon_12	616,0	321,0	0,521	0,061	0,002	0,292	0,014	0,035	0,001	0,011	0,000	0,814	260,0	11,0	646,0	73,0	221,2	7,3	14,9	
BZircon_42	381,0	355,0	0,932	0,052	0,002	0,258	0,010	0,035	0,001	0,011	0,000	0,191	232,7	8,2	288,0	95,0	223,5	4,5	4,0	
AZircon_13	149,9	109,7	0,732	0,058	0,004	0,280	0,016	0,036	0,002	0,010	0,001	0,048	250,0	13,0	500,0	150,0	226,9	9,1	9,2	
~~AZircon_30~~	~~123,6~~	~~102,4~~	~~0,828~~	~~0,076~~	~~0,005~~	~~0,375~~	~~0,023~~	~~0,036~~	~~0,001~~	~~0,013~~	~~0,001~~	~~0,120~~	~~326,0~~	~~20,0~~	~~1100,0~~	~~130,0~~	~~227,1~~	~~7,5~~	~~30,3~~	
~~AZircon_17~~	~~177,8~~	~~68,0~~	~~0,382~~	~~0,072~~	~~0,004~~	~~0,353~~	~~0,018~~	~~0,036~~	~~0,001~~	~~0,013~~	~~0,001~~	~~0,011~~	~~306,0~~	~~13,0~~	~~970,0~~	~~110,0~~	~~229,8~~	~~6,3~~	~~24,9~~	
AZircon_33	63,5	35,6	0,560	0,052	0,004	0,261	0,019	0,037	0,001	0,012	0,001	0,097	237,0	15,0	240,0	160,0	233,9	8,2	1,3	
~~AZircon_48~~	~~145,4~~	~~114,1~~	~~0,785~~	~~0,065~~	~~0,003~~	~~0,338~~	~~0,018~~	~~0,037~~	~~0,001~~	~~0,012~~	~~0,001~~	~~0,293~~	~~295,0~~	~~14,0~~	~~777,0~~	~~99,0~~	~~234,8~~	~~7,7~~	~~20,4~~	
BZircon_30	156,0	155,0	0,994	0,053	0,004	0,267	0,018	0,037	0,001	0,012	0,001	0,019	244,0	13,0	270,0	150,0	235,3	6,6	3,6	
BZircon_09	223,0	336,0	1,507	0,054	0,003	0,270	0,015	0,037	0,001	0,012	0,001	0,382	242,0	12,0	380,0	120,0	236,7	6,5	2,2	
~~BZircon_47~~	~~38,0~~	~~31,0~~	~~0,816~~	~~0,063~~	~~0,007~~	~~0,341~~	~~0,037~~	~~0,038~~	~~0,002~~	~~0,013~~	~~0,001~~	~~-0,053~~	~~305,0~~	~~30,0~~	~~730,0~~	~~250,0~~	~~238,0~~	~~11,0~~	~~22,0~~	
BZircon_24	205,0	160,0	0,780	0,052	0,003	0,272	0,018	0,038	0,001	0,012	0,001	0,067	244,0	14,0	250,0	140,0	238,5	8,3	2,3	
AZircon_40	178,0	133,0	0,747	0,061	0,004	0,321	0,019	0,038	0,001	0,012	0,001	0,341	282,0	14,0	590,0	120,0	239,7	8,8	15,0	
AZircon_06	158,3	153,2	0,968	0,053	0,003	0,280	0,013	0,038	0,000	0,012	0,001	-0,048	250,0	10,0	350,0	110,0	240,9	7,3	3,6	

Sample																					
AZircon_31	253,0	117,3	0,464	0,059	0,003	0,314	0,012	0,039	0,001	0,012	0,001	0,567	244,4	8,9	276,9	9,8	535,0	92,0	244,4	8,9	11,7
AZircon_25	305,5	183,3	0,600	0,053	0,003	0,275	0,013	0,039	0,001	0,012	0,000	-0,161	244,5	6,2	248,0	11,0	280,0	110,0	244,5	6,2	1,4
AZircon_42	446,0	183,6	0,412	0,055	0,003	0,286	0,015	0,039	0,001	0,012	0,000	-0,160	245,7	7,1	255,0	12,0	400,0	110,0	245,7	7,1	3,6
AZircon_37	290,0	171,3	0,591	0,053	0,002	0,284	0,011	0,039	0,001	0,011	0,000	0,412	247,3	8,2	253,9	9,1	332,0	78,0	247,3	8,2	2,6
AZircon_38	277,0	206,7	0,746	0,056	0,002	0,301	0,013	0,040	0,001	0,012	0,000	-0,209	249,7	6,6	266,0	10,0	443,0	93,0	249,7	6,6	6,1
AZircon_55	272,0	265,0	0,974	0,054	0,002	0,290	0,014	0,040	0,001	0,013	0,000	0,284	250,6	6,7	259,0	11,0	330,0	100,0	250,6	6,7	3,2
AZircon_28	194,4	137,2	0,706	0,054	0,003	0,297	0,019	0,041	0,001	0,012	0,001	-0,792	256,7	8,2	264,0	14,0	350,0	130,0	256,7	8,2	2,8
AZircon_41	213,2	122,8	0,576	0,054	0,003	0,310	0,014	0,042	0,001	0,013	0,000	-0,137	264,1	6,9	274,0	11,0	370,0	100,0	264,1	6,9	3,6
BZircon_05	393,0	348,0	0,885	0,065	0,004	0,370	0,024	0,042	0,001	0,015	0,001	0,222	264,3	7,6	321,0	17,0	820,0	110,0	264,3	7,6	17,7
AZircon_05	126,7	81,0	0,639	0,065	0,008	0,385	0,035	0,043	0,002	0,015	0,001	-0,317	270,0	14,0	330,0	26,0	830,0	330,0	270,0	14,0	18,2
AZircon_21	380,0	308,0	0,811	0,054	0,004	0,313	0,016	0,043	0,002	0,013	0,000	-0,052	271,4	9,5	276,0	13,0	360,0	170,0	271,4	9,5	1,7
AZircon_57	145,0	97,3	0,671	0,052	0,003	0,312	0,019	0,043	0,001	0,014	0,000	0,535	273,1	8,0	275,0	14,0	270,0	120,0	273,1	8,0	0,7
AZircon_56	351,0	187,2	0,533	0,053	0,002	0,318	0,011	0,044	0,001	0,014	0,000	0,055	274,6	6,6	280,3	8,3	330,0	85,0	274,6	6,6	2,0
AZircon_16	257,0	138,7	0,540	0,052	0,002	0,310	0,012	0,044	0,001	0,014	0,000	-0,031	275,3	6,9	273,7	9,4	271,0	92,0	275,3	6,9	-0,6
AZircon_10	460,0	490,0	1,065	0,053	0,002	0,319	0,014	0,044	0,001	0,013	0,000	0,050	276,0	7,2	281,0	11,0	290,0	100,0	276,0	7,2	1,8
AZircon_36	146,3	134,4	0,919	0,053	0,003	0,321	0,015	0,044	0,001	0,014	0,001	-0,039	276,5	7,5	282,0	12,0	320,0	110,0	276,5	7,5	2,0
AZircon_14	92,5	58,6	0,634	0,055	0,005	0,333	0,026	0,044	0,002	0,013	0,001	-0,201	276,5	9,6	291,0	20,0	410,0	190,0	276,5	9,6	5,0
BZircon_57	175,0	153,0	0,874	0,051	0,003	0,311	0,017	0,044	0,001	0,014	0,001	0,096	276,7	7,4	274,0	13,0	240,0	120,0	276,7	7,4	-1,0
AZircon_59	289,7	267,8	0,924	0,053	0,002	0,318	0,011	0,044	0,001	0,014	0,000	0,204	277,3	6,8	280,4	8,8	321,0	79,0	277,3	6,8	1,1
BZircon_55	171,0	112,0	0,655	0,052	0,003	0,314	0,021	0,044	0,001	0,014	0,001	0,121	277,4	6,1	276,0	16,0	280,0	140,0	277,4	6,1	-0,5
BZircon_39	209,0	108,0	0,517	0,051	0,003	0,317	0,018	0,044	0,001	0,014	0,001	0,136	277,4	6,6	278,0	14,0	250,0	110,0	277,4	6,6	0,2
BZircon_45	211,0	185,0	0,877	0,054	0,004	0,332	0,022	0,044	0,001	0,014	0,001	-0,106	278,9	6,9	289,0	16,0	350,0	140,0	278,9	6,9	3,5
BZircon_36	356,0	161,0	0,452	0,054	0,004	0,328	0,030	0,044	0,002	0,015	0,001	0,546	279,0	10,0	287,0	22,0	360,0	130,0	279,0	10,0	2,8
BZircon_34	205,0	113,0	0,551	0,053	0,003	0,327	0,020	0,044	0,001	0,014	0,001	-0,147	279,3	7,5	291,0	15,0	320,0	140,0	279,3	7,5	4,0
BZircon_40	213,0	227,0	1,066	0,055	0,004	0,342	0,022	0,045	0,001	0,014	0,001	-0,186	282,4	7,1	298,0	17,0	400,0	140,0	282,4	7,1	5,2
AZircon_61	128,6	109,3	0,850	0,053	0,003	0,321	0,019	0,045	0,001	0,015	0,001	0,178	282,8	7,4	281,0	15,0	350,0	140,0	282,8	7,4	-0,6
BZircon_29	138,0	108,0	0,783	0,055	0,004	0,332	0,021	0,045	0,001	0,014	0,001	-0,099	283,0	6,6	290,0	16,0	340,0	150,0	283,0	6,6	2,4
AZircon_07	124,6	93,3	0,749	0,057	0,006	0,363	0,032	0,045	0,002	0,015	0,001	-0,050	283,0	11,0	313,0	24,0	520,0	190,0	283,0	11,0	9,6

AZircon_53	165,8	124,9	0,753	0,056	0,003	0,359	0,018	0,045	0,001	0,015	0,001	0,119	283,2	7,6	310,0	13,0	450,0	100,0	283,2	7,6	8,6
BZircon_33	287,0	187,0	0,652	0,056	0,003	0,344	0,015	0,045	0,001	0,014	0,001	0,020	283,4	6,7	302,0	11,0	440,0	110,0	283,4	6,7	6,2
AZircon_08	255,8	129,1	0,505	0,054	0,003	0,334	0,019	0,045	0,001	0,015	0,001	-0,047	283,8	7,3	292,0	15,0	330,0	130,0	283,8	7,3	2,8
BZircon_17	161,0	145,0	0,901	0,053	0,003	0,330	0,018	0,045	0,001	0,014	0,001	-0,002	284,6	6,7	288,0	14,0	270,0	140,0	284,6	6,7	1,2
AZircon_60	93,5	61,0	0,652	0,053	0,003	0,322	0,017	0,045	0,001	0,014	0,001	0,036	285,6	7,9	283,0	13,0	310,0	120,0	285,6	7,9	-0,9
BZircon_51	270,0	231,0	0,856	0,052	0,003	0,323	0,015	0,045	0,001	0,014	0,001	-0,017	285,7	6,2	283,0	11,0	260,0	110,0	285,7	6,2	-1,0
AZircon_18	186,4	134,5	0,722	0,053	0,002	0,326	0,012	0,045	0,000	0,015	0,001	-0,020	285,7	7,9	287,4	9,6	327,0	95,0	285,7	7,9	0,6
AZircon_09	284,0	345,0	1,215	0,053	0,003	0,335	0,019	0,045	0,001	0,014	0,001	-0,162	285,7	8,8	293,0	15,0	310,0	150,0	285,7	8,8	2,5
BZircon_54	240,0	183,0	0,763	0,056	0,003	0,352	0,020	0,045	0,001	0,014	0,001	0,149	285,9	7,1	305,0	15,0	410,0	120,0	285,9	7,1	6,3
BZircon_38	346,0	206,0	0,595	0,051	0,002	0,323	0,013	0,045	0,001	0,015	0,001	0,043	286,1	6,1	284,8	9,8	220,0	96,0	286,1	6,1	-0,5
BZircon_16	76,0	63,0	0,829	0,059	0,005	0,362	0,030	0,045	0,002	0,015	0,002	-0,459	286,2	9,2	312,0	22,0	590,0	180,0	286,2	9,2	8,3
AZircon_45	143,9	112,0	0,778	0,056	0,002	0,361	0,015	0,046	0,001	0,016	0,001	0,040	287,2	7,5	312,0	12,0	454,0	97,0	287,2	7,5	7,9
BZircon_12	250,0	247,0	0,988	0,057	0,003	0,355	0,020	0,046	0,001	0,014	0,001	0,002	287,6	6,0	308,0	15,0	440,0	130,0	287,6	6,0	6,6
AZircon_15	161,9	106,4	0,657	0,055	0,004	0,336	0,024	0,046	0,001	0,015	0,001	0,496	288,3	8,5	294,0	18,0	390,0	150,0	288,3	8,5	1,9
BZircon_25	346,0	338,0	0,977	0,064	0,003	0,406	0,020	0,046	0,001	0,015	0,001	-0,172	288,5	6,4	346,0	14,0	762,0	98,0	288,5	6,4	16,6
AZircon_50	196,9	106,4	0,540	0,053	0,002	0,339	0,014	0,046	0,001	0,015	0,001	0,031	288,6	7,1	296,0	11,0	306,0	90,0	288,6	7,1	2,5
BZircon_35	221,0	143,0	0,647	0,050	0,003	0,316	0,020	0,046	0,001	0,014	0,001	-0,016	288,8	7,9	278,0	15,0	170,0	140,0	288,8	7,9	-3,9
BZircon_21	412,0	445,0	1,080	0,057	0,003	0,349	0,015	0,046	0,001	0,014	0,001	0,147	289,1	6,9	303,0	12,0	480,0	110,0	289,1	6,9	4,6
AZircon_04	198,4	119,1	0,600	0,053	0,003	0,339	0,019	0,046	0,001	0,015	0,001	-0,173	289,2	8,4	296,0	14,0	290,0	130,0	289,2	8,4	2,3
BZircon_32	220,0	137,0	0,623	0,051	0,003	0,327	0,018	0,046	0,001	0,014	0,001	-0,056	289,4	6,6	289,0	13,0	220,0	130,0	289,4	6,6	-0,1
BZircon_20	377,0	297,0	0,788	0,053	0,002	0,339	0,013	0,046	0,001	0,015	0,001	0,246	289,7	5,9	298,1	9,8	318,0	89,0	289,7	5,9	2,8
BZircon_37	176,0	144,0	0,818	0,065	0,003	0,419	0,021	0,046	0,001	0,017	0,001	-0,194	289,7	7,2	354,0	15,0	760,0	110,0	289,7	7,2	18,2
BZircon_27	200,0	139,0	0,695	0,053	0,003	0,341	0,016	0,046	0,001	0,014	0,001	-0,148	289,8	6,9	299,0	12,0	360,0	110,0	289,8	6,9	3,1
AZircon_39	72,4	38,4	0,530	0,062	0,004	0,381	0,020	0,046	0,002	0,016	0,001	0,222	289,9	8,9	327,0	14,0	660,0	120,0	289,9	8,9	11,3
AZircon_34	143,5	95,7	0,667	0,057	0,004	0,366	0,023	0,046	0,001	0,015	0,001	0,095	290,1	8,8	316,0	17,0	470,0	140,0	290,1	8,8	8,2
BZircon_56	209,0	154,0	0,737	0,054	0,003	0,344	0,019	0,046	0,001	0,015	0,001	0,164	290,4	7,8	299,0	14,0	350,0	120,0	290,4	7,8	2,9
AZircon_24	84,3	69,8	0,828	0,054	0,003	0,336	0,020	0,046	0,001	0,015	0,001	-0,044	290,8	8,1	293,0	15,0	400,0	140,0	290,8	8,1	0,8
AZircon_02	164,5	108,5	0,660	0,057	0,006	0,361	0,036	0,046	0,002	0,016	0,002	0,258	291,0	11,0	312,0	27,0	460,0	240,0	291,0	11,0	6,7

Sample																					
AZircon_03	85,5	49,9	0,584	0,064	0,005	0,412	0,027	0,046	0,002	0,017	0,001	-0,084	291,0	10,0	349,0	19,0	720,0	160,0	291,0	10,0	16,6
AZircon_54	218,2	137,7	0,631	0,052	0,002	0,337	0,014	0,046	0,001	0,015	0,000	-0,024	291,1	7,4	295,0	10,0	288,0	96,0	291,1	7,4	1,3
BZircon_52	89,0	57,0	0,640	0,055	0,005	0,345	0,029	0,046	0,001	0,016	0,001	0,066	291,2	8,7	306,0	20,0	390,0	190,0	291,2	8,7	4,8
BZircon_44	230,0	208,0	0,904	0,054	0,003	0,345	0,019	0,046	0,001	0,015	0,001	0,074	291,7	6,6	300,0	14,0	310,0	120,0	291,7	6,6	2,8
BZircon_14	166,0	104,0	0,627	0,055	0,003	0,345	0,022	0,046	0,001	0,015	0,001	-0,053	291,9	8,1	300,0	17,0	360,0	140,0	291,9	8,1	2,7
AZircon_01	72,6	43,9	0,605	0,056	0,005	0,371	0,028	0,046	0,002	0,016	0,001	-0,009	292,0	10,0	319,0	21,0	500,0	200,0	292,0	10,0	8,5
AZircon_35	236,4	187,7	0,794	0,053	0,003	0,337	0,019	0,046	0,001	0,015	0,001	0,280	292,1	7,3	294,0	14,0	280,0	110,0	292,1	7,3	0,6
AZircon_22	310,2	298,0	0,961	0,054	0,002	0,337	0,011	0,046	0,001	0,015	0,000	0,106	292,1	7,4	294,9	8,5	384,0	74,0	292,1	7,4	0,9
AZircon_58	185,0	134,0	0,724	0,053	0,002	0,340	0,016	0,046	0,001	0,015	0,001	0,038	292,2	7,5	297,0	12,0	330,0	100,0	292,2	7,5	1,6
BZircon_08	156,0	231,0	1,481	0,056	0,004	0,343	0,021	0,046	0,001	0,015	0,001	-0,046	292,4	6,5	302,0	16,0	410,0	130,0	292,4	6,5	3,2
AZircon_29	191,9	141,9	0,739	0,052	0,002	0,331	0,013	0,046	0,001	0,014	0,000	-0,156	292,7	7,2	290,3	9,6	296,0	93,0	292,7	7,2	-0,8
BZircon_28	100,0	52,0	0,520	0,068	0,005	0,436	0,033	0,047	0,001	0,019	0,001	0,093	292,9	8,7	365,0	23,0	890,0	180,0	292,9	8,7	19,8
BZircon_43	245,0	322,0	1,314	0,061	0,003	0,392	0,021	0,047	0,001	0,015	0,001	0,114	293,4	6,8	335,0	15,0	620,0	110,0	293,4	6,8	12,4
AZircon_52	132,4	80,2	0,606	0,053	0,003	0,360	0,019	0,047	0,001	0,015	0,001	-0,036	293,8	7,8	311,0	14,0	340,0	120,0	293,8	7,8	5,5
BZircon_02	171,0	138,0	0,807	0,053	0,003	0,333	0,018	0,047	0,001	0,015	0,001	0,190	294,0	8,1	291,0	14,0	340,0	120,0	294,0	8,1	-1,0
BZircon_46	133,0	80,0	0,602	0,058	0,004	0,378	0,023	0,047	0,001	0,016	0,001	0,075	294,0	6,8	324,0	17,0	470,0	140,0	294,0	6,8	9,3
AZircon_49	216,6	170,1	0,785	0,052	0,002	0,340	0,013	0,047	0,001	0,015	0,000	0,232	294,1	7,4	296,6	9,4	305,0	78,0	294,1	7,4	0,8
~~BZircon_07~~	~~222,0~~	~~204,0~~	~~0,919~~	~~0,071~~	~~0,004~~	~~0,437~~	~~0,023~~	~~0,047~~	~~0,001~~	~~0,017~~	~~0,001~~	~~0,045~~	~~294,1~~	~~7,6~~	~~368,0~~	~~17,0~~	~~940,0~~	~~110,0~~	~~294,1~~	~~7,6~~	~~20,1~~
BZircon_11	581,0	385,0	0,663	0,052	0,002	0,339	0,011	0,047	0,001	0,015	0,001	-0,052	294,5	5,8	295,9	8,5	297,0	85,0	294,5	5,8	0,5
AZircon_23	809,0	330,0	0,408	0,053	0,002	0,337	0,010	0,047	0,001	0,014	0,000	0,280	294,9	7,2	295,3	7,1	346,0	59,0	294,9	7,2	0,1
BZircon_22	254,0	174,0	0,685	0,053	0,003	0,342	0,015	0,047	0,001	0,015	0,001	0,198	294,9	6,8	298,0	12,0	300,0	110,0	294,9	6,8	1,0
BZircon_59	288,0	203,0	0,705	0,051	0,003	0,332	0,015	0,047	0,001	0,015	0,001	-0,006	295,5	6,6	290,0	11,0	230,0	110,0	295,5	6,6	-1,9
BZircon_01	150,0	94,0	0,627	0,053	0,004	0,341	0,020	0,047	0,001	0,015	0,001	-0,178	295,6	7,4	297,0	15,0	290,0	140,0	295,6	7,4	0,5
BZircon_41	55,0	34,0	0,618	0,055	0,006	0,344	0,031	0,047	0,002	0,015	0,001	0,006	296,2	9,2	304,0	24,0	430,0	200,0	296,2	9,2	2,6
BZircon_15	201,0	233,0	1,159	0,068	0,005	0,441	0,030	0,047	0,001	0,016	0,001	-0,157	296,2	7,0	369,0	21,0	830,0	160,0	296,2	7,0	19,7
BZircon_26	233,0	177,0	0,760	0,067	0,003	0,436	0,020	0,047	0,001	0,017	0,001	0,159	296,3	6,7	366,0	14,0	825,0	94,0	296,3	6,7	19,0
BZircon_10	213,0	168,0	0,789	0,054	0,003	0,345	0,016	0,047	0,001	0,015	0,001	-0,003	296,4	7,0	302,0	12,0	360,0	110,0	296,4	7,0	1,9
AZircon_43	186,2	117,4	0,631	0,051	0,003	0,335	0,016	0,047	0,001	0,015	0,000	0,032	297,3	7,7	296,0	12,0	230,0	110,0	297,3	7,7	-0,4

227

Analysis																							
AZircon_26	303,9	242,0	0,796	0,053	0,002	0,337	0,011	0,047	0,001	0,015	0,000	0,109	297,5	7,2	295,4	9,0	295,0	74,0	297,5	7,2	-0,7	
~~BZircon_49~~	229,0	106,0	0,463	0,072	0,004	0,476	0,025	0,048	0,001	0,022	0,004	0,128	299,7	7,1	395,0	16,0	961,0	99,0	299,7	7,1	24,1	
AZircon_46	81,1	41,8	0,515	0,050	0,004	0,333	0,023	0,048	0,001	0,015	0,001	-0,067	299,8	8,8	292,0	17,0	230,0	150,0	299,8	8,8	-2,7	
AZircon_32	173,9	147,1	0,846	0,053	0,004	0,345	0,015	0,048	0,002	0,016	0,001	0,273	300,0	11,0	300,0	12,0	300,0	140,0	300,0	11,0	0,0	
BZircon_13	344,0	269,0	0,782	0,066	0,050	0,400	1,800	0,047	0,049	0,016	0,073	0,499	300,0	210,0	370,0	270,0	820,0	440,0	300,0	210,0	18,9	
~~BZircon_48~~	40,0	25,0	0,625	0,094	0,011	0,616	0,074	0,048	0,002	0,021	0,002	0,162	301,0	13,0	489,0	45,0	1450,0	240,0	301,0	13,0	38,4	
BZircon_53	329,0	258,0	0,784	0,053	0,002	0,356	0,013	0,048	0,001	0,015	0,001	-0,349	301,2	6,1	309,0	9,9	338,0	97,0	301,2	6,1	2,5	
BZircon_58	138,0	78,0	0,565	0,052	0,004	0,338	0,021	0,048	0,001	0,017	0,001	0,021	303,2	8,2	298,0	16,0	230,0	150,0	303,2	8,2	-1,7	
BZircon_19	120,0	70,0	0,583	0,061	0,004	0,404	0,027	0,048	0,001	0,016	0,001	0,291	303,6	8,7	343,0	19,0	570,0	140,0	303,6	8,7	11,5	
BZircon_31	154,0	104,0	0,675	0,054	0,003	0,357	0,023	0,049	0,001	0,016	0,001	0,106	309,6	8,6	312,0	17,0	360,0	130,0	309,6	8,6	0,8	
~~BZircon_06~~	54,0	55,0	1,019	0,074	0,036	0,510	0,640	0,049	0,006	0,048	0,044	-0,055	340,0	34,0	440,0	130,0	980,0	350,0	340,0	34,0	24,4	
~~BZircon_04~~	162,0	168,0	1,037	0,082	0,004	0,559	0,023	0,050	0,001	0,049	0,004	0,236	346,6	7,2	450,0	15,0	1230,0	90,0	346,6	7,2	29,6	
AZircon_20	484,0	260,6	0,538	0,056	0,003	0,427	0,020	0,056	0,002	0,016	0,002	0,330	353,7	9,6	360,0	14,0	447,0	96,0	353,7	9,6	1,8	
BZircon_50	203,0	115,0	0,567	0,057	0,003	0,599	0,027	0,075	0,002	0,024	0,002	-0,185	467,0	10,0	475,0	17,0	480,0	110,0	467,0	10,0	1,7	
BZircon_18	418,0	244,0	0,584	0,057	0,002	0,590	0,018	0,076	0,002	0,024	0,002	0,128	469,8	8,7	470,0	12,0	478,0	70,0	469,8	8,7	0,0	
~~BZircon_03~~	233,0	175,0	0,751	0,255	0,011	2,035	0,075	0,058	0,001	0,057	0,002	0,124	362,4	7,7	1129,0	24,0	3217,0	67,0	3217,0	67,0	67,9	
~~AZircon_47~~	154,0	108,2	0,703	0,512	0,037	10,000	220,000	0,100	1,800	0,200	4,200	0,949	800,0	2000,0	2330,0	610,0	4268,0	86,0	4268,0	####	65,7	
CPV-15-350 (IZ)									Weighted mean age: 210.7 ±3.4 Ma (MSWD = 0.2)													
Zircon_28	1261,0	1419,0	1,125	0,052	0,003	0,236	0,012	0,033	0,001	0,311	0,011	0,000	209,3	5,8	215,0	9,6	270,0	110,0	209,3	5,8	2,7	**
Zircon_26	248,0	269,0	1,085	0,053	0,003	0,242	0,015	0,033	0,001	0,173	0,011	0,000	211,2	5,9	219,0	12,0	340,0	130,0	211,2	5,9	3,6	**
Zircon_25	356,0	291,0	0,817	0,054	0,003	0,252	0,013	0,033	0,001	-0,266	0,012	0,000	211,7	6,1	228,0	10,0	420,0	120,0	211,7	6,1	7,1	**
Zircon_11	260,0	435,0	1,673	0,056	0,004	0,268	0,020	0,034	0,001	-0,083	0,011	0,000	216,9	6,7	241,0	16,0	470,0	130,0	216,9	6,7	10,0	
Zircon_23	1046,0	426,0	0,407	0,051	0,002	0,243	0,011	0,035	0,001	0,307	0,012	0,001	219,0	5,8	220,8	8,9	221,0	92,0	219,0	5,8	0,8	
Zircon_20	628,0	518,0	0,825	0,053	0,003	0,253	0,014	0,035	0,001	0,286	0,011	0,000	220,7	6,2	228,0	11,0	290,0	110,0	220,7	6,2	3,2	
Zircon_31	125,0	69,0	0,552	0,050	0,004	0,246	0,021	0,035	0,001	0,074	0,012	0,001	221,9	7,5	224,0	17,0	170,0	180,0	221,9	7,5	0,9	
Zircon_15	411,0	506,0	1,231	0,052	0,003	0,247	0,012	0,035	0,001	0,240	0,011	0,000	223,0	6,3	225,0	10,0	260,0	110,0	223,0	6,3	0,9	

Sample																					
Zircon_29	111,0	85,0	0,766	0,053	0,004	0,256	0,021	0,035	0,001	0,022	0,012	0,001	224,0	8,4	230,0	17,0	290,0	170,0	224,0	8,4	2,6
Zircon_24	66,0	66,0	1,000	0,066	0,006	0,329	0,027	0,035	0,002	0,099	0,013	0,001	224,2	9,1	287,0	21,0	790,0	200,0	224,2	9,1	21,9
Zircon_06	705,0	468,0	0,664	0,051	0,003	0,253	0,013	0,035	0,001	-0,112	0,011	0,000	224,5	6,7	229,0	10,0	260,0	100,0	224,5	6,7	2,0
Zircon_10	82,0	47,0	0,573	0,073	0,007	0,349	0,032	0,036	0,004	0,063	0,014	0,001	224,9	8,9	308,0	25,0	870,0	210,0	224,9	8,9	27,0
Zircon_17	180,0	156,0	0,867	0,058	0,003	0,288	0,017	0,036	0,001	0,053	0,012	0,001	225,7	7,2	258,0	13,0	480,0	130,0	225,7	7,2	12,5
Zircon_09	169,0	136,0	0,805	0,053	0,004	0,258	0,017	0,036	0,001	0,269	0,012	0,001	226,1	7,4	235,0	13,0	280,0	160,0	226,1	7,4	3,8
Zircon_32	234,0	259,0	1,107	0,056	0,005	0,279	0,024	0,036	0,001	-0,326	0,012	0,001	226,9	6,7	250,0	18,0	560,0	150,0	226,9	6,7	9,2
Zircon_30	203,0	113,0	0,557	0,053	0,003	0,257	0,015	0,036	0,001	-0,002	0,012	0,001	227,7	7,1	232,0	12,0	290,0	140,0	227,7	7,1	1,9
Zircon_27	284,0	339,0	1,194	0,052	0,003	0,256	0,019	0,036	0,001	0,362	0,012	0,001	228,0	7,0	231,0	15,0	240,0	140,0	228,0	7,0	1,3
Zircon_12	258,0	239,0	0,926	0,055	0,004	0,277	0,020	0,036	0,001	0,057	0,012	0,001	228,3	7,4	248,0	16,0	390,0	160,0	228,3	7,4	7,9
Zircon_13	446,0	258,0	0,578	0,056	0,003	0,279	0,016	0,036	0,001	-0,036	0,012	0,001	229,2	6,4	250,0	12,0	450,0	120,0	229,2	6,4	8,3
Zircon_02	138,0	94,0	0,681	0,053	0,005	0,268	0,024	0,036	0,001	0,045	0,013	0,001	230,5	8,1	240,0	19,0	270,0	190,0	230,5	8,1	4,0
Zircon_22	280,0	147,0	0,525	0,052	0,003	0,258	0,014	0,037	0,001	0,070	0,012	0,001	230,9	6,9	233,0	11,0	250,0	120,0	230,9	6,9	0,9
Zircon_14	64,0	32,0	0,500	0,055	0,006	0,277	0,030	0,036	0,002	0,136	0,014	0,001	231,0	11,0	245,0	24,0	350,0	180,0	231,0	11,0	5,7
Zircon_04	153,0	98,0	0,641	0,053	0,004	0,268	0,019	0,037	0,001	0,157	0,012	0,001	232,3	7,6	240,0	15,0	280,0	150,0	232,3	7,6	3,2
Zircon_08	299,0	260,0	0,870	0,052	0,003	0,264	0,017	0,037	0,001	0,259	0,012	0,001	233,9	8,1	239,0	13,0	260,0	130,0	233,9	8,1	2,1
Zircon_18	411,0	255,0	0,620	0,051	0,003	0,268	0,016	0,038	0,001	0,120	0,011	0,001	237,3	6,9	241,0	13,0	250,0	130,0	237,3	6,9	1,5
Zircon_16	625,0	1204,0	1,926	0,051	0,003	0,258	0,015	0,038	0,001	0,212	0,012	0,001	237,7	7,6	233,0	12,0	210,0	110,0	237,7	7,6	-2,0
Zircon_19	74,0	56,0	0,757	0,148	0,031	0,790	0,260	0,040	0,002	0,209	0,021	0,003	255,0	14,0	588,0	97,0	2070,0	340,0	255,0	14,0	56,6
Zircon_21	164,0	151,0	0,921	0,057	0,004	0,347	0,026	0,045	0,001	0,194	0,014	0,001	280,8	8,9	306,0	18,0	440,0	140,0	280,8	8,9	8,2
Zircon_07	154,0	144,0	0,935	0,055	0,004	0,353	0,022	0,045	0,001	0,056	0,014	0,001	282,8	8,4	307,0	15,0	430,0	150,0	282,8	8,4	7,9
Zircon_05	290,0	436,0	1,503	0,052	0,003	0,325	0,018	0,045	0,001	-0,194	0,014	0,001	284,6	8,1	285,0	13,0	270,0	130,0	284,6	8,1	0,1
Zircon_03	140,0	110,0	0,786	0,053	0,004	0,336	0,024	0,045	0,001	-0,185	0,014	0,001	286,1	8,7	292,0	19,0	280,0	170,0	286,1	8,7	2,0
CPV-15-400 (IZ)												Concordance age: 208.4 ±2.3 Ma (MSWD = 2.2)									
Zircon_64	245,6	178,3	0,726	0,050	0,002	0,224	0,009	0,032	0,001	0,181	0,010	0,000	204,4	5,4	204,8	7,8	221,0	92,0	204,4	5,4	0,2
Zircon_70	190,6	100,0	0,525	0,051	0,003	0,223	0,011	0,032	0,001	0,365	0,010	0,000	203,8	5,3	204,2	9,2	190,0	100,0	203,8	5,3	0,2
Zircon_78	331,2	202,8	0,612	0,051	0,004	0,237	0,018	0,034	0,001	-0,052	0,011	0,000	213,9	5,7	216,0	14,0	210,0	130,0	213,9	5,7	1,0

Zircon																					
Zircon_75	252,8	144,6	0,572	0,051	0,003	0,234	0,011	0,033	0,001	0,040	0,011	0,000	211,3	5,5	211,3	213,7	8,6	220,0	100,0	211,3	5,5	1,1
Zircon_83	545,0	488,0	0,895	0,051	0,003	0,223	0,011	0,032	0,001	0,151	0,010	0,000	201,8	5,5	201,8	204,5	8,8	230,0	100,0	201,8	5,5	1,3
Zircon_66	187,7	97,6	0,520	0,052	0,003	0,235	0,010	0,033	0,001	0,171	0,012	0,000	211,4	5,6	211,4	214,3	8,7	290,0	110,0	211,4	5,6	1,4
Zircon_67	360,0	216,0	0,600	0,052	0,002	0,231	0,010	0,033	0,001	0,434	0,011	0,000	207,9	5,9	207,9	210,8	8,7	252,0	85,0	207,9	5,9	1,4
Zircon_68	104,0	48,2	0,463	0,051	0,004	0,237	0,016	0,033	0,001	-0,124	0,011	0,001	211,7	5,9	211,7	215,0	13,0	230,0	150,0	211,7	5,9	1,5
Zircon_62	126,2	60,4	0,479	0,052	0,003	0,238	0,012	0,033	0,001	0,196	0,011	0,001	212,3	6,1	212,3	217,0	10,0	290,0	120,0	212,3	6,1	2,2
Zircon_63	120,0	44,3	0,369	0,053	0,003	0,229	0,014	0,032	0,001	0,139	0,011	0,001	201,2	5,9	201,2	208,0	11,0	290,0	130,0	201,2	5,9	3,3
Zircon_74	185,9	97,2	0,523	0,054	0,002	0,248	0,013	0,034	0,001	0,353	0,011	0,000	213,1	5,9	213,1	224,0	10,0	310,0	100,0	213,1	5,9	4,9
Zircon_79	230,0	124,1	0,540	0,053	0,003	0,232	0,011	0,031	0,001	0,356	0,011	0,000	199,6	5,5	199,6	211,3	9,4	290,0	110,0	199,6	5,5	5,5
Zircon_81	125,9	54,3	0,431	0,059	0,003	0,276	0,014	0,034	0,001	-0,163	0,013	0,001	215,0	6,3	215,0	247,0	11,0	550,0	120,0	215,0	6,3	13,0
Zircon_71	179,1	101,3	0,566	0,059	0,003	0,248	0,014	0,030	0,001	-0,019	0,010	0,000	193,0	5,1	193,0	225,0	11,0	530,0	120,0	193,0	5,1	14,2
Zircon_65	234,2	159,5	0,681	0,059	0,003	0,258	0,013	0,032	0,001	0,343	0,011	0,000	201,5	5,6	201,5	237,0	10,0	590,0	120,0	201,5	5,6	15,0
Zircon_76	140,8	69,2	0,491	0,059	0,004	0,243	0,015	0,029	0,001	-0,007	0,010	0,001	183,9	6,3	183,9	220,0	12,0	550,0	130,0	183,9	6,3	16,4
Zircon_80	179,8	154,8	0,861	0,062	0,004	0,211	0,013	0,025	0,001	-0,076	0,007	0,000	159,9	5,6	159,9	194,0	11,0	610,0	130,0	159,9	5,6	17,6
Zircon_82	138,6	102,6	0,740	0,065	0,005	0,270	0,018	0,030	0,001	0,156	0,010	0,001	190,9	5,8	190,9	244,0	14,0	740,0	140,0	190,9	5,8	21,8
Zircon_73	98,2	56,8	0,578	0,068	0,009	0,326	0,075	0,035	0,001	0,014	0,014	0,002	218,9	7,6	218,9	286,0	42,0	830,0	200,0	218,9	7,6	23,5
Zircon_72	239,0	178,0	0,745	0,067	0,008	0,285	0,037	0,030	0,001	0,122	0,011	0,001	191,7	7,6	191,7	254,0	26,0	810,0	140,0	191,7	7,6	24,5
Zircon_69	172,0	124,0	0,721	0,088	0,005	0,360	0,019	0,032	0,001	-0,128	0,013	0,001	201,9	8,1	201,9	311,0	15,0	1300,0	120,0	201,9	8,1	35,1

Anexo 9: 40Ar-39Ar detrital muscovite results.

Run_ID	Sample	Ar40Rad/Ar39	Ar40Rad/Ar39_Er	%Ar40Rad	Age	Age_Error (1sigma)	Age_Er_ with_J_er (1sigma)	Ar39_Moles
2200-01A	CPV-16-391	26,7054	0,0227729	88,13142	207,6422	0,1673904	0,3233688	1,76E-14
2200-02A	CPV-16-391	26,6137	0,0566206	91,80254	206,9681	0,4163395	0,4994173	5,33E-15
2200-03A	CPV-16-391	28,72031	0,0441136	83,87791	222,393	0,3216508	0,4365526	9,02E-15
2200-04A	CPV-16-391	29,96286	0,0469767	86,95884	231,4306	0,3408397	0,458323	7,91E-15
2200-05A	CPV-16-391	25,96751	0,0184102	89,63772	202,2103	0,1357252	0,3020403	2,21E-14
2200-06A	CPV-16-391	26,08267	0,0264965	89,87725	203,0591	0,1952488	0,3339285	1,29E-14
2200-07A	CPV-16-391	31,82841	0,0178928	92,43671	244,9164	0,1288686	0,3478518	2,60E-14
2200-08A	CPV-16-391	27,20144	0,0304474	89,62658	211,2847	0,2233563	0,3591524	1,13E-14
2200-09A	CPV-16-391	26,67908	0,0763784	90,93321	207,4487	0,5614734	0,6258319	3,65E-15
2200-10A	CPV-16-391	29,01338	0,0652817	89,2246	224,5287	0,4754416	0,56102	5,20E-15
2200-11A	CPV-16-391	25,30437	0,0369571	85,72345	197,315	0,2731875	0,3796554	8,68E-15
2200-12A	CPV-16-391	27,33206	0,0948531	90,85623	212,2427	0,6954609	0,7506306	3,38E-15
2200-13A	CPV-16-391	25,87227	0,0138533	88,87785	201,5081	0,1021696	0,2876944	6,91E-14
2200-14A	CPV-16-391	25,52167	0,0407224	88,90912	198,9205	0,3007571	0,4012936	7,08E-15
2200-15A	CPV-16-391	25,90223	0,0462617	94,34315	201,729	0,3411441	0,4345789	5,96E-15
2200-16A	CPV-16-391	26,09548	0,0331563	89,09995	203,1535	0,2443119	0,3648821	9,86E-15
2200-17A	CPV-16-391	26,28605	0,0874879	92,22949	204,5572	0,6441589	0,6995383	3,35E-15
2200-18A	CPV-16-391	26,2149	0,0349784	89,77469	204,0332	0,2576135	0,3747238	9,20E-15
2200-19A	CPV-16-391	28,38728	0,0359513	88,3442	219,9632	0,2624845	0,3927271	1,02E-14
2200-20A	CPV-16-391	26,80187	0,0219623	91,92441	208,3512	0,16137	0,3210646	1,64E-14
2200-21A	CPV-16-391	25,9836	0,0491722	91,99163	202,3289	0,3624876	0,4519791	6,01E-15
2200-22A	CPV-16-391	29,44721	0,0386854	88,27639	227,6855	0,281257	0,4125068	9,55E-15
2200-23A	CPV-16-391	26,87687	0,0192546	90,83069	208,9021	0,1414321	0,3121384	2,05E-14
2200-24A	CPV-16-391	26,25835	0,0395083	92,88484	204,3533	0,2909256	0,398636	7,79E-15
2200-25A	CPV-16-391	26,75222	0,0406112	89,95732	207,9863	0,2984536	0,4072618	7,92E-15
2200-26A	CPV-16-391	26,41193	0,0924237	88,80166	205,4838	0,6801557	0,7332553	2,99E-15
2200-27A	CPV-16-391	28,68091	0,06949	88,80284	222,1058	0,5067608	0,5862711	4,82E-15
2200-28A	CPV-16-391	24,77218	0,0441487	91,60828	193,3767	0,3270511	0,4169695	6,44E-15
2200-29A	CPV-16-391	27,99118	0,028482	87,55186	217,0689	0,2082795	0,3558298	1,41E-14
2200-30A	CPV-16-391	28,46697	0,0211009	90,66716	220,5449	0,154011	0,3308793	1,89E-14
2200-31A	CPV-16-391	25,68924	0,0269642	84,67238	200,1577	0,1990109	0,3331971	1,79E-14
2200-32A	CPV-16-391	25,69309	0,0379906	87,94394	200,1861	0,2803873	0,3873645	8,35E-15
2200-33A	CPV-16-391	28,84158	0,0484848	91,23959	223,277	0,3533527	0,4611176	6,99E-15
2200-34A	CPV-16-391	25,47052	0,0498319	89,96162	198,5427	0,3681115	0,4536895	5,85E-15
2200-35A	CPV-16-391	27,34469	0,0567606	86,39077	212,3352	0,4161465	0,5030149	5,62E-15
2200-36A	CPV-16-391	25,6534	0,0770024	86,38962	199,8931	0,5684026	0,6279475	3,54E-15
2200-37A	CPV-16-391	25,04516	0,0241657	86,8757	195,3978	0,1788208	0,3165592	1,78E-14
2200-38A	CPV-16-391	25,65587	0,0376377	87,35817	199,9114	0,2778241	0,3852726	8,54E-15
2200-39A	CPV-16-391	27,48495	0,030395	86,40266	213,3633	0,2227194	0,3608056	1,33E-14
2200-40A	CPV-16-391	27,92804	0,1430037	79,85962	216,6071	1,046002	1,084906	2,27E-15
2200-41A	CPV-16-391	30,33246	0,1111445	87,85036	234,1103	0,80523	0,8627472	3,22E-15
2200-42A	CPV-16-391	28,01487	0,0305248	92,09178	217,2422	0,2231967	0,3649335	1,14E-14
2200-43A	CPV-16-391	25,30373	0,0372804	90,35989	197,3102	0,2755787	0,3813754	8,14E-15
2200-44A	CPV-16-391	27,80395	0,0473192	92,84302	215,6992	0,3462887	0,449626	6,84E-15
2200-45A	CPV-16-391	25,76076	0,0566817	85,42371	200,6854	0,418222	0,4966703	5,51E-15
2200-46A	CPV-16-391	27,66766	0,0644739	89,34101	214,7016	0,4720865	0,5517227	5,19E-15
2200-47A	CPV-16-391	25,9433	0,0159328	87,28595	202,0318	0,1174723	0,2940838	5,74E-14
2200-48A	CPV-16-391	26,00138	0,0887951	88,36598	202,46	0,6545326	0,7080891	3,08E-15
2200-49A	CPV-16-391	25,7529	0,0508643	91,112	200,6274	0,3753104	0,4610753	5,92E-15
2200-50A	CPV-16-391	26,36958	0,0387222	87,99464	205,1721	0,2850095	0,395053	8,42E-15

2200-51A	CPV-16-391	27,70535	0,0438495	85,67676	214,9775	0,3210232	0,4298672	8,04E-15
2200-52A	CPV-16-391	25,6824	0,0520876	89,93075	200,1072	0,3844457	0,468166	5,66E-15
2200-53A	CPV-16-391	25,304	0,207202	92,09209	197,3122	1,531645	1,554169	1,25E-15
2200-54A	CPV-16-391	24,99303	0,1295383	85,63404	195,0121	0,958756	0,9935748	2,16E-15
2200-55A	CPV-16-391	26,73166	0,0357314	90,19284	207,8352	0,2626136	0,3816388	9,14E-15
2200-56A	CPV-16-391	31,24075	0,1462148	92,95151	240,679	1,055515	1,10234	2,19E-15
2200-57A	CPV-16-391	31,26804	0,0764906	90,56015	240,876	0,5521214	0,637208	4,72E-15
2200-58A	CPV-16-391	25,77724	0,0569844	91,47787	200,8071	0,4204273	0,4986113	5,39E-15
2200-59A	CPV-16-391	25,31998	0,1311805	90,01946	197,4303	0,9696284	1,00487	2,00E-15
2200-60A	CPV-16-391	25,82957	0,0317232	89,21788	201,1931	0,2340022	0,356192	1,02E-14
2200-61A	CPV-16-391	27,11403	0,0477026	88,86866	210,6433	0,3500598	0,4485441	6,18E-15
2200-62A	CPV-16-391	25,77628	0,053523	86,61066	200,7999	0,3948904	0,4772711	5,85E-15
2200-63A	CPV-16-391	24,91889	0,0301761	87,19294	194,4632	0,22341	0,342823	1,20E-14
2200-64A	CPV-16-391	28,50346	0,0789622	90,25091	220,8112	0,5762452	0,646541	3,83E-15
2200-65A	CPV-16-391	25,2171	0,1142056	85,29047	196,6697	0,8445088	0,8844613	2,55E-15
2200-66A	CPV-16-391	30,10521	0,0553057	94,61327	232,4632	0,4010446	0,5054823	6,25E-15
2200-67A	CPV-16-391	26,3404	0,1073602	87,58777	204,9573	0,7903024	0,8362215	2,82E-15
2200-68A	CPV-16-391	28,81049	0,03002	89,88825	223,0504	0,2188102	0,3680785	1,23E-14
2200-69A	CPV-16-391	27,71462	0,0353572	91,53229	215,0454	0,2588412	0,3857165	9,20E-15
2200-70A	CPV-16-391	30,72308	0,1056759	92,05776	236,9381	0,7644282	0,8261181	3,01E-15
2200-71A	CPV-16-391	25,88814	0,0332264	88,93301	201,6251	0,2450327	0,3639368	9,71E-15
2200-72A	CPV-16-391	26,27382	0,040173	85,25706	204,4671	0,2958018	0,4023058	8,37E-15
2200-73A	CPV-16-391	30,2592	0,0701629	93,19924	233,5795	0,5084699	0,5950393	4,48E-15
2200-74A	CPV-16-391	28,10257	0,1316611	88,4288	217,8833	0,9623658	1,004973	2,26E-15
2200-75A	CPV-16-391	27,03711	0,031566	86,75865	210,0788	0,2317149	0,3632416	1,17E-14
2200-76A	CPV-16-391	28,25296	0,0724627	84,10092	218,9822	0,5293419	0,6040069	4,50E-15
2200-77A	CPV-16-391	29,2713	0,5142327	88,78864	226,4061	3,741277	3,753299	5,89E-16
2200-78A	CPV-16-391	29,48183	0,1482851	95,05246	227,9372	1,077939	1,119464	2,36E-15
2200-79A	CPV-16-391	28,53563	0,0689703	90,61591	221,0459	0,5032622	0,5825819	5,02E-15
2200-80A	CPV-16-391	26,1272	0,0568453	85,20691	203,3872	0,4188103	0,4990116	5,56E-15
2200-81A	CPV-16-391	26,80594	0,0243408	85,31054	208,381	0,1788431	0,330224	1,96E-14
2200-82A	CPV-16-391	29,72829	0,0591533	86,2171	229,7279	0,4295864	0,5264414	6,07E-15
2200-83A	CPV-16-391	25,90341	0,0375612	93,0881	201,7377	0,2769834	0,386271	8,10E-15
2200-84A	CPV-16-391	27,83427	0,1096331	82,73555	215,9211	0,8022133	0,852029	2,97E-15
2200-85A	CPV-16-391	27,18809	0,044353	87,08059	211,1867	0,3253831	0,4300086	7,35E-15
2200-86A	CPV-16-391	26,87091	0,0306153	90,08584	208,8583	0,2248864	0,3577297	1,11E-14
2200-87A	CPV-16-391	26,72604	0,0313527	87,49631	207,7939	0,2304368	0,3602147	1,23E-14
2204-01A	CPV-16-408	34,55183	0,1185183	99,37855	264,4267	0,8445459	0,9130639	4,83E-15
2204-02A	CPV-16-408	34,42699	0,077038	98,70513	263,5369	0,5492301	0,6490988	7,43E-15
2204-03A	CPV-16-408	34,8951	0,2998348	98,4691	266,8712	2,133732	2,162249	1,84E-15
2204-04A	CPV-16-408	34,10088	0,1944731	99,10226	261,2105	1,388228	1,429998	2,90E-15
2204-05A	CPV-16-408	34,85954	0,0950158	97,72685	266,6181	0,6762599	0,7613256	6,09E-15
2204-06A	CPV-16-408	34,16813	0,1625431	98,70736	261,6905	1,159994	1,209838	3,34E-15
2204-07A	CPV-16-408	34,88022	0,3501344	99,44599	266,7653	2,491826	2,51627	1,59E-15
2204-08A	CPV-16-408	34,00879	0,3748727	98,1886	260,553	2,676955	2,69875	1,44E-15
2204-09A	CPV-16-408	34,55049	0,1424047	98,73593	264,4172	1,014763	1,072457	4,02E-15
2204-10A	CPV-16-408	34,64876	0,2466285	96,53073	265,1173	1,75678	1,79089	2,36E-15
2204-11A	CPV-16-408	34,04172	0,1058856	98,60432	260,7881	0,7560288	0,8300262	5,13E-15
2204-12A	CPV-16-408	34,66278	0,2013683	99,48625	265,2172	1,434305	1,475916	2,73E-15
2204-13A	CPV-16-408	34,13388	0,1552147	99,21034	261,446	1,107843	1,159841	3,60E-15
2204-14A	CPV-16-408	34,26723	0,2183298	98,20285	262,3976	1,557516	1,595171	2,60E-15
2204-15A	CPV-16-408	34,88719	0,179261	99,52993	266,8149	1,275725	1,322849	3,19E-15
2204-16A	CPV-16-408	34,65183	0,1855527	99,42912	265,1392	1,32171	1,36673	2,98E-15
2204-17A	CPV-16-408	34,69432	0,119687	99,56351	265,4418	0,8524014	0,9208022	4,80E-15

2204-18A	CPV-16-408	34,85454	0,0864965	99,16906	266,5825	0,615637	0,7080027	6,69E-15
2204-19A	CPV-16-408	33,48559	0,2750543	97,8609	256,813	1,968172	1,996937	1,93E-15
2204-20A	CPV-16-408	34,85207	0,1474831	99,43913	266,5649	1,049718	1,106414	3,91E-15
2204-21A	CPV-16-408	34,14638	0,3604788	99,1791	261,5352	2,572787	2,595616	1,59E-15
2204-22A	CPV-16-408	34,31789	0,0853333	99,0029	262,7589	0,6086282	0,6996054	6,67E-15
2204-23A	CPV-16-408	34,58554	0,0899035	98,89073	264,6669	0,6405565	0,728659	6,38E-15
2204-24A	CPV-16-408	34,59012	0,2941985	99,19517	264,6996	2,096108	2,124695	1,87E-15
2204-25A	CPV-16-408	34,06304	0,1064497	98,46301	260,9404	0,759993	0,8337151	5,25E-15
2204-26A	CPV-16-408	34,46089	0,4260865	99,28582	263,7786	3,037313	3,056984	1,29E-15
2204-27A	CPV-16-408	34,65159	0,0905703	98,47683	265,1374	0,6451415	0,7329651	6,28E-15
2204-28A	CPV-16-408	34,93127	0,1802611	98,36744	267,1286	1,282622	1,329603	3,10E-15
2204-29A	CPV-16-408	34,77518	0,1771246	97,91111	266,0176	1,261071	1,308464	3,12E-15
2204-30A	CPV-16-408	34,45582	0,2148942	98,86191	263,7425	1,531881	1,570512	2,66E-15
2204-31A	CPV-16-408	34,87307	0,0937037	99,72957	266,7144	0,6668863	0,7530661	6,24E-15
2204-32A	CPV-16-408	34,59743	0,1784092	99,13904	264,7516	1,271095	1,31772	3,09E-15
2204-33A	CPV-16-408	34,47076	0,1523708	99,36569	263,849	1,086117	1,139996	3,75E-15
2204-34A	CPV-16-408	34,27097	0,0970689	99,22472	262,4243	0,6924578	0,7734568	5,85E-15
2204-35A	CPV-16-408	34,81532	0,0617471	99,30485	266,3033	0,439551	0,5614501	9,36E-15
2204-36A	CPV-16-408	34,94213	0,2413601	99,39686	267,2058	1,717291	1,752678	2,31E-15
2204-37A	CPV-16-408	34,08602	0,1694408	98,70107	261,1044	1,209607	1,25729	3,33E-15
2204-38A	CPV-16-408	32,46862	0,2478044	96,35092	249,5215	1,780262	1,810365	2,09E-15
2204-39A	CPV-16-408	34,95969	0,0844798	99,31557	267,3308	0,601038	0,6958044	6,87E-15
2204-40A	CPV-16-408	34,72751	0,1492958	98,80796	265,6781	1,063136	1,118815	3,70E-15
2204-41A	CPV-16-408	33,70202	0,6906192	98,86376	258,361	4,9376	4,949266	7,77E-16
2204-42A	CPV-16-408	34,81661	0,1068319	99,42713	266,3125	0,7604863	0,8368802	5,41E-15
2204-43A	CPV-16-408	35,01183	0,1081703	99,84598	267,7017	0,7694292	0,8457159	5,36E-15
2204-44A	CPV-16-408	34,21656	0,0650526	99,1479	262,0361	0,464162	0,577804	8,63E-15
2204-45A	CPV-16-408	34,61068	0,2330368	99,17254	264,846	1,66021	1,696196	2,36E-15
2204-46A	CPV-16-408	34,85207	0,5023549	99,03898	266,5649	3,575536	3,59259	1,10E-15
2204-47A	CPV-16-408	34,57688	0,0753899	99,48261	264,6052	0,5371663	0,6396301	7,61E-15
2204-48A	CPV-16-408	34,47509	0,203721	99,08421	263,8798	1,452123	1,492859	2,80E-15
2204-49A	CPV-16-408	34,59447	0,0611977	99,55088	264,7305	0,4360146	0,557489	9,38E-15
2204-50A	CPV-16-408	35,20799	0,6937635	99,18425	269,0965	4,931071	4,94367	8,08E-16
2204-51A	CPV-16-408	34,49119	0,1784915	98,9164	263,9946	1,272207	1,31855	3,17E-15
2204-52A	CPV-16-408	34,10534	0,4479594	99,26146	261,2423	3,197659	3,216018	1,21E-15
2204-53A	CPV-16-408	35,53808	1,587042	92,81388	271,4411	11,26579	11,2714	3,57E-16
2204-54A	CPV-16-408	32,19147	0,487898	97,42787	247,5294	3,508946	3,524086	1,05E-15
2204-55A	CPV-16-408	35,01615	0,4561992	99,5002	267,7324	3,24495	3,263884	1,22E-15
2204-56A	CPV-16-408	34,70521	0,3250075	99,51455	265,5194	2,314579	2,340647	1,70E-15
2204-57A	CPV-16-408	34,55743	0,24498	96,65408	264,4666	1,745658	1,779827	2,34E-15
2204-58A	CPV-16-408	34,88681	0,3440055	98,00019	266,8122	2,448145	2,473029	1,61E-15
2204-59A	CPV-16-408	35,05962	0,7373517	99,65374	268,0416	5,243905	5,255668	7,56E-16
2204-60A	CPV-16-408	34,82207	0,3392832	99,18041	266,3514	2,415147	2,440286	1,70E-15
2204-61A	CPV-16-408	35,35474	0,3408778	99,5285	270,1393	2,421481	2,447218	1,65E-15
2204-62A	CPV-16-408	32,33894	1,977724	98,97536	248,5896	14,21548	14,21926	2,59E-16
2204-63A	CPV-16-408	34,49649	0,5530468	98,27534	264,0323	3,94179	3,956994	9,92E-16
2204-64A	CPV-16-408	33,60394	0,2878042	98,88452	257,6597	2,058453	2,086141	1,86E-15
2204-65A	CPV-16-408	35,20193	0,8171244	98,84239	269,0534	5,808021	5,818718	6,85E-16
2204-66A	CPV-16-408	30,0736	1,86644	92,28718	232,2339	13,53603	13,53952	2,55E-16
2204-67A	CPV-16-408	34,48687	0,0970021	99,01852	263,9638	0,6913994	0,7733494	5,84E-15
2204-68A	CPV-16-408	35,10334	0,213554	98,16005	268,3525	1,518498	1,558719	2,69E-15
2204-69A	CPV-16-408	35,41708	0,6325869	99,56068	270,582	4,492597	4,506563	8,89E-16
2204-70A	CPV-16-408	34,43514	0,2614296	98,46182	263,595	1,86376	1,895607	2,21E-15
2204-71A	CPV-16-408	31,4625	1,25953	97,20774	242,2791	9,084519	9,090148	3,96E-16

2204-72A	CPV-16-408	35,19266	0,2564462	99,86867	268,9875	1,822854	1,85664	2,18E-15
2204-73A	CPV-16-408	33,78947	0,6744741	98,14994	258,9862	4,820524	4,832526	7,98E-16
2204-74A	CPV-16-408	35,07375	0,2898645	99,2913	268,1421	2,061348	2,091111	1,92E-15
2204-75A	CPV-16-408	34,07204	0,6945983	96,84114	261,0046	4,958882	4,97072	7,83E-16
2204-76A	CPV-16-408	33,28916	0,4926871	94,49892	255,4069	3,52817	3,544133	1,07E-15
2204-77A	CPV-16-408	35,00311	0,4804003	99,65422	267,6397	3,417266	3,435239	1,15E-15
2204-78A	CPV-16-408	34,732	0,3713432	99,55432	265,7101	2,644289	2,667167	1,49E-15
2204-79A	CPV-16-408	32,82655	16,40086	86,05633	252,0911	117,6608	117,6613	3,16E-17
2204-80A	CPV-16-408	33,38929	0,4723407	96,67402	256,1238	3,381143	3,397884	1,16E-15
2204-81A	CPV-16-408	35,00072	0,195571	99,59303	267,6227	1,391182	1,43476	2,83E-15
2204-82A	CPV-16-408	35,01504	0,3923982	98,67964	267,7245	2,791145	2,813134	1,42E-15
2204-83A	CPV-16-408	34,45909	0,2606431	99,55838	263,7657	1,85798	1,889963	2,19E-15
2204-84A	CPV-16-408	24,81545	0,2595038	89,55433	193,6972	1,922054	1,939434	1,54E-15
2204-85A	CPV-16-408	35,00375	0,1324531	99,80016	267,6442	0,9421861	1,005425	4,38E-15
2204-86A	CPV-16-408	34,61385	0,8500318	99,91782	264,8686	6,055754	6,06572	6,53E-16
2204-87A	CPV-16-408	25,97902	0,4882691	88,25111	202,2952	3,59949	3,609597	8,52E-16
2202-01A	CPV-16-409	33,82013	0,0931796	92,82708	259,2053	0,6658829	0,7479583	4,71E-15
2202-02A	CPV-16-409	34,15203	0,0793991	97,69485	261,5756	0,5666701	0,6626758	5,87E-15
2202-03A	CPV-16-409	34,19114	0,0937902	98,25009	261,8547	0,669277	0,7524562	4,97E-15
2202-04A	CPV-16-409	33,5867	0,1899315	96,65548	257,5364	1,358533	1,400095	2,37E-15
2202-05A	CPV-16-409	34,38984	0,0709769	96,58057	263,272	0,5060915	0,6128463	6,63E-15
2202-06A	CPV-16-409	32,65144	0,4310633	89,05406	250,8344	3,0946	3,112186	9,70E-16
2202-07A	CPV-16-409	34,16995	0,0977158	95,38002	261,7034	0,6973473	0,7774476	4,50E-15
2202-08A	CPV-16-409	33,81694	0,3055624	93,15565	259,1825	2,183647	2,210053	1,41E-15
2202-09A	CPV-16-409	33,60369	0,0664793	96,3333	257,6579	0,4754782	0,5838103	7,05E-15
2202-10A	CPV-16-409	33,955	0,1092481	98,33243	260,1688	0,7803013	0,8518896	4,23E-15
2202-11A	CPV-16-409	34,12775	0,1729872	94,97801	261,4023	1,234723	1,281569	2,52E-15
2202-12A	CPV-16-409	34,93309	0,0585086	99,211	267,1415	0,416307	0,5441021	8,14E-15
2202-13A	CPV-16-409	30,89688	0,8631647	85,91851	238,1949	6,239594	6,24753	4,55E-16
2202-14A	CPV-16-409	34,20849	0,1109298	96,69921	261,9785	0,7915296	0,8630653	4,14E-15
2202-15A	CPV-16-409	34,1457	0,1874153	93,43663	261,5304	1,337613	1,381012	2,34E-15
2202-16A	CPV-16-409	34,206	0,1991215	92,44975	261,9607	1,420827	1,461882	2,39E-15
2202-17A	CPV-16-409	34,06834	0,1596372	96,77605	260,9782	1,139699	1,190142	2,85E-15
2202-18A	CPV-16-409	32,89988	0,1549012	93,25526	252,6171	1,110951	1,159663	2,72E-15
2202-19A	CPV-16-409	33,66037	0,3167177	91,62566	258,0633	2,26475	2,290018	1,45E-15
2202-20A	CPV-16-409	34,13385	0,17821	95,84057	261,4458	1,271971	1,317508	2,47E-15
2202-21A	CPV-16-409	33,22727	0,2655351	94,68821	254,9636	1,901978	1,931334	1,67E-15
2202-22A	CPV-16-409	33,1184	0,1307457	94,8305	254,1836	0,9369063	0,9948275	3,25E-15
2202-23A	CPV-16-409	34,08845	0,1591903	98,27847	261,1217	1,13642	1,187052	2,86E-15
2202-24A	CPV-16-409	33,80513	0,076588	97,6212	259,0981	0,5473477	0,6446252	6,03E-15
2202-25A	CPV-16-409	32,86031	0,0973186	94,84631	252,3333	0,698077	0,7731014	4,70E-15
2202-26A	CPV-16-409	32,70418	0,3079563	87,6659	251,213	2,210358	2,234982	1,37E-15
2202-27A	CPV-16-409	31,0411	0,1063894	91,18336	239,2371	0,7686239	0,8310799	4,09E-15
2202-28A	CPV-16-409	34,71745	0,1557361	97,65942	265,6065	1,10904	1,162496	2,99E-15
2202-29A	CPV-16-409	33,55313	0,187281	91,6977	257,2962	1,33975	1,381805	2,31E-15
2202-30A	CPV-16-409	34,13599	0,1543656	96,48817	261,4611	1,101773	1,15405	2,83E-15
2202-31A	CPV-16-409	35,9687	0,0718067	98,4845	274,4954	0,5088776	0,622925	6,95E-15
2202-32A	CPV-16-409	33,14505	0,2099317	95,48848	254,3746	1,504185	1,54098	2,02E-15
2202-33A	CPV-16-409	33,50869	0,2351192	93,72569	256,9783	1,682262	1,715866	1,82E-15
2202-34A	CPV-16-409	33,88276	0,0569352	95,68215	259,6528	0,4067724	0,5309223	8,20E-15
2202-35A	CPV-16-409	34,20865	0,130074	96,43758	261,9796	0,9281304	0,9898432	3,38E-15
2202-36A	CPV-16-409	33,99662	0,2892059	95,45732	260,4661	2,065308	2,093464	1,50E-15
2202-37A	CPV-16-409	34,44682	0,1389681	98,43473	263,6783	0,9906738	1,049395	3,32E-15
2202-38A	CPV-16-409	32,36029	0,1632391	92,02963	248,7431	1,173232	1,218168	2,71E-15

2202-39A	CPV-16-409	34,5079	0,0642669	98,67512	264,1137	0,4580356	0,5744211	7,33E-15
2202-40A	CPV-16-409	32,7589	0,1786304	93,22463	251,6057	1,281846	1,323975	2,51E-15
2202-41A	CPV-16-409	34,05748	0,1661999	96,48487	260,9006	1,186603	1,235105	2,63E-15
2202-42A	CPV-16-409	33,59865	0,2418675	91,37934	257,6219	1,729937	1,762784	1,79E-15
2202-43A	CPV-16-409	34,25197	0,0517835	96,60807	262,2887	0,3694341	0,5050792	9,26E-15
2202-44A	CPV-16-409	33,98534	0,1424876	96,74066	260,3855	1,017593	1,073556	3,20E-15
2202-45A	CPV-16-409	32,17356	0,2366772	93,51559	247,4005	1,702294	1,733259	1,82E-15
2202-46A	CPV-16-409	34,55661	0,2562573	98,15717	264,4608	1,826022	1,858713	1,71E-15
2202-47A	CPV-16-409	28,84566	0,7839933	74,33585	223,3068	5,713576	5,721254	4,70E-16
2202-48A	CPV-16-409	34,32095	0,1826965	96,13913	262,7807	1,303043	1,347946	2,52E-15
2202-49A	CPV-16-409	34,35059	0,0448951	97,97762	262,9922	0,3201675	0,4708749	1,07E-14
2202-50A	CPV-16-409	31,18296	0,2390356	95,30411	240,2617	1,725977	1,75491	1,75E-15
2202-51A	CPV-16-409	33,90551	0,0863113	97,01115	259,8153	0,6165945	0,7047973	5,28E-15
2202-52A	CPV-16-409	28,03294	0,4025712	85,64189	217,3743	2,943378	2,957521	9,51E-16
2202-53A	CPV-16-409	33,99441	0,0944139	95,19808	260,4503	0,6742445	0,7560998	4,95E-15
2202-54A	CPV-16-409	30,4101	0,4114399	85,73686	234,6728	2,979922	2,996048	9,47E-16
2202-55A	CPV-16-409	34,53621	0,1121859	98,37546	264,3154	0,7994711	0,8714859	3,97E-15
2202-56A	CPV-16-409	32,82231	0,0971771	95,41472	252,0607	0,6971663	0,7721352	4,55E-15
2202-57A	CPV-16-409	34,189	0,2121071	96,51668	261,8394	1,513586	1,552156	2,05E-15
2202-58A	CPV-16-409	33,54902	0,0638958	94,44293	257,2668	0,4570982	0,5686558	7,13E-15
2202-59A	CPV-16-409	34,95715	0,1278854	99,40213	267,3127	0,9098592	0,9750515	3,49E-15
2202-60A	CPV-16-409	33,38738	0,0670639	96,65332	256,1102	0,4800649	0,5864609	6,82E-15
2202-61A	CPV-16-409	33,85245	0,0959571	95,94313	259,4362	0,6856451	0,7657306	4,82E-15
2202-62A	CPV-16-409	30,83428	0,0749643	92,97598	237,7423	0,5420313	0,6265328	5,59E-15
2202-63A	CPV-16-409	31,44621	0,123422	89,18226	242,1616	0,8902539	0,945918	3,51E-15
2202-64A	CPV-16-409	34,2216	0,0716197	97,92376	262,072	0,5110098	0,6160943	6,52E-15
2202-65A	CPV-16-409	34,16034	0,0857932	95,96303	261,6349	0,6122846	0,7021157	5,36E-15
2202-66A	CPV-16-409	33,63823	0,0737162	97,16972	257,9049	0,5271671	0,6267895	6,26E-15
2202-67A	CPV-16-409	33,95959	0,1674844	97,14801	260,2016	1,196231	1,244123	2,72E-15
2202-68A	CPV-16-409	34,00807	0,2160205	98,19347	260,5478	1,5426	1,58012	2,11E-15
2202-69A	CPV-16-409	34,71607	0,1476335	98,25306	265,5967	1,051345	1,107586	3,16E-15
2202-70A	CPV-16-409	33,77599	0,0839972	97,08745	258,8898	0,6003669	0,6900863	5,49E-15
2202-71A	CPV-16-409	34,30394	0,1563891	97,49738	262,6594	1,115485	1,16758	2,81E-15
2202-72A	CPV-16-409	31,89944	0,033965	94,08779	245,4279	0,244556	0,4057206	1,33E-14
2202-73A	CPV-16-409	29,78996	0,1897688	91,36998	230,1758	1,377813	1,411136	2,09E-15
2202-74A	CPV-16-409	34,33332	0,1588642	96,87635	262,869	1,13301	1,184409	2,94E-15
2202-75A	CPV-16-409	31,52007	0,3974135	91,5062	242,6943	2,865746	2,883596	1,01E-15
2202-76A	CPV-16-409	33,24742	0,1090631	95,11928	255,108	0,7811366	0,8501896	3,96E-15
2202-77A	CPV-16-409	33,76338	0,2990869	96,46843	258,7997	2,137817	2,164709	1,45E-15
2202-78A	CPV-16-409	34,13346	0,1119148	98,39464	261,443	0,7987916	0,8694717	4,15E-15
2202-79A	CPV-16-409	34,38963	0,7154431	97,39008	263,2705	5,101377	5,113071	6,13E-16
2202-80A	CPV-16-409	34,14324	0,1323326	98,30415	261,5128	0,9444872	1,005001	3,46E-15
2202-81A	CPV-16-409	33,73267	0,0750615	97,17354	258,5801	0,5365897	0,6351768	6,05E-15
2202-82A	CPV-16-409	33,88676	0,0802068	96,24109	259,6813	0,5730272	0,6669324	5,78E-15
2202-83A	CPV-16-409	34,87032	0,1525482	99,02711	266,6948	1,085692	1,14065	3,11E-15
2202-84A	CPV-16-409	34,48024	0,0841404	98,0928	263,9165	0,5997407	0,692593	5,25E-15
2202-85A	CPV-16-409	35,57636	0,8202555	99,00443	271,7129	5,821811	5,832679	5,53E-16
2202-86A	CPV-16-409	34,56548	0,1504279	98,48072	264,524	1,071873	1,126686	2,94E-15
2202-87A	CPV-16-409	31,18821	2,158729	99,54583	240,2997	15,58696	15,59019	1,84E-16
2201-01A	CPV-16-411	31,05073	0,1069829	96,75169	239,3068	0,7728823	0,8350525	3,96E-15
2201-02A	CPV-16-411	34,54837	0,0418784	98,45315	264,4021	0,2984243	0,4576725	1,13E-14
2201-03A	CPV-16-411	10,36458	0,0294838	79,14691	83,40724	0,2319411	0,2588504	5,64E-15
2201-04A	CPV-16-411	13,59999	0,0362681	86,99504	108,6839	0,2813976	0,3182832	5,41E-15
2201-05A	CPV-16-411	28,48264	0,0559213	96,13985	220,6592	0,4081327	0,502412	6,89E-15

2201-06A	CPV-16-411	16,56833	0,9633718	69,82121	131,5711	7,381733	7,383901	2,20E-16
2201-07A	CPV-16-411	11,62049	0,0323527	67,54997	93,26057	0,2531432	0,2837343	8,78E-15
2201-08A	CPV-16-411	11,88025	0,0290548	71,72559	95,29195	0,2270867	0,2621	1,01E-14
2201-09A	CPV-16-411	31,7343	0,0746867	97,24134	244,2384	0,5381108	0,62723	5,81E-15
2201-10A	CPV-16-411	12,27481	0,0455638	70,14604	98,37315	0,3555185	0,3802849	4,38E-15
2201-11A	CPV-16-411	35,11664	0,0441345	98,73259	268,447	0,3138068	0,4715152	1,09E-14
2201-12A	CPV-16-411	10,15352	0,0521752	84,45557	81,74618	0,4108199	0,4259936	2,72E-15
2201-13A	CPV-16-411	10,42683	0,1041653	67,4317	83,89694	0,8192197	0,827333	1,42E-15
2201-14A	CPV-16-411	10,9749	0,0381139	73,46993	88,20222	0,2990469	0,3227378	4,56E-15
2201-15A	CPV-16-411	11,74871	0,0339941	67,75612	94,26355	0,2658407	0,2957042	6,71E-15
2201-16A	CPV-16-411	13,60492	0,0458969	82,22612	108,7222	0,3560982	0,3859283	4,11E-15
2201-17A	CPV-16-411	11,88208	0,0410674	69,4494	95,30628	0,320972	0,3466353	5,00E-15
2201-18A	CPV-16-411	9,562026	0,039047	73,38145	77,08289	0,3082348	0,3260789	3,63E-15
2201-19A	CPV-16-411	12,45253	0,0554206	79,3606	99,75932	0,4321001	0,4532513	3,26E-15
2201-20A	CPV-16-411	11,53812	0,0358601	83,48219	92,61598	0,2806857	0,3082005	4,74E-15
2201-21A	CPV-16-411	11,28579	0,0510427	52,6683	90,63986	0,3999548	0,4189266	6,78E-15
2201-22A	CPV-16-411	8,924076	0,0229842	68,99788	72,04	0,1819364	0,2073986	8,89E-15
2201-23A	CPV-16-411	11,9451	0,0408193	61,90344	95,79874	0,318947	0,3450118	5,99E-15
2201-24A	CPV-16-411	11,79189	0,0441758	79,17699	94,60122	0,3453994	0,3690362	3,96E-15
2201-25A	CPV-16-411	14,08546	0,057588	69,96802	112,4468	0,4458972	0,4716502	3,81E-15
2201-26A	CPV-16-411	11,13925	0,0437809	74,10038	89,49124	0,3432693	0,3646747	3,97E-15
2201-27A	CPV-16-411	11,84017	0,0532154	69,83243	94,97868	0,4159923	0,435968	3,29E-15
2201-28A	CPV-16-411	13,88367	0,0547151	79,75544	110,8837	0,4240142	0,4503163	3,49E-15
2201-29A	CPV-16-411	33,20203	0,0890585	97,18342	254,7829	0,6379721	0,7206864	5,09E-15
2201-30A	CPV-16-411	31,01277	0,033456	98,5833	239,0324	0,241734	0,3977266	1,27E-14
2201-31A	CPV-16-411	10,32525	0,0146237	79,21956	83,09782	0,1150599	0,162327	1,55E-14
2201-32A	CPV-16-411	10,67084	0,0318403	71,43016	85,81491	0,2501493	0,2766529	5,86E-15
2201-33A	CPV-16-411	11,07824	0,0180153	76,23068	89,01285	0,1412881	0,1869717	1,39E-14
2201-34A	CPV-16-411	11,31867	0,0455119	86,35278	90,8975	0,3565671	0,3778385	3,48E-15
2201-35A	CPV-16-411	10,71756	0,0490656	67,77964	86,18195	0,3854001	0,4032521	3,24E-15
2201-36A	CPV-16-411	9,487899	0,0432123	71,64575	76,49764	0,341225	0,3571912	3,39E-15
2201-37A	CPV-16-411	9,620414	0,0387288	64,92343	77,54374	0,3056463	0,3238384	4,31E-15
2201-38A	CPV-16-411	11,272	0,0415603	82,85414	90,53177	0,3256729	0,3486579	3,71E-15
2201-39A	CPV-16-411	11,42925	0,0250346	72,10513	91,76359	0,196043	0,2331231	1,21E-14
2201-40A	CPV-16-411	11,51816	0,0637658	47,0686	92,45971	0,4991528	0,5150761	5,56E-15
2201-41A	CPV-16-411	11,99189	0,0358351	65,94635	96,16428	0,2799468	0,3095239	6,69E-15
2201-42A	CPV-16-411	11,26323	0,0218579	81,35558	90,46307	0,171288	0,2116982	8,54E-15
2201-43A	CPV-16-411	12,2114	0,0634552	84,37131	97,87829	0,4952531	0,5131478	2,58E-15
2201-44A	CPV-16-411	12,34332	0,0549475	78,60442	98,90764	0,4286106	0,4495814	3,27E-15
2201-45A	CPV-16-411	28,40479	0,1116152	94,37245	220,091	0,8148582	0,8656927	3,48E-15
2201-46A	CPV-16-411	11,30935	0,1950036	40,74011	90,82443	1,527834	1,53293	9,83E-16
2201-47A	CPV-16-411	9,99522	0,0355229	64,70909	80,49931	0,279893	0,3011006	6,34E-15
2201-48A	CPV-16-411	35,75584	0,0933293	98,7921	272,9863	0,6619493	0,752292	5,22E-15
2201-49A	CPV-16-411	14,84884	0,0664285	90,31448	118,348	0,5126923	0,537536	3,10E-15
2201-50A	CPV-16-411	12,78597	0,0319223	79,04463	102,3572	0,2485371	0,2854073	6,33E-15
2201-51A	CPV-16-411	10,70079	0,0469249	61,28154	86,05023	0,3686122	0,3871846	4,09E-15
2201-52A	CPV-16-411	12,56643	0,0799289	84,50982	100,6472	0,6228828	0,6379929	2,06E-15
2201-53A	CPV-16-411	12,31538	0,0764787	73,50317	98,68964	0,5966332	0,6118077	2,34E-15
2201-54A	CPV-16-411	11,65596	0,0336501	63,69109	93,53807	0,2632545	0,2929538	8,27E-15
2201-55A	CPV-16-411	11,98482	0,0625595	65,59904	96,10908	0,488734	0,5062373	2,93E-15
2201-56A	CPV-16-411	12,08781	0,0993789	75,90685	96,91346	0,7760379	0,7873596	1,72E-15
2201-57A	CPV-16-411	11,27199	0,0461538	82,49132	90,53173	0,3616681	0,3824962	3,32E-15
2201-58A	CPV-16-411	11,68343	0,0726616	56,79753	93,75302	0,568386	0,5827999	2,84E-15
2201-59A	CPV-16-411	34,35452	0,1494517	98,6412	263,0202	1,065792	1,120336	2,92E-15

2201-60A	CPV-16-411	9,525073	0,0293635	72,10088	76,79116	0,2318306	0,2549126	6,65E-15
2201-61A	CPV-16-411	12,49579	0,0576393	80,71948	100,0966	0,449316	0,469824	2,92E-15
2201-62A	CPV-16-411	12,89636	0,0859339	82,14796	103,2165	0,6687403	0,683537	1,98E-15
2201-63A	CPV-16-411	11,08564	0,0537278	68,30114	89,07087	0,4213554	0,4388115	3,16E-15
2201-64A	CPV-16-411	11,95416	0,0476456	76,64792	95,86949	0,3722706	0,3948623	3,75E-15
2201-65A	CPV-16-411	9,87027	0,070839	68,62355	79,51454	0,5584572	0,5691245	2,07E-15
2201-66A	CPV-16-411	11,35775	0,0639129	65,95945	91,20363	0,5006478	0,5161133	3,08E-15
2201-67A	CPV-16-411	11,37637	0,0391188	74,26938	91,34951	0,3064041	0,3311454	4,57E-15
2201-68A	CPV-16-411	11,18939	0,0304439	82,03401	89,88438	0,2386478	0,2687689	5,57E-15
2201-69A	CPV-16-411	13,49676	0,1639471	72,52807	107,8829	1,272592	1,28113	1,08E-15
2201-70A	CPV-16-411	33,80238	0,0963956	98,16514	259,0784	0,6889131	0,7684641	4,86E-15
2201-71A	CPV-16-411	10,64342	0,0361366	79,83754	85,59954	0,2839359	0,3074302	4,91E-15
2201-72A	CPV-16-411	11,38512	0,0443376	88,26151	91,41804	0,3472681	0,3693129	3,63E-15
2201-73A	CPV-16-411	13,70922	0,0717635	81,74839	109,5313	0,5565417	0,5763629	2,73E-15
2201-74A	CPV-16-411	12,42757	0,1057462	77,49861	99,56468	0,8245635	0,8357992	1,61E-15
2201-75A	CPV-16-411	9,095438	0,0282487	67,26824	73,39596	0,2234432	0,2453758	7,76E-15
2201-76A	CPV-16-411	11,57601	0,0741978	72,01791	92,91253	0,5806697	0,5945432	2,14E-15
2201-77A	CPV-16-411	11,41699	0,1389704	86,91923	91,66764	1,088318	1,09559	1,07E-15
2201-78A	CPV-16-411	12,37753	0,078667	83,79436	99,17446	0,6135425	0,6284485	2,07E-15
2201-79A	CPV-16-411	12,23495	0,0405891	73,90769	98,06208	0,3167564	0,3441595	4,79E-15
2201-80A	CPV-16-411	9,95434	0,0259812	75,32358	80,17718	0,2047482	0,2326951	7,94E-15
2201-81A	CPV-16-411	25,73456	0,0923107	77,66039	200,4922	0,6811795	0,7318788	4,06E-15
2201-82A	CPV-16-411	33,92107	0,300709	92,23576	259,9265	2,148089	2,17507	1,45E-15
2201-83A	CPV-16-411	13,44141	0,1701861	82,1797	107,4532	1,321331	1,329493	1,03E-15
2201-84A	CPV-16-411	9,86036	0,0577269	71,48238	79,43641	0,4551078	0,4681113	2,39E-15
2201-85A	CPV-16-411	12,576	0,0673191	70,78765	100,7218	0,5245936	0,5424738	3,05E-15
2201-86A	CPV-16-411	12,44506	0,1163544	60,15761	99,70104	0,9072143	0,9174654	1,62E-15
2201-87A	CPV-16-411	11,95206	0,1155782	50,60323	95,85309	0,9030589	0,9126009	1,53E-15
2198-01A	FCs-F1	3,454071	0,0018525	99,86439	28,22049	0,0150191	0,0422318	3,12E-14
2198-02A	FCs-F1	3,446794	0,0029036	99,79184	28,16149	0,023542	0,0458881	2,16E-14
2198-03A	FCs-F1	3,451735	0,0093887	99,22967	28,20155	0,0761201	0,085733	7,49E-15
2198-04A	FCs-F1	3,450403	0,0022467	99,82388	28,19075	0,0182153	0,0434338	2,52E-14
2198-05A	FCs-F1	3,449916	0,0035934	99,82729	28,18681	0,029134	0,049021	1,43E-14
2198-06A	FCs-F1	3,448762	0,0098422	99,71277	28,17745	0,0797978	0,0889996	5,08E-15
2198-07A	FCs-F1	3,461679	0,0056366	99,74498	28,28218	0,0456978	0,0604401	9,91E-15
2198-08A	FCs-F1	3,500607	0,0025268	98,26737	28,59775	0,0204816	0,0449339	2,25E-14
2198-09A	FCs-F1	3,53714	0,0030186	98,41962	28,89385	0,0244644	0,0472345	1,85E-14
2198-10A	FCs-F1	3,49436	0,0090503	92,90554	28,54711	0,0733623	0,0835223	6,07E-15
2198-11A	FCs-F1	3,620935	0,0101737	96,83271	29,57285	0,0824231	0,0922125	5,29E-15
2198-12A	FCs-F1	3,931592	0,0130497	98,5329	32,08792	0,1055779	0,1147026	4,24E-15
2198-13A	FCs-F1	3,521743	0,0026438	96,65986	28,76907	0,0214285	0,045583	2,42E-14
2198-14A	FCs-F1	3,519421	0,0109184	98,19612	28,75024	0,0884959	0,097201	4,73E-15
2198-15A	FCs-F1	3,570393	0,0058222	98,8003	29,16334	0,0471794	0,0623605	9,84E-15

The Early Stages of the Magmatic Arc in the Southern Central Andes

Verónica Oliveros, Javiera González, Mauricio Espinoza Vargas, Paulina Vásquez, Pablo Rossel, Christian Creixell, Fernando Sepúlveda and Francisco Bastias

Abstract A temporal and tectonic framework for the initiation of the Andean magmatism at its earliest stages is presented in this work, based on the current geological, geochemical, and geochronological information available in northern Chile between 20º and 30º S. This information has been collected from Triassic and Jurassic plutonic, volcanic, and volcanosedimentary units cropping out at the Coastal, Domeyko, Frontal Cordilleras, and the Precordillera, as two roughly parallel belts that extend for more than 1,000 km in the Chilean territory. Petrological and geochemical data suggest that the magmatism during the Triassic and Jurassic was dominantly intermediate in composition and had arc or subduction affinities. Even though magma sources should have had a clear mantle component, a crustal influence was more important during the Triassic. Geochronological information shows a significant magmatic lull near the Triassic–Jurassic boundary, associated with the retraction of the arc to the present-day Coastal Cordillera. Based on these data, the early stages of the Andean magmatism can be tracked backup to the Triassic igneous units in northern Chile.

Keywords Andes · Jurassic · Triassic · Arc

V. Oliveros (✉) · J. González · M. Espinoza Vargas · F. Sepúlveda · F. Bastias
Departamento de Ciencias de la Tierra, Universidad de Concepción, Casilla 160-C, Concepción, Chile
e-mail: voliveros@udec.cl

P. Vásquez · C. Creixell
Servicio Nacional de Geología y Minería, Av. Santa María 0140, Providencia, Santiago, Chile

P. Rossel
Universidad Andres Bello, Autopista Concepción-Talcahuano 7100, Concepción, Chile

165

238

1   Introduction

For the last decades, the Lower Jurassic volcanic deposits of the Coastal Cordillera between 18° and 30° S were considered the earliest volcanic products of the Andean arc (García 1967; Rogers and Hawkesworth 1989), produced by subduction of an oceanic plate under the continent after a period of within-plate extension and rifting of the western margin of the South American during the Late Permian to Early Jurassic (Charrier et al. 2007; Mpodozis and Ramos 1989, 2008). Consequently, the onset of Andean subduction would have taken place roughly at 200 Ma. After this, the voluminous magmatism developed during the Jurassic to Early Cretaceous in the Coastal Cordillera of southern Peru and northern central Chile was mainly produced during a protracted transtensional tectonic regime (Charrier et al. 2007; Scheuber and González 1999). The oblique subduction of the Phoenix plate under the continent resulted in a rollback of the oceanic plate, retreat of the trench, and progressive thinning of the continental crust (Charrier et al. 2007). This paleogeographic configuration was characterized by intensive volcanism and plutonism in the arc region (the present-day Coastal Cordillera from 17° to 35° S) and along strike back-arc extension (Mpodozis and Ramos 1989).

Contrastingly, the Permian to Triassic period for the southwestern Gondwana margin was associated with a significant magmatic lull resulting from the lack of subduction and related to the orogenic collapse that followed the Permian "San Rafael" contractional event (Mpodozis and Ramos 1989; Nasi et al. 1990; Mpodozis and Kay 1992; Kleiman and Japas 2009). In this context, the magmatic sources would have changed significantly, decreasing the crustal component, between the Late Permian and the Early Jurassic (Mpodozis and Kay 1992; Hervé et al. 2014). However, recent works dealing with igneous units in the Frontal and Coastal Cordilleras of Chile and westernmost Argentina have failed to sustain the model in which subduction ceased for most of the Triassic and instead have proposed a setting characterized by an extensional overriding plate in an active subduction setting (Vásquez et al. 2011; del Rey et al. 2016; Coloma et al. 2017).

In this chapter, we present a compilation of geological, geochemical, and geochronological data for Triassic and Jurassic (ca. 250–150 Ma) volcanic, volcanosedimentary, and plutonic rocks cropping out in the Coastal, Domeyko, and Frontal Cordilleras of northern Chile between 20° S and 30° S. We critically review these existing data with the aim of establishing the initiation of the Andean volcanic arc and the overall tectonic setting in the continental margin for the aforementioned period.

2   Geological Framework for the Early Andes

Thanks to the semiarid climate of the present-day forearc region, the Triassic and Jurassic magmatic rocks are well exposed in northern Chile, where Cretaceous to Cenozoic deformation exhumed upper crustal plutonic roots (Mpodozis and

Ramos 1989) (see Chap. "Mechanisms and Episodes of Deformation Along the Chilean–Pampean Flat-Slab Subduction Segment of the Central Andes in Northern Chile"). Different morphostructural systems in this part of the margin are N-oriented and vary in number and surficial expression along strike in response to the Chilean–Pampean flat subduction segment between 26°–30° S (Fig. 1). The westernmost system is the Coastal Cordillera that limits to the east with the central depression north of the flat subduction segment at 26° S. South of this latitude, this low-relief zone is absent and a series of E-incised valleys cut several minor mountain systems. To the east, the Domeyko Cordillera (22°–26° S) and Precordillera (26°–30° S) constitute a series of fault-bounded ranges exposing mostly Mesozoic stratified rocks and a Paleozoic basement. South of 26° S, the Frontal Cordillera considered a product of the flat subduction segment is a thick-skinned system that exposes deep Paleozoic plutonic and metamorphic rocks, covered by Mesozoic and Cenozoic volcanic and sedimentary sequences.

The studied Triassic rocks crop out mainly in the Precordillera/Domeyko and Frontal Cordilleras. Plutonic rocks correspond to middle and upper crustal intrusions that form the Montosa–Chollay Batholith between 27° and 30° S. Volcanic and volcanosedimentary rocks crop out as tilted and folded sequences that overlie the Paleozoic plutonic rocks and underlie Jurassic marine or continental sequences between 24° and 30° S (SERNAGEOMIN 2002; Salazar et al. 2013). These rocks are commonly crosscut by numerous Mesozoic dykes and less often intruded by Cenozoic plutons (Parada et al. 1991; Creixell et al. 2009; Salazar et al. 2013). Triassic rocks in the Coastal Cordillera are volumetrically restricted, although recent works indicate that these units are more widely exposed than previously thought, particularly at 20°–22° S and 25°–26° S (Sepúlveda et al. 2014; Álvarez et al. 2016). Volcanic and volcanosedimentary rocks crop out as relatively restricted homoclinal sequences, spatially associated with, although not controlled by, the N-S trending Atacama Fault System (AFS), a 1,000 km trench–parallel structure segmented by minor oblique NW-structures that accommodated strike–slip displacements during the Mesozoic (Espinoza et al. 2015), whereas the Triassic intrusions consist mostly of minor plutons and plutonic complexes at 26°30′ and 28° S (Fig. 1). These rocks overlie and intrude the Late Paleozoic Chañaral Epimetamorphic Complex and other Permian igneous units (Marinovic et al. 1995; Godoy and Lara 1998; Creixell et al. 2016). During this period, the dominant crustal stress was extensional, which led to the deposition of volcanosedimentary sequences in NW-oriented basins (Charrier et al. 2007). Fault-bounded Triassic plutonic complexes also denote extensional conditions during their emplacement (Grocott et al. 2009), while a roughly N-trending Middle Triassic mylonitic belt recognized along the Frontal Cordillera at 29° S indicates deep-seated deformation under sinistral transtensional conditions (Murillo et al. 2013). Additionally, an exhumation event would have taken place during the Middle to Late Triassic (Salazar et al. 2013; Kato and Godoy 2015).

Contrastingly, the Jurassic volcanic and plutonic rocks are widely exposed in the Coastal Cordillera between 20° and 28° S, in close relation to the AFS. The main geological units that represent the magmatic arc are the La Negra Formation, a thick
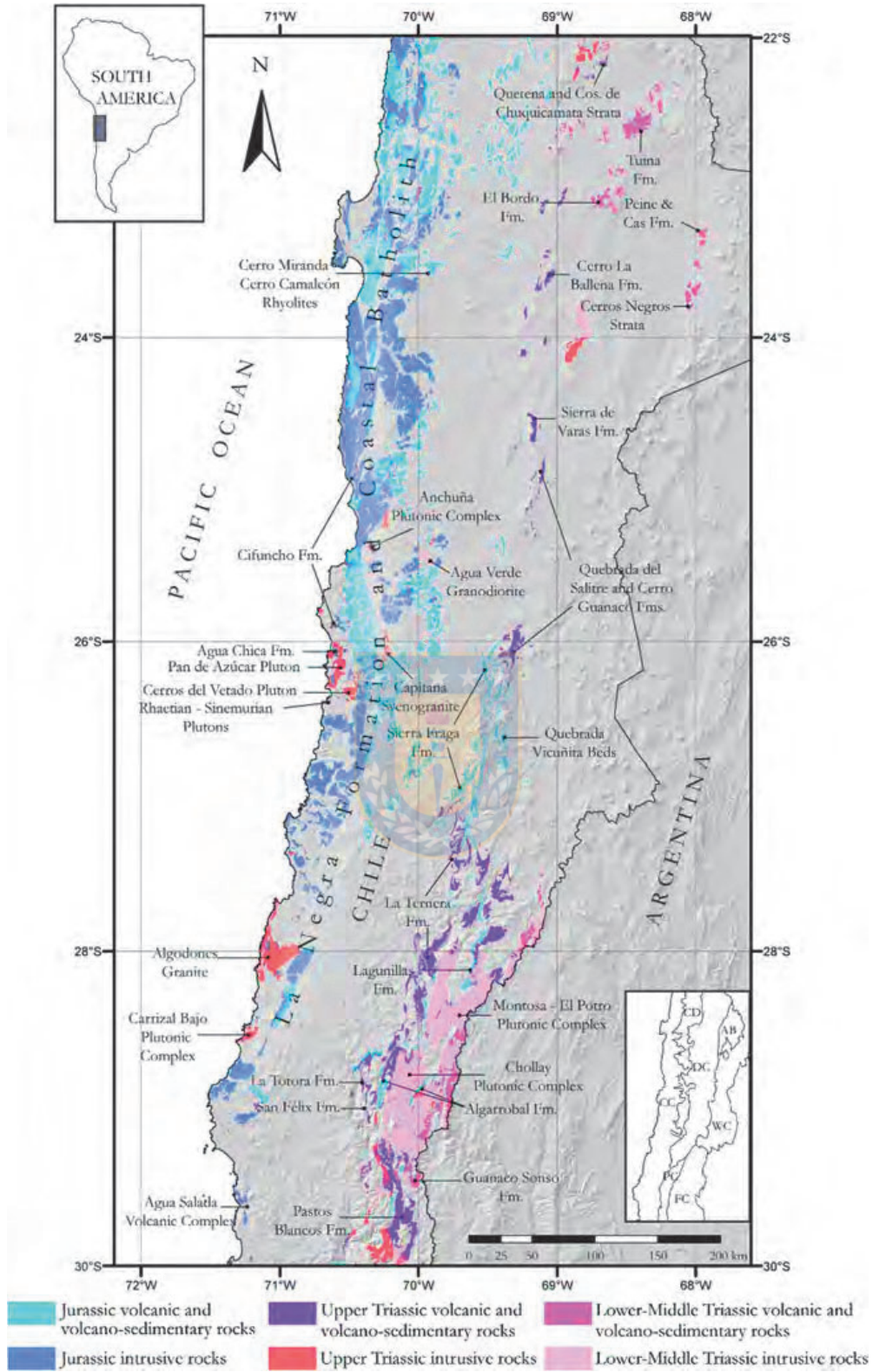
Fig. 1 Location of the outcrops of Triassic and Jurassic igneous rocks in the Southern Central Andes between 22° and 30° S. The inset shows the present-day morphotectonic units at these latitudes (CC: Coastal Cordillera; CD: Central Depression; DC: Domeyko Cordillera; PC: Precordillera; AB: Salar de Atacama Basin; FC: Frontal Cordillera and WC: Western Cordillera). The simplified geological map is based on the recently updated cartography done by the Chilean Geological and Mining Survey. For specific references see the text

241

homoclinal volcanic sequence, and the Coastal Batholith (Fig. 2). Marine sedimentary beds representing the back-arc domain are exposed in the eastern flank of the Coastal Cordillera, in the central depression and in the Domeyko Cordillera at the same latitudes (SERNAGEOMIN 2002; Vicente 2006). A more restricted belt of Jurassic volcanosedimentary units is exposed in the Precordillera and Domeyko Cordillera between 25° and 30° S. Structural studies carried out between 23° and 28° S suggest that throughout the Jurassic the subduction system developed under an extensional regime that later shifted to a transtensional setting (Scheuber and González 1999). The arc zone accommodated most of the extensional deformation, as evidenced by the structures observed in syntectonic plutonic bodies that were intruded at relatively deep crustal levels, whereas the back-arc basins were submitted to a slow thermal subsidence (Scheuber and González 1999; Grocott and Taylor 2002). A short episode of transpressive deformation has been detected along the Jurassic arc south of 31° S (Creixell et al. 2011; Ring et al. 2012), but this has not been documented north of that latitude. The shift from extensional to transtensional conditions would have occurred likely at the Jurassic–Cretaceous boundary (Scheuber and González 1999; Grocott and Taylor 2002) followed by the main phase of transtensive and transpressive deformation in the AFS at ∼135–120 Ma (Scheuber and González 1999; Arévalo and Creixell 2009). The magmatic arc and associated rift system were aborted after ca. 118–106 Ma, when the magma foci shifted to the east and a compressive tectonic regime started during the Late Cretaceous (Grocott and Taylor 2002; Escribano et al. 2013;
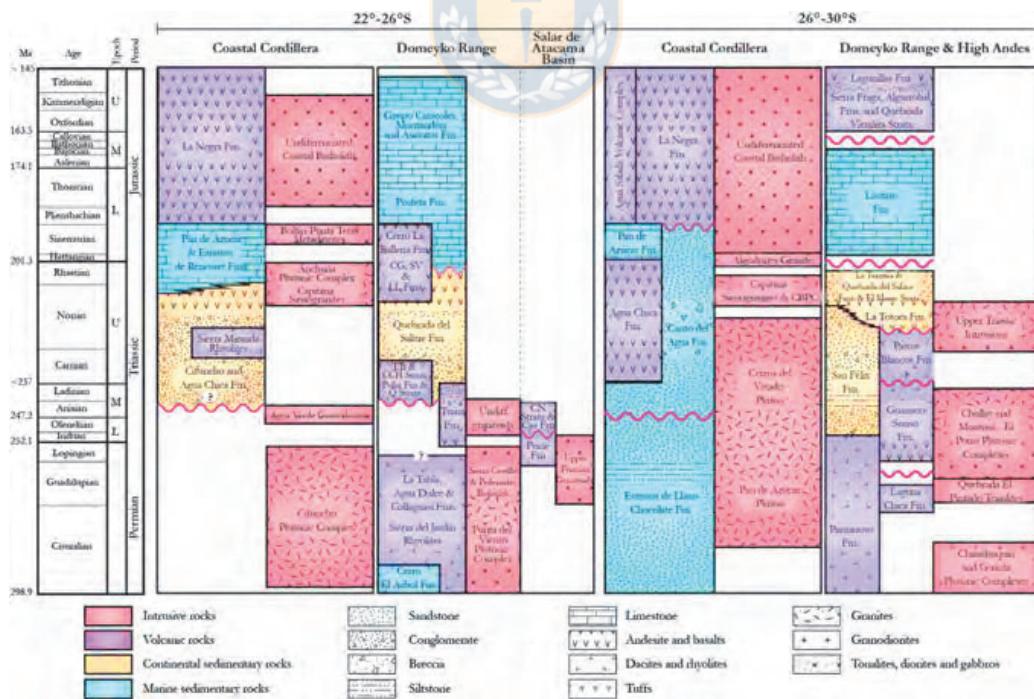
Fig. 2 Chronostratigraphic chart with Triassic and Jurassic rocks in the studied segments and morphotectonic units. Based on the recently updated cartography done by the Chilean Geological and Mining Survey. For specific references see the text

Sepúlveda et al. 2014) (see Chap. "Mechanisms and Episodes of Deformation Along the Chilean–Pampean Flat-Slab Subduction Segment of the Central Andes in Northern Chile").

3 Petrography and Geology of the Triassic–Jurassic Igneous Units in Northern Chile

3.1 Triassic–Jurassic Igneous Units Between 20° and 22° S

The studied volcanic units in this segment are as follows: Sierra de Lagunas Beds (Upper Triassic–Lower Jurassic), Oficina Viz Formation (Toarcian–Bajocian), and the volcanic facies from the Huantajaya Group corresponding to the Caleta Lígate Formation (Bajocian) and the El Godo Formation (Bajocian–Oxfordian). Sierra de Lagunas Beds are exposed in both Coastal Cordillera and Precordillera, whereas in the Precordillera, volcanic formations younger than Lower Jurassic are absent.

Sierra de Lagunas Beds and Oficina Viz Formation consist in monotonous homoclinal sequences of subaereous andesitic to basaltic andesitic lava flows and minor pyroclastic rocks in the Sierra de Lagunas Beds. The contact relation between these units is unclear because of late tectonic deformation. Additionally, a plutonic event took place at 180–175 Ma, represented by the Vetarrón Monzonite, which intruded the Sierra de Lagunas Beds (Sepúlveda et al. 2014). The Sierra de Lagunas Beds are located at the central and eastern portion of the Coastal Cordillera and are composed of porphyritic andesitic and basaltic andesitic lavas with a total thickness of 2,250 m. These lavas are dark gray and contain scarce lenses of laminated sandstone and crystal and lithic tuffs. Locally, they vary to amygdule-bearing and red-colored glassy andesitic lavas. Along the Precordillera, Tomlinson et al. (2015) recognized this unit as composed of massive and brecciated pyroxene and horn-blende andesites with porphyritic, glomeroporphyritic and seriate textures, minor lithic tuffs, volcanic and volcanosedimentary breccias, conglomerates, and sand-stones. The Oficina Viz Formation consists mostly in a dark green to gray sequence of aphiric, porphyritic, and amygdaloidal basaltic-andesite and andesite lavas, andesitic volcanic breccias, sandstone lenses, and scarce reddish brown tuff layers, with a minimum thickness of 1,000–1,500 m. Locally, andesitic dykes cut the lava piles (Thomas 1970; Kramer et al. 2005; Sepúlveda et al. 2014). The volcanic rocks are affected by very low-grade metamorphism, but fresh clinopyroxene, plagioclase, and amphibole phenocrysts do occur in most of the lava flows (Oliveros et al. 2006). The Oficina Viz Formation is covered concordantly by the Caleta Lígate Formation with a Bajocian age (Thomas 1970; Kossler 1998; Vásquez and Sepúlveda 2013).

The volcanic lithofacies of Caleta Lígate Formation has been recognized south of Iquique town and consist of pyroclastic breccias, basalts, and tuffs intercalated with fossiliferous sandstones (Kossler 1998; Vásquez and Sepúlveda 2013).

The pyroclastic breccias contain long rhyolithic blocks (juvenile) of decimetric size, and minor centimetric andesitic and sedimentary clasts, both included in a glassy groundmass. The pyroclastic rocks vary from breccias to glassy lapilli tuffs, with "fiamme" structures and lithics fragments mostly of andesitic composition. There are also basaltic lavas with a greenish gray color with pillow tubes. The volcanic rocks of El Godo Formation correspond mainly to basalt and basaltic andesites with pillowed or brecciated structure. Locally, olistoliths, humid intrusive dikes, and peperites associated with subaqueous lapilli tuffs, denote that volcanism interacted with water-rich sediments. Andesites and basalts have subophitic and porphyritic texture with plagioclase, pyroxene, and minor amphibole phenocrysts, in a crystal-bearing glassy groundmass. The volcanic rocks associated with the Huantajaya Group were deposited in a submarine environment, intercalated in marine sedimentary rocks, while their ages have been determined on the base of the fossiliferous content and radiometric dating (Thomas 1970; Kossler 1998; Marquardt et al. 2008; Vásquez and Sepúlveda 2013). Both formations are unconformably covered by the Lower Cretaceous Punta Barranco Formation.

3.2 Triassic–Jurassic Igneous Units Between 22° and 26° S

In addition to the two morphostructural units where the Triassic rocks usually crop out in northern Chile, the Triassic rocks are also found in the vicinity of the Salar de Atacama basin in this segment (Figs. 1 and 2). Near the Peine locality, volcanic sequences of reddish and greenish andesitic lava flows and breccias, vitric and crystalline tuffs, interbedded with conglomeratic sedimentary rocks are grouped in the Peine Formation (Upper Permian?—Middle Triassic). This unit is unconformably overlain by porphyritic andesitic lavas and breccias and dacitic agglomerates of the Cas Formation (Niemeyer 2013). Partially coetaneous andesitic volcanism and continental sedimentation in fluvial systems are represented by the volcanosedimentary sequences of the Cerros Negros Beds (Lower Triassic) (Niemeyer 2013) (Fig. 2).

In the Domeyko Cordillera, the Triassic units also represent volcanic activity and continental sedimentation, where they unconformably overlie Carboniferous to Lower Permian strata. Near the city of Calama, the Quetena Beds composed of conglomerates and sandstones (Middle Triassic) (Tomlinson et al. 2010) are overlain by the andesitic lavas, with minor dacitic and rhyolitic rocks, of the Chuquicamata Beds (Carnian) (Tomlinson and Blanco 2008) (Fig. 2). The latter sequence is intruded by small granodiorites plutons of Carnian age (Proffett and Dilles 2007; Tomlinson et al. 2010). In the eastern flank of the Domeyko Cordillera, the Tuina Formation crops out, which is composed of andesitic lava flows and minor dacites and rhyolites (Lopingian—Middle Triassic) (Henríquez et al. 2014). Also in this flank, andesitic and dacitic lava flows are interbedded with lacustrine deposits that correspond to the El Bordo Beds (Middle Triassic) (Basso and Mpodozis 2012) and their equivalents further south in Sierra Mariposas and Imilac

(Cortés 2012; Solari et al. 2015). In the southern part of the Domeyko Cordillera, the Exploradora, Vaquillas, and Castillo ranges, Triassic sequences of the vol-canosedimentary Quebrada del Salitre Formation crop out extensivelly (Middle?—Upper Triassic) (Fig. 2). Its lower member is composed of basaltic lava flows, dacites, and pyroclastic and volcanoclastic rocks interbedded with sedimentary rocks that represent an alluvial–fluvial environment (Mpodozis and Cornejo 1997; Venegas et al. 2013), and it is intruded by rhyolitic domes dated at ca. 232 Ma (Cornejo et al. 1998, 2009). Its upper member (Norian-Rhaetian) is composed of thick piles of andesitic and dacitic lava flows, breccias, and tuffs, interbedded with fluvial and alluvial sedimentary strata that grade into shallow marine beds that mark an important transgression in the area (Venegas et al. 2013; Espinoza et al. 2015), which lasted until the Middle Jurassic and is represented by units such as the Rencoret Beds and Profeta Formation (Chong 1973; Tobar 1966; Marinovic 2007; Cornejo et al. 1998, 2009). Other units, with similar composition to the Quebrada del Salitre Formation, that represent significant volcanic activity contemporaneous with lacustrine and alluvial continental sedimentation in the area are the Las Lomas Beds, the Cerro La Ballena, Cerro Guanaco, and Sierra de Varas formations (Norian—Rahetian) (Marinovic and García 1999; Marinovic 2007; Basso and Mpodozis 2012; González et al. 2015) (Fig. 2).

In the Coastal Cordillera at ~23° S, Triassic volcanic activity is recorded by tuffs and domes of rhyolitic composition and restricted volume (Basso 2004). Further south, a volcanosedimentary sequence that constitutes so far the oldest known Triassic unit (Middle to Upper Triassic) in the coast of northern Chile crops out near the Paposo town (Álvarez et al. 2016). It has been assigned to the Cifuncho Formation (Álvarez et al. 2016), although the latter is mainly Upper Triassic in age in its type locality, where it is composed mainly by braided fluvial sedimentary and pyroclastic rocks (Contreras et al. 2013). The Agua Chica Formation, the south-ernmost Triassic unit in the Coastal Cordillera, is composed by andesitic lava flows and subvolcanic bodies, interbedded with sandstones and conglomerates repre-senting an alluvial and fluvial environment (Godoy and Lara 1998). Triassic magmatism in the Coastal Cordillera is also represented by small plutons and plutonic complexes, such as the Middle Triassic granodioritic intrusions (Espinoza et al. 2011), the Upper Triassic (Norian) two mica monzo and syenogranites near Taltal (Escribano et al. 2013), and minor tonalitic intrusions in Mejillones (Casquet et al. 2014) (Fig. 2). The Upper Triassic marine transgression identified in the Domeyko Cordillera is also recorded in the Coastal Cordillera by the Rencoret Beds and the Pan de Azúcar Formation (González and Niemeyer 2005; Contreras et al. 2013) (Fig. 2).

3.3 Triassic Igneous Units Between 26° and 30° S

The Triassic igneous units between 26° and 30° S crop out as two roughly sub-parallel belts in the Coastal Cordillera and in the Precordillera/Frontal Cordillera

(Fig. 1). The outcrops in the western belt, in the Coastal Cordillera, are volumetrically more restricted than their eastern counterparts (Fig. 1). Igneous rocks in this belt are mainly plutonic, and they intrude or overlie schists, metasandstones, and metapsamites of the Chañaral Epimetamorphic and Punta de Choros metamorphic complexes (Devonian—Permian) (Godoy and Lara 1998; Creixell et al. 2016). Among these units are the Cerros del Vetado Pluton composed by hornblende and two mica syenogranites and monzogranites (Triassic); the Capitana Syenogranite, a two mica suite of monzo and syenogranites (Norian); the Peralillo, Bufadero, Barquito, and Cerro Castillo plutons, which include biotite and hornblende gneissic granodiorites, diorites and tonalites (with paragneiss inclusions), and monzogranites (Rhaetian—Sinemurian) (Godoy and Lara 1998; Cruden et al. 2004; Espinoza et al. 2014) (Fig. 2). Further south in the Coastal Cordillera, outcrops of the Carrizal Bajo Plutonic Complex (Rhaetian) are composed by a bimodal suite of pyroxene–hornblende–biotite diorites, quartz-diorites and gabbronorites, and biotite–hornblende granites and granodiorites. This complex is intruded by the biotite–hornblende monzogranites and granodiorites of the Algodones Granite (Triassic—Jurassic boundary) (Cruden et al. 2004; Arévalo and Welkner 2008) (Fig. 2).

A small portion of the volcanosedimentary Agua Chica Formation (Upper Triassic) crops out in this segment, and it is composed of andesitic lava flows, crystalline and lithic tuffs, shales and basal conglomerates, and breccias. The beds are interdigitated with the Cifuncho Formation and overlaid by the marine Pan de Azúcar Formation (Godoy and Lara 1998) (Fig. 2). Further south, the Canto del Agua Formation (Middle—Upper Triassic) is exposed in two main depocenters and composed by sandstones, shales, conglomerates, minor calcareous sedimentary rocks and volcanoclastic breccias, and tuffaceous sandstones (Arevalo and Welkner 2008). Most of the sedimentary and volcanic rocks that were exposed in the southern depocenter have been recently assigned to the Carboniferous—Permian Llanos de Chocolate beds based on radiometric ages and fossil content (Welkner et al. 2006; Creixell et al. 2016).

In the Precordillera and Frontal Cordillera, a thick sequence of intermediate to acidic volcanic rocks, the Guanaco Sonso Formation (Lopingian—Middle Triassic), covers a large area near the Chile—Argentina border, overlying the Late Carboniferous basement (Las Placetas Formation). It is composed of andesitic to rhyolitic lavas flows and domes, interbedded with glass and lithic tuffs and a minor proportion of siliciclastic rocks (Ortiz and Merino 2015). This unit is temporal and spatially related to the Chollay Plutonic Complex (Lower—Middle Triassic), a NNE-elongated series of plutonic bodies that along with the Montosa—El Potro Plutonic Complex (Lopingian—Middle Triassic) represent the largest Mesozoic batholith in the Frontal Cordillera, cropping out to the west of the Guanaco Sonso Formation (Fig. 2). This plutonic unit is composed mainly by hornblende–biotite monzogranites, granodiorites and tonalites, with minor amounts of gabbros and syenogranites. It intrudes the Paleozoic metasedimentary sequences and abundant xenoliths of mid-crustal metamorphosed plutonic rocks, known as La Pampa Gneisses, are incorporated in its western flank (Álvarez et al. 2013; Salazar et al. 2013; Coloma et al. 2017). The Chollay Plutonic Complex is overlaid by the Pastos

Blancos Formation (Upper Triassic) (Fig. 2), formerly assigned to the Pastos Blancos Group along with the Guanaco Sonso Formation by Martin et al. (1999), a volcanic bimodal succession composed by a basal section of basaltic lava flows and pyroclastic rocks, and an upper section of dacitic to rhyolitic domes, lava flows, and tuffs. The Colorado Syenogranites (Upper Triassic) intrudes both the Chollay complex and the Pastos Blancos Formation (Fig. 2); it is a spatially restricted suite of biotite syeno- and monzogranites of characteristic pink color (Martin et al. 1999; Salazar et al. 2013; Coloma et al. 2017). Numerous dykes of basaltic-andesite and rhyolite (pink colored) composition cross cut the aforementioned units; their contacts with the wall rock are irregular, suggesting that they are partly contemporaneous with the Pastos Blancos Formation and the Colorado Syenogranite (Martin et al. 1999; Creixell et al. 2009).

To the west of the Chollay Plutonic Complex crops out the La Totora Formation (Upper Triassic), a volcanic sequence that discordantly overlies the Guanaco Sonso Formation, the Carboniferous—Permian intrusions, and the Permian Laguna Chica Formation (Fig. 2). It is in gradational contact with the Triassic sedimentary San Felix Formation; in fact, the upper member of the latter has been assigned to the La Totora Formation based on their lithological similarity (Coloma et al. 2017). It is composed by basaltic and basaltic-andesite lava flows, ash and lapilli tuffs, rhyolitic domes, and sedimentary beds of breccias and lithic arkose (Salazar et al. 2013; Maksaev et al. 2014). The shallow marine deposits of the Lower—Middle Jurassic Lautaro Formation overlie the Triassic volcanics in slight unconformity (Salazar et al. 2013). North of 28°30′S, the La Ternera Formation (Upper Triassic—Hettangian), discordantly overlies Late Paleozoic intrusions and older stratified units and it is in turn overlaid by the Lautaro Formation (Iriarte et al. 1996; Iriarte et al. 1999; Arévalo 2005; Matthews et al. 2006; Mpodozis et al. 2012; Peña et al. 2013). This volcanosedimentary sequence is composed by andesitic and basaltic andesitic lava flows, minor rhyolitic domes, glass and lithic tuffs, conglomerates, quartz sandstones, and shales (Iriarte et al. 1996). Further north of 27°30′, the outcrops of the El Mono Beds (Lopingian) and the Quebrada del Salitre Formation are located in a similar position as the La Ternera and La Totora within the eastern belt of Triassic rocks at the Frontal Cordillera (Fig. 2).

3.4   *Jurassic Igneous Units Between 22° and 26° S*

In contrast to the Triassic units, the present-day Coastal Cordillera of northern Chile was the main locus of Jurassic magmatism as it is attested by the vast outcrops of volcanic and plutonic rocks of the period aligned along more than 1,000 km (Fig. 1). The Jurassic volcanic and sedimentary rocks are assigned to the La Negra Formation and crop out as a homoclinal sequence that can reach thicknesses of 7,000–10,000 m (Buchelt and Tellez 1988). They mainly consist of porphyritic lavas with phenocryst contents up to 25%, with basaltic andesites and andesites as the main compositional types, although basalts, dacites, and rhyolites (ignimbrites)

have been reported from several areas (Boric et al. 1990; Cortés 2000; Kramer et al. 2005). Volcanic breccias, tuffs, and sedimentary rocks as well as epiclastic sandstone lenses are less abundant. The age of volcanism has traditionally been established on the basis of contact relationship with sedimentary units or the fossiliferous content of interbedded sediments, from Early to lowermost Upper Jurassic (Rogers and Hawkesworth 1989; González and Niemeyer 2005) (Fig. 2), although some authors argue that the main volume of volcanism and sedimentation is restricted to the Middle and Upper Jurassic (Oliveros et al. 2006, 2008). Large and widely distributed plutonic bodies, the Coastal Batholith (Figs. 1 and 2), of gabbroic to granitic in composition, intrude the volcanic sequence together with dykes and stocks of mainly basic to intermediate composition (Jurassic—Early Cretaceous) (Pichowiak 1994; Dallmeyer et al. 1996; Lucassen and Thirlwall 1998; González and Niemeyer 2005; Oliveros et al. 2006, 2008).

3.5 Jurassic Igneous Units Between 26º and 30º S

The units that represent the Early Andean magmatism in this segment can be divided into two main areas that form two parallel belts of outcrops (Fig. 1). As in the northern segment, the first group of rocks, representing the Jurassic arc, is located in the present-day Coastal Cordillera and comprises thick sequences of volcanic and volcanoclastic material and large batholitic bodies. The second group of rocks has been interpreted as the Jurassic back-arc domain, and it is located in the Precordillera and Frontal Cordillera (Charrier et al. 2007; Rossel et al. 2013). The back-arc domain can be further subdivided into western and eastern belts of outcrops, both of them composed almost exclusively by volcanic and volcaniclastic rocks (Rossel et al. 2013, 2015).

The volcanism in the Coastal Cordillera is represented in this segment by the thick deposits of the La Negra Formation (26º–29º S) and the volcanic and subvolcanic rocks of the Agua Salada Volcanic Complex (29º30′–31º S). This last unit can be correlated with the lower member of the Punta del Cobre Formation that is intruded by 143 Ma tonalites (Creixell et al. 2012). The sequence crops out mainly as large roof pendants as a consequence of the intrusion of Upper Jurassic and Cretaceous plutonic bodies; therefore, its base is in general not well exposed. Locally, it can be observed that the La Negra Formation overlies in concordance the Pan de Azúcar (Rhaetian—Sinemurian) and Canto del Agua (Upper Triassic) formations (Naranjo and Puig 1984; Welkner et al. 2006; Arévalo and Welkner 2008, Creixell et al. 2016) or unconformably the Chañaral Epimetamorfic Complex of Permian age (Naranjo and Puig 1984; Espinoza et al. 2015) (Fig. 2). On the basis of its fossil content, stratigraphic relationships and scarce radiometric data, an age ranging from Pliensbachian to Upper Jurassic, are assigned to this unit (Charrier et al. 2007 and references therein) (Fig. 2).

Plutonic rocks of the Coastal Batholith cropping out in this segment range compositionally from gabbro to granite, but correspond mostly to diorites,

248

monzonites, tonalites, and granodiorites with typical metaluminous mafic mineralogy, that intruded in several magmatic pulses during the Jurassic (Fig. 2). Structural analyses suggest that the intrusion of these bodies was facilitated mostly by tensional fractures and faults (Grocott et al. 1994; Creixell et al. 2011), but it is possible to observe forced intrusions induced by sequential emplacement of magmatic pulses in early stages (Rodríguez et al. 2016).

In the Precordillera and Frontal Cordillera, a series of volcanosedimentary units (Fig. 2) would represent a back-arc volcanism during the Late Jurassic (Rossel et al. 2013). The rocks are distributed in two parallel chains and, due to their position relative to the arc domain, would resemble the configuration of some of the modern island arc magmatic systems of western Pacific (Rossel et al. 2013). The westernmost chain of volcanic rocks is represented by the Sierra Fraga (26–27º S) and Algarrobal-Picudo (28–31º S) formations. These units are composed by thick piles of more than 1,500 m of volcanic and pyroclastic material, intercalated with sedimentary continental and marine beds in the case of Sierra Fraga Formation and with continental sedimentary beds in the Algarrobal Formation (Iriarte et al. 1996; Rossel et al. 2013; Salazar et al. 2013). The eastern chain is represented by the Quebrada Vicuñita Beds (26º–27º S) and the Lagunillas Formation (27º30′–30º S) (Fig. 1). These units are characterized by homogeneous sequences of basaltic and basaltic andesitic lavas with a maximum thickness of 200 m, interbedded with minor limestones and calcareous sandstones in the Quebrada Vicuñita Beds, (Cornejo et al. 1998; Iriarte et al. 1999; Salazar et al. 2013). Only two minor Jurassic intrusive bodies crop out in the Frontal Cordillera at 29º S, the Quebrada Lopez (150 Ma), and the Río Potrerillos (144 Ma.) tonalitic stocks (Merino and Ortiz 2015).

4 Age Distribution of the Triassic and Jurassic Magmatism

The Mesozoic volcanic and plutonic rocks cropping out between 22° and 30° S have been dated mainly through the K-Ar (Ar–Ar) and U-Pb methods in primary mineral phases such as zircon, amphibole, biotite, and plagioclase (Oliveros et al. 2006; Parada et al. 2007; Hervé et al. 2014; Maksaev et al. 2014, and references therein). In terms of the total volume of units and rocks sampled for geochronology, there is a slight bias toward plutonic rocks due to the higher abundance of suitable mineral phases in these rocks and the lower alteration degree that they exhibit. Volcanic rocks in general lack of amphibole and biotite, and their phenocrystals and groundmass are strongly altered and replaced by minerals typical of very low to low-grade metamorphism, which is particularly problematic when dating with the K-Ar and Ar–Ar methods (Oliveros et al. 2006, 2008). Consequently, the Coastal Batholith and the Triassic plutons in the High Andes have extensively been more dated than the Triassic and Jurassic volcanic units. Taking this into account, the

volume of magmatism seems invariant throughout most of the Triassic, with a significant peak at ca. 245–250 Ma and an important decrease toward the Triassic–Jurassic boundary (Fig. 3). The Jurassic igneous rocks are volumetrically more abundant than their Triassic counterparts (Fig. 1), and the same pattern is observed in terms of age distribution (Fig. 3). The peaks in the Middle and Late Jurassic have higher magnitudes than the Triassic, with the c. 150 Ma peak being the largest of the studied time frame (Fig. 3). The opposite is observed in the Latest Triassic and Early Jurassic, where igneous ages are scarce. A relatively similar pattern of age distribution is observed in the back-arc marine and continental sedimentary units representative of the Tarapacá and Neuquén basin (Naipauer et al. 2015) (see Chap. "A Provenance Analysis from the Lower Jurassic Units of the Neuquén Basin. Volcanic Arc or Intraplate Magmatic Input?"). The detrital zircons of different localities of these Jurassic basins yield a frequency distribution with two prominent peaks at ca. 243 Ma and 144–152 Ma and a magmatic lull at ca. 197 Ma, which those authors interpreted as the onset of Andean subduction. Overall, the amount to Triassic detrital zircons is smaller than the Jurassic material (Fig. 3). Given the current geochronological database, it is therefore possible to infer that the volume of magmatism would have remained relatively constant during most of the Triassic, decreasing notoriously at ca, 200 Ma, and later increasing to its maximum for the studied period at the Late Jurassic.
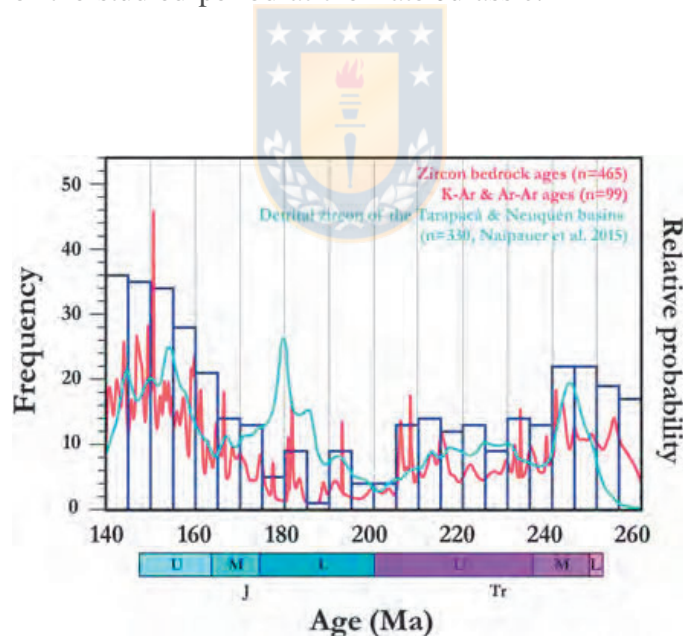
Fig. 3 Frequency distribution histogram for mineral U-Pb and K-Ar (Ar–Ar) radiometric ages from rocks of northern Chile (20°–30° S) and model distribution of detrital zircon U-Pb ages for Tr-Jr rocks of the Neuquén and Tarapacá back-arc basins. Data from Breitkreuz and Van Schmus (1996), Oliveros et al. (2006), Parada et al. (2007), Maksaev et al. (2014), Hervé et al. (2014), Naipauer et al. (2015) and references therein, and geological maps of the Chilean Geological and Mining survey between 20° and 30° S

5   Geochemistry of the Triassic and Jurassic Magmatism

The significant compositional contrasts between the Jurassic and Triassic magmatism in northern Chile are one of the main reasons for which these two periods have been associated with specific and distinctive evolutionary stages of the South American margin. From a purely petrographic perspective (Fig. 4), most of the exposed Triassic igneous rocks are intermediate to acid in composition (Fig. 4a), whereas the Jurassic magmatism was predominantly basic to intermediate (Fig. 4b). Previously, the bimodal character of the Triassic volcanism has been invoked as evidence of continental rifting during that stage (Ramos and Kay 1991; Parada et al. 1999; Morata et al. 2000). However, in spite of the more evolved character of the Triassic rocks, no bimodality in their composition is observed when integrating either the petrography or the major elements content of all the reported igneous units in northern Chile (Figs. 4 and 5a); in fact, the volcanism is largely andesitic in composition for the studied 100 my interval. The Triassic rocks are mainly sub-alkaline (Fig. 5a), with few samples escaping to this trend, and also follow a calk-alkaline trend in the AFM diagram (Fig. 5b). The plutonic Jurassic rocks are mostly metaluminous, whereas the majority of the Triassic intrusions are peraluminous (Fig. 5c), indicating an important crustal component in the magma source. However, the metaluminous intrusions correspond to the less evolved lithologies, which suggest that a mantle component must have also been involved in the generation of these magmas (Coloma et al. 2017). Due to the significant alteration exhibited by the volcanic rocks, the use of mobile major elements, such as K, Na, Ca, Fe, and Mg, is not recommended (Oliveros et al. 2007; Rossel et al. 2015; Coloma et al. 2017) and most of the tectonic classifications are made based on the more immobile trace elements (Fig. 5d, e). The two selected diagrams show that the vast majority of the Triassic and Jurassic rocks plot either in the field of "volcanic arc basalts" or "volcanic arc granites", with few samples in other fields. These Triassic igneous rocks with transitional to alkaline affinities have been interpreted as precursors to the establishment of the arc at the present-day Coastal Cordillera, which took place at some point after ca. 215 Ma (Vásquez and Franz 2008; Coloma et al. 2017). The "arc-signature" for the Triassic and Jurassic rocks is further reinforced by the primitive mantle-normalized trace element abundances (Fig. 5f) in which there is a marked enrichment in LIL elements over the HFS elements, with characteristics troughs in Nb, Ta, P, and Ti. High abundances of Pb and Zr would suggest an important crustal component, which is more evident for the Triassic rocks.

In terms of the REE abundances, when considering the whole dataset for each stage, it is difficult to find distinctive patterns as both groups have rather flat slopes or LREE to HREE ratios (Fig. 5g). However, a systematic decrease in the La/Yb and La/Sm parameters from the Triassic to the Jurassic has been reported (Oliveros et al. 2016). For a group of Triassic rocks, the Eu anomaly is markedly more negative than for the whole population of samples, suggesting more reduced conditions for the magmatism. There is also a particular group of Jurassic samples for
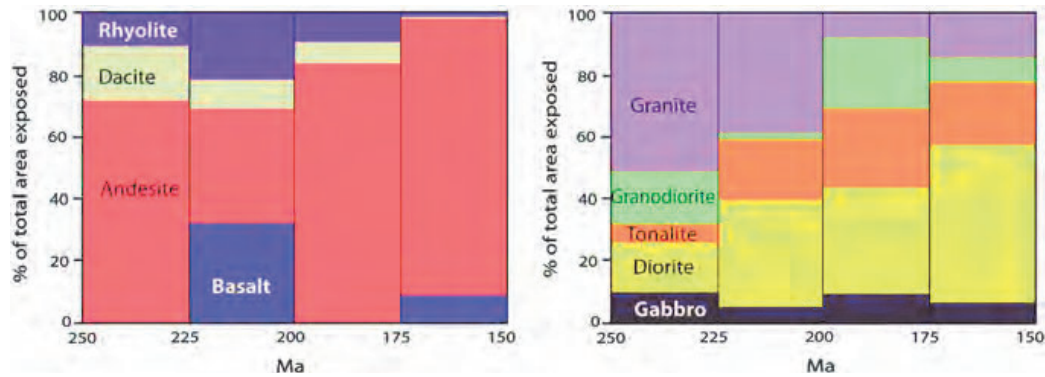
Fig. 4 Compositional distribution of the Triassic and Jurassic igneous rocks cropping out in the Chilean territory between 20° S and 30° S. The percentages of each lithology are calculated from the petrographic, stratigraphic and geochronological information available for ca. 20,000 km^2 of surficial exposure of relevant units according to the geological maps published by the Chilean Geological and Mining Survey

which the slope and abundances of REE are lower, indicating the less evolved magmas would have been generated under a thinned crust.

The isotope composition of the Mesozoic rocks suggests that the magma source must have had a mantle component as they plot along the mantle array, and most of the Jurassic and a significant portion of the Triassic rocks plot above and to the left of the "bulk silicate earth" values, in the Nd-Sr diagram (Fig. 5h). Some of the Triassic rocks have undoubtedly a crustal component in their source due to the elevated $^{87}Sr/^{86}Sr$ and low $^{143}Nd/^{144}Nd$ that they exhibit. The Jurassic rocks with the more radiogenic signature are those representing the back-arc domain (Late Jurassic volcanism), and they are thought to have a more enriched mantle source because of their inferred position relative to the mantle wedge in the subduction zone at that time (Rossel et al. 2013, 2015). The Pb isotopic composition of the Triassic rocks is very similar to the Jurassic ones and both groups plot in a field that suggest a rather restricted crustal or sediment influence in the magma sources (Fig. 5i). The Late Jurassic rocks mark a distinctive, more radiogenic group, for which their Pb signature is interpreted as a more enriched mantle source behind the main arc at that time (Rossel et al. 2013, 2015).

6 Tectonic Setting and Initiation of the Andean Magmatism

The geochemical signature of the Triassic magmatism, along with its intermediate to acid composition, would require a depleted mantle source that melted in presence of fluids enriched in mobile incompatible elements. The most likely tectonic setting to produce such magmatic products is the subduction of the oceanic plate beneath the continent (Fig. 6a, b). Although some authors have recently speculated with a
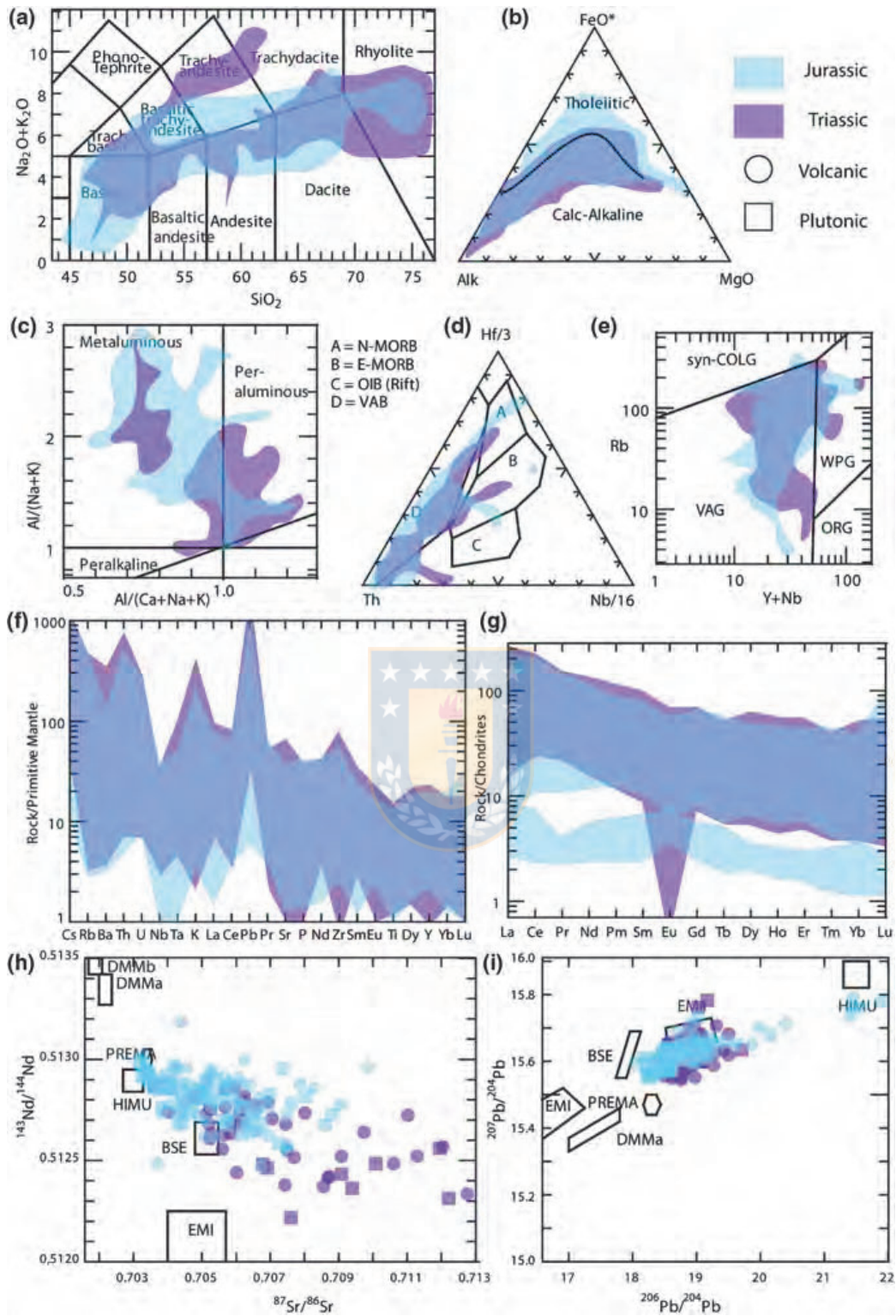
◄**Fig. 5** **a** TAS (Le Bas et al. 1986), **b** AFM (Irvine and Baragar 1971) **c** alumina saturation index diagrams for plutonic rocks (Shand 1943), **d** Th-Nb-Hf for basic and intermediated volcanic rocks (Wood 1980) **e** Rb versus Y+Nb diagram for plutonic and acid volcanic rocks (Pearce et al. 1984). Spider diagrams of **f** chondrite-normalized rare earth and **g** primitive mantle-normalized trace elements abundances in plutonic and volcanic rocks. Normalizing values are from Sun and McDonough (1989). **h** $^{87}Sr/^{86}Sr$ versus $^{143}Nd/^{144}Nd$ and **i** $^{207}Pb/^{204}Pb$ versus $^{206}Pb/^{204}Pb$ diagrams for the studied rocks, showing the mantle components after Zindler and Hart (1986). Data are from Rogers and Hawkesworth (1989), Brown (1991), Vergara et al. (1991), Mpodozis and Kay (1992), Pichowiak (1994), Parada et al. (1999), Morata et al. 2000, Llambías et al. (2003), Kramer et al. (2005) Lucassen et al. (2006), Llambías et al. (2007), Oliveros et al. (2007), Vásquez and Franz (2008), D'Elia et al. (2012), Vásquez et al. (2011), Creixell et al. (2012), Parada (2013), Rossel et al. (2013), Salazar et al (2013), Coloma et al. (2017) and Oliveros et al. (2016)

scenario like this for the Triassic magmatism (Vásquez et al. 2011; del Rey et al. 2016; Coloma et al. 2017), the more generalized hypothesis is that during this period, subduction ceased and magmatism was generated merely by continental rifting (Mpodozis and Kay 1992; Charrier et al. 2007 and references therein).

At a continental scale, the tectonic forces during the Triassic were indeed dominated by the Pangea–Gondwana breakup that imposed tensional stresses along the proto-south american part of the continental plate (Frizon de Lamotte et al. 2015). This resulted firstly in extensive crustal anathexis, generating the acidic Choiyoi province, and then in the formation of NW- oriented rift basins (Llambías et al. 1993, 2003; Charrier et al. 2007; Bechis et al. 2014), with a minor component of N-S extensional stresses, such as the Ichigualasto and Cuyo basins in the present-day Argentinian territory, which accumulated large volumes of siliciclastic sediments and OIB-like or anorogenic bimodal magmatism (Ramos and Kay 1991; Llambías et al. 2007). All this features are well-documented in Argentina and allow constraining the tectonic model of orogenic collapse, continental extension, and rifting without subduction. However, Chilean units show that closer to the continental margin, volcanic and plutonic rocks do not exhibit a bimodal compositional distribution, with dominant intermediate lithologies that show systematic enrichment in LILE over HFSE. Given the evidence of a crustal component in the Triassic magmas, i.e., the peraluminous character of several plutonic units, part of the LILE enrichment could have been generated from melting or assimilation of the preexisting continental crust, during the ascent of the magmas to the surface or middle-upper crustal levels. Nevertheless, the Sr–Nd–Pb isotope signature of volcanic and plutonic rocks requires a magmatic source with a depleted mantle component (Fig. 5h, i); thus, the Triassic magmatism cannot be solely attributed to dehydration melting of a preexisting crust bearing an arc-signature nor to decompression melting of an asthenospheric mantle beneath the continent. The features of the Triassic volcanic and plutonic rocks are better explained if fluid-induced melting of a depleted mantle source generated basaltic magmas that latter evolved due to different degrees of continental crust assimilation, in the context of active subduction under tensional stresses along the margin.

The progressive stretching of the continental lithosphere due to the Gondwana breakup would have resulted, during the Jurassic, in a paleogeographic
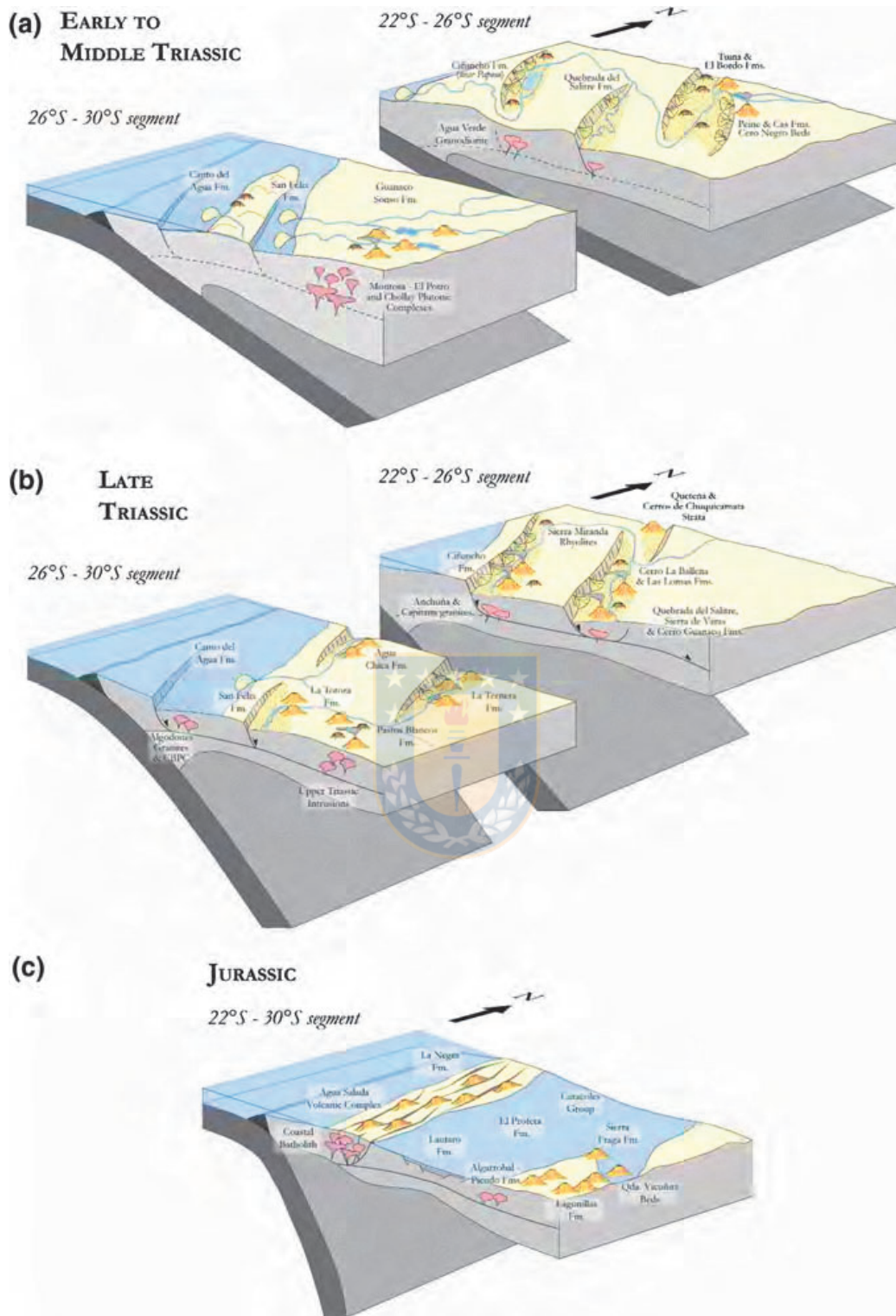
Fig. 6 Paleography and tectonic setting for the magmatism at the northern Chile margin during the Triassic and Jurassic. Location of the segments corresponds to the present-day latitudes

255

configuration that resembled an ocean–ocean convergent margin, with a low-relief, partly submarine, arc chain, and a back-arc marine basin (Rossel et al. 2013) (Fig. 6c). The Jurassic arc magmatism is remarkably homogeneous both lithologically and geochemically, with basaltic-andesite, andesite, and diorite being by far the most abundant type of products, while major and trace elements composition groups the samples tightly in the different trends of calc-alkaline (Fig. 5b) or arc affinities (Fig. 5d, e). The small crustal contribution to the magma sources and the protracted extensional regime during the Jurassic resulted in a large addition of juvenile magmas to the continent in this period (Lucassen et al. 2006; Oliveros et al 2007). Back-arc magmatism was much more restricted in terms of volume and duration, but also more heterogeneous in its composition, including calc-alkaline and transition to alkaline volcanism. It took place during a marine regression that left the back-arc basin partially emerged and that would have resulted from transpressional conditions in the arc region (Rossel et al 2013, 2015).

Therefore, subduction associated with extensional stresses, indeed persisted during the Triassic and the Jurassic, indicating that the beginning of the "Andean cycle" or "Andean subduction" was arbitrarily placed at the Early Jurassic. In spite of their similar origin, Triassic igneous rocks are somewhat different to the Jurassic ones, as they are more acidic (Fig. 4) and their deposits in general lack of thick piles of effusive lava flows, which is the norm in the "La Negra arc" representative units. Pyroclastic and volcanoclastic deposits are the most common occurrence of the Triassic volcanics, which reflects in part its more evolved character. The crustal component in the Jurassic magmas is significantly lower than the older magmatism, with the Jurassic volcanic rocks being partly tholeiitic having MORB-like isotopic signatures (Figs. 5b, h and 6). Thus, even though the mechanism for magma generation would have remained invariant through the ca. 100 Ma, the lithospheric contributions to the magmatic processes significantly diminished in the same period (Oliveros et al. 2016). In addition to the geochemical and petrological differences, a potential "break" in the magmatism could have been occurred near the Triassic–Jurassic boundary because both igneous and detrital ages exhibit a marked lull around this time frame (Fig. 3). The settlement of the volcanic arc in the present-day Coastal Cordillera is thought to have taken place at the Hettangian or Sinemurian age (Mpodozis and Ramos 1989; Charrier et al. 2007 and references therein), but the recent finding of the Estratos de Sierra Lagunas (Sepúlveda et al. 2014) suggests that the typical volcanism of the "La Negra arc" could have started during the Rhaetian age. Still, this event roughly coincides in time with the magmatic lull and the shift from a rifting stage to a thermal sag stage in the Neuquén basin (see Chap. "A Provenance Analysis from the Lower Jurassic Units of the Neuquén Basin. Volcanic Arc or Intraplate Magmatic Input?"), suggesting that probably a common tectonic phenomenon existed associated with the decrease in the magma production rates prior to the focus of the arc in a narrow position along the margin. Further studies are necessary to determine the nature of such phenomenon and more precisely constrain the exact time when it started. This work argues for the need to redefine the beginning of the "Andean Cycle" to be placed

either at sometime during the Triassic or after the end of the Choiyoi event during the Late Permian–Early Triassic (Sato et al. 2015).

7   Pre-Andean Segmentation of the Convergent Margin

Even though Mesozoic subduction may have taken place along the entire section of the Andean margin between 22° and 30° S, this could have had different characteristics evidenced by different deformation styles affecting the uppermost crust evidenced in the geological record that could reflect a tectonic segmentation of the margin. During the Early to Middle Triassic, the magmatism in the northern segment was less abundant and closely related to continental basins, whereas in the southern segment, large volumes of both volcanic and plutonic rocks were emplaced in the crust, relatively far from the marine forearc basins (Fig. 6). During the Late Triassic, the differences between both segments are less notorious but still the magma production was likely higher in the northern region, where volcanism was closely related to rifting in continental-marine basins (Fig. 6).

The segmentation of the margin becomes especially evident during Late Jurassic in the back-arc, with exclusively marine sedimentation north of 27º S and continental deposition between 27º and 36º S. However, it is possible to observe a second-order segmentation related to magmatic activity (Rossel et al. 2013). Thus, Rossel et al. (2015) suggest the following scenario: (a) 20º–25º S, marine sedimentation without volcanism, (b) 25–27º S, mainly marine sedimentation and submarine calc-alkaline-tholeitic volcanism, (c) 27º–31º S, continental sedimentation and heterogeneous volcanism.

References

Álvarez J, Mpodozis C, Blanco-Quintero I, García-Casco A, Arriagada A, Morata D (2013) U-Pb ages and metamorphic evolution of the La Pampa Gneisses: Implications for the evolution of the Chilenia Terrane and Permo-Triassic tectonics of north Central Chile. J S Am Earth Sci 47:100–115

Álvarez J, Jorquera R, Miralles C, Padel M, Martinez P (2016) Cartas Punta Posallaves y Sierra Vicuña Mackenna, Región de Antofagasta. Servicio Nacional de Geología y Minería. Carta Geológica de Chile, Geología Básica (1:100.000)

Arévalo C (2005) Carta Los Loros, Región de Atacama. Servicio Nacional de Geología y Minería. Serie Geología Básica 92 (1:100.000)

Arévalo C, Creixell C (2009) The Atacama Fault System and its role on the migration and deposition of Iron Oxide Copper Gold and Magnetite-Apatite ores: an evaluation from the Los Choros and Huasco valleys. In: Wörner G, Möller-McNett S (eds) International Lateinamerika – Kolloquium, Alemania, pp 23–25

Arévalo C, Welkner D (2008) Geología del área Carrizal Bajo-Chacritas, Región de Atacama. Servicio Nacional de Geología y Minería. Serie Geología Básica 111:67 (1:100.000)

Basso M (2004) Carta Baquedano, Región de Antofagasta. Servicio Nacional de Geología y Minería. Carta Geológica de Chile, Serie Geología Básica 82 (1:100.000)

Basso M, Mpodozis C (2012) Carta Cerro Quimal, Región de Antofagasta. Servicio Nacional de Geología y Minería. Carta Geológica de Chile, Serie Geología Básica 143 (1:100.000)

Bechis F, Cristallini EO, Giambiagi LB, Yagupsky DL, Guzmán CG, García VH (2014) Transtensional tectonics induced by oblique reactivation of previous lithospheric anisotropies during the Late Triassic to Early Jurassic rifting in the Neuquén basin: insights from analog models. J Geodyn 79:1–17

Boric R, Díaz F, Maksaev V (1990) Geología y yacimientos metalíferos de la Región de Antofagasta. Servicio Nacional de Geología y Minería, Santiago, Boletín 40:246

Breitkreuz C, Van Schmus WR (1996) U-Pb geochronology and significance of Late Permian ignimbrites in Northern Chile. J S Am Earth Sci 9(5):281–293

Brown M (1991) Comparative geochemical interpretation of Permian-Triassic plutonic complexes of the Coastal Range and Altiplano (25 30′ to 26 30′ S), northern Chile. Geol Soc Am Spec Pap 265:157–178

Buchelt M, Tellez C (1988) The Jurassic La Negra formation in the area of Antofagasta, northern Chile (lithology, petrography, geochemistry). In: Bahlburg H, Breitkreuz C, Giese P (eds) The Southern Central Andes, vol. 17. Springer, Heidelberg. Lecture Notes in Earth Sciences, pp 171–182

Casquet C, Hervé F, Pankhurst RJ, Baldo E, Calderón M, Fanning CM, Dahlquist J (2014) The Mejillonia suspect terrane (Northern Chile): Late Triassic fast burial and metamorphism of sediments in a magmatic arc environment extending into the Early Jurassic. Gondwana Res 25 (3):1272–1286

Charrier R, Pinto L, Rodríguez M (2007) Tectonostratigraphic evolution of the Andean Orogen in Chile. In: Gibbonds W, Moreno T (eds) The Geology of Chile. Geo Soc London, Special Publications:21–116

Chong G (1973) Reconocimiento geológico del área Catalina-Sierra de Varas y estratigrafía del Jurásico del Profeta, Provincia de Antofagasta. Memoria de Título (Unpubl.), Departamento de Geología, Universidad de Chile, p 284

Coloma F, Valin X, Oliveros V, Vásquez P, Creixell C, Salazar E, Ducea MN (2017) Geochemistry of Permian to Triassic igneous rocks from northern Chile (28º–29º30′S): implications on the dynamics of the proto-Andean margin. Andean Geology 44(2): 147–178

Contreras JP, Espinoza M, De la Cruz R, Jorquera R, Kraus S, Ramírez C, Naranjo JA, Escribano J, Martínez P (2013) Carta Cifuncho, Regiones de Antofagasta y Atacama. Servicio Nacional de Geología y Minería. Carta Geológica de Chile, Serie Geología Básica 161 (1:100.000)

Cornejo P, Mpodozis C, Tomilnson A (1998) Hoja Salar de Maricunga. Región de Atacama. Servicio Nacional de Geología y Minería. Mapas Geológicos, Serie Geología Básica 7 (1:100.000)

Cornejo P, Mpodozis C, Rivera O, Matthews S (2009) Carta Exploradora, Regiones de Antofagasta y Atacama. Servicio Nacional de Geología y Minería. Carta Geológica de Chile, Serie Geología Básica 119, p 99 (1:100.000)

Cortés J (2000) Carta Palestina, Región de Antofagasta. Servicio Nacional de Geología y Minería. Carta Geológica de Chile, Serie Geología Básica 19 (1:100.000)

Cortés J (2012) Carta Sierra Mariposa, Región de Antofagasta. Servicio Nacional de Geología y Minería. Carta Geológica de Chile, Serie Geología Básica 144, p 30 (1:100.000)

Creixell C, Parada MA, Morata D, Roperch P, Arriagada C (2009) The genetic relationship between mafic dike swarms and plutonic reservoirs in the Mesozoic of central Chile (30°–33° 45′S): insights from AMS and geochemistry. Int J Earth Sci 98(1):177–201

Creixell C, Parada MÁ, Morata D, Vásquez P, Pérez de Arce C, Arriagada C (2011) Middle-Late Jurassic to Early Cretaceous transtension and transpression during arc building in Central Chile: evidence from mafic dike swarms. Andean Geol 38(1):37–63

Creixell C, Ortiz M, Arévalo C (2012) Geología del área Carrizalillo-El Tofo, Regiones de Atacama y Coquimbo. Servicio Nacional de Geología y Minería. Carta Geológica de Chile, Serie Geología Básica 133–134, p 82 (1:100.000)

Creixell C, Oliveros V, Vásquez P, Navarro J, Vallejos D, Valin X, Godoy E, Ducea MN (2016) Geodynamics of Late Carboniferous Early Permian forearc in north Chile (28°30–29°30′S). J Geol Soc. https://doi.org/10.1144/jgs2016-010

Cruden A, Arévalo C, Davis D, Grocott J (2004) Magmatic migration and pluton construction rates in the Mesozoic chilean coastal cordillera batholith (27° to 29° S). International Geological Congress N°32, Florence in CD-ROM

D'Elia L, Muravchik M, Franzese JR, Bilmes A (2012) Syn-rift volcanism of the Neuquen Basin, Argentina: relationships with the Late Triassic-Early Jurassic evolution of the Andean margin. Andean Geol 39:106–132

Dallmeyer D, Brown M, Grocott J, Taylor G, Treloar PJ (1996) Mesozoic magmatic and tectonic events within the Andean Plate boundary zone, 26º–27º30′S, North Chile: constraints from 40Ar/39Ar mineral ages. J Geol 104:19–40

del Rey A, Deckart K, Arriagada C, Martínez F (2016) Resolving the paradigm of the late Paleozoic-Triassic Chilean magmatism: isotopic approach. Gondwana Res. https://doi.org/10.1016/j.gr.2016.06.008

Escribano J, Martínez P, Domagala J, Padel M, Espinoza M, Jorquera R, Contreras J, De la Cruz R, Calderón M (2013) Cartas Bahía Isla Blanca y Taltal, Región de Antofagasta. Servicio Nacional de Geología y Minería. Carta Geológica de Chile, Serie Geología Básica 164–165 (1:100.000)

Espinoza F, Matthews S, Cornejo P, Venegas C (2011) Carta Catalina, Región de Antofagasta. Servicio Nacional de Geología y Minería. Carta Geológica de Chile, Serie Geología Básica 129 (1:100.000)

Espinoza M, Contreras JP, Jorquera R, De La Cruz R, Kraus S, Ramírez C (2014) Carta Cerro del Pingo, Regiones de Antofagasta y Atacama. Servicio Nacional de Geología y Minería. Carta Geológica de Chile, Serie Geología Básica N° 169, p 109 (1:100.000)

Espinoza M, Oliveros V, Vásquez P, Bechis F (2015) U-Pb geochronology and kinematic preliminary analyses of Late Triassic-Early Jurassic basins in northern Chile (24.5°–26° S). XIV Congreso Geológico Chileno, La Serena. Actas, vol I, pp 840–843

Frizon de Lamotte D, Fourdan B, Leleu S, Leparmentier F, Clarens P (2015) Style of rifting and the stages of Pangea breakup. Tectonics 34(5):1009–1029

García F (1967) Geología del Norte Grande de Chile. Sociedad Geológica de Chile, Santiago, Chile, p 138

Godoy E, Lara L (1998) Hojas Chañaral y Diego de Almagro, Región de Atacama. Servicio Nacional de Geología y Minería. Mapas Geológicos 5–6 (1:100.000)

González G, Niemeyer H (2005) Cartas Antofagasta y Punta Tetas, Región Antofagasta. Servicio Nacional de Geología y Minería. Carta Geológica de Chile, Serie Geología Básica 89 (1:100.000)

González R, Wilke G-H, Menzies AH, Riquelme R, Herrera C, Matthews S, Espinoza F, Cornejo P (2015) Carta Sierra de Varas, Región de Antofagasta. Servicio Nacional de Geología y Minería. Carta Geológica de Chile, Serie Geología Básica 178 (1:100.000)

Grocott J, Taylor GK (2002) Magmatic arc fault systems, deformation partitioning and emplacement of granitic complexes in the Coastal Cordillera, north Chilean Andes (25º30′S to 27º30′S). J Geol Soc, London 159:425–442

Grocott J, Brown M, Dallmeyer RD, Taylor GK, Treloar PJ (1994) Mechanisms of continental growth in extensional arcs: an example from the Andean plate-boundary zone. Geology 22(5):391–394

Grocott J, Arévalo C, Welkner D, Cruden A (2009) Fault-assisted vertical pluton growth: Coastal Cordillera, north Chilean Andes. J Geol Soc 166(2):295–301

Henríquez SM, Becerra J, Arriagada C (2014) Geología del área San Pedro de Atacama, Región de Antofagasta. Servicio Nacional de Geología y Minería. Carta Geológica de Chile, Serie Geología Básica 171 (1:100.000)

Hervé F, Fanning CM, Calderón M, Mpodozis M (2014) Early Permian to Late Triassic batholiths of the Chilean Frontal Cordillera (28°–31° S): SHRIMP U-Pb zicon ages and Lu–Hf and O isotope systematics. Lithos 184–187:436–446

Iriarte S, Arévalo C, Mpodozis C, Rivera O (1996) Mapa Geológico de la Hoja Carrera Pinto, Región de Atacama. Servicio Nacional de Geología y Minería. Mapas Geológicos 3 (1:100.000)

Iriarte S, Arévalo C, Mpodozis C (1999) Hoja La Guardia, Región de Atacama. Servicio Nacional de Geología y Minería. Mapas Geológicos 13 (1:100.000)

Irvine TN, Baragar WRA (1971) A guide to the chemical classification of the common volcanic rocks. Can J Earth Sci 8(5):523–548

Kato TT, Godoy E (2015) Middle to late Triassic mélange exhumation along a pre-Andean transpressional fault system: coastal Chile (26°–42° S). Int Geol Rev 57(5–8):606–628

Kleiman LE, Japas MS (2009) The Choiyoi volcanic province at 34° S–36° S (San Rafael, Mendoza, Argentina): Implications for the Late Palaeozoic evolution of the southwestern margin of Gondwana. Tectonophysics 473(3):283–299

Kossler A (1998) Der Jura in der Küstenkordillere von Iquique (Nordchile): Paläontologie, Lithologie, Stratigraphie, Paläogeographie. Berliner Geowissenschaftliche Abhandlungen (A, 197)

Kramer W, Siebel W, Romer RL, Haase G, Zimmer M, Ehrlichmann R (2005) Geochemical and isotopic characteristics and evolution of the Jurassic volcanic arc between Arica (18º30′S) and Tocopilla (22º S), North Chilean Coastal Cordillera. Chem Erde 65(1):47–78

Le Bas MJ, Maitre RWL, Streckeisen A, Zanettin B (1986) A chemical classification of volcanic rocks based on the total alkali-silica diagram. J Petrol 27(3):745–750

Llambías EJ, Kleiman LE, Salvarredi JA (1993) El Magmatismo Gondwánico. In: Ramos VA (ed) Geología y Recursos Naturales de Mendoza. Relatorio, XII Congreso Geológico Argentino y II Congreso de Exploración de Hidrocarburos, Mendoza, pp 53–64

Llambías EJ, Quenardelle S, Montenegro T (2003) The Choiyoi Group from central Argentina: a sub-alkaline transitional to alkaline association in the craton adjacent to the active margin of the Gondwana continent. J S Am Earth Sci 16:243–257

Llambías EJ, Leanza HA, Carbone O (2007) Evolución tectono-magmática durante el Pérmico al Jurásico temprano en la Cordillera del Viento (37°05′S – 37°15′S): Nuevas evidencias geológicas y geoquímicas del inicio de la Cuenca Neuquina. Revista de la Asociación Geológica Argentina 62(2):217–235

Lucassen F, Thirlwall M (1998) Sm-Nd ages of mafic rocks from the Coastal Cordillera at 24º S, northern Chile. Geol Rundsch 86:767–774

Lucassen F, Kramer W, Bartsch V, Wilke HG, Franz G, Romer RL, Dulski P (2006) Nd, Pb and Sr isotope composition of juvenile magmatism in the Mesozoic large magmatic province of northern Chile (18°–27° S): indications for a uniform subarc mantle. Contrib Miner Petrol 152:571–589

Maksaev V, Munizaga F, Tassinari C (2014) Timing of the magmatism of the paleo-Pacific border of Gondwana: U-Pb geochronology of Late Paleozoic to Early Mesozoic igneous rocks of the north Chilean Andes between 20° and 31° S. Andean Geol 41(3):447–506

Marinovic N (2007) Carta Oficina Domeyko, Región de Antofagasta. Servicio Nacional de Geología y Minería. Carta Geológica de Chile, Serie Geología Básica 105, p 41 (1: 100.000)

Marinovic N, García M (1999) Hoja Pampa Unión, Región de Antofagasta. Servicio Nacional de Geología y Minería. Mapas Geológicos 9 (1:100.000)

Marinovic N, Smoje I, Maksaev V, Hervé M, Mpodozis C (1995) Hoja Aguas Blancas, Región de Antofagasta. Servicio Nacional de Geología y Minería. Carta Geológica de Chile 70, p 150 (1:250.000)

Marquardt C, Marinovic N, Muñoz V (2008) Geología de las Ciudades de Iquique y Alto Hospicio, Región de Tarapacá. Servicio Nacional de Geología y Minería. Carta Geológica de Chile, Serie Geología Básica 133, p 33 (1:25.000)

Martin MW, Clavero RJ, Mpodozis MC (1999) Late Paleozoic to Early Jurassic tectonic development of the high Andean Principal Cordillera, El Indio Region, Chile (29-30° S). J S Am Earth Sci 12:33–49

Matthews S, Cornejo P, Riquelme R (2006) Carta Inca de Oro, Región de Atacama. Servicio de Geología y Minería. Carta Geológica de Chile, Serie Geología Básica 102, p 79 (1:100.000)

Merino R, Ortiz M (2015) Nuevos antecedentes de rocas volcánicas e intrusivas del Jurásico Superior – Cretácico Inferior de la Alta Cordillera de Vallenar. Área Río Chollay – Matancilla (29°–29°30′S). XIV Congreso Geológico Chileno, La Serena. Actas, vol I, pp 747–750

Morata D, Aguirre L, Oyarzún M, Vergara M (2000) Crustal contribution in the genesis of the bimodal Triassic volcanism from the Coastal Range, central Chile. Rev Geol Chile 27:83–98

Mpodozis C, Cornejo P (1997) El rift triásico-sinemuriano de Sierra Exploradora, Cordillera de Domeyko (25º–26º S): asociaciones de facies y reconstrucción tectónica. In VIII Congreso Geológico Chileno, Antofagasta. Actas, vol I, pp 550–554

Mpodozis C, Kay S (1992) Late Paleozoic to Triassic evolution of the Gondwana margin: Evidence from Chilean Frontal Cordilleran batholiths (28° S to 31° S). Geol Soc Am Bull 104:999–1014

Mpodozis C, Ramos VA (1989) The Andes of Chile and Argentina. In: Ericksen GE, Cañas Pinochet MT, Reinemund JA (eds) Geology of the Andes and its relation to hydrocarbon and mineral resources. Houston, Texas, Circum-Pacific Council for Energy and Mineral Resources, Earth Sciences Series 11:59–90

Mpodozis C, Ramos VA (2008) Tectónica Jurásica en Argentina y Chile: extensión, subducción oblicua, rifting, deriva y colisiones? Rev Asoc Geol Argentina 63(4):481–497

Mpodozis C, Iriarte S, Gardeweg M, Valenzuela M (2012) Carta Laguna del Negro Francisco, Región de Atacama. Servicio Nacional de Geología y Minería. Carta Geológica de Chile, Serie Geología Básica 145, p 30 (1:100.000)

Murillo I, Álvarez J, Montecinos P, Creixell C, Salazar E, Arriagada C (2013) Geochronology and kinematics of the El Portillo Mylonites: relation with San Rafael Orogeny and Middle Triassic extensión in north-Central Chile. In International Geological Congress on the Southern Hemisphere GEOSUR. Bollettino di Geofisica teorica ed applicata (Supplement 2):54

Naipauer M, Tunik M, Marques JC, Rojas Vera E, Vujovich GI, Pimentel MM, Ramos VA (2015) U-Pb detrital zircon ages of Upper Jurassic continental successions: implications for the provenance and absolute age of the Jurassic-Cretaceous boundary in the Neuquén Basin. Geol Soc, London, Special Publications 399(1):131–154

Naranjo JA, Puig A (1984). Hojas Taltal y Chañaral, Regiones de Antofagasta y Atacama. Servicio Nacional de Geología y Minería. Carta Geológica de Chile 62–63, p 140 (1:250.000)

Nasi C, Moscoso R, Maksaev V (1990) Hoja Guanta. Servicio Nacional de Geología y Minería. Carta Geológica de Chile, Serie Geología Básica 67, p 141 (1:250.000)

Niemeyer H (2013) Geología del Área Cerro Lila-Peine, Región de Antofagasta. Servicio Nacional de Geología y Minería. Carta Geológica de Chile, Serie Geología Básica 147 (1:100.000)

Oliveros V, Féraud G, Aguirre L, Fornari M, Morata D (2006) The Early Andean Magmatic Province (EAMP): 40Ar/39Ar dating on Mesozoic volcanic and plutonic rocks from the Coastal Cordillera, northern Chile. J Volcanol Geoth Res 157(4):311–330

Oliveros V, Morata D, Aguirre L, Féraud G, Fornari M (2007) Jurassic to Early Cretaceous subduction–related magmatism in the Coastal Cordillera of northern Chile (18°30′–24° S): geochemistry and petrogenesis. Rev Geol Chile 34:209–232

Oliveros V, Féraud G, Aguirre L, Ramírez LE, Fornari M. Palacios C, Parada MA (2008) Detailed 40Ar/39Ar dating of geological events associated with the Mantos Blancos copper deposit, northern Chile. Miner Deposita 43(3):281–293

Oliveros V, Vásquez P, Creixell C, Lucassen F, Ducea M, González J, Ciocca I (2016) Lithospheric evolution at the Early Andean convergent margin, Chile. Goldschmidt conference, Yokohama, Japan

Ortiz M, Merino N (2015) Geología de las áreas Río Chollay – Matancilla y Cajón del Encierro, Regiones de Atacama y Coquimbo. Servicio Nacional de Geología y Minería. Carta Geológica de Chile 175–176 (1:100.000)

261

Parada F (2013) Geoquímica de las rocas ígneas del Carbonífero-Triásico de la Alta Cordillera, Región de Atacama, Chile. Memoria de Título (Unpubl), Departamento de Geología, Universidad de Chile, p 93

Parada MA, Levi B, Nystrom JO (1991) Geochemistry of the Triassic to Jurassic plutonism of Central Chile (30 to 33 S); petrogenetic implications and a tectonic discussion. Geol Soc Am Spec Pap 265:99–112

Parada MA, Levi B, Nyström JO (1999) Multiple sources for the Coastal Batholith of central Chile (31–34° S): geochemical and Sr–Nd isotopic evidence and tectonic implications. Lithos 46:505–521

Parada MA, López-Escobar L, Oliveros V, Fuentes F, Morata D, Calderón M, Aguirre L, Féraud F, Espinoza F, Moreno H, Figueroa O (2007) Andean magmatism. In: Moreno T, Gibbons W (eds) The Geology of Chile. The Geological Society, London:115–146

Pearce JA, Harris NBW, Tindle AG (1984) Trace element discrimination diagrams for the tectonic interpretation of granitic rocks. J Petrol 25(4):956–983

Peña M, Becerra J, Martinez F, Arriagada C (2013) Geología del área Yerbas Buenas – Tres Morros, Región de Atacama. Servicio Nacional de Geología y Minería. Carta Geológica de Chile 155, p 78 (1:100.000)

Pichowiak S (1994) Early Jurassic to Early Cretaceous magmatism in the Coastal Cordillera and the Central Depression of North Chile. In: Reutter KJ, Scheuber E, Wigger PJ (eds) Tectonics of the Southern Central Andes. Structure and evolution of a continental margin. Springer Verlag, Stuttgart, pp 203–217

Proffett JM, Dilles JH (2007) SHRIMP-RG ion microprobe U-Pb age determinations of intrusive rock units northeast of the Chuquicamata mine, Chile. CODELCO, Informe (Unpubl.), p 15

Ramos VA, Kay SM (1991) Triassic rifting and associated basalts in the Cuyo basin, central Argentina. In Harmon RS, Rapela CW (eds) Andean magmatism and its tectonic setting. Geol Soc Am, Special Papers 265:79–91

Ring U, Willner A, Layer P, Richter P (2012) Jurassic to Early Cretaceous postaccretional sinistral transpression in north-central Chile (latitudes 31–32° S). Geol Mag 149(2):202–220

Rodríguez N, Díaz-Alvarado J, Rodríguez C, Riveros K, Fuentes P (2016) Petrology, geochemistry and thermobarometry of the northern area of the Flamenco pluton, Coastal Range batholith, northern Chile. A thermal approach to the emplacement processes in the Jurassic andean batholiths. J S Am Earth Sci 67:122–139

Rogers G, Hawkesworth CJ (1989) A geochemical traverse across the North Chilean Andes: Evidence for crust generation melt from the mantle wedge. Earth and Planet Sci Lett 91:271–285

Rossel P, Oliveros V, Ducea M, Charrier R, Scaillet S, Retamal L, Figueroa O (2013) The Early Andean subduction system as an analogue to island arcs: evidence from across-arc geochemical variations in northern Chile. Lithos 179:211–230

Rossel P, Oliveros V, Ducea MN, Hernández L (2015) Across and along arc geochemical variations in altered volcanic rocks: Evidence from mineral chemistry of Jurassic lavas in northern Chile, and tectonic implications. Lithos 239:97–113

Salazar E, Coloma F, Creixell C (2013) Geología del área El Tránsito - Lagunillas, Región de Atacama. Servicio Nacional de Geología y Minería. Carta Geológica de Chile, Serie Geología Básica 149, p 121 (1:100.000)

Sato AM, Llambías EJ, Basei MA, Castro CE (2015) Three stages in the Late Paleozoic to Triassic magmatism of southwestern Gondwana, and the relationships with the volcanogenic events in coeval basins. J S Am Earth Sci 63:48–69

Scheuber E, González G (1999) Tectonics of the Jurassic – Early Cretaceous magmatic arc of the north Chilean Coastal Cordillera (22°–26° S): A story of crustal deformation along a convergent plate boundary. Tectonics 18:895–910

Sepúlveda F, Vásquez P, Quezada A (2014) Cartas Patillos y Oficina Victoria, Región de Tarapacá. Servicio Nacional de Geología y Minería. Carta Geológica de Chile, Serie Geología Básica 167–168 (1:100.000)

SERNAGEOMIN (2002) Mapa Geológico de Chile. Servicio Nacional de Geología y Minería, Chile. Carta Geológica de Chile, Serie Geología Básica 75 (1:1.000.000)

Shand S (1943) Eruptive rocks: their genesis, composition, and classification, with a chapter on meteorites. John Wiley Sons, Inc. p 444

Solari M, Montecinos D, Venegas C, Espinoza F (2015). Hallazgo de unidades volcánicas del Triásico Medio en la Sierra de Imilac, Segunda Región de Antofagasta. XIV Congreso Geológico Chileno, La Serena. Actas, vol III, pp 398–400

Sun S-s, McDonough WF (1989) Chemical and isotopic systematics of oceanic basalts: implications for mantle composition and processes. Geol Soc London, Special Publications 42 (1):313–345

Thomas A (1970) Cuadrángulos Iquique y Caleta Molle. Instituto de Investigaciones Geológicas, Chile. Carta Geológica de Chile 21–22. 2 maps (1:50.000)

Tobar A (1966) Estratigrafía del área Baquedano-Rencoret, Provincia de Antofagasta. Memoria de Título (Unplub.), Departamento de Geología, Universidad de Chile, p 69

Tomlinson AJ, Blanco N (2008) Geología de la franja El Abra-Chuquicamata, II Región (21°45′–22°30′S). Servicio Nacional de Geología y Minería, Informe Registrado IR-08–35, p 196

Tomlinson AJ, Blanco N, Dilles JH (2010) Carta Calama, Región de Antofagasta. Servicio Nacional de Geología y Minería. Carta Geológica de Chile, Serie Preliminar 8: 3 anexos (1:50.000)

Tomlinson A, Blanco N, Ladino M (2015) Carta Mamina, Región de Tarapacá. Servicio Nacional de Geología y Minería. Carta Geológica de Chile, Serie Geología Básica (1:100.000)

Vásquez P, Franz G (2008) The Triassic Cobquecura Pluton (Central Chile): An example of a fayalite-bearing A-type intrusive massif at a continental margin. Tectonophysics 459(1):66–84

Vásquez P, Sepúlveda F (2013) Cartas Iquique y Pozo Almonte, Región de Tarapacá. Servicio Nacional de Geología y Minería. Carta Geológica de Chile, Serie Geología Básica 162–163 (1:100.000)

Vásquez P, Glodny J, Franz G, Frei D, Romer RL (2011) Early Mesozoic Plutonism of the Cordillera de la Costa (34–37º S), Chile: constraints on the onset of the Andean Orogeny. J Geol 119(2):159–184

Venegas C, Cervetto M, Astudillo N, Espinoza F (2013) Carta Sierra Vaquillas Altas, Regiones de Antofagasta y Atacama. Servicio Nacional de Geología y Minería. Carta Geológica de Chile, Serie Geología Básica 159 (1:100.000)

Vergara M, López-Escobar L, Cancino A, Levi B (1991) The Pichidangui Formation; Some geochemical characteristics and tectonic implications of the Triassic marine volcanism in central Chile (31°55′ to 32°20′S) In: Harmon R S, Rapela C W (eds) Andean magmatism and its tectonic setting. Geol Soc Am Spec Pap 265:93–98

Vicente JC (2006) Dynamic Paleogeography of the Jurassic Andean Basin: pattern of regression and general considerations on main features. Revista de la Asociación Geológica Argentina 61 (3):408–437

Welkner D, Arévalo C, Godoy E (2006) Geología del área Freirina-El Morado, Región de Atacama. Servicio Nacional de Geología y Minería. Carta Geológica de Chile, Serie Geología Básica 100 (1:100.000)

Wood DA (1980) The application of a Th-Hf-Ta diagram to problems of tectonomagmatic classification and to establishing the nature of crustal contamination of basaltic lavas of the British Tertiary Volcanic Province. Earth Planet Sci Lett 50:11–30

Zindler A, Hart S (1986) Chemical geodynamics. Ann Rev of Earth Planet Sci 14(1):493–571

ORIGINAL ARTICLE

WILEY **Basin Research** AS EAGE

The synrift phase of the early Domeyko Basin (Triassic, northern Chile): Sedimentary, volcanic, and tectonic interplay in the evolution of an ancient subduction-related rift basin

Mauricio Espinoza[1] 🔟 | Diego Montecino[2] | Verónica Oliveros[1] | Natalia Astudillo[2] |
Paulina Vásquez[2] | Robinson Reyes[1] | Christopher Celis[1] | Rodrigo González[3] |
Juan Contreras[4] | Christian Creixell[2] | Amancay Martínez[5]

[1]Departamento Ciencias de la Tierra, Universidad de Concepción, Concepción, Chile

[2]Servicio Nacional de Geología y Minería (SERNAGEOMIN), Providencia, Santiago, Región Metropolitana, Chile

[3]Departamento de Ciencias Geológicas, Universidad Católica del Norte, Antofagasta, Chile

[4]Área de Minería y Metalurgia, Universidad Tecnológica de Chile (INACAP), Iquique, Chile

[5]Departamento de Geología, FCFMyN, Universidad Nacional de San Luis, San Luis, Argentina

Correspondence
Mauricio Espinoza, Departamento Ciencias de la Tierra, Universidad de Concepción, Víctor Lamas 1290, Casilla 160-C, Concepción, Chile.
Email: mauricespinoza@udec.cl

Abstract

The geodynamic setting along the SW Gondwana margin during its early breakup (Triassic) remains poorly understood. Recent models calling for an uninterrupted subduction since Late Palaeozoic only slightly consider the geotectonic significance of coeval basins. The Domeyko Basin initiated as a rift basin during the Triassic being filled by sedimentary and volcanic deposits. Stratigraphic, sedimentological, and geochronological analyses are presented in order to determine the tectonostratigraphic evolution of this basin and to propose a tectonic model suitable for other SW Gondwana-margin rift basins. The Domeyko Basin recorded two synrift stages. The Synrift I (~240–225 Ma) initiated the Sierra Exploradora sub-basin, whereas the Synrift II (~217–200 Ma) reactivated this sub-basin and originated small depocentres grouped in the Sierra de Varas sub-basin. During the rift evolution, the sedimentary systems developed were largely controlled by the interplay between tectonics and volcanism through the accommodation/sediment supply ratio (A/S). High-volcaniclastic depocentres record a net dominance of the syn-eruptive period lacking rift-climax sequences, whereas low-volcaniclastic depocentres of the Sierra de Varas sub-basin developed a complete rift cycle during the Synrift II stage. The architecture of the Domeyko Basin suggests a transtensional kinematic where N-S master faults interacted with ~NW-SE basement structures producing highly asymmetric releasing bends. We suggest that the early Domeyko Basin was a continental subduction-related rift basin likely developed under an oblique convergence in a back-arc setting. Subduction would have acted as a primary driving mechanism for the extension along the Gondwanan margin, unlike inland rift basins. Slab-induced dynamic can strongly influence the tectonostratigraphic evolution of subduction-related rift basins through controls in the localization and style of magmatism and faulting, settling the interplay between tectonics, volcanism, and sedimentation during the rifting.

264

1 | INTRODUCTION

Subduction-related rift basins are the result of mechanical subsidence driven by lithospheric thinning at the vicinity of a subduction zone in extensional arcs (Merle, 2011; Sengör & Natal'in, 2001) (see Supplementary Material SM1). Current examples of such arcs are less common than their compressional or neutral stress counterparts (Busby, 2012; Jarrard, 1986) and they often develop in oceanic crust (e.g., Western Pacific subduction zones). Few examples of extensional, subduction-related rift basins in continental settings are known: the Okinawa Trough (Lee, Shor, Bibee, Lu, & Hilde, 1980), the intra-arc rift basins of the Taupo arc (Villamor et al., 2017), and the grabens of southern Japan (Kamata & Kodama, 1994), whereas extinct examples are the Eo-Oligocene evolution of the Basin and Range (Ingersoll, 2012) and the Late Cretaceous Western Peruvian Trough (Polliand, Schaltegger, Frank, & Fontboté, 2005). Recent studies from the Taupo intra-arc rift, have shed light on the uniqueness of subduction-related rifts, such as their rapid evolution compared to intraplate continental rifts, which is due to the role of active magmatism in weakening of the crust during the early rift stages (Ellis, Heise, Kissling, Villamor, & Schreurs, 2014; Villamor et al., 2017).

Even though continental subduction-related rifts are scarce in modern settings, they could have been far more common along the "Pangean rim of fire" developed during the Late Triassic (Hadlari, Midwinter, Poulton, & Matthews, 2017), where unique global tectonic conditions such as very low convergence rates and subduction of relatively old and cold oceanic plates (Matthews et al., 2016; Müller et al., 2016) would have favoured the development of continental rift basins (Schellart, 2005; Stephenson & Schellart, 2010) associated with contemporaneous arc magmatism along the northwestern (Busby-Spera, 1988) and southwestern (Coloma et al., 2017; González et al., 2018; Oliveros et al., 2017; Poma et al., 2014) Gondwana margins. The identification and study of those basins in the Triassic Gondwanean record is crucial to understand the processes that took place at the margin of the supercontinent during the early stages of its breakup (~ 200 Ma; Lamotte, Fourdan, Leleu, Leparmentier, & Clarens, 2015).

In addition to their scarcity in the global geological record, subduction-related rift basins are difficult to identify because of their intrinsic relationship to arc volcanism, generating complex stratigraphic records where primary and secondary volcano-sedimentary deposits evolve in tandem (Németh & Martin, 2007; D'Elia, Martí, Muravchik, Bilmes, & Franzese, 2016), in strong contrast to the non-volcanic basins for which most tectonostratigraphic models have been proposed (e.g., Gulf of Suez and North Sea rifts; Schlische, 1991; Gawthorpe & Leeder, 2000; Withjack,

Highlights

- The synrift phase of the Domeyko Basin took place during two synrift stages: Synrift I (242-225 Ma) and Synrift II (217-200 Ma).
- Tectonic subsidence and volcanism largely controlled the development of sedimentary systems through the evolution of the A/S ratio.
- Rift climax sequences related to a fault linkage process were developed during the Synrift II in the Sierra de Varas sub-basin.
- The Domeyko Basin synrift architecture suggests a transtensional kinematic for the rifting process.

Schlische, & Olsen, 2002). For example, the larger volume and supply rates of sedimentation in magma-rich basins (Muravchik, D'Elia, Bilmes, & Franzese, 2011) results in low accommodation space-sediment supply ratios (A/S) during the syn-eruptive period, creating thick aggradational successions that often interfere with normal siliciclastic or carbonatic deposition (Németh & Martin, 2007). Hence, typical features developed in many nonvolcanic intracontinental rifts such as the tripartite succession representing the alluvial-lacustrine-fluvial deposition (Schlische, 1991; Withjack et al., 2002), are not always observed in volcano-sedimentary basins. Furthermore, new advances in the study of subduction-related rift basins have highlighted the link between key volcanic parameters (type of edifices, style, and scale of eruptions, etc.) and main features of the basin internal dynamics (synrift stratigraphic infill and subsidence pattern), distinguishing two-end members models depending on the amount of volcaniclastic input to the basin (low/high volcaniclastic depocentres; e.g., D'Elia et al., 2016). How can these models be applied to continental subduction-related rift basins? What controls the development of low/high volcaniclastic depocentres in this particular tectonic scenario? A detailed characterization of the main volcanic parameters and their impact on the accommodation and material supply ratios is key to address these questions.

The Domeyko Basin of northern Chile (Figs. 1 and 2) provides an excellent opportunity to study the relationship between tectonism, magmatism, and sedimentation in a subduction-related rift developed on the Gondwana continent. It began as a rift basin during the Triassic (Charrier, 1979; Suárez & Bell, 1992), though its position with respect to the arc remains unknown (Oliveros et al., 2017; Poma et al., 2014; Suárez & Bell, 1992). During the synrift stage, continental and later marine deposition was coeval with profuse volcanism of variable composition, ranging

from basalts to rhyolites (Astudillo et al., 2017; Chong & Hilldebrandt, 1985; Cornejo, Mpodozis, Rivera, & Matthews, 2009; Venegas et al., 2013), with mainly calcalkaline affinities (Espinoza, Oliveros, & Celis, 2016; González et al., 2015; Oliveros et al., 2017). The end of the mechanical subsidence at the postrift stage is thought to have taken place during the earliest Jurassic (Ardill, Flint, Chong, & Wilke, 1998; Suárez & Bell, 1992). Even though the continental infill dominates the synrift succession, previous works focused on the postrift marine successions, paying little attention to the initial volcano-sedimentary successions (Ardill et al., 1998; Bell & Suárez, 1991; Chong & Hilldebrandt, 1985; Marinovic, Smoje, Maksaev, Hervé, & Mpodozis, 1995; Prinz, Wilke, & von Hillebrandt, 1994). This was partly due to the lack of adequate chronostratigraphic constraints in the fossil-poor continental syn-rift

successions and to the strong deformation resulting from the tectonic inversion of the basin since the Late Cretaceous (Amilibia et al., 2008; Bascuñán, Arriagada, Le Roux, & Deckart, 2015), that hampered the understanding of the synrift architecture of the Domeyko Basin. Recent geological field surveys have generated significant geochronological and stratigraphic information of the Triassic successions (Astudillo et al., 2017; Cornejo et al., 2009; González et al., 2015; Venegas et al., 2013) without interpreting that information in the context of the architecture, kinematics, and driving mechanisms of the synrift stage. Thus, tectonostratigraphic models which integrate this data at the entire basin scale are still lacking.

The aims of this paper are twofold. In order to get insights about the evolution of subduction-related basins, we attempt to unravel the tectonostratigraphic evolution of the synrift
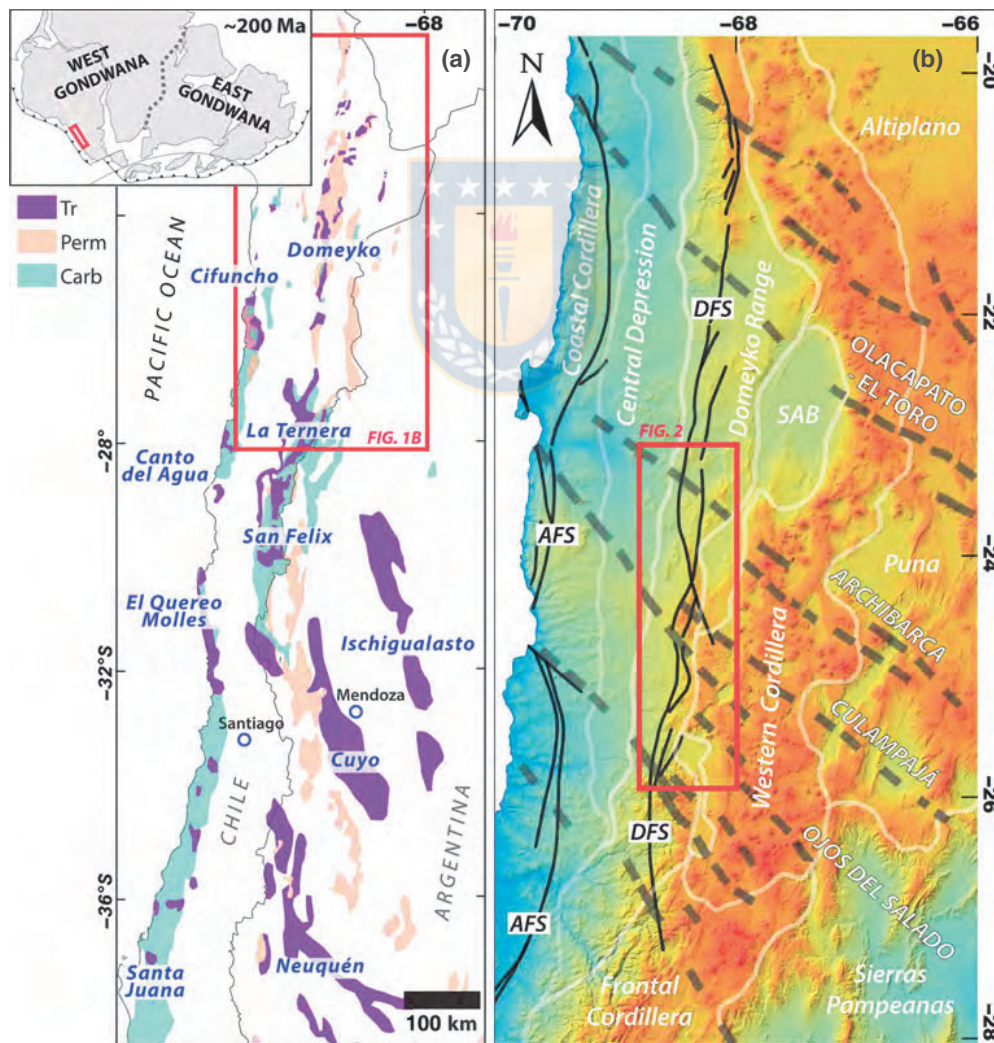
FIGURE 1 (a) Distribution of Triassic basins of Chile and Argentina. The inset shows the reconstruction of Gondwana at 200 Ma according to Torsvik and Cocks (2013). (b) Map of NW Chile and adjacent Argentina, showing main morphostructural units. Main tectonic features include the Atacama Fault System (AFS), the Domeyko Fault System (DFS) and main continental NW-SE lineaments (Abels & Bischoff, 1999; Petrinovic, Riller, & Brod, 2005). The red rectangle indicates the study area showed in Figure 2

Domeyko Basin by addressing the interplay between volcanic, sedimentary, and tectonic processes. Secondly, on a broader scale, we aim to assess the geologic processes acting at the southwestern margin of Gondwana during the early stages of its breakup and propose a coherent tectonic model for extensional basins developed on a continental margin. To achieve these goals we carried a sedimentological and U-Pb geochronological study focused on the continental Triassic deposits cropping out in the Domeyko Range (Fig. 2).

2 | GEOLOGICAL SETTING

2.1 | Overview of the Domeyko Basin

The Domeyko Basin comprises deposits from the Triassic to Lower Cretaceous (Ardill, 1996; Ardill et al., 1998), cropping out in the western margin of the Domeyko Range of northern Chile, between 21° and 27°S (Figs. 1 and 2). The Domeyko Basin developed in its earliest stages under active lithospheric stretching, producing a continental rift basin (Charrier, 1979; Suárez & Bell, 1992). The synrift deposits comprise mainly volcanic and continental sedimentary rocks, which unconformably overlie "upper" Carboniferous to Permian acidic igneous rocks (Fig. 3). Master extensional faults have been inferred to have been inverted postrifting (Amilibia et al., 2008), whereas secondary normal faults show displacements from metres to tens of metres (Fig. 4). The prerift basement in part comprises rocks of the Choiyoi magmatic province, which is typically exposed across the Principal Cordillera of Chile and Argentina (Kleiman & Japas, 2009; Llambías, Quenardelle, & Montenegro, 2003).

Overlying the synrift deposits are sedimentary rocks that represent a marine transgression that took place in several depocentres during the Late Triassic (Chong, 1973; Chong & Hilldebrandt, 1985). This transgression was followed by an abrupt global rise of the sea level during the Hettangian (Ardill et al., 1998). The positive tectonic inversion of the basin took place during the Andean orogeny, which shaped the Domeyko Range through the Domeyko Fault System since the Late Cretaceous (Amilibia et al., 2008; Muñoz et al., 2005). The subsequent deformation imposed on the synrift successions hindered the recognition of the primary basin geometry and most of its large-scale architectural elements.

2.2 | Sub-basins and synrift lithostratigraphic units

In the study area (Fig 2; 24°-26°30′S), the Domeyko Basin comprises two major synrift sub-basins: the Sierra de Varas sub-basin (SVSB) and the Sierra Exploradora sub-basin (SESB). In this section, we briefly describe the synrift units

following the lithostratigraphic schemes outlined by recent studies (Fig. 3; Álvarez, 2003; Cornejo et al., 2009; Venegas et al., 2013; González et al., 2015; Montecino, 2015; Astudillo et al., 2017).

2.2.1 | Sierra de Varas sub-basin

The units representing the SVSB crop out as several small synrift depocentres disrupting the continuity of the current Domeyko Range (Fig. 2). The synrift units unconformably overlie acidic volcanic and granitic rocks of Upper Carboniferous-Early Permian age (La Tabla Formation and Punta del Viento Plutonic Complex) and are conformably overlain by the lower member of the Profeta Formation.

At the Cerro La Ballena depocentre (24°45′S–24°09′S), the Cerro La Ballena Formation comprises ~650 m of welded tuffs, calcarenites, stromatolitic limestones, and basalts to basaltic andesites (Astudillo et al., 2017; Marinovic, 2007; Muñoz, 1989; Valenzuela, 2014). Zircon U-Pb ages indicate an age interval of ca. 218–203 Ma for this unit (Matthews et al., 2007 in Valenzuela, 2014; Astudillo et al., 2017). A mildly younger age for this unit (194.4 + 7.9 -9.2 Ma; Marinovic, 2007) is based on just two zircons with a different weighted mean age as the reported, so we discard it due to its poor statistical signification.

At the Sierra de Varas depocentre (24°11′S and 24°42′S), ~600 m of bouldery-grained conglomerates and breccias from the Cerro Rincones Beds crop out at the western flank of the Sierra de Varas range (Astudillo et al., 2017; Montecino, 2015). A maximum depositional zircon U-Pb age of ca. 276.2 ± 6.6 Ma and stratigraphic relationships constrain its age to the Permian-Late Triassic (Astudillo et al., 2017). In the same depocentre, the Sierra de Varas Formation comprises >650 m of siliciclastic and carbonate sedimentary rocks intercalated with pyroclastic rocks (Astudillo et al., 2017; Contreras, 2014; González et al., 2015; Marinovic et al., 1995; Montecino, 2015). U-Pb ages indicate a range of ~211–206 Ma for this unit (Astudillo et al., 2017; González et al., 2015).

In the Cerro Guanaco depocentre (24°47′S and 25°10′S), the Cerro Guanaco Formation crops out along the flanks of the Sierra de Varas range and is composed of ~1300 m of andesitic to dacitic lavas and pyroclastic rocks (Alfaro, 2014; González et al., 2015). U-Pb zircon geochronology constrains the age of this unit to ca. 213–200 Ma (González et al., 2015). Isolated gravel-rich outcrops which are similar to those from the Cerro Rincones Beds have been assigned by González et al. (2015) to the basal member of the Sierra de Varas Formation. These breccias unconformably overlie Permian plutonic rocks (288 ± 7 Ma; Marinovic et al., 1995) and are discordantly overlain by Hettangian marine rocks from the Profeta Formation (Chong, 1973; Marinovic et al., 1995), though a

FIGURE 3 Lithostratigraphic scheme of the western margin of the Domeyko Range based on the work of Tomlinson et al. (1999); Álvarez (2003); Cornejo et al. (2009); Naranjo and Puig (1984); González et al. (2015) and Astudillo et al. (2017)

fault contact between these units has been proposed recently (González et al., 2015).

The Late Triassic marine transgression is represented by the lower member of the Profeta Formation (Astudillo et al., 2017; Chong & Hilldebrandt, 1985; González et al., 2015; Venegas et al., 2013), which comprises gravel-rich siliciclastic beds, calcareous sandstones, and coral-rich boundstones of a Rhaetian age (Astudillo et al., 2017; Chong & Hilldebrandt, 1985; González et al., 2015; Prinz-Grimm, 1995). This unit concordantly overlies the previous synrift units, though local angular unconformities are observed in Quebrada La Carreta (Fig. 4A) and Quebrada Punta del Viento (Chong & Hilldebrandt, 1985; Fig. 5).
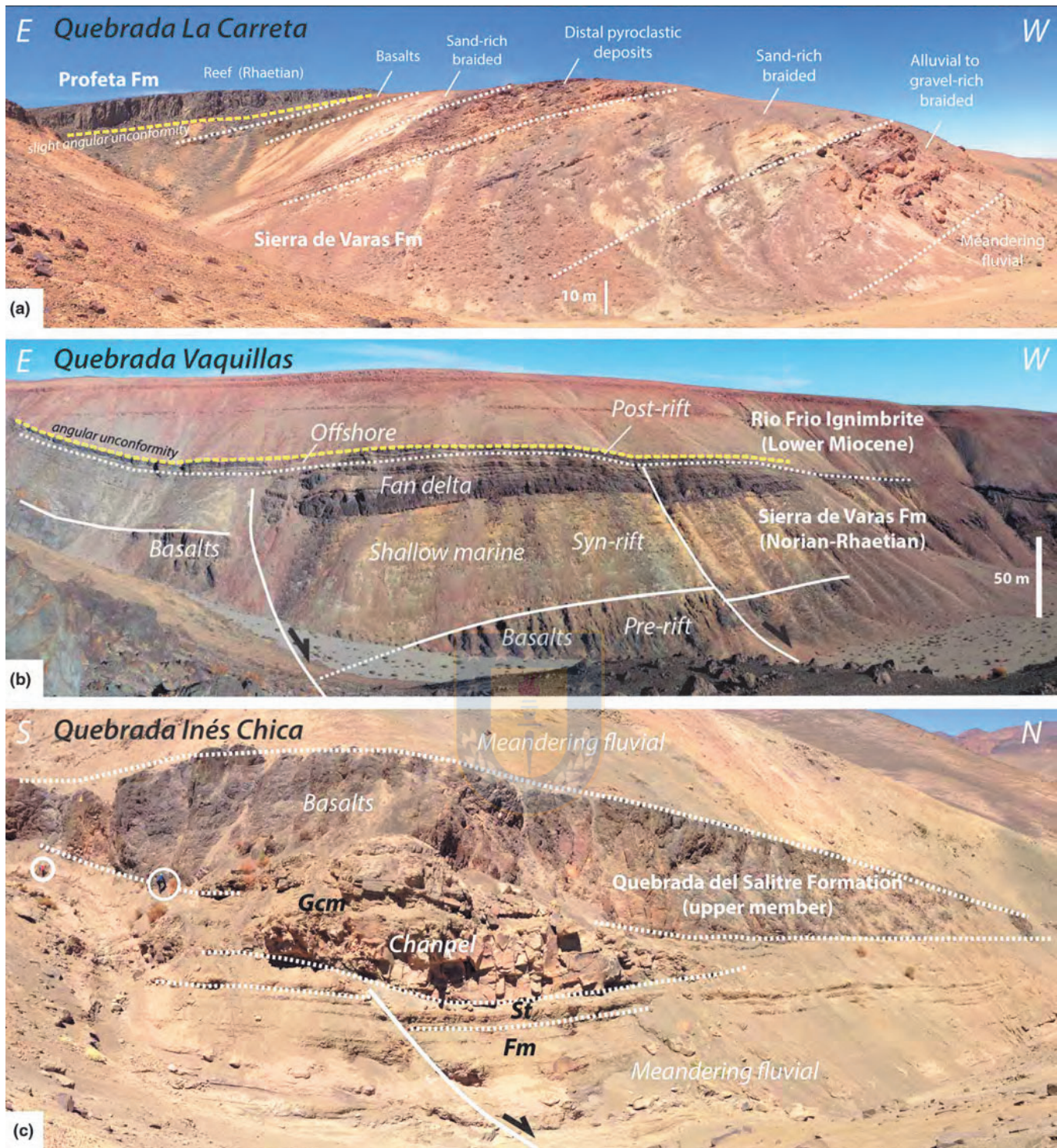
FIGURE 4 (a) Slight angular unconformity between the reef facies of the Profeta Formation and the fluvial and volcanic successions of the Sierra de Varas Formation (SVF) at S8. (b) Synrift listric faults affecting deltaic facies from the SVF at S7. (c) Synsedimentary extensional fault controlling the location of a fluvial palaeochannel, growth strata and basaltic lava flow thickness from the Quebrada del Salitre Formation at S11

2.2.2 | Sierra Exploradora sub-basin

To the south of the study area (Fig 2), the SESB is represented by a voluminous succession of volcanic and sedimentary rocks known as the Quebrada del Salitre Formation (Cornejo et al., 2009; Naranjo & Puig, 1984; Tomlinson, Cornejo, & Mpodozis, 1999). The lower member of this unit unconformably overlies Permian plutonic rocks (Cornejo et al., 2009; Tomlinson et al., 1999), including a thick succession of coarse sedimentary rocks and a suite of dacitic, rhyolitic, and basaltic volcanic rocks (Cornejo & Mpodozis, 1996; Cornejo et al., 2009).
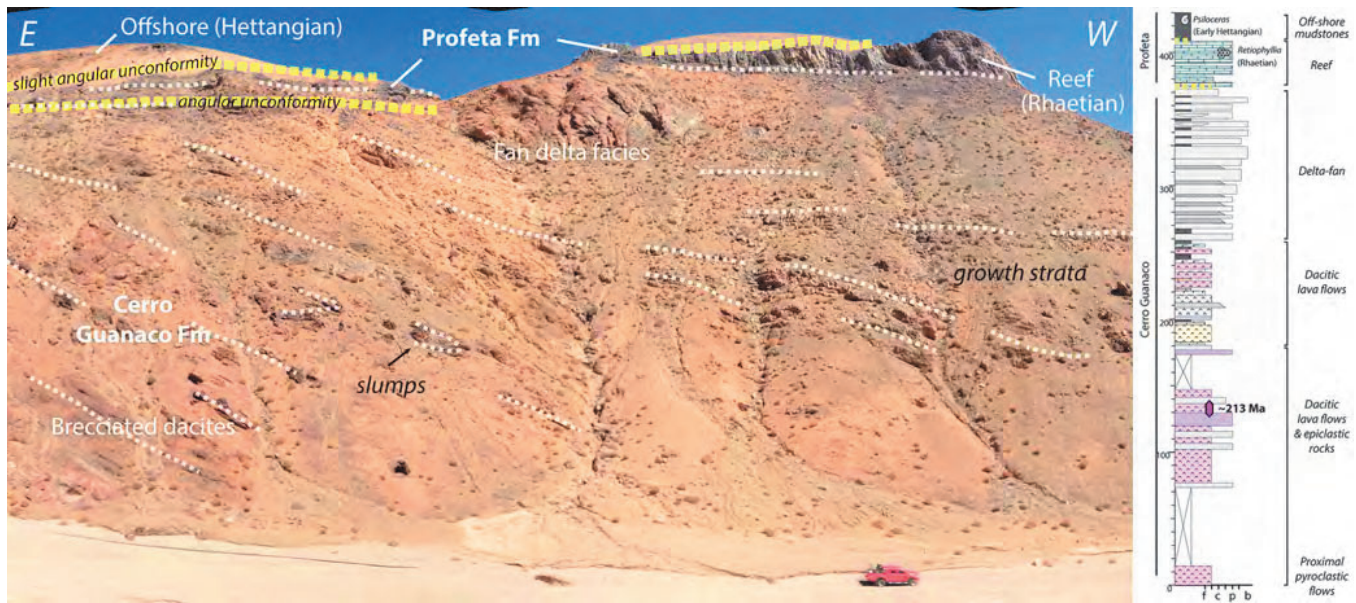
FIGURE 5 Angular unconformity between the delta fan facies from the Cerro Guanaco Formation and the Profeta Formation at S6. A slight angular unconformity between the Rhaetian reef (early postrift) and the offshore facies of the Profeta Formation marks a maximum flooding surface during the Hettangian global sea rise (Ardill et al., 1998)

According to Cornejo et al. (2009), the upper member corresponds to transitional to marine facies, which underlies Pliensbachian beds from the Montandón Formation. However, based on the difference between the continental and marine lithofacies, we agree with the proposal of Álvarez (2003) who separates the initial shallow marine succession in the Las Bateas Formation (Rhaetian – Sinemurian). Hence, we consider the upper member of the Quebrada del Salitre Formation corresponds mainly to the continental and transitional successions developed prior to the well-developed marine deposits (Las Bateas Formation). This division has lithostratigraphic and chronostratigraphic significance, helping to make regional correlations between the sub-basins. The lower levels of the Las Bateas Formation comprise quartz-rich sandstones, conglomerates, and coral-rich boundstones (Rhaetian?; Álvarez, 2003) correlating with the basal member of the Profeta Formation (Astudillo et al., 2017; González et al., 2015).

3 | LITHOFACIES ASSOCIATION AND DEPOSITIONAL ENVIRONMENTS

We performed a comprehensive facies analysis focused in the continental volcanic and sedimentary Triassic successions of the Domeyko Basin (24°–26°S). A summary of the volcanic and sedimentary facies, their codes and interpreted genetic processes is presented in Table 1, whereas a detailed description of individual facies and interpretations can be found in the Supplementary Material SM2. Facies

nomenclature follows Miall (2006) for sedimentary siliciclastic rocks, Branney and Kokelaar (2002) for pyroclastic rocks and D'Elia, Muravchik, Franzese, and López (2012) for volcanic and volcano-sedimentary rocks. Facies analysis was based on measured stratigraphic sections, field survey of key localities and complemented with lithostratigraphic studies carried out by Suárez and Bell (1992), Cornejo et al. (2009) and Mpodozis and Cornejo (2002) in the southern part of the studied area.

3.1 | Facies associations

The sedimentary versus volcanic infill of the synrift stage of the Domeyko Basin present large variations across the depocentres with sedimentary deposits comprising ~60% of the observed rocks. The sedimentary assemblages developed during this stage include alluvial fan, sand-rich braided, and meandering fluvial systems, lacustrine, deltaic, and shallow carbonate platform assemblages. Here we present a synthesis of main facies associations and the interpreted depositional environments where they were originated (Table 2). Main localities of facies associations are listed in Supplementary Material SM7.

3.1.1 | Alluvial fan

Facies Association A1: *Debris flows (Gmm, Sm)*
This facies assemblage is mainly represented by *Gmm* gravel facies, corresponding to massive, matrix-supported and poorly sorted breccias (Fig. 6A), developing crude horizontal stratification (<5 m thick). Decimetre- to metre-scale

intercalations of massive sandstone facies (*Sm*) are common. *Gmm* facies represent debris flows deposits, developed in subaerial to subaqueous conditions (Miall, 2006). Due to the lack of marine or lacustrine features (e.g., wave reworking, subaqueous fossils, calcareous, or muddy matrix) we interpret this association as corresponding to the proximal portion of alluvial fans (Blair & McPherson, 1994; Nemec & Steel, 1984). Given that the generation of this type of *en-masse* flows is favored by steep slopes, and its preservation in the geological record requires a high subsidence, these assemblages are inferred here to be deposited in proximity to uplifted structural blocks (Blair & McPherson, 1994, 2009). Given the inferred extensional setting, these structural blocks were likely formed via fault slip along high-angle, predominantly dip-slip normal faults.

Facies Association A2: *Channelized flows (Gcm, St, Sm)*

Channelized gravel bodies show lenticular to tabular geometries and are formed by clast-supported, poorly to moderately sorted, massive conglomerates of decimetric to metric scale thick (*Gcm* facies, Fig. 7G). This facies occasionally grade upward into medium- to pebbly-sized massive (*Sm*) and trough cross-bedded sandstones (*St*). This association represents the deposition of channels and/or longitudinal bars (*Gcm*) and sediment gravity flows (*Sm*) in the active lobes of alluvial fans (Miall, 2006; Nichols, 2009; Selley, 2000).

Facies Association A3: *Sheetfloods (Gcm, Sh)*

This facies association is mainly represented by well-stratified, tabular bodies of oligomictic and clast-supported conglomerates (*Gcm*), occasionally intercalated with sheets of horizontal laminated and normal graded tuffaceous sandstones (*Sh*). *Gcm* facies were originated by pseudo-plastic debris flows, whereas parallel-laminated sandstones (*Sh*) were deposited under upper flow regime conditions (Miall, 1978, 2006). This association records sheetfloods originated by turbulent flows (Koster & Steel, 1984; Nichols, 2009).

3.1.2 | Fluvial

Facies Association F1: *Sand-rich braided rivers (Gcm, St, Sp, Sh, Sm, Fm)*

The architecture of this facies assemblage corresponds to channel bedforms embedded in thick overbank deposits (Fig. 6). Channelized bedforms are represented by trough cross-bedded sandstones (*St*) formed by 3-D dune migration, and massive sandstones (*Sm*). Fine facies (*Fm*) represents deposition from standing water in the floodplain during low-stage abandonment of channels. Occasional *Sh* facies would represents sporadic spill out floods into the overbank area (Miall, 2006).

Facies Association F2: *Meandering rivers (Fl, Fm, Sm, Sh)*

This facies association corresponds to massive and laminated fine facies (*Fm* and *Fl*), formed by quartz-rich siltstones to very fine sandstones, intercalated with thin sheets of massive (*Sm*), and horizontally stratified sandstones (*Sh*) (Fig. 6C). Fine facies occasionally incorporates Late Triassic fossil flora (Fig. 6B; see Supplementary Material SM6 for detailed descriptions) indicating deposition in a floodplain with abundant vegetation (Miall, 2006). The presence of siderite nodules points to a deposition under reducing conditions with a mixing of seawater and freshwater (Nichols, 2009), suggesting a coastal meandering fluvial origin for these facies. On the other hand, sandy facies represents sediment gravity flows (*Sm*) and deposition under upper plane conditions (*Sh*), probably related to sporadic bank collapse and/or crevasse splays over the floodplain environment (Miall, 2006; Walker & James, 1992).

3.1.3 | Lacustrine

Facies Association L1: *Basinal lacustrine (Fl, Sm)*

Finely laminated mudstones (*Fl* facies) correspond to greyish to greenish mudstones, displaying millimetric lamination ("*laminites*", Fig. 6E), with common intercalations of pyroclastic fall deposits (*//sT* facies). Occasionally, they present centimetric-scale "*cast and flame*" load structures and ripple bedding. Fine facies represents deposition by suspension and weak traction currents (Miall, 2006). The well-preserved "*laminites*" indicates the absence of bioturbating bottom fauna and seasonal variation in phytoplankton production, pointing to a deposition under open water lake conditions in a deep basinal setting (Platt & Wright, 1991), whereas *Sm* facies and the load-cast features suggest the development of sporadic sandy turbidites (Nichols, 2009), probably in a *high-gradient, bench type margin* lake (Platt & Wright, 1991).

Facies Association L2: *Marginal lacustrine facies (Fo, Bs, Gmm, Gcm)*

Stromatolitic boundstone facies (*Bs*), is formed by dark-greyish microbial limestones (*algal mats* and *stromatolites*) showing parallel and convolute bedding, originated in shallow lake shorelines under good illumination conditions (Nichols, 2009). Oncolytic floatstone facies (*Fo*, Fig. 6F) exhibits intercalations of coarse siliciclastic beds (*Gmm, Gcm*), indicating progradation of alluvial fans over swamps in a palustrine environment (Alonso-Zarza & Tanner, 2009; Wright & Platt, 1995). These marginal lacustrine facies were formed in shallow and ephemeral lakes associated with a *low-gradient ramp margin*, where the sediment supply and accommodation space were similar (Platt & Wright, 1991).

TABLE 1 Lithofacies code and corresponding depositional process

Code	Lithology	Description	Geometry and thickness	Interpretation
Sedimentary				
Gmm	Breccia	Poorly sorted, massive, matrix-supported conglomerate showing crude horizontal stratification. Gravel clasts are angular to subangular ranging from pebbles to boulders	Irregular to poorly tabular bodies, making up metres to tens of metres thick	High-strength debris flow
Gcm	Conglomerate	Moderately sorted, massive, clast-supported conglomerate. Clasts range from pebble to large boulder and are moderately to well rounded	Lenticular to tabular. Decimetric- to metric-scale thickness (< 4 m)	Debris flows; hyper-concentrated flows
Gmg	Conglomerate	Matrix-supported conglomerate, normal or inverse grading	Irregular to poorly tabular bodies, up to 2 m thick	Low-strength debris flow
Sh	Sandstone	Medium- to fine-grained sandstones with horizontal lamination	Tabular, 10–30 cm thick	Plane bed flow (critical flow)
Sm	Sandstone	Massive, very fine- to coarse-grained sandstone containing roots	Tabular, <40 cm thick	Sediment gravity flow
Sp/St	Sandstone	Cross stratified, medium to coarse-grained sandstone	Tabular, Foresets up to 60 cm thick	2-D and 3-D dune migration under lower regime conditions
Ss	Sandstone	Thin-bedded stratified sandstones; occurs as thin lenses within or alternates with facies Gmm	Tabular, 10–40 cm thick	Scour fills
Fl	Siltstone	Interlaminated, mudstone, siltstone, and fine-grained sandstone; locally containing plant fossils	Laminar, milli-to centi-metre scale lamination (< 3 cm)	Overbank, abandoned channel, or warning flood deposits
Fm	Siltstone	Massive siltstone and mudstone; locally containing plant fossils	Tabular, 10–30 cm thick	Deposition from suspension; back swamp, abandoned channel deposits
W, M	Limestone	Laminated and massive calcareous mudstones and wackestones	Tabular, < 30 cm thick.	Calcareous deposition from suspension in restricted shallow marine environment
Fo	Limestone	Oncolytic floatstone	Irregular, 20–30 cm thick	Algae originated under shallow subaqueous conditions
R	Limestone	Coarse, clast-supported bioclastic mudstones	Irregular, up to 1.5 m thick.	Deposition in carbonate platform in high-energy conditions
B	Limestone	Coral-rich boundstones	Irregular, deci- to metre- scale thick (up to 1.5 m)	Framework reefal carbonate
Bs	Limestone	Stromatolitic boundstone	Irregular, 20–30 cm thick	Stromatolites and algal mats originated under shallow subaqueous conditions and low siliciclastic input
P	Limestone	Packstone limestones	Irregular, 10–30 cm	Deposition in carbonate platform in high to medium energy conditions

(Continues)

TABLE 1 (Continued)

Code	Lithology	Description	Geometry and thickness	Interpretation
Extrusive				
cB	Basalt	Coherent aphanitic and microporphiritic lava flows. Highly vesiculated and amygdaloidal, very altered	Tabular to lenticular, metre-scale beds making up tens to hundreds of metres (<600 m)	Subaerial mafic lava flows related to fissural volcanism
brB	Basalt	Brecciated and highly vesiculated lava flows with moderate development of pseudo pillows, peperitic textures, and hyaloclastic textures	Tabular to irregular, <3 m thick	Hydroclastic reaction of mafic flows in contact with water or wet sediments. Subaqueous lava flows
cA	Andesite	Coherent porphyritic lavas. Locally highly amygdaloidal	Tabular, 0.4 – 2 m thick	Subaerial intermediate lava flows
cD	Dacite	Coherent and massive lava flows, show aphanitic and porphyritic texture		Subaerial acidic lava flows
brA/brD	Andesite/Dacite	Autobrecciated lava flows with angular clasts in a matrix-supported fabrics and crystalline groundmass	Tabular, < 2 m thick	Subaerial acidic lava flows
bcR/cjD	Rhyolite/Dacite	Coherent vitrophiric and porphyritic lavas showing flow banded textures with vertical disjunctions. Fault related	Irregular to dome-shaped, circular to highly elongated. Related to extensional faults. Tens of metre thick (<40 m)	Silicic domes and necks
Pyroclastic				
mBr	Pyroclastic breccia	Massive monomictic breccia, nongraded, seriated, poorly sorted, and ash supported. Juvenile pyroclasts are dacitic porphyritic rocks	Tabular, 1–5 m thick	Block and ash pyroclastic flows related to dome collapse
mLT	Lapilli tuff	Massive lapilli tuff	Tabular, cm to m thick horizons or amalgamated beds making up tens of metres (<40 m)	Ignimbrite deposit. Rapid aggradation from fluid escape-dominated flow boundary zone of a pyroclastic density current
mT	Tuff	Massive vitric and vitric-crystal tuff	Tabular or lenticular, <1 m thick	Distal ignimbrite or fallout deposits
//sT	Tuff	Thin stratified, laminated well-sorted fine tuff	Tabular, 10–30 cm thick	Fallout deposits
p-//sT	Tuff	Pumice rich, parallel-laminated tuff		Pumice rich fallout deposits

3.1.4 | Shallow marine

Facies Association SM1: *Delta fans (Gmg, Gmm, Gcm, St, Ss, M)*

Gravel-facies consist of pale grey *Gmm*, *Gcm,* and *Gmg* facies, corresponding to debris flows (Miall, 2006) deposited first in alluvial fans, and then into a shallow marine carbonate platform as indicated by the intercalations of limestones (*M* facies) and the increasing input of bioclastic fragments (Benvenuti, 2003; Blair & McPherson, 2009; McPherson, Shanmugam, & Moiola, 1987). Conglomerates display poor sorting and coarsening-upward cycles with clast sizes ranging from pebbles to large boulders (Fig. 5)

with outsized clasts that are up to 1.12 m in diameter (Fig. 6D), immersed in a fine-grained calcareous matrix. Intercalated in these facies are green calcareous mudstones and medium- to pebble-sized calcareous sandstones, with trough cross stratification (*St* facies) and scoured bases (*Ss* facies).

Facies Association SM2: *Rimmed carbonate shelf (B, R, P, W, M, Sm)*

This facies association is characterized by calcareous coral-rich facies formed by greyish, irregular beds of coral-rich *boundstones* (*B* facies, Figs. 5 and 6G), bearing Late Triassic *Retiophyllia* sp. and *Thecosmilia* sp. fossils

TABLE 2 Facies association codes

Type	Depositional environment	Facies association	Code	Facies
Sedimentary	Alluvial fan	Debris flow	A1	*Gmm, Sm*
		Channelized flows	A2	*Gcm, St, Sm*
		Sheetflood flows	A3	*Gcm, Sh*
	Fluvial	Sand-rich braided river	F1	*Gcm, St, Sp, Sh, Sm, Fm*
		Meandering river	F2	*Fl, Fm, Sm, Sh*
	Lacustrine	Marginal lacustrine	L1	*Fo, Bs, Gmm, Gcm*
		Basinal lacustrine	L2	*Fl, Sm*
	Shallow marine	Delta-fan	SM1	*Gmg, Gmm, Gcm, St, Ss, M*
		Rimmed carbonate shelf	SM2	*B, R, P, W, M, Sm*
Volcanic	Basaltic volcanism	Basaltic subaerial & partly subaqueous volcanism	VB1	*cB, brB*
	Intermediate volcanism	Intermediate subaerial lava flows	VI1	*cA, cD, brA, brD*
	Silicic explosive volcanism	Silicic domes & proximal pyroclastic deposits	VS1	*bcR, cjD, mBr, mLT*
		Medium to distal pyroclastic deposits	VS2	*mT,//sT, p-//sT*

corresponding to the core of reefal frameworks (Ardill et al., 1998; Chong, 1977; González et al., 2015; Montecino, 2015). Intercalations of rudstone (*R* facies) and packstone limestones (*P* facies) are composed of fragments of bivalves, brachiopods, shell debris, and corals. Locally, intercalations of massive litharenites (*Sm*) and laminated calcareous mudstones (*M* facies), indicate a deposition by suspension fallout in protected areas, probably in a back-reef to lagoon environment (Nichols, 2009). This assemblage represents a shallow marine carbonate platform limited by a mounded-reef ("rimmed carbonate shelf") with an intermittent siliciclastic input (Nichols, 2009). This reefal facies marks the beginning of a marine transgression of regional significance along the Domeyko Range (Chong, 1973; Chong & Hilldebrandt, 1985; Gröschke, v. Hillebrandt, Prinz, Quinzio, & Wilke, 1988). The presence of *Retiophyllia* sp. and *Choristoceras* sp. in equivalent facies across the Domeyko Basin indicates a Rhaetian age for the onset of the marine transgression (Ardill, 1996; Chong & Hilldebrandt, 1985; Navea, Wilke, & González, 2015).

3.2 | Volcanic facies

Volcanic lithofacies present important variations across the sub-basins, with a mainly intermediate composition (andesites to dacites) at the Sierra de Varas sub-basin and a predominant mafic composition (basalts to basaltic andesites) with silicic and minor intermediate volcanism at the Sierra Exploradora sub-basin.

3.2.1 | Basaltic volcanism

Facies Association VB1: *Basaltic subaerial and partly subaqueous volcanism (cB, brB)*

Mafic volcanic rocks crop out extensively in the southern portion of the study area, with thicknesses varying from tens of metres (~ 60 m) in Quebrada Los Pozos (S7, Fig. 2) to hundreds of metres (>1300 m, Fig 7C) in Quebrada del Salitre (S10, Fig. 2). This facies assemblage mainly corresponds to dark-green, coherent basalts, and basaltic andesites (*cB* facies, Fig. 7C) which form decimetric to metric scale irregular beds displaying a high proportion of vesicles and calcite-filled amygdales. Coherent basaltic facies (*cB*) represents subaerial mafic effusive volcanism (McPhie, Doyle, & Allen, 1993). Locally, basalts exhibit a brecciated texture (*brB* facies), corresponding to mixed lava fragments and silicified red-coloured sediments (peperitic texture, Fig. 7E), indicating interaction of lava with soft and wet sediments (Busby-Spera & White, 1987; Doyle, 2000), or pillow-breccias (Fig. 7B), evidencing partial deposition under subaqueous conditions (Cas & Wright, 1988; White & Houghton, 2006).

3.2.2 | Intermediate volcanism

Facies Association VI1: *Intermediate subaerial lava flows (cA, cD, brA, brD)*

Intermediate composition volcanic rocks crop out discontinuously across the entire Domeyko Range. Andesitic

TABLE 3 Geochronological data from this study

U-Pb geochronology			Sample location			Igneous Zircon (IZ)		Detrital Zircon (DZ)	
Sample	Lithology	Lithostratigraphic unit	UTM N	UTM E	n	Concordia age (Ma)	Weighted mean age (Ma)	Maximum depositional age (Ma)[a]	Major peak (Ma)
CPV-14-157	Volcanic breccia	Cerro Guanaco	7225857	475701	33	211.5 ± 1.8 (n = 28)	–	–	–
CPV-15-400	Vitric tuff	Sierra de Varas	7197540	477638	15	208.4 ± 2.3 (n = 8)	–	–	–
CPV-14-268	Vitric tuff	Sierra de Varas	7311340	480355	35	–	203.5 ± 1.6 (n = 20)	–	–
CPV-15-310	Rhyolite	Quebrada del Salitre	7114194	462332	38	–	225.2 ± 1.5 (n = 26)	–	–
CPV-15-350	Lapilli tuff	Sierra de Varas	7201630	471834	31	–	210.7 ± 3.4 (n = 3)	–	–
CPV-15-342	Quart-rich sandstone	Sierra de Varas.	7201928	471961	107	–		213.8 ± 3.1 (n = 4)	~292
CPV-14-254	Quartz-rich sandstone	Sierra de Varas	7200644	475282	105	–		234.4 ± 4.8 (n = 2)[b]	~297
CPV-14-261	Breccia	Sierra de Varas	7252939	479730	35	–	–	303.3 ± 2.1 (n = 33)	~303
CPV-15-316	Sandstone	Quebrada del Salitre	7125508	468083	120	–	–	241.5 ± 4.0 (n = 3)	~294
CPV-15-324	Sandstone	Quebrada del Salitre	7115254	470733	35	–	–	208.4 ± 3.4 (n = 3)	~260

[a]Maximum depositional age calculated from the 3 or more zircons overlapping at 2σ which define a separate peak.
[b]Maximum depositional age calculated from the 2 youngest zircons overlapping at 1σ.

volcanism is common in the northern portion of the study area (Cerro La Ballena depocentre), whereas dacitic and subordinate andesitic volcanism predominates to the south (Vaquillas Altas depocentre and SESB).

Andesitic to dacitic coherent facies (*cA* and *cD* facies), form massive and vesiculated beds (0.4–2 m thick), showing a porphyritic texture (Fig. 5) composed by medium-grained phenocrysts (pg + amph ± qtz) embedded in a glassy or microcrystalline groundmass. These facies correspond to lava flows originated under low shear rates in subaerial conditions (Stewart & McPhie, 2003). Locally, matrix-supported, brecciated dacites and andesites (*brD*, Fig. 7F, and *brA* facies) were originated by an autoclastic, brittle fragmentation mechanism, due to the lateral transport of lava flows under subaerial conditions (McPhie et al., 1993; Stewart & McPhie, 2006).

3.2.3 | Silicic effusive and explosive volcanism

Facies Association VA1: *Silicic domes and proximal pyroclastic deposits (bcR, cjD, mBr, mLT)*

Coherent vitrophyric rhyolites (*bcR*) and dacites (*cjD*) present flow banding and vertical columnar jointing (Fig. 7D), indicating the flow advance and cooling margins of small domes and vents (Fink & Anderson, 2000). At SESB, these domes form elongated bodies (1.6 to 2.2 km long) which are spatially associated with ~NS trending extensional faults (Cornejo et al., 2009). Large vents are recorded by subcircular silicic domes bounded by arcuate ring normal faults (~5 km of diameter, Tomlinson et al., 1999) associated with dome-margin breccias (*mBr*), suggesting an extensional origin for these vents, with a plate (piston) mechanism for the subsidence (Lipman, 2000).

At Cerro Guanaco depocentre (S5 and S6 in Fig. 9), matrix-supported, and monomictic massive pyroclastic breccias (*mBr*) are spatially associated with dacitic domes and are interpreted as block-and-ash pyroclastic flow deposits related to the gravitational collapse of lava domes (Branney & Kokelaar, 2002; Cas & Wright, 1988; Freundt, Wilson, & Carey, 2000).

Ignimbrite deposits are recorded by very poorly sorted massive lapilli-tuffs (*mLT* facies), which are formed by lapilli-sized pumice, crystal fragments and lithics in a vitric matrix. The common thickness of *mLT* facies at Vaquillas Altas depocentre are up to ~30 m thick, though similar facies can be thicker at Cerro Guanaco (Alfaro, 2014; González et al., 2015) and Cerro La Ballena (Valenzuela, 2014) depocentres. There is a general lack of evidence of high-temperature welding (e.g., sintering of glass shards, rheomorphism, etc.), with some ignimbrites showing a pseudo-eutaxitic texture due to diagenetic alteration.
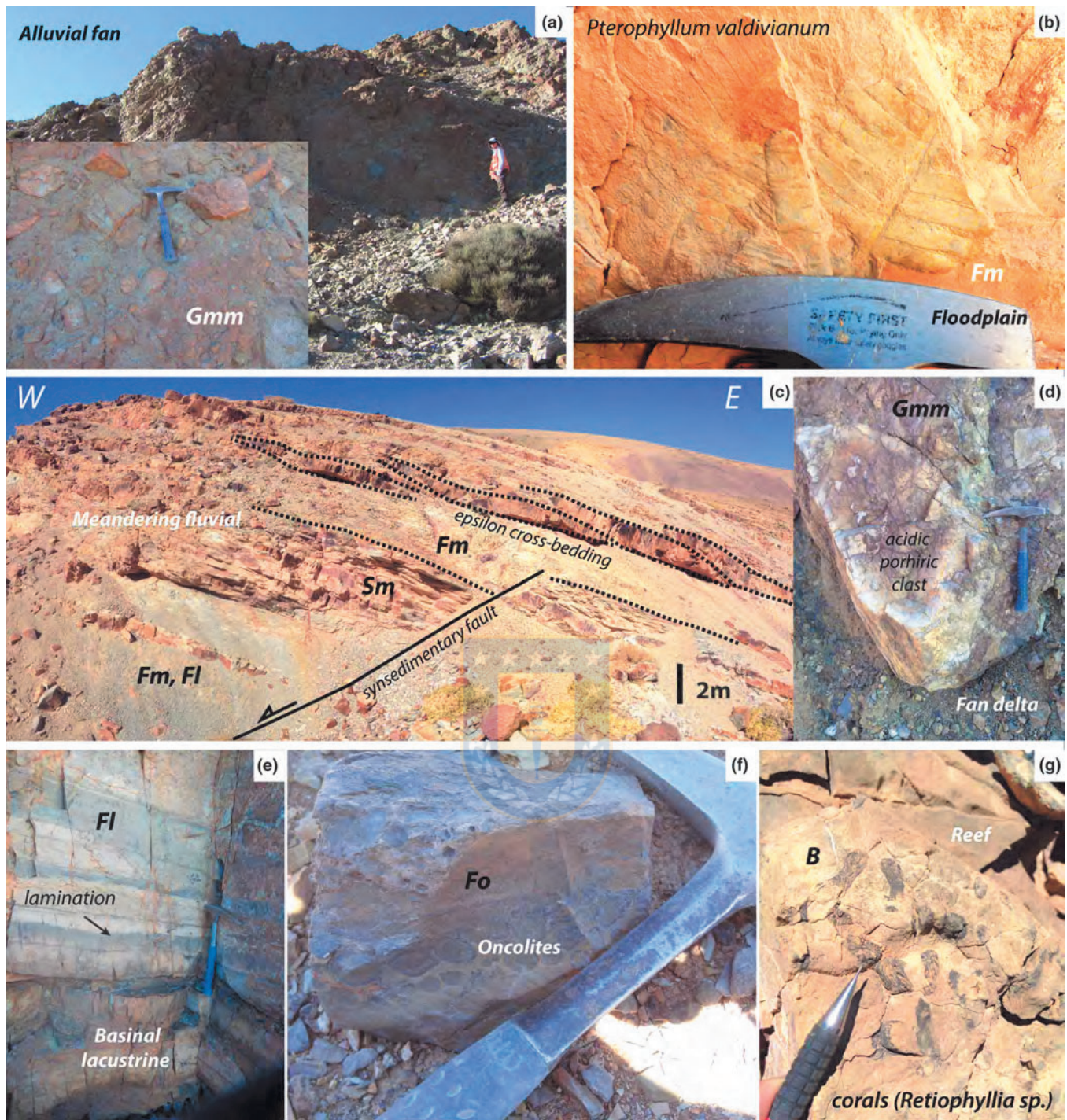
FIGURE 6 (a) *Gmm* facies developed in proximal alluvial fan facies (debris flows) from the basal member of Sierra de Varas Formation (SVF) at Sierra de Varas depocentre. (b) Late Triassic fossil flora developed in floodplain assemblage from SVF at S7. (c) A synsedimentary extensional fault affecting meandering fluvial assemblages from basal successions of the SVF at S7. (d) Matrix-supported gravel facies developed in a fan delta assemblage from the Cerro Guanaco Formation at S6. (e) Basinal lacustrine facies (*Fl* facies) from SVF at S7. (f) Oncolite-bearing floatstone facies deposited in marginal lacustrine conditions from the SVF at S3. (g) Boundstone facies from the Las Bateas Formation bearing Late Triassic corals (*Retiophyllia* sp.) at S11

Facies Association VA2: *Medium to distal pyroclastic deposits (mT, //sT, p-//sT)*

Reddish- to greenish- massive tuffs (*mT*) are composed of well-sorted pumice, crystals, and minor lithics in a vitreous ash-sized matrix, making up centimetric beds (<1 m). This facies can corresponds to the deposition of fine-grained distal ignimbrites or fallout deposits (Branney & Kokelaar, 2002; Cas & Wright, 1988; Fisher & Schmincke, 1984).
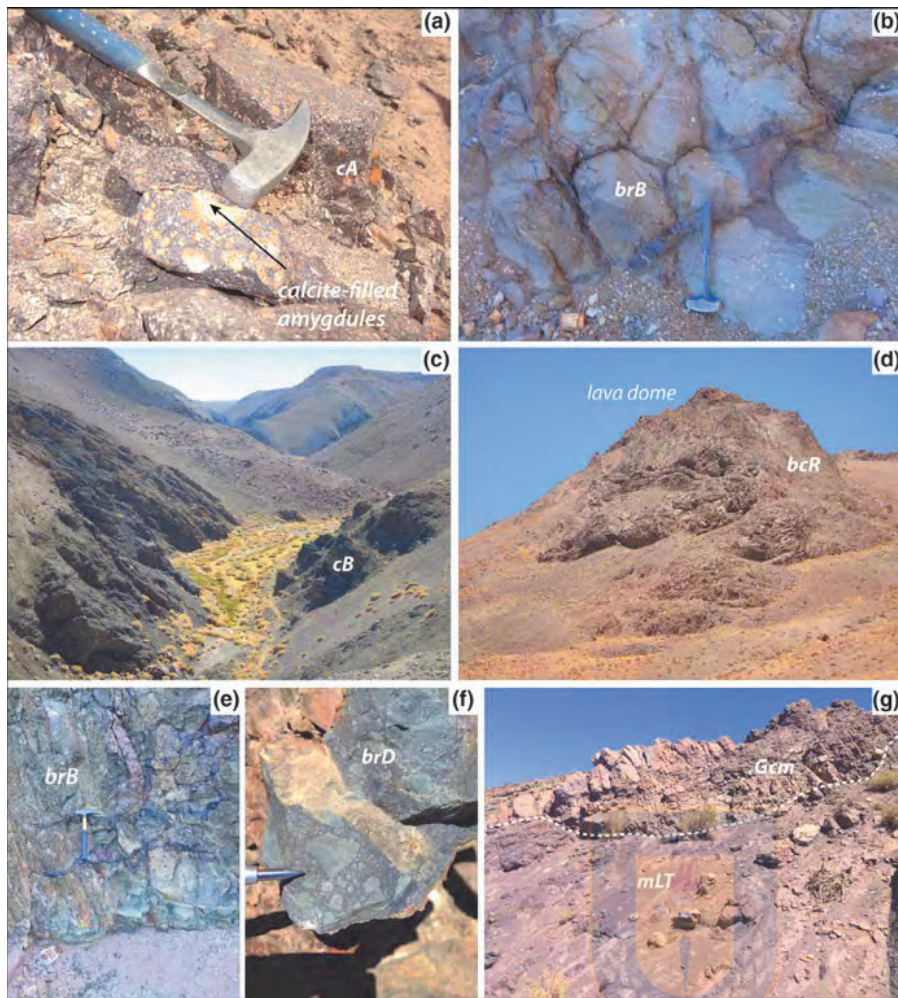
FIGURE 7 (a) Coherent andesites (*cA*) from Cerro La Ballena Formation at S1. (b) Brecciated basalts (*brB*) from Quebrada del Salitre Formation (QSF) showing pseudo-pillow structures at S7. (c) Coherent basalts (*cB*) successions at S10. (d) Silicic lava dome formed by coherent rhyolites (*bcR*) from the QSF showing vertical columnar jointing at Cerro Colorado. (e) Peperites. (f) Brecciated dacites facies (*brD*) at S6. (g) Channelized flows (alluvial fan) incised over massive lapilli-tuffs (*mLT*) from the SVF at S7

On the other hand, well-stratified (occasionally laminated) and very well-sorted //s*T* facies present a similar composition that *mT* facies. The //s*T* facies could represent distal fallout of eruption plumes, ash-rich pyroclastic density currents or surges deposits (Branney & Kokelaar, 2002; Cas & Wright, 1988), however, its common association with lacustrine mudstones, its generally low thickness (0.3-0.6 m) and the absence of lateral transport evidence (scours, cross stratification, low-angle truncations), points to a fallout origin (Branney & Kokelaar, 2002; Cas & Wright, 1988; D'Elia et al., 2012; McPhie et al., 1993). Occasionally, similar pumiceous-rich tuffs (*p-//sT* facies) show subangular pumice clasts indicating a similar fallout origin (Branney & Kokelaar, 2002).

4 | RESULTS

4.1 | Analytical methods

U-Pb igneous and detrital zircon analyses were performed using laser-ablation inductively coupled-plasma mass-spectrometry (LA-ICP-MS and LA-MC-ICP-MS) method in 10

samples. Lithostratigraphic units sampled correspond to the continental, sedimentary, and volcanic, Sierra de Varas, Cerro Guanaco and, Quebrada del Salitre formations.

Heavy minerals were concentrated by standard crushing, Gemini table, LST heavy liquid (2.9 g/cm^3), and magnetic separation techniques at Servicio Nacional de Geología and Minería and University of Concepción. Finally, zircon grains were handpicked under a binocular microscope, mounted in epoxy, and polished to expose grain centres for cathodoluminescence (CL) imaging. U-Pb analysis of samples CPV-14-157, CPV-14-254, CPV-14-261, and CPV-14-268 were performed at the Arizona LaserChron Center (ALC), University of Arizona, whereas samples CPV-15-310, CPV-15-316, CPV-15-324, CPV-15-342, CPV-15-350, and CPV-16-400 were analysed at the Laboratorio de Estudios Isotópicos (LEI), Centro de Geociencias, UNAM. Concordia and average ages were calculated using Isoplot v. 4.15 (Ludwig, 2008). We apply a discordance filter of <15% for igneous analyses, whereas for detrital analyses, a discordance filter <25%, and a reverse discordance filter of > -5% were used. ^{206}Pb/^{238}U ages are preferred for zircons younger than <1.0 Ga, whereas ^{207}Pb/^{206}Pb ages are

reported for zircons older than that age (Gehrels, 2011). A detailed description of the analytical techniques is in Supplementary Material SM5.

4.2 | U-Pb geochronology

Geochronological results and sample locations are summarized in Table T3 and Figures 2 and 8. Errors are reported as 2σ and maximum depositional ages (MDA) were calculated averaging the 3 or more zircons overlapping at 2σ error, except for sample CPV-14-254, where 2 zircons overlapping at 1σ error was used (Dickinson & Gehrels, 2009). Detailed isotopic and rejected data of U-Pb analysis are found in Supplementary Material SM3 and SM4.

4.2.1 | Sierra de Varas Formation

Detrital zircons (DZ) from a coarse-grained sandstone intercalated in monomictic massive breccias (CPV-14-261) corresponding to the Lower Member of the Sierra de Varas Formation (González et al., 2015), yielded a unimodal age distribution with a weighted mean age of 303.3 ± 2.1 Ma which is interpreted as the MDA. The breccias overly in unconformity Permian plutonic rocks with a K-Ar (biotite) age of 288 ± 7 Ma (Marinovic et al., 1995), suggesting a significant gap between the MDA and the depositional age for this unit.

DZ age distribution from a coarse sandstone intercalated in conglomeratic facies at the base of the Sierra de Varas Formation (CPV-15-342) shows the main peak at ca. 292 Ma (~80%) and a minor peak at ca. 246 Ma (~12%) with an MDA of 213.8 ± 3.1 Ma. Another DZ sample from this unit (CPV-14-254), a quartz-rich sandstone directly overlying Carboniferous-Permian plutonic rocks (Punta del Viento Plutonic Complex), shows a main age peak at ~297 Ma (77%) and two smaller groups at ~479 Ma (9%) and ~246 Ma (3%), with scarce zircons older than 500 Ma and a MDA of 234.4 ± 4.8 Ma. Thus, both samples from the basal successions indicate the main source from the Permian basement (292-297 Ma), with more restricted secondary sources from Middle Triassic (~246 Ma) and Ordovician (~478 Ma) rocks.

Igneous zircon (IZ) from a lapilli-tuff sampled 40 m above the base of the unit (CPV-15-350) yielded a major peak at ca. 227 Ma and a secondary peak at ca. 211 Ma. We interpret the youngest peak as the age of the eruptive event, yielding a weighted mean age (WMA) of 210.7 ± 3.4, whereas the secondary peak at ca. 227 Ma would correspond mostly to accessory sources. A vitric tuff (CPV-14-268) intercalated in the upper levels of a lacustrine succession (Fig. 8) yielded a WMA of 203.5 ± 1.6 Ma interpreted as the age of the volcanic event. An older small peak at ca. 283 Ma is probably associated to accidental fragments. On the other hand, an IZ sample from a vitric tuff intercalated in fluvial deposits (CPV-15-400) yielded a Concordia age of 208.6 ± 2.3 Ma, interpreted as the crystallization age of the pyroclastic event.

4.2.2 | Cerro Guanaco Formation

Igneous zircon from a brecciated dacite (CPV-14-157) yielded a Concordia age of 211.5 ± 1.8 interpreted as the crystallization age. This lithostratigraphic unit was formerly assigned to the Carboniferous-Permian La Tabla Formation (Venegas et al., 2013). However, taking into account the Norian crystallization age and the interpretation of the dated level as part of proximal acidic dome deposits, we assign these outcrops to the Cerro Guanaco Formation (Alfaro, 2014; González et al., 2015).

4.2.3 | Quebrada del Salitre Formation

Igneous zircon from a banded rhyolite belonging to a silicic dome (CPV-15-310) yielded a WMA of 226.7 ± 1.4 Ma interpreted as the timing of the volcanic event, whereas a secondary group at ca. 241 Ma is inferred to represent accessory material from the volcanic conduit. A litharenite corresponding to sand-rich fluvial deposits from the basal member of this unit (CPV-15-316) yielded an MDA of 241.5 ± 4.0 Ma with a major peak at ca 294 Ma (41%) and a secondary peak at ~267 Ma (12%). Another DZ sample from a tuffaceous sandstone corresponding to meandering fluvial facies from the upper continental member of this unit, shows an MDA of 208.4 ± 3.4 Ma and major peaks at ca. 258 Ma (47%) and ca. 272 Ma (24%).

5 | DISCUSSION

5.1 | Stratigraphic correlations across the Domeyko Basin

Given the abrupt facies changes across depocentres and the common incomplete exposure of many sections due to basin inversion process, there are scarce correlations for the logged synrift deposits. The most easily correlated unit is the "upper" Rhaetian marine transgression marked by the presence of coral-rich reef boundstones (Fig. 6G) at the base of the Profeta and Las Bateas formations (Álvarez, 2003; Ardill et al., 1998; Astudillo et al., 2017; Chong & Hilldebrandt, 1985; Cornejo et al., 2009; González et al., 2015; Venegas et al., 2013), which is observed in most of the depocentres (Fig. 9). The beginning of the synrift can be correlated at the base of the sections S7 and S8 in the Vaquillas Altas depocentre for the Sierra de Varas Formation and between the base of S4 and S5 sections in the Sierra de Varas and the Cerro Guanaco
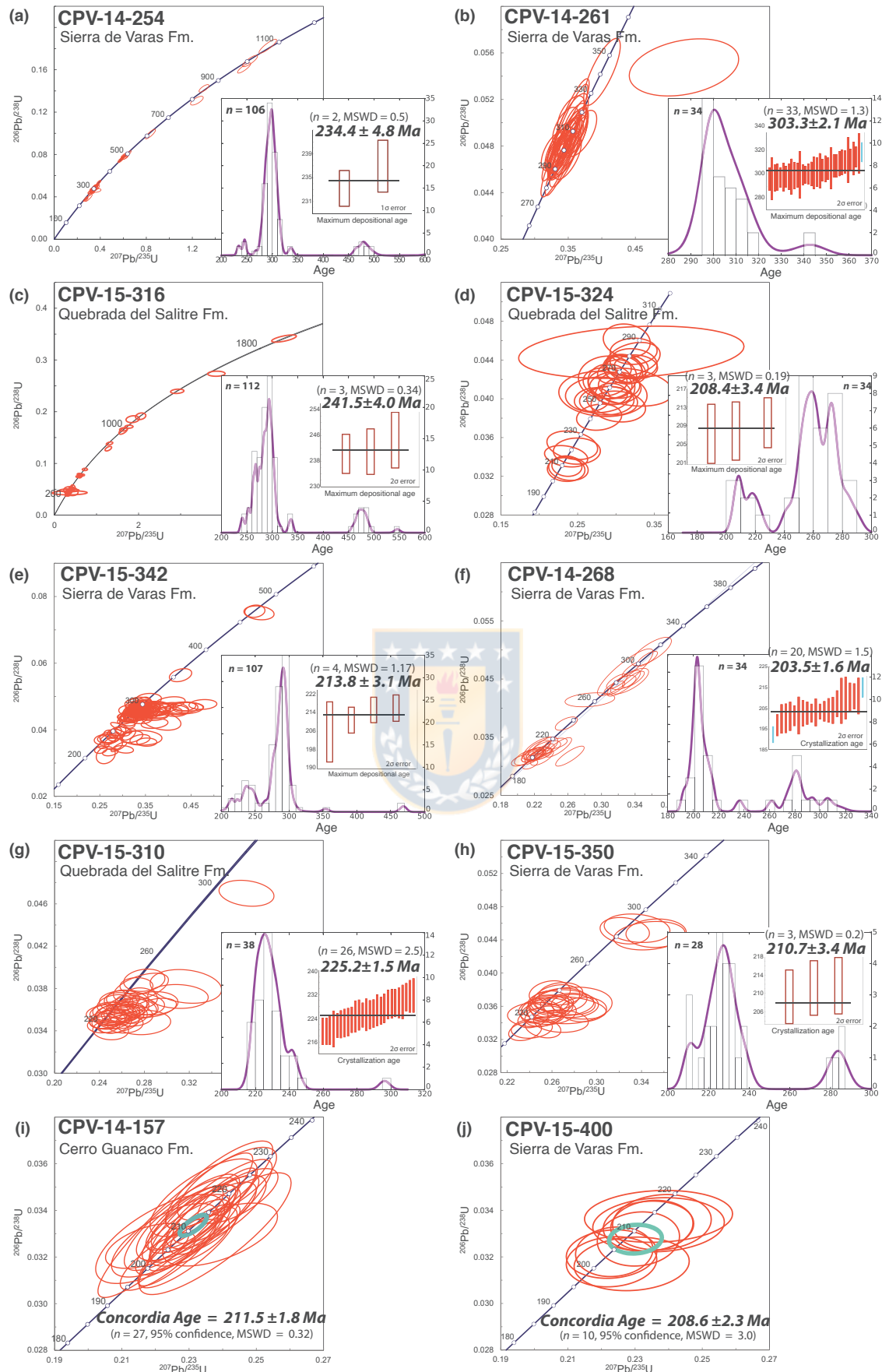
FIGURE 8 U-Pb geochronological data from this study

depocentres for the Sierra de Varas and the Cerro Guanaco formations respectively. Secondary correlations based on sedimentary facies can be suggested between the meandering fluvial systems that follow the thick basaltic successions of the Quebrada del Salitre Formation (S10 and S11) and the Sierra de Varas Formation (S7 and S8) at the Vaquillas Altas depocentre (Fig. 9).

5.2 | Timeframe of the synrift activity

In the Domeyko Basin, we propose that two stages of major mechanical subsidence and associated sedimentation were developed during the Triassic (Fig. 11). The Synrift I would have taken place in the SESB, during the Ladinian – Carnian (~240–225 Ma). The lower limit is constrained by the DZ MDA of 241.5 ± 4.0 Ma from sand-rich braided fluvial facies (CPV-15-316; Figs. 8 and 9) and the upper limit by the IZ age of rhyolitic domes which have been dated at 225.2 ± 1.5 Ma (CPV-15-310, Fig. 8 and S10 in Fig. 9). The Synrift II ("upper" Norian – Rhaetian; 217-200 Ma) is well constrained by the initiation of the SVSB at ca. ~213-210 Ma (Figs. 9 and 10). The upper limit of the Synrift II is constrained by the Rhaetian marine transgression and a U-Pb IZ age of 200 ± 2 Ma (González et al., 2015) from the uppermost synrift beds in the Cerro Guanaco depocentre (section S5, Fig. 9). The activity of the SESB during the Synrift II can be established by the DZ MDA of meandering fluvial facies (208.4 ± 3.4 Ma) which are overlain by Rhaetian shallow marine facies from the Las Bateas Formation (Álvarez, 2003). The initiation age of the Synrift II at SESB is very problematic to resolve due to the low zircon fertility of basaltic lavas inferred to represent the basal part of the Synrift II (S10, Fig. 9). The latter raises the possibility that a relatively continuous deposition took place at the SESB, without the inferred hiatus between the two synrift stages. However, considering a more regional context, the scattered sedimentary record from the "Synrift I stage" occurred in isolated basins peripheral adjacent to the Domeyko Range which do not record deposition during the Synrift II stage, such as the El Bordo (Basso & Marinovic, 2003), Tuina (Henríquez, Becerra, & Arriagada, 2014) and Pular (Solari, Montecinos, Venegas, & Espinoza, 2015) formations, suggesting that the volcanism and sedimentation during the Synrift I stage was discontinuous with respect to the Synrift II stage. On the other hand, the well-marked initiation of depocentres at ~212 Ma such as the SVSB and the Cifuncho basin at the Coastal Cordillera (Contreras et al., 2013; spinoza, Oliveros, Vásquez, & Bechis, 2015) seems to indicate that the Synrift II stage was a well-distinguishable event across the palaeo-margin. Therefore, we propose that both stages were clearly differentiated and infer that the activity of the SESB during the Synrift II stage took place in a similar timeframe as the SVSB, though further

geochronological constraints are needed to confirm this hypothesis.

5.3 | Tectonostratigraphic evolution of the synrift Domeyko Basin: an interaction between sedimentary, volcanic, and tectonic processes

Sedimentary systems are the result of the balance between the accommodation space (A) and sediment supply (S) to the basin. The accommodation space is related to the space available below the base level in order for sediments to accumulate (Jervey, 1988). In nonmarine environments, base level is better defined by the "stratigraphic base level" (Martinsen et al., 1999), which is the equilibrium surface that "describes the direction in which a stratigraphic system is likely to move, towards sedimentation and stratigraphic preservation or sediment bypass and erosion" (Shanley & McCabe, 1994). Thus, we use the "subaerial accommodation space" defined as "the space developed between successive depositional surfaces of different ages" (Muto & Steel, 2000), which is most commonly driven by changing subsidence, uplift or eustatic sea level and is represented by the thickness of preserved sediment in the stratigraphic record (Muto & Steel, 2000). In nonmarine basins, eustatic level changes are negligible (Martinsen et al., 1999). On the other hand, in rift basins tectonic subsidence may affect the accommodation space more strongly than climatic effects (Derer, Schumacher, & Schäfer, 2005; Martins-Neto & Catuneanu, 2010; Prosser, 1993; Schlische, 1991). However, the latter can account for higher frequency changes in sedimentary environments (Carroll & Bohacs, 1999), as observed in some rift lakes from East Africa (Lake Tanganyika, Lake Malawi, and Lake Turkana; Scholz, Rosendahl, & Scott, 1990; Scholz et al., 2007; Johnson, Halfman, Rosendahl, & Lister, 1987) and United States (Lake Lahonton; Benson & Thompson, 1987). During the Triassic, major climatic fluctuations at the Domeyko Basin are poorly recorded, maintaining a main subtropical climate, though sporadic drought episodes have been proposed at the Coastal Cordillera (Suárez & Bell, 1994, 2010). However, the development of very different sedimentary environments in both sub-basins during a similar period (Synrift II stage), such as lacustrine and alluvial facies associations in the SVSB and meandering rivers in the SESB, let us to infer that the base level variations were mainly controlled by local variations in the subsidence regime rather than climatic fluctuations which should have allowed the development of similar sedimentary environments in a broader area. In the following section, the evolution of the synrift stages in the SVSB and SESB is analysed interpreting changes in the stratigraphic record (A/S) as due to the interplay between sedimentary, volcanic, and tectonic processes.
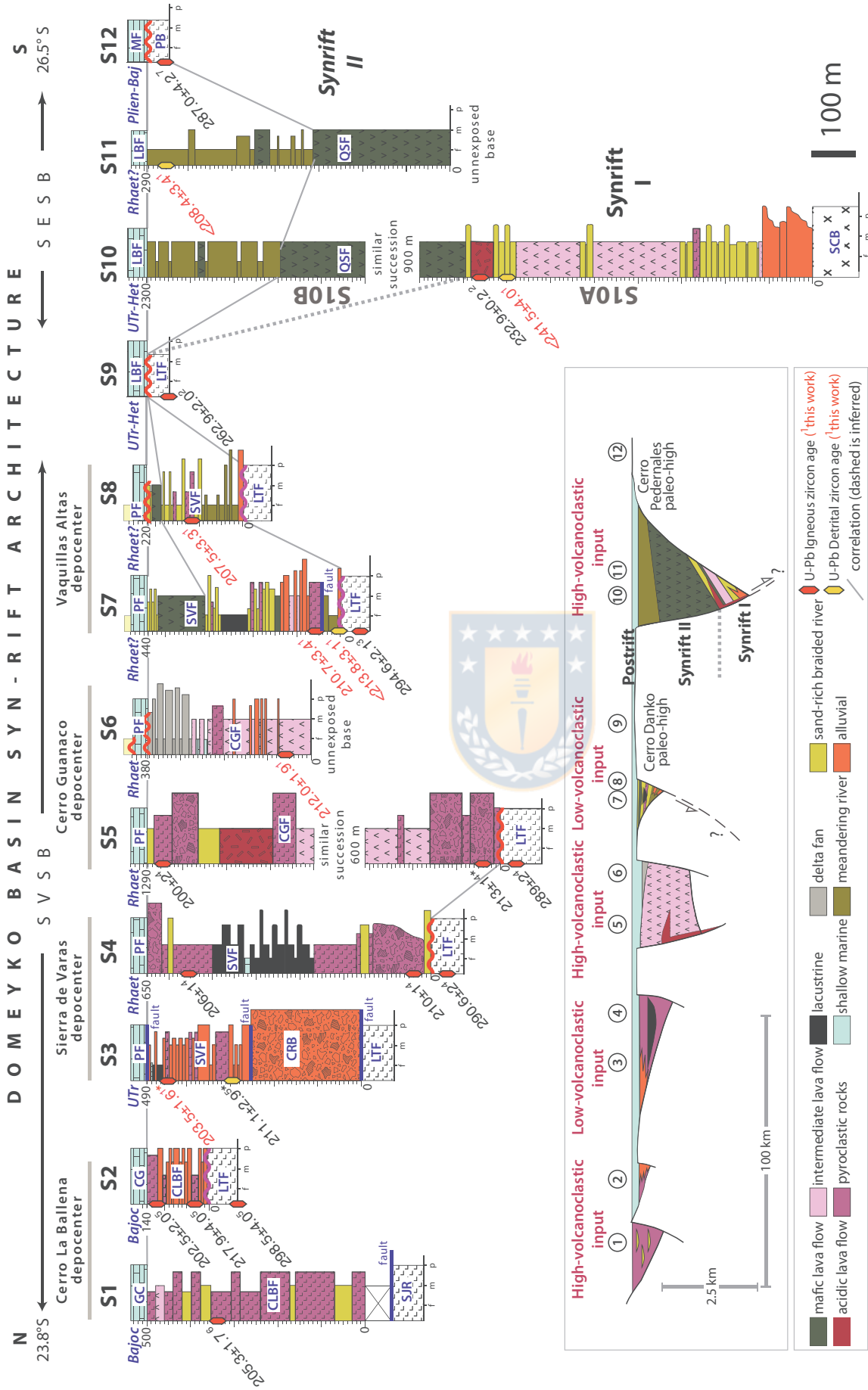
FIGURE 9 Domeyko Basin synrift architecture based in generalized sections across the Domeyko Range (extensional structures correspond to oblique NW-SE inferred basin margin faults). References for sections are: this work (S2, S3, S6, S7, and S8); this work and Cornejo et al., 2009 (S10); this work and Suárez & Bell, 1992 (S11); Valenzuela, 2014 (S1); Contreras, 2014 (S4): González et al., 2015 (S5); Cornejo et al., 2009 (S9) and Tomlinson et al., 1999 (S12) (for section locations see Figure 2). Different depocentres have been classified as "lower/high-volcaniclastic" based on the impact of volcanism in the evolution of sedimentary systems (D'Elia et al., 2016). Lithostratigraphic unit abbreviations are as follow: SJR (Sierra Jardín Rhyolites), CLBF (Cerro La Ballena Formation), CG (Caracoles Group), LTF (La Tabla Formation), PF (Profeta Formation), SVF (Sierra de Varas Formation), CRB (Cerro Rincones Beds), CGF (Cerro Guanaco Formation), LBF (Las Bateas Formation), QSF (Quebrada del Salitre Formation), SCB (Sierra Castillo batholith), MF (Montandón Formation) and PB (Pedernales batholith). References for U-Pb ages are: [1] (this work, red coloured), [2] (Cornejo et al., 2009), [3] (Venegas et al., 2013), [4] (González et al., 2015), [5] (Astudillo et al., 2017), [6] (Matthews et al., 2007 in Valenzuela, 2014), [7] (Maksaev, Munizaga, & Tassinari, 2014).

Synrift II at Quebrada Los Pozos (section S7)
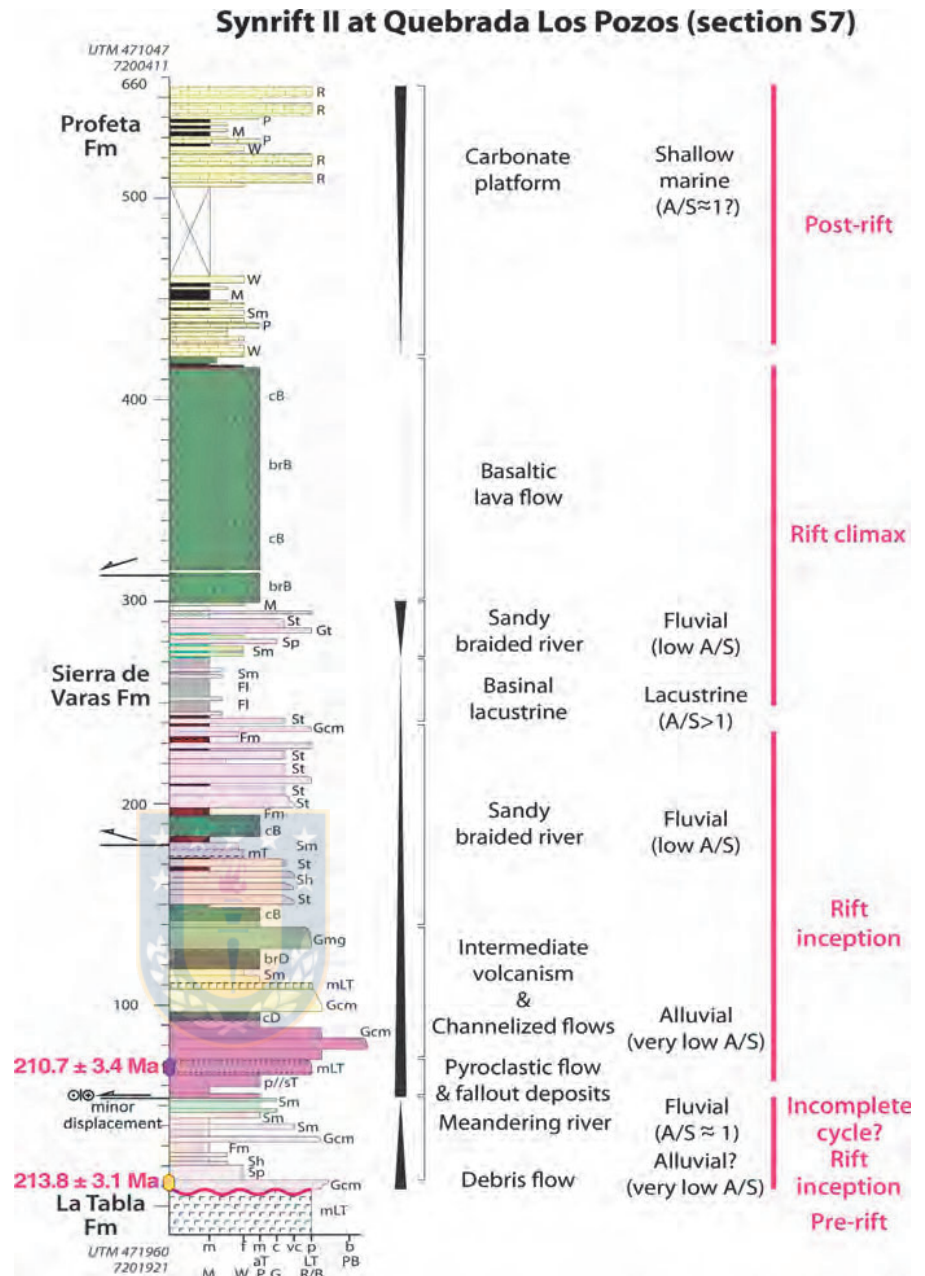
FIGURE 10 Generalized stratigraphic section S7 showing a complete rift cycle during the Synrift II stage. Rift inception records alluvial and fluvial with an A/S < 1, rift climax records basinal lacustrine facies with an A/S > 1 indicating an abrupt increase of subsidence and the postrift phase is marked by shallow marine facies indicating a decrease of the subsidence and supply to the basin. Approximate lithology outcrop-colour is indicated

5.3.1 | Synrift I (~240–225 Ma)

Sierra Exploradora sub-basin
The Synrift I stage (Fig. 12A) recorded the deposition of coarse alluvial fan facies (A/S < 1; Martinsen et al., 1999) with a thickening-upward trend (base of S10, Fig. 9), that resulted from very low A/S due to low subsidence rates during basin initiation (Gawthorpe & Leeder, 2000). The alluvial fans are followed by sand-rich braided rivers indicating a slight increase in the A/S ratio (S10 in Fig. 9). This was accompanied by subaerial intermediate volcanism which added a significant supply to the basin (S10, Fig. 9). During the Carnian, deposition to the basin was marked by a profuse silicic magmatism evidenced by the extrusion of

rhyolitic domes spatially related to high-angle extensional structures with a current ~NS trend (Fig. 12A). Explosive volcanism is recorded by the proximal deposition of ign-imbrites near to silicic vents. The scarcity of major epiclas-tic sedimentation indicates the predominance of a high volcaniclastic material supply during this period, with restricted deposition of sand-rich braided fluvial facies (A/S < 1 ratio).

5.3.2 | Synrift II (~217–200 Ma)

Sierra de Varas sub-basin
The initiation of rifting in the Sierra de Varas sub-basin (Norian) was accompanied by the deposition of proximal

alluvial fan facies (A/S < 1) from the Cerro Rincones Beds (S3 in Fig. 9) and the basal member of the Sierra de Varas Formation (S4 in Fig. 9). At the Vaquillas Altas depocentre (S7 in Fig. 9), the alluvial deposition (A/S < 1) was followed by meandering rivers (A/S ≈ 1, Martinsen et al., 1999) carrying a Late Triassic fossil flora (Fig. 6B), evidencing an increase in the accommodation space during the inception of the rift. This phase experienced negligible volcanism, evidenced by the mature composition of sediments and scarce DZ juvenile sources (Fig. 8E).

During the Norian-Rhaetian, the variable supply of volcanic products across the SVSB resulted in "high- or low-volcaniclastic" depocentres based on the sedimentary systems developed (Fig. 9; D'Elia et al., 2016). At the Cerro La Ballena and Cerro Guanaco volcanic depocentres, intermediate to silicic volcanism formed composite vents and proximal pyroclastic deposits (block-and-ash and ignimbrites). Restricted coarse-grained sedimentary systems were developed (A/S < 1), such as alluvial fans and braided rivers at Cerro La Ballena depocentre and progradational delta-fans at the Cerro Guanaco depocentre (S2 and S6, Fig. 9).

In Sierra de Varas and Vaquillas Altas depocentres, a low-volcaniclastic input allowed the deposition of sedimentary systems with medial to distal pyroclastic assemblages (distal ignimbrites and/or fallout deposits). A complete synrift cycle is recorded at the Vaquillas Altas depocentre (S7 in Fig. 9 and Fig. 10), from alluvial fans (A/S < 1), basinal lacustrine (A/S > 1) and braided fluvial systems, with restricted pyroclastic (mainly fallout deposits) and dacitic to basaltic volcanism (Fig. 10). This succession would represents the transition from rift inception (very low A/S), climax (high A/S), and postrift sequences (moderate A/S), reflecting the rapid increase and posterior cease of mechanical subsidence (Barredo et al., 2012; Prosser, 1993; Schlische & Anders, 1996; Withjack et al., 2002). The rift climax is referred as the "time of maximum rate of displacement on a fault" (Prosser, 1993). This period is characterized by the linkage of previous small and isolated faults into a fully linked fault array (Cowie, Gupta, & Dawers, 2000; Gawthorpe & Leeder, 2000) producing a maximum subsidence where the sedimentation is likely to be outpaced by the accommodation space, generating characteristic relatively fine-grained basinal depositional systems (lacustrine, marine gulf) due to the starvation of the basin (McCann & Saintot, 2003; Prosser, 1993). Thus, the development of basinal lacustrine rift-climax facies (Prosser, 1993) across the Sierra de Varas and the Vaquillas Altas depocentres (e.g., at S4, S7 sections), suggests an abrupt increase of the accommodation space which would be related to the fault linkage and consequent increase in mechanical subsidence across the SVSB (Fig. 12B; Schlische, 1991; Gawthorpe & Leeder, 2000; Withjack et al., 2002).

It should be noted that the succession recording the complete rift cycle (S7), was previously assigned to the Quebrada del Salitre Formation (Naranjo & Puig, 1984; Venegas et al., 2013). We suggest that these deposits would be better assigned to the Sierra de Varas Formation based on: (1) the presence of lacustrine facies which are absent in the type locality of the Quebrada del Salitre Formation, (2) its Norian-Rhaetian age which is younger than a significant portion of the Quebrada del Salitre Formation, and (3) its location in a structurally separated depocentre.

Sierra Exploradora sub-basin

The Synrift II stage in the SESB (Fig. 12 B), recorded the deposition of meandering rivers and mafic lava flows (S10 and S11) with no development of rift-climax sequences (Prosser, 1993). The development of meandering rivers (A/S ≈ 1, Martinsen et al., 1999) suggest that the thick basaltic infill (>1300 m in S10, Fig. 9) match the high accommodation space and inhibited the development of water-deep facies during the high-subsidence of the basin. An outcrop scale example of this is preserved in the Quebrada del Salitre Formation (Fig. 4C), where syntectonic troughs were filled by basaltic lavas during meandering fluvial deposition (S11 in Fig. 9). This indicates an important role of the volcanism in the depositional systems developed in the SESB (high-volcaniclastic input).

5.3.3 | Postrift transition ("latest" Rhaetian)

During the uppermost Rhaetian (Fig. 12C), a broad and thin (<50 m) shallow marine surface formed in carbonate shelves mantled the hanging- and footwalls of both sub-basins (see section 5.1), indicating a generalized and abrupt reduction of the mechanical subsidence and the onset of the postrift stage. At the Vaquillas Altas depocentre, exceptional exposures of synsedimentary faults evidence the postrift character of the carbonate platform assemblage (Fig. 4B). Previous works roughly delineated the onset of the postrift at the Hettangian, when deep marine facies were developed during a global sea rise (Ardill et al., 1998). However, these facies are better assigned to a late postrift phase (Fig. 12D; Prosser, 1993).

5.4 | Synrift architecture of the Domeyko Basin

Regarding to the main rift structures of the Domeyko Basin, we suggest that major N-S basin bounding faults were located at the western margin of the basin based on the predominance of thick, monomictic and coarse debris flow deposits, covering small areas near to the westernmost N-S faults of the Cenozoic Domeyko Fault System (DFS; Fig. 2). This proximal alluvial fan facies requires

high-slopes to be formed and fast subsidence to be preserved, suggesting the proximity to high-angle faults (Blair & McPherson, 1994, 2009), in contrast to wider medial to distal assemblages (sheetfloods and channelized flows) developed at flexural margins. The proximity of this facies to the DFS suggests the reactivation of this structure, which usually occurs at the master faults of previous extensional systems (Amilibia et al., 2008; Bonini, Sani, & Antonielli, 2012; Butler, 1989). At the SESB, elongated silicic domes were associated with ~N-S trending faults (Fig. 12A).

On the other hand, abrupt lithofacies changes and strong thickness asymmetry of the Domeyko Basin through the N-S direction, suggest basin segmentation was controlled by oblique, NW-SE striking faults (inset in Fig. 9). Moreover, several palaeo-highs can be recognized longitudinally across the Domeyko Basin (e.g., Cerro Danko and Cerro Pedernales palaeo-highs) based on the unconformable contact between the prerift basement and postrift marine facies (Fig. 9). Major palaeo-highs coincide with the tip of SVSB and SESB and correlates with large-scale NW lineaments (Figs. 1 and 2; Salfity, 1985; Abels & Bischoff, 1999;

Petrinovic, Riller, & Brod, 2005), suggesting pre-existing basement fabrics exhibit a strong control on the segmentation of the basin (Fig. 12). Additionally, Triassic NW-SE trending cataclasites (238 ± 10 Ma, K-Ar whole rock age) crop out at the Sierra de Varas depocentre (Niemeyer, Berríos, & Ruiz Cruz, 2004; Padilla, 1988) while prevailing, centi- to metre-scale Triassic NNW-SSE to NW-SE synsedimentary extensional faults have been identified at the SVSB (Espinoza et al., 2016).

We suggest that the interaction between major N-S structures and NW-SE oblique discontinuities can be explained by a transtensional model, partitioning the deformation into extensional and sinistral strike-slip components, where the NW-SE structures acted as releasing bends (Fig. 12). Several key features developed in transtensional basins are recognized in the Domeyko Basin: (a) a strong longitudinal and lateral asymmetry (Christie-Blick & Biddle, 1985), (b) narrow basins and rapid changes in lateral and vertical facies, thickness, and geometry of near depocentres (Belt, 2012; Christie-Blick & Biddle, 1985; Dorsey & Umhoefer, 2012), (c) common unconformities from one basin to another marking the migration of
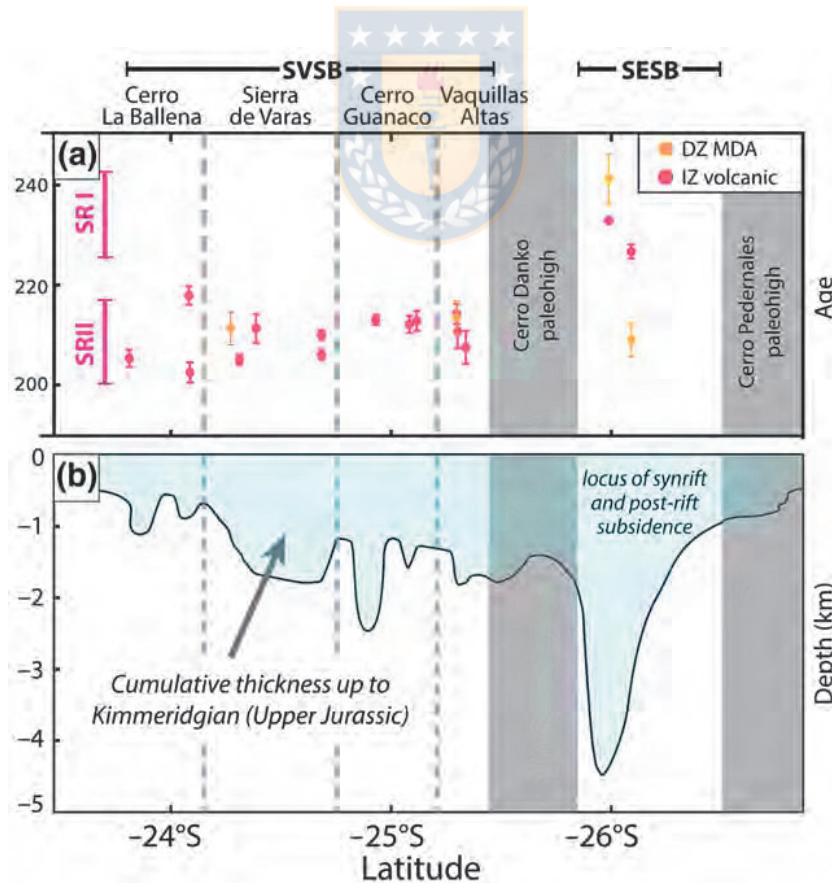
FIGURE 11 (a) Compilation of volcanic and detrital (MDA) U-Pb ages from Triassic units exposed at the western margin of the Domeyko Range (69°–69.5°W). The two synrift stages are indicated. References for geochronological data are the same that in Fig. 9. (b) Minimum cumulative thickness of outcropping successions up to Kimmeridgian (based in the work of Prinz et al. (1994) and graphically updated by the thickness of Triassic successions presented in this work)

depocentres (Busby & Bassett, 2007; Christie-Blick & Biddle, 1985), such as those recorded at S6 and S8 in Vaquillas Altas and Cerro Guanaco depocentres (Fig. 9), (d) prominent topographic margins (Nilsen & Sylvester, 1998), which is in agreement with the unimodal provenance evidenced by the DZ data (Fig. 8), pointing to close and highly compartmentalized depocentres. Additionally, a strike-slip component has been suggested for the Jurassic back-arc phase of the Domeyko Basin, based on the "*en-echelon*" distribution of depocentres (Prinz et al., 1994; Vicente, 2005). Similar transtensional continental rift basins were developed during the Late Triassic-Lower Jurassic arc of the northwestern Gondwana (Busby, 2012; Busby & Bassett, 2007). In modern times, the dextral transtensional Walker Lane belt (United States) host the largest volcanic vents at releasing bends (Busby, 2013), and we infer a similar setting for the major volcanic centres developed in the Domeyko Basin.

During the postrift stage (mainly Jurassic to Lower Cretaceous), the location of the thickest cumulative infills coincides with the deepest subsiding depocentres formed during the synrift stage (Fig. 11), suggesting a strong control of the synrift architecture over the differential thermal subsidence during the postrift phase of the Domeyko Basin, similar to that proposed by Cristallini et al. (2009) for the Jurassic back-arc Neuquén Basin of South America.

5.5 | Geotectonic significance of the Domeyko Basin in the Southwestern Gondwana

During the Synrift II stage, the Cifuncho Basin (Fig. 1) was filled by volcanic and sedimentary rocks in the Coastal Cordillera in a similar timespan (212-200 Ma; Contreras et al., 2013; Espinoza et al., 2015). The scattered plutonic rocks of this age (Escribano et al., 2013; Espinoza et al., 2014; Godoy & Lara, 1998) and the intermediate to silicic, calcalkaline volcanism at the Coastal Cordillera would indicate a back-arc position for the synrift Domeyko Basin which hosts both calcalkaline and tholeiitic magmas (Espinoza et al., 2016; Oliveros et al., 2017). The later points to a more distal position of the Domeyko Basin with respect to the arc-axis, where the influence of released fluids from the slab in the genesis of magmas is less pronounced (Hochstaedter, Gill, & Morris, 1990; Sayit, Bedi, Tekin, Göncüoglu, & Okuyucu, 2017; Stern et al., 1990).

The strong possibility that the subduction would have been active in northern Chile at least during the Late Triassic (Coloma et al., 2017; González et al., 2018; Oliveros et al., 2017; Poma et al., 2014; del Rey, Deckart, Arriagada, & Martínez, 2016), suggests that the slab-pull would have played an important role as a driving mechanism of rifting

at the southwestern margin of Gondwana during its early breakup. The oblique convergence required to sustain the sinistral transtension for the Domeyko Basin is in agreement with recent Triassic kinematic reconstructions (Matthews et al., 2016; Müller et al., 2016). The slab-pull in a retreating trench, would be coexisting with others driving mechanisms, such as far-field stresses (Giambiagi et al., 2009), which would have been more relevant for inboard basins at this time, such as the Ischigualasto and Cuyo basins (Fig. 1A). We suggest that the influence of the subduction system at the Gondwanan margin would have controlled the basin geometry, kinematics and ultimately the tectonostratigraphic evolution of the synrift Domeyko Basin.

6 | CONCLUSIONS

In the Domeyko Basin, two synrift periods were developed during the Triassic: The Synrift I (~240–225 Ma) with the aperture of the Sierra Exploradora sub-basin (SESB) and the Synrift II (217-200 Ma), which led to the opening of the Sierra de Varas sub-basin (SVSB) and the reactivation of the SESB. These volcano-sedimentary sub-basins present striking differences in the sedimentary and volcanic infill of their depocentres, evidencing a strong influence of the volcanic input (low or high) and the mechanical subsidence in the sedimentary depositional systems developed (A/S ratio). In low-volcaniclastic depocentres, a complete rift cycle is recorded (alluvial-lacustrine-fluvial), with rift-climax basinal lacustrine facies (A/S > 1) indicating the fault linkage of the SVSB during the Synrift II. In high-volcaniclastic depocentres of the SVSB and SESB, the development of low to very low A/S facies (A/S ≤ 1) during high mechanical subsidence suggests that volcanic supply inhibited the development of rift-climax facies (basinal deep-water facies). The postrift transition took place at the "latest" Rhaetian where the thermal subsidence allowed a wide transgression of shallow marine facies, bypassing the footwalls of the Domeyko Basin.

We suggest that the architecture of the synrift Domeyko Basin was controlled by the interaction between major N-S faults and oblique ~NW-SE discontinuities, generating asymmetric half-graben depocentres and structural highs in a left-lateral transtensional model (pull-apart or releasing bend). The oblique discontinuities would correspond to NW-SE continental-scale lineaments, suggesting that inherited basement weaknesses controlled the segmentation of the Domeyko Basin.

The strong possibility that the Domeyko Basin would have been formed as subduction-related rift basin in a back-arc position during the Late Triassic, highlights the slab-pull as a probable driving mechanism for extension at the Southwestern Gondwana margin during its early breakup, unlike
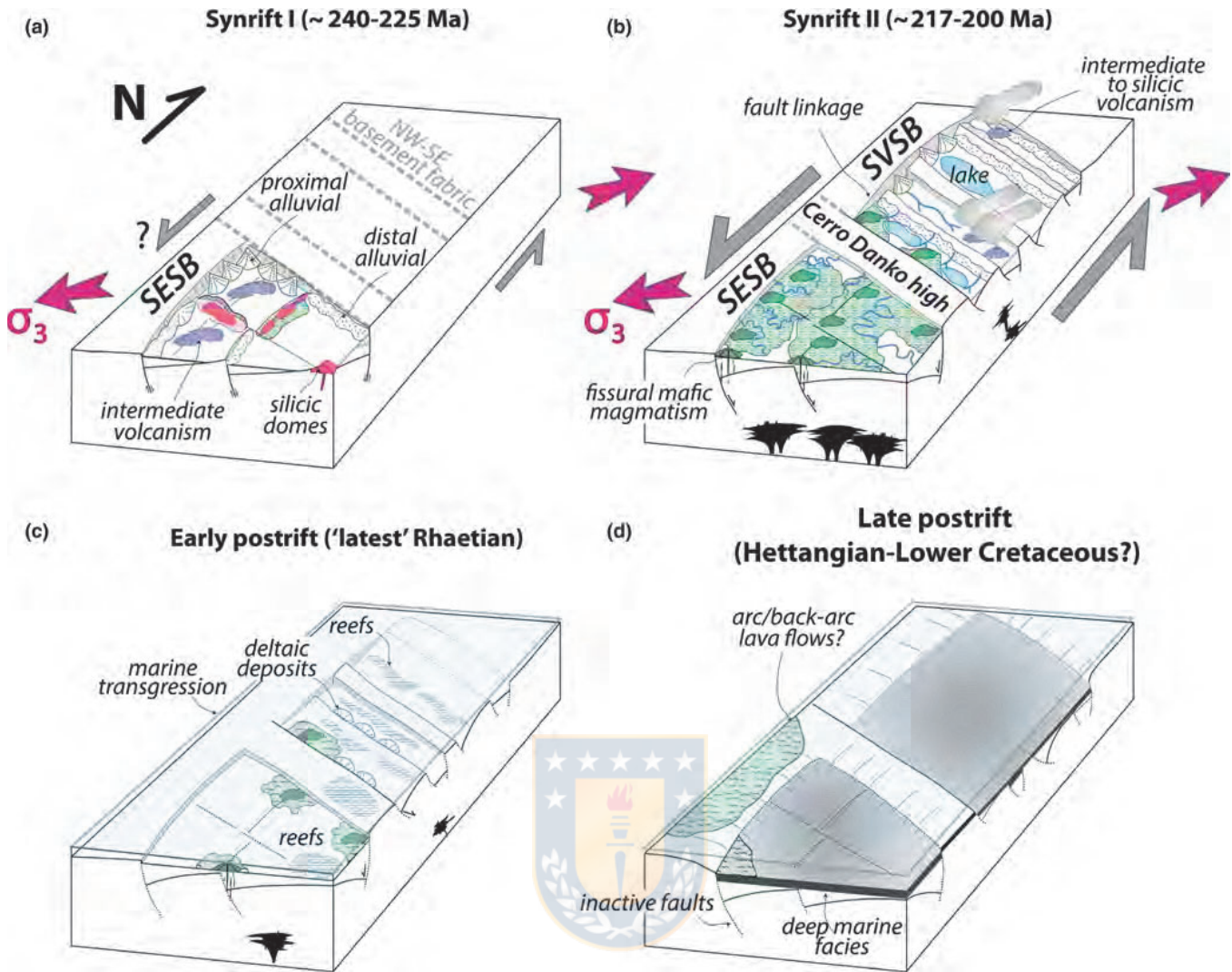
FIGURE 12 Conceptual basin-evolution model of the Synrift I, II and postrift phase of the Domeyko Basin. (a) Synrift I stage (~240–225 Ma): Initiation of the SESB in a mainly extensional setting occupying the NW-SE basement fabric. (b) Synrift II stage (~217–200 Ma): Aperture of the SVSB and likely reactivation of the SESB in a mainly transtensional (sinistral) setting. During this stage, rift inception to rift climax sequences were developed at the SVSB due to an ongoing fault linkage through a ~N-S trending fault system. (c) Early Postrift ("latest" Rhaetian): An abrupt reduction of the mechanical subsidence allowed the settlement of a shallow sea due to the initiation of the thermal subsidence phase. (d) Late Postrift stage (Hettangian-Lower Cretaceous?): The ongoing thermal subsidence coupled with a global rise of the sea level controlled the deposition of deep marine facies across the mechanically inactive sub-basins

other inland rift basins driven by far-field stresses (Cuyo, Ischigualasto and Neuquén basins). Therefore, slab-induced tectonics can control the first-order features of subduction-related rifts, such as the rift position (e.g., intra-arc or back-arc basins), the style and composition of volcanism, and the rift kinematics (purely extensional versus transtensional tectonics). These features would have controlled the tectonostratigraphic evolution of the synrift stage of the Domeyko Basin through the localization of volcanic centres (high-volcaniclastic depocentres) and the deformation at releasing stepovers (transtensional kinematics). Given that only a moderate amount of subduction obliquity would be required to develop a strike-slip component during rifting (> ~30°; Philippon & Corti, 2016), the transtensional

Domeyko rift may correspond to an underestimated example of the tectonostratigraphic evolution of Gondwanean continental subduction-related basins.

for the constant help that Jorge Lemp gave us in the field. Dr. Cathy Busby and an anonymous reviewer are thanked for the constructive comments on the manuscript that helped to significantly improve the quality of the final text. Dr.Cynthia Ebinger is thanked for editorial handling.

ORCID

Mauricio Espinoza http://orcid.org/0000-0003-2557-1603

REFERENCES

Abels, A., & Bischoff, L. (1999). Clockwise block rotations in northern Chile: Indications for a large-scale domino mechanism during the middle-late Eocene. *Geology*, *27*, 751–754. https://doi.org/10.1130/0091-7613(1999)027<0751:CBRINC>2.3.CO;2

Alfaro, R. (2014). Estratigrafía de las rocas triásicas de la Formación Cerro Guanaco (Nueva Unidad) en la Cordillera de Domeyko, sector Sierra de Varas. Región de Antofagasta.(24° 48′–25° 00′ Lat. Sur). *Memoria de título, Antofagasta* (unpublished), pp. 95. Chile.

Alonso-Zarza, A. M., & Tanner, L. H. (2009). *Carbonates in continental settings: facies, environments, and processes*, Vol. 61. Amsterdam, the Netherlands: Elsevier.

Álvarez, P. (2003). Análisis litofacial de la Formación Las Bateas. In X Congreso Geológico Chileno. Concepción, Chile.

Amilibia, A., Sàbat, F., McClay, K. R., Muñoz, J. A., Roca, E., & Chong, G. (2008). The role of inherited tectono-sedimentary architecture in the development of the central Andean mountain belt: Insights from the Cordillera de Domeyko. *Journal of Structural Geology*, *30*, 1520–1539. https://doi.org/10.1016/j.jsg.2008.08.005

Ardill, J. (1996). *Sequence stratigraphy of the Mesozoic Domeyko basin, northern Chile*. University of Liverpool.

Ardill, J., Flint, S., Chong, G., & Wilke, H. (1998). Sequence stratigraphy of the Mesozoic Domeyko Basin, northern Chile. *Journal of the Geological Society of London*, *155*, 71–88. https://doi.org/10.1144/gsjgs.155.1.0071

Astudillo, N., Ferrando, R., Montecino, D., Espinoza, F., Matthews, S., Cornejo, P., & Arévalo, C. (2017). *Carta Augusta Victoria, Región de Antofagasta. Servicio Nacional de Geología y Minería*. Carta Geológica de Chile, Serie Geología Básica 189. 1 mapa escala 1:100.000. Santiago, Chile.

Barredo, S., Chemale, F., Marsicano, C., Ávila, J. N., Ottone, E. G., & Ramos, V. A. (2012). Tectono-sequence stratigraphy and U-Pb zircon ages of the Rincón Blanco Depocenter, northern Cuyo Rift. *Argentina. Gondwana Res.*, *21*, 624–636. https://doi.org/10.1016/j.gr.2011.05.016

Bascuñán, S., Arriagada, C., Le Roux, J., & Deckart, K. (2015). Unraveling the Peruvian Phase of the Central Andes: stratigraphy, sedimentology and geochronology of the Salar de Atacama Basin (22°30-23°S), northern Chile. *Basin Research*, *28*, 365–392.

Basso, M., & Marinovic, N. (2003). Antecedentes geocronológicos de volcanismo triásico en la zona de los Estratos El Bordo, Antofagasta, Chile. In X Congreso Geológico Chileno. Concepción.

Bell, C. M., & Suárez, M. (1991). Late Triassic fluvial and marine shelf succession, Quebrada Doña Inés Chica, Atacama region, northern Chile. *J. South Am. Earth Sci.*, *4*, 287–293. https://doi.org/10.1016/0895-9811(91)90002-3

Belt, L. (2012). Active transtensional intracontinental basins: Walker Lane belt in the Western Great Basin. In C. Busby, & A. Azor (Eds.), *Tectonics of Sedimentary Basins: Recent Advances*, pp. 226–248. Oxford, UK: Wiley-Blackwell.

Benson, L. V., & Thompson, R. S. (1987). Lake-level variation in the Lahontan basin for the past 50,000 years. *Quat. Res.*, *28*, 69–85. https://doi.org/10.1016/0033-5894(87)90034-2

Benvenuti, M. (2003). Facies analysis and tectonic significance of lacustrine fan-deltaic successions in the Pliocene-Pleistocene Mugello Basin, Central Italy. *Sediment. Geol.*, *157*, 197–234. https://doi.org/10.1016/S0037-0738(02)00234-8

Blair, T. C., & McPherson, J. G. (1994). Alluvial Fans and their Natural Distinction from Rivers Based on Morphology, Hydraulic Processes, Sedimentary Processes, and Facies Assemblages. *SEPM J. Sediment. Res.*, *64A*, 450–489.

Blair, T. C., & McPherson, J. G. (2009). Processes and Forms of Alluvial Fans. In A. J. Parsons, & A. D. Abrahams (Eds.), *Geomorphology of Desert Environments*, 2nd ed. (pp. 413–467). Netherlands: Springer. https://doi.org/10.1007/978-1-4020-5719-9

Bonini, M., Sani, F., & Antonielli, B. (2012). Basin inversion and contractional reactivation of inherited normal faults: A review based on previous and new experimental models. *Tectonophysics*, *522*, 55–88. https://doi.org/10.1016/j.tecto.2011.11.014

Branney, M., & Kokelaar, P. (2002). Interpreting ignimbrite lithofacies. In *Pyroclastic Density Currents and the Sedimentation of Ignimbrites* (pp. 51–85). London: The Geological Society of London.

Busby, C. (2012). Extensional and transtensional continental arc basins: case studies from the southwestern United States. In C. Busby & A. Azor (Eds.), *Tectonics of Sedimentary Basins: Recent Advances* (pp. 382–404). Oxford, UK: Wiley-Blackwell.

Busby, C. (2013). Birth of a plate boundary at ca. 12 Ma in the Ancestral Cascades arc, Walker Lane belt of California and Nevada. *Geosphere*, *9*, 1147–1160. https://doi.org/10.1130/GES00928.1

Busby, C., & Bassett, K. N. (2007). Volcanic facies architecture of an intra-arc strike-slip basin, Santa Rita Mountains, Southern Arizona. *Bulletin of Volcanology*, *70*, 85–103. https://doi.org/10.1007/s00445-007-0122-9

Busby-Spera, C. J. (1988). Speculative tectonic model for the early Mesozoic arc of the southwest Cordilleran United States. *Geology*, *16*, 1121–1125. https://doi.org/10.1130/0091-7613(1988)016<1121:STMFTE>2.3.CO;2

Busby-Spera, C. J., & White, J. D. L. (1987). Variation in peperite textures associated with differing host-sediment properties. *Bulletin of Volcanology*, *49*, 765–776. https://doi.org/10.1007/BF01079827

Butler, R. W. H. (1989). The influence of pre-existing basin structure on thrust system evolution in the Western Alps. *Geol. Soc. London. Spec. Publ.*, *44*, 105–122. https://doi.org/10.1144/GSL.SP.1989.044.01.07

Carroll, A. R., & Bohacs, K. M. (1999). Stratigraphic classification of ancient lakes: Balancing tectonic and climatic controls. *Geology*, *27*, 99–102. https://doi.org/10.1130/0091-7613(1999)027<0099:SCOALB>2.3.CO;2

Cas, R., & Wright, J. V. (1988). *Volcanic successions modern and ancient: A geological approach to processes, products and successions*. London, UK: Chapman & Hal.

Charrier, R. (1979). El Triásico en Chile y regiones adyacentes de Argentina: Una reconstrucción paleogeográfica y paleoclimática. *Comun. Dep. Geol. Univ. Chile*, *26*, 1–47.

Chong, G. (1973). Reconocimiento Geológico del Área Catalina, Sierra de Varas y estratigrafía del Jurásico del Profeta, Provincia de Antofagasta. *Memoria de título, Universidad de Chile* (unpublished), pp. 284.

Chong, G. (1977). Contribution to the knowledge of the Domeyko range in the Andes of northern Chile. *Geol. Rundschau*, *66*, 374–404.

Chong, G., & Hilldebrandt, A. (1985). El Triásico PreAndino de Chile entre los 23°30′ y 26°00′ de lat. sur. In IV Congreso Geológico Chileno. Antofagasta, Chile.

Christie-Blick, N., & Biddle, K. (1985). Deformation and Basin Formation Along Strike-Slip Faults. *SEPM (Society Sediment. Geol. Spec. Publ.*, *37*, 1–33.

Coloma, F., Valin, X., Oliveros, V., Vásquez, P., Creixell, C., Salazar, E., … Vallejos, D. (2017). Geochemistry of Permian to Triassic igneous rocks from northern Chile (28°-29°30′S): Implications on the dynamics of the proto-Andean margin. *Andean Geology*, *44*, 147–178. https://doi.org/10.5027/andgeoV44n2-a03

Contreras, J. F. (2014). Estratigrafía de la Formación Sierra de Varas, Cordillera de Domeyko, Región de Antofagasta entre las coordenadas 7.273. 103–7.268. 892 m N; 481.320–482.290 m E, *Memoria de título, Antofagasta* (unpublished), pp. 105. Universidad Católica del Norte, Antofagasta, Chile.

Contreras, J. P., Espinoza, M., Jorquera, R., Kraus, S., Ramírez, C., De la Cruz, R., … Martínez, P. (2013). *Carta Cifuncho, Regiones de Antofagasta y Atacama. Servicio Nacional de Geología y Minería*. Carta Geológica de Chile, Serie Geología Básica 161, 1 mapa escala. 1:100.000. Santiago, Chile.

Cornejo, P., & Mpodozis, C. (1996). *Geología de la Región de Sierra Exploradora (Cordillera de Domeyko 25°–26°S)*. Servicio Nacional de Geología y Minería – CODELCO, Informe Registrado, IR-96-09, 1-330, 9 mapas escala 1:50.000. Santiago.

Cornejo, P., Mpodozis, M., Rivera, O., & Matthews, S. (2009). *Carta Exploradora, Regiones de Antofagasta y Atacama*. Servicio Nacional de Geología y Minería, Carta Geológica de Chile, Serie Geología Básica, 119, 1–103. 1 mapa escala 1:100.000.Santiago, Chile.

Cortés, J. (2012). *Carta Sierra Mariposa, Región de Antofagasta. Servicio Nacional de Geología y Minería*. Carta Geológica de Chile, Serie Geología Básica 119, 30. 1 mapa escala 1:100.000. Santiago, Chile.

Cowie, P. A., Gupta, S., & Dawers, N. H. (2000). Implications of fault array evolution for synrift depocentre development: Insights from a numerical fault growth model. *Basin Research*, *12*, 241–261. https://doi.org/10.1046/j.1365-2117.2000.00126.x

Cristallini, E., Tomezzoli, R. N., Pando, G., Gazzera, C., Martínez, J. M., Quiroga, J., … Zambrano, O. (2009). Controles precuyanos en la estructura de la cuenca neuquina. *Rev. La Asoc. Geológica Argentina*, *65*, 248–264.

D'Elia, L., Martí, J., Muravchik, M., Bilmes, A., & Franzese, J. R. (2016). Impact of volcanism on the sedimentary record of the Neuquén rift basin, Argentina: Towards a cause and effect model. *Basin Research*, *30*, 311–335.

D'Elia, L., Muravchik, M., Franzese, J. R., & López, L. (2012). Tectonostratigraphic analysis of the Late Triassic-Early Jurassic syn-rift sequence of the Neuquén Basin in the Sañicó depocentre, Neuquén Province. *Argentina. Andean Geol.*, *39*, 133–157.

Derer, C. E., Schumacher, M. E., & Schäfer, A. (2005). The northern Upper Rhine Graben: basin geometry and early syn-rift tectonosedimentary evolution. *International Journal of Earth Sciences*, *94*, 640–656. https://doi.org/10.1007/s00531-005-0515-y

Dickinson, W. R., & Gehrels, G. E. (2009). Use of U-Pb ages of detrital zircons to infer maximum depositional ages of strata: A test against a Colorado Plateau Mesozoic database. *Earth and Planetary Science Letters*, *288*, 115–125. https://doi.org/10.1016/j.epsl.2009.09.013

Dorsey, R. J., & Umhoefer, P. J. (2012). Influence of Sediment Input and Plate-Motion Obliquity on Basin Development Along an Active Oblique-Divergent Plate Boundary: Gulf of California and Salton Trough. In C. Busby & A. Azor (Eds.), *Tectonics of Sedimentary Basins: Recent Advances* (pp. 209–225). Oxford, UK: Wiley-Blackwell.

Doyle, M. G. (2000). Clast shape and textural associations in peperite as a guide to hydromagmatic interactions: Upper Permian basaltic and basaltic andesite examples from Kiama. *Australia. Aust. J. Earth Sci.*, *47*, 167–177. https://doi.org/10.1046/j.1440-0952.2000.00773.x

Ellis, S., Heise, W., Kissling, W., Villamor, P., & Schreurs, G. (2014). The effect of crustal melt on rift dynamics: Case study of the Taupo Volcanic Zone. *New Zealand Journal of Geology and Geophysics*, *57*, 453–458.

Escribano, J., Martínez, P., Domagala, J., Padel, M., Espinoza, M., Jorquera, R., … Calderón, M. (2013). *Cartas Bahía Isla Blanca y Taltal. Escala 1:100.000*. Servicio Nacional de Geología y Minería, Carta Geológica de Chile, Serie Geología Básica, 164-165. 1–75. 1 mapa escala 1:100.000. Santiago.

Espinoza, M., Contreras, J. P., Kraus, S., De la Cruz, R., Jorquera, R., Ramirez, C., & Naranjo, J. A. (2014). *Carta Cerro del Pingo, Regiones de Antofagasta y Atacama*. Servicio Nacional de Geología y Minería, Carta Geológica de Chile, Serie Geología Básica 169. 1 mapa escala 1:100.000. Santiago.

Espinoza, M., Oliveros, V., & Celis, C. (2016). Geochronology, Geochemistry and Tectonics of Subduction-Related Late Triassic Rift Basins in Northern Chile (24°-26°S). *American Geophysical Union, Fall General Assembly 2016* (pp. T51D–2975). San Francisco: United States.

Espinoza, M., Oliveros, V., Vásquez, P., & Bechis, F. (2015). U-Pb geochronology and kinematic preliminary analyses of Late Triassic-Early Jurassic basins in northern Chile (24.5°-26°S). In *XIV Congreso Geológico Chileno*, La Serena, Chile, pp. 840–843.

Fink, J. H., & Anderson, S. W. (2000). Lava domes and coulees. In B. F. Houghton, S. McNutt, H. Rymer & J. Stix (Eds.), *Encyclopedia of volcanoes* (pp. 307–319). San Diego: Academic Press.

Fisher, R. V., & Schmincke, H.-U. (1984). Pyroclastic rocks and tectonic environment. In R. V. Fisher, & H.-U. Schmincke (Eds.), *Pyroclastic rocks* (pp. 383–409). Berlin, Germany: Springer.

Freundt, A., Wilson, C. J. N., & Carey, S. N. (2000). Ignimbrites and block-and-ash flow deposits. In H. Sigurdsson (Ed.), *Encyclopedia of volcanoes* (pp. 581–599). New York: Academic Press.

Gawthorpe, R., & Leeder, M. (2000). Tectono-sedimentary evolution of active extensional basins. *Basin Research*, *12*, 195–218. https://doi.org/10.1046/j.1365-2117.2000.00121.x

Gehrels, G. (2011). Detrital Zircon U-Pb Geochronology: Current Methods and New Opportunities. In C. J. Busby & A. Azor (Eds.), *Tectonics of Sedimentary Basins: Recent Advances* (pp. 45–62). Oxford, UK: Wiley-Blackwell.

Giambiagi, L., Tunik, M., Barredo, S., Bechis, F., Ghiglione, M., Alvarez, P., & Drosina, M. (2009). Cinemática de apertura del sector norte de la cuenca neuquina. *Rev. La Asoc. Geológica Argentina*, *65*, 278–292.

Godoy, E., & Lara, L. (1998). *Hojas Chañaral y Diego de Almagro, Región de Atacama*. Servicio Nacional de Geologia y Minería, Mapas Geológicos No. 5-6. 1 mapa escala 1:100.000, Santiago.

González, J., Oliveros, V., Creixell, C., Velásquez, R., Vásquez, P., & Lucassen, F. (2018). The Triassic magmatism and its relation with the Pre-Andean tectonic evolution: Geochemical and petrographic constrains from the High Andes of north central Chile (29° 30′–30° S). *J. South Am. Earth Sci*, *87*, 95–112.

González, R., Wilke, H. G., Menzies, A. H., Espinoza, F., Riquelme, R., & Herrera, C. (2015). *Carta Sierra de Varas, Región de Antofagasta*. Servicio Nacional de Geología y Minería, Carta Geológica de Chile, Serie Geología Básica 178. 114 p, 1 mapa escala 1:100.000. Santiago.

Gröschke, M., v. Hillebrandt, A., Prinz, P., Quinzio, L. A., & Wilke, H.-G. (1988). Marine mesozoic paleogeography in Northern Chile between 21°–26°S. In H. Bahlburg, C. Breitkreuz & P. Giese (Eds.), *The Southern Central Andes SE – 7* (Vol. 17, pp. 103–117). Berlin, Germany: Springer. https://doi.org/10.1007/BFb0045170

Hadlari, T., Midwinter, D., Poulton, T. P., & Matthews, W. A. (2017). A Pangean rim of fire: Reviewing the Triassic of western Laurentia. *Lithosphere*, *L643*, 1.

Henríquez, S, Becerra, J., & Arriagada, C.. (2014). *Geología del área San Pedro de Atacama, Región de Antofagasta*. Servicio Nacional de Geología y Minería. Carta Geológica de Chile, Serie Geología Básica 171. 111 p., 1 mapa escala 1:100.000. Santiago.

Hochstaedter, A. G., Gill, J. B., & Morris, J. D. (1990). Volcanism in the Sumisu Rift, II. Subduction and non-subduction related components. *Earth and Planetary Science Letters*, *100*, 195–209. https://doi.org/10.1016/0012-821X(90)90185-Z

Ingersoll, R. V. (2012). Tectonics of Sedimentary Basins, with Revised Nomenclature. In C. Busby & A. Azor (Eds.), *Tectonics of Sedimentary Basins: Recent Advances* (pp. 1–43). Oxford, UK: Wiley-Blackwell.

Jarrard, R. D. (1986). Relations among subduction parameters. *Reviews of Geophysics*, *24*, 780–783.

Jervey, M. T. (1988). Quantitative geological modeling of siliciclastic rock sequences and their seismic expression. In C. K. Wilgus, H. W. Posamentier, C. K. Ross & G. G. St. C. Kendall (Eds.), *Sea level changes: An integrated approach* (pp. 47–69). Tulsa, OK: SEPM Special Publication 42.

Johnson, T. C., Halfman, J. D., Rosendahl, B. R., & Lister, G. S. (1987). Climatic and tectonic effects on sedimentation in a rift-valley lake: Evidence from high-resolution seismic profiles, Lake Turkana. *Kenya. Geol. Soc. Am. Bull.*, *98*, 439–447. https://doi.org/10.1130/0016-7606(1987)98<439:CATEOS>2.0.CO;2

Kamata, H., & Kodama, K. (1994). Tectonics of an arc-arc junction: An example from Kyushu Island at the junction of the Southwest Japan Arc and the Ryukyu Arc. *Tectonophysics*, *233*, 69–81. https://doi.org/10.1016/0040-1951(94)90220-8

Kleiman, L. E., & Japas, M. S. (2009). The Choiyoi volcanic province at 34°S–36°S (San Rafael, Mendoza, Argentina): Implications for the Late Palaeozoic evolution of the southwestern margin of Gondwana. *Tectonophysics*, *473*, 283–299. https://doi.org/10.1016/j.tecto.2009.02.046

Koster, E. H., & Steel, R. J. (1984). *Sedimentology of gravels and conglomerates*, Vol. *10*. Calgary: Canadian Society of Petroleum Geologists.

De Lamotte, D. F., Fourdan, B., Leleu, S., Leparmentier, F., & Clarens, P. (2015). Style of rifting and the stages of Pangea breakup. *Tectonics*, *34*, 1009–1029.

Lee, C.-S., Shor, G. G., Bibee, L. D., Lu, R. S., & Hilde, T. W. C. (1980). Okinawa Trough: Origin of a back-arc basin. *Marine Geology*, *35*, 219–241. https://doi.org/10.1016/0025-3227(80)90032-8

Lipman, P. W. (2000). Calderas. In H. Sigurdsson, B. Houghton, S. McNutt, H. Rymer & J. Stix (Eds.), *Encyclopedia of Volcanoes* (pp. 643–662). San Diego, CA: Academic Press.

Llambías, E. J., Quenardelle, S., & Montenegro, T. (2003). The Choiyoi Group from central Argentina: A subalkaline transitional to alkaline association in the craton adjacent to the active margin of the Gondwana continent. *J. South Am. Earth Sci.*, *16*, 243–257. https://doi.org/10.1016/S0895-9811(03)00070-1

Ludwig, K. R. (2008). Isoplot 3.7: A geochronological toolkit for Microsoft Excel. Berkeley Geochronology Center Special Publication.

Maksaev, V., Munizaga, F., & Tassinari, C. (2014). Timing of the magmatism of the paleo-Pacific border of Gondwana: U-Pb geochronology of late paleozoic to early mesozoic igneous rocks of the north Chilean Andes between 20° and 31°S. *Andean Geology*, *41*, 447–506.

Marinovic, N. (2007). *Carta Oficina Domeyko, Región de Antofagasta*. Servicio Nacional de Geología y Minería, Carta Geológica de Chile, Serie Geológica Básica, 105, 1–41. 1 mapa escala 1:100.000, Santiago.

Marinovic, N., Smoje, I., Maksaev, V., Hervé, M., & Mpodozis, C. (1995). *Hoja Aguas Blancas*. Servicio Nacional de Geología y Minería, Carta Geológica de Chile, 70, 1-150. 1 mapa escala 1:250.000, Santiago.

Martinsen, O. J., Ryseth, A. L. F., Helland-Hansen, W., Flesche, H., Torkildsen, G., & Idil, S. (1999). Stratigraphic base level and fluvial architecture: Ericson Sandstone (Campanian), Rock Springs Uplift, SW Wyoming, USA. *Sedimentology*, *46*, 235–263. https://doi.org/10.1046/j.1365-3091.1999.00208.x

Martins-Neto, M. A., & Catuneanu, O. (2010). Rift sequence stratigraphy. *Marine and Petroleum Geology*, *27*, 247–253. https://doi.org/10.1016/j.marpetgeo.2009.08.001

Matthews, K. J., Maloney, K. T., Zahirovic, S., Williams, S. E., Seton, M., & Miller, R. D. (2016). Global plate boundary evolution and kinematics since the late Paleozoic. *Glob. Planet. Change*, *146*, 226–250. https://doi.org/10.1016/j.gloplacha.2016.10.002

McCann, T., & Saintot, A. (2003). Tracing tectonic deformation using the sedimentary record: An overview. *Geological Society of London. Special Publication*, *208*, 1–28. https://doi.org/10.1144/GSL.SP.2003.208.01.01

McPherson, J. G., Shanmugam, G., & Moiola, R. J. (1987). Fan-deltas and braid deltas : Varieties of coarse- grained deltas. *Geological Society of America Bulletin*, *99*, 331–340. https://doi.org/10.1130/0016-7606(1987)99<331:FABDVO>2.0.CO;2

McPhie, J., Doyle, M. G., & Allen, R. (1993). *Volcanic textures: A guide to the interpretation of textures in volcanic rocks*. Hobart: CODES-University of Tasmania.

Merle, O. (2011). A simple continental rift classification. *Tectonophysics*, *513*, 88–95. https://doi.org/10.1016/j.tecto.2011.10.004

Miall, A. D. (1978). Lithofacies types and vertical profile models in braided river deposits: A summary. *Fluv. Sedimentol.*, *5*, 597–600.

Miall, A. D. (2006). *The Geology of Fluvial Deposits*. Berlin: Springer. https://doi.org/10.1007/978-3-662-03237-4

Montecino, D. (2015). Nuevo esquema estratigráfico, condiciones de sedimentación y evolución de la cuenca triásica entre los 24°00′-24°30′ S y 69°00′-69°30′ W, Región de Antofagasta, Chile. *Memoria de título, Universidad de Concepción* (unpublished), pp. 177. Concepción.

Mpodozis, C., & Cornejo, P. (1997). El rift triásico-sinemuriano de Sierra Exploradora, Cordillera de Domeyko (25°–26°S): Asociaciones de facies y reconstrucción tectónica. In *VIII Congreso Geológico Chileno*, Antofagasta, Chile. pp. 550–554.

Müller, R. D., Seton, M., Zahirovic, S., Williams, S. E., Matthews, K. J., Wright, N. M., … Cannon, J. (2016). Ocean basin evolution and global-scale reorganization events since Pangea breakup. *Annu. Rev. Earth Planet. Sci. Lett.*, *44*, 107–138. https://doi.org/10.1146/annurev-earth-060115-012211

Muñoz, N. (1989). Estudio geológico estratigráfico de las Hojas Baquedano y Pampa Unión, II Región de Antofagasta, Chile. *Memoria de Título, Universidad de Chile* (unpublished), Departamento de Geología, pp. 161. Santiago.

Muñoz, J., Amilibia, A., Carrera, N., Mon, R., Chong, G., Roca, E., & Sàbat, F. (2005). A geological cross-section of the Andean orogen at 25.5° LS. In *VI International Symposium on Andean Geodynamics*, Barcelona, España, pp. 536–539.

Muravchik, M., D'Elia, L., Bilmes, A., & Franzese, J. R. (2011). Syn-eruptive/inter-eruptive relations in the syn-rift deposits of the Precuyano Cycle, Sierra de Chacaico, Neuquén Basin. *Argentina. Sediment. Geol.*, *238*, 132–144. https://doi.org/10.1016/j.sedgeo.2011.04.008

Muto, T., & Steel, R. J. (2000). The accommodation concept in sequence stratigraphy: Some dimensional problems and possible redefinition. *Sediment. Geol.*, *130*, 1–10. https://doi.org/10.1016/S0037-0738(99)00107-4

Naranjo, J. A., & Puig, A. (1984). *Hojas Taltal y Chañaral, Regiones de Antofagasta y Atacama*. Servicio Nacional de Geología y Minería, Carta Geológica de Chile, 62–63, 1–146. 1 mapa escala 1:250.000, Santiago.

Navea, A., Wilke, H.-G., & González, R. (2015). Naturaleza de la transgresión marina triásica superior en Sierra Áspera de Argomedo y Sierra de Varas, Región de. *XIV Congreso Geológico Chileno* (pp. 808–811). La Serena: Universidad de Chile.

Nemec, W., & Steel, R. J. (1984). Alluvial and coastal conglomerates: Their significant features and some comments on gravelly mass-flow deposits. *Sedimentol. Gravels Conglomerates*, *10*, 1–31.

Németh, K., & Martin, U. (2007). Practical Volcanology. Lecture notes for understanding volcanic rocks from field-based studies. In *Occasional Papers of the Geological Institute of Hungary* (*27*, pp. 1–221). Budapest: Geological Institute of Hungary.

Nichols, G. (2009). *Sedimentology and stratigraphy*. London, UK: John Wiley & Sons.

Niemeyer, H., Berríos, H., & Ruiz Cruz, M. D. (2004). Temperaturas de formación en cataclasitas triásicas de la Cordillera Domeyko, Antofagasta. *Chile. Rev. Geológica Chile*, *31*, 3–18.

Nilsen, T. H., & Sylvester, A. G. (1998). Strike-Slip Basins. In C. Busby & R. Ingersoll (Eds.), *Tectonics of sedimentary basins* (pp. 425–456). Cambridge, UK: Willey.

Oliveros, V., González, J., Espinoza Vargas, M., Vásquez, P., Rossel, P., Creixell, C., … Bastías, F. (2017). The early stages of the magmatic arc in the Southern Central Andes. In A. Folguera, E. Contreras-Reyes, N. Heredia, A. Encinas, V. Oliveros, F. Dávila & G. Collo (Eds.), *The Evolution of the Chilean-Argentinean Andes* (pp. 185–212). Cham, Switzerland: Springer.

Padilla, H. (1988). Eventos intrusivos y deformaciones en la Cordillera de Domeyko a la latitud del Salar de Punta Negra. Antecedentes geocronológicos K-Ar. In *V Congreso Geológico Chileno*, Santiago, Chile, pp. 229–243.

Petrinovic, I. A., Riller, U., & Brod, J. A. (2005). The Negra Muerta Volcanic Complex, southern Central Andes: Geochemical characteristics and magmatic evolution of an episodically active volcanic centre. *J. Volcanol. Geotherm. Res.*, *140*, 295–320. https://doi.org/10.1016/j.jvolgeores.2004.09.002

Philippon, M., & Corti, G. (2016). Obliquity along plate boundaries. *Tectonophysics*, *693*, 171–182. https://doi.org/10.1016/j.tecto.2016.05.033

Platt, N. H., & Wright, V. P. (1991). Lacustrine carbonates: Facies models, facies distributions and hydrocarbon aspects. *Spec. Publ. Internatinal Assoc. Sedimentol.*, *13*, 57–74.

Polliand, M., Schaltegger, U., Frank, M., & Fontboté, L. (2005). Formation of intra-arc volcanosedimentary basins in the western flank of the central Peruvian Andes during Late Cretaceous oblique subduction: Field evidence and constraints from U-Pb ages and Hf isotopes. *International Journal of Earth Sciences*, *94*, 231–242. https://doi.org/10.1007/s00531-005-0464-5

Poma, S., Zappettini, E. O., Quenardelle, S., Santos, J. O., Koukharsky, M., Belousova, E., & McNaughton, N. (2014). Geochemistry, U-Pb SHRIMP zircon dating and Hf isotopes of the Gondwanan magmatism in NW Argentina : Petrogenesis and geodynamic implications. *Andean Geology*, *41*, 267–292.

Prinz, P., Wilke, H.-G., & von Hillebrandt, A. (1994). Sediment accumulation and subsidence history in the Mesozoic marginal basin of northern Chile. In K. J. Reutter, E. Scheuber, & P. J. Wigger (Eds.), *Tectonics of the Southern Central Andes* (pp. 219–232). Berlin: Springer-Verlag. https://doi.org/10.1007/978-3-642-77353-2

Prinz-Grimm, P. (1995). Triassiche Korallen der südlichen Zentral-Anden. *Geologica et Palaeontologica*, *29*, 233–234.

Prosser, S. (1993). Rift-related linked depositional systems and their seismic expression. *Geol. Soc. London. Spec. Publ.*, *71*, 35–66. https://doi.org/10.1144/GSL.SP.1993.071.01.03

del Rey, A., Deckart, K., Arriagada, C., & Martínez, F. (2016). Resolving the paradigm of the late Paleozoic-Triassic Chilean magmatism: Isotopic approach. *Gondwana Research*, *37*, 172–181.

Salfity, J. A. (1985). *Lineamentos transversales al rumbo andino en el Noroeste Argentino*. In IV Congreso Geologico Chileno, Antofagasta, Chile, Vol. 2, pp. 119–137.

Sayit, K., Bedi, Y., Tekin, U. K., Göncüoglu, M. C., & Okuyucu, C. (2017). Middle Triassic Back-arc Basalts from the Blocks in the Mersin Mélange, southern Turkey: Implications for the Geodynamic Evolution of the Northern Neotethys. *Lithos*, *268–271*, 102–113. https://doi.org/10.1016/j.lithos.2016.10.032

Schellart, W. P. (2005). Influence of the subducting plate velocity on the geometry of the slab and migration of the subduction hinge. *Earth and Planetary Science Letters*, *231*, 197–219. https://doi.org/10.1016/j.epsl.2004.12.019

Schlische, R. W. (1991). Half-graben basin filling models: New constraints on continental extensional basin development. *Basin Research*, *3*, 123–141. https://doi.org/10.1111/j.1365-2117.1991.tb00123.x

Schlische, R. W., & Anders, M. H. (1996). Stratigraphic effects and tectonic implications of the growth of normal faults and extensional basins. *Geological Society of America Special Paper*, *303*, 183–203.

Scholz, C. A., Johnson, T. C., Cohen, A. S., King, J. W., Peck, J. A., Overpeck, J. T., … Pierson, J. (2007). East African megadroughts between 135 and 75 thousand years ago and bearing on early-modern human origins. *Proceedings of the National Academy of Sciences*, *104*, 16416–16421. https://doi.org/10.1073/pnas.0703874104

Scholz, C. A., Rosendahl, B. R., & Scott, D. L. (1990). Development of coarse grained-facies in lacustrine rift basins: Example from East Africa. *Geology*, *18*, 140–144. https://doi.org/10.1130/0091-7613(1990)018<0140:DOCGFI>2.3.CO;2

Selley, R. C. (2000). *Applied sedimentology*. San Diego, CA: Academic Press.

Sengör, A. M. C., & Natal'in, B. A. (2001). Rifts of the world. In *Special Paper 352: Mantle plumes: Their identification through time* (Vol. 352, pp. 389–482). https://doi.org/10.1130/0-8137-2352-3

Shanley, K. W., & McCabe, P. J. (1994). Perspectives on the sequence stratigraphy of continental strata. *American Association of Petroleum Geologists Bulletin*, *78*, 544–568.

Solari, M., Montecinos, D., Venegas, C., & Espinoza, F. (2015). Hallazgo de unidades volcánicas del Triásico Medio en la sierra de Imilac, Segunda Región de Antofagasta. In XIV Congreso Geológico Chileno, pp. 0–2.

Stephenson, R. A., & Schellart, W. P. (2010). The Black Sea back-arc basin: Insights to its origin from geodynamic models of modern analogues. *Geol. Soc. London. Spec. Publ.*, *340*, 11–21. https://doi.org/10.1144/SP340.2

Stern, R. J., Lin, P. N., Morris, J. D., Jackson, M. C., Fryer, P., Bloomer, S. H., & Ito, E. (1990). Enriched back-arc basin basalts from the northern Mariana Trough: Implications for the magmatic evolution of back-arc basins. *Earth and Planetary Science Letters*, *100*, 210–225. https://doi.org/10.1016/0012-821X(90)90186-2

Stewart, A. L., & McPhie, J. (2003). Internal structure and emplacement of an Upper Pliocene dacite cryptodome, Milos Island. *Greece. J. Volcanol. Geotherm. Res.*, *124*, 129–148. https://doi.org/10.1016/S0377-0273(03)00074-X

Stewart, A. L., & McPhie, J. (2006). Facies architecture and Late Pliocene – Pleistocene evolution of a felsic volcanic island, Milos. *Greece. Bull. Volcanol.*, *68*, 703–726. https://doi.org/10.1007/s00445-005-0045-2

Suárez, M., & Bell, C. (1992). Triassic rift-related sedimentary basins in northern Chile (24°-29°S). *J. South Am. Earth Sci.*, *6*, 109–121. https://doi.org/10.1016/0895-9811(92)90001-F

Suárez, M., & Bell, C. M. (1994). Braided Rivers, Lakes and Sabkhas of the Upper Triassic Cifuncho Formation, Atacama Region. *Chile. J. South Am. Earth Sci.*, *7*, 25–33. https://doi.org/10.1016/0895-9811(94)90031-0

Suárez, M., & Bell, C. (2010). Sabkhas continentales y costeros en el Triásico Superior-Cretácico Inferior de Atacama, Chile. *Rev. Geológica Chile*, *25–26*, 145–153.

Tomlinson, A. J., Cornejo, P., & Mpodozis, C. (1999). Hoja Potrerillos, Región de Atacama. Servicio Nacional de Geología y Minería (Chile), Mapas Geológicos, No. 14, 1 mapa escala 1:100.000, Santiago.

Torsvik, T. H., & Cocks, L. R. M. (2013). Gondwana from top to base in space and time. *Gondwana Research*, *24*, 999–1030. https://doi.org/10.1016/j.gr.2013.06.012

Urzúa, F. (2009). *Structural Evolution of La Escondida Copper District, Northern Chile*. Hobart, TAS: University of Tasmania.

Valenzuela, J. (2014). Estratigrafía y geología estructural de la región de Cerro La Ballena-Portezuelo Azabache (Cordillera de Domeyko 23° 40′-24° 00′S). MSc. Thesis, Universidad de Chile, pp. 147. Santiago de Chile.

Venegas, C., Cervetto, M., Astudillo, N., Espinoza, F., Cornejo, P., Mpodozis, C., & Rivera, O. (2013). Carta Sierra Vaquillas Altas, Regiones de Antofagasta y Atacama. Servicio Nacional de Geología y Minería, Carta Geológica de Chile, Serie Geología Básica 159, 1-87. 1 mapa escala 1:100.000. Santiago.

Vicente, J. C. (2005). Dynamic paleogeography of the Jurassic Andean Basin: Pattern of transgression and localisation of main straits through the magmatic arc. *Rev. La Asoc. Geológica Argentina*, *60*, 221–250.

Villamor, P., Berryman, K. R., Ellis, S. M., Schreurs, G., Wallace, L. M., Leonard, G. S., … Ries, W. F. (2017). Rapid Evolution of Subduction-Related Continental Intraarc Rifts: The Taupo Rift, New Zealand. *Tectonics*, *36*, 2250–2272. https://doi.org/10.1002/2017TC004715

Walker, R. G., & James, N. P. (1992). *Facies models: Response to sea level change*. Ontario, Canadá: Geological Association of Canada.

White, J. D. L., & Houghton, B. F. (2006). Primary volcaniclastic rocks. *Geology*, *34*, 677–680. https://doi.org/10.1130/G22346.1

Withjack, M. O., Schlische, R. W., & Olsen, P. E. (2002). Rift-basin structure and its influence on sedimentary systems. In R. Renaut & G. M. Ashley (Eds.), *Sedimentation in continental Rifts* (pp. 57–81). Society of Economic Paleontologists and Mineralogists (SEPM), Special Publication 73, Tulsa. https://doi.org/10.2110/pec.02.73

Wright, V. P., & Platt, N. H. (1995). Seasonal wetland carbonate sequences and dynamic catenas: A re-appraisal of palustrine limestones. *Sediment. Geol.*, *99*, 65–71. https://doi.org/10.1016/0037-0738(95)00080-R

SUPPORTING INFORMATION

Additional supporting information may be found online in the Supporting Information section at the end of the article.

A TECTONOSTRATIGRAPHIC STUDY OF LATE TRIASSIC-EARLY JURASSIC BASINS IN NORTHERN CHILE (24.5º-26ºS): KINEMATIC PRELIMINARY RESULTS

Mauricio Espinoza [1]*, **Verónica Oliveros** [1], **Paulina Vásquez** [2] **Florencia Bechis** [3]

(1) Departamento de Ciencias de la Tierra, Facultad de Ciencias Químicas, Universidad de Concepción, Casilla 160-C, Concepción.

(2) Servicio Nacional de Geología y Minería. Avda. Santa María 0104, Providencia, Santiago.

(3) Universidad Nacional de Río Negro, Isidro Lobo 516, General Roca, Argentina.

*Mail: mauricespinoza@udec.cl

Resumen. The Pre-Andean cycle (Late Permian-Early Jurassic), has been characterized typically as a stationary stage of Gondwana with an abortion of the subduction system (Mpodozis and Kay, 1990). Consequently, it would have predominated an extensional tectonic with the development of a NNW trending continental rifting and a magmatic bimodality (Charrier et al., 2007). These features are well recognized in Argentina. However, along the Chilean side, the outcrops are more scarce and discontinuous than in Argentina and have been strongly affected by magmatism and tectonism of the Cenozoic era, hindering the recognition of primary features of basins and discouraging systematic studies of this important period.

On the other hand, previous and recent works in Chile and Argentina, have proposed models invoking the development of subduction during the Late Triassic (Llambías et al., 2007; Suárez et al., 1985; Coloma et al., 2013; Oliveros et al., 2014) which would modify the classic interpretation of these basins as continental rifting non-related to subduction.

In northern Chile (24.5°-26°S) cropping out two depocenters of the Pre-Andean cycle: the Cifuncho basin in Coastal Cordillera, and El Profeta basin in Precordillera. This area records volcano-sedimentary rocks, which allow us to evaluate the position of the basins relative to the locus of magmatism (intra-arc versus back-arc basins). These probable arc-related basins are important proxies to characterize the geodynamic framework of the Late Triassic-Early Jurassic

Thus, in order to unravel the geologic evolution during this period and to evaluate the possible influence of subduction process in the strain field of the crust, we propose a tectonostratigraphic study focused in stratigraphic (chronostratigraphy, provenance and environmental studies) and tectonic methodologies (syn-rift kinematic analysis and restoration of structural sections).

We carried a preliminary structural analysis of third and four order extensional faults affecting Late Triassic-Early Jurassic successions of the El Profeta depocenter. Most of the data (Punta del Viento, Quebrada Encuentro, Quebrada Doña Inés Chica and Quebrada La Perra) show a clear synrift character with the development of fault controlled growing strata. Besides, the extensional structures present in Cerro Manchón are analyzed together because of its presumable synrift origin. These data and their kinematic analysis are summarized in the Figure 1.

The kinematic analysis shows a great variability in the bedding-corrected orientation of tensional axis (T). This principal direction vary from NW to NE. Also, most of the corrected extensional structures show normal faulting with little strike-slip component except the Quebrada Doña Ines Chica data which correspond to a main sinistral faulting with a minor extensional component.

However, significant clockwise rotations close to ~30º have been reported in the vicinity of the study area. Moreover this rotations can vary highly in magnitude and even in sense of movement, like those reported near the south of Potrerillos area related to complex local tectonics (Arriagada et al., 2006).

Thus, although the principal directions distribution are probably reflecting a variation in the strain field across the El Profeta basin, this orientations need to be corrected by vertical axis rotations to get original principal strain directions. This paleomagnetic data is absent in the study area and is acquisition is beyond the scope of this work.
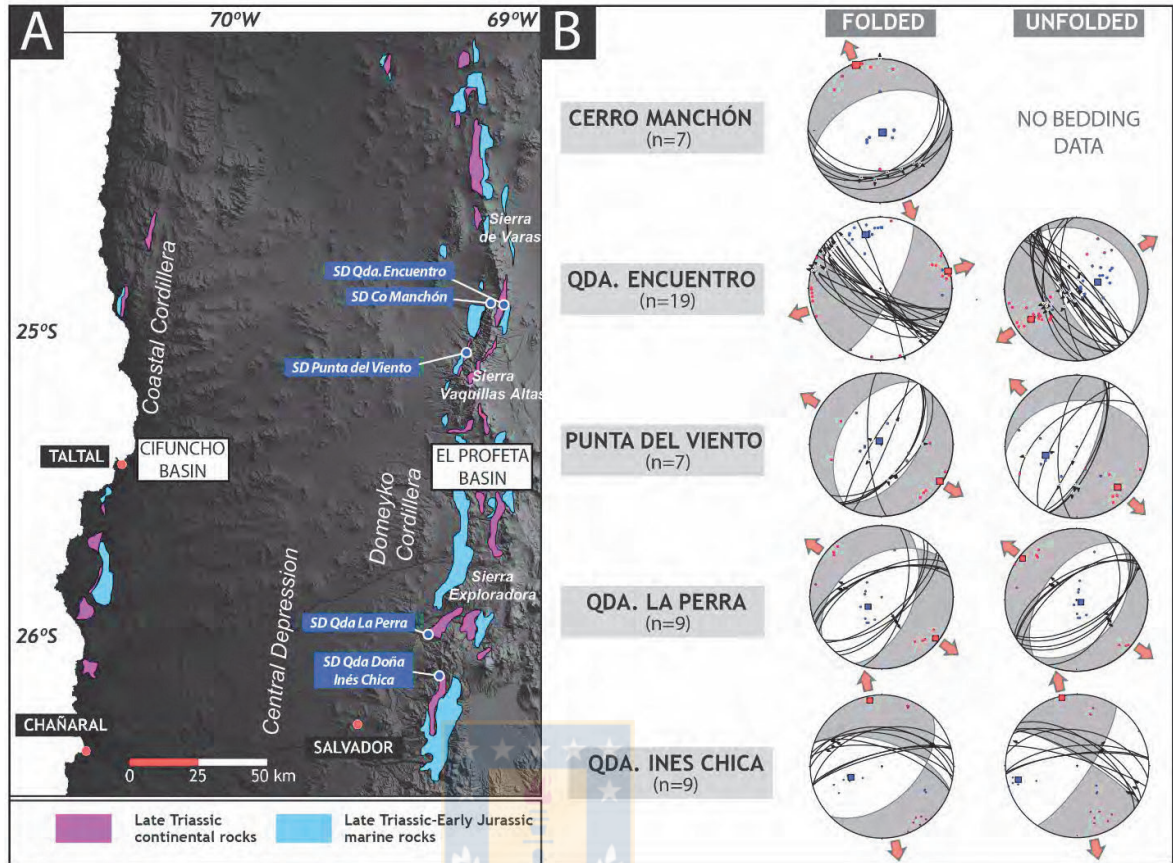
Figura 1: A) Área de estudio mostrando la ubicación de las cuencas de Cifuncho y El Profeta. En azul se muestra las localidades donde análisis cinemáticos de fallas fueron realizados. B) Estereogramas mostrando los planos de falla y la solución de estos planos. Los cuadrados rojos marcan la posición del eje T de tension y los azules marcan los ejes de presión P. Las flechas marcan la dirección de extension estimada para la posición del eje de tensión.

VI. References

Arriagada, C., Roperch, P., Mpodozis, C., Fernandez, R., 2006. Paleomagnetism and tectonics of the southern Atacama Desert (25-28°S), northern Chile. Tectonics 25.

Charrier, R., Pinto, L., Rodriguez, M.P., 2007. Tectonostratigraphic evolution of the Andean Orogen in Chile, in: The Geology of Chile. pp. 21–114.

Coloma, F., Creixell, C., Salazar, E., 2013. Arc development during continuous subduction from Carboniferous to Triassic: Evidence from geochemistry of intrusive rocks in the Vallenar Cordillera (El Tránsito valley), Andes of northern Chile, in: International Geological Congress on the Southern Hemisphere. p. 281.

Llambías, E.J., Leanza, H. A., Carbone, O., 2007. Evolución Tectono-magmática durante el pérmico al Jurásico temprano en la Cordillera del Viento (37°05′S - 37°15′S): Nuevas evidencias geológicas y geoquímicas del inicio de la Cuencas Neuquina. Rev. de la Asoc. Geol. Argentina 62, 217–235.

Mpodozis, C., Kay, S., 1990. Provincias magmáticas ácidas y evolución tectónica de Gondwana: Andes chilenos (28º-31º S). Revista Geológica de Chile.

Oliveros, V., Valin, X., Vásquez, P., Creixell, C., Vallejos, D., 2014. Estudio geoquímico y geocronológico de las sucesiones volcano-sedimentarias pre-Jurásicas en el norte de Chile (28º00`-29º30`): Implicancias para el inicio de la subducción andina, in: XIX Congreso Geológico Argentino.

Suárez, M., Naranjo, J., Puig, A., 1985. Estratigrafia de la Cordillera de la Costa al sur de Taltal, etapas iniciales de la evolucion andina. Rev. Geológica Chile 19–28.

U-Pb geochronology and kinematic preliminary analyses of Late Triassic-Early Jurassic basins in northern Chile (24.5º-26ºS).

Mauricio Espinoza [1*], Verónica Oliveros [1], Paulina Vásquez [2], Florencia Bechis [3]

(1) Departamento de Ciencias de la Tierra, Facultad de Ciencias Químicas, Universidad de Concepción, Casilla 160-C, Concepción.
(2) Servicio Nacional de Geología y Minería. Avda. Santa María 0104, Providencia, Santiago.
(3) Instituto de Investigaciones en Diversidad Cultural y Procesos de Cambio (IIDyPCa), CONICET - Universidad Nacional de Río Negro, Mitre 630, San Carlos de Bariloche, Argentina

*Mail: mauricespinoza@udec.cl

Abstract. In northern Chile (24.5 -26 S) two Late Triassic-Early Jurassic depocenters crop out: the Cifuncho basin in Coastal Cordillera, and Profeta basin in Precordillera. There is scarce systematic studies of these basins resulting in major gaps in the knowledge of its chronostratigraphy and structural framework.

In this contribution we present preliminary results (U-Pb geochronological and structural syn-rift data) of a tectonostratigraphic study of the Cifuncho and Profeta basins. The geochronological data along the Cifuncho and Profeta basins shows a main continental sedimentary deposition during the Norian to Raethian. Volcanosedimentary rocks shows a main detrital supply of Early Permian age (2 -2 3 Ma). This input can be associated with the volcanic La Tabla Formation and/or the exhumation of Permian granitoids. A minor supply close to 4 Ma is related to a source from the Lower Ordovician arc (4 Ma), suggesting the tectonic exhumation of this source to the east of the Profeta basin during the Late Triassic. On the other hand, the kinematic analyses evidence a variability in the orientation of the maximum strain axes from a main north-est to a subordinate northeast direction of extension, probably reflecting local variation in the strain field across the basins during.

Keywords: Triassic, syn-rift, U-Pb geochronology.

I. Introduction

The Pre-Andean cycle (Late Permian-Early Jurassic, Charrier et al., 2007) has been characterized as a stationary stage of Gondwana with an abortion of the subduction system (Mpodozis and Kay, 1990) and the development of a NNW trending continental rifting (Charrier et al., 2007). However, previous works in Chile and Argentina, have proposed alternative models invoking the development of subduction during the Late Triassic (Coloma et al., 2013; Llambías et al., 2007; Oliveros et al., 2014). The latter

evidences that the first order driving mechanisms for extension in the Pre-Andean basins are poorly understood.

On the other hand, the best preserved successions of Pre-Andean basins are recorded in Argentina, while along the Chilean side, the outcrops are scarce, scattered and have been strongly affected by magmatism and tectonism of the Cenozoic era. The later causes major gaps in the knowledge of the geochronology, stratigraphy and structural framework of these basins in Chile.

The study of these basins is an important proxy in order to characterize the geodynamic framework of the Late Triassic-Early Jurassic evolution of the southwestern margin of Gondwana during the transition to the Andean orogeny. In this work, we present first results (U-Pb geochronology and kinematic analyses) of a tectonostratigraphic study of the Pre-Andean Cifuncho and Profeta basins, cropping out in the Coastal Cordillera and the Precordillera of northern Chile (Figure 1).

II. Background

II.1 Geological setting

The units corresponding to the **Cifuncho basin** crops out along the Coastal Cordillera and its infill is composed by the Cifuncho, Agua Chica, Pan de Azúcar and Posada de los Hidalgo formations. The Cifuncho Formation overlies in unconfomity the Paleozoic metasedimentary basement and is composed mainly by continental fluvial-alluvial facies and piroclastic rocks. To the south, this unit grades laterally to the volcaniclastic Agua Chica Formation. Recent data have assigned the main part of the Cifuncho Formation to the Norian (Contreras et al., 2013). A marine transgression was developed diacronically in the 'late' Norian and Hettangian-Sinemurian represented by the shallow marine Pan de Ázucar Formation (Contreras et al., 2013).

The units representing the **Profeta basin** are located along the Precordillera and correspond to Late Triassic-Early

Jurassic stratified volcanic and sedimentary rocks. The older unit of this basin is the continental volcaniclastic Quebrada del Salitre Formation, which overlies the Punta del Viento Plutonic Complex and the La Tabla Formation (Carboniferous-Permian). Quebrada del Salitre Formation records lacustrine and alluvial-fluvial facies with volcanic intercalations. In the Sierra de Varas, the Cerro Guanaco and Sierra de Varas formations overlie in unconformity the La Tabla Formation with an age constrained as late Norian-Raethian (González et al., 2015). A wide marine transgression begins in the Raethian represented by the Profeta Formation and the upper member of the Quebrada del Salitre Formation in Sierra Exploradora (Cornejo et al., 2009). These rocks overlie in transition the previous volcaniclastic rocks (Cornejo et al., 2009).

II.2 Structural framer

In the Coastal Cordillera, the structures controlling the Cifuncho basin have been referred as the Tigrillo Fault System. Yet, according to Contreras et al. (2013) there is not clear evidence of the synrift character for this structural system. Thus, the characterization of the faults controlling the Cifuncho basin remains an open issue. On the other hand, a complex tectonic evolution has been suggested for the Precordillera. This evolution involves strike slip faulting, inversion of the Mesozoic synrift structures, and vertical axis rotations. However, an important number of mesoscopic synrift structures are well preserved in some ravines. The kinematic analysis of these structures allow us to compare the strain field along the Cifuncho-El Profeta basins with those reported in Argentina for the same period (Bechis et al., 2010).

III. Methoolog

U-Pb zircon geochronology (LA-MC-ICPMS) was conducted at the Arizona LaserChron Center. The statistical analysis were carried out using the Isoplot/Ex version 4.15 (Ludwig, 2011). Kinematic analyses were made using FautKin7 software (Allmendinger et al., 2012).

IV. Resuls

IV.1 Geochronological U-P aa

The geochronological results of this work are summarized in the Figure 2. In the north portion of Sierra de Varas two samples belonging to the Sierra de Varas Formation were collected. A fine grained tuff intercalated in lacustrine mudstones (CPV-14-268) shows a main peak of ~205 Ma interpreted as the approximate age of the pyroclastic event. A secondary peak of ~283 Ma is probably associated with an accidental source. On the other hand, a tuffaceous sandstone (CPV-14-266), shows a detrital signal with two marked peaks, a primary close to ~295 Ma and a younger

peak of ~212 Ma. In this sample, the weighted average of the three youngest grains yields an age of 207.3±3.2 as the maximum depositional age.

In Sierra Vaquillas Altas two samples corresponding to the Quebrada del Salitre Formation were analyzed. A tuffaceous breccia (CPV-14-157), formerly assigned to the La Tabla Formation (Venegas et al., 2013) cropping out ~220 m under the contact with Profeta Formation, yielded a crystallization age of 212.1 +1.7/-1.6 Ma according to the TuffZirc algorithm (Ludwig, 2011). On the other hand, a coarse grained sandstone directly overlying Permian granites in Quebrada Vaquillas (CPV-14-254), displays a detrital signal with a major peak close to ~297 Ma and two minor peaks at ~246 Ma and ~478 Ma. In this sample, the weighted average of the three youngest grains estimates an age of 245.9±3.6 Ma as the maximum depositional age.
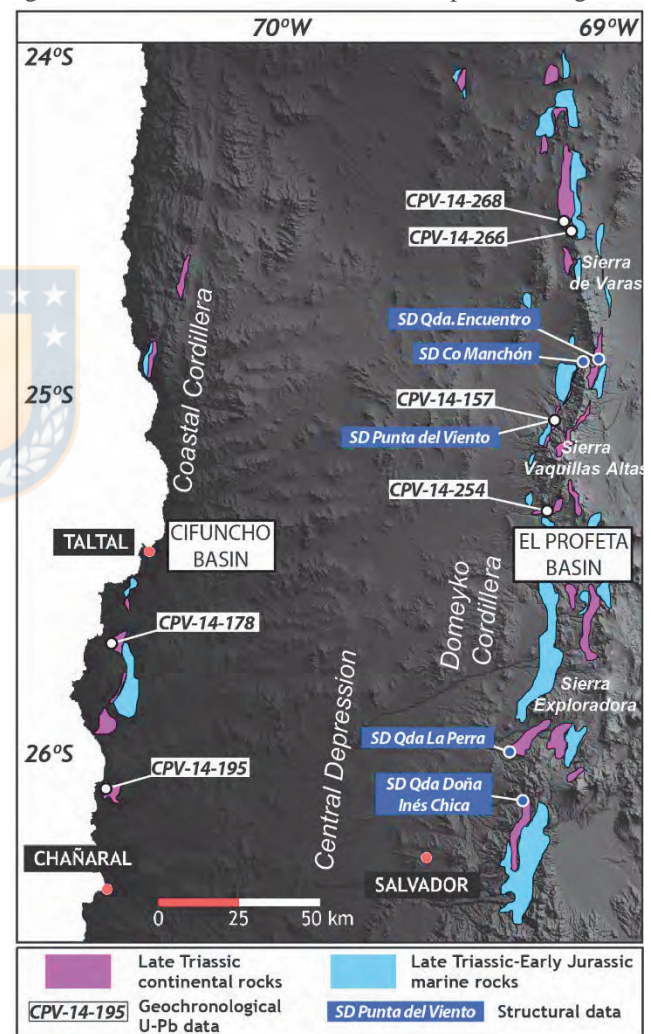
Figure 1: Study area showing outcrops of Cifuncho and Profeta basins. Samples codes associated with geochronological U-Pb and structural data locations are included.

In the Coastal Cordillera, two samples corresponding to the Cifuncho and Agua Chica formations were collected. A tuffaceous breccia of Cifuncho Formation (CPV-14-178), yield a concordia age of 208.9±2.1 Ma. On the other hand,

a tuff belonging to the Agua Chica Formation in the Quebrada Pan de Ázucar (CPV-14-195) shows a main peak close to the ~200 Ma and a secondary peak close to ~264 Ma. The estimate age of the youngest cluster based in TuffZirc algorithm yield an age of 200.7 +2.29/-3.32 Ma interpreted as the age of the pyroclastic event.

IV.1 Kinema ic a a

We carried a preliminary structural analysis of third and four order extensional faults affecting Late Triassic-Early Jurassic strata (<10 m of slip). Most of the data (Punta del Viento, Quebrada Encuentro, Quebrada Doña Inés Chica and Quebrada La Perra localities) show a clear synrift character with the development of fault controlled growing strata. Three of the sites correspond to the continental underlying successions (Quebrada La Perra and Cerro Manchón localities) while the others correspond to the marine overlying succesions (Quebrada Encuentro, Quebrada Doña Inés Chica and Punta del Viento localities) These data and their kinematic analysis are summarized in the Figure 3.

The kinematic analysis after the tilting correction evidence that tensional axis (T) range from NW to NE directions with a slight predominance of the NW to NNW extension directions. Also, most of the corrected extensional structures show normal faulting with little strike-slip component except the data from the Quebrada Doña Ines Chica data which correspond to a main sinistral faulting with a minor extensional component.

V. Discussion

In the northern section of the study area, the crystallization ages presented (CPV-14-157,268) constrain the main activity of deposition to the upper part of the Late Triassic. These data are in agreement with recent works in the Sierra de Varas constraining the continental deposition to the interval between the Norian to Raethian (Gonzalez et al., in press). On the other hand, the detrital zircons at the base of the Quebrada del Salitre Formation (CPV-14-254) only yield a maximum age of deposition close to ~246 Ma. Thus, it can not be discarded that in Sierra Vaquillas Altas the rifting began earlier than the well-recognized activity close to ~212-214 Ma (Venegas et al., 2013).

Moreover, the detrital signal of samples in Precordillera shows an main source of Early Permian rocks (~283-297 Ma), related to supplies from La Tabla Formation, Permian granitoids (Punta del Viento or Sierra de Varas plutonic complexes) or a combination of both. A minor input close to ~478 Ma is observed at the base of Quebrada del Salitre Formation (CPV-14-254), which could be associated with the Lower Ordovician arc (~480 Ma). This magmatism has been recognized to the northeast of the study area (Zimmermann et al., 2009), suggesting a tectonic control in the exhumation of this source during the Late Triassic.

In the Coastal Cordillera, the age obtained in the Cifuncho Formation (208 ± 2.1 Ma) is in agreement with those presented by Contreras et al. (2013), ranging from 209 to 212 Ma. Also, we report the first absolute age of the Agua Chica Formation (~200 Ma), which indicates that part of this unit is younger than Cifuncho Formation and that the continental facies reached the Triassic-Jurassic limit.

The kinematic analysis shows a variability in the bedding-corrected orientation of tensional axis (T) from a main NW to subordinate NE directions. However, significant clockwise rotations close to ~30° have been reported in the vicinity of the study area. These rotations can vary in magnitude and even in the sense of movement (Arriagada et al., 2006). Thus, although the principal directions distribution are probably reflecting a variation in the strain field across the El Profeta basin, vertical axis rotations needs to be considered to get original principal strain directions.

VI. Conclusions

The geochronological data along the Cifuncho and Profeta basins, show a main continental sedimentary deposition during the Norian to Raethian. Volcanosedimentary rocks show a main detrital supply of Early Permian age (~297-283 Ma). This input can be associated with the volcanic La Tabla Formation and/or the exhumation of Permian granitoids. A minor supply close to ~478 Ma is related to a source from the Lower Ordovician arc (~480 Ma), suggesting the tectonic exhumation of this source to the east of the Profeta basin during the Late Triassic.

The kinematic analyses evidence a variability in the orientation of the maximum strain axes from a main northwest to a subordinate northeast direction of extension, probably reflecting local variation in the strain field across the basins during the aperture of Pre-Andean depocenters.

VIII. References

Allmendinger, R.W., Cardozo, N.C., Fisher, D., 2012. Structural Geology Algorithms: Vectors & Tensors. Cambridge, England, Cambridge University Press.

Arriagada, C., Roperch, P., Mpodozis, C., Fernandez, R., 2006. Paleomagnetism and tectonics of the southern Atacama Desert (25-28°S), northern Chile. Tectonics 25, TC4001.

Bechis, F., Giambiagi, L., García, V., Lanés, S., Cristallini, E., Tunik, M., 2010. Kinematic analysis of a transtensional fault system: The Atuel depocenter of the Neuquén basin, southern Central Andes, Argentina. J. Struct. Geol. 32, 886–899.

Charrier, R., Pinto, L., Rodriguez, M.P., 2007. Tectonostratigraphic evolution of the Andean Orogen in Chile, in: The Geology of Chile. pp. 21–114.

Contreras, J.P., Espinoza, M., Jorquera, R., Kraus, S., Ramírez, C., De la Cruz, R., Naranjo, J. a., Escribano, J., Martínez, P., 2013. Carta Cifuncho, Regiones de Antofagasta y Atacama. Servicio

Nacional de Geología y Minería, Carta Geológica de Chile, Serie Geología Básica 161, 1 mapa escala 1:100.000. Santiago.

Cornejo, P., Mpodozis, M., Rivera, O., Matthews, S., 2009. Carta Exploradora, Regiones de Antofagasta y Atacama. Servicio Nacional de Geología y Minería, Carta Geológica de Chile, Serie Geología Básica 119: 103 p., 1 mapa escala 1:100.000.

González, R., Contreras, J., n.d. Carta Sierra de Varas, Región de Antofagasta. Servicio Nacional de Geología y Minería, Carta Geológica de Chile, Serie Geología Básica XXX, 1 mapa escala 1:100.000. Santiago.

Llambías, E.J., Leanza, H. A., Carbone, O., 2007. Evolución Tectono-magmática durante el pérmico al Jurásico temprano en la Cordillera del Viento (37°05′S - 37°15′S): Nuevas evidencias geológicas y geoquímicas Del Inicio de la Cuencas Neuquina. Rev. la Asoc. Geol. Argentina 62, 217–235.

Mpodozis, C., Kay, S., 1990. Provincias magmáticas ácidas y evolución tectónica de Gondwana: Andes chilenos (28-31 S). Revista Geológica de Chile.

Oliveros, V., Valin, X., Vásquez, P., Creixell, C., Vallejos, D., 2014. Estudio geoquímico y geocronológico de las sucesiones volcano-sedimentarias pre-Jurásicas en el norte de Chile (28°00`-29°30`): Implicancias para el inicio de la subducción andina, en: XIX Congreso Geológico Argentino.

Venegas, C., Cervetto, M., Astudillo, N., Espinoza, F., Cornejo, P., Mpodozis, C., Rivera, O., 2013. Carta Sierra Vaquillas Altas, Regiones de Antofagasta y Atacama. Servicio Nacional de Geología y Minería, Carta Geológica de Chile, Serie Geología Básica XXX, 1 mapa escala 1:100.000. Santiago.

Zimmermann, U., Niemeyer, H., Meffre, S., 2010. Revealing the continental margin of Gondwana: the Ordovician arc of the Cordón de Lila (northern Chile). Int. J. Earth Sci. 99, S39–S56.

Figure 2: Geochronological U-Pb data of igneous and detrital zircons.
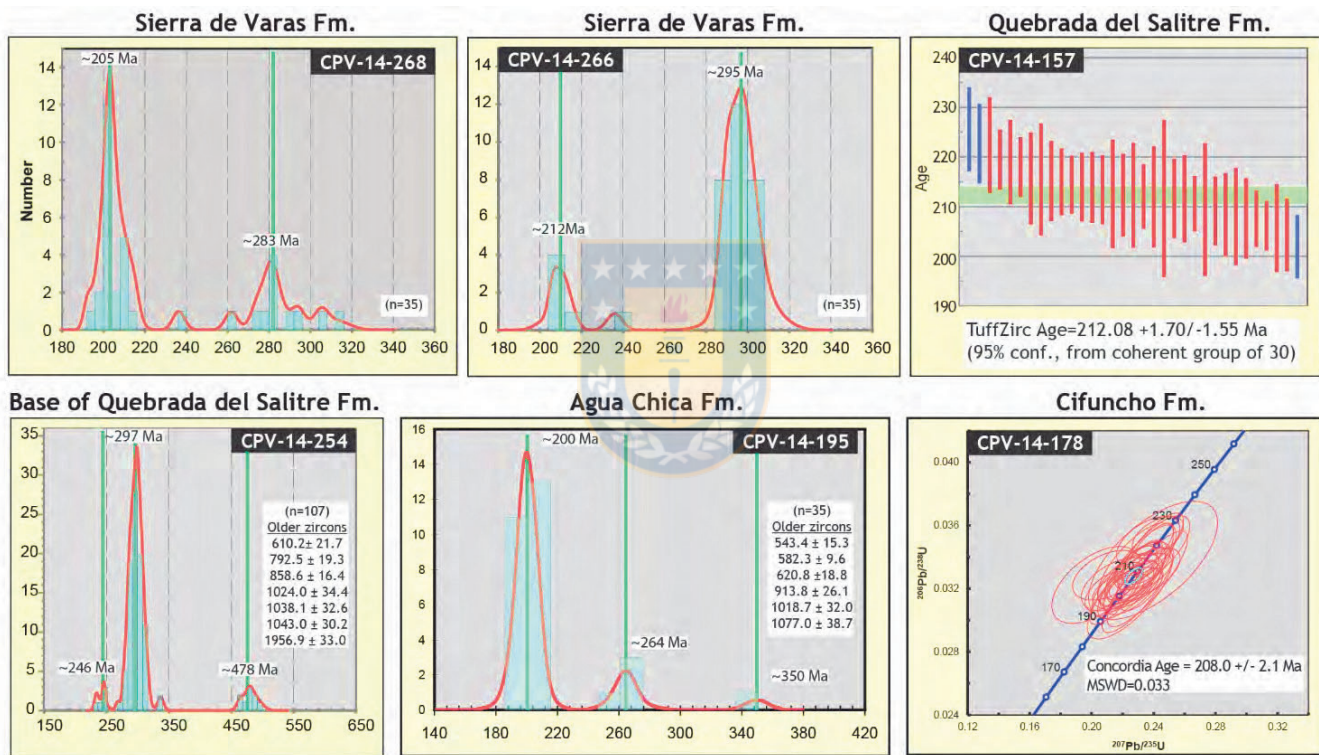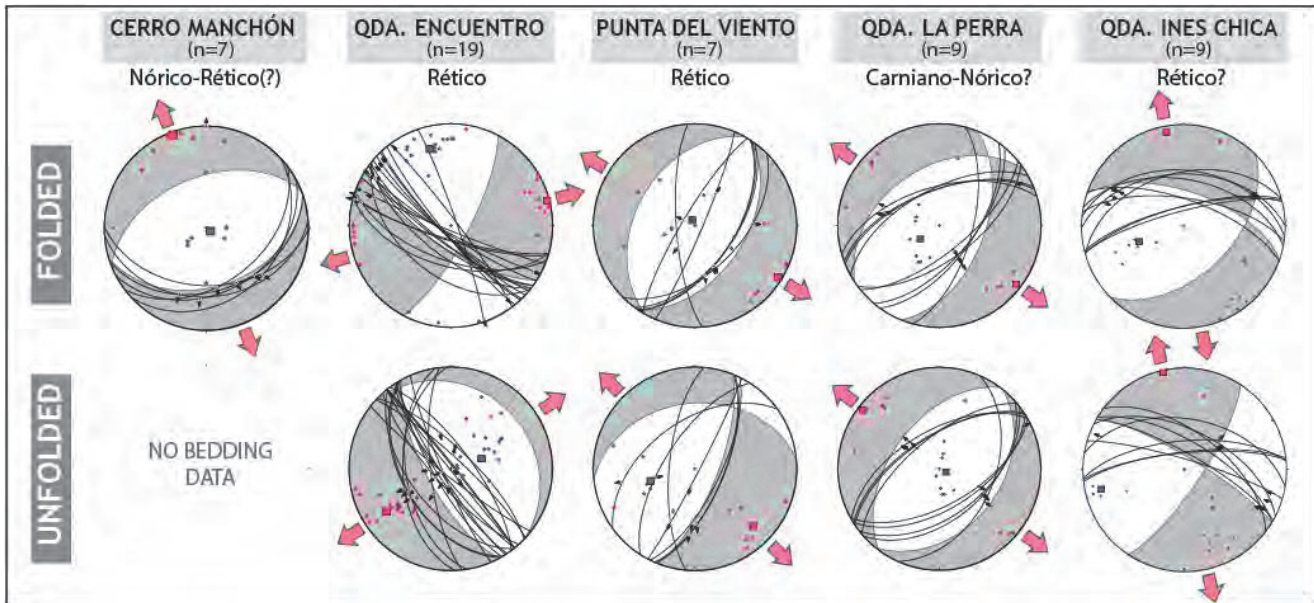
Figure 3: Kinematic analysis of synrift data. Red (blue) squares represent the maximum (minimum) axes of the strain ellipsoid (Allmendinger et al., 2012).

Geochronology, Geochemistry and Tectonics of subduction-related Late Triassic rift basins in northern Chile (24º-26ºS).

Mauricio Espinoza, Verónica Oliveros, Chistopher Celis, Paulina Vásquez, Florencia Bechis

Abstract

As plate-tectonic processes ultimately control the location, initiation, and evolution of sedimentary basins, the study of these is crucial to understand the geodynamic framework of a specific period. In northern Chile, Late Triassic depocenters crop out along the Coastal Cordillera and Precordillera. These basins have been typically associated to a continental rifting unrelated to subduction prior to the Andean orogeny. In this work, we characterize these basins and present field and analytical data suggesting the development of these basins during an active subduction system.

U-Pb geochronology show the opening of these basins probably during the Anisian-Carnian (>233 Ma) with the deposition of highly mature sediments in fluvial systems, followed by the initiation of the volcanism and associated fluvial-alluvial redeposition. Furthermore, a continental (fluvial and lacustrine) deposition and its transition to shallow marine facies are recorded during the Norian to Raethian (212-200 Ma), contemporaneous with the development of acidic volcanic centers. The sedimentary provenance evidence a main detrital supply of Early Permian age (~297-283 Ma) corresponding to volcanic and plutonic basement rocks and a minor supply close to ~478 Ma related to the exhumed Famatinian arc to the east.

Geochemical results from volcanic products present in the basins show a typical subduction signal (calc-alkaline trend, low HFS/LILE ratio and Nb-Ta negative anomalies), while petrography indicate a wide compositional variation more than a bimodal distribution.

These basins present half-graben geometries with the recognition of structural highs separating local depocenters. Kinematic analyses carried in synrift extensional faults show a bimodal distribution of the maximum strain axes from a NE-SW to a subordinate NW-SE direction of elongation. This bimodality could be related to the co-existence of two competing strain directions associated to the breakup of Pangea and the presence of a subducting slab.

These results integrates the magmatic, sedimentary and tectonic record pointing to a subduction-related extensional basin model developed over a continental substratum. The recognition of this ancient examples are important to understand an actual underrepresented basin setting.

The synrift evolution of the early Domeyko Basin (Domeyko Range, northern Chile): Coupling detrital ^{40}Ar-^{39}Ar white mica and U-Pb zircon analysis into a tectonostratigraphic framework

Mauricio Espinoza, Verónica Oliveros, Leah Morgan, Michael Cosca, Luigi Solari

Abstract

Compressional tectonics that shaped the western flank of the Andes seems to have been strongly influenced by the heritage of extensional basins developed during the break-up of Gondwana. However, major questions remain about the exact timing, architecture and driving mechanism of these basins (subduction-related rift versus continental rift). In this work, we coupled U-Pb detrital zircon (DZ) and ^{39}Ar-^{40}Ar in detrital muscovites (DM) into a tectonostratigraphic framework in order to unravel the synrift evolution of the Domeyko Basin (northern Chile, 24° - 26° S).

U-Pb data indicate that the rifting in the Domeyko Basin occurred in two stages; a first from ca. 240-225 Ma which led to the formation of the Sierra Exploradora sub-basin (SESB) and a second from ca. 217-200 Ma, opening the Sierra de Varas sub-basin (SVSB) and reactivating the SESB. The competition between mechanical subsidence and the volcanic supply rates in these magma-rich depocenters, led to the dominance of the inter-eruption period in the SVSB and a predominance of the syn-eruptive period along the SESB.

Geochronology of detrital minerals deposited during the second rift stage reveal significant differences between both sub-basins. At the SVSB, DZ ages show a main peak at ca. 285-295 Ma and much younger WDM ages, with a main peak close to ca. 200 Ma, slightly younger than the depositional age at ca. 213-210 Ma, likely due to partial resetting of the WDM ages by burial. A lack of muscovite-bearing plutonic sources of 230-200 Ma, leads us to interpret that WDM ages indicate a significant cooling of the Permian plutonic sources close to the basin aperture. On the contrary, along the SESB, WDM ages (260-265 Ma) are only slightly younger than DZ ages (280-270 Ma). The small difference between the WDM and the DZ ages, points to a rapid cooling of plutonic source rocks at ca. 260 Ma, coinciding with the age of the San Rafael orogenic phase in northern Chile.

DZ data of the Domeyko Basin show a predominance of sediments from the Gondwanic basement with a scarcity of zircons >500 Ma, indicating erosion from the margins of fault-bounded closed basins. All samples fall in the convergent regime of tectonic discriminator plots for DZ data, suggesting a subduction-related origin for these basins, which contrasts with the classical view of these basins as having a continental rift origin.

**Evolución geológica   c onica   e las cuencas riásicas en el nor e   e Chile
(C. Cos a   C. Dome   o, 24 -26 S): Evi encias e un rif asocia o a su   ucción.**

Mauricio Espinoza [1]**, Verónica Oliveros** [1]**, Paulina Vásquez** [2]**, Chris opher Celis**[1]**, Ro inson Re es**[1]

[1] Departamento de Ciencias de la Tierra, Facultad de Ciencias Químicas, Universidad de Concepción, Casilla 160-C, Concepción. E-mail: mauricespinoza@udec.cl
[2] Servicio Nacional de Geología y Minería. Avda. Santa María 0104, Providencia, Santiago.

En las C. de la Costa y C. de Domeyko del norte de Chile (24°-26°S) se albergan un volumen importante de sucesiones volcánicas y sedimentarias de origen continental y marino depositadas en cuencas durante el Triásico Medio-Superior.

Recientes avances en la geocronología U-Pb indican que la apertura de estas cuencas se habría desarrollado en dos periodos bien reconocibles. Durante el Ladiniense-Nórico bajo (242-225 Ma), tendría lugar una sedimentación fluvial sincrónica a un volcanismo intermedio-ácido y durante el Noriano-Rhaetiano (212-200 Ma) una sedimentación a través de sistemas fluviales y lacustres, contemporánea al desarrollo un magmatismo de gran variación composicional, sucedida por una sedimentación marina somera con característicos arrecifes coralinos.

En C. de Domeyko, la geometría de estas cuencas corresponde a hemigrábenes que describen una profundización general hacia el sur (Qda. Doña Inés Chica) con altos del basamento Carbonífero Superior-Pérmico separando estos depocentros. En la Cordillera de la Costa, la distribución del registro triásico estaría controlada por el Sistema de Fallas Tigrillo y el Sistema de Fallas de Atacama, infiriéndose una posible actividad precursora en el Triásico para éste ltimo.

Los análisis cinemáticos obtenidos desde fallas synrift del Triásico Superior-Jurásico Inferior, muestran una distribución bimodal de los ejes de deformación, con una dirección de elongación principal NE-SW y una subordinada NW-SE. Esta bimodalidad pareciera ser independiente de la edad del fallamiento y podría estar relacionada a dos direcciones de deformación competentes, una asociada al desmembramiento de Pangea y otra correspondiente a la presencia de una losa subductante.

Por otro lado, los resultados geoquímicos de los productos volcánicos del Triásico Superior intercalados en las cuencas, presentan una geoquímica típica de un volcanismo asociado a subducción, describiendo una tendencia calcoalcalina, altas razones LILE HFSE y anomalías negativas de Nb y Ta. De esta manera, el conjunto de resultados obtenidos indicaría que estas cuencas se habrían desarrollado bajo una tectónica extensional con una sedimentación continental y posteriormente marina, íntimamente relacionada al desarrollo de volcanismo asociado a subducción, al menos durante el Triásico Superior.

SYNRIFT STAGE OF THE DOMEYKO BASIN (TRIASSIC): ARCHITECTURE, PROVENANCE AND TECTONICS OF A SUBDUCTION-RELATED BASIN (DOMEYKO RANGE, 23°30'-26°30'S)
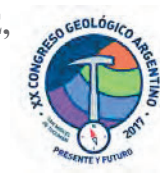
Mauricio ESPINOZA [1], Verónica OLIVEROS [1], Diego MONTECINO[2], Paulina VÁSQUEZ[2]

1.-Departamento de Ciencias de la Tierra, Facultad de Ciencias Químicas, Universidad de Concepción, Casilla 160-C, Concepción. mauricespinoza@udec.cl

2.-Servicio Nacional de Geología y Minería. Avda. Santa María 0104, Providencia, Santiago

LA ETAPA 'SYNRIFT' DE LA CUENCA DE DOMEYKO (TRIÁSICO): ARQUITECTURA, PROVENIENCIA Y TECTÓNICA DE UNA CUENCA ASOCIADA A SUBDUCCIÓN (CORDILLERA DE DOMEYKO, 23°30'-26°30'S)

Resumen

Durante la etapa synrift (Triásico) de la Cuenca de Domeyko (21°-27°S), esta estuvo segmentada en dos depocentros principales: la subcuenca de Sierra de Varas (SVSB) y la subcuenca de Sierra Exploradora (SESB). Ambas subcuencas presentaron un margen activo hacia el oeste a través de estructuras actualmente orientadas N-S y una segmentación que sugiere la interacción con estructuras oblicuas (WNW-ESE?). Geocronología U-Pb indica que la apertura de ambas cuencas fue diacrónica, con una primera etapa de apertura de la SESB durante el Ladiniano (?)-Carniano y una segunda etapa de apertura de la SVSB, durante el Nórico 'alto'-Rético (ca. 218-200 Ma). Por otro lado, los circones detríticos de ambas subcuencas, evidencia una predominancia de fuentes del basamento ígneo Gondwánico con una fuente menor asociada a la orogenia Famatiniana (ca. 460-480 Ma). Sin embargo, la proveniencia de ambas subcuencas presenta importantes diferencias, registrándose una predominancia de fuentes del Pérmico 'inferior' (ca. 280-290 Ma) y del volcanismo coetáneo en la SVSB, mientras en la SESB las fuentes principales corresponden al Pérmico 'superior' (ca. 260-270 Ma), con un escaso registro de volcanismo coetáneo. Por otro lado, la distribución de edades de los

circones detríticos, sugiere que la sedimentación se desarrolló en un contexto de subducción activa (Cawood et al. 2014).

Finalmente, la segmentación observada entre las subcuencas SVSB y SESB, controló la temporalidad de apertura, el grado de extensión, la distribución de facies y la proveniencia sedimentaria de ambos depocentros. Más aún, la localización de los altos de basamento durante el synrift, se mantuvo durante la etapa de subsidencia termal de la CD (Jurásico al Cretácico Inferior) y posteriormente, determinó el estilo estructural de la deformación compresiva desarrollada durante el Cretácico Superior al Neógeno, sugiriendo que la segmentación de la Cuenca de Domeyko constituyó una herencia estructural de primer orden en la evolución de la posterior Cordillera de Domeyko.

Palabras clave: Cuenca Synrift, Triásico, Cordillera de Domeyko, U-Pb detrítico

Keywords: Triassic, synrift basin, U-Pb detrital geochronology, Domeyko Range

Expanded Abstract

The Domeyko Basin comprises deposits from the Upper Permian (?)-Triassic to Lower Cretaceous, cropping out in the western margin of the Domeyko Range of northern Chile (21°-27°S). During an early stage, the Domeyko Basin recorded the deposition of volcanic and sedimentary rocks under active lithospheric stretching, giving place to a continental rift basin (Suárez and Bell 1992). The synrift deposits consist of volcanic and continental sedimentary rocks, which unconformably overlie 'upper' Carboniferous to Permian acidic igneous rocks, partly equivalent to the Choiyoi magmatic province (Kleiman and Japas 2009). Overlying the synrift deposits, a marine transgression took place in several depocenters during the 'latest' Late Triassic (Rhaetian) (González et al. 2015).

In the study area, the Domeyko Basin comprises two major synrift sub-basins: the Sierra de Varas sub-basin (SVSB, 23°47'S - 25°20'S) to the north and the Sierra Exploradora sub-basin to the south (SESB, 25° 50'S – 26° 20'S). These sub-basins were separated by a structural paleo-high approximately at 25°30'S. To the north, the SVSB comprises a series of depocenters which accumulated proximal volcanic successions or mainly lacustrine deposits associated with distal pyroclastic products (González et al. 2015; Astudillo et al., *in prep*). Our new U-Pb igneous zircon

data, as well as the compilation of recent published data (González et al. 2015; Astudillo et al. 2017), indicate that the deposition of synrift deposits in SVSB, occurring during ca. 218-200 Ma ('upper' Norian-Rhaetian). On the other hand, detrital zircon ages show a main peak spanning ~283-297 Ma, indicating a predominant source from the Gondwanan orogeny, matching the 'lower Choiyoi' magmatic event (ca. 280 Ma, Kleiman and Japas, 2009), with minor Triassic peaks at 250 Ma, 245 Ma and 225 Ma. A subordinate Ordovician peak at ca. 478 Ma is recorded to the southern of the basin, indicating minor contribution from the Famatinian arc while scarce zircons older than 500 Ma are observed. Besides, MDA is very similar to the depositional age and systematically younger upward, indicating the record of active volcanism through the successions, which is in agreement with field observations.

To the south, in the SESB, a first stage of deposition comprises the most voluminous successions across the Domeyko Basin (>2000 m), formed by coarse sedimentary, and volcanic dacitic, rhyolitic and basaltic rocks (Cornejo et al., 2009). Acidic dome complexes were plumbed out by NNE-SSW trending extensional faults. One of these rhyolitic domes yielded an age of 226.7 ± 1.4 Ma, which is similar to the ca. 233 Ma age obtained by Cornejo et al. (2009) in an equivalent dome, indicating a profuse acidic volcanic activity during the Carnian. These domes intruded fine conglomerates corresponding to braided fluvial systems, which yielded a MDA of 241.5 ± 4.0 Ma. Hence, in the SESB, part of the lower member deposition occurred at least in the Middle Triassic (Ladinian). After that, thick successions of basaltic lava flows and associated meandering fluvial deposits filled the depocenter. Fluvial tuffaceous sandstones which underlie marine transgressive facies, yielded a MDA of 208.4±3.4 Ma, indicating a large time span between the deposition of the lower and the upper member (>25 Ma), though no unconformities have been observed within those members. Detrital zircon ages from the lower member indicate a main peak at ca. 295 Ma and a secondary group at ca. 265 Ma. On the other hand, age peaks from the upper member show a main group at ca. 260-268 Ma and a subordinate peak at ca. 278 Ma, while minor peaks of Ordovician (ca. 460-475 Ma) and Carboniferous ages are well defined in most of the samples. These patterns indicate a main source from the Gondwanan orogen, particularly the 'upper Choiyoi' event (ca. 265 Ma, Kleiman and Japas 2009) and a secondary source from the Famatinian arc. Moreover, the MDA appears to have a

significant difference respect to the depositional age (~15 Ma in the upper member) and no systematic younger upward of MDA is recorded.

The overall detrital zircon data of the synrift stage of Domeyko Basin show a predominance of sources from the Gondwanic local basement with a scarcity of zircons >500 Ma, interpreted as the direct erosion and deposition from the margins of fault-bounded closed basins. On the other hand, in the tectonic setting discriminator plot proposed by Cawood et al. (2012) based in the cumulative plot difference between the crystallization and the depositional ages of the detrital zircons, all the samples fall in the convergent setting, suggesting a subduction related origin which is in agreement with the geochemical data of the volcanic products.

Finally, as we have shown, the first order segmentation of SVSB and SESB controlled the timing of basin aperture, the amount of extension, the volcanic and sedimentary facies assemblages and the sedimentary sources of these depocenters. Furthermore, the SESB recorded the thickest infill of the Domeyko Basin, including a huge deposition of mafic magmas, interpreted here as the zone where the lithospheric stretching was greater, allowing the free ascent of primitive magmas. Moreover, during the Jurassic and Early Cretaceous the SESB reached the thickest infill of the Domeyko Basin (Prinz et al. 1994), indicating that the locus of the Triassic extension conditioned the later evolution of the Domeyko Basin. Furthermore, a segmentation in the plutonic basement and an abrupt change in the structural style of the Late Cretaceous to Neogene deformation of the Domeyko Range coincides with the position of the structural paleo-high strongly suggesting that the first order segmentation acquired during the synrift stage has prevailed during most of the geologic history of the region.

References

Astudillo, N., Ferrando, R., Montecino, D., Espinoza, F.; Matthews, S.; Cornejo, P. y Arévalo, C. in prep. Carta Augusta Victoria, Región de Antofagasta. Servicio Nacional de Geología y Minería, Carta Geológica de Chile, Serie Geología Básica XXX, 1 mapa escala 1:100.000. Santiago.

Cornejo, P., Mpodozis, M., Rivera, O. and Matthews, S. 2009. Carta Exploradora, Regiones de Antofagasta y Atacama. Servicio Nacional de Geología y Minería, Carta Geológica de Chile, Serie Geología Básica 119: 103 p., 1 mapa escala 1:100.000.

Cawood, P., Hawkesworth, C. J., Dhuime, B. 2012. Detrital zircon record and tectonic setting: Geology, 40 (10): 875–878.

González, R., Cornejo, P., Espinoza, F., and Herrera, C., Matthews, S., Menzies, A., Riquelme, R., Wilke, H. 2015. Carta Sierra de Varas, Región de Antofagasta. Servicio Nacional de Geología y Minería, Carta Geológica de Chile, Serie Geología Básica 178: 114 p., 1 mapa escala 1:100.000.

Kleiman, L.E. and Japas, M.S. 2009. The Choiyoi volcanic province at 34°S–36°S (San Rafael, Mendoza, Argentina): Implications for the Late Palaeozoic evolution of the southwestern margin of Gondwana: Tectonophysics, 473 (3–4): 283–299.

Prinz, P., Wilke, H.-G. and von Hillebrandt, A. 1994. Sediment accumulation and subsidence history in the Mesozoic marginal basin of northern Chile, in Tectonics of the Southern Central Andes, Springer. 219–232.

Suárez, M. and Bell, C. 1992. Triassic rift-related sedimentary basins in northern Chile (24°-29°S): Journal of South American Earth Sciences, 6 (3):109–121.

The interplay between volcanic, tectonic and sedimentary processes in an ancient subduction-related rift basin: The early Domeyko Basin (Triassic, northern Chile)

Espinoza, M.; Oliveros, V.; Montecino, D.; González, R.; Vásquez, P.

The geodynamic setting along the SW Gondwana margin during its early breakup (Triassic) remains poorly understood. However, main models only slightly consider the geotectonic significance of coeval basins. The Domeyko Basin initiated as a rift basin during the Triassic being filled by sedimentary and volcanic deposits. Stratigraphic, sedimentological and geochronological analyses are presented in order to determine the tectonostratigraphic evolution of this basin (22º-26º S) and to propose a tectonic model suitable for other SW Gondwana-margin rift basins.

The Domeyko Basin recorded two synrift stages. The Synrift I (~240-225 Ma) initiated the Sierra Exploradora sub-basin (SESB) while the Synrift II (~217-200 Ma) reactivated this sub-basin and originated small depocenters grouped in the Sierra de Varas sub-basin (SVSB). During the rift evolution, the sedimentary systems developed were largely controlled by the interplay between tectonics and volcanism through changes in the accommodation/sediment supply ratio (A/S). High-volcaniclastic depocenters record a net dominance of the syn-eruptive period, lacking rift-climax sequences due to the decreasing of the A/S ratio by the high volcanic supply. On the other hand, low-volcaniclastic depocenters of the SVSB record a tripartite succession (alluvial-lacustrine-fluvial) indicating the development of a complete rift cycle with a fault-linkage phase during the Synrift II stage. An early post-rift phase took place during the latest Rhaetian with the ubiquitous development of shallow marine facies marked by typical reefal deposits over the former foot- and hanging- walls of the basin.

The inferred architecture of the Domeyko Basin suggests a transtensional kinematic (sinistral) where N-S master faults interacted with ~NW-SE basement structures producing narrow and highly asymmetric releasing bends. Detrital zircon data show a predominance of sediments from the Gondwanic basement with a scarcity of zircons >500 Ma, indicating erosion from the margins of fault-bounded closed basins. All detrital zircon samples fall in the convergent regime for tectonic discriminator plots. We propose that the early Domeyko Basin was a continental subduction-related rift basin likely developed under an oblique convergence in a back-arc setting. Subduction would have acted as a primary driving mechanism for the extension along the Gondwanan margin, unlike inland rift basins (Ischigualasto, Cuyo and Neuquén basins).

Revealing the Early Mesozoic tectonic inheritance of the western Central Andes (Domeyko Range, northern Chile): A structural, geochronological and ^{39}Ar-^{40}Ar thermochronological approach.

Espinoza, M.; Oliveros, V.; Giambiagi, L.; Bechis, F.; Vásquez, P.; Morgan, L.

The Domeyko Range defines the western edge of the Central Andes and hosts some of the gigantic porphyry Cu-Mo deposits in the world. This range is a complexly deformed belt formed by a core of Late Paleozoic rocks uplifted over a Mesozoic stratified cover. The building of this range seems to have been strongly controlled by the inversion of the former Mesozoic basin (Domeyko Basin). However, major questions rely on the primary structure of this basin and its control over the later deformation. This study aims to unravel the tectonic evolution of the Triassic rifting and relate it with the later building of the Domeyko Range (northern Chile 22º - 26º S).

U-Pb data show that the Domeyko Basin was formed during two synrift stages. The Synrift I (~240-225 Ma) initiated the Sierra Exploradora sub-basin (SESB), while the Synrift II (~217-200 Ma) originated the Sierra de Varas sub-basin (SVSB). During the Synrift II, rift-climax sequences were developed at the SVSB evidencing a fault-linkage process which created a major N-S fault array in the present position of the Domeyko Fault System (Eocene-Oligocene). Structural mapping and kinematic analyses indicate a transtensional rifting kinematic with a main ~NE-SW stretching direction, where major N-S faults interacted with NW-SE basement structures producing deep releasing bends.

On the other hand, at the SVSB, U-Pb detrital zircon ages (DZ) show the main peak at ca. 290 Ma and much younger ^{40}Ar-^{39}Ar detrital muscovites ages (DM), suggesting the begin of the sources exhumation at ~245 Ma. On the contrary, along the SESB, the main exhumation of sources took place at ~265 Ma (DM ages), only slightly after its crystallization (DZ peak at ~270 Ma). The latter reveals a different history of sources exhumation between both sub-basins, pointing to a segmentation of the basement structure prior to ~265 Ma. Moreover, main spatial variations in the structural style along the range axis correlate with the sub-basins edges (vergence direction, thick- versus thin- skin and shortening ratios), with thick-skinned belts occurring at the site of former synrift border faults.

We propose that the rifting architecture strongly determined the main structural style of the Domeyko Range and controlled the inception of the prolific Domeyko Fault System. The main structure which segmented the sub-basins would have been present at least since the Late Paleozoic (~265 Ma) and correlates with a major NW lineament of the present forearc.